38766.2-EL CF

QUANTUM CONFINEMENT V: NANOSTRUCTURES



Edited by

M. Cahay
D. J. Lockwood
J. P. Leburton
S. Bandyopadhyay

REPORT DOCUMENTATION PAGE

Form Approved
OMB NO. 0704-0188

Public reporting burden for this collection of information is estimated to average 1 hour per response, including the time for reviewing instructions, searching existing data sources, gathering and maintaining the data needed, and completing and reviewing the collection of information. Send comment regarding this burden estimates or any other aspect of this collection of information, including suggestions for reducing this burden, to Washington Headquarters Services, Directorate for information Operations and Reports, 1215 Jefferson Davis Highway, Suite 1204, Arlington, VA 22202-4302, and to the Office of Management and Budget, Paperwork Reduction Project (0704-0188), Washington, DC 20503.

1. AGENCY USE ONLY *(Leave blank)*	2. REPORT DATE	3. REPORT TYPE AND DATES COVERED
		Book

4. TITLE AND SUBTITLE

Quantum Confinement V: Nanostructures

5. FUNDING NUMBERS

DAAG55-98-1-0357

6. AUTHOR(S)

Marc Cahay, principal investigator

7. PERFORMING ORGANIZATION NAMES(S) AND ADDRESS(ES)

Electrochemical Society, Inc.
10 South Main St.
Pennington, NJ 08534-2896

8. PERFORMING ORGANIZATION REPORT NUMBER

9. SPONSORING / MONITORING AGENCY NAME(S) AND ADDRESS(ES)

U.S. Army Research Office
P.O. Box 12211
Research Triangle Park, NC 27709-2211

10. SPONSORING / MONITORING AGENCY REPORT NUMBER

ARO 38766.2-EL-CF

11. SUPPLEMENTARY NOTES

The views, opinions and/or findings contained in this report are those of the author(s) and should not be construed as an official Department of the Army position, policy or decision, unless so designated by other documentation.

12a. DISTRIBUTION / AVAILABILITY STATEMENT

Approved for public release; distribution unlimited.

12 b. DISTRIBUTION CODE

13. ABSTRACT *(Maximum 200 words)*

SEE PREFACE

14. SUBJECT TERMS

15. NUMBER IF PAGES

16. PRICE CODE

17. SECURITY CLASSIFICATION OR REPORT	18. SECURITY CLASSIFICATION OF THIS PAGE	19. SECURITY CLASSIFICATION OF ABSTRACT	20. LIMITATION OF ABSTRACT
UNCLASSIFIED	UNCLASSIFIED	UNCLASSIFIED	UL

PROCEEDINGS OF THE FIFTH INTERNATIONAL SYMPOSIUM ON

QUANTUM CONFINEMENT: NANOSTRUCTURES

Editors

M. Cahay
Dept. of Electrical and Computer Engineering
and Computer Science
University of Cincinnati
Cincinnati, Ohio

D. J. Lockwood
Institute for Microstructural Sciences
National Research Council
Ottawa, Canada

J. P. Leburton
Beckman Institute
Urbana, Illinois

S. Bandyopadhyay
Dept. of Electrical Engineering
University of Nebraska
Lincoln, Nebraska

19990706 127

DIELECTRIC SCIENCE AND TECHNOLOGY, ELECTRONICS, AND LUMINESCENCE AND DISPLAY MATERIALS DIVISIONS

Proceedings Volume 98-19



THE ELECTROCHEMICAL SOCIETY, INC.,
10 South Main St., Pennington, NJ 08534-2896, USA

DTIC QUALITY INSPECTED 4

Copyright 1999 by The Electrochemical Society, Inc.
All rights reserved.

This book has been registered with Copyright Clearance Center, Inc.
For further information, please contact the Copyright Clearance Center,
Salem, Massachusetts.

Published by:

The Electrochemical Society, Inc.
10 South Main Street
Pennington, New Jersey 08534-2896, USA

Telephone (609) 737-1902
Fax (609) 737-2743
e-mail: ecs@electrochem.org
Web site: http://www.electrochem.org

ISBN 1-56677-213-3

Printed in the United States of America

PREFACE

This book is a collection of the some of the papers presented at the Fifth International Symposium on Quantum Confinement: Nanostructures, held November 2-5 in Boston, USA, as part of the 194th Meeting of the Electrochemical Society. This symposium was a follow-up of previous meetings held in St Louis (Spring '92), San Francisco (Spring '94), Chicago (Fall '95), and Montreal (Spring '97). Forthcoming meetings will be held in Honolulu (Fall '99) and in Washington (Fall '01).

The symposium was sponsored by the Dielectric Science and Technology, the Electronics, and the Luminescence and Display Materials Divisions of the Electrochemical Society. There was a one day session organized jointly with the EXCON' 98 (Excitonic Processes in Condensed Matter) meeting.

The symposium was organized to address recent developments in the area of nanoscale semiconducting and metallic structures with emphasis on ultrasmall clusters and their potential for device applications. Papers were presented on silicon nanostructures, porous silicon, quantum dot structures, excitons in nanostructures, self-ordered nanostructures and clusters, quantum devices, architectures, and circuits.

This Proceedings Volume includes 55 of the 68 papers presented at the meeting. The symposium was organized into oral presentations that spanned four days including one day organized jointly with the EXCON' 98 (Excitonic Processes in Condensed Matter) meeting. Posters were also presented during an evening session. Invited papers are indicated by an asterisk in the Table of Contents.

The editors thank all the speakers and session chairpersons for their contributions to the success of the symposium. We also thank the Electrochemical Society staff for their constant support and for their help in preparing the volume for publication.

Finally, we would like to conclude by expressing our appreciation for the financial support provided by the U.S. Army Research Office and the Electrochemical Society.

M. Cahay
D. J. Lockwood
J. P. Leburton
S. Bandyopadhyay

TABLE OF CONTENTS

PREFACE iii

Silicon Nanostructures

A Review on Epitaxial Si/Oxygen Superlattice as: Si Light Emitter and Insulating Barrier 3
*R. Tsu**

Measurement of Photocarrier Lifetimes in Silicon Nanoclusters 17
A. Kenyon, S. Botti, P. F. Trwoga, and C. W. Pitt

Characterization of RTCVD Grown Si Films on SiO_2 for Nanotechnology Applications 27
J. Vizoso, F. Martin, X. Martinez, M. Garriga, and X. Aymerich

Effects of Thermal Processing on Photoluminescence of Si Nanocrystallites Prepared by Pulsed Laser Ablation 40
I. Umezu, K. Shibata, S. Yamaguchi, H. Sato, A. Sugimura, Y. Yamada, and T. Yoshida

Observation of an Electron Charging Effect in Si Nanocrystals Embedded in an Ultrathin Gate Oxide 49
T. Maeda, E. Suzuki, I. Sakata, M. Yamanaka, and K. Ishii

Formation and Characterization of Erbium Doped Silicon Nanocrystals .. 61
J. St. John, J. L. Coffer, Y. Chen, and R. F. Pinizzotto

Structural and Electrical Characterization of Nanocrystalline Silicon Superlattices 76
L.Tsybeskov, G. F. Grom, P. M. Fauchet, J. P. McCaffrey, J.-M. Baribeau, H. J. Labbe, G. I. Sproule, and D. J. Lockwood*

Ordering and Crystallization in Ultra Thin Si/SiO_2 Superlattices 94
M. Zacharias, J. Blaäsing, P. Veit, L. Tsybeskov, K. D. Hirschman, and P. M. Fauchet

Optical Properties of Silicon Nanocrystals Formed by Ion Implantation .. 106
M. H. Wu, A. Ueda, R. Mu, D. O. Henderson, R. Zuhr, A. Meldrum, and C. W. White

Nonlinear Optical Phenomena in the Luminescence from Si Nanocrystals 118
D. Kovalev, H. Heckler, B. Averboukh, M. Ben-Chorin, and F. Koch

Magnetospectroscopy of Si Nanocrystals 128
H. Heckler, D. Kovalev, G. Polisski, N. N. Zinov'ev, and F. Koch

Porous Silicon

Light Emitting Micropatterns of Porous Semiconductors Created at Surface Defects 141
D.J. Lockwood, P. Schmuki, and L. E. Erickson
Quenching of Red Photoluminescence of Porous Silicon with Adsorption of Alcohols 151
M. Shimura, K. Kiyama, and T. Okumura
Quantum Size Controlled Percolation Effects on Electron Transport in Nanoparticle Thin Films 163
J. Jacbos, B. Hamilton, D. Teehan, and L. T. Canham

Excitons in Nanostructures

Optical Properties of Semiconductor Nanocrystals Embedded in Dielectric Media 177
Al.L.Efros and M. Rosen*
Excitonic Optical Nonlinearity and Exciton Dephasing in Quantum Dots 192
*T.Takagahara**
Optical Properties of Charged InAs Quantum Dots 213
K.Schmidt , J. Garcia, G. Medeiros-Ribeiro, U. Kunze, and P. M. Petroff*
Internal Transitions of Neutral and Charged Magneto-excitons in GaAs Nanostructures by Optically Detected Resonance Spectroscopy 227
B.D.McCombe, H. A. Nickel, G. Kioseoglou, G. S. Herold, T. Yeo, H. D. Cheong, A. Petrou, A. D. Dzyubenko, A. Yu. Sivachenko, and D. Broido*
Optical Properties of Excitons in Semiconductor Quantum Wires 241
V. Dneprovskii, E. Zhukov, E. Mulyarov, S. Tikhodeev, and Y. Masumoto

Quantum Dot Structures

How to Describe the Electronic Structure of Semiconductor Quantum Dots 259
*A.Zunger**
Spectroscopy of a Few Electron Lateral Dot 270
C. Gould, A.Sachrajda , P. Hawrylak, P. Zawadzki, Y. Feng, and Z. Wasilewski*
Stark Spectroscopy Investigation of Spectral Diffusion In Single CdSe Quantum Dots 280
K. Shimizu, S. A. Empedocles, R. Neuhauser, and M. G. Bawendi
Carrier Relaxation in InGaAs/GaAs Quantum Dots with Tunable Intersublevel Transitions 286
N. Perret, D. Morris, and R. Leon
Engineering of the Ferro-Magnetic and Ferro-Electric Properties of Strained Quantum Dots 297
J.B. Khurgin and F. Jin
Optical properties of ZnSe/Cdse-based QD structures 312
A. D. Andreev, R. P. Seisyan, R. M. Datsiev, and S. V. Ivanov
Effects of Carrier Relaxation and Emission on Photoluminescence of InAs Quantum Dots 318
H. Zhu, Z. M. Wang, B. Q. Sun, S. L. Feng, D. S . Jiang, and H. Z. Zheng
Dynamical And Spectral Peculiarities Of Quantum Dot Lasers Under Different Operation Conditions 320
D. Bhattacharyya, E. A. Avrutin, A. C. Bryce, J. M. Gray, J. H. Marsh, D. Bimberg, F. Heinrichsdorff, V. M. Ustinov, S. V. Zaitsev, N. N. Ledentsov, Z. I. Alferov, A. I. Onishchenko, and E. P. O' Reilly

Self-Ordered Nanostructures

Size-controllable Nanostructure Array Fabrication with Self-Assembly ... 335
C. Haginoya, M. Ishibashi, and K. Koike
Carrier Dynamics in Stacked Self-Assembled InAs/GaAs Quantum Dots . 348
D. Morris and S. Fafard
Intraband Excited States and Relaxation Time in InAs/GaAs Self-Assembled Quantum Dots 357
S. Sauvage, P. Boucaud, F. Glotin, R. Prazeres, J.-M. Ortega, A. Lemaître, J.-M. Gérard, and V. Thierry-Mieg
Electronic Bistability in An Electrochemically Self-Assembled Array of Semiconductor Quantum Dots 371
S. Bandyopadhyay, N. Kouklin, L. Menon, L. Balandin, D. Zaretsky, A. Varfolomeev, and S. Tereshin

Clusters and Other Nanostructures

Magneto-optical properties of II-VI semiconductor nanoparticles, either embedded in glass matrix or covered by epitaxial capping 381
E. Lifshitz, H.-E. Porteanu, I. D. Litvin, and A. Glozman,

Photoluminescence of Nanocrystalline ZnO Particles 392
A. van Dijken, E. A. Meulenkamp, D. Vanmaekelbergh, and A. Meijerink

Photo-induced Nano-Patterns on the Surface of C_{60} Single Crystals 402
L. Jiang, Y. Kim, T. Iyoda, J. Lin, K. Kitazawa, A. Fujishima, and K. Hashimoto

Photoresponse of Spray-Pyrolytically Synthesized Nanocrystalline n-Fe_2O_3 Thin Film Electrodes Towards The Water-Splitting Reaction 410
S.U.M. Khan and J. Akikusa

Modification of One Phonon Emission Rates Due to Finite Size Effects in $Y_2O_3Eu^{3+}$ Nanocrystals 430
H.-S. Yang, R. S. Meltzer, W. M. Dennis, S. P. Feofilov, and B. M. Tissue

Optical Properties of Au Nanocrystals Confined in Porous Vycor Glass .. 439
R. Mu, A. Ueda, M. H. Wu, D. O. Henderson, K. Malone, G. Mills, and A. Meldrum

Copper Doped CdSe Nanocrystalline Thin Films 454
N. Chandrasekharan, S. Gorer, and G. Hodes

Calculation of Structure and Properties of Semiconductor Clusters: Influence of Extended Defects 464
K. Masuda-Jindo, M. Menon, K. R. Subbaswamy, and M. Aoki

Computer Simulation Study of The Properties of Strained Layer Superlattices by TBMD and PPM 475
K. Masuda-Jindo and R. Kikuchi

Interface Light Absorption in Nanostructures 489
L. Braginsky and V. Shklover

Quantum Devices, Architectures, and Circuits

Role of Small Dimensions and Quantum Confinement in Small Silicon Memories 507
S.Tiwari, F. Rana, A. Kumar, J.J. Welser, and C.T. Balck*

Electron Waveguide Pumped Quantum Wire Far IR Laser 529
E. Forsberg, J.-O. Wesström, L. Thylen, and T. Palm

3D Computer Modeling of Silicon Quantum-Dot Floating Gate Flash Memory Device 542
A. Thean and J.-P. Leburton

Simulation of Nanoscale Silicon Conduction Channels 551
A. Trellakis and U. Ravaioli

Magneto-capacitance of Multiprobe Mesoscopic Systems 563
P. Pomorski

Adaptive Control of Single-Electron Circuit Signatures for Computation . 574
R. Rendell

Fault Rates in Nanochips 582
S. Spagocci and T. Fountain

Influence of the Spin-Orbit Split-Off Band on the Tunneling Properties of Holes Across InAlAs/InGaAs and InP/InGaAs Interfaces 597
S. Ekbote, M. Cahay, and K. Roenker

Johnson Noise in Quantum Wires: Temperature Dependence and the Effect of High Electric Fields 618
A. Svizhenko, S. Bandyopadhyay, and M. Stroscio

Visible Light Emitting Device with Schottky Contact on Ultra-thin Amorphous Silicon Layer Containing Silicon Nanocrystals 629
S. Fujita and N. Sugiyama

Quantum Transport Through an Atomic Cluster 640
J. Taylor, H. Guo, anf J. Wang

Nonlinear Resonant Tunnelling Through a Double Degenerate Local State and Strong Electron-Phonon Interaction 650
V. N. Ermakov

The Domains of Current in the Resonant Tunneling Diodes 663
M. Feiginov and V. A. Volkov

Radioactivity - Induced Degradation of Si PIN Photodetectors 670
E. A. Anagnostakis

* Invited Speaker

AUTHOR INDEX 681

SUBJECT INDEX 687

FACTS ABOUT THE ELECTROCHEMICAL SOCIETY, INC.

The Electrochemical Society, Inc., is an international, nonprofit, scientific, educational organization founded for the advancement of the theory and practice of electrochemistry, electrothermics, electronics, and allied subjects. The Society was founded in Philadelphia in 1902 and incorporated in 1930. There are currently over 7,000 scientists and engineers from more than 70 countries who hold individual membership; the Society is also supported by more than 100 corporations through Contributing Memberships.

The Technical activities of the Society are carried on by Divisions and Groups. Local Sections of the Society have been organized in a number of cities and regions. Major international meetings of the Society are held in the Spring and Fall of each year. At these meetings, the Divisions and Groups hold general sessions and sponsor symposia on specialized subjects.

The Society has an active publications program which includes the following:

Journal of The Electrochemical Society - The *Journal* is a monthly publication containing technical papers covering basic research and technology of interest in the areas of concern to the Society. Papers submitted for publication are subjected to careful evaluation and review by authorities in the field before acceptance, and high standards are maintained for the technical content of the *Journal.*

Electrochemical and Solid-State Letters - *Letters* is the Society's rapid-publication, electronic journal. Papers are published as available at http://www3.electrochem.org/letters.html. This peer-reviewed journal covers the leading edge in research and development in all fields of interest to ECS. It is a joint publication of the ECS and the IEEE Electron Devices Society.

Interface - *Interface* is a quarterly publication containing news, reviews, advertisements, and articles on technical matters of interest to Society Members in a lively, casual format. Also featured in each issue are special pages dedicated to serving the interests of the Society and allowing better communication among Divisions, Groups, and Local Sections.

Meeting Abstracts *(formerly Extended Abstracts)* - Meeting Abstracts of the technical papers presented at the Spring and Fall Meetings of the Society are published in serialized softbound volumes.

Proceedings Series - Papers presented in symposia at Society and Topical Meetings are published as serialized Proceedings Volumes. These provide up-to-date views of specialized topics and frequently offer comprehensive treatment of rapidly developing areas.

Monograph Volumes - The Society sponsors the publication of hardbound Monograph Volumes, which provide authoritative accounts of specific topics in electrochemistry, solid-state science, and related disciplines.

For more information on these and other Society activities, visit the ECS Web site:

http://www.electrochem.org

Silicon Nanostructures

A Review on Epitaxial Si / Oxygen Superlattice as: Si Light Emitter and Insulating Barrier

R. Tsu
Department of Electrical and Computer Engineering
University of North Carolina at Charlotte
Charlotte, NC 28223 USA

ABSTRACT

A coherent review of the work in the past several years on epitaxially formed Si/O-superlattice is presented. The Si growth beyond the adsorbed monolayer of oxygen is epitaxial having fairly low defect density consisting of stacking faults and dislocations. At present, such a structure shows electroluminescence and insulating behavior, useful for optoelectronic and SOI applications. Since this type of superlattice consisting of monolayers of adsorbed atoms or molecules sandwiched between thin epitaxially grown silicon (1-2nm), results in very thin barriers, some materials on the fundamental aspects of quantum wells and superlattices, though already in the literatures, are presented here for a better exposition of what one can expect from this type of semiconductor-atomic-superlattices.

INTRODUCTION

Without a suitable heterojunction barrier, silicon has not made a significant contribution to quantum devices. Silicon dioxide with a barrier height of 3.2 eV in the conduction band of silicon is amorphous, preventing the building of a quantum well structure on top of the a-SiO_2 barrier. Several years ago, it was proposed that the oxides of one or two monolayers might allow the continuation of epitaxy. [1] After several failures in attempting to realize the SLB (Superlattice Barrier) with thin silicon layers separated by thin oxides, a new method, involving the exposure to molecular oxygen followed by epitaxial growth of silicon using the in-situ RHEED (reflection high energy electron diffraction) for monitoring epitaxy, was introduced. The arriving silicon beam has sufficient energy to convert the adsorbed molecular oxygen to bonded Si-O. [2] Silicon growth beyond a barrier structure consisting of 1 or 2nm of silicon sandwiched between adjacent layers of adsorbed oxygen up to 100 Langmuir of exposure for each layer is epitaxial and almost free of stacking faults as

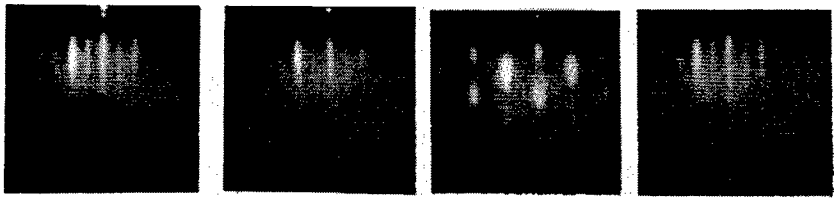
determined in high resolution X-TEM. [3] The effective barrier height measured is almost 0.5eV.[4] It is presented in the section that follows that the best theoretically estimated barrier height between silicon and mono-oxide is 1.5eV. The difficulties involved in the determination of extremely thin barrier leads to lower values. This barrier structure may be repeated for achieving desired carrier insulation. Therefore we now have a method to build an epitaxial SOI. Forming a superlattice by many repeats of the basic period, Si/O, results in a structure that exhibits visible photo-luminescence and electro-luminescence.[5,6] It is worth pointing out that our electro-luminescent diode has been life-tested for eight months of continuous operation without any degradation. Thus the SAS is ready for playing an important role in optoelectronics with silicon.

This type of superlattice, semiconductor-atomic-superlattice, (SAS), has extremely thin barriers. The unavoidable defects such as strains, dangling bonds, etc. at the interfaces, may degrade the degree of quantum confinement, particularly obvious when amorphous silicon or a-Si:H followed by crystallization is involved [7,8]. These concerns have been treated by using the quantum mechanical Langevin's equation, [9,10] and by introducing a relaxation time. [11,12] Results of these studies, Refs.9-12, indicates that quantum confinement effects may be easier to manifest than the usual rule that the mean free path must be greater than the well width, or $k\ell \geq n\pi$. Some phase of these published works is repeated here to bring out the principles involved, with an emphasis on clarity and physical meanings, rather than mathematical details.

The method has been extended to replacing the exposure to molecular oxygen by exposure to carbon mono-oxide. In this case, perhaps the name SAS should be replaced by SMS, semiconductor-molecular-superlattices. Results are just as exciting. Hopefully many other systems should be possible. The fact is that it is rather difficult to wipe out effects of epitaxy short of amorphizing by ion bombardment.[13]

EPITAXY ON Si (100) WITH ADSORBED OXYGEN

Silicon depositions are performed in a MBE system generally at relatively low substrate temperature of 550-600°C. The exposure to molecular oxygen is at a lower temperature of <200°C. Figure 1 shows the in-situ RHEED: (a), buffer (25nm), showing the 1x1 and 1x2 reconstructions; (b), after exposure to 10L (One Langmuir is an exposure of 100 seconds at 10^{-8} Torr) of molecular oxygen; (c), after 1.1nm of silicon deposition at 0.03nm / 550 °C, showing 2D pattern changing to 3D pattern and the disappearance of the 1x2. The pattern of (a) is restored after more than 5nm of Si MBE shown in (d). The transformation from 2D to 3D pattern is mainly due to surface roughness.



(a). (b) (c) (d)

Fig.1 In-situ RHEED of Si (100)

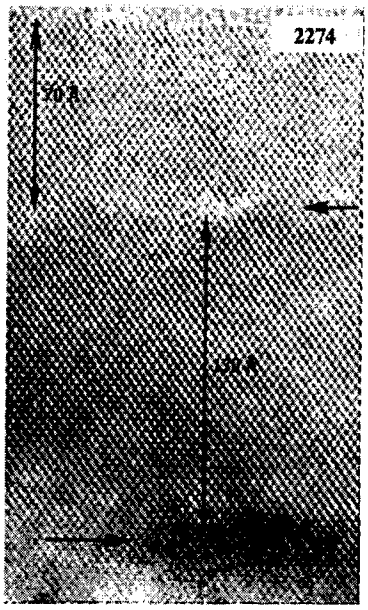


Fig.2 High resolution X-TEM (Middle arrow shows O/Si/O cluster)

Figure 2, a high resolution X-TEM shows the buffer (25nm) and 2 repeats of adsorbed oxygen (10L each). Note that oxygen forms a cluster (middle vertical arrow) of size generally in the neighborhood of 2.5x10 nm. The lattice image does not show the details of the disordered oxygen. Low resolution X-TEM shows almost void of stacking faults. Distler *et al.*[13] reported the oriented nucleation of gold on NaCl precoated with amorphous carbon layers below a critical thickness, and concluded that a sufficiently thin amorphous intermediate layer between substrate and deposit failed to inhibit epitaxy. Electrical measurements show that up to 0.5 eV of barrier height [5] is possible with several repeats of the double-barrier structure [14], Si-O/Si/O-Si.

The process has been repeated up to nine periods forming the SAS, between the n-doped substrate and a Schottky front contact. This structure allows hot electrons injected through the Schottky junction resulting in e-h pair generation for radiative recombination to take place in the superlattice structure.[15,16] Figure 3 shows the hot electron injection through the front Schottky into the SMS while avalanching in the deep depletion of the substrate results in e-h pairs for radiative recombination .

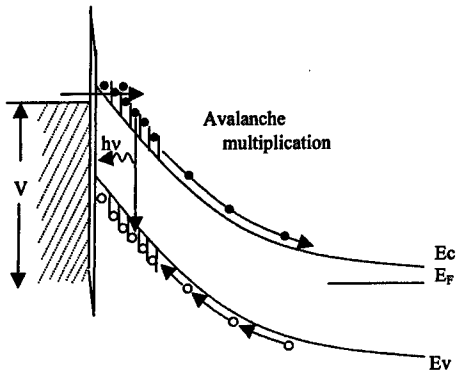


Fig. 3 Band profile of the Si/O superlattice EL device under reverse bias. Electrons undergo avalanche multiplication providing holes for recombination with light emission

The observed PL (photoluminescence) peaks at 2.2eV while the EL (electro-luminescence) spectrum extends beyond the cutoff of the PL spectrum dictated by the 457.9nm Ar laser line. The diode device has been in continuous operation for more than eight months without signs of degradation with efficiency better than porous silicon. It is frequently suggested that the visible light from nanoscale structures comes mostly from the interface regions. Although it has been shown quite convincingly that in the case of silicon superlattices [7], quantum confinement plays an important role. Actually, as the structure is reduced to the point that an appreciable fraction of the atoms are at the interface, the important question is whether control can be maintained and fabrication can be reproducible. The SAS is really quite different from the conventional superlattices or even the strain-layer superlattice. Here, the quantum states are determined by the effective barrier depending on the atomic orbitals of the oxygen-silicon atoms, rather than the usual quantum confinement effected by the band-edge offset. The use of surface adsorption to limit the oxygen atoms to, at most one monolayer seems to be the main ingredient of the continuation of epitaxy, although the precise mechanism is yet to be established.

BARRIER HEIGHT OF Si-O-Si SAS

The conventional superlattices [16] and quantum wells [14] utilize the band-edge offset of two semiconductors heterojunctions, such as GaAs / GaAlAs. The class of available materials is further widened after the introduction of the strain-layered superlattices.[17] Si/SiO_2 does not form an epitaxial junction because the oxide is amorphous. Figure 4 shows the atomic energy states of silicon and oxygen.[18] Note that the separation between the unoccupied states to the occupied ground state is about 9eV, not too different from the SiO_2 band structure.[19,20] Since we know that the conduction band-edge offset between Si and SiO_2 is 3 eV, the half way point is 1.5 eV because only half of the electron transfer is necessary for silicon mono-oxide. This is the basis of assigning 1.5eV for the barrier height of Si and Si-O system. Thus far we have not experimentally shown that the SAS indeed consists of Si-O rather than SiO_2. Further experiment is necessary, using the electron loss measurement for example, to determine whether Si-O is indeed involved in the SAS. However, the measured barrier height is 0.5eV. As we know that it is very difficult to measure extremely thin barrier heights, it is possible that the true barrier height is 1.5 eV or the lower value is correct which represents SiO_x with $x < 1$. As mentioned earlier, preliminary experiments indicated that we have also succeeded [21] in substituting CO for O in the SAS (Semiconductor-Atomic-Superlattice).

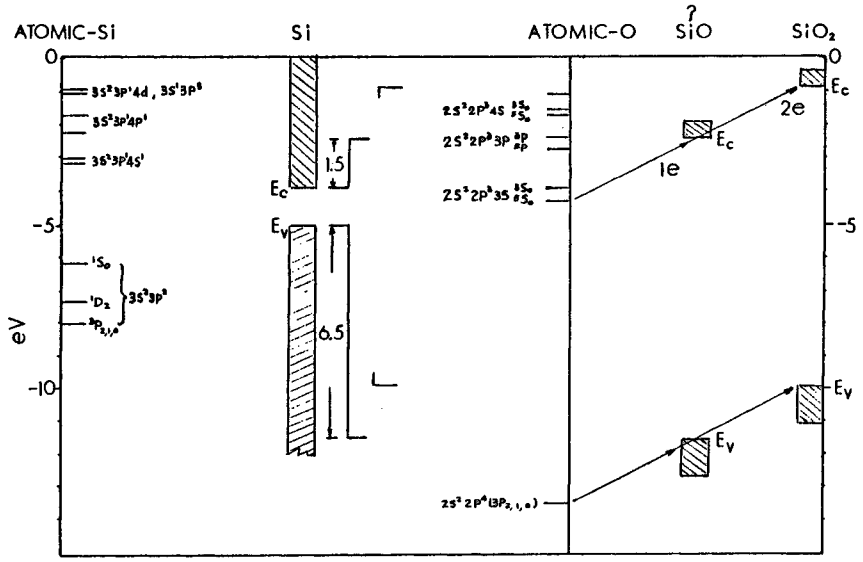


Fig. 4 Atomic energy states for Si and O. The high electro-negativity of O takes electrons away from Si resulting in moving up the O states with respect to Si

ISSUES IMPORTANT TO QUANTUM CONFINEMENT

It is well known that quantum confinement is involved whenever the observed spectra of luminescence is shifted up. However, apart from quantum confinement, damping, inelastic scattering leading to a finite mean-free-path or finite mean-free-time can also push up the states. What is important is to be able to compare the line broadening with the level shift. Although these issues were presented in Ref's 9-12, the present discussion is to focus more on the physical principle rather than mathematical

results. We introduce the quantum analog of the Langevin equation [22] for finite mean- free-path, and a relaxation time for mean-free-time into the Schroedinger equation. In any damped system, the Green function G can be obtained and the Im G gives the spectral density. Results give resonant states with or without damping. At first sight, damping removes the electron density, which might be viewed as a violation of quantum mechanics. However, we are dealing with an open system where electrons are removed from a given state into other states in which we have no intention of keeping track. In other words, as far as we are concerned, once removed from a given state, they are lost to the universe, an open system. This is quite similar to the classical treatment by Breit and Wigner [23] on the capture of slow neutrons where the quasi-stationary bound states are coupled to the incident particle of a continuum. In essence, eigenstates are unique but quasi-stationary states are not, rather, they depend on initial conditions.

The Green function for a 1D wave equation having a velocity dependent damping term characterized by the operator $H_1 = 2q\frac{d}{dx}$, with $q = (2\ell)^{-1}$ is [9,10,11]

$$G_{\pm}(k) = \frac{1}{(k_o^2 - k^2) \pm i2kq}, \tag{1}$$

in which (+) sign for x>0 and (-) sign for x<0, and $k_o^2 \equiv 2mE/\hbar^2$, q, spatial damping constant and k, the wave vector. The spectral density Im $G_+(k)$ has a maximum at

$$k^2 = k_o^2 - q^2(1 - q^2/k_o^2), \tag{2}$$

and the poles of $G_{\pm}(k)$ are located at $k = \pm(k_o^2 - q^2)^{1/2} \pm iq$.

Thus, the presence of damping up-shifts the peak of the spectral density. Incidentally in an RLC circuit, the peak position is independent of damping, R in this case, because wavelength is not involved. To understand the physical meaning of the up-shift, we need to go back to the fundamentals. In a quantum well, the eigenstates are shifted down due to tunneling out of the confining barriers because the effective deBroglie wavelength is longer with tunneling. On the other hand, finite mean free path lowers the effective deBroglie wavelength resulting in the up-shift. There is an important point

to be stressed, i.e. phase coherence is not entirely destroyed after the particle traverses a mean-free-path, rather there is still 1/e of the coherence left.

The finite mean free path leads to a different boundary condition. Starting with the current operator

$J = \frac{\hbar}{i2m}(\psi^*\psi' - \psi\psi^{*'})$, using Schroedinger equation, there results the continuity equation

$$\frac{dJ}{dx} + 2qJ = 0, \tag{5}$$

which has the solution

$$\frac{1}{m_1}\frac{d\psi_1}{dx}\exp(2q_1x) = \frac{1}{m_2}\frac{d\psi_2}{dx}\exp(2q_2x). \tag{4}$$

For $q_1 = q_2 = 0$, Eq.(6) gives the usual condition applicable for the boundary condition at a hetero-junction.

We can also introduced a relaxation time with $H_1 = -i\hbar/\tau$. There are two possible solutions. The first has complex energy and real momentum, which applies to time damping such as cyclotron resonance and atomic transitions. The second has complex momentum and real energy, which is discussed here. With $k = k_r + k_i$,

$k_r^2 = k_o^2 + k_i^2$, and $k_i = Q^2/2k_r$, where $Q^2 = 2m/\hbar\tau$. (5)

The density of state

$n(E) = k_r / k_o^2$, has a maximum at $k_o^2 = 0.75\,Q^2$, or $k_r \ell \geq 1$, (6)

which is same as $\ell \geq W/n\pi$, where W is the width of the quantum well, and $k_i = (2\ell)^{-1}$. **Comparison between direct computation with the Schroedinger equation with an added damping term with materials presented here gives a condition for quantum effects, $k_c \ell \geq 0.3$, where k_c demarcates the local and non-local states. This last condition is far less stringent than the general rule of $\ell \geq W$.**

The real part of k and n(E) for the mean-free-path case is plotted in Fig. 5 for q = 1 and 0. Note that the peak in n(E) is up-shifted. The propagation, or non-local case is for E lying above the maximum of n(E), while localized states lie below the maximum as shown.

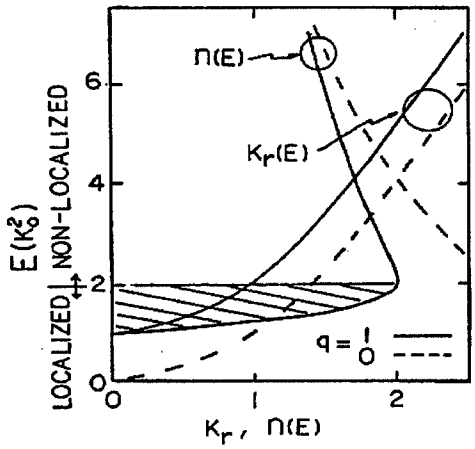


Fig. 5 k_r and n(E) versus energy for damping with mean free path

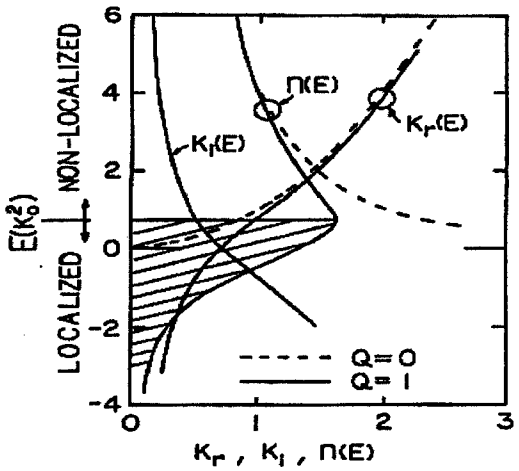


Fig. 6 k_r, k_i, and n(E) versus energy for damping in time

The maxumum DOS for 1D with q = 0 is at E = 0. With damping, the maximum is shifted up. Figure 6 shows the real and imaginary parts of k and n(E) for time damping. Note that damping actually results in states in the gap shown as shaded in the figure, having an exponential-like tail below the "mobility gap" defined by the maximum in n(E). In 3D, the Green function is e^{ikr} / r giving $n(E) \propto k_r$, which describes disordered solids quite well. The consequence of damping is to broaden the quasi-states, or the resonant states, and shifts up the states in energy. Since localized states are already confined, confinement in a quantum well serves to move up the extended states with respect to the localized states, resulting in a decrease in trapping.[12] It is well known that quantum confinement shifts up the energy states, and damping broadens these states, however, it is not generally known that damping results in further upshift!

We close this section with an example this author worked out many years ago, [25] for a double barrier structure with barrier height 0.4eV, $m^* = 0.07m$, well width of 8nm. The quality factor $Q \equiv E / \Delta E$, with ΔE being the linewidth, and the shift in energy δE, are calculated for the mean free path ℓ in nm.

ℓ (nm)	E(eV)	Q	ΔE	δE
∞	0.0712	∞	0	0
50	0.07125	13.24	0.005	0.00003
20	0.07162	5.32	0.014	0.00043
5	0.07221	1.39	0.06	0.0068
3	0.08961	0.88	0.10	0.02

In calculating the above, $Q = k_r \ell$, $\Delta E \approx 2E_o / Q$, and $\delta E \approx E_o / 4Q^2$, have been used. Note that as Q decreases with larger and larger damping (shorter and shorter mean free path), eventually the shift can even exceed the linewidth. For good materials, which apply to most epitaxially grown semiconductors, the energy shift can be neglected comparing with the line broadening. However, for bad materials

such as amorphous semiconductors, the shift can exceed the line broadening. Thus, with superlattices and quantum wells having extremely thin wells, interface states may degrade the mobility to the point that the energy up-shift can be larger than the line broadening. In our context, such as the luminescence from extremely thin wells, 1-2nm well width, the luminescence spectra can not only be broad, but also can further shift up in energy!

PHOTO-LUMINESCENCE AND ELECTRO-LUMINESCENCE OF Si/O SUPERLATTICE

The fabrication procedure for the Si/O epitaxy superlattice is used to form a diode consisting of nine periods of Si/O with thin silicon layers of 1.1nm separated by adsorbed oxygen. The front aluminum contact forms a Schottky barrier to serve as hot electron injection as shown in Fig.3. The hot electrons tunnel out of the superlattice into the substrate result in avalanche multiplication of e-h pairs. The trapped holes into the valence band of the Si/O structures provide radiative recombination.[6,15,25] It should be noted that the EL is produced with reverse bias, because avalanche in the deep depletion is needed. Couple of typical spectra are shown in Fig.7. Note that the cut-off in PL is due to the 457.9nm Ar laser line used. The visible PL appears red to the eye , but the EL appears yellow to the eye due to the presence of sufficient blue component in the spectra. The diode has been under life-test for more than eight months without signs of degradation. Figure 8 shows a plot of the life-test. Since the light intensity is proportional to the current, the stability of the current gives a measure for the stability of the light output.

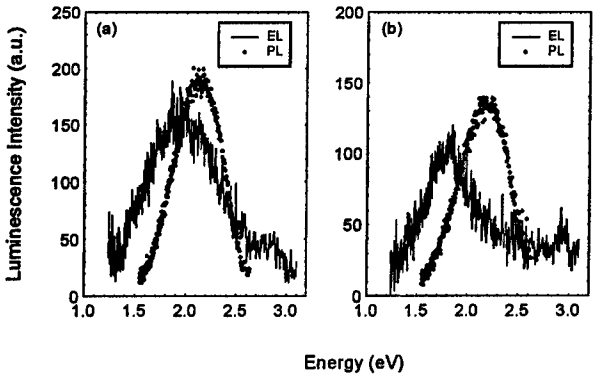


Fig. 7 The EL and PL spectra measured at room temperature of (a) sample 1 at reverse bias V=14 V, and (b) sample 2 at reverse bias V=20 V. The applied voltage includes the voltage drop over the substrate. The EL extends beyond the 457.9nm Ar laser line, used for the excitation of PL

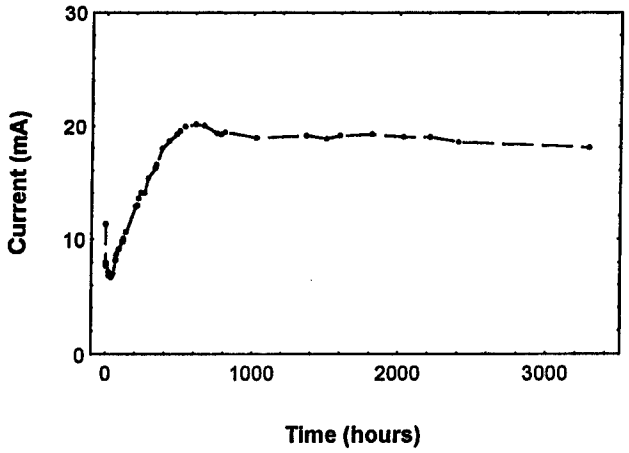


Fig. 8 Current versus time under reverse bias of 10.4V of sample 1

CONCLUSION

This development, the successful construction of a semiconductor-atomic-superlattice may have opened the door to the fabrication of a wide variety of electronic and optoelectronic structures. In particular, the present structure, consisting of silicon and bonded oxygen most probably in the form of SiO rather than SiO_2, is the key to allowing the continuation of epitaxial growth. Possible applications such as silicon-on-insulator (SOI), and even silicon based quantum devices cannot be ruled out. The realization that finite mean free path or finite mean free time, even at the point of $k\ell < 1$ can exhibit quantum confinement is good news for optoelectronic device fields.

ACKNOWLEDGMENTS

The author would like to express his gratitude for the support of this work by ONR, particularly by ARO, and by NanoDynamics, Inc. The contributions by C. Lofgren, A. Filios, and Q. Zhang are gratefully acknowledged.

REFERENCES

1. R.Tsu, *Nature,* **364**, 19 (1993).

2. R. Tsu, D. Martin, J. Hernandez, and S.R. Ovshinsky, *Phys. Rev.* B **35**, 2385 (1987)

3. R. Tsu, A. Filios, C. Lofgren, K.Dovidenko and C.G. Wang, *Electrochem and Solid State Lett.*, **1** (2) 80 (1998).

4. J.Ding and R. Tsu, *Appl. Phys. Lett.* **71**, 2124 (1997).

5. R. Tsu, A Filios, C.Lofgren, J. Ding, Q. Zhang, J. Morias and C.G.Wang, *ECS Proc.* **97-11**, 341 (1997)

6. R.Tsu, Q.Zhang, and A. Filios, *SPIE* **3220**, 246 (1998).

7. Z.H. Lu, D.J. Lockwood and J.M. Baribeau, *Nature* **378**, 258 (1995)

8. L.Tsybeskov,K.D.Hirschman,S.P.Duttagupta,P.M.Fauchet,M.Zacharias,P.Kohlert,J. P.McCaffrey and D.J. Lockwood, *ECS Proc.* **97-11**,134 (1997)

9. R. Tsu, in " Tetrahedrally - bonded Amorphous Semiconductors" edited by D. Adler and H.Fritzshe (Plenum Publ. Corp.,1985) p.433

10. R. Tsu, *J. Non-crystalline Solids*, **75** 463 (1985).

11. R. Tsu, *J. Non-crystalline Solids* **114**, 708 (1989).

12. R. Tsu and F. Zypman, *Surface Science* **228**, 418 (1990).

13. G.I.Distler, B.B. Zvyagin, *Nature*, **212**, 807 (1966).

14. R. Tsu and L.Esaki, *Appl. Phys. Lett.* **22**, 562 (1973).

15. R. Tsu, A.Filios and Q.Zhang, "Perspectives of Light Emitters in Nanoscale Silicon", 9th CIMTEC, SX-1:IL01, Florence, Italy, 1998

16. L.Esaki and R. Tsu, *IBM J. Res. and Devlop.* **14**, 61 (1970)

17. J. Matthews and A. E. Blakeslee, *J. Crystal Growth*, **32**, 265 (1976)

18. In Atomic Spectra and Atomic Structure, G. Herzberg, (Dover Publ. N.Y. 1944)

19. Y.P.Li, and W.Y.Ching, *Phys. Rev.* B**31**, 2172 (1985)

20. R.P.Gupta, Phys. Rev. B 32, 8278 (1985)

21. To be published

22. A. Isihara, Statistical Physics, (Academic, Press, N.Y. 1971)

23. G. Briet and E. Wigner, *Phys. Rev.* **49** 519 (1936)

24. Unpublished

25. Q.Zhang,A.Filios, C.Lofgren and R. Tsu, "Ultra-stable Visible Electroluminescence from Crystalline Si/O Superlattice", *Physica E*, North-Holland, 1998.

MEASUREMENT OF PHOTOCARRIER LIFETIMES IN SILICON NANOCLUSTERS

A.J. Kenyon[1], S. Botti[2], P.F. Trwoga[1] and C.W. Pitt[1]

[1]Dept. Electronic & Electrical Engineering
University College London
Torrington Place, London WC1E 7JE
United Kingdom

[2]ENEA, Via Enrico Fermi, 45 - Casella Postale n. 65
00044 Frascati (Roma)
Italy

ABSTRACT

Carrier lifetimes in silicon nanoclusters have been determined using measurements of photogenerated free-carrier absorption. Two classes of samples were studied: silicon nanoclusters deposited using laser pyrolysis of silane, and silicon nanoclusters in a silica matrix prepared by plasma-enhanced chemical vapour deposition. Photocarriers were generated using modulated 514nm light from an argon-ion laser and the induced transient absorption probed using an 840nm probe laser.

All samples showed visible and near-ir photoluminescence and a band edge absorption in the visible typical of silicon nanoclusters. The silicon nanopowders may find useful application in the field of nanophosphors while the silicon-rich silica samples are of interest from the point of view of producing all-silicon optoelectronics.

Our results consistently show very long carrier lifetimes in silicon nanoclusters. Lifetimes are of the order of several milliseconds, in contrast to the tens to hundreds of microseconds typical of bulk silicon. We attribute this increase to a combination of defect and impurity-free clusters with a fully oxidised or hydrogenated surface. The absence of non-radiative recombination centres in such a system leads to slow thermally-assisted recombination of carriers, and hence long lifetimes.

I. INTRODUCTION

The lack of a silicon-based light source, a consequence of the indirect bandgap of silicon, has so far frustrated attempts at true large-scale optoelectronic integration. However, the huge benefits that would result from the achievement of efficient light emission from silicon have continued to spur investigators to investigate novel methods for manipulating the band structure of silicon. Over the past eight years or so, this area of study has been developing rapidly following the discovery of light emitting porous silicon by Canham[1]. The field now encompasses a number of novel forms of silicon that exhibit favourable optical properties. In addition to porous silicon[1-3], silicon-silica multilayers[4,5], spark-processed silicon[6,7], and silicon nanoclusters[8-10] have all received varying amounts of attention in recent years, and both photo- and electroluminescence have been demonstrated. There has been, and still remains, much vigorous debate over the luminescence mechanism in these materials[11-13], and in the case of electroluminescence, the process of electron transport remains unclear[14,15]. Broadly speaking, the field can be divided into two camps: those who invoke quantum confinement as an explanation for the observed luminescence, and those who prefer to think of it as being a result of defects, chemical species, or defect-mediated transitions. Much of the difficulty lies in the often contradictory nature of the results reported in the literature. Whatever the explanation, it can at least be stated that this is a complex problem and the jury is still out on the fundamental optical physics of this class of material. This is undoubtedly an area of extreme technological importance and clearly there remains much to be investigated in the way of fundamental physical processes in nanoscale materials for optoelectronics.

Our particular interest is nanoclustered silicon; that is, aggregates of silicon atoms in the size range 20-100Å. Such material offers confinement in all three dimensions and exhibits many of the same optical properties as porous silicon. We have observed bright visible an near-ir light emission from silicon nanoclusters in a silica matrix ('silicon-rich silica') and have proposed in previous studies that the two distinct luminescence bands present are the result of two separate mechanisms: radiative recombination of confined excitons, and defect luminescence related to oxygen atom vacancies in the silica matrix[16,17]. The former is indicated by the very clear red-shift of the first luminescence band on annealing: the latter is suggested by the correlation between the disappearance of the second luminescence band at high annealing temperatures and the annealing out of oxygen-vacancy defects as shown by FTIR and ESR studies. A great deal of the uncertainty surrounding light emission from silicon may thus be due to differences in the production technique favouring one or other of these mechanisms. We have also demonstrated electroluminescence from simple metal-oxide-semiconductor (MOS) structures fabricated using thin films of this material[18].

Of equal interest is material consisting of nanoclustered silicon in powder form. Such material may be of great importance as a nanophosphor for use in low-voltage field emission displays or may be embedded in a dielectric host to form electroluminescent devices. It also allows the study of silicon nanoclusters isolated from a surrounding oxide matrix. We have demonstrated production of this material using laser pyrolysis of silane and have obtained bright visible luminescence from silicon nanopowders[19,20].

II. EXPERIMENTAL

For the present study we have produced two classes of nanoclustered material: silicon nanoclusters in silica deposited by plasma enhanced chemical vapour deposition (PECVD) and silicon nanopowders generated by CO_2 laser pyrolysis of silane.

To produce silicon-rich silica thin films, a number of films were deposited on lightly doped p-type <100> CZ silicon wafers in a capacitively-coupled PECVD deposition chamber. The sample wafers were first thoroughly cleaned, placed in the reaction chamber and cleaned again with an argon plasma for 5 minutes. Precursor gases were a silane/argon mix (5% silane (SiH_4) in argon) and nitrous oxide (N_2O) as silicon and oxygen sources respectively. The nitrous oxide flow rate was fixed at 10 sccm and the silane/argon mixture flow rate at 180 sccm. This mixture has been shown in previous studies[16] to give good quality luminescent silicon-rich silica films. A 13.56 MHz RF generator was used to dissociate the precursor gases, the power being varied from run to run between 10 W and 30 W. Substrate temperature was set at 200 °C.

The nanopowders were produced by introducing a mixture of silane and an inert carrier gas (argon or helium) into a high vacuum chamber and dissociating the silane using 10.6μm light from a CO_2 laser. Further details of deposition can be found elsewhere[19,20].

Photoluminescence spectra were measured for each film using a Coherent argon-ion laser as the excitation source. Spectra were dispersed using a Bentham M300 monochromator and detection was via a Bentham 231 side window photomultiplier tube, a current preamplifier and lock-in amplifier. Both the detection electronics and monochromator were computer controlled; care was taken to ensure that the spectra were as accurate and repeatable as possible by calibrating the system response using a white light source of known spectral distribution. A diffraction grating was used as a premonochromator to filter out laser plasma lines and both a high-pass dielectric filter and a Schott glass filter (OG495) placed immediately following the collection optics removed any unwanted laser scatter.

One of the powder samples (sample E) was measured as-deposited, the second (sample G) was oxidised in the reaction chamber prior to measurement. In the case of the silicon-rich silica films, the samples were used as-deposited, i.e. without further post-process annealing. Both classes of sample exhibited luminescence when excited using the 476nm line of an argon-ion laser, though the lineshapes showed a strong dependence on the presence of the oxide layer in the case of the nanopowders. This is illustrated in figure 1 which shows photoluminescence spectra of as-deposited and oxidised silicon nanopowders along with that of a silicon-rich silica film.

Optical absorption spectra were taken of all samples using a tungsten-halogen light source, a Bentham M300 monochromator and either a silicon photodiode or side-window photomultiplier tube for detection. Figure 2 illustrates absorption spectra for both a silicon-rich silica film and a nanopowder sample. Clearly apparent is a strong fundamental absorption band edge in the visible region. The large shift in band edge energy from the bulk silicon value of 1.1eV must be due to a change in the bandgap of the material and can be attributed to quantum confinement effects.

Carrier lifetimes were measured using the technique of photoinduced free-carrier absorption that we have applied in previous work to measure carrier lifetime distributions in silicon wafers and devices[21]. A similar technique has been used by other groups to measure carrier lifetimes in bulk silicon[22] and porous silicon[23]. The sample is illuminated with a pulsed light source having a photon energy greater than the band gap energy of the material. In this way, photocarrier pairs are excited in the bulk of the sample, down to a depth corresponding to the penetration depth of the light used. In this case, the source used was the 514nm line of an argon ion laser, modulated using a rotating blade optical chopper. At the same time, a near-ir source with a photon energy just less than the band gap energy is transmitted through the sample. When photogenerated free carriers are present in the sample, this probe beam is attenuated by free-carrier absorption. Thus, by modulating the photocarrier population and monitoring the increase in probe transmission following switch-off of the 514nm pump source, the free-carrier lifetime, τ, can be obtained. Care was taken to characterise the response time of the experimental apparatus by increasing the speed of rotation of the chopper wheel and focusing the laser onto the edge of the blade. Using this mechanical method we were able to resolve cut-off times down to 10μsec. This is the practical limit set on this measurement by the speed of rotation of the chopper blade and the diameter of the laser spot on the blade. For the experiments described here, the probe source was a diode laser operating at 849nm, delivering a power of approximately 20mW into a multimode fibre. Butting the fibre up to the sample allowed the experiment to probe a small area. The samples studied were either in the form of thin (approximately 1μm) films of silicon-rich silica on glass or nanocluster powders held between microscope slides.

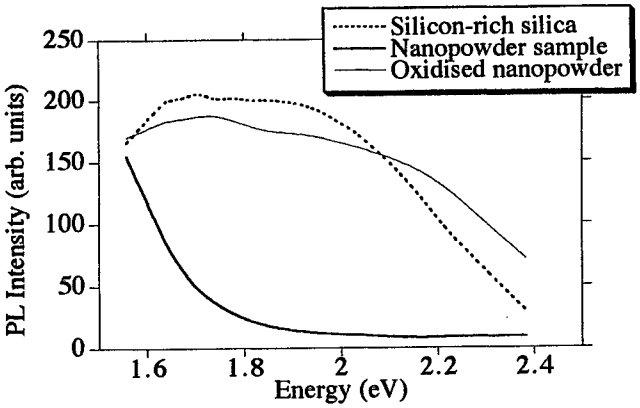


Figure 1: Photoluminescence spectra of silicon-rich silica thin film, as-deposited silicon nanopowder, and oxidised silicon nanopowder

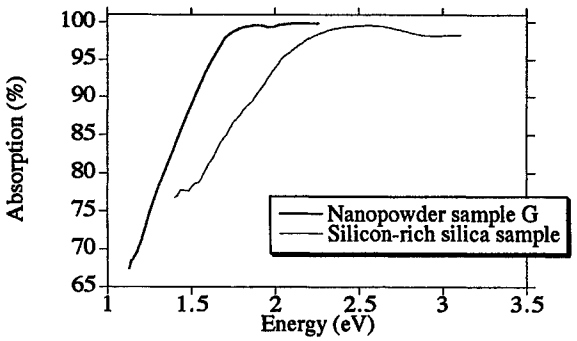


Figure 2: Absorption spectra of nanopowder sample G and silicon-rich silica thin film

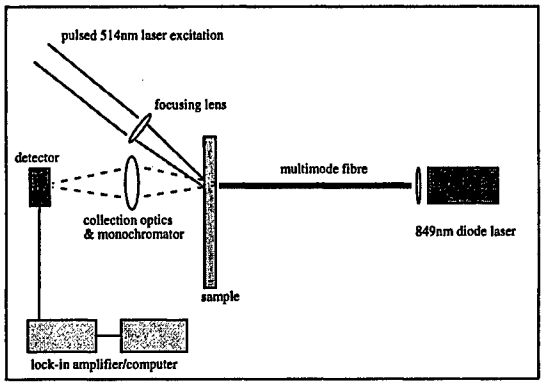


Figure 3: Experimental set-up for measurement of transient free-carrier absorption

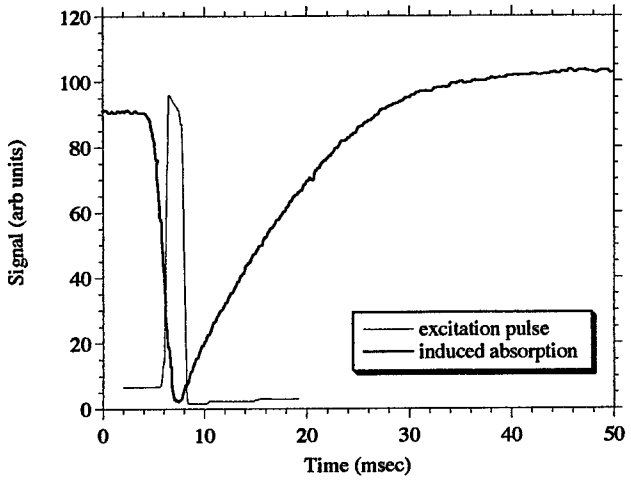


Figure 4: Transient free-carrier absorption for silicon-rich silica film. Also shown is the excitation pulse, demonstrating that the measured decay is not limited by the system response.

All measurements were performed at room temperature. Figure 3 details the experimental set-up. No photoinduced absorption was detectable when a glass slide was substituted for the silicon nanocluster samples, confirming that the effect is due to photoinduced free carrier absorption. Measurements were also taken over a range of excitation powers to ensure that the powers used were not sufficient for Auger recombination to dominate. Over the range of powers used (1-40mW at the sample), the measured lifetimes were constant.

III. RESULTS AND DISCUSSION

Figure 1 shows photoluminescence spectra of both silicon nanopowder samples: the strong band around 2-2.2eV appears only in the case of the oxidised sample. This is the band we have previously assigned to luminescent oxygen-vacancy defects (non-bridging oxygen hole centres). Sample E (as-grown, non-oxidised) shows only a band around 1.6eV that we have assigned to quantum confinement effects.
Cluster size distributions were obtained for the powder samples by neutron diffraction measurements. There were two strong peaks in the distribution around 3Å and 30Å: well within the region within which quantum confinement effects become important (i.e. cluster sizes which are less than the excitonic Bohr radius: 49Å for silicon[24]).

Figure 4 shows the time evolution of free-carrier absorption for a silicon nanopowder sample. Also shown is the time evolution of the 514nm excitation pulse. The carrier lifetime is given by the rise time of the absorption signal following turn-off of the excitation pulse (taken as the 1/e point of the rise). Decay curves were fitted with an exponential function and the 1/e times extracted. For this sample, this is 7.9msec. Lifetime measurements were taken for a number of film and powder samples: the results are detailed in table I.

The carrier lifetimes detailed in table I are very long compared to those obtained for bulk silicon. In previous work using the same technique, carrier lifetimes in lightly doped silicon wafers were in the region of 100 to 500μsec: those measured for the silicon nanoclusters are approximately an order of magnitude greater than this. In the case of bulk silicon, carrier recombination largely takes place via surface 'traps' or defect states in the bulk. Thus, carrier lifetimes in bulk silicon are heavily dependent on doping level, density of defect states and surface quality. In the case of silicon nanoclusters, there is a very high surface-to-volume ratio, so it may be expected that surface recombination would dominate and hence carrier lifetimes would be correspondingly short. It is often stated that the presence of dangling bonds at the surface of silicon nanoclusters serves to quench luminescence by acting as non-radiative recombination centres[25]. In a highly localised system such as a nanocluster, this recombination should be very rapid, and hence luminescence yield should be low and carrier lifetime short. However, in previous studies we have demonstrated an increase in photoluminescence following removal of the large amount of hydrogen present in as-deposited silicon-rich silica films[16]. This hydrogen is removed by thermal annealing at temperatures in excess of 600°C. Associated with this removal is an increase in defect-related luminescence and an eventual compensation of these defects by diffusion of interstitial oxygen. It is also noteworthy that the carrier lifetimes measured for the two powder samples were very similar. Given that the very large surface area of the silicon nanopowders would be reasonably expected to form a native oxide layer extremely readily, it would be surprising if there was a significant population of dangling bonds present in these samples. In fact, it was noticed that when a laser beam of even moderate power (in the region of 60-80mW of 514nm light) is focused onto any of the nanopowder samples in air, the sample very readily oxidises to form a porous glass. This oxidation takes place very exothermically and a small flame is visible.

Sample name	Sample type	Carrier lifetime (msec)
E	Si nanopowder	7.9±0.5
G	Oxidised Si nanopowder	5.7±0.4
SS23	Silicon-rich silica film	6.98±0.5

Table I: Carrier lifetimes for nanopowder and silicon-rich silica samples

It is our contention, therefore, that for the case of the silicon nanoclusters produced in this study, the cluster surfaces are highly passivated. In the case of silicon-rich silica films, we propose that hydrogen mops up those dangling bonds that are not taken up by oxygen. FTIR spectra demonstrate the presence of significant amounts of hydrogen in as-grown films. In the case of silicon nanopowders, the rapid formation of a native oxide layer readily compensates those dangling bonds not taken up by hydrogen from the silane precursor. Thus there are very few non-radiative carrier recombination centres. In addition, the clusters are of high purity (chemical analysis of the silicon-rich silica films have shown very little contamination with carbon, some nitrogen and very little else). As a result, carrier recombination is largely thermally-assisted and therefore slow. Both silicon-rich silica films and silicon nanopowders are produced using silane as a precursor gas, so there is an abundance of hydrogen in the forming reaction. Incomplete dissociation of silane will lead to the inclusion of large amounts of hydrogen into both films and powders, as is confirmed by FTIR studies[16]. We must stress at this point that we are not suggesting that all of the silicon nanoclusters have completely passivated surfaces and therefore long carrier lifetimes. Our results merely indicate that there are sufficient such clusters to produce a strong long-lifetime component in the decay times observed. It is probable that there is a significant proportion of clusters that have very short lifetimes due to the presence of non-radiative recombination centres, but these cannot be resolved by our detection technique. Another possibility is that the carriers produced within the silicon clusters become trapped in defect sites within the silica matrix. This is known to happen very rapidly and could lead to the observed lifetimes being controlled by the lifetime of the charge traps rather than that of carriers within the silicon clusters. However, we discount this possibility as a result of the observation that the carrier lifetimes in both as-received and oxidised nanopowder samples are similar. Inspection of the PL spectra of these two samples shows a lack of luminescence from defects in the former case.

IV. CONCLUSIONS

We have measured transient free carrier absorption in silicon nanoclusters. We have investigated two classes of clusters: those in the form of powders and those embedded in a silica matrix. Both sets of samples exhibit surprisingly long free carrier lifetimes which we assign to a significant population of nanoclusters having a high degree of surface passivation, thereby reducing the available non-radiative de-excitation pathways via dangling bonds. We do not believe these measurements are significantly influenced by charge trapping at defect sites in the silica matrix, as similar decay times are observed for non-oxidised powder samples.

V. ACKNOWLEDGEMENTS

We would like to express our thanks to the Engineering and Physical Sciences Research Council, UK, for financial support.

REFERENCES

[1] L.T. Canham, Appl. Phys. Lett. **57**, 1046 (1990)

[2] L.T. Canham, Physica Status Solidi B-Basic Research **190**, 9 (1995)

[3] R.T. Collins, P.M. Fauchet, and M.A. Tischler, Physics Today **50**, .24 (1997)

[4] B. Abeles and T. Tiedje, Phys. Rev. Lett, **51**, 2003, (1983)

[5] D.J. Lockwood, Z.H. Lu, and J.M. Baribeau, Phys. Rev. Lett. **76 (3)**, 539 (1996)

[6] M.A. Ludwig, A. Augustin, R.E. Hummel, and Th. Gross, J. Appl. Phys. **80**, 1 (1996)

[7] R.E. Hummel and S.S. Chang, Appl. Phys. Lett. **61**, 1965 (1992)

[8] I.T.H. Chang, F. Niu, D. Slimovici, C. Wildig, P.A. Leigh, P.J. Dobson, and B. Cantor, Mat. Sci. Forum, **225**, 175 (1996)

[9] T. Shimizu-Iwayama, K. Fujita, S. Nakao, K. Saitoh, T. Fujita, and N. Itoh, J. Appl. Phys. **75**, 7779 (1994)

[10] S. Veprek, Thin Solid Films, **297**, 145 (1997)

[11] G. Qin and G.G. Qin, J. Appl. Phys. **82**, 2572 (1997)

[12] Y. Kanemitsu, Thin Solid Films, **276**, 44 (1996)

[13] L.T. Canham, A. Loni, P.D.J. Calcott, A.J. Simons, C. Reeves, M.R. Houlton, J.P. Newey, K.J. Nash, and T.I. Cox, Thin Solid Films, **276**, 112 (1996)

[14] D.W. Boeringer and R. Tsu, Mat. Res. Symp. Proc. **358**, 569 (1995)

[15] H. Cruz, D. Luis, N.E. Capuj, and L. Pavesi, J. Appl. Phys. **83**, 7693 (1998)

[16] A.J. Kenyon, P.F. Trwoga, C.W. Pitt, and G. Rehm, J. Appl. Phys. **79**, 9291 (1996)

[17] P.F. Trwoga, A.J. Kenyon, and C.W. Pitt, J. Appl. Phys. **83**, 3789 (1998)

[18] P.F. Trwoga, A.J. Kenyon, and C.W. Pitt, Electron. Lett. **32**, 1703 (1996)

[19] E. Borsella, S. Botti, S. Martelli, R.M. Montereali, W. Vogel, and E. Carlino, Mat. Sci. Forum, **235**, 967 (1997)

[20] E. Borsella, S. Botti, M. Cremona, S. Martelli, R.M. Montereali, and A. Nesterenko, J. Mat. Sci. Lett. **16**, 221 (1997)

[21] S. Amirhaghi, A.J. Kenyon, M. Federighi, and C.W. Pitt, Mat. Res. Soc. Symp Proc. **428**, 455 (1996)

[22] V. Grivickas, J. Linnros, A. Vigelis, J. Seckus, and J.A. Tellefsen, Solid State Elec. **35**, 299 (1992)

[23] V. Grivickas and J. Linnros, Mat. Res. Soc. Symp Proc. **358**, 543 (1995)

[24] A.G. Cullis, L.T. Canham, and P.D.J. Calcott, J. Appl. Phys. **82**, 909 (1997)

[25] M. Lannoo, C. Delerue, and G. Allan, J. Luminesc. **57**, 243 (1993)

Characterization of RTCVD grown Si films on SiO_2 for Nanotechnology Applications

J. Vizoso[a], F. Martín[a], X. Martínez[b], M. Garriga[b] and X. Aymerich[a].
[a] Departament d'Enginyeria Electrònica, Universitat Autònoma de Barcelona
[b] Institut de Ciència de Materials de Barcelona, CSIC.
08193 - BELLATERRA. Spain.

ABSTRACT

A RTCVD reactor has been used to grow very thin Si films on SiO_2 under a wide variety of conditions, with the aim of obtaining appropriate process parameters for the control of nuclei uniformity and size at the nanometer scale. This has applications as an alternative to traditional lithographic methods for the patterning of surfaces at the nanometer scale length. The use of a RTCVD reactor comes from the fact that the fast temperature transitions allow an easy control of the growth. Films were characterized by means of spectroscopic ellipsometry (SE) for effective thickness and structure determination, whereas an estimation of grain size and roughness are given by TEM and AFM measurements. For deposition times around the incubation time a precise control in nuclei size and uniformity is demonstrated.

I. INTRODUCTION

The Chemical Vapor Deposition (CVD) growth of Si on SiO_2 is one of the most largely studied processes with a vast variety of applications in the semiconductor industry: polycrystalline films are used for the fabrication of Thin Film Transistor (TFT) [1], Metal Oxide Semiconductor (MOS) gates [2] and Electrical Erasable Programable Read Only Memories (EEPROMs) [3], among other devices. The main requirements for each of them may vary, what has led to a good knowledge and improvement of this process. Thus, large grain sizes are suitable for TFT active areas

[1] and smoothness is the most stringent requirement for EEPROMs and MOS gates [2,3].

Because of the continuous scaling down of integration, the fabrication of nanostructures has emerged as a new forefront in technology, in which Si/SiO_2 can contribute in promising applications such as nanocrystal memories [4,5] and Si-based light emission devices [6]. For the fabrication of such structures one can take advantage of the important technological background involved in the applications mentioned at the beginning [1-3]. However, this represents only a first approach to get success in nanofabrication, since the main challenge in this new area is the control on the nuclei size and location [7-10], and further investigations are needed to this end. This can have potential applications in the fabrication of quantum dot based devices, and is an alternative to optical based lithography which has a limited resolution that does not fit to the requirements needed for the development of nanostructures. Other alternatives to the fabrication of nanostructures have been proposed: among them, we can cite Selective Epitaxial Growth (SEG) [7,8], as well as those based in self-organization [9] or using a Scanning Near Microscopy (SNM) [10,11].

In this work, the optimal process conditions to obtain Si nuclei grown on SiO_2 with size control are reported. However, to determine such conditions it has been necessary to grow thin Si films on SiO_2. The estimation of growth rate, surface roughness, grain size and incubation time on these films has provided us the necessary conditions to success in the formation of nanoscale Si nuclei, as is demonstrated later in this work.

II. EXPERIMENTAL

Films have been grown on thermal SiO_2 (100nm thick) under various conditions, using SiH_4 as a precursor gas in a Jipelec Jet Star 100 ST RTCVD reactor. Briefly, our RTCVD system consists in a water refrigerated stainless steel chamber, into which silane, hydrogen and nitrogen can flow through separated gas lines with its corresponding mass flow controllers. The wafer is heated by twelve oil and air cooled tungsten lamps which enable the pyrolisis of silane, whereas the temperature is controlled by a feedback circuitry which uses a pyrometer to sense the optical radiation emitted by the wafer.

To perform nano-scaled structures with application in quantum devices, the use of a RTCVD system is suitable because low thermal budget has to be much more in consideration for these ultra small structures. RTP-based systems with fast transitions in temperature (in our processes up to 50°C/s) minimize the area enclosed for the

temperature-vs-time graph, as thermal budget is defined [12], when the process is starting (ramp up in temperature) and stopping (cooling down). These fast transitions allow the formation of nanostructures during times as short as few minutes since this yields a high enough deposition to transition time ratio to consider that no growth occurs during ramp up in temperature and cooling down. Thus, the shorter the transitions times are, the shorter the deposition time that can be used.

Before each process, the wafers are cleaned by introducing them in a H_2O_2/H_2SO_4 (3:1) bath for 15 min. followed by 5 min. rinse in de-ionized water and spin dry. Once in the chamber, and before the initiation of the growth, the samples are subjected to an ultimate vacuum of 10^{-6} mb during two hours, achieved by a turbomolecular pump (the usual process pressures are ranged between 0.2 and 1.5 mb). Films were characterized by SE to determine film structure and effective thickness, plan-view TEM for morphology and AFM to estimate surface roughness, grain size and to determine the dimensions of the grown Si dots.

III. RESULTS AND DISCUSSION

The conditions for accurate control on Si nuclei formation must be given in terms of temperature, deposition time and pressure. We analyze the effects of these parameters on GR, incubation time, structure, morphology and nuclei size in this section in order to establish the best process conditions.

According to the argument explained in section II, a minimum deposition time is always desirable for low thermal budget. However, transition times of several seconds, to start and stop the growths, lead us to consider deposition times above 1 min to avoid significant growth and undesirable thermal processes during transitions. Therefore, to form structures in the nanometer scale with high controlability in size, a GR of units of nm/min is suitable for our processes. For a fixed 0.2 mb of pressure, from a series of samples grown at various temperatures, the GR vs temperature is plotted in fig.1, while the resulting thickness and structure are reported in Table I. For temperatures below 560°C, the GR is corrected according to the incubation time, which has been inferred from fig.2, whereas for temperatures above 560°C the evaluation of the incubation time has been disregarded because it decreases exponentially with an increase in temperature [13] and the samples are thick enough. Thus, we find that the GR values for 540°C (5.3 nm/min) and 520°C (3.7 nm/min) are within the desired range whereas those obtained at high temperatures have a deposition time too short for nanometer dimensional structures. The delay for the initial growth due to the incubation times at 520°C (2.7 min.) and 540°C (1.55 min.) does not represent an important increase to the total process time. Therefore, temperatures

around 530°C give an appropriate GR and incubation time to grow nanostructures with accuracy.

Temperatures below 560°C tend to produce a-Si, as is shown in fig. 3 from SE measurements. Since a crystalline structure is required for most nanostructure applications, a thermal annealing can be used after processing to achieve nanocrystals. This avoids the use of higher temperatures, whose corresponding GR would lead us to an extremely short deposition time for our purposes, resulting in a coarse control, as has been explained earlier. A first attempt to corroborate our control predictions is shown in the sample of fig.4, in which some nuclei have started to coalesce, with a height of 15 nm and a diameter of 30 nm. Thus, for temperature of 540°C, this experiment guarantees the formation of nuclei without coalescence and with precise control on size by considering times below that used in figure 4 (around the incubation time, 1.55 min).

We are also interested in the effect of pressure variation on sample structure and morphology. Increasing pressure from 0.2 mb to 1.5 mb in samples grown at 540°C, does not affect the structure, which is amorphous in all cases, in accordance to other results obtained under similar process conditions [14]. To reliably estimate the RMS surface roughness for these series of samples, which is shown in conjunction with their thickness in fig.5, the data acquired by the AFM system are post-processed. This allows us to overcome non idealities occurred during measurements (usually non linear scan, thermal drifts and slight support inclination). The final roughness of a surface is strongly dependent on grain size during its initial growth, a fact that has been related to the density of primary nuclei [8,13]. This is corroborated from comparative AFM observations shown in fig.6 for samples grown at the lowest (0.2mb) and highest (1.5 mb) pressure with a similar thickness, where a decrease in the grain size is obtained at the highest pressure following the same tendency as roughness in fig.5. This is argued because a pressure increase leads to an enhancement of small size nuclei density, which eases the formation of smooth surfaces. This suggests that for the conditions in which the smoothest surface results, at 1.5 mb, smaller grains for initial growth result. From the images shown in fig.6 and fig.4, high uniformity in grain size is observed. This is of paramount importance for process reproducibility and future nanostructure-based applications as quantum devices [4-6]. In contrast, in the sample shown in fig.7, which has been grown while adding H_2 to the process, a non uniform grain size results. Therefore, we can conclude that the use of SiH_4 diluted in H_2 has negative effects to the formation of Si quantum dots with regular size, something which is required in most Si dot based applications.

According to the previous results obtained on the basis of very thin silicon films grown on SiO_2, it follows that to form Si nuclei with uniform size, process

temperatures of about 520-540°C with deposition times around the incubation time are suitable. The process pressure is unimportant from the point of view of nuclei uniformity. We have carried out depositions under these conditions with the aim to obtain nanoscale Si nuclei on SiO_2. The results are shown in figure 8, where two process times (above and below the incubation time) have been considered for temperatures of 520°C and 540°C. In view of the figures, the size of the nuclei is quite uniform in all cases. For the higher temperature, a more dense distribution of nuclei is observed, regardless of the process time considered. On the other hand, if we compare samples grown at the same temperature and different time, no significant differences regarding nuclei density are observed. This means that the times considered in these experiments are close to those for density saturation. Times well below the incubation time are therefore necessary in order to have control on nuclei density. It is interesting to compare the AFM images corresponding to the samples with nuclei grown during 2 min and different temperatures. Even though both temperatures are very close, the nuclei size as well as the mean separation of nuclei is rather different (at 540°C nuclei almost coalesce), which reveals the high sensitivity of nuclei formation with temperature.

Finally, in figure 9 we depict two 3D AFM images corresponding to the samples of figures 8(a) and 8(c) to show how the height of the nuclei is also quite uniform. The image ranges have been reduced to the nanometer scale to appreciate more clearly the size of the nuclei. The heights of these are between 3.5nm and 4nm for the lower temperature and between 5.2nm and 6.1nm for the highest temperature, while the diameters are of the order of 25nm and 35nm in each case (these diameters are probably overestimated due to the limited lateral resolution of the AFM system, so that TEM images are currently being obtained to determine the lateral dimensions of the nuclei with more precision). These results are promising since the dimensions of the obtained nuclei are convenient to the fabrication of devices based on Si nanodots, and reveal that our UHV-RTCVD system is suitable for the fabrication of nanoscale quantum devices.

IV. CONCLUSIONS

This work has been focused to obtain the optimal conditions for the fabrication of Si nanostructures on SiO_2 by means of a UHV-RTCVD system. Under these conditions, structures of nanometer dimensions have been grown during times around the incubation time with high uniformity in size if pure SiH_4 is used during process. Temperatures in the reaction-limited growth regime and pressure of 0.2 mb have been established to obtain a GR of few nm/min which gives a convenient time scale for the formation of nanometer Si structures. A variety of pressures have been considered to study its effect in the morphology resulting, from comparative AFM measurements, a

decrease in the roughness and grain size for an increase in the pressure. The dilution of silane in hydrogen has a negative effect on nuclei features, since cluster size uniformity is lost. This is undesirable for applications requiring a regular size distribution of islands (quantum dots). The main conclusion of the work is that with appropriate process conditions, a RTCVD reactor can be used to the fabrication of quantum devices based on the formation of Si nanoscale dots on SiO_2. We have found process conditions suitable to obtain accurate control on nuclei properties. Work is in progress to control also the position of the islands.

ACKNOWLEDGEMENTS

This work has been supported by the *Dirección General de Enseñanza Superior* under project number PB96-1162. Thanks to Drs. F. Pérez-Murano, K. Birkelund and P. Gorostiza for AFM measurements and Y. Maniette for TEM images.

References

1. T. Noma, T. Yonehara and H. Kumoni, Appl. Phys. Lett., **59** (6), 653 (1991).

2. E. Ibok and S. Garg, J. Electrochem. Soc., **140** (10), 2927 (1993).

3. C. Cobianu, O. Popa and D. Dascalu, IEEE Electron Device Lett. EDL-14, 213 (1993).

4. H. I. Hanafi, S. Tiwari and Imran Khan, IEEE Trans. Electron Devices, **43** (9), 1553 (1996).

5. L. Guo, E. Leobandung and S. Y. Chou, Science, **275**, 649 (1997).

6. Z. H. Lu, D. J. Lockwood and J. M. Baribeau, Nature **378**, 258 (1995).

7. H. Kumoni, T. Yonehara and T. Noma, Appl. Phys. Lett., **59** (27), 3565 (1991).

8. K. E. Violette, M. K. Sanganeria, M. C. Öztürk, G. Harris and D. M. Maher, J. Electrochem. Soc., **141** (11), 3269 (1994).

9. Y. H. Xie, S. B. Samavedam, M. Bulsara, T. A. Langdo and E. A. Fitzgerald, Appl. Phys. Lett., **71** (24), 3567 (1997).

10. M. Wendel, S. Kühn, H. Lorenz, J. P. Kotthaus and M. Holland, Appl. Phys. Lett. 65 (14), 1775 (1994).

11. T. Fayfield and T. K. Higman, J. Vac. Sci. Technol. B, **12** (6), 3731 (1994).

12. R. Ditchfield and E. G. Seebauer, J. Electrochem. Soc., **144** (5), 1842 (1997).

13. Y. Z. Hu, D. H. Diehl, C. Y. Zhao, C. L. Wang, Q. Liu and E. A. Irene, J. Vac. Sci. Technol. B, **14** (2), 744 (1996).

14. A. Voutsas and M. K. Hatalis, J. Electrochem. Soc., **139** (9), 2659 (1992).

15. D.E. Aspnes ans A.A. Studna, Phys. Rev. B **27**, 985 (1983).

Temperature (°C)	Structure	Deposition Time (min)	Thickness (nm)	Inc. Time (min)
520	a-Si	30	90	2.71
540	a-Si	60	310	1.55
560	a-Si	35	325	-
580	p-Si	13.5	166	-
600	p-Si	13.8	229	-

Table I: Structure, thickness and GR for samples grown at several temperatures. The incubation time for the lowest temperatures is also reported. Samples were grown with 50 sccm of undiluted SiH_4 at 0.2mb.

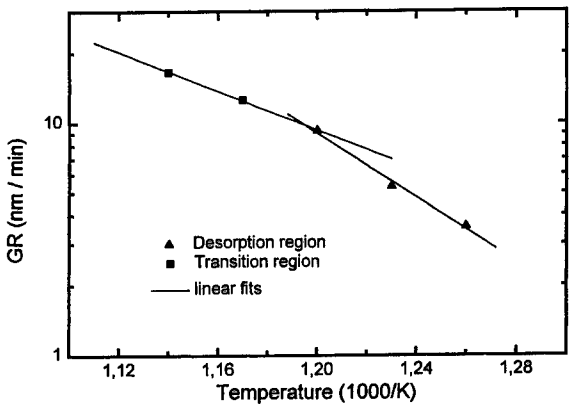


Figure 1. Arrhenius plot for films grown at 0.2mb and 50sccm of undiluted SiH_4. The data for the lowest temperatures is corrected by the corresponding incubation time. Two different regions are shown with its corresponding linear fit.

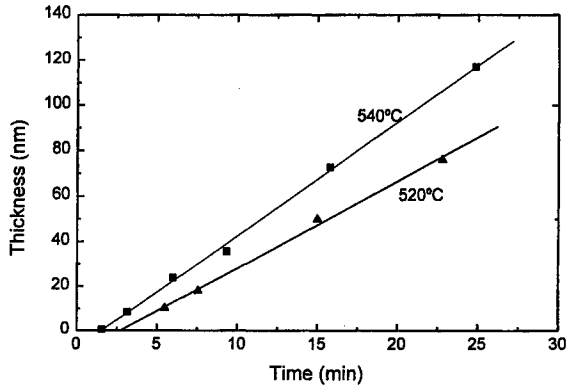


Figure 2. Effective thickness-vs-time (0.2 mb) for T=520° and T=540°. The incubation time measured at the intersection with X axes is 2.71 min. and 1.55 min. respectively for each temperature. The GR, extracted from the slope of the graphs, is 3.5 nm/min and 5.3 nm/min respectively.

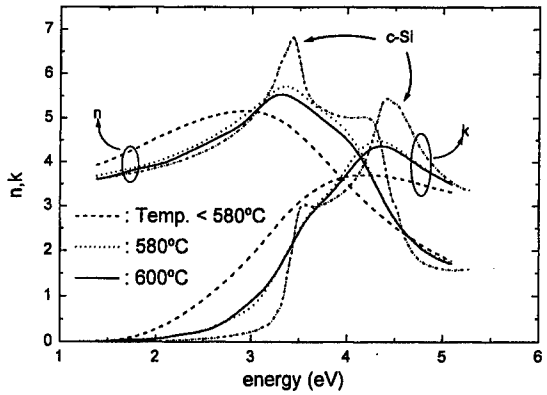


Figure 3. Real (n) and imaginary (k) part of refractive index for samples grown at several deposition temperatures together with spectrum of c-Si (from Ref. 15). Spectra for temperatures below 580°C show the broad structure spectrum of a-Si, whereas for 580°C and 600°C the spectra start to show the electronic transitions characteristic of c-Si.

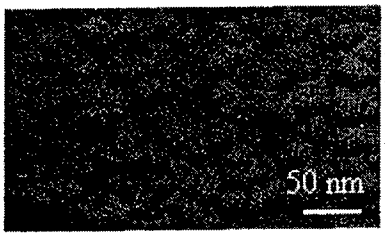


Figure 4. Plan-view TEM of a film grown during 190s at 0.2mb and 540°C.

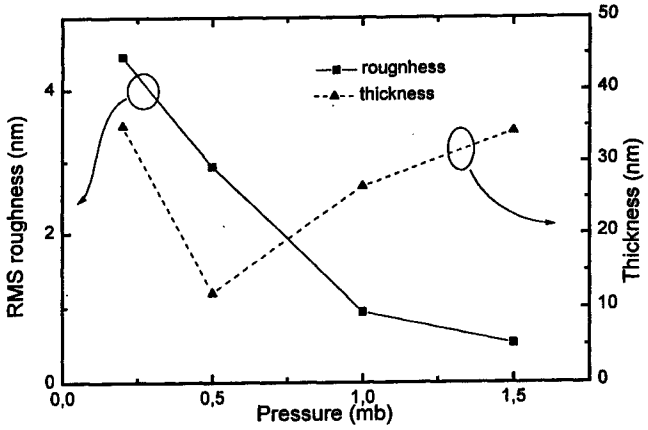
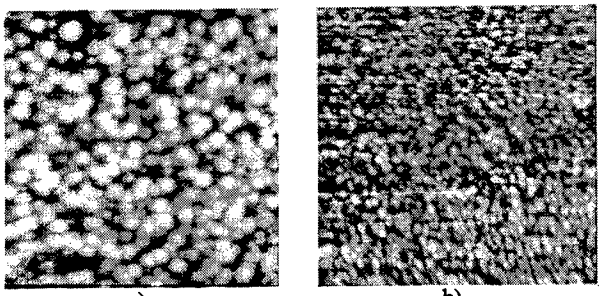


Figure 5. RMS surface roughness variation with pressure for samples grown at 540°C. The corresponding thickness is shown for comparison.



a) b)

Figure 6. Top view AFM images of two samples grown with undiluted SiH_4 at 540°C and a) at 0.2 mb and b) at 1.5 mb. The range of the images is 1.5μ x 1.5μ.

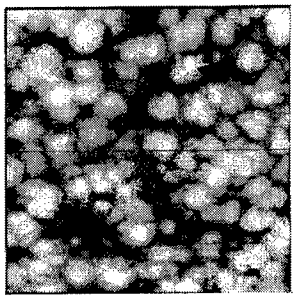


Figure 7. Top view AFM image of a sample grown with a 0.2mb of SiH_4 and 0.8mb of H_2. The image range is 1.5μ x 1.5μ.

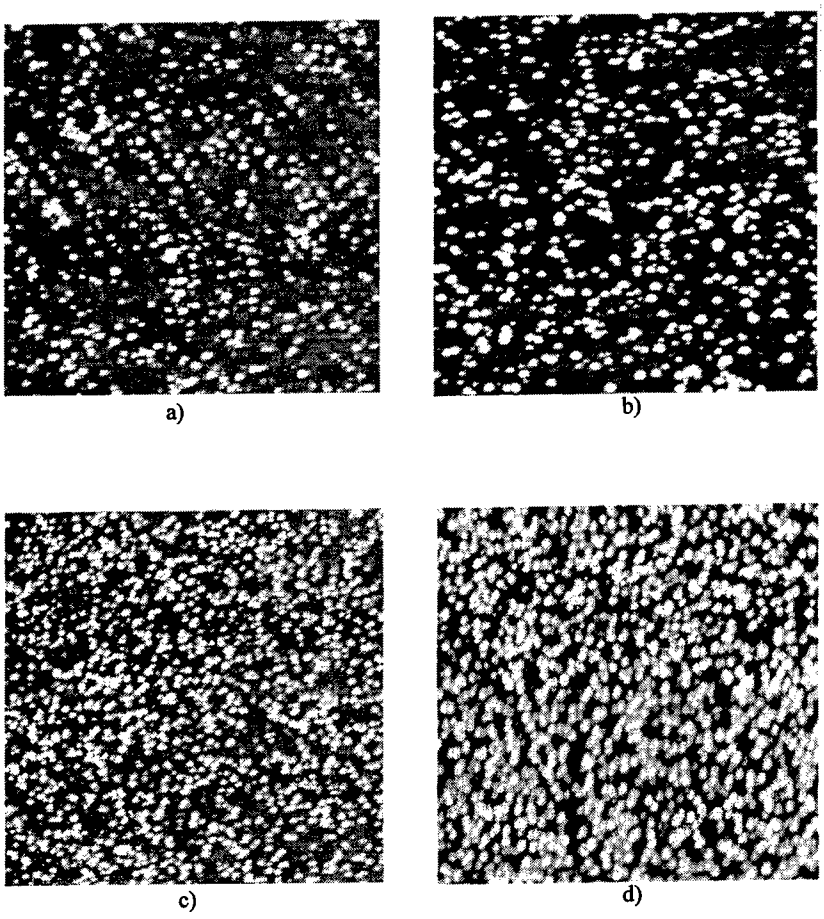
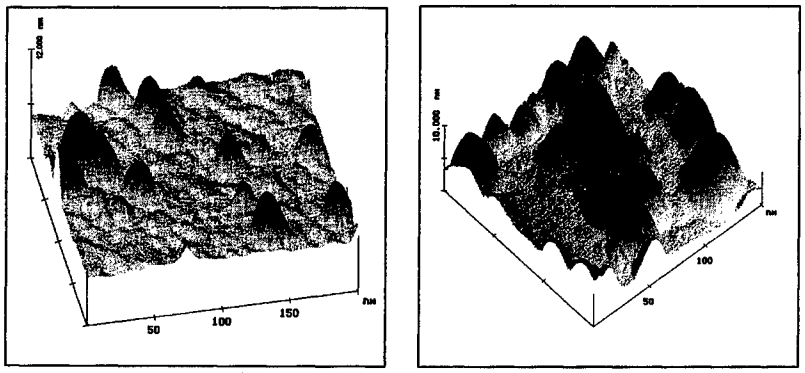


Figure 8: Top view AFM images showing Si islands obtained at different temperatures and times: a) T = 520°C, t = 2 min, b) T = 520°C, t = 3 min, c) T =

540°C, t = 1.50 min, d) T = 540°C, t = 2 min. The process pressure is 0.2mb in all cases.



a) b)

Figure 9: AFM images corresponding to the samples of figures 8a) and 8 c). The smaller range considered allows to appreciate better the uniformity of the grown Si dots.

EFFECTS OF THERMAL PROCESSING ON PHOTOLUMINESCENCE OF Si NANOCRYSTALLITES PREPARED BY PULSED LASER ABLATION

I. Umezu, K. Shibata, S. Yamaguchi, H. Sato and A. Sugimura,
Department of Applied Physics, Konan University,
Kobe, 658-8501, Japan

Y. Yamada and T. Yoshida
Matsushita Research Institute Tokyo, Inc.,
Kawasaki 214-8501, Japan

ABSTRACT

The photoluminescence (PL) properties of Si nanocrystallites prepared using an inert-gas-ambient pulsed laser ablation technique was characterized. We performed subsequent thermal processing to the Si nanocrysallites in N_2 or O_2 gas. Although the PL intensity of as-deposited Si nanocrystallites was very weak at room temperature, it increased with annealing in N_2 or O_2 gas. The PL intensity of the nanocrystallites annealed in O_2 gas was the largest at room temperature. The strong PL intensity of O_2 annealed sample corresponded to long PL lifetime. The nonradiative recombination process which reduces PL intensity is discussed in terms of the temperature dependence of the PL intensity and lifetime. Our results suggest that annealing of Si nanocrystallites in O_2 gas reduces the nonradiative recombination of electron-hole pairs.

INTRODUCTION

Over the past several years, observation of visible photoluminescense (PL) spectra at room temperature have led to extensive studies on nanometer-sized silicon structures.[1-3] The strong PL from Si materials is important to investigate physics of nanometer sized materials and to realize Si based optelectronic devices. The nanometer-sized silicon structures had been prepared using numerous methods. The most of the researches are focused on porous Si since the fabrication of the specimen is convenient. For the present study, the laser ablation technique combined with constant-pressure gas evaporation has been adopted to prepare size-controlled spherical Si nanocrystallites.[4] It is well known that the PL intensity of porous Si increases with thermal oxidation.[5] This suggests that properties of nanoscaled Si materials are sensitive to the post-deposition processing. This correlation between the post-deposition processing and PL characteristics is a key to understanding the large PL quantum efficiency in Si nanocrystallites at room temperature. Many reports pointed out that

the origin of the efficient PL of nanocrystallites is the increase in the oscillator strength due to confinement of electron-hole pair. The nonradiative recombination processes are discussed in few reports.[6] Since the PL intensity is the result of competitions between radiative and nonradiative recombination processes, we measured temperature dependence of PL intensity and lifetime and discussed PL properties by means of radiative and nonradiative processes.

EXPERIMENT

In the present study, Si nanocrystallites were prepared using a pulsed laser ablation method.[4,7] During the growth process, helium gas was introduced into a vacuum chamber and a pressure of 333 Pa was maintained. An ArF excimer laser was focused on the surface of a single-crystal Si wafer, and the resulting Si nanocrystallites were deposited on single-crystal Si substrates. The mean diameter of the as-deposited nanocrystallites was determined by high resolution scanning electron microscope (HRSEM) to be 13 nm. One sample was then annealed in N_2 gas and another was annealed in O_2 gas. Annealing was performed at a temperature of 800 °C for 10 min. In this paper, we refer to these as the "N_2-annealed" and "O_2-annealed" samples. Additional samples were annealed in O_2 gas at a temperature that was varied from 700 to 900 °C. Since all samples were left in air at room temperature for about 2 years, native oxide layer was observed on all kind of samples. The temperature dependence of PL spectra was measured in a cryostat kept at a pressure of 10^{-2} Pa. An Ar ion laser with a wavelength of 488 nm and a power of 30 mW was used as an excitation light source. A 25 cm monochromator with a photomultiplier was used as a detection system. The signal from the photomultiplier was amplified by Lock-in method. Frequencies of optical chopper of Ar ion laser beam for the Lock-in detection were 15, 150 and 3 kHz.

RESULTS

Figure 1 shows the PL spectra for the as-deposited, N_2- and O_2-annealed samples. The temperature and the frequency of the optical chopper during the measurements were 12 K and 15 Hz, respectively. The intensity ratios for the three samples are not exact due to an optical alinement but are accurate within a few factor. The intensity of the as-deposited sample was smallest among the results for the three samples. The broken line in this figure indicates the results for O_2-annealed sample at room temperature. The PL spectra of as-deposited and N_2-annealed samples were not shown since they are very weak. All samples had two peaks around the green (~2.1 eV) and red (1.2~1.6 eV) regions as shown in Fig. 1. Although the peak energies in the green PL spectra did not depend on post-deposition processing, those in the red PL spectra were sensitive to this. The PL peak energies for as-deposited, N_2- and O_2-annealed samples were about 1.3 eV, 1.4 eV and 1.6 eV, respectively.

The temperature dependence of the PL intensity for the red band of the O_2-annealed sample under the chopping frequency of 15 Hz is shown in Fig. 2. We can observe two regions in this figure: a plateau in a region of low temperature, and a

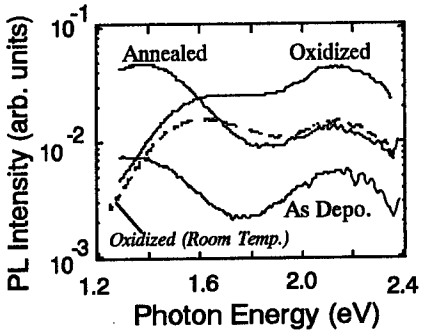


Fig. 1.
PL spectra of as-deposited, N_2- and O_2-annealed samples at 12K. The broken line is a result for the O_2-annealed sample at room temperature. The PL spectra of the as-deposited and N_2-annealed samples measured at room temperature had very small amplitude.

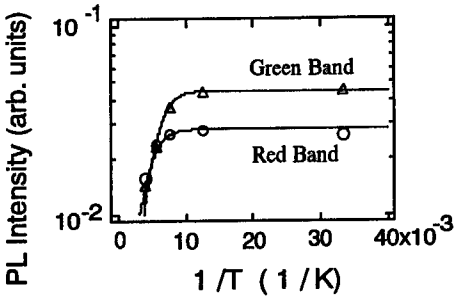


Fig. 2.
Temperature dependence of the red and green band PL intensity for the O_2-annealed sample. The solid lines are the results of curve fitting. (see eq.[3])

decrease in the intensity in a region of high temperature. Every sample that we prepared had a kink point which corresponded to the transition temperature between the low and high temperature regions. A simple model of the temperature dependence of the PL intensity is obtained by assuming a temperature-independent radiative recombination probability, P_r, and a thermal-activation nonradiative recombination probability, P_{nr}.[8] This PL intensity is described as

$$\eta(T) \propto P_r/(P_r+P_{nr}(T)). \quad [1]$$

Here, P_r is the radiative transition probability and $P_{nr}(T)$ is the nonradiative transition probability. P_{nr} is written as

$$P_{nr}(T)=P_{nr0}\exp(-E^*/kT) . \quad [2]$$

Here, P_{nr0} is a constant pre-exponential factor and E^* is the activation energy. Therefore, the temperature dependence of the PL intensity is written as

$$\eta(T) \propto 1/(1+(P_{nr0}/P_r)\exp(-E^*/kT)) . \quad [3]$$

The kink point of temperature dependence in Fig. 2 is a function of P_{nr0}/P_r and E^*. A small value of P_{nr0}/P_r or large value of E^* corresponds to a large value of kink temperature.

The P_{nr0}/P_r and E^* values in eq.[3] can be obtained by curve fitting. The obtained P_{nr0}/P_r values were on the order of 10-100 and E^* values were on the order of 0.01-0.1 eV for the O_2- and N_2-annealed samples. The solid lines in Fig. 2 are the results of curve fitting. Here we define a characteristic temperature, T_K, to express the kink temperature. This is the temperature at which the PL intensity reduces to half its value at the low temperature plateau. The radiative recombination probability, P_r, and the nonradiative recombination probability, P_{nr}, are equal at this temperature as derived from eq.[3].

The T_K values obtained through our experiments are shown in Table I. The T_K values for the red PL of the as-deposited, N_2- and O_2-annealed samples are 90, 160 and 270 K, respectively. The PL intensity of the O_2-annealed sample was the largest and that of the as-deposited sample was the smallest at room temperature. The results of annealing temperature dependence are shown in Table II. The peak energy and T_K value of the red PL of the sample annealed at 700°C were smaller than those for the sample annealed at 800°C, and similar to those for the N_2-annealed sample.

Table I
PL peak energy and T_K for the as-deposited, N_2- and O_2-annealed samples, for an annealing temperature of 800°C.

Process Gas	Annealing Temp.(°C)	PL Peak Energy(eV)	T_K(K)
(as-deposited)	-	1.3	90
		2.2	190
N2	800	1.4	160
		2.1	200
O2	800	1.7	270
		2.2	210

Table II
PL peak energy and T_K for samples annealed in O_2 gas at 700, 800 and 900°C.

Process Gas	Annealing Temp.(°C)	PL Peak Energy(eV)	T_K(K)
O2	700	1.3	150
		2.2	230
O2	800	1.7	270
		2.2	200
O2	900	-	-
		2.2	170

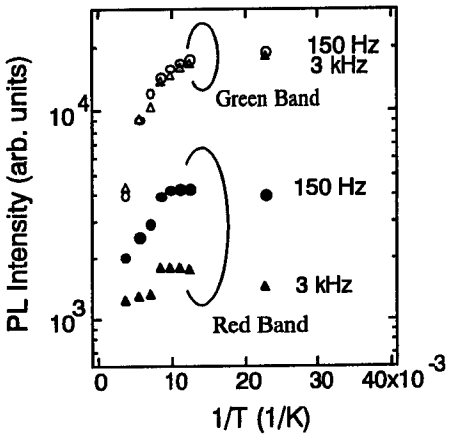


Fig. 3.
Chopper frequency dependence of PL intensity for red band of O_2-annealed nc-Si. The circles and triangles are for 150 Hz and 3 kHz, respectively. The solid and open symbols are for the red band and green band, respectively.

Since we employed Lock-in detection, the chopper frequency dependence of PL intensity and the phase delay of PL signal to the reference signal give us information on the PL lifetime. The correlation between phase delay, ϕ, and lifetime, τ_{PL} is expressed as

$$\omega_c \tau_{PL} = \tan \phi . \qquad [4]$$

Here, ω_c is the chopping frequency, τ_{PL} is the PL lifetime and ϕ is the phase delay. Temperature dependences of PL intensities of O_2-annealed sample when the chopper frequencies are 150 Hz and 3 kHz are shown in Fig.3. The PL intensity of the red band drastically decreased at the chopping frequency of 3 kHz. On the other hand, green PL intensity did not change. PL intensity of as deposited and N_2- annealed samples also did not change under the frequency of 3 kHz. These results indicate that red PL lifetime of O_2-annealed sample is about 0.3 ms and that of as-deposited and N_2-annealed sample was much less than 0.3 ms. The phase delay of the red PL of O_2-annealed sample is shown in Fig.4(a). The phase delay of as-deposited and N_2-annealed sample was under detection limit in our system. This indicates faster lifetime in as-deposited and N_2-annealed samples. The estimated lifetime, τ_{PL}, of O_2-annealed sample estimated by eq. [4] is shown in Fig. 4(b). The value of τ_{PL} was about 0.3 ms at low temperature and was about 0.03 ms at room temperature. The temperature dependence of τ_{PL} is expressed as

$$\tau_{PL}^{-1}(T) = \tau_r^{-1} + \tau_{nr}(T)^{-1}$$
$$= P_r + P_{nr}(T) \ . \qquad [5]$$

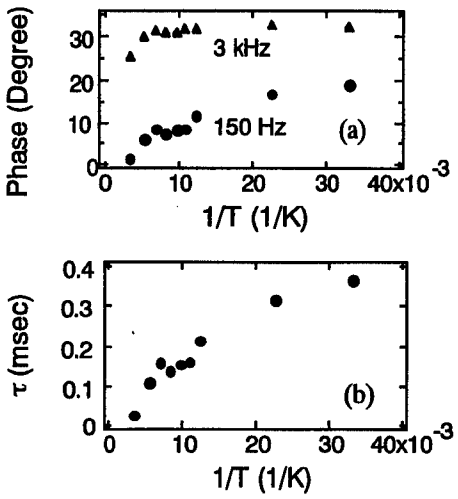


Fig.4.
(a) Chopper frequency dependence of PL phase for the red band of the O_2-annealed sample. (b) Lifetime for red PL of O_2-annealed sample estimated from the data chopped at 150 Hz shown in Fig.4(a).

Here, τ_r and τ_{nr} are the radiative and nonradiative lifetime, respectively. The increase in $P_{nr}(T)$ with increasing temperature corresponds to the decrease in $\eta(T)$ and $\tau_{PL}(T)$ as shown in Fig. 2 and 4(b).

DISCUSSION

The large PL intensity of the O_2-annealed sample at room temperature is the result of the large T_K value. The large T_K value corresponds to a small P_{nr0}/P_r value or a large E^* value. This suggests three possible conditions for large PL intensity at room temperature: small P_{nr0}, large P_r and large E^*. Here we compare the temperature dependence of the PL intensity with that of hydrogenated amorphous Si (a-Si:H) film to investigate the origin of the large T_K value in the O_2-annealed sample. Although a-Si:H film is well known as a bulk-photoluminescent Si material, the PL intensity at room temperature is much smaller than that of O_2-annealed Si nanocrystallites. The E^* and P_{nr0}/P_r values for a-Si:H are about 10^{-1} eV and 10^6, respectively.[9] These results indicate that the large value of the quantum efficiency of the Si nanocrystallites at room temperature is mainly due to the small value of P_{nr0}/P_r because the difference in the values of E^* between a-Si:H and Si nanocrystallites is not so large. There are two possibilities for the small value of P_{nr0}/P_r; small P_{nr0} or large P_r. The P_r value in nanocrystallites should not be so much larger than that in a-Si:H because the PL lifetime of a-Si:H, which is on the order of μs~ms[10], is close to that of our O_2-annealed sample. If the origin of large PL is the increase in P_r value due to confinement, τ_{PL} value in the sample which shows strong PL should decrease with increasing PL intensity. This is not consistent with our results. Therefore, it can be concluded that the large T_K value, i.e. the small P_{nr0}/P_r value, in O_2-annealed Si nanocrystallites is due to the small P_{nr0} value.

The effects of thermal processing of Si nanocrystallites shown in Table II can be also discussed in the view point of nonradiative recombination process. The lifetime of as-deposited and N_2-anneald samples was much faster than that of O_2-annealed sample. If the origin of the increase in the T_K value of O_2-annealed sample is the increase in P_r value, lifetime of the sample should be smaller. This indicates that the difference of the T_K value between the O_2-annealed and other, as-deposited and N_2-annealed, samples is due to the nonradiative recombination probability, P_{nr0}. These results suggest that the origin of the large PL intensity in the O_2-annealed sample is decrease in the nonradiative recombination probability rather than the increase in the radiative recombination probability.

We could find some similarity between the as-deposited Si nanocrystallites and a-Si:H film. The T_K value and PL peak energy of a-Si:H were 110 K and 1.3 eV, respectively.[9] These values are close to that of as-deposited Si nanocrystallites. This suggests a possibility that the as-deposited sample includes considerable number of amorphous-like Si nanoparticles. The increase in the T_K value after annealing in N_2 gas may be attributed to the recrystallization of the nanoparticles because oxidation does not take place during this annealing process. The difference in the PL properties of the N_2- and O_2-annealed samples indicates the importance of the surface reaction with oxygen. Because the T_K value corresponds to the P_{nr0} value, the O_2-annealing

processing decreases the P_{nro} value. This indicates that the origin of the large PL intensity for the O_2-annealed sample is the reduction of the nonradiative recombination probability.

To clarify the effect of the oxidation, we measured the strength of Si-O IR absorption. No remarkable difference in the peak intensity for the as-deposited, N_2- and O_2-annealed samples was observed. This indicates that the surface of the as-deposited sample was already covered by a native oxide layer, and that the increase in the oxide thickness due to annealing in O_2 gas was smaller than the thickness of this original native oxide layer. This suggests that the PL intensity is not strongly dependent on the thickness of the oxide layer, but that it is very dependent on the quality of Si/SiO_2 interface. Thus, the origin of the large T_K, that is small P_{nr0}, value is the existence of a high quality Si/SiO_2 interface. This high quality interface results in small interface defect density. Furthermore, abrupt potential difference at the interface induce strong confinement of electron-hole pair. These effects should reduce nonradiative recombination channel in O_2-annealed sample.

As shown in Table II, the peak energy and the T_K value of the red PL of the sample annealed at 700°C were smaller than those for the sample annealed at 800°C, and similar to those for the N_2-annealed sample. This indicates that an annealing process similar to that for the N_2-annealed sample occurred, but that the oxidation process was incomplete at this temperature. When the annealing temperature was raised to 900°C, the red PL was hardly observed. This result is similar to that for porous Si.[5] Observation of a reduction in the number of nanocrystallites after annealing at temperatures above 800°C has been reported.[5] The emission results for the green band were much different from those for the red band. The changes in the values of T_K and the PL peak energies were smaller than those for the red PL spectra as shown in Tables I and II. The PL lifetime of the green PL estimated by the phase delay in the O_2-annealed sample is much faster than that of red band as shown in Fig.3. The origin of the green band emissions is more complicated than that for the red band. The intensity of the red PL in air was comparable with that in a vacuum. On the other hand, the intensity of the green PL decreased with irradiation of excitation light to about 1/10 of its initial state in air, then recovered with subsequent vacuum evacuation.[7] The existence of an ambient dependence of the PL intensity suggests that the origin of the green band correlates to processes occurring in the surface region.

CONCLUSIONS

We measured the temperature dependence of the PL spectra of Si nanocrystallites prepared by the inert-gas-ambient pulsed laser ablation technique. The temperature dependence of peak energy and intensity of the red PL was found to be dependent on the post deposition processing. We observed strong PL at room temperature when the sample had been annealed in O_2 gas at 800 °C. The temperature dependence of PL intensity was smallest and that of PL lifetime was largest in the O_2-annealed sample among the specimens we prepared. These results suggest that the origin of the large PL intensity in the O_2-annealed sample is decrease in the nonradiative recombination probability rather than the increase in the radiative recombination probability. Our results indicate importance of nonradiative recombination processes

of red band PL in Si nanocrystallites.

ACKNOWLEDGMENTS

This work was partially supported by The Hirao Taro Foundation of the Konan University Association for Academic Research and by a Grant-in-Aid for Scientific Research from the Ministry of Education, Science and Culture of Japan. Part of this work was conducted in the program "Advanced Photon Processing and Measurement Technologies" of the Agency of Industrial Science and Technology, the Ministry of International Trade and Industry, consigned to the R&D Institute for Photonics Engineering from the New Energy and Industrial Technology Development Organization.

REFERENCES

1. L.T. Canham, Appl. Phys. Lett. **57**, 1046 (1990).
2. S. Furukawa and T. Miyasato, Jpn. J. Appl. Phys. L2207 (1988).
3. H. Takagi, H. Ogawa, Y. Yamazaki, A. Ishizaki and T. Nakagiri, Appl. Phys. Lett. **56**, 2379 (1990).
4. Y. Yosida, S. Takeyama, Y. Yamada and K. Mutoh: J. Appl. Phys. **68**, 1772 (1996).
5. Y. Kanemitsu: Physics Reports **263**, 1 (1995).
6. C. Delerue, G. Allan and M. Lannoo. ; in *Semoconductor and semimetals Vol.49*, D. J. Lockwood, Editor, p253, Academic Press, San Diego, (1998).
7. Y. Yamada, T. Orii, I. Umezu, S. Takeyama and T. Yoshida, Jpn. J. Appl. Phys. **35**, 1361 (1996).
8. J.I. Pankove; *Optical processes in Semiconductors*, Dover, New York (1971).
9. I.G. Austin, W.A. Jackson, T.M. Searle, P.K. Bhat and R.A. Gibson, Philos. Mag. B **52**, 271 (1985).
10. R. A. Street ; in *Semoconductor and semimetals Vol.21 Pt.B*, J. I. Pankove, Editor, p197, Academic Press, New York (1984).

Observation of an Electron Charging Effect in Si Nanocrystals Embedded in an Ultrathin Gate Oxide

Tatsuro Maeda, Eiichi Suzuki, Isao Sakata, Mitsuyuki Yamanaka and Kenichi Ishii

Electrotechnical Laboratory, 1-1-4, Umezono, Tsukuba-shi, Ibaraki 305, Japan
Electric mail: tmaeda@etl.go.jp

Abstract

We have investigated the electrical characteristics of Si nanocrystals fabricated by the rapid thermal oxidation (RTO) of an ultrathin chemical vapor deposition (CVD) amorphous Si (a-Si:H) film(<10nm). It is found from the transmission electron microscope (TEM) observation that the ultrathin RTO film contains Si nanocrystals of less than 5nm in diameter. The dynamic measurement of the electrical conduction through the ultrathin RTO film reveals novel features indicating a tunnel current modulation such as the current peak and valley and the hysteresis. The electron charging effect in Si nanocrystals and the consequent screening effect on reducing the tunnel current can explain these experimental results. We also fabricated the 3-terminal device with Si nanocrystals, which shows the similar charging effect, modulated by the gate voltage

Introduction

The semiconductor nanoscale structure has led to several significant observations of low dimensional phenomena and demonstrations of their usefulness in electronic and optoelectronic devices. Especially, Si nanocrystals have received much attention[1,2,3], and shown interesting phenomena in a MOS structure[4,5] and some remarkable performances in a single electron transistor[6,7,8], a single electron memory[9,10], and a nano-crystal memory[11]. To widely apply such a new electronic material to novel devices, it is desirable not only to exactly understand the electron

transport characteristics but also to develop the fabrication method, which is simple and compatible with a conventional Si technology.

In this paper, we report on a fascinating fabrication method of Si nanocrystals embedded in the ultrathin oxide by the rapid thermal oxidation (RTO) of an ultrathin chemical vapor deposition (CVD) amorphous Si (a-Si:H) film. The dynamic current vs. voltage (I-V) characteristics present the novel features such as a current peak and valley and a hysteresis in the tunnel current through the ultrathin RTO film including Si nanocrystals. The electron charging in Si nanocrystals and its screening effect on the tunnel current can explain this tunnel current modulation.

Experiment

We fabricated the RTO diode structure with Si nanocrystals as schematically shown in Fig. 1. At first, an n-type, (100)-oriented, 2 Ω-cm Si substrate was oxidized to form a field oxide of 230nm in thickness in dry O_2 at 1100℃. The active device area of $3x3\mu m^2$ was formed by etching the window of the field oxide. A 1.9nm-thick tunnel oxide was thermally grown in this active device area in dry O_2 (0.7%) and N_2 at 900℃. This tunnel oxide acts as the first barrier layer electrically. Next, an ultrathin thermal CVD a-Si:H (10nm) film was deposited on the tunnel oxide at 430℃ in Si_2H_6 (18cc/min) and H_2 (100cc/min) atmosphere. Then, the RTO processing was performed in pure O_2 at 800℃ for 30sec and 10min followed by gradual cooling for 20min in pure N_2. During the RTO, thermal crystallization and oxidation of the ultrathin a-Si:H film simultaneously occur. Finally, the aluminum gate was formed on some samples to fabricate the diode structure for the electrical measurement.

For fabricating a 3-terminal device, the ultrathin RTO film was formed on the V-shaped ditch between two n^+-Si areas isolated by an anisotropic etching of Silicon-on-insulator (SOI). Si nanocrystals embedded in an ultrathin gate oxide are placed between the source and the drain. Poly-Si gate was formed on the ultrathin RTO film.

All the electrical measurement was carried out at room temperature in dark by using a semiconductor parameter analyzer (HP4156A).

Results and discussion

Figures 2 shows the cross-sectional transmission electron microscope (TEM) images of (a) 30sec and (b) 10min RTO diode samples. In the 30sec RTO diode sample, random Si lattice images can be seen clearly in a 7nm-thick layered structure between the tunnel oxide layer and the upper amorphous layer. That is, a part of the a-Si:H film of 3nm was partially oxidized during the 30sec RTO process. This upper amorphous layer was identified as SiOx (x<2) by the energy disperse X-ray spectroscopy (EDX) analysis. Oxidation of the a-Si:H film proceeds from the surface, whereas the remainder is poly-crystallized on the tunnel oxide during the RTO process. On the other hand, in the 10min RTO diode sample, it is difficult to distinguish a poly-Si layer between the upper oxide and tunnel oxide layers, compared with the case of the 30sec RTO sample. It should be noted, however, that many Si lattice image regions of less than 5nm are dispersed in the amorphous SiOx matrix. During the prolonged RTO process for 10min, it is considered that oxygen penetrates through grain boundaries and Si nanocrystals are formed possibly with a self-limiting oxidation of small Si grains. Consequently, we obtained Si nanocrystals by the proper RTO processing of the ultrathin a-Si:H films.

Before discussing the electrical properties, it is important to explain the present I-V measurement of the diode structures in time scale. Since a transient current is usually observed in the I-V measurement when a carrier charging occurs, we have to distinguish between the static and the dynamic I-V characteristics. To obtain the static characteristic at each gate voltage, it is necessary to wait for some time. We define this waiting time as a "delay time". Figure 3 shows the round sweep I-V characteristics of the 10min RTO diode sample, where the delay time is (a) 60sec and (b) 0sec. An electron current flows from the Si substrate to the gate through the tunnel oxide and RTO film. It is apparent from Fig. 3 (a) that only the simple Fowler-Nordheim tunnel current flows and the I-V curves of the forward and reverse sweeps coincide completely. We consider these I-V characteristics to be the static behavior. On the other hand, I-V characteristics measured under the delay time of 0sec (Fig. 3 (b)) indicate the novel features of the current peak and valley at the gate voltage Vg from 2.5V to 4.2V in the forward sweep. The reverse sweep I-V curve shows no current peak and valley, and corresponds to the steady-state tunnel current. Therefore, the current peak and valley in the forward sweep are not attributed to a resonant tunneling. These characteristics

were quite reproducible. In Fig. 3 (b), the I-V characteristic of the 30sec RTO diode sample is shown additionally to compare with that of the 10min RTO diode sample. For the 30sec RTO diode sample, we never observed these notable features even under the delay time of 0sec.

To investigate this novel dynamic behavior carefully, the time dependence of the tunnel current for the 10min RTO diode sample was measured. The tunnel current vs. time (I-t) characteristics are summarized in Fig. 4, where the gate bias voltage is from 2V to 5.5V and the measurement time scale is from 100msec to 100sec. At Vg=2V, only the initial tunnel current decrease is observed. This initial gradual decrease of the tunnel current is attributed to the slight electron trapping effect in both oxide layers and/or at the interfaces. This supplementary current decrease is not considered here. At Vg=2.5~4.5V, however, the time-dependent tunnel current indicates the clear current reduction from the higher level to the lower level. At Vg=3.5V, for example, the constant tunnel current of around 200pA flows until 1sec. Consecutively, the tunnel current reduces in the period from 1sec to 10sec, and is eventually settled down only at 2pA after 10sec. The reduction in the tunnel current during this transient period (1~10sec) indeed amounts to 1/100. This tunnel current reduction is directly related to the current peak and valley as shown in the forward sweep I-V curve in Fig. 3 (b). In the case that the tunnel current is measured at the time when the tunnel current level at higher Vg underlies that at lower Vg, the tunnel current peak and valley appear in the I-V characteristic. When the current is measured in the steady-state current period (after 60sec), we obtain the static characteristics of the tunnel current. At the higher gate voltage of more than 5V, any tunnel current reduction is not observed in this measurement time sale.

The above-mentioned experimental results can be explained by the electron charging in the Si nanocrystals and the consequent screening effect on the tunnel current as illustrated in Fig. 5. Figure 5 shows the schematic Ig vs. Vg and Ig vs. time characteristics and the corresponding real space models at each gate voltage. At first, we observe the tunnel current (A state) at the gate voltage higher than the first threshold voltage (V_{t1}; 3V in Fig. 3(b)). There are many electron tunnel paths via relatively large Si nanocrystals, and the tunnel current increases with increasing Vg. Simultaneously, the electron charging at the Si nanocrystals starts (B state). Once electrons are trapped in small Si nanocrystals, the screening to the tunnel current paths occurs in the vicinity

of the charged Si nanocrystals. Because the charging in the Si nanocrystals forces up the surrounding electronic potential that makes narrowing of the tunnel current paths in parallel with the charged Si nanocrystals (C state; around 4V in Fig. 3(b)). The incubation time until the start of the screening depends on the electron charging efficiency at each Si nanocrystals. By increasing the gate voltage furthermore, the tunnel current rises up again, keeping the charged state in Si nanocrystals. The second threshold voltage (V_{t2}; 4.2V in Fig. 3(b)) refers to the starting voltage of the screened tunneling current. The reverse sweep current consists of the fully screened tunnel current and coincides, therefore, with the static tunnel current curve shown in Fig. 3(a). The fixed spacing between the first and second threshold voltage suggests the definite electron charging effect in the Si nanocrystals. The exact charging sites in the Si nanocrystals are not known at present. But we emphasize here that the 10min RTO sample contains so small Si nanocrystals that we can observe the electron charging as the screening effect on the tunnel current even at room temperature. When the size of Si nanocrystals is more than 5nm as in the case of the 30sec RTO sample, it is difficult to observe the screening effect because of the small charging energy in larger Si nanocrystals. We consider that our experimental result is the substantial demonstration of the tunnel conductance modulation utilizing the screening effect of electron charging.

We also fabricated the 3-terminal device with Si nanocrystals embedded in ultrathin gate oxide as schematically shown in the inset of Fig. 6. An electron current laterally flows from the source to the drain via Si nanocrystal. In the drain current vs. voltage characteristics (Fig. 6), we find the similar one or two current peaks and valleys as I-V characteristics in the RTO diode structure due to the charging and screening effect. Besides, the gate voltage modifies the Id-Vd characteristics. We consider that the gate voltage changes the electric potential of several charging sites as well as the tunnel barrier height between source and drain and consequently controls the threshold voltage of the tunnel current.

Conclusion

In summary, we have studied the dynamic and static electron conduction behavior of the RTO film of the ultrathin CVD a-Si:H film using the MOS diode and 3-terminal structure. The RTO ultrathin film contains Si nanocrystals of less than 5nm

in diameter. The dynamic I-V measurement of these films reveals novel features such as the tunnel current peak and valley, and the hysterisis characteristic. Based on the time-dependent current measurement, these phenomena can be elucidated by the electron charging in Si nanocrystals and the consequent screening effect on the tunnel current. Such the tunnel current modulation is expected to open the way to novel Si devices.

Acknowledgment

The authors would like to thank Drs. T. Sakamoto and T. Sekigawa for their encouragement.

References

[1] Q.Ye, R.Tsu, and E.H.Nicollian, Phys. Rev. B, 44, 1806 (1991).

[2] A.Kohno, H.Murakami, M.Ikeda, S.Miyazaki and M.Hirose, Proc. of SSDM'97, p567 (1997).

[3] J.Lutzen, A.H.Kamal, B.A.Sanborn, M.V.Sidorov and M.N.Koziki, D.J.Smith, and D.K.Ferry, Abstracts of Silicon Nanoelectronics Workshop, 1997, p24.

[4] S. Y. Chou and A. E. Gordon, Appl. Phys. Lett. 60, 1827 (1992).

[5] E.H.Nicollian and R.Tsu, J. Appl. Phys., 74, 4020 (1993).

[6] Y. Takahashi, M. Nagase, H. Namatsu, K. Kurihara, K. Iwadate, Y. Nakajima, S. Horiguchi, K. Murase, and M. Tabe, Electron. Lett. 31, 136 (1995).

[7] E. Leobandung, L. Guo, Y. Wang, and S. Y. Chou, Appl. Phys. Lett. 67, 938 (1995).

[8] K. Yano, T. Ishii, T. Hashimoto, T. Kobayashi, F. Murai, and K. Seki, Appl. Phys. Lett. 67, 828 (1995).

[9] K. Yano, T. Ishii, T. Hashimoto, T. Kobayashi, F. Murai, and K. Seki, IEEE Trans. Electron Devices 41, 1628 (1995).

[10] L. Guo, E. Leobandung, and S. Y. Chou, Appl. Phys. Lett. 70, 850 (1997).

[11] S. Tiwari, F. Rana, H. Hanai, A. Hartstein, E. F. Crabbe, and K. Chan, Appl. Phys. Lett. 68, 1377 (1996).

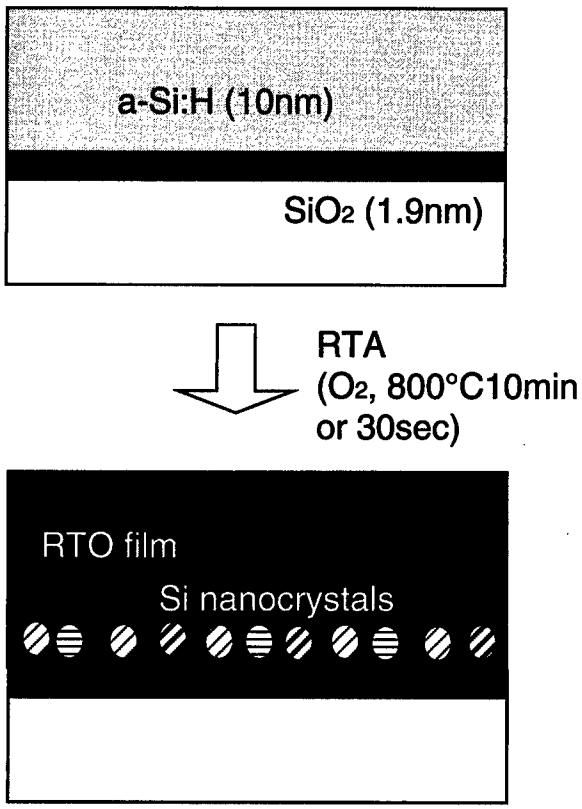
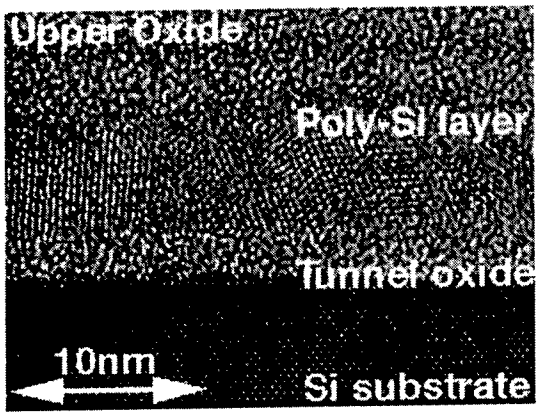
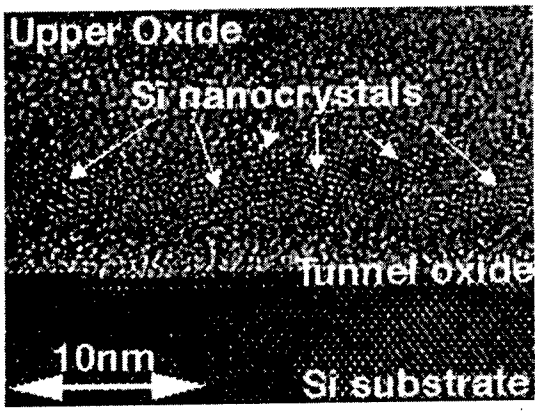


Fig. 1. Schematic cross section of the RTO sample structure fabricated.



(a)



(b)

Fig. 2. Cross-sectional TEM images of (a) 30sec and (b) 10min RTO samples.

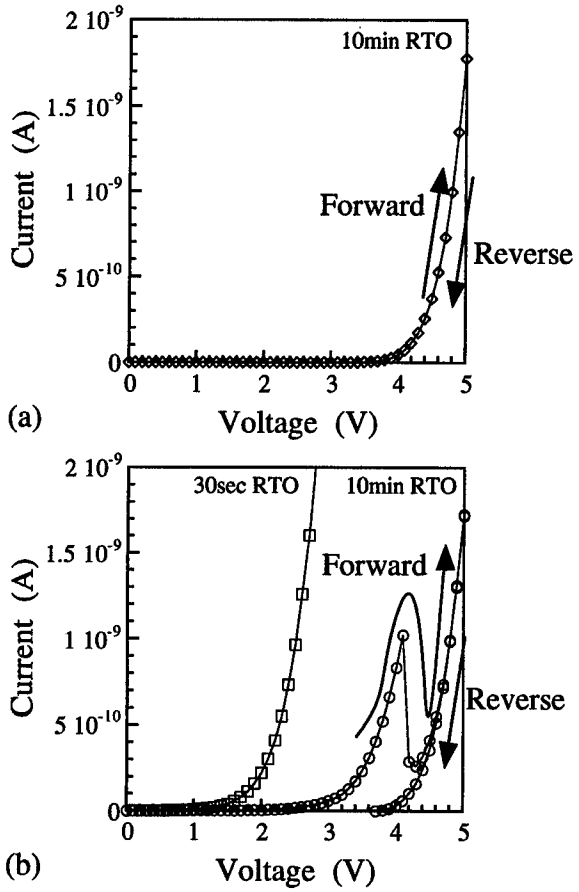


Fig. 3. I-V characteristics of the 10min RTO diode sample measured at room temperature, where the measurement delay time is 60sec (a) and 0sec (b). In Fig. 3 (b), the I-V characteristic of the 30sec RTO diode sample is shown additionally.

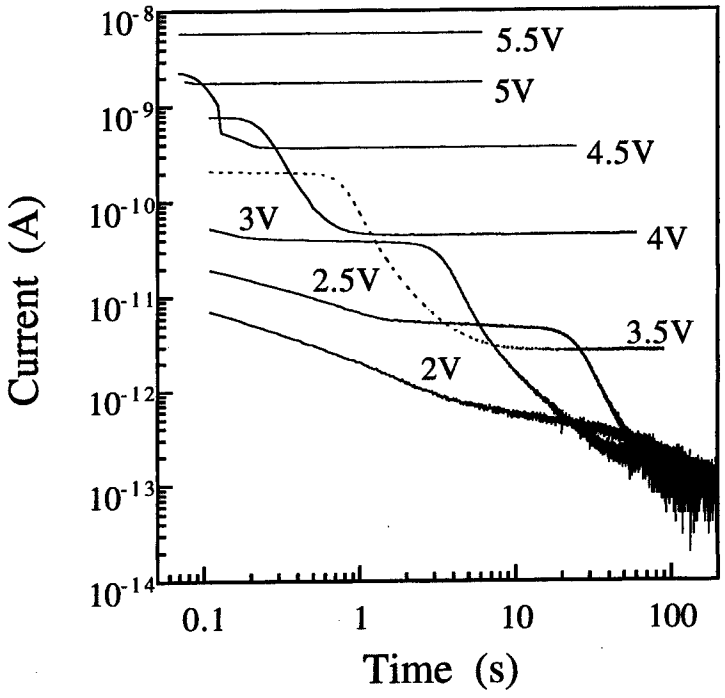


Fig. 4. Time dependence of the tunnel current of the 10min RTO diode sample with the gate voltage as a parameter measured at room temperature. Dashed line indicates Vg=3.5V.

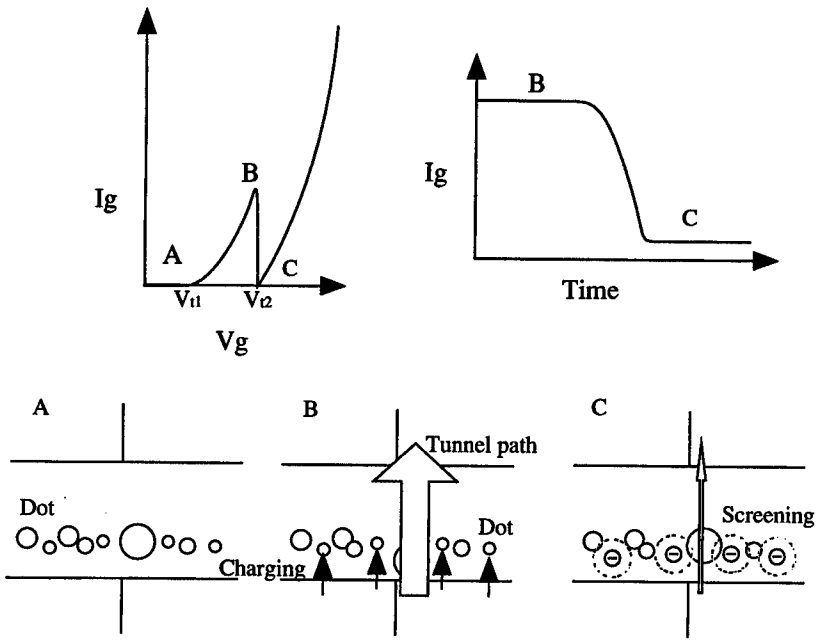


Fig. 5 Schematic Ig vs. Vg and Ig vs. time characteristics and the corresponding real space models at each state.

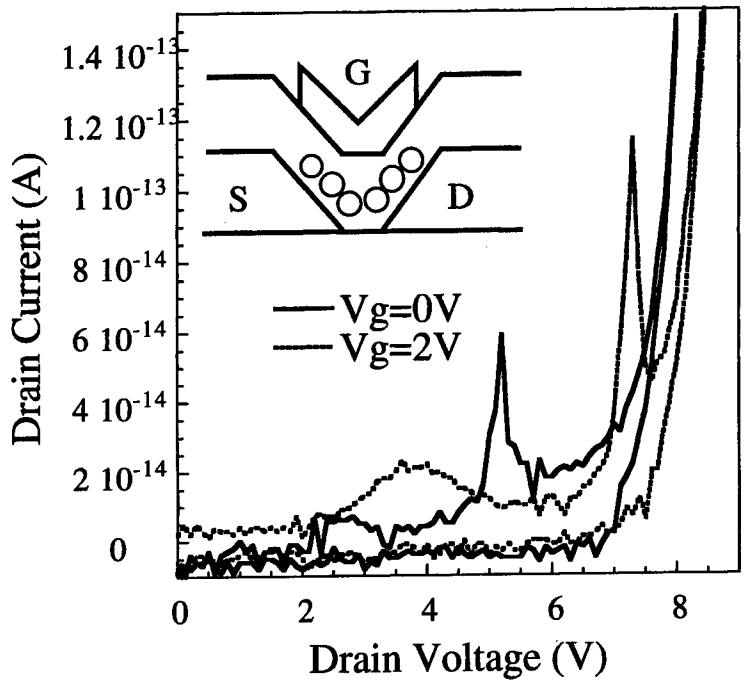


Fig. 6 Id vs. Vd characteristics of 3-terminal device. Vg=0, 2V

FORMATION AND CHARACTERIZATION OF ERBIUM-DOPED SILICON NANOCRYSTALS

John V. St. John and Jeffery L. Coffer*
Department of Chemistry,
Texas Christian University, Fort Worth, Texas 76129

Yandong Chen and Russell F. Pinizzotto*
Materials Science Department
University of North Texas, Denton, Texas 76203

ABSTRACT

Two common approaches to the formation of efficient light-emitting silicon are quantum confinement and the incorporation of luminescent rare earth ions such as Er^{3+} into crystalline Si. This paper describes the synthesis and characterization of discrete Er^{3+}-doped Si nanocrystals produced in the vapor phase by the pyrolysis of disilane gas in the presence of the volatile Er^{3+} complex $Er(tmhd)_3$ (tmhd = 2,2,6,6 tetramethyl-3,5-heptanedionato). Individual Er^{3+}-doped Si nanocrystals are found to aggregate into larger clusters; the size distributions of those clusters can be controlled by varying the length of the pyrolysis oven. Energy dispersive X-ray analyses of Er^{3+}-doped Si nanocrystals detect Er and Si while control samples produced in the absence of $Er(tmhd)_3$ detect only Si. High resolution electron microscopy (HREM) shows the presence of lattice defects in all samples. Room temperature near IR PL at 1540 nm, associated with Er^{3+}, was detected from the doped nanoparticles. The mechanism for Er^{3+} photoluminescence excitation in Er^{3+}-doped Si nanocrystals is thought to be a carrier mediated process through energy transfer from a silicon exciton.

* To Whom Correspondence Should Be Addressed.

INTRODUCTION

The desire to integrate Si into optoelectronic platforms is hampered by the lack of a suitable Si-based light emitter [1]. Though several routes for light emission from Si have been explored, two of the more promising avenues include: 1) the shrinking of Si to nanoscale dimensions giving rise to kinetic quantum-confined visible luminescence [2, 3], and 2) the incorporation of luminescent rare earth ions such as Er^{3+} which produce defect luminescence ascribed to electronic transitions of $4f$ orbitals [4-7]. To date, most studies of Er^{3+} luminescence have focused on erbium which has been ion-implanted in bulk Si [8], or erbium and Si co-deposited as thin films [9]. It is desirable to understand the properties of isolated, individual silicon nanocrystals with dimensions below those necessary for quantum confinement which have been doped with luminescent rare earth ions. We describe here the preparation of discrete erbium-doped silicon nanocrystals prepared by the co-pyrolysis of disilane and the volatile complex $Er(tmhd)_3$ (tmhd = 2,2,6,6 tetramethyl-3,5-heptanedionato). These nanocrystals are characterized by transmission electron microscopy (TEM), high resolution transmission electron microscopy (HREM), energy dispersive X-ray analysis, and infrared (IR) vibrational spectroscopy. The optical properties of Er^{3+}-doped Si nanocrystals are probed using UV-visible absorption spectroscopy, and near IR photoluminescence (PL) spectroscopy.

EXPERIMENTAL

Discrete Si nanocrystals have been produced by several methods including laser ablation of bulk crystalline Si [10], the gas phase pyrolysis of silane or disilane [11-14], and the reduction of halosilanes [15]. The method chosen for the production of Er^{3+}-doped Si nanocrystals involves a modification of a high temperature aerosol reaction involving the pyrolysis of disilane (Si_2H_6) in a He carrier gas followed by oxidation and isolation as a colloidal solution in ethylene glycol [11-13]. The modified pyrolysis apparatus allows the introduction of an additional vapor phase reactant into the gas stream. The reactor is constructed from 7 mm ID quartz tubing. Gas flow is regulated using mass-flow controllers (MKS Inc.) which are connected to the pyrolysis system with O-ring fittings (Cajon Inc). The disilane (0.48% Si_2H_6 in He (Praxair)) is maintained at a fixed flow rate during the course of an experiment; flow rates employed ranged from 2.8 to 4.0 sccm. A He carrier gas (Praxair, UHP semiconductor grade) is used to further dilute the disilane mixture at a flow rate of 3000 sccm. If desired, the He carrier gas can be diverted through a bubbler which contains a MOCVD precursor. The Er precursor chosen for these reactions is the well known Er^{3+} chemical vapor

deposition precursor, $Er(tmhd)_3$. The gases mix and flow through a short pyrolysis oven operating at 1000° C. The length of the oven remained constant for a given 24 hour pyrolysis run, but could be varied for different experiments from 1.5 to 3.0 to 6.0 cm. After pyrolysis the reaction mixture travels downstream where the aerosol is collected as a colloid in acidified ethylene glycol (5% acidified H_2O at pH = 1). After a 24 hour pyrolysis reaction period, the product consists of a yellow colloid and brown solid in the ethylene glycol bubbler. Nanocrystals were extracted from the solution, washed, and purified to separate the as-formed nanoparticles from an unreacted, physisorbed Er^{3+} present in solution.

Structural characterization of Er^{3+}-doped Si nanocrystal aggregates was performed using a JEOL 200CX TEM at the University of North Texas. Samples were deposited on carbon coated copper grid and the ethylene glycol allowed to evaporate prior to imaging. Structural characterization of individual Er^{3+}-doped Si nanocrystals by HREM was performed using a Hitachi H9000 at UNT. X-ray energy dispersive spectroscopy (XEDS) analyses of Er^{3+}-doped Si aggregates were performed in the scanning transmission electron microscopy (STEM) mode of the JEOL 200CX. Selected area electron diffraction patterns (SADP) were obtained in conjunction with TEM analyses. UV-visible spectroscopy was obtained using a Hewlett-Packard 8452A diode array spectrometer.

Optical characterization of Er^{3+}-doped Si nanocrystals was performed using low resolution (±4 nm) near IR photoluminescence (PL) spectra were obtained using an Applied Detector Corp. liquid N_2 cooled Ge detector in conjunction with a Stanford Research Systems chopper/lock-in amplifier and an Acton Research Corp. 0.25 m monochromator. Sample excitation was provided by a Coherent Ar^+ laser. A 10 cm lens was used to focus light emitted from the samples on the monochromator entrance slit. Emitted light was collected at right angles to excitation. A 1000 nm cutoff filter (Melles Griot) was positioned over the monochromator entrance slit to filter out second and third order harmonics from the exciting line.

RESULTS

A conventional low resolution, bright-field transmission electron micrograph of a washed Er^{3+}-doped Si nanocrystal sample collected from a pyrolysis run using a 3.0 cm long oven is shown in Figure 1. The micrograph shows two distinct types of material: (1) light contrast areas (L) and (2) dark contrast areas (D). The clusters are actually aggregates composed of smaller Si nanocrystallites. Selected area diffraction patterns (SADP) obtained from both the light and dark contrast areas show diffraction rings consistent with the diamond cubic phase of Si. SADP obtained for control samples produced

without the introduction of $Er(tmhd)_3$ to the reactor also show diffraction rings consistent with diamond cubic Si.

The average size of these Er^{3+}-doped Si nanoparticle aggregates have been determined by measuring the diameters of 400 to 700 structures for each type of sample. Since these structures are aggregates of smaller nanocrystals, structure sizes are described using lognormal statistics. Average sizes and standard deviations for three reaction furnace lengths are presented in Table 1.

Table 1 Statistical data for structure size versus reaction furnace length

Reaction Furnace Length (cm)	Average Structure Size Linear Statistics (nm)	σ (Linear Statistics) (nm)	Average Structure Size Lognormal Statistics (log nm)	σ (Lognormal Statistics) (log nm)
1.5	11.3	3.8	1.03	0.14
3.0	13.8	4.8	1.11	0.15
6.0	15.2	6.6	1.15	0.16

High resolution electron microscopy (HREM) was used to probe the structure of the dark aggregates observed in the TEM analyses. It was hoped that the location of Er in the Si lattice could be elucidated. Figure 2 is a HREM image of one of the dark contrast areas observed by TEM from a sample produced with a 3.0 cm oven. The aggregates are composed of numerous discrete Si nanoparticles with a mean diameter of 3 nm. This size distribution is well within the regime required for kinetic quantum confinement. Many of the nanocrystals observed contain various types of lattice defects. Similar studies of control samples without Er^{3+} show the same types of lattice defects. The defects are most likely the result of rapid growth caused by the short high temperature anneal times.

Analysis of light and dark contrast areas by XEDS was used to probe for the presence of erbium. Figure 3a is an energy dispersive X-ray spectrum obtained from a dark contrast are similar to D in Figure 1. The peaks present in this spectrum are assigned to Si, Fe, Cu-Kα, Cu-Kβ, Er-L, and Er-M. The Si and Er peaks are from the sample itself, the Cu peaks arise from the Cu grid used to support the sample, and the Fe is an artifact from the sample chamber. Quantitative analysis of multiple spectra yields an estimated Er^{3+} concentration of 2-3%. Figure 3b shows a typical x-ray energy dispersive spectrum for a light contrast area similar to L in Figure 1. The spectrum shows only peaks for Si, Fe, Cu-Kα, and Cu-Kβ. There is no evidence of Er in this type of particle. Control samples produced without $Er(tmhd)_3$ have spectra similar to Figure 3b.

Both the absorption and photoluminescence spectra of the Er^{3+}-doped Si nanocrystals have been measured. A typical UV/visible absorption spectrum is shown in Figure 4 for an ethylene glycol solution of Er^{3+}-doped Si nanoparticles with a mean particle size of 3 nm. A broad absorption tail is observed with the onset of absorption near 600 nm. This type of absorption spectrum is observed in all samples produced with and without the presence of $Er(tmhd)_3$ in the reaction stream. This tail is indicative of an indirect-gap semiconductor and has been observed for solutions of homogeneous oxide-capped Si nanocrystallites produced by pyrolysis of disilane gas in previous studies [11].

A KBr pellet of the washed Er-doped Si nanocrystals was formed for analysis by infrared (IR) absorption, the spectrum is shown in Figure 5. The IR absorbance spectrum shows a Si-O stretch near 1100 cm^{-1} (strong), and the O-H stretch at approximately 3500 cm^{-1}. The sharp peaks which show up near 1400, and 1700 cm^{-1} are residual THF solvent. This indicates that the Er^{3+}-doped Si nanocrystals are capped with an oxide shell.

The room temperature photoluminescence of Er^{3+}-doped Si nanoparticles has also been measured. Upon excitation at 488 nm, the anticipated Er^{3+} emission maximum near 1540 nm, associated with the $(^4I_{13/2})\rightarrow(^4I_{15/2})$ transition, is observed. Figure 6 shows representative photoluminescence spectra for Er^{3+}-doped Si nanocrystals in ethylene glycol from three different pyrolysis experiments. No visible luminescence associated with kinetically quantum-confined Si nanocrystals is detected, however [11]. Two scenarios are possible for the fundamental luminescence mechanism of the Er^{3+} centers [15]: 1) Si carrier-mediated excitation of the Er centers by energy transfer, or 2) direct absorption into energy levels associated with the Er^{3+} centers. Carrier mediated excitation is dependent on energy transfer from excitons in Si which excites the Er^{3+} ion to produce the 1540 nm transition. Direct absorption is prevalent in insulating systems such as glasses in which excitation at 488 nm results in the population of the $^4F_{7/2}$ energy level which can then undergo non-radiative decay to the $^4I_{13/2}$ level leading to the fluorescence transition at 1540 nm.

Preliminary measurements of wavelength and power dependencies have been carried out to elucidate the mechanism for Er^{3+} excitation in Si nanocrystals. For an excitation wavelength range of 475 to 514 nm at a constant power of 50 mW, we find that there is a monotonic decrease in the 1540 nm luminescence intensity as the excitation wavelength increases. Figure 7 illustrates the dependence of normalized emission intensity as a function of wavelength for a sample of Er^{3+}-doped Si nanocrystallites in ethylene glycol prepared from a pyrolysis in a 3.0 cm oven. Carrier-mediated excitation relies on an electronic level of the Er^{3+} ion close in energy to the Si conduction band to trap an exciton from Si, which then transfers energy through an Auger process to the Er^{3+} ion for excitation [15].

Measurements were made of the dependence of emission intensity on excitation power (Figure 8). This sub-linear PL power dependency has been reported for Er^{3+} in several systems [16-18]. Sub-linear power dependency is found in direct absorption systems as a consequence of the saturation of optically active Er^{3+} centers with exciting light. It is also consistent with a carrier mediated process involving non-radiative Auger quenching.

Visible photoluminescence ascribed to quantum confined Si nanocrystals was not detected from Er^{3+}-doped Si nanocrystal samples or for control samples produced in the absence of $Er(tmhd)_3$, even though the Er^{3+}-doped Si nanocrystals are below the size limits required for kinetic quantum confinement. The absence of this emission in Er^{3+}-doped Si samples can be explained by the carrier-mediated excitation process as energy transfer occurs between the Si exciton and the Er^{3+} centers. The Er^{3+}-doped Si nanocrystal samples also show evidence for lattice defects which act as sites for non-radiative recombination. Homogeneous Si nanocrystals produced via disilane pyrolysis in a 3.0 cm oven without the presence of $Er(tmhd)_3$ have an average size of 12 nm, well above the size limit required for kinetic quantum confinement. However, these "control" Si nanocrystals produced without $Er(tmhd)_3$ also show evidence of lattice defects, which can act as sites for non radiative recombination (Figure 9).

CONCLUSIONS

These experiments show that it is possible to form discrete erbium doped Si nanoparticles. This revelation is important from a fundamental perspective in that it is now possible to study the effects of quantum confinement on rare earth centers incorporated within a Si host. Er^{3+}-doped Si nanocrystals show characteristic 1.54 μm photoluminescence ascribed to the $^4I_{13/2} \rightarrow {}^4I_{1/2}$ electronic transition of Er^{3+}. Er^{3+}-doped Si nanocrystals show a sub-linear dependency on pump laser power which is either a manifestation of Er^{3+} center saturation or evidence of Auger quenching processes from the Si lattice. Er^{3+}-doped Si nanocrystals show a monotonic decrease in 1.54 μm emission intensity as the excitation wavelength increases, consistent with a carrier-mediated process. A carrier-mediated excitation process gives further evidence that the Er^{3+} centers reside within the Si lattice.

ACKNOWLEDGEMENTS

The authors gratefully thank the Robert A. Welch Foundation for their financial support of this research.

REFERENCES

[1] Iyer, S.; Xie, Y.-H. *Science*, **260**, 40, (1993).

[2] Canham, L., *Appl. Phys. Lett.* **57**, 1046 (1990).

[3] For an extensive compilation of fundamental and applied research concerning porous silicon see *Properties of Porous Silicon*, Leigh Canham, Ed., EMIS Datareviews Series, INSPEC / IEEE Press (UK), 1997.

[4] Ennen, H.; Schneider, J.; Pomrenke, G.; Axmann, A. *Appl. Phys. Lett.* **90**, 943 (1983).

[5] Ennen, H.; Schneider, J.; Pomrenke, G.; Axmann, A.; Eisele, K.; Haydl, W.; Schneider, J. *Appl. Phys. Lett.* **90**, 943, (1983).

[6] Benton, J. L.; Michel, J.; Kimerling, L. C.; Jacobson, D. C.; Xie, Y,-H.; Eaglesham, D. J.; Fitzgerald, E. A.; Poate, J. M. *J. Appl. Phys.* **70**, 2667, (1991).

[7] Adler, D. L.; Jacobsen, D. C.; Eaglesham, D. J.; Marcus, M. A.; Benton, J. L.; Poate, J. M.; Citrin, P. H. *Appl. Phys. Lett.* **61**, 2181 (1992).

[8] Polman, A. *J. Appl. Phys.* **82**, 1 (1997).

[9] Thilderkvist, A.; Michel, J.; Ngiam, S.; Kimerling, L.; Kolenbrander, K. D. *Appl. Phys. Lett.* **64**, 1821 (1994).

[10] Werwa, E.; Seraphin, A. A.; Chiu, L. A.; Zhou, C.; Kolenbrander, K. D. *Appl. Phys. Lett.* **64**, 1821 (1994).

[11] Littau, K.; Szajowski, P.; Muler, A.; Kortan, A.; Brus, L. *J. Phys. Chrm.* **97**, 1224 (1993).

[12] Brus, L.; Szajowski, P. F.; Wilson, W.; Harris, T.; Schupler, S.; Citrin, P. *J. Am. Chem. Soc.* **117**, 2915 (1995).

[13] Wilson, W. L.; Szajowski, P. F.; Brus, L. E. *Science*, **262**, 1242 (1993).

[14] Murthy, T.; Miyamoto, N.; Shibo, M.; Nishizawa, J. *J. Cryst. Growth*, **33**, 1 (1976).

[15] Polman, A.; van den Hoven, G. N.; Cluster, J. S.; Shin, J. H.; Serna, R.; Alkemade, P. F. F. *J. Appl. Phys.* **77**, 1256, (1995)

[16] Coffa, S.; Franzó, G.; Priolo, F.; Polman, A.; Serna, R. *Phys. Rev. B.* **49**, 313, (1994).

[17] Hömmerich, U.; Namavar, F.; Cremins, A.; Bray, K. *Appl. Phys. Lett.* **68**, 1951 (1996).

[18] Kimura, T.; Yokio, A.; Horiguchi, H.; Saito, R.; Ikoma, T.; Sato, A. *Appl. Phys. Lett.*, **65**, 983 (1994).

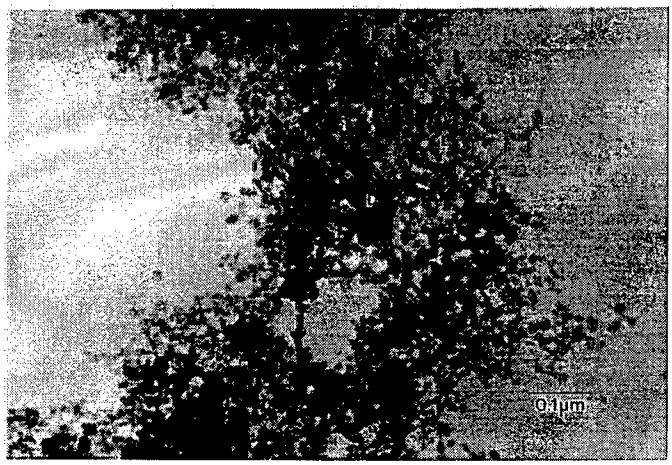


Figure 1: A conventional low resolution transmission electron micrograph of a sample collected from a 3.0 cm long reaction furnace. There are two distinct morphologies with light (L) and dark (D) contrast. Dark contrast areas contain Er while light contrast areas do not.

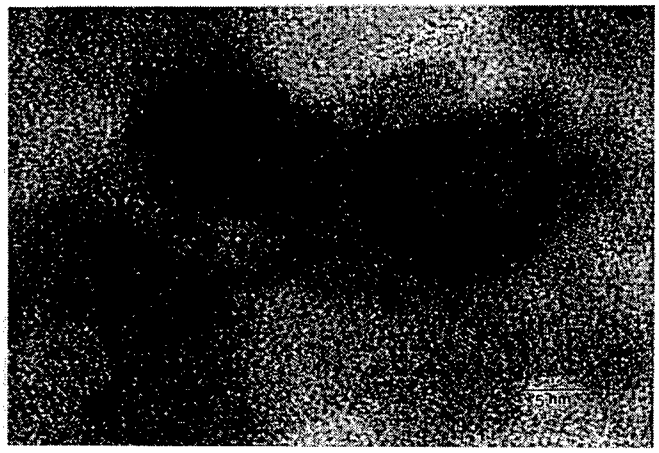


Figure 2: High resolution electron micrograph of a sample from the 3.0 cm long furnace. The structures visible in Figure 1 are seen to be composed of an agglomeration of nanoparticles.

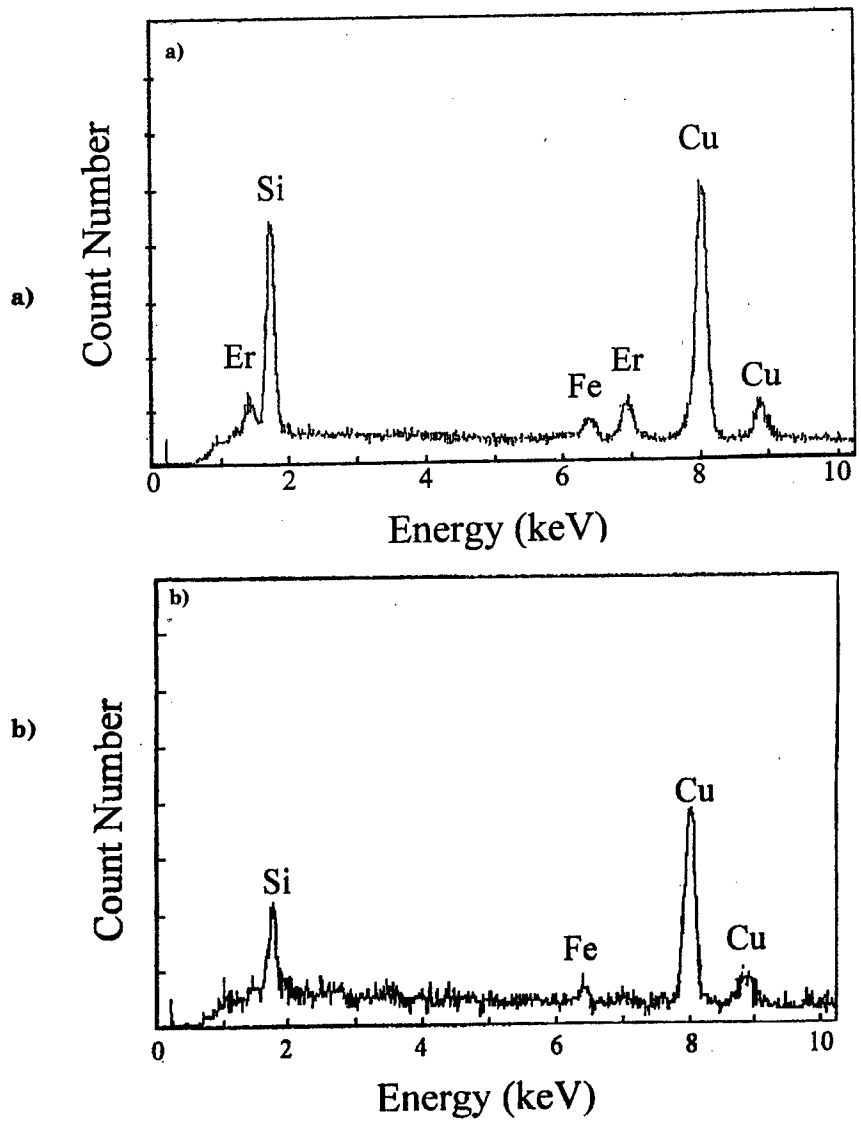


Figure 3: X-ray energy dispersive spectra from (a) a dark contrast area similar to D in Figure 1 and (b) a light contrast area similar to L in Figure 1.

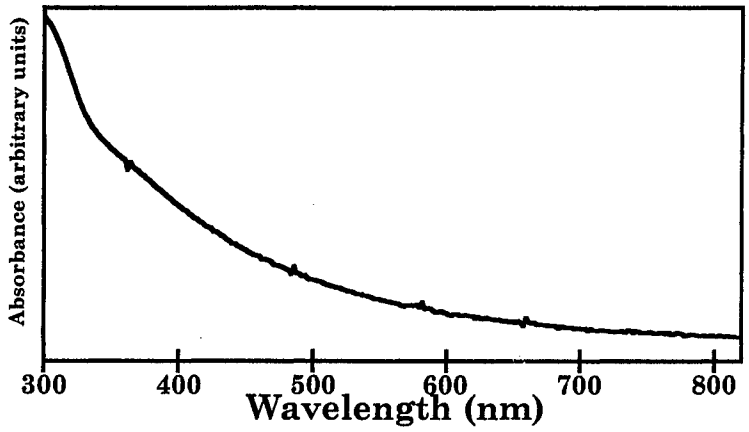


Figure 4: Room temperature UV/visible absorption spectrum of Er^{3+}-doped Si nanoparticles in ethylene glycol solution and produced from disilane pyrolysis (3.2 sccm) in a 3.0 cm furnace.

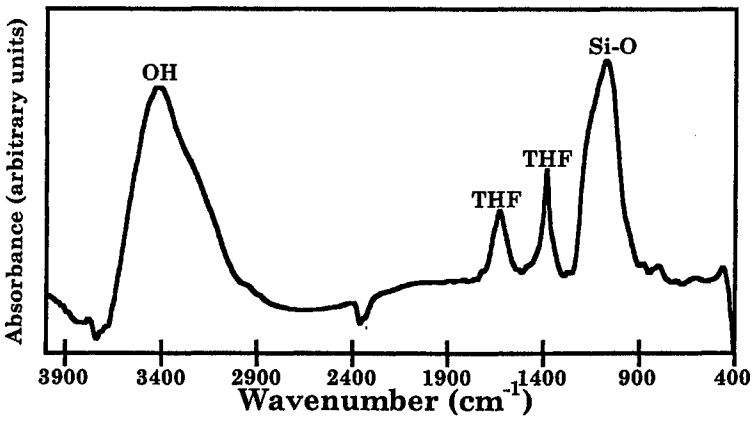


Figure 5: Infrared spectrum of Er^{3+}-doped Si nanocrystallites prepared from a pyrolysis experiment using a 3.0 cm furnace.

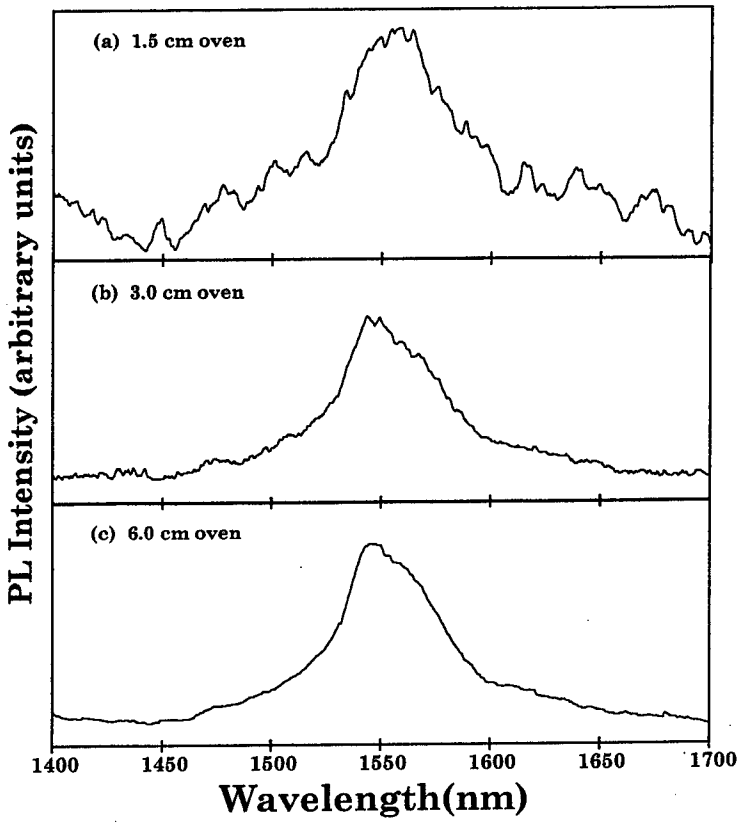


Figure 6: Room temperature near-IR Photoluminescence spectra for Er^{3+}-doped Si nanocrystals from 1.5, 3.0, and 6.0 cm pyrolysis ovens.

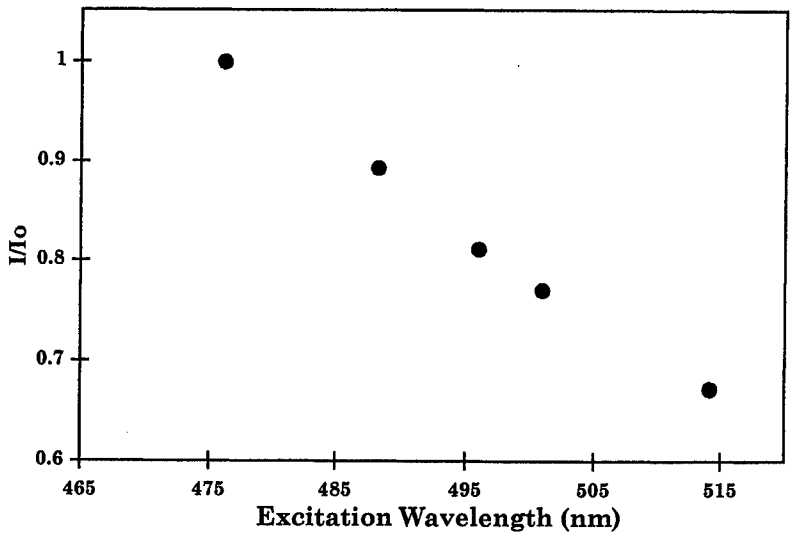


Figure 7: Excitation wavelength dependence of the integrated near infrared PL intensity for Er^{3+}-doped Si nanocrystals in ethylene glycol solution produced from disilane pyrolysis in a 3.0 cm furnace.

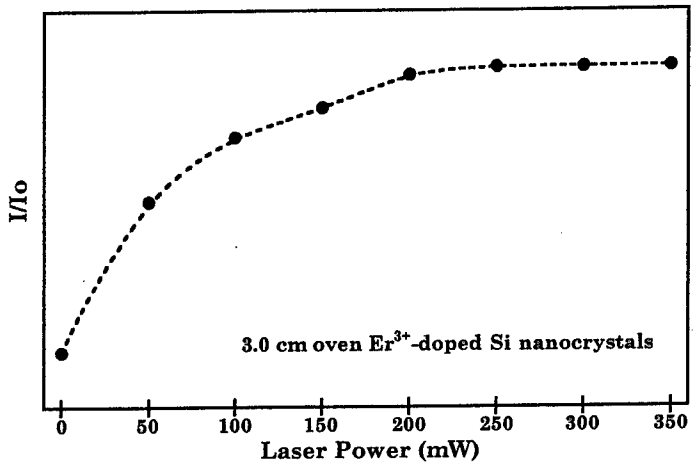


Figure 8: Power dependence of the integrated near infrared PL intensity of Er^{3+}-doped Si nanoparticles in ethylene glycol solution produced from the pyrolysis of disilane in a 3.0 cm furnace.

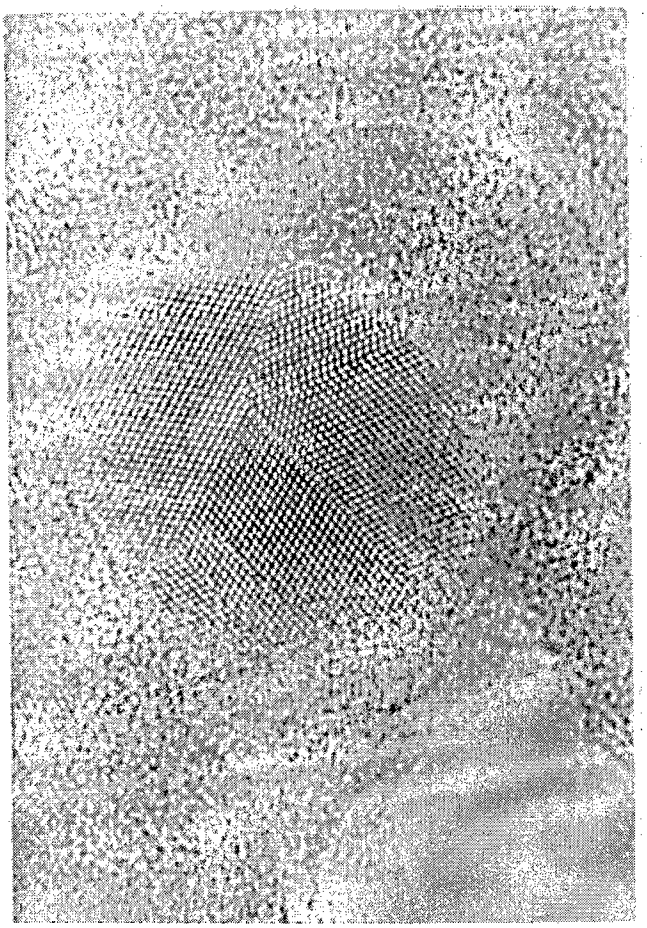


Figure 9: High resolution electron micrograph showing the image of one nanoparticle produced in a 3.0 cm long furnace without the presence of $Er(tmhd)_3$.

STRUCTURAL AND ELECTRICAL CHARACTERIZATION OF NANOCRYSTALLINE SILICON SUPERLATTICES

L. Tsybeskov, G. F. Grom, and P. M. Fauchet
Department of Electrical Engineering, University of Rochester, Rochester, NY, USA

J. P. McCaffrey, J.-M. Baribeau, H. J. Labbe, G. I. Sproule and D. J. Lockwood
Institute for Microstructural Sciences, National Research Council, Ottawa, Canada

ABSTRACT

We report on the characterization of nanocrystalline-Si/SiO_2 (nc-Si/SiO_2) superlattices (SLs) prepared by magnetron sputtering of nanometer-thick amorphous Si layers followed by high-temperature crystallization. The crystallization was performed in two steps, i.e., rapid thermal annealing (RTA) and slow ramp-up furnace annealing, and monitored by a number of characterization methods including: transmission electron microscopy (TEM) and atomic force microscopy (AFM), X-ray diffraction and X-ray small angle reflection, Raman scattering, and tunneling spectroscopy. Our fabrication technique is able to control the size, shape, and packing density of the Si nanocrystals. The interfaces between the nc-Si and SiO_2 layers in the nc-Si/SiO_2 SL are shown to be flat and chemically abrupt. Our measurements showed that a post-treatment oxidation and annealing induce lateral self-organization of the nc-Si and a transition from sphere-like nanocrystals to rectangular or brick-shaped nanocrystals. Phonon-assisted tunneling was observed in a bipolar nc-Si based structure, which confirmed that the nc-Si/SiO_2 interface is abrupt and nearly defect-free. These results hold promise for nc-Si SL quantum device applications.

I. INTRODUCTION

The electronic structure and major physical properties of 3-dimensional or bulk crystalline semiconductors are determined by their chemical composition and crystal lattice. Therefore, to manufacture semiconductor heterostructures and superlattices (SLs) of high quality, precise control of the changes in chemical composition and a near-perfect lattice match is required. Examples include GaAs/GaAlAs-based structures grown by molecular beam epitaxy (MBE). Semiconductor nanocrystals represent a new class of materials where, in general, the electronic structure is now also determined by the size of the nanocrystals. Semiconductor nanocrystals, also called quantum dots (QDs), can be produced by a wide variety of techniques such as aerosol reactions (gas phase), precipitation in organic liquids (liquid phase) or Stranski-Krastanow growth (solid phase). Existing chemical synthesis methods work well in partially ionic II-VI materials and are also applicable to III-V materials. In the case of covalent group IV semiconductors such as Si and Ge, however, a narrow size distribution of nanocrystals has not yet been achieved [1]. Nevertheless, silicon is the dominant material in microelectronics and there is an increasing interest in silicon nanocrystals due to their potential application in nanoelectronics.

Among the many approaches to fabricate Si QDs, the thermal crystallization of amorphous Si (a-Si)/SiO_2 layered structures [2] shows great potential. The crystallized Si nanocrystals are packed in the form of ordered layers, and their size and packing density can be controlled precisely. This type of structure has been called a nanocrystalline Si (nc-Si) SL because it consists of periodically alternating layers of Si nanocrystals and SiO_2.

In this work we show that the nc-Si SL prepared by controlled crystallization exhibits nearly perfect nc-Si/SiO_2 interfaces and a narrow nanocrystal size distribution. We demonstrate that accurate control of the nanocrystal shape and packing density can be obtained using post-treatment steps. As an example, we show two types of Si nanocrystal shape: sphere-like and rectangular (brick-shaped). In addition, we discuss the electrical properties of nc-Si SLs and their application in nanoelectronics.

II. SAMPLE PREPARATION & STRUCTURAL CHARACTERIZATION

The magnetron sputtering of the a-Si/SiO_2 multilayers was performed at Rochester in a Perkin-Elmer 2400 sputtering system by radio-frequency (RF) sputtering and plasma oxidation. In the sputtered samples, the a-Si thickness ranged from ~ 20 to 250 Å and that of the SiO_2 from 25 to 60 Å. The number of periods varied from 1 to 60. The crystallization was performed by rapid (40-60 s) thermal annealing (RTA) at 800-900°C followed by furnace annealing. In the furnace annealing step, the temperature was increased by ~ 10°C per minute from 600 to 1050°C. This annealing is defined as quasi-equilibrium annealing (QEA). Several post-treatment steps such as wet (or dry) oxidation and annealing have been performed in order to test the nc-Si SL thermal stability and oxidation resistance, as well as to control the nanocrystal size and shape: these tests include a combination of oxidation at moderate temperature (~ 600-700°C) and high temperature (~ 1000° C) annealing.

The thermal crystallization of a-Si/SiO_2 multilayers is controlled by several factors. Silicon has a very low diffusivity in SiO_2 and the initial RTA process forms nanocrystals without distorting the SL periodic structure. The shape of the Si nanoclusters is expected to be close to spherical due to the competition between surface and volume tension. The strain in nc-Si/SiO_2 multilayers can be released by QEA. High-temperature annealing also results in a decrease of the Si/SiO_2 interface defect density (see Ref. 3 for details).

The role of the double-step annealing is to create crystalline nuclei by RTA (nucleation stage) and to complete the crystallization of the Si nanocrystals and improve their surface passivation by QEA (growth stage). After nucleation, the nanocrystalline nuclei are surrounded by an amorphous tissue and occupy not more than ~ 20-30% by volume of the Si layer (estimated from Raman scattering). After furnace annealing and completed crystallization, nearly 90-95% of the Si layer volume was found to be crystallized in samples with Si nanocrystals greater than 30 Å in diameter.

A wide variety of characterization techniques have been applied to study the nc-Si SLs. X-ray specular reflectivity measurements were carried out using a Philips PW1820

vertical goniometer and simulated using the Philips HRS calculation package. The Raman experiments were carried out at room temperature in a quasi backscattering geometry using a Jobin-Yvon triple spectrometer or a Spex 14018 double spectrometer. Low-frequency Raman scattering was also measured using a SOPRA DMDP 2000 double monochromator with a cooled Hamamatsu R928P photomultiplier. The excitation source was 300 mW of 457.9 nm Ar^+ laser light with an angle of incidence of 77.7°. The incident light was polarized in the scattering plane, while the scattered light was collected without polarization analysis.

Auger elemental microanalysis was performed on a Physical Electronics Industries PHI 650 instrument with a 5 keV electron beam 30° off normal. An argon ion gun operating at 1 keV and 51° off normal was used for depth profiling. The Si LMM and O KLL Auger lines at 96 eV and 510 eV, respectivly, were used to obtain the SL composition profile.

The TEM analysis was performed on a Philips EM 430 microscope operated at 300 kV. Samples were prepared by a cleavage method [4].

Electrical measurements were performed at temperatures ranging from 20 to 300 K in a closed-cycle CTI-Cryogenic system using a Keithly 220 current source and a Keithly 595 quasi-static CV meter. High frequency C-V measurements were obtained using a Bonton 72BD 1 MHz capacitance meter.

Figure 1 shows a TEM picture of a crystallized a-Si/SiO_2 sample. The nc-Si/SiO_2 layers are very flat with an average roughness less than 3-4 Å. The size of the Si nanocrystals within the layers is close to the thickness of the a-Si layer while the volume packing density is controlled by the thickness of the SiO_2 layer. A quantitative analysis of the nc-Si size distribution is difficult, but the difference between crystallized spheres is not greater than a few monolayers. Figure 1(b) shows the same sample at higher magnification and depicts individual nanocrystals of nearly perfect spherical shape. The nanocrystal size is around 40Å with size distribution of ~ 2-3 %.

The lateral size distribution has been studied by a Digital Instruments AFM using commercial software for crystallite size recognition: in all cases, the grain size distribution was found to be narrow, ~ 5% on average (Fig. 2). Selected area electron diffraction measurements proved that the material is nanocrystalline rather than amorphous (see Fig. 2).

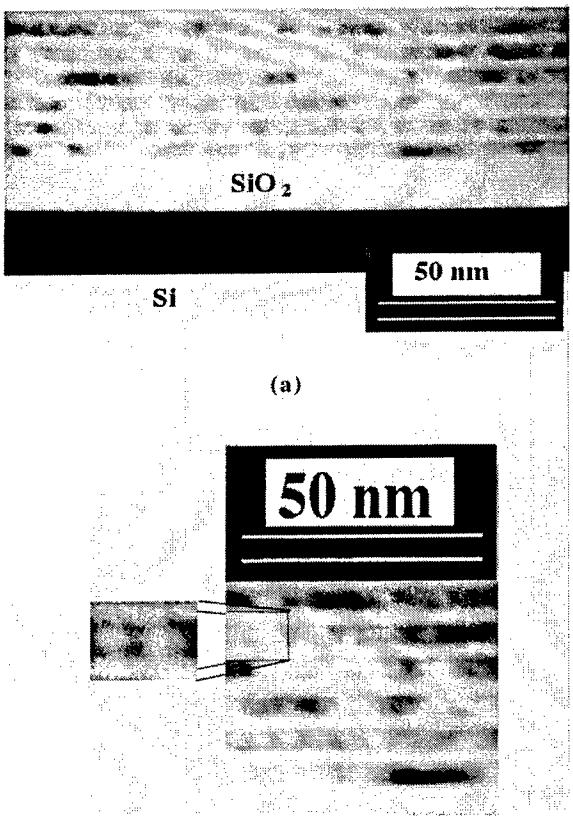
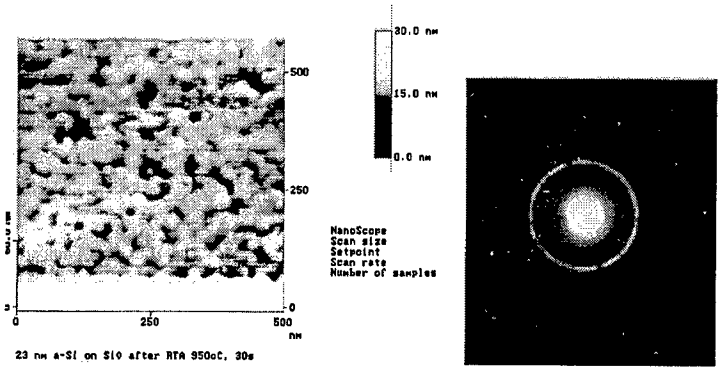


Figure 1. TEM images showing (a) an example of a nc-Si SL and (b) a magnified picture detailing two individual Si nanocrystals.

Raman scattering in low-dimensional systems is a well known method to study the phonon dispersion relationship and crystal translational symmetry. In addition, periodicity and interface quality in the layered structure can be studied using low-energy accoustic phonon scattering. Figure 3 shows Raman scattering data in nc-Si SLs with different crystalite sizes and compares it with similar measurements in crystalline Si (c-Si). For example, a peak that corresponds to first-order (1-O) optical zone-center phonon (OZCP) scattering in samples with 130 Å Si nanocrystals is broader, and slightly shifted toward lower wavenumber compared to the Raman peak in c-Si (Fig. 3(a)). The nanocrystal size of ~ 130 Å is too large to provide any significant effects in phonon dispersion due to phonon confinement [5], and the observed differences can be explained as being due to strain, an influence of the nc-Si/SiO_2 interface or "bulk" defects (including grain boundary, dislocation, etc.) and non-stoichiometric SiO (the shoulder near 505 cm^{-1}). Figure 3(a) shows progressive changes in the 1O OZCP Raman scattering during high-temperature (~ 1000°C) annealing: the Raman peak narrows, shifts to ~ 519 cm^{-1}, and the shoulder at ~ 505 cm^{-1} continuously decreases. Therefore, we can conclude that annealing decreases the defect density and improves the SiO_2 stoichiometry in the nc-Si SLs.



(a) (b)

Figure 2. (a) AFM plan-view of the surface of a nc-Si SL showing the spherical shape of the Si nanocrystals, which are nearly the same size. (b) Selected area electron diffraction pattern proves that after crystallization the material is crystalline, not amorphous.

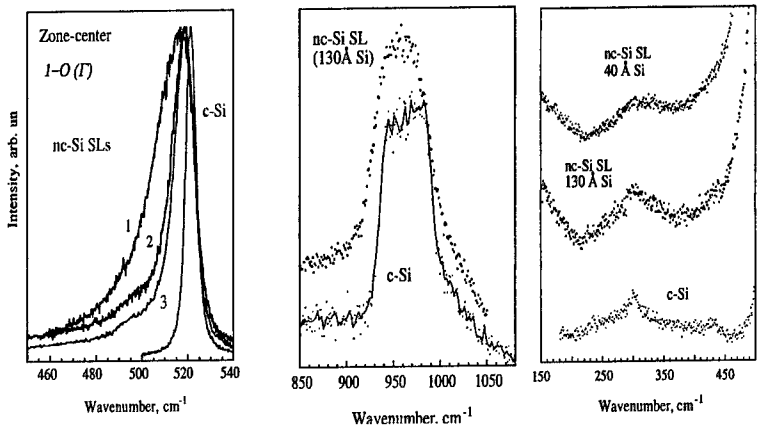


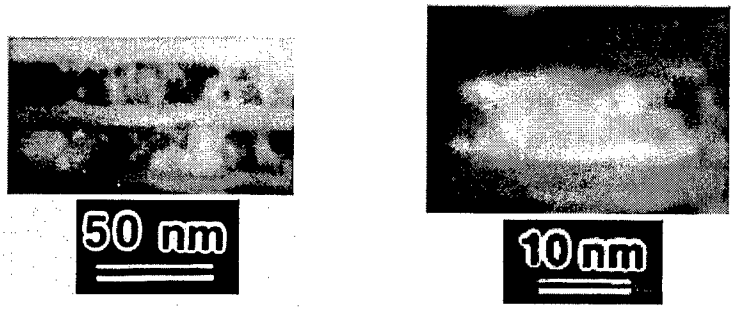
Figure 3. Raman spectra in crystallized SLs: (a) The first-order (1-O) zone-center phonon mode. The spectra labeled from 1 to 3 show progressive changes due to 20 min. annealing steps at 1050°C. The spectrum of c-Si is given for comparison. (b) Second order optical phonon scattering in an annealed SL (corresponds to spectrum #3 in Fig. 3(a)) and in c-Si. (c) Second order TA phonon scattering in c-Si and SLs with different size Si nanocrystals.

Additional information can be provided by the second-order Raman scattering in nc-Si SLs. Generally speaking, the second-order Raman scattering is more sensitive to stress and crystallographic imperfections then the first-order Raman scattering. Such high sensitivity of the second-order Raman scattering is due to a contribution to the scattering process from phonons propagating in different directions within Brillouin zone. Figure 3(b) shows that even after annealing at ~ 1000°C the second-order Raman scattering in Si nanocrystals of ~ 130 Å diameter is very different compared to c-Si: the intensity of scattering is larger, the peak is shifted toward lower wavenumbers, and the spectrum is broader. Figure 3(b) shows a spectrum with contributions from the second-order OZCP or 2-O (Γ) at 1040 cm^{-1}, 2TO (L) at 991 cm^{-1}, 2TO (W) at 947 cm^{-1} and 2TO (X) at 930 cm^{-1} [6]. The observed enhancement of the second-order Raman scattering intensity can also be explained in part by broken or reduced translational symmetry.

Raman scattering near 150 and 300 cm^{-1} (second-order) in c-Si has been explained as phonon scattering from acoustic phonons at wavevectors away from the zone center

[6], and the overtone at 302 cm^{-1} is associated with the 2TA (X) phonon. This feature is relatively sharp in c-Si. It increases in intensity, but changes shape in the nc-Si SL with ~ 130 Å Si nanocrystals, and becomes much broader in samples with 40 Å Si nanocrystals (Fig. 3 (c)). This weak scattering in c-Si is also enhanced when the translational symmetry is disrupted. However, in all our Raman measurements, a pure a-Si phase with a peak at 480-490 cm^{-1} was clearly absent. Thus, our Raman data is consistent with selected area electron diffraction and X-ray diffraction data (not shown): the treated material is not amorphous, but crystalline, with more or less random crystallographic orientation of the Si crystallites. This conclusion is important because a-Si is a highly defective material and these defects can strongly affect the performance of a nanoscale device.

Also, our Raman data clearly shows that the structural properties of nc-Si SLs can be improved by high temperature annealing. This post-treatment step, however, can be dangerous for our layered structure: diffusion at high temperature can be efficient and an abrupt nc-Si/SiO_2 profile can be damaged. To address this question we have performed series of post-treatment experiments such as annealing and oxidation at different temperatures. Samples subjected to anealing have been investigated by TEM. These measurements have demonstrated that the nc-Si SL structure retains its layered structure with sharp nc-Si/SiO_2 interfaces. At the same time, the shape of the Si nanocrystals is found to be changed.



(a) (b)

Figure 4. (a) TEM image of the nc-Si SL after a combination of steam oxidation (~ 10 min at ~ 900°C) and annealing at 1050°C. (b) TEM image of an individual nanocrystal, which is believed to be made from the merging of three nanocrystals. The brick-like shape is clearly observed.

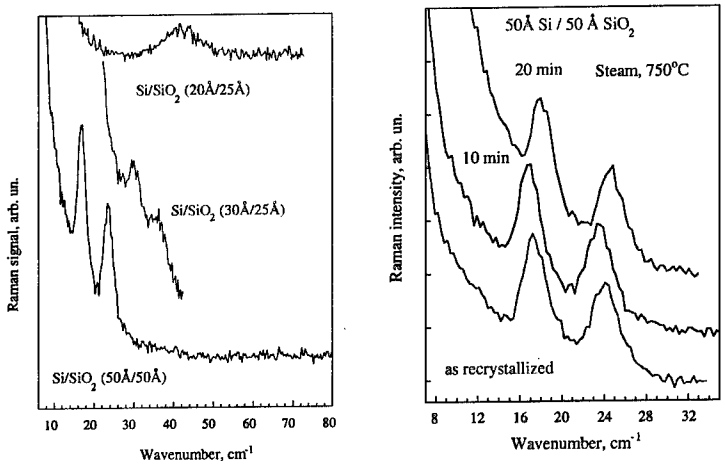


Figure 5. Low-frequency Raman scattering in nc-Si SLs: (a) SLs with different Si nanocrystal sizes and (b) Raman spectra in a nc-Si SL before and after steam oxidation (750°C) and annealing at ~ 1050°C post-treatment steps.

Figure 4 shows that after annealing in combination with a short oxidation time, the Si nanocrystals are not spherical but rather rectangular, or brickshaped. At the same time the nc-Si/SiO_2 interface remains at least the same as before the annealing. The avarage size of the "bricks" is found to be nearly the same. Thus, the nanocrystal merging and lateral self-organization is possibly controlled by the thermal budget (e.g., annealing time and temperature).

The TEM analysis is a very useful method to study individual nanocrystals. However, it is difficult to do any statistics or to provide a quantitative picture in a length scale of 10^{-10} - 10^{-6} m and investigate the nc-Si SL local-, medium- and long-range organization. Therefore, a TEM study must be combined with several other analytical techniques such as Auger elemental microanalysis, small-angle X-ray reflection, and Raman spectroscopy of folded acoustic phonon modes.

A quantization effect of the phonon vibrations could be observed in the case when the phonon coherence length is larger than the nc-Si layer thickness. Low frequency

accoustic modes fulfill this condition because they are an in-phase motion of a large number of atoms and are not strongly influenced by the disruption of the translational symmetry. Low frequency accoustic modes reflect the average bulk elastic properties of the materials and can be very useful to help estimate the periodicity and the interface roughness in a multilayer structure.

Figure 5a shows low frequency Raman scattering in nc-Si SLs having different nanocrystal layer thicknesses. A first approximation to the accoustic phonon dispersion in a bulk material is $\omega_m(k) = v_s k$ and is modified in the case of a multilayer structure to $\omega_m(k) = v_s|k + 2\pi m/L|$, where v_s is the sound velocity in SLs, $k$is the phonon wave vector, $m = 0, \pm 1, \pm 2...$ is Brillouin zone folding index, and L is the multilayer spacing, or period. The periodicity of the multilayers introduces an artificial Brillouin zone boundary at π / L along the growth direction and the folding of the phonon dispersion. In Raman backscattering experiments, the choice of the excitation wavelength $\lambda = 4\pi n / k_p$, where n is the SLs average refractive index and $k_p$the photon wavevector, provides the possibility to probe near the center or near the boundary of the artificial Brillouin zone. In our samples, the first pair of the folded acoustic phonon mode with $m = \pm 1$ is observed, and the mode frequencies are in a good agreement with theory (our calculations are based on Ref. [7] and will be discussed elsewhere [8].) More importantly, the post treatment steps such as steam oxidation at 750°C following annealing at 1050°C do not change the folded mode spectra (Fig. 5(b)). The small peak frequency shift of ~ 0.5 cm^{-1} is not a systematic one, and is due to a small lateral non-uniformity in the multilayer thickness across the wafer arising from the growth conditions. A simple calculation shows that folded acoustic phonon modes will disappear from Raman spectrum in the case of an average interface rougthness larger than ~ 3Å [7].

We would like to emphasize that nc-Si SLs represent a new class of layered structures with a unique thermal stability. Our result from the folded accoustic mode spectroscopy study is supported by TEM, Auger elemental microanalyses, and small-

angle X-ray reflection (Fig. 6). In all measurements, damage of the multilayer structure from annealing has not been indicated. Indeed, the simulation of the X-ray reflection data (Fig. 6(b)) shows that the nc-Si/SiO_2 interface in nc-Si SLs even improves after annealing at ~ 1000°C.

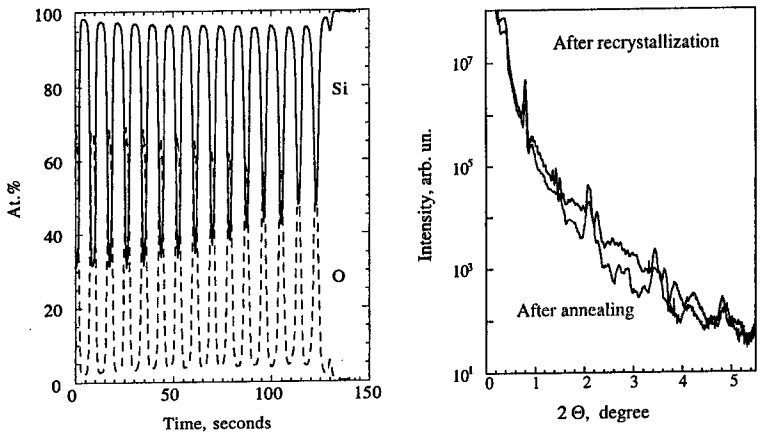


Figure 6. (a) Auger elemental microanalysis showing no diffusion or layered structure disruption after ~ 1050°C annealing. (b) Small-angle X-ray reflection data confirming no damage in the layered structure after crystallization and annealing.

III. ELECTRICAL CHARACTERIZATION

Structural characterization of the nc-Si SLs shows that we are able to fabricate a good quality, thermally-stable layered structure consisting of nc-Si and SiO_2 layers. However, similar structures can be used in a device applications only in the case of defect-free material. The defects, located within Si nanocrystals or at their surface can play a critical role in carrier transport and significantly affect electron coherence, which is an important condition for nanoscale devices and quantum electronics. Thus, the electronic properties of nc-Si SLs is another very important issue and will now be discussed.

The quality of the nc-Si/SiO_2 interface can be tested using tunneling spectroscopy in, for example, an Esaki diode or a double-barrier structure. There are several quantitative characteristics of the carrier tunneling in such structures (excess current,

peak-to-valley ratio, etc.). In the case of Si or other indirect bandgap semiconductors, a qualitative test could be performed. In an indirect bandgap semiconductor, tunneling across the gap (interband tunneling) requires phonon assistance to provide momentum conservation. Thus, the tunnel structure should contain a p-type substrate and an n-type top contact separated by a thin layer of an insulator. The signature of phonon assistance can be traced only in the case of a very low interface defect density. Otherwise, carrier inelastic scattering due to interaction with interface defects will change the carrier momentum and phonon assistance will not be necessary.

A tunnel junction with a single nc-Si layer of ~ 130 Å Si nanocrystal diameter was fabricated. Figure 7 shows the current-voltage (I-V) data exhibiting very clear steps with a spacing of ~ 60 meV, which is close to that of the most energetic TO-phonon in Si (~ 57 meV). Thus, a 130 Å Si nanocrystal is too large to change the electronic structure of the material due to quantum confinement, but the well demonstrated phonon-assisted tunneling clearly indicates a very low density of interface defects.

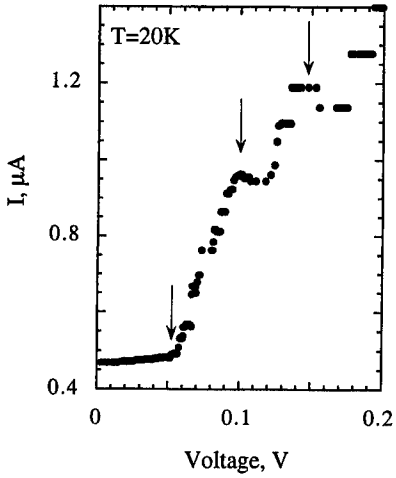


Figure 7. A signature of phonon-assisted tunneling at temperature of 20 K in a single nc-Si layer of ~ 130 Å Si nanocrystals sandwiched between a p+ c-Si substrate and an n-type top contact.

An other technique that may be used to estimate the defect density in Si/SiO_2 structures is capacitance-voltage (C-V) measurements. A nc-Si SL can be deposited on thermally grown SiO_2 on Si, so that Si nanocrystals are imbedded in an isolated gate, and C-V measurements can be appropriate. Assuming that the applied voltage will partially appear across the thermally grown SiO_2 of ~200 Å thickness, the nc-Si SL structure, and the Si substrate, the total potential is $V = V_{SiO_2} + V_{nc-SiSL} + V_{Si}$. The total system capacitance (per unit area) is a combination of the SiO_2 capacitance $C_{SiO_2} = \varepsilon_{SiO_2} / d$, the capacitance of the nc-Si SL $C_{nc-Si\,SL} = \varepsilon^*_{ncSi} / d_{SL}$, and the c-Si depletion layer capacitance C_{Si}^{SC}. The total capacitance is $C_{\Sigma}^{-1} = (\sum_i C_i)^{-1}$, so the smallest capacitance (or thickest layer) contribution will be dominant. In the case of n-type Si with the a resistivity of ~ 5 Ω cm, a maximum depletion length of ~ 3000-5000 Å is expected [9], and that is an order of magnitude larger than the total thickness of the thermally-grown SiO_2 (~ 200Å) and nc-Si SL layers (~ 150 Å). Thus, our structure is suitable for such measurements.

Figure 8(a) shows relatively sharp room-temperature high-frequency (1MHz) C-V characteristics of the nc-Si SL and the C-V data in a similar structure with a uniform SiO_2 layer grown by magnetron sputtering following high-temperature annealing. The capacitance modulation by reverse bias is due to a stretching of the Si depletion layer, and the presence of defects can be found by comparison with the calculated C-V curve for an ideal MOS structure (see Ref. 9 for detals). The result of our simulation is a defect density of ~ 10^{11} cm^{-2} for the structure containing an eigth period nc-Si SL and a slightly higher number for the structure with a uniform SiO_2 layer. This means that the majority of the defects are in the "bulk" of SiO_2. Also, for a surface density of the Si nanocrystals higher than 10^{12} cm^{-2}, only one Si nanocrystal per **100** or **1, 000** is defective!

Figure 8(a) shows a hysteresis (or a memory effect) in the C-V curve with a width equal to the charge $Q = CV \approx ne$, where e is electron charge and n is a number that is always surprisingly close to the calculated number of the Si nanocrystals

in the sample. The experiments on sample discharging have been performed and clearly demonstrated that the "memory" effect depends on the Si nanocrystal sizes (Fig. 8(b)). In addition, the discharging kinetics trigger interesting speculations.

The question is: What is the nature of charge relaxation in the nc-Si SL? After carriers have been injected and localized, presumably charging Si nanocrystals, carriers should eventually recombine or escape. Recombination requires carriers of opposite charge (e.g., holes in the case of electron injection). A sequence of charge-transfer steps from one localized site to another in the presence of an applied electric field (external or built-in) is a possible charge relaxation scenario. This process is qualitatively different in the case of nearly monoenergetic localized states than in the case of a disordered structure with a broad energy-level distribution. Due to the disorder (including defects, nanocrystal size and shape distribution, etc.) the transfer time can be a random variable, characterized by the probability $\psi(t)dt$. The time for an individual transfer is in the range t to $t + dt$. The accumulative sequence of these events in the motion of a charge carrier has been described as a "random walk" and the associated carrier transport has been named "dispersive transport" (see Ref. 10 for details).

For a probability distribution $\psi(t)$ with a "tail" given by $\psi(t) \sim t^{-(1+\beta)}$, the mean position of the spatially biased time-evolving packet varies as $l(t) \propto t^{\beta}$ with $0 < \beta \leq 1$. The average packet velocity then is $dl(t)/dt \sim t^{-(1-\beta)}$. When a reasonable fraction of the carriers (~ 10%) reach the electrode at $t = t_r$, the current begins to decrease at a faster rate which is given by $\sim t^{-(1+\beta)}$ for $t > t_r$. Therefore, a double logarithmic plot of current or charge relaxation is simply two lines with slopes of $-(1-\beta)$ and $-(1+\beta)$ separated by a narrow transition region. The sum of the slopes is **-2**; it is independent of the index β that defines the algebraic probability distribution. In the case of charging of the Si nanocrystals due to Coulomb blockade, β could be assosiated with the Si nanocrystal size distribution.

The discharging kinetics in the nc-Si Si are very different from the expected dispersive type of carrier transport. The initial part $(t < t_r)$ is flat, which gives $\beta \approx 0$. Also, the second part of the kinetics with $t > t_r$ is very sharp, and this leads us to conclude that the charge relaxation mechanism in the nc-Si SL is not a random walk, and that carrier transport is not dispersive transport. This conclusion is important, because dispersive transport is a signature of a disorder (Ref. 10), or in the case of Coulomb blockade is associated with a very broad crystallite size distribution. Recent measurements of drift mobility in porous silicon reveal dispersive transport and a carrier mobility of $\mathbf{10^{-4}}$ - $\mathbf{10^{-5}}$ $\mathbf{cm^2/Vs}$ [11]. Currently, we have a strong evidence that porous silicon is a disordered (not an amorphous) material with a very broad Si nanocrystal size distribution (See Ref. 12).

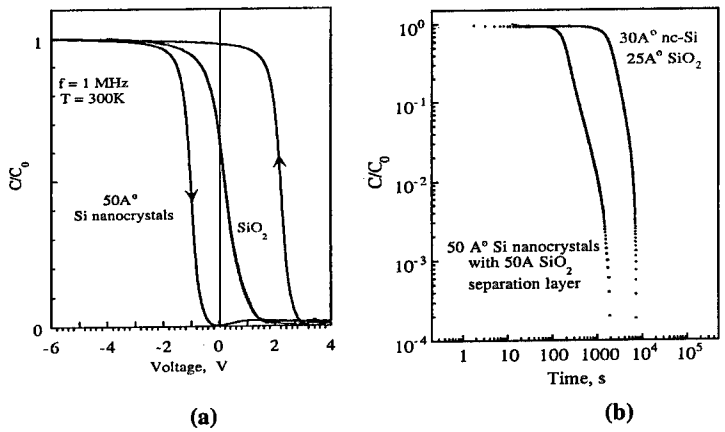


Figure 8. (a) C-V characteristics showing a hysteresis at room temperature in a structure with nc-Si layers imbedded in the isolated gate. No hysteresis is observed in a test structure with a uniform SiO_2 layer. (b) Room temperature charge relaxation measured by capacitance recovery. The C(t) kinetics indicate a non-dispersive carrier transport and a significant retention time dependence as a function of the Si nanocrystal size.

For comparison, we now estimate drift mobility in the nc-Si SL. The definition of drift mobility is $\mu_d = d/(t_r E)$, where d is the sample thickness, and the built-in electric field is in order of $\mathbf{E \sim 10^4\ V/cm}$. The transition time at room temperature varies from 200 s in a sample with 50 Å Si nanocrystals to > 2000 s in sample with 30 Å Si nanocrystals (Fig. 7). This means that the drift mobility at room temperature is in the range of $\mathbf{10^{-12}\text{-}10^{-14}\ cm^2/Vs}$. It is approximately **15 - 17** orders of magnitude lower then the drift mobility in c-Si (~ $\mathbf{1000\ cm^2/Vsec}$) and **10** orders of magnitude lower than the carrier mobility in porous silicon!

IV. CONCLUSION

In conclusion, we list several important results from this study:

(a) Nanocrystalline silicon superlattices can be reproducibly fabricated using nearly standard microelectronic fabrication steps.

(b) The nc-Si/SiO_2 SL exhibits an excellent interface roughness (< 4 Å), which has been established by a number of characterization techniques including small angle X-ray reflection and low-frequency Raman scattering.

(c) The structure demonstrates extraordinary thermal stability; it can survive heat treatment at > 1000°C when most of the structural ("bulk" and interface) defects are annealed.

(d) The size of the Si nanocrystal in the nc-Si SL is controlled by the original a-Si layer thickness, and the shape of the Si nanocrystal can be changed using post-treatments. Ordering and a transition from a spherical nanocrystal to rectangular or "brick"-shaped objects is demonstrated.

(e). The perfect structure of the nc-Si/SiO_2 interface is accompanied by a very low interface defect density, or in other words, Si nanocrystal surface defect density . The number of defected nanocrystals is estimated to be from one per 100 to one per 1,000. This low density is verified by a number of electrical measurements.

(f). A very unusual carrier transport mechanism is indicated from charge-relaxation measurements and a memory effect in nc-Si SLs. The estimated carrier mobility is 10^{-12}-10^{-14} cm^2/Vs, which is **15 - 17** orders of magnitudes lower then the drift mobility in c-Si and **10** orders of magnitude lower than the carrier mobility in porous silicon. Carrier transport is not dispersive and exhibits a size dependence.

ACKNOWLEDGMENTS

This work was supported by the US Army Research Office and Motorola.

REFERENCES

1. P. M. Fauchet, J. Luminescence **70**, 294 (1996).

2. L. Tsybeskov, K. D. Hirschman, S. P. Duttagupta, P. M. Fauchet, M. Zacharias, P. Kohlert, J. P. McCaffrey and D. J. Lockwood, in *Quantum Confinement IV: Nanoscale Materials, Devices, and Systems*, edited by M. Cahay, J.-P. Leburton, D.J. Lockwood, and S. Bandyopadhyay (The Electrochemical Society, Pennington, NJ, 1997), pp 134-145.

3. L. Tsybeskov, K. D. Hirschman, S. P. Duttagupta, M. Zacharias, P. M. Fauchet, J. P. McCaffrey and D. J. Lockwood, Appl. Phys. Lett. **72**, 43 (1998).

4. J. P. McCaffrey, Microsc. Res. Tech. **24**, 180 (1993).

5. I. H. Campbell and P. M. Fauchet, Solid State Commun. **58**, 739 (1986).

6. P. A. Temple and C. E. Hathaway, Phys. Rev. B. **7**, 3685 (1973).

7. D. J. Lockwood, M. W. C. Dharma-wardana, J.-M. Baribeau, and D. C. Houghton, Phys. Rev. B **35**, 2243 (1987).

8. G. F. Grom et. al., to be published.

9. S. M. Zee, *Physics of Semiconductor Devices* (Wiley Inter-Science, NY 1969), p. 812.

10. H. Scher, M. F. Shlesinger, and J. T. Bendler, Physics Today, January 1991, pp. 26-34.

11. P. Rao, E. A. Schiff, L. Tsybeskov, and P. M. Fauchet, in Advances in Microcrystalline and Nanocrystalline Semiconductors-1996, Mat. Res. Soc. Symp. Proc. **454**, p. 613 (1997).

12. L. Tsybeskov, MRS Bulletin, April 1998, pp. 33-39.

ORDERING AND CRYSTALLIZATION IN THIN Si/SiO_2 SUPERLATTICES

M. Zacharias, J. Bläsing, P. Veit
Department of Solid State Physics , Otto- von- Guericke University, Magdeburg, Germany

L. Tsybeskov, K.D. Hirschman, P.M. Fauchet,
Department of Electrical and Computer Engineering, University of Rochester, Rochester, NY, USA

ABSTRACT

A detailed investigation of thermal crystallization of amorphous Si/SiO_2 superlattices is presented. A one-step conventional furnace annealing and a two- step annealing process combining rapid thermal annealing and furnace annealing are studied by transmission electron microscopy (TEM) and X-ray diffraction. The increase of the crystallization temperature for sublayer thickness below 10 nm is demonstrated. The dependence of the nanocrystal size and the size asymmetry is monitored as a function of the sublayer thickness. Growth faults are shown with high resolution electron microscopy (HRTEM) in nanocrystals of sizes larger than 7 nm. The influence of growth fault on the Scherrer size is discussed.

INTRODUCTION

Nanocrystalline silicon (nc-Si) has been the subject of an increasing number of papers due to its potential application in novel optoelectronic devices based on Si.

Different preparation techniques are reported including anodic etching [1], ion implantation [2], chemical vapor deposition [3] and molecular beam epitaxy [4]. The preparation normally results in a broad distribution of nanocrystal sizes. Some processes like ion irradiation induce defects in the SiO_2 films which quenche the luminescence. Methods are desirable for a fabrication of ordered arranged nanocrystals with selected sizes.

The first evidence for self organization of Si nanocrystals in a Si/SiO_2 structure has been reported previously [3]. Such structures could be very attractive due to the low cost in production and the compatibility with standard integration technology. Decreasing the a-Si layer thickness increases the crystallization temperature and the inhomogeneous strain [5]. The understanding of thermally induced Si self-organization requires an extended investigation of relaxation, diffusion and crystallization of nanometer-size Si sublayers separated by oxide interfaces. It is reported based on TEM and Raman studies that both the nucleation rate and the crystal growth rate drastically decrease for sublayer thickness below 10 nm [6].

In this paper, we focus on key aspects of the thermal crystallization of amorphous Si/SiO_2 superlattices. The effect of a two-step annealing process (rapid thermal annealing at 950°C (2x1min) and conventional furnace annealing at 1050°C) has been compared to that of a single-step furnace annealing process at different temperatures (700-1050°C). The crystallization procedures are studied in a wide thickness range. The interface roughness, size, shape and growth fault of the Si nanocrystals are analyzed. Our studies have been performed using x-ray reflection, x-ray diffraction, TEM, and HRTEM.

EXPERIMENTAL DETAILS

Amorphous Si/SiO_2 superlattices are deposited on Si wafers by alternating rf sputtering and plasma oxidation in a conventional Perkin-Elmer 2400 RF sputterer. The use of the substrate rotation improves the homogeneity of the superlattice. The crystallization is performed as a one-step or a two-step process. The one-step process is

based on normal furnace annealing under Ar atmosphere at different temperatures (700-1050°C, ΔT = 50K). Every sample is annealed at the desired temperature in a one step conventional furnace process. The two-step procedure is a combination of rapid thermal annealing (RTA) at 950°C (2x1min) and furnace annealing (for details see [7]). The RTA forms nanosized nuclei within the Si sublayer. The following furnace annealing completes the crystallization, releases the strain, and decreases the interface defect density. During it, the temperature is raised from 800 to 1050°C with a slow ramp of only 10K/min. All these steps are frequently used in conventional microelectronic technology.

The superlattice structure, the interface quality, the size of the nanocrystals and the growth fault are studied with transmission electron microscopy (TEM) and high resolution transmission electron microscopy (HRTEM) using a Philip CM 200 system with 200kV. The results are compared with x-ray diffraction and x-ray reflectivity investigations. For wide angle scattering we use a thin film attachment on a URD6 (Seifert/FPM) goniometer with Cu/Kα radiation and 1° degree constant angle of incidence. The specular reflectivity of the thin film system is measured with a symmetric slit system (resolution 0.04°, Co/Kα). Further details can be found in [7].

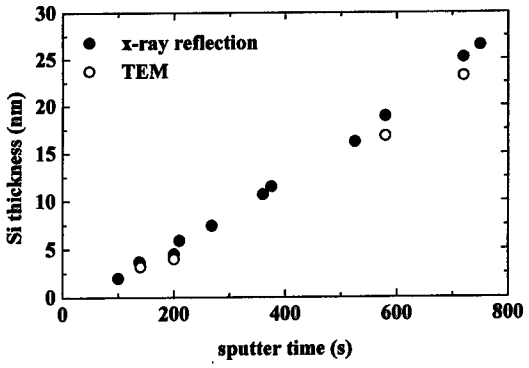


Fig. 1: Si layer thickness as a function of sputtering time.

RESULTS AND DISCUSSION

As expected we found a nearly linear dependence between the layer thickness and the sputtering time (Fig. 1). The thickness is calculated from x-ray reflection and compared with the TEM results of selected films. The average interface roughness after crystallization is less than 10Å, as estimated from x-ray reflection. The high quality of the films is shown by TEM (Fig. 2). The TEM image shows 40 periods of a Si/SiO_2 (3.2/3.5nm) superlattice after the crystallization. The dark and bright stripes represent the element and density contrast of the Si and SiO_2 layers, respectively.

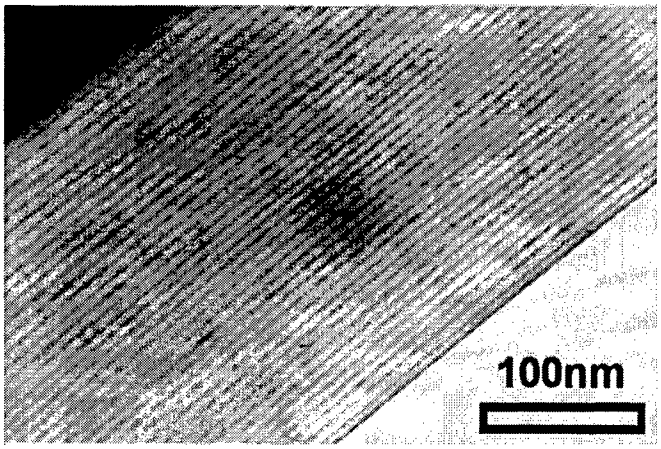


Fig. 2: TEM image of nc- Si/SiO_2 (3.2/3.5 nm) superlattices with 40 periods. The film is crystallized using conventional furnace annealing at 1000°C.

The two-step crystallization process is monitored by x-ray diffraction as shown in Fig. 3a for a film containing thick (19 nm) Si layers. It shows the amorphous (curve **a**) and nanocrystalline (curves **b, c**) state of the superlattice film. Small nc-Si nuclei of an average size of 8 nm can be found (curve **b**) after rapid thermal annealing. Further conventional annealing completes the crystallization and releases part of the strain caused from the RTA process (curve **c**). Using the Scherrer analysis we estimate the

average crystallite size to be 13.8 nm which is close to the thickness of the film (17 nm, TEM).

The increase in crystallization temperature for very thin Si sublayers is demonstrated in Fig. 3b for the one step annealing process. The Si layer thickness in this structure is 3.2 nm. A Scherrer size of 4 nm is found after crystallization which is in agreement with the initial Si layer thickness, within the accuracy of the measurements. The nucleation does not start until 900°C and is finished at 950°C. This clearly demonstrates the increase of the crystallization temperature for thin a-Si layers. It is reported that bulk a-Si crystallize rapidly at 700°C [6]. Decreasing the layer thickness below 10 nm exponentially increases the crystallization temperature. An empirical model with takes into account the Si layer thickness, the bulk crystallization temperature, and a material specific constant has been developed [5].

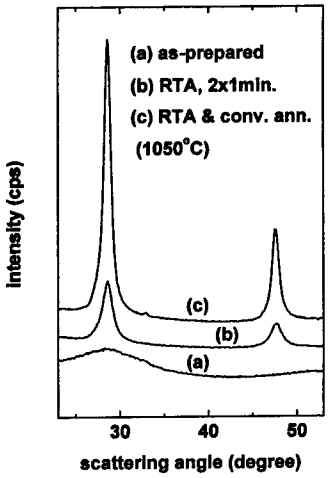


Fig. 3a: X-ray diffraction of a structure with thick (19 nm) Si layers. (a) as-prepared, (b) after RTA, (c) after RTA & furnace annealing.

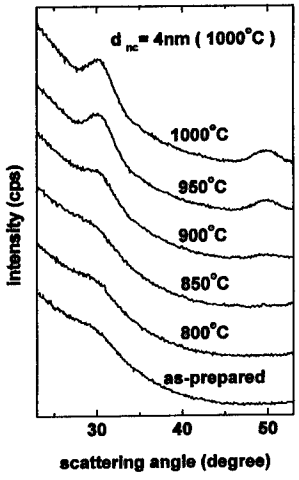


Fig. 3b: X-ray diffraction from a structure with a thin (3.2 nm) Si layer following the one-step furnace annealing at varied temperature.

Using a temperature above the crystallization temperature did not change the size significantly as demonstrated in Fig. 4. The Scherrer size is shown as a function of the annealing temperature. However, a significant deviation between the Scherrer size and the Si layer thickness is found in the limit of thick layers. The asymmetry of the nanocrystals can be analyzed using a constant angle of grazing incident (1°) and the angle dependence of the Scherrer size by using different Bragg lines. A significant size asymmetry is found between the sizes in plane or perpendicular to the growth direction. The analysis presented in Fig. 4 is done for the one step annealing. Two trends are found. First, films with a Si layer thickness above 7-8 nm did not show a significant size asymmetry. However, the Scherrer size does not significantly exceed 7 nm, which is far below the Si thickness. Second, films with a Si layer thickness below 7 nm did show an agreement among the average size of the nanocrystals, the in-plane size and the Si layer thickness. But the size perpendicular to the layers is 2 nm below the in-plane size. This can be interpreted as the influence of the oxide interface. Evidence for a retarded crystallization near the SiO_2 interface was first reported in [8].

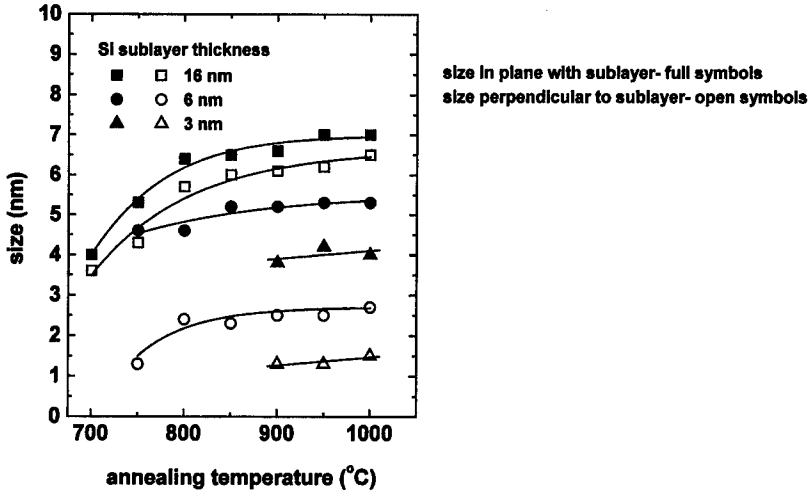


Fig. 4: Scherrer size as a function of annealing temperature. A significant size asymmetry is found for the size in plane or perpendicular to the growth direction.

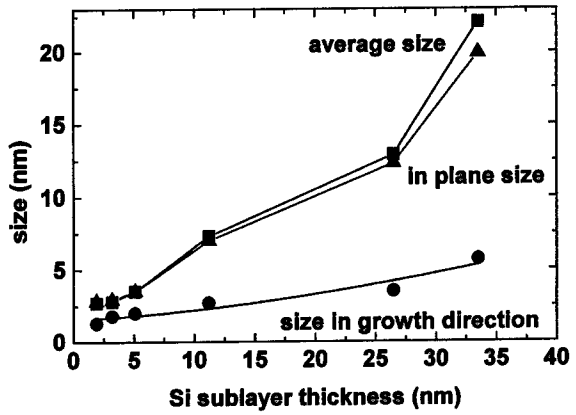


Fig. 5: Asymmetry in Scherrer size analyzed for the two step procedure.

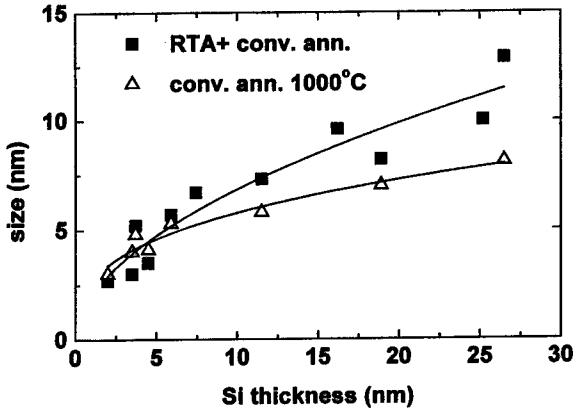


Fig. 6: Comparison of the average Scherrer size of the two crystallization procedures as a function of Si layer thickness.

Similar trends in size asymmetry can be found for the two step process (Fig. 5). The size in the growth direction deviates by nearly 2 nm from the average size and the in-plane size for layers below 7 nm. However, a clear trend to larger average and in-plane sizes compared to the one-step process can be found, more consistent with the layer thickness. Fig. 6 demonstrates significant deviation between the Scherrer size and layer thickness for both annealing procedures. It also show that this discrepancy can be decreased by using the two-step process.

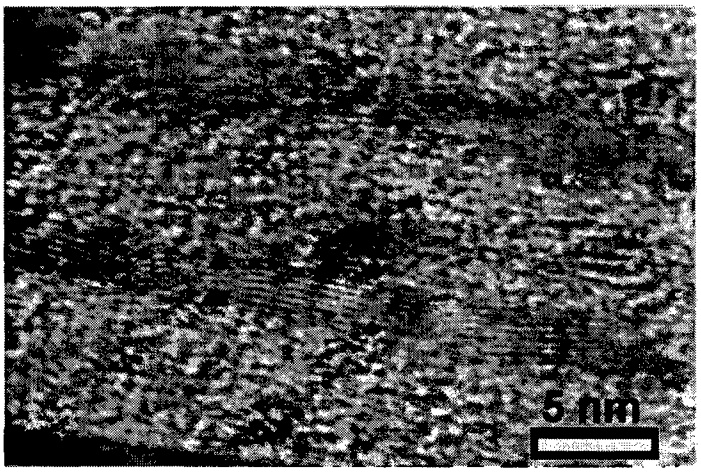


Fig. 7: HRTEM showing the crystallized Si/SiO_2 superlattice with an average nanocrystal size of 3.6 nm. Only crystals having the right orientation can be seen.

The following discussion is focused on the origin of this discrepancy which seems to be in disagreement with previous reports [6]. The HRTEM image of a film with very thin Si layers (Fig. 7) and the TEM image of a film with thick Si layers (Fig. 8) clearly demonstrate the complete crystallization of the Si layers. Nanocrystals extend over the whole layer. As can be seen in Fig. 8, large holes also extending over the whole layer thickness are found after the crystallization process in case of thick layers. Such holes can not be found in the as- prepared film and for Si layer thickness below 10 nm.

On the other hand, prefect nanocrystals with a rectangle shape are found as direct neighbor of such holes (HRTEM, Fig. 9).

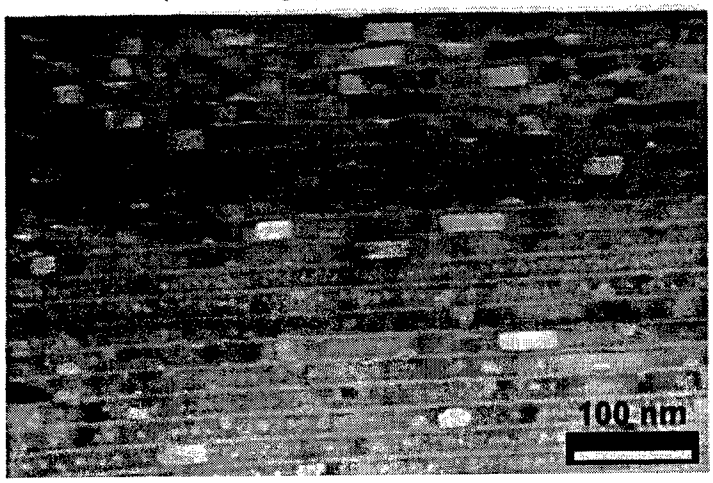


Fig. 8: Large crystals and holes extending over the whole layer are seen in the TEM image (one-step furnace annealing) of a sample with thick layers.

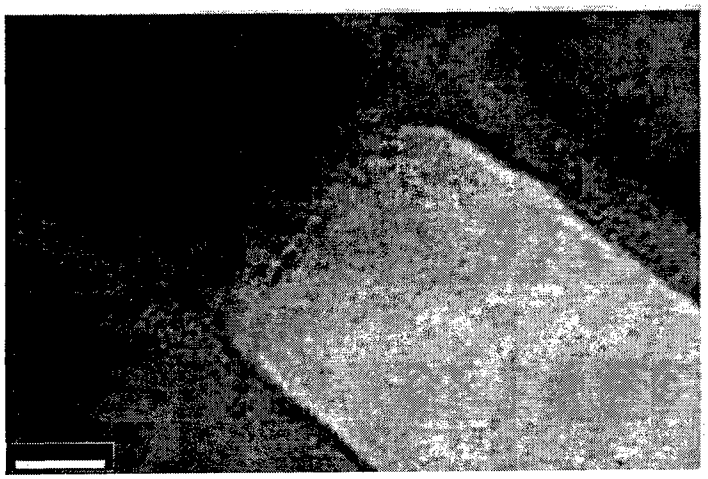


Fig. 9: The HRTEM image demonstrates the interface between a large, perfect nanocrystal and a hole also extending over the whole layer (two-step annealing procedure).

Variations in electron diffraction and contrast are used to check that these regions are really holes and not nanocrystals having a different orientation. With such technique we estimated that the depth extension of such holes is in the range of the Si layer thickness, too. These holes are detected for both the conventional furnace process and the two step procedure.

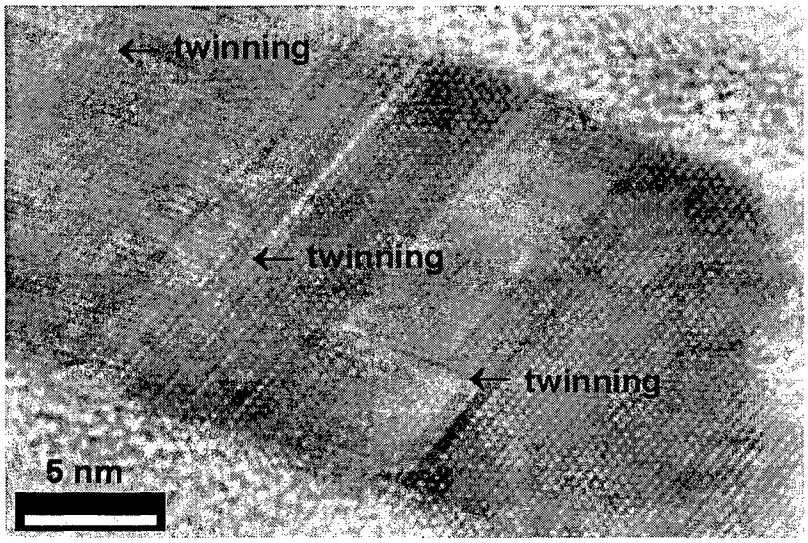


Fig. 10: HRTEM demonstrates growth faulting in large crystals grown in thick (17nm) layers. Dislocations and twinning borders can be seen.

Raman investigations as shown in [6] do not monitor details such as growth faults. Fig. 10 demonstrates a large imperfect nanocrystal extending over the whole layer. During the crystal growth the formation of twin borders is related to the energy relaxation. Obviously, a large numbers of such growth faults can be found in large nanocrystals. While the undisturbed range in-plane with the layer is larger, more twin borders can be found in the perpendicular direction. Such twins disturb the coherence of the x-ray scattering. As a consequence, the Scherrer size does not monitor the size of the entire nanocrystal but the distance between the twin borders which explain the

difference between the sizes obtained with x-ray diffraction and TEM results. However, such crystallographic imperfections have not been found in small nanocrystals. In this case, a good agreement between the Scherrer size and the Si layer thickness is found.

We expect an influence of surface tension (related to the stable SiO_2 interface), nucleation density and Si diffusion directed to the nc-Si nuclei during the thermal growth of the crystals. Let assume that the crystals are grown very rapidly from SiO_2 interface to SiO_2 interface. These crystals operate like timbers in a tunnel and prevent a large shrinkage of the superlattice layers. Further annealing can only increase the lateral size of the crystals by diffusion of Si atoms from the remaining amorphous Si parts to the crystals. The diffusion process dilutes the remaining amorphous region in the lateral direction. On the other hand, the crystal is slowly growing in lateral direction under the influence of the diffusion. As a consequence large undisturbed regions with a nearly perfect crystal structure are found in the lateral direction of the crystals, in agreement with our results.

CONCLUSION

In this paper, the results of a detailed investigation of the crystallization of Si/SiO_2 superlattices are presented. The increase in crystallization temperature for very thin Si layers is demonstrated using x-ray diffraction. Perfect nanocrystals arranged like pearls in a chain can be seen in the HRTEM images. An agreement among the average size of the nanocrystals, the in-plane size, and the Si layer thickness is obtained for layer thicknesses below 7 nm, independent of the crystallization process. The perpendicular size is decreased by around 2 nm due to the influence of the SiO_2 interfaces. These crystallized superlattices do not contain any holes.

On the other hand, films with a Si layer thickness above 7-8 nm did not show a significant size asymmetry in different directions, but the Scherrer size is dependent on the crystallization process. A clear trend to larger average and in-plane sizes is found for the two-step process compared to the one step process, more consistent with the layer thickness. Large holes are visible for thick Si layers, independent of the crystallization process. The discrepancy between the TEM size and the Scherrer size is related to

growth faults which disturbs the x-ray coherence. Twin borders can be seen in large nanocrystals. Consequently, the Scherrer size monitors the undisturbed range of the crystal only, which explains the discrepancy between the Scherrer size and the TEM size.

ACKNOWLEDGEMENTS

Financial support by the Deutsche Forschungsgemeinschaft (DFG), the Kultusministerium Sachsen-Anhalt, and the US Army Research Office is gratefully acknowledged.

REFERENCES

1. L.T. Canham, Appl. Phys. Lett. 57, 1046 (1990).
2. K.S. Min, K.S. Shcheglov, C.M. Yang, H.A. Atwater, M.L. Brongersma, A. Polman, Appl. phys. Lett. 69, 2033 (1996).
3. L. Tsybeskov, K. D. Hirschman, S.P. Duttagupta, M. Zacharias, P.M. Fauchet, J. McCaffrey, D.J. Lockwood, Appl. Phys. Lett.72, 43 (1998).
4. Z.H. Lu, D.J. Lockwood, J.M. Baribeau, Nature 378, 258 (1995).
5. M. Zacharias, J. Bläsing, P. Veit, L. Tsybeskov, K. Hirschman, P. M. Fauchet, submitted.
6. P.D. Persans, A. Ruppert, B. Abeles, J. Non-Cryst. Solids **102**, 130 (1988).
7. M. Zacharias, L. Tsybeskov, K.D. Hirschman, P.M. Fauchet, J. Bläsing, P. Kohlert, P. Veit, J. Non-Cryst. Solids 227-230, 1132 (1998).
8. J. Gonzalez-Hernandez, R. Tsu, Appl. Phys. Lett. **42**, 90 (1983).

OPTICAL PROPERTIES OF SILICON NANOCRYSTALS FORMED BY ION IMPLANTATION

M. H. Wu, A. Ueda, R. Mu. and D. O. Henderson
Chemical Physics Laboratory, Department of Physics
Fisk University, Nashville TN 37208

A. Zuhr, A. Meldrum and C. W. White
Solid State Division, Oak Ridge National Laboratory
Oak Ridge, TN 37831

ABSTRACT

Photoluminescence from silicon nanocrystals fabricated by ion implantation has been investigated using size selective optical excitation techniques. A comparison of the results from size selective excitation measurements for a fixed ion dose to data from measurements at a fixed photon energy for several different ion doses has been made to separate size effects from secondary effects associated with variations in the ion dose. The data show a much greater dependence on ion dose than on excitation photon energy. Both the photoluminescence spectra and the decay of the photoluminescence are virtually unchanged for samples of a given dose as the excitation photon energy is varied from 3.50 eV to 1.91 eV. Photoluminescence spectra for a fixed excitation photon energy, on the other hand, show a redshift of ~ 0.2 eV as the ion dose is changed from 1 x 10^{21} ions/cm^{3}to 1 x 10^{22}ions/cm^3. Photoluminescence decay times extracted from time resolved measurements as a function of implanted ion density also show much larger variations than those observed as a result of tuning the excitation photon energy, ranging from ~250 μs for the lowest dose sample to ~ 600 μs for the highest dose sample. These measurements give greater weight to theories which exclude recombination of excitons within the nanocrystals as the source of the bright visible photoluminescence observed previously in silicon nanocrystals.

INTRODUCTION

The optical properties of quantum confined semiconductors have attracted much interest due to potential device applications and due to basic physical questions concerning the effects of confinement. Silicon nanocrystals (Nanocrystals), in particular, are of great interest for both reasons following the initial observation of efficient luminescence in the

visible region.[1] A red photoluminescence (PL) band has been noted in many different types of quantum confined silicon, including porous silicon[1], colloidal silicon[2] and silicon nanocrystals formed via vacuum deposition[3] and ion implantation.[4] Decay times reported for the red PL range from μs to ms. Faster emission with lifetimes in the nanosecond regime in the green and blue regions has been reported, but is often weaker and appears highly dependent on sample processing.[5] Conflicting theories concerning the origin of the red PL from Si nanocrystals have been presented. Three possible mechanisms have been suggested: radiative recombination of excitons within the Si nanocrystals;[6] luminescence from a trap state localized on the surface of the nanocrystal[7] and carrier tunneling to a "radiative center" outside the NC followed by emission from the radiative center.[8] Studies of the photoluminescence of Si nanocrystals created by ion implantation have been performed to shed more light on this subject.

Silicon and other semiconductor nanocrystals have been successfully fabricated in a number of dielectric hosts by ion implantation followed by thermal annealing. Ion implantation is a technique that is very familiar to the semiconductor industry and results in samples which exhibit extremely good mechanical, thermal and chemical stabilities. Disadvantages of using ion implantation to produce nanocrystals are the relatively broad size distributions which result and the generation of defects in the host material by the high energy ions. Silicon nanocrystals produced by implantation of ions into thermally grown SiO_2 layers on bulk Si and into bulk SiO_2 have been investigated by many authors. Great care must be taken in the interpretation of photoluminescence data from these samples, since SiO_2 is well known to have a number of defects which luminesce in the ultraviolet and the visible regions of the spectrum.[9] Luminescence from these samples is thus highly dependent on implantation and post - implantation thermal annealing conditions. The observed luminescence from Si nanocrystals formed by ion implantation falls into the two categories mentioned above: fast (nanosecond or faster lifetime) emission in the green and blue regions now attributed to defects and slow (microsecond - millisecond lifetime) emission in the red region that has been conclusively connected to nanocrystal formation. These conclusions have been drawn after consideration of a number of points of evidence. First, the higher energy emission is present in inert gas (e. g. Ar, Kr) implanted samples, while the lower energy band is not observed.[10] Second, the higher energy band decreases in intensity with increasing time and/or temperature, beginning at 400°C. This coincides with the behavior of E' and D type defects in SiO_2 as determined by EPR spectroscopy.[11] The intensity of the lower energy band increases with annealing time and/or temperature above 1000°C, which is consistent with the growth of nanocrystals by nucleation.[12] The position of the peaks from XPS measurements indicate a shift from a position reported for SiO_x to a peak position previously reported for Si at these temperatures.[12] We have therefore focused on the red emission band in our current report.

While the lower energy photoluminescence band is associated with the formation of Si nanocrystals, the emission mechanism is still unclear. Photoluminescence most likely occurs after absorption of a photon by the nanocrystal core and the resulting generation of an exciton. We report here experiments designed to distinguish between the two

suggested emission mechanisms: recombination within the nanocrystal and defect mediated relaxation. Measurements of both the photoluminescence spectra and the photoluminescence decay as a function of both ion dose and excitation photon energy have been performed. Variations in the ion dose should result in differing nanocrystal sizes and different levels of defect generation, while size selective excitation for a given dose sample should show differences due only to size differences. If excitonic recombination is solely responsible for the observed photoluminescence, both types of measurements should show the same results. Defect mediated photoluminescence dominates if the measurements do not agree.

EXPERIMENTAL

White and co-workers[13] have shown that the mean size of the nanocrystals formed by ion implantation into bulk SiO_2 substrates can be controlled by varying the ion energy and the post - implantation thermal annealing conditions. The nanocrystals used in the current are identical to those used by White, et. al.[13] Si^+ ions were implanted into SiO2 at energies selected to achieve planar concentration profiles. Samples with implanted ion densities of 1×10^{21}, 2×10^{21}, 5×10^{21} and 1×10^{22} ions/cm^3 were studied. All samples were annealed a reducing atmosphere (96%Ar + 4% H_2) at 1100°C for one hour. Temperatures above 1100°C is required to efficiently produce nanocrystalline silicon, as discussed above. Annealing in a reducing atmosphere is well known to enhance the luminescence efficiency in nanocrystalline and porous silicon, possibly by passivating either dangling bonds at the surface of the nanocrystals or defects in the host matrix.[5] Transmission electron microscopy was used to measure nanoparticle sizes and to establish the presence of crystalline silicon through electron diffraction measurements. Time resolved and static PL measurements were performed using the output of an optical parametric generator/amplifier pumped by the third harmonic of a Nd:YAG laser (30ps pulse width). Emission was monitored at a photon energy of 1.65 eV, where the emission curves of all samples overlap. The pump energy was limited to 2 microjoules to avoid nonlinear or thermal effects. The PL was focused into a 1/4 m monochromator, measured with a photomultiplier tube and digitized by a 500MHz oscilloscope. PL spectra were meaured with an intensified photodiode array mounted to the same monochromator used for the time resolved measurements. All spectra were taken with the intensifier in CW mode.

RESULTS AND DISCUSSION

The presence of silicon nanocrystals in the samples studied here was confirmed by transmission electron microscopy (TEM). TEM micrographs of three of the samples and a virgin SiO_2 substrate are shown in Fig. 1.

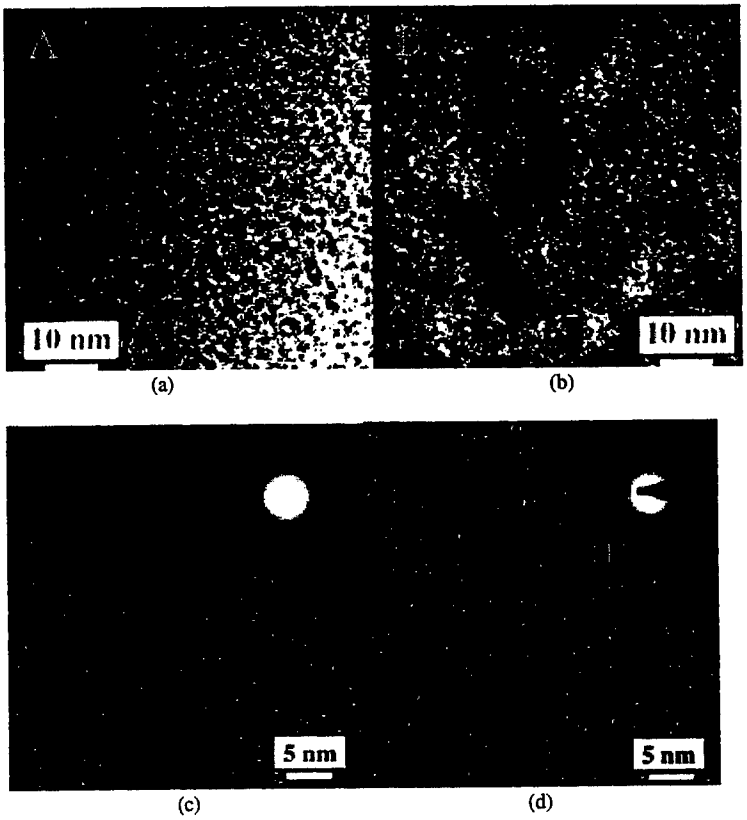


Figure 2. TEM micrographs of (a) 5 x $10^{21}/cm^3$, (b) 1 x $10^{22}/cm^3$ (c) virgin SiO_2 and (d) 2 x $10^{21}/cm^3$. The implanted samples have been annealed for at 1100°C fpr one hour in a reducing atmosphere.

It proved difficult to accurately determine the size of the nanoparticles in the two lowest dose samples, largely because of the low contrast between the SiO_2 matrix and the Si nanocrystals. Figure 1(d), an image from the 2 x $10^{21}/cm^3$ sample, demonstrates the difficulty in imaging the lower dose samples. The "roughness" in fig. 2(d) is the most obvious difference between fig. 1(d) and fig 1(c), an image from an unimplanted substrate. This feature has been observed in many low dose implant of Si into SiO_2 and most likely represents small silicon rich regions. Electron diffraction (as shown in the inset of fig.

1(d)), however, establishes the presence of crystalline silicon. Increasing the dose to 5 x $10^{21}/cm^3$ leads to formation of nanoparticles with dimensions ranging from 1.5 - 4 nm. These particles, shown in fig. 1(a), are clearly resolved at a lower resolution than that used for the lower doses. This established an upper limit of 1.5 nm to the size of the nanoparticles in the two lowest dose samples. Another dramatic change occurs when the implanted dose is increased to 1 x $10^{22}/cm^3$, where the particle size distribution appears to be bimodal (fig. 1(b)). Much larger particles, with diameters of 10 nm or larger, co - exist with smaller particles. These large particles are clearly nanocrystalline silicon, as lattice fringes were observed. The micrographs shown above are believed to be representative of the entire sample, but it must be noted that these TEM micrographs provide images of only a very small region of the samples. The size of the micrographs shown above are much smaller than the beam size of a few square mm used in the photoluminescence and absorption measurements reported below.

The linear absorption spectra of the four samples (shown in fig. 2) illustrates the effect of ion dose on the location of the absorption edge.

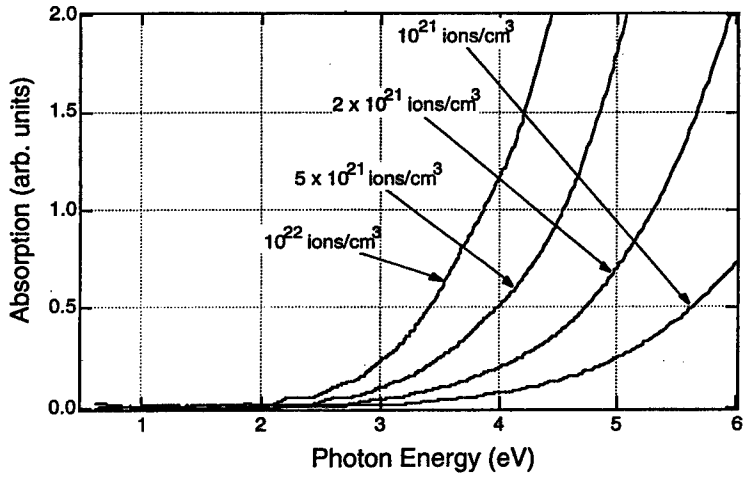


Figure 2. UV-visible absorption spectra of the implanted samples after annealing.

All spectra are normalized against a spectrum from a virgin SiO_2 substrate. Oscillations appearing between 2 eV and 3 eV in the spectra are caused by interference effects caused by reflections from the silicon nanocrystal layer. The absorption edges for all samples are considerably blue shifted from the bulk edge near 1.1 eV. White, et. al. reported that optical absorption edge shifts from 3 eV to < 2 eV as the dose is increased over a range similar to that considered here. This trend is consistent with the increase of the average

particle size as seen from TEM measurements as the implanted ion dose is increased. The excitation photon energies for the experiments reported here range from 1.9 eV to 3.5 eV, spanning the range of the absorption edges shown above.

Photoluminescence Spectra

The dependence of the photoluminescence spectra after "global" excitation at 3.5 eV on the ion dose is shown in Fig. 3.

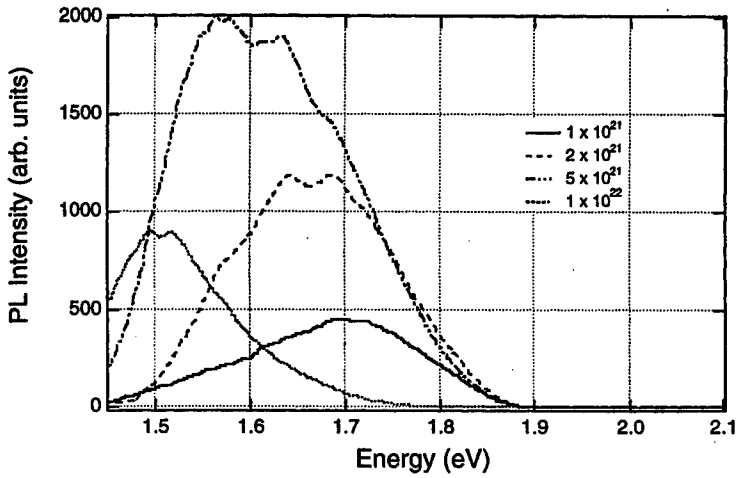


Figure 3. Dose dependence of the photoluminescence spectra after global excitation. Excitation photon energy = 3.50 eV and T = 10K.

There is quite a large gap between the absorption onsets and the onset of the photoluminescence peaks. Furthermore, the position of the peaks in photoluminescence spectra show a much smaller dependence on the ion dose than do the absorption onsets. The peaks of the spectra gradually redshift from 1.70 eV to 1.50 eV with increasing dose, while the absorption edges shift by more than 1 eV. Emission from all samples are fairly broad, with FWHM of roughly 0.25 eV. Emission intensity also increases with increasing dose for the three lowest doses, as expected. The decrease in the efficiency of the highest dose sample may result from the appearance of larger nanocrystals.

The dose dependent PL spectra described above have been complemented by measurements of the PL spectra of each sample as the excitation photon energy was

varied from 1.91 eV to 3.50 eV. This corresponds roughly to the range of the absorption onsets shown in Fig. 1.

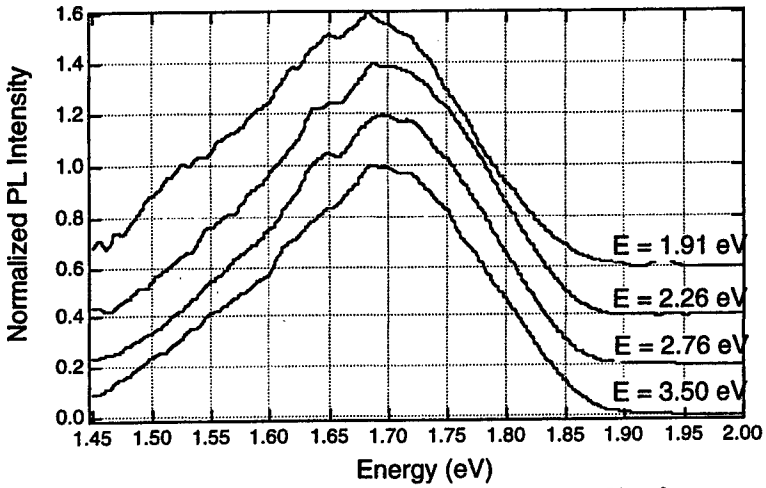


Figure 4. Dependence of the photoluminescence spectra of the 1 x $10^{21}/cm^3$ sample on the excitation photon energy. Spectra are normalized and offset for clarity of presentation.

The spectra show little change as the excitation photon energy is varied over a wide range. The peaks of the spectra show a very small redshift of less than 0.02 eV at the lowest excitation photon energy. This redshift is insignificant compared to the shift of approximately 0.2 eV that occurs between the lowest and highest dose sample under global excitation. The width of the peak remains largely unchanged, with the exception of a slight broadening measured at the lowest photon energy. This is an unexpected result if the photoluminescence is assumed to occur from excitonic recombination within the nanocrystals. Decreasing the excitation photon energies reduces the size range of the excited nanocrystals and therefore should lead to narrowing of the PL spectrum. Similar measurements (not shown) for the intermediate dose samples show similar effects. Small redshifts of ~0.05 eV can be seen for the lowest excitation photon energy in those samples. Noticeable broadening also occurs at the lowest photon energy in both cases. Spectra for the highest dose sample, do not show any significant shifts in peak position or any appreciable broadening.

Time Resolved Photoluminescence

Measurements of the time resolved photoluminescence were carried out in a manner analogous to that described above for the photoluminescence spectra. The excitation photon energy was tuned while the emission was monitored at 1.65 eV. The dose dependence of the photoluminescence lifetime under global excitation is shown below in Fig. 5.

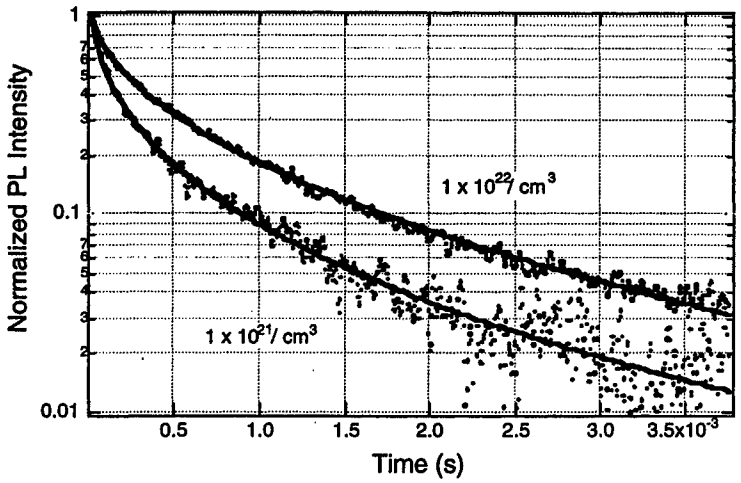


Figure 5. Dose dependence of PL decay after global excitation.

The decay curves observed are strongly nonexponential for all doses. The PL decay are fit well by a stretched exponential function

$$I(t) = I_O e^{-(t/\tau)^{\beta}} \qquad [1]$$

which is often used to describe relaxation dynamics in systems with broad distributions of decay times.[14] The parameter β ranges between 0 and 1, with smaller values indicating a broader distribution and the upper limit of one resulting a single exponential decay. The decay of experimental curves fitted to this model can be characterized by a mean lifetime[15]

$$\langle \tau \rangle = \frac{\tau}{\beta} \Gamma\left(\frac{1}{\beta}\right) \qquad [2]$$

The lifetimes of the globally excited samples increase with increasing dose for the three lowest doses, from ~250 μsec for the lowest dose to ~575 μsec for the 5 x 10^{21}/cm^3 sample. The lifetime of the 1 x 10^{22}/cm^3 sample is ~ 450 μsec, but this is most likely due to the fact that the lifetime is measured at an emission energy approximately 0.15 eV above the peak of the spectrum. Several earlier investigations have shown that the lifetime as the measured position approaches the peak of the spectrum.[8]

The dose dependence of the time resolved measurements described above can be compared to measurements performed on a individual samples while the excitation energy is varied. The variation of the lifetimes for the lowest dose sample is shown below in figure 6.

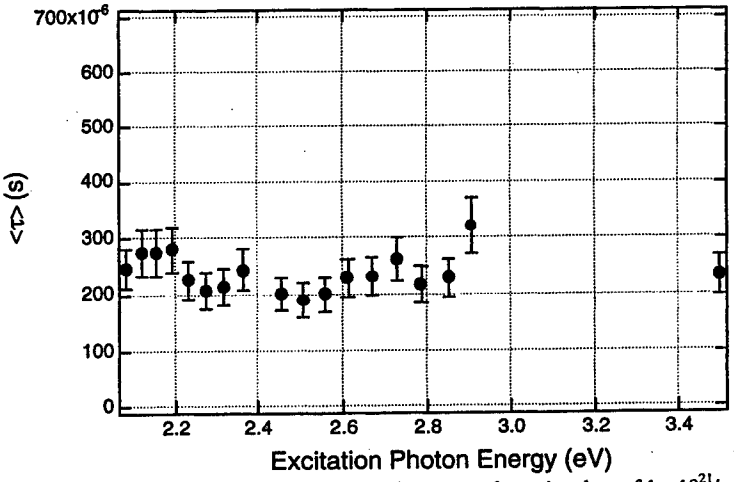


Figure 6. Dependence of PL lifetime on excitation energy for an ion dose of 1 x 10^{21}/cm^3.

The mean lifetimes, while showing some scattering due to a relatively large uncertainty, are grouped between 190 μsec and 310 μsec. This is a small variation compared to lifetimes up to 575 μsec observed in the dose dependent measurements. No definitive trend can be observed as the excitation photon energy is tuned. Measurements of the 2 x 10^{21}/cm^3 sample show much the same results, with the lifetimes scattered in a range between 390 μsec and 510 μsec. The range of lifetimes increases to 500 μsec and 600 μsec for the 5 x 10^{21}/cm^3 sample. The lifetimes for the highest dose sample largely

overlaps that of the 5 x 10^{21}/cm^3 sample. The time resolved PL data is summarized below in Figure 7.

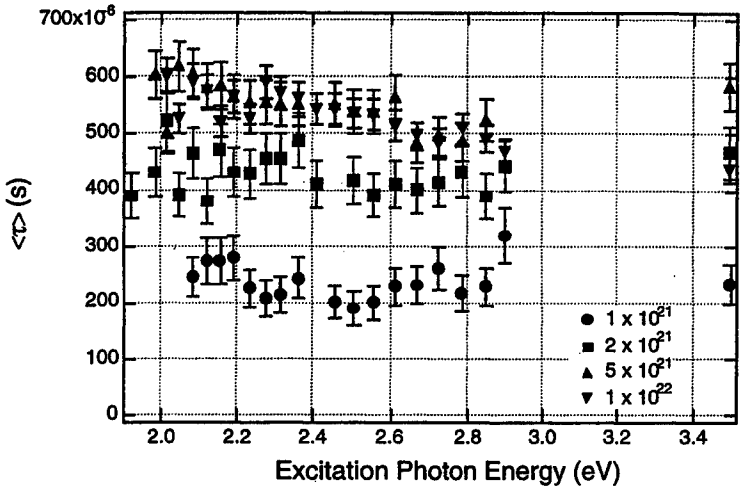


Figure 7. Dependence of the PL lifetime on the excitation photon energy for four ion doses.

The data for the three lowest dose samples is another clear indication that the ion dose has a greater impact than nanocrystal size on the photoluminescence. There is virtually no overlap between the lifetimes of the different dose samples, regardless of the excitation photon energy considered. The overlap between the 1 x 10^{22}/cm^3 sample and the 5 x 10^{21}/cm^3 sample may result from the energy of the PL detected for the time resolved measurements. Studies on porous silicon have shown that lifetimes increase with decreasing emission photon energy. The reason for this increase is not clear. The monitored emission photon energy of 1.65 eV is on the low energy side of the peaks of the spectra of the three lower doses, but is considerably redshifted from the peak of the spectra for the highest dose sample.

CONCLUSIONS

Comparisons between the ion dose dependence and the excitation photon energy dependence of the photoluminescence decay and spectra show that emission from silicon nanocrystals fabricated by ion implantation is influenced far more by the ion dose. This leads to the conclusion that photoluminescence from these nanocrystals is unlikely to result from excitonic recombination within the nanocrystals. If the dominant mechanism

for emission was recombination within the nanocrystals, the spectral and time resolved data should show a greater dependence on the excitation photon energy - which effectively selects the size of the emitting nanocrystals. The main emission mechanisms remaining are emission from excitons trapped at surface states and emission from "luminescence centers" located outside of the nanocrystals. Ion dose can affect the emission by these mechanisms in a number of ways, including changing the type or density of defects present in the host matrix and on the surface of the nanocrystal. Further investigation, including implantation into different matrices and alteration of the annealing conditions, are being conducted to determine the nature of the emission process.

REFERENCES

1. L. T. Canham, *Appl. Phys. Lett.* **57**, 1046 (1990).

2. See, for example, W. L. Wilson, P. F. Szajowski and L. E. Brus, *Science* **262**, 1242 (1993).

3. See, for example, L. N. Dinh, L. L. Chase, M. Balooch, W. J. Siekhaus and F. Wooten, *Phys. Rev. B* **54**, 5029 (1996).

4. See, for example, T. Shimizu-Iwayama, S. Nakao and K. Saitoh, *Appl. Phys. Lett.* **65**, 1814 (1994).

5 . K. S. Min, K. V. Shcheglov, C. M. Yang, H. A. Atwater, M. L. Brongersma and A. Polman, *Appl. Phys. Lett.* **69**, 2033 (1996).

6. See, for example, K. Kim, *Phys. Rev. B* **57**, 13072 (1998).

7. Y. Kanemitsu, T. Ogawa, K. Shiraishi and K. Takeda, *Phys. Rev. B* **48**, 4883 (1993).

8. J. C. Vial, A. Bsiesy, F. Gaspard, R. Herino, M. Ligeon, F. Muller, R. Romestain and r. M. Macfarlane, *Phys. Rev. B* **45**, 14171 (1992).

9. T. shimizu-Iwayama, M. Ohshima, T. Niimi, S. Nakao, K. Saitoh, T. Fujita and N. Itoh, *J. Phys. Cond. Matt.* **5**, L375 (1993).

10. S. Guha, M. D. Pace, D. N. Dunn and I. L. Singer, *Appl. Phys. Lett.* **70**, 1207 (1997).

11. L. S. Liao, X. M. Bao, X. Q. Zheng, N. S. Li and N. B. Min, *Appl. Phys. Lett.* **68**, 550 (1996).

12. H. Z. Song and X. M. Bao, *Phys. Rev. B* **55**, 6988 (1997).

13. C. W. White, S. P. Withrow, A. Meldrum, J. D. Budai, D. M. Hembree, J. G. Zhu, D. O. Henderson and S. Prawer, *Mat. Res. Soc. Symp. Proc.*, to be published

14. K. D. Singer, R. Dureiko, J. Khaydarov and R. Fuerst, *Mat. Res. Soc. Symp. Proc.* **328**, 499 (1994).

15. A. Dhinojwala, J. C. Hooker and J. M. Torkelson, *Mat. Res. Soc. Symp. Proc.* **328**, 443 (1994).

NONLINEAR OPTICAL PHENOMENA IN THE LUMINESCENCE FROM SI NANOCRYSTALS

D. Kovalev, H. Heckler, B. Averboukh, M. Ben-Chorin*, F. Koch
Technische Universität München, Physik-Department E16, D-85747 Garching, Germany
*Weizmann Institute of Science, Department of Chemical Physics, Rehovot 76100, Israel

ABSTRACT

We review some of our recent work on the porous Si luminescence and emphasize the importance of the nonradiative Auger-process in the description of the Si nanocrystal photoluminescence (PL) properties. Due to a very long radiative time already at weak levels of optical excitation a double occupation of crystallites by *e-h* pairs is achieved. This results in PL saturation, an efficient photoluminescence suppression by a resonant pump beam and persistent hole burning phenomena. The hole burnt in the luminescence spectrum in a pump-to-probe or persistent mode has two well defined onsets related to the TO momentum conserving phonons of Si. The amplitude of the spectral hole is 90% from the total PL. These results allow us to conclude that most of the luminescence of porous Si arises from radiative recombination of indirect excitons confined inside the nanocrystals.

One of the most important properties of the nanocrystal assemblies is their strong nonlinear optical response. Recently the importance of the competition between radiative and Auger recombination for the electronic and optical properties of semiconductor quantum dots has been recognized [1]. A very efficient breakdown of the *k*-conservation rule due to a strong spatial confinement [2] considerably accelerates the rate of Auger process. Even in direct bandgap quantum dots with radii of the order of a few nanometers this rate is expected to be larger than that of radiative transitions. Porous Si films are ensembles of differently sized and shaped quantum dots. Experimental and theoretical investigations of porous Si [3] show that Si nanocrystals still have an indirect band gap. The radiative times at room temperature are ~10 μs and at low temperatures as long as a few ms. A simple estimate shows that at room temperature at 100 W/cm^2 and at He temperature at 1W/cm^2 of CW optical excitation in average each crystallite is already occupied by one *e-h* pair. This leads to a variety of phenomena like saturation of the PL and a persistent PL hole burning already under mediate levels of optical excitation. First studies demonstrating such kind of effects in

porous Si were done by injection of additional carriers from electrolyte. The Auger process was considered as a good candidate to explain voltage selective quenching of PL and voltage tunable electroluminescence [4]. In this paper we intend to explain our current understanding how the nonradiative Auger-process influences the basic PS photoluminescence properties. The results of our experiments combined together allow us to conclude that most of the luminescence of PS arises from radiative recombination of indirect excitons affected by spatial confinement.

The luminescence mechanism in porous silicon has been a subject of a long-standing debate. In his first article on PS luminescence Canham [5] attributed the PL to radiative transitions between quantum confined levels inside the Si nanoparticles. Some researchers suggested different models [3] including radiative recombination via surface states [6], Si based luminescing compounds like a-Si [7], siloxene [8] and light emission from certain defects in SiO_2 [9].

The first spectroscopic evidence that at least a part of the luminescence results from quantum-confined states inside the Si nanocrystals came from the experiments of Calcott et al [10]. They excite the luminescence resonantly and observe clear onsets in the PL spectrum. The energy of the onsets is identical to that of the TO and the TA momentum conserving phonons of c-Si. Since two structures are observed (for each phonon) the only possible processes in the absorption-emission cycle involve zero, one or two momentum-conserving phonons. These processes correspond to no-phonon transitions in both emission and absorption, to a phonon-assisted process in either the absorption or the emission, and to phonon-assisted transitions in both the emission and the absorption.

Several experimental observations, especially regarding the influence of the surface chemistry of PS on its light emission, are difficult to reconcile with the notion that all the light originates from quantum confined states. For instance in [11] it was suggested that most of the light comes from a very efficient luminescence source, which is not the Si nanocrystals. This proposed source is efficiently excited only above 2.5 eV, and there is a strong Stokes shift of the emission, so its PL peak is at 1.6-2 eV. The weak luminescence from the Si nanocrystals can be seen only when the excitation of the strong source is impossible (as in the case of the resonant excitation) [11]. In order to support this conjecture the efficiency of light emission under resonant and non-resonant excitations has been measured, and the luminescence is found to be much weaker under resonant excitation, when the phonon structures are seen. The increase in the luminescence efficiency with rising excitation energy is accompanied by a smearing of the phonon onsets. They conclude that under usual excitation conditions most of the light does not involve phonon assisted processes, and therefore it is not a result of radiative transitions between confined exciton states.

We use luminescence hole burning in order to determine accurately how much of the light is emitted from quantum-confined states. This method has been employed for a variety of nanocrystal systems (see, for example [12]). The luminescence is excited by a weak probe beam ($\hbar\omega_{ex.} = 2.8$ eV). Because of the high energy of the photons all the emitters are excited efficiently. Then, an intense pump beam is used to quench the

luminescence. If a probe photon is absorbed in a nanocrystal which is already occupied by an electron-hole pair created by the strong pump beam, non-radiative Auger recombination will occur [4]. Therefore, the luminescence due to the probe beam is suppressed by the presence of the pump beam.

In order to identify the light emission from the strong source we use a resonant pump beam ($\hbar\omega_{pump}$ = 1.68 eV). At this pump energy the strong source is supposedly not absorbing [11]. Therefore, the fraction of the PL suppressed by the pump beam is emitted from the quantum confined states. This is confirmed by the observation of onsets due to the TO momentum conserving phonons in the spectral shape of the "hole" burnt in the PL spectrum. We find that the magnitude of the "hole" reaches 90 % in the region of the second phonon step, what implies that most of the luminescence is due to indirect exciton transitions.

Persistent hole burning is also observed as a result of Auger ionization. If two *e-h* pairs occupy simultaneously the same nanocrystal one pair would recombine non-radiatively via the Auger process. One of the carriers left gains the energy of the recombined pair and can escape from the crystallite. As a result the nanocrystal is charged, and all further radiative recombination inside it is suppressed due to sequence of Auger processes. At low temperatures the nanocrystal remains ionized for long times, resulting in a persistent degradation of the PL [13,14,15]. We show that Auger-induced charging of the nanocrystallites leads to the persistent hole-burning phenomena in the PL with the same phonon onsets structure. Increasing the temperature of the sample washes out the hole burnt in the PL spectrum and this is accompanied by a thermoluminescence signal with similar phonon onsets.

The details of the sample preparation and the optical setup can be found elsewhere [16]. The experiments are done using a pump-probe technique. A dye laser tunable in the spectral range of 600--690 nm or Ti-Sapphire laser are used to excite resonantly the PL or as a pump beam source. For nonresonant pump-probe experiments an Ar^+ laser with $\hbar\omega_{ex.}$ = 2.54 eV is used. A He-Cd laser (2.8 eV) beam is used as a probe. The intensity of the probe beam is kept low (I_{probe}=10 mW/cm^2) so the PL intensity is in the linear regime. A microscope is used to ensure that the pump spot overlaps completely the smaller spot of the probe laser. The probe beam is modulated at a frequency of 12 Hz and the PL is measured using conventional lock-in technique at the same frequency. The pump beam is modulated at a high frequency (260 Hz) to achieve quasi-steady-state pumping conditions with respect to the excited carriers lifetimes [10]. To suppress stray light from the pump laser the entrance slit of monochromator is blocked when the pump beam illuminates the sample. To avoid overheating of the sample by the pump beam all the experiments are done in superfluid He at T=1.5 K and the intensity of the pump beam is kept below the He boiling threshold ($I_{pump}\leq$ 50 W/cm^2).

On the Fig.1 we show the dependence of the PL response on the probe beam as a function of the pump beam intensity. Introduction of both resonant and nonresonant pump beams induces an efficient quenching of the PL. Under non-resonant pump beam illumination ($\hbar\omega_{pump}$=2.54 eV) the maximal suppression value is of the order of 20 while

for the low pump beam energy the effect is significantly weaker. The additional carriers injection rate is a product of the radiative lifetime, absorption cross-section of nanocrystals and the pump beam intensity. In order to give an estimate of the ratio of the absorption cross-sections at resonant and non-resonant excitations, we assume that the PL induced by the probe beam at $\hbar\omega_{det.}$ is proportional to the density of crystallites with a „gap" $\hbar\omega_{det.}$, which are left unoccupied by the pump beam (at energy $\hbar\omega_{pump}$). We solve a system of rate equations and obtain the density of empty crystallites as a function of the pump intensity[15] (Eq. 1):

$$N_{empty}(\hbar\omega_{det.}, I_{pump}) = \frac{N_{total}(\hbar\omega_{det.})}{1+\tau_R(\hbar\omega_{det.})\sigma(\hbar\omega_{det.},\hbar\omega_{pump})I_{pump}}$$

Here τ_R $(\hbar\omega_{det.})$ is the radiative lifetime, σ $(\hbar\omega_{det.}, \hbar\omega_{pump})$ is the cross section for absorption of photons with an energy $\hbar\omega_{pump}$ in a nanocrystal with a „gap" $\hbar\omega_{det.}$, I_{pump} is the intensity of the pump light expressed in an areal flux of incident photons. The solid curves in Fig. 1 are fits using Eq. 1. We neglect the fact that light emission at $\hbar\omega_{det.}$ originates from crystallites with gaps $\hbar\omega_{det.}$ (via no-phonon process) and $\hbar\omega_{det.} + \hbar\Omega_{phonon}$ (via phonon-assisted emission). Since we would like to get an order of magnitude estimate of the ratio between the cross section at non-resonant and resonant excitation we can assume safely that the cross sections at $\hbar\omega_{det.}$ and $\hbar\omega_{det.} + \hbar\Omega_{phonon}$ are the same, and therefore it can be replaced by an average value. Although we used this simplification the results are fitted very well. Substituting the measured values of τ_R=4 ms we obtain an approximate value of σ ($\hbar\omega_{det.}$ = 1.88 eV, $\hbar\omega_{pump}$ = 1.94 eV) = $4\cdot10^{-19}$ cm^2, while for high energy pumping σ ($\hbar\omega_{det.}$ = 1.77 eV, $\hbar\omega_{pump}$ = 2.54 eV) = 10^{-17} cm^2. The difference in these values reflects the increase in the density of electronic states with increasing energy above the "gap".

The resonant beam suppresses the non-resonant PL intensity at energies below that of the pump photons. This effect is present for all excitation energies used (1.5-2.5 eV). The PL intensity at higher emission energies is almost not affected. Two well defined onsets, separated by ~56 meV, are seen in the resulting PL spectra. No influence on the PL is observed in the close vicinity of the excitation line. These PL features are related to the TO-phonon replicas and the exciton gap observed in the resonant PL spectrum [10,11,17]. The maximal suppression we have achieved is as large as 10 and it reaches factor of 3 already in the region of the first phonon step. The effect is far from saturation and the measured suppression values are limited by the experimental setup (the power of the laser). Note that the actual suppression value is even higher since the detected signal is a result of averaging over the pump laser on and off periods (time ratio is 5:7). The same tendency can be seen at room temperature except of the phonon onsets smeared due to interaction with acoustical phonons.

In Fig.2 we compare the degree of PL suppression (the difference between the PL intensity with and without pump beam) with the resonant PL spectrum. The resonant PL spectrum is excited at the same wavelength as that of the pump. There is an obvious

correlation between the spectral dependence of the degree of quenching and the resonant PL spectrum. In particular, the two steps in the suppression spectrum coincide with the TO momentum conserving phonon onsets observed in the resonant PL spectrum. The intensity of the suppressed PL is a large fraction of the PL intensity under non-resonant excitation when all the "emitters" are efficiently excited.

In order to assert that the luminescence dynamic hole burning phenomena do not arise from bleaching of the band edge absorption (occupation of the electron or the hole ground states can affect the transition energy and quantum dot oscillator strength [18] we have looked for changes in the absorption of free standing layers, induced by the pump beam. However, no induced effect on the absorption is seen within the experimental error. This is probably due to the small fraction of luminescing particles.

The presence of *two* phonon steps in the quenching spectrum proves that the luminescence that has been suppressed involves momentum-conserving phonons also in the emission process [10]. We assume that the probe beam does not induce light emission in a crystallite in which an *e-h* pair is excited by the pump beam. The probability of a crystallite to be occupied is proportional to σ (E_g, $\hbar\omega_{pump}$) the absorption cross section for photons with an energy $\hbar\omega_{pump}$ in a nanocrystal with a "gap" E_g, what in fact reflects the average density of electronic states at $\hbar\omega_{pump}$ in the nanocrystal. However, since the absorption involves no-phonon and phonon-assisted processes, , σ (E_g, $\hbar\omega_{pump}$) has one phonon onset at $\hbar\Omega_{phonon}$ above E_g. The second phonon onset comes from the emission process. The occupied crystallite does not emit light either at E_g (minus the small exciton gap) or at $E_g - \hbar\Omega_{phonon}$. We point out that if only the absorption takes place inside the nanocrystal, but the emission involves localized states (surface or SiO_x defect states), only one phonon step should be seen.

We observe that 90% of the total luminescence is suppressed by the presence of the resonant pump. The spectral shape of the "hole" demonstrates two phonon onsets. Combining these facts we conclude that the origin of the PL is radiative recombination between quantum confined states inside the Si nanocrystals. The observations that the resonantly excited PL is much weaker than that excited at high energies is explained by the difference of the absorption cross sections. Indeed, the light emission under non-resonant excitation is much more efficient than under resonant one as it was shown in [11], but this is due to the large difference in the density of states. We point out that this factor we have obtained from the hole burning experiments has a similar magnitude to that deduced from the luminescence intensity [11].

We turn now to discuss persistent hole burning phenomena. These effects are studied in the following way. After measuring the usual PL spectrum under non-resonant conditions ($\hbar\omega_{ex.}$ = 2.8 eV), we switch off the weak probe beam and expose the sample to a strong resonant beam I_{pump} = 10 W/cm^2. The intense resonant pump beam is used to create a long term degradation of the luminescence via an Auger ionization. After each light soaking step (with varied exposure time), we switch off the strong beam and measure the luminescence again using the same weak probe beam.

The burnt luminescence spectra are shown in Fig. 3. They are very similar to those seen in Fig. 2. A clear decrease in PL efficiency is recorded for emission energies

below that of the degrading beam, while no influence is detected above it. Again two phonon replicas and a forbidden gap known from the resonant PL measurements are observed. The degradation becomes less efficient at low detection energies as in the case of the non-resonant fatigue effect [15]. The amplitude of the spectral hole increases continuously with resonant light exposure time. At low temperatures, the spectrum of the "hole" and its magnitude do not change during tens of hours. Heating heals the hole and at 300 K washes it out completely. Again the same effect can be seen over the whole PL band.

On the Fig.4 we show a detailed PL spectrum in the vicinity of the burning laser energy. The onset of the spectral hole is spectrally delayed with respect to the burning laser energy. This spectroscopic gap labeled Δ is well known from the resonant PL measurements and is due to the *e-h* exchange exciton splitting [10]. This observation has very important implications for the understanding of the nature of the PL. First it shows that electronic states of all possible luminescing species are splitted in the same way as it does for resonantly excited emitters. Second, it evidences that there is no Stokes shift between absorbing and luminescing state. Observed and widely discussed significant Stokes shift between absorption edge and PL band energy is an artificial fact arising from the small density of electronic states near to the exciton ground state. Our hole burning experiments show that the energy difference between absorbing and luminescing state is equal to Δ even at 2.5 eV excitation energy.

Electrons or holes ejected from the Si nanocrystals during the Auger ionization process are either captured by surface traps or transferred to a neighboring nanocrystals. When the sample is heated the trapped carriers can be thermally reexcited into the nanocrystals. A carrier injected into a charged nanocrystal recombines with the carrier which has been left there. This process restores the initial optical properties of the sample, since the nanocrystals become neutral (hole healing process). If the recombination is radiative a thermoluminescence signal appears. This effect is known for semiconductor doped glasses [13]. Thermoluminescence is measured during the heating of the sample (after persistent hole burning) using a spectrograph combined with a silicon CCD array or with a photomultiplier in an integral mode.

The thermoluminescence from a sample that has been exposed to resonant light at 1.5 K is measured while the sample is heated to 20K. The spectra are shown in Fig. 5 and demonstrate the same spectral features seen in the hole burning experiments. The emission spectra shift with the burning light energies. Furthermore, two TO phonon onsets are seen as well. These TO phonon replicas are seen better in the first derivative of the thermoluminescence spectrum (inset of Fig.5). The presence of a weak anti-Stokes thermoluminescence at energies above the burning energy indicates that a part of the carriers is ejected via Auger process to crystallites with higher bandgaps. According to our estimates the total number of photons emitted during the heating procedure is roughly equal to the number of photodegraded nanocrystals. The spectrally-integrated thermoluminescence signal measured at a constant heating rate has a broad temperature distribution from 1.5K to 300K with a maximum around 150 K. Following the procedure described in [19] we deduce an average activation energy of 300 meV. This

energy is in a good agreement with measured energy positions of surface traps in porous silicon [20]. It is slightly smaller than the activation energy of the DC transport (about 0.5 eV) [21].

The fact that the hole burnt at low temperatures persists for a few hours and that heating can cause thermoluminescence has important implication for the understanding of the mechanism of PS luminescence. In several of the suggested models for the PL, it is argued that electrons and holes, optically excited in the core of the nanocrystal, relax in energy to different types of localized states, from which they recombine radiatively. The relaxation energy is assumed to be about 0.3-0.5 eV, thus explaining the Stokes shift of the non-resonantly excited PL. Indeed such trap states can exist as it is evident from the thermoluminescence data. However, the lifetime of captured carriers is very long (of the order of tens hours at low temperatures). Radiative recombination between these states is impossible at low temperatures, and thus the light emission can not involve such transitions. The hole burning spectra clearly show that Stokes shift between absorbing and luminescing states is only due to the exchange splitting of the absorbing and luminescing exciton states confined in Si nanocrystals.

To summarize, we have demonstrated that Auger non-radiative processes result in spectral hole burning in the PL of PS. At low temperatures the hole can persist for long times, and its healing is accompanied by thermoluminescence. The presence of two phonon steps as a general feature in all these phenomena allows us to conclude that the luminescence of porous Si arises from radiative transitions between quantum confined indirect exciton states inside the Si nanocrystals.

ACKNOWLEDGEMENT

We acknowledge the support of this work by INTAS (grant No. 93-3325 ext) and Deutsche Forschungsgemeinschaft.

References

[1] V. A. Kharchenko and M.Rosen, Journal of Luminescence 70, p.158 (1996).
[2] D. Kovalev, H. Heckler, M. Ben-Chorin, G. Polisski, M. Schwartzkopff, and F. Koch, Phys. Rev. Lett. 81, p.2803 (1998).
[3] L. T. Canham, Phys. Stat. Sol. (b) 190, p.9 (1995).
[4] I. Mihalcescu, J. C. Vial, A. Bsiesy, F. Muller, R. Romestain, E. Martin, C. Delerue, M. Lannoo, G. Allan, Phys. Rev. B 51, p.17605 (1995); C.Delerue, M. Lannoo, G. N. Allan, E. Martin, I. Mihalcescu, J. C. Vial, R. Romestain, F. Muller, A. Bsiesy Phys. Rev. Lett. 75, p.2228 (1995).
[5] L. T. Canham, Appl. Phys. Lett. 57, p.1046 (1990).
[6] F. Koch, Mat. Res. Soc. Symp. Proc. 298, p.319 (1993).
[7] R. P. Vasques, R. W. Fathauer, T. George, A. Ksendzov, and T. L. Lin, Appl. Phys. Lett. 60, p.1004 (1992).
[8] M. S. Brandt, H. D. Fuchs, M. Stutzmann, J. Weber, and M. Cardona, Solid State Commun. 81, p.307 (1992).

[9] S. M. Prokes and W. E. Carlos, J. Appl. Phys. 78, p.2671 (1995).
[10] P. D. J. Calcott, K .J. Nash, L. T. Canham, M.J. Kane, and D. Brumhead, J.Phys. Condens. Matter 5, L91 (1993).
[11] M. Rosenbauer, S. Finkbeiner, E. Bustarret, J. Weber, M. Stuzmann, Phys. Rev.B 51, p.10539 (1995).
[12] T. Kawazoe and Y. Masumoto, Phys. Rev. Lett. 77, p.4942 (1996).
[13] A. I. Ekimov and Al. L. Efros, Phys. Stat. Sol. (b) 150, p.627 (1988).
[14] V. Grivickas, J. Linnros, and J. A. Tellefsen, Thin Solid Films 255, 208 (1995).
[15] D. Kovalev, B. Averboukh, M. Ben-Chorin, F. Koch, Al. L. Efros, and M. Rosen, Phys. Rev. Lett. 77, p.2089 (1996); Al. L. Efros, M. Rosen, B. Averboukh, D. Kovalev, M. Ben-Chorin, and F. Koch, Phys. Rev. B 56, p.3875 (1997).
[16] D. Kovalev, M. Ben-Chorin, J. Diener, F. Koch, Al. L. Efros, M. Rosen, N. A. Gippius, S. G. Tikhodeev, Appl. Phys. Lett. 67, p.1585 (1995).
[17] T. Suemoto, T. Kanaka, A. Nakajima, T. Itakura, Phys. Rev. Lett. 70, p.3659 (1993).
[18] Y. Masumoto, Journal of Luminescence, 70, p.386 (1996).
[19] D. Curie, *Luminescence in Crystals* (Methuen and co., London 1963).
[20] M. Ben-Chorin, F. Möller, and F. Koch, Mat. Res. Soc. Symp. Proc. 358, p.575 (1995).
[21] M. Ben-Chorin, F. Möller, and F. Koch, Phys. Rev. B 49, p.2981 (1994).

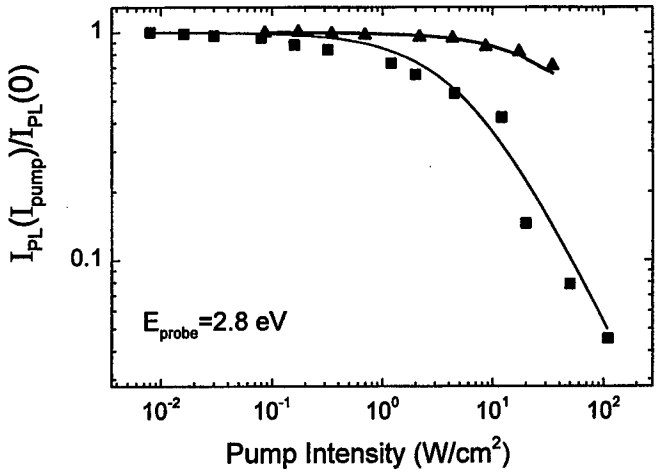


Figure 1: The intensity of the PL induced by probe beam as a function of the pump beam intensity. Triangles: $\hbar\omega_{pump}$ = 1.946 eV, $\hbar\omega_{det.}$ = 1.879 eV. Squares: $\hbar\omega_{pump}$ = 2.54 eV, $\hbar\omega_{det.}$ = 1.77 eV. Solid lines are fits to Eq. 1.

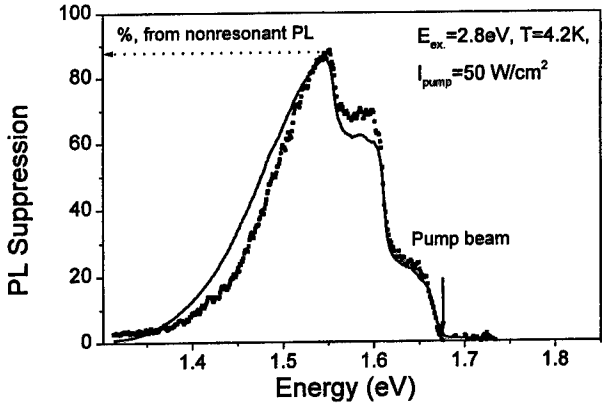


Figure 2: A comparison between the spectral dependence of the suppression of the non-resonantly excited PL by a pump beam (solid squares) and the resonant PL of PS at the same excitation energy (solid line). The laser energy is shown by arrow.

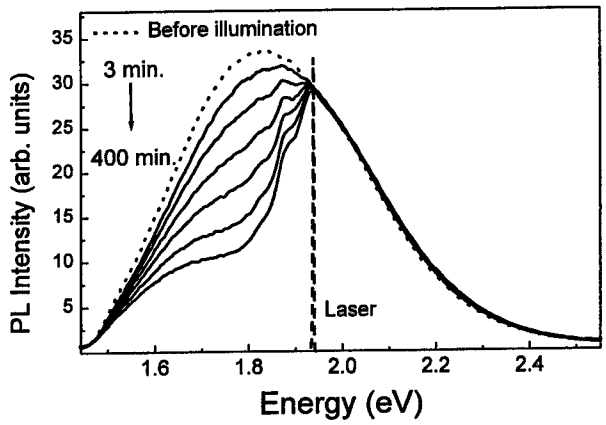


Figure 3: Persistent hole burning spectra of PS luminescence for different resonant light soaking time (solid lines). The illumination exposure times are 3, 10, 40, 100, 220 and 400 minutes, respectively. For comparison the initial PL spectrum is also shown (dashed line).

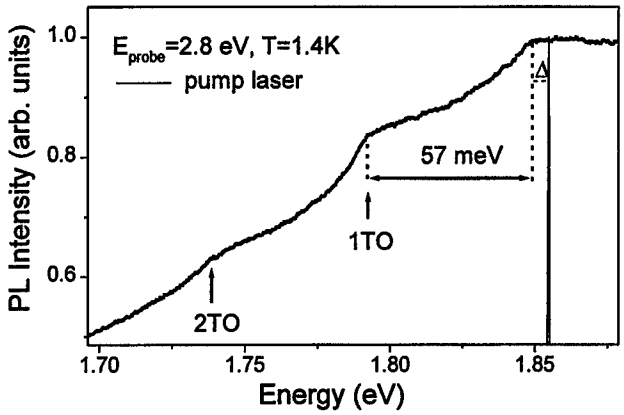


Figure 4: Detailed PL spectrum in the vicinity of the burning laser energy. The energy position of Si momentum-conserving TO-phonons with account for the exchange gap is indicated by arrows.

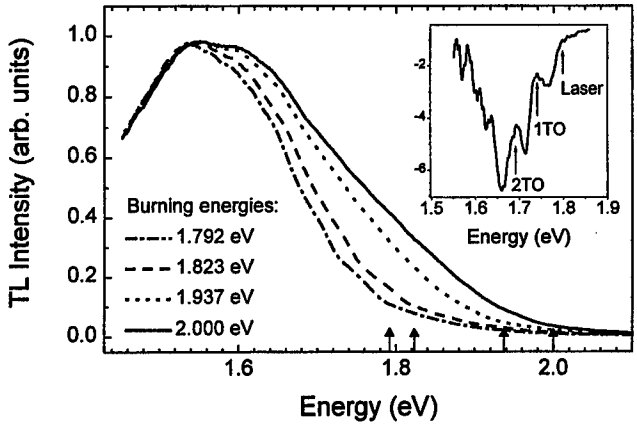


Figure 5: Thermoluminescence spectra (heating range is 1.5-20 K) measured after spectral hole burning at different energies (shown by arrows). Inset: The first derivative of one of the spectra. A better discrimination of the TO phonon-related structure is possible.

MAGNETOSPECTROSCOPY OF SILICON NANOCRYSTALS

H. Heckler, D. Kovalev, G. Polisski
N.N. Zinov'ev[+], F. Koch
Technische Universität München, Physik Department E 16,
D-85747 Garching, Germany
[+]A. F. Ioffe Physikotechnical Institute
Politechnicheskaya 26, 194021 St. Petersburg, Russia

ABSTRACT

We report on the photoluminescence properties of nanocrystalline porous silicon in presence of an external magnetic field. As a result of the Zeeman splitting of the exciton ground level the spectroscopic gap between the excitation and photoluminescence onset energies increases linearly with magnetic field, and spectral features due to momentum conserving phonons are following the shift towards lower energy. The photoluminescence lifetimes in the presence of the magnetic field become longer. The effect is stronger for smaller exciton confinement energies when the value of the Zeeman splitting is comparable with the electron-hole exchange interaction splitting term. Our experimental results confirm the exciton nature of the luminescing states responsible for the light emission from porous silicon.

The detailed nature of photoexcited luminescing state in porous Si has been debated for some time in the literature. While evidence in favor of the picture of a quantum-confined exciton in the Si-bandstructure, as originally and consistently proposed by the group of researchers around L. Canham [1-3], has been accruing, a definitive experiment that allows one to access relevant microscopic parameters of the electronic state has been lacking. Magneto-optical spectroscopy is a most powerful tool for such an investigation and has been widely applied to other low-dimensional structures. A magnetic field is capable in principle of probing both the spin and orbital characteristics of the state. It can decisively influence the energies, relaxation lifetimes and polarization characteristics of the luminescence.

In spite of several attempts cited in the literature [4,5] to observe an influence of the magnetic field on the porous Si luminescence, no conclusive results have been obtained. Contrary to the case of other quantum dot materials [6] the fabrication of porous Si yields nanoparticles with a wide range of sizes and shapes. The electrochemical anodization generates a significant fraction of oxide or hydride material in boundary layers. The result is a photoluminescence (PL) line that is inhomogeneously broadened by hundreds of meV and whose origin has been attributed variously to molecular complexes in the boundary layers [7], to surface-layer modified Si-sates in which the electron and hole are partly separated in the particle [8], and the aforementioned Si-exciton in a bounded geometry [1].

Because magnetic energies for a 10 T laboratory field and a g-factor in the vicinity of 2 are of the order of 1 meV (compared to a line width of 300-400 meV) it is necessary to use low temperatures and the resonant excitation technique to generate sharp spectral features on the PL curve. We remind the reader of the well-studied phonon replica and point to recent work where the use of selective excitation spectroscopy on the low energy side of the PL line (the latter centered at an energy only 0.3 eV above the Si bulk band-gap) has yielded sharp, resonance-like phonon replica peaks in the spectra [2,9]. Using these one has no difficulty at all in observing a significant influence of the magnetic field on basic emission characteristics of porous Si.

According to the Si-exciton model [1-3] there exist two spin-states for the photo-excited Coulomb-bound electron-hole complex. The optically-allowed singlet state (S) has a short lifetime (~μsec) and lies in energy above a partly forbidden, long-lived (~msec) triplet state (T). The singlet-triplet splitting Δ_{ST} separating these states is a confinement-dependent exchange energy. Calcott identified and measured this energy from the value of a gap in the PL under resonant excitation conditions [2]. The temperature dependence of the PL lifetime is quantitatively described at low temperatures by this 2-level, singlet-triplet model [2,10].

The magnetic field can provide an essential test of the exciton hypothesis, measure the g-factor of the triplet state and allows one to verify the lifetime mechanism. If, as in the schematic of Fig. 1, the spectroscopic gap Δ_{ST} separates a low-lying triplet (S = 1) from the singlet (S = 0) that is photoexcited via the transition (broken arrow up) the application of a field B will split this ground state due to the Zeeman effect. For temperatures such $k_BT<<\Delta_{ST}$, $g\mu_BB$ all PL emission will occur from the lowest member of the triplet. The spectrum should shift to lower energy linearly with rising B (emission, broken arrow down). The separation of PL onset and excitation energy is $\Delta_{ST}(B) = \Delta_{ST}+g\mu_BB$. In a second regime where $k_BT\sim\Delta_{ST}\sim g\mu_BB$ we may expect major changes in the decay time of PL because of redistribution of the thermal population between the states with B.

We use resonant excitation at low T to introduce sharply defined features in the spectrum analogous to Calcott et al [2]. The sample used for the data of Fig. 1 is conventional porous Si (PL peak energy at 1.7eV) prepared by anodic electrochemical etching [11]. The excitation is via a dye laser. The light is guided to and from sample via fiber optics. A superconducting solenoid provides fields up to 12 T. The detector is a SiCCD array, a photomultiplier or a Ge-detector with time resolution of 50 μs. The temperature T can be varied between 2 and 200 K.

The spectra in Fig. 1 are for excitation at 2.006 eV. At B = 0 T we record the spectroscopic gap of about 7 meV in agreement with Calcott [2]. Increasing the field B up to 11.5 T we record an approximately linear displacement of the curves to lower energy. Averaging over such data and in particular correcting for the small and consistent tendency of the PL intensity to decrease (this is a known degradation effect that slowly reduces the overall PL during the 6 hours of measurement) we arrive at a shift of ~120μeV/T. Other characteristics of the overall PL spectrum such as the amplitude of the phonon replica steps, the PL peak position and intensity, as well as the lifetime re-

main unaffected by the magnetic field. The linear shift of the curves in Fig.1 is identical for Faraday and Voigt geometries. It does not depend on the excitation energy.

The limit of $\Delta_{ST} \sim k_B T$, $g\mu_B B$ is best explored in samples for which the nanoparticles luminesce is closer to the Si-band-gap energy. Using a Ti:Sapphire laser as an excitation source and samples prepared to have their PL peak at energies near 1.5eV, very sharp and reproducible phonon features are found under resonant excitation conditions.

Figure 2 shows a resonantly excited PL spectrum excited at the low energy end of the distribution of emission energies. The energy Δ_{ST} is not resolved here (the reduced confinement implied by the lower energy of luminescence leads to a lower value of the exchange energy that separates the S and T states. Moreover at T = 4.2 K an appreciable fraction of the transitions take place via S), but the spectral replicates of momentum conserving TO and TA phonons are very sharply developed and allow to be traced while applying a magnetic field. A magnification of the marked phonon features is shown in figure 3. The figure shows a succession of PL intensity curves for field strengths increasing in appropriate steps. Both features shift parallel and again linearly with the field to lower energy. One can trace in the same way the shift of the TO+TA feature. When all of these are combined there results the plot of Fig. 4. The averaged slope is 0.12±0.01 meV/T. At low field the data points vary more slowly. For 0-2 T the shift is more nearly parabolic for the data of Fig. 4 (solid points). Because of the small Δ_{ST} (estimated as ~2 meV) and T $\cong$ 4.2 K some transitions take place via the S state. With rising B the splitting $\Delta_{ST}(B)$ increases and the linear dependence applies as more and more luminescent transitions proceed from the T state. With rotation of the magnetic field in the sample plane there is no discernible shift in the slope. We conclude that there is no dependence on the crystal axes. The same slope applies in Voigt and Faraday configurations.

The model description of the PL relaxation rate involves a fast lifetime through the S state, a slower one from T. The observed time depends on the relative populations. A magnetic field-dependent lifetime will be observed when the field B significantly changes the relative populations of S and T. This applies for small Δ_{ST} and hence PL energies near the Si band-gap. For bulk Si the splitting has been estimated as $\Delta_{ST} \sim 150$ μeV [12]. In the weak confinement limit with PL detected at 1.19 eV (as in Fig. 5) the magnetic shift of the triplet state by ±1 meV should bring about major changes in the lifetime at 4.2 K. This is indeed observed. The decay appears monoexponential over the entire range and changes decisively with B. The inset of Fig. 5 shows the behaviour of the PL lifetime at a fixed temperature of 4.2 K and a varying magnetic field. For $k_B T \sim 300$ μeV the PL decay time is significantly longer at B = 10 T due to a shift of the thermal equilibrium towards the slow, lowest triplet state. At higher temperatures the effect vanishes, because all participating levels are then equally populated. At very thermal energy predominantly the slow ground state is populated and thus the magnetic field induced enhancement of the PL lifetime becomes weaker. We follow [2] in modeling the decay based on singlet time τ_S and a triplet time τ_T. The relative occupations are taken from a Boltzmann distribution with statistical weighting of 1 and 3 for these levels. The data points nicely fit the model variation in Fig. 5 for relevant range of

B and T (parameters are $\tau_T = 12$ ms, $\tau_S = 0.75$ ms, $\Delta_{ST} = 0.5$ meV and $E_{Zeeman} = 0.12$ meV/T). The solid line in the inset is a fit based on the same set of parameters.

Contrary to the CdSe quantum dot system [13] where the B-field changes the relaxation rate of the triplet state, the Si case studied here involves the population changes mainly. The reason is the comparatively weak spin-orbit coupling energy in Si. For CdSe the main effect is a field–dependent change of coupling and admixture of S and T in the ground state.

The observations of a magnetic-field dependent energy shift linear in field (Fig. 1, 3, 4) and the influence of B on the lifetime as in Fig. 5 leave us to conclude that we are dealing with the spin-dynamics of an excitonic state. The ground state is a triplet with a significant Δ_{ST} even in the low confinement limit. The value 0.5 meV is larger than that for bulk Si, probably because of reduced screening in the porous medium for which the dielectric constant of order 3-4 applies. There is no way to make a consistent picture of the energy shift or lifetime changes with B in terms of a model of the porous Si PL where the electron and hole are separated in a surface potential. Together with the now well established fact that the PL of hydrided porous Si can be continuously tuned to the Si-band-gap in small incremented step [14] and that the phonon-resonances relate to Si momentum-conserving phonons in the expected way [9], there is no other way to account for the dominant light emission of porous Si. The exciton picture in a quantum-confined geometry in Si gives a correct description.

There is no evidence in the magneto-spectroscopy experiment, even in the low confinement limit with the PL energy only ~100 meV above the band-gap, of diamagnetic energy shifts that vary quadratically with field. The orbital effects in terms of compression of the wave function in a field, or the breakup of the exciton in favor of the independent cyclotron motion of the electron and hole, are not observed. It follows, that the calculation of the size-effect in terms of an independent particle picture where the electron and hole separately and independently move in a confining potential, is not adequate even in this limit where the size-effect induced shifts are only of order 100 meV. The excited state is an exciton in which the electron and hole are bound by the Coulomb interaction with a strength that exceeds relevant orbital magnetic energies which at 11.5 T are of order 5 meV. In the absence of orbital and diamagnetic effects, the magnetospectroscopy results for magnetic fields up to 11.5 T are accounted for solely by the Zeeman splitting of the spin-state of the coupled electron and hole as shown in this account.

References

[1] L. T. Canham, Appl. Phys. Lett., **57**, 1046 (1990)

[2] P. D. J. Calcott, K. J. Nash. L. T. Canham, M. J. Kane and D. Brumhead, J. Phys. Condens. Matter, **5**, L91 (1993)

[3] K. J. Nash, P. D. J. Calcott, L. T. Canham and R. J. Needs, Phys. Rev., **B51**, 17698 (1995)

[4] C. H. Perry, F. Lu, F. Namavar, N. M. Kalkhoran and R. A. Soref, Appl. Phys. Lett., **60**, 3117 (1992)

[5] X. L. Zheng, H. C. Chen, W. Wang and D. Heiman, Mat. Res. Soc. Proc., **256**, 59 (1992)
[6] C. B. Murray, D. J. Norris and M. G. Bawendi, J. Am. Chem. Soc., **115**, 8706 (1993)
[7] S. M. Prokes, O. J. Glembocki, V. M. Bermudez, R. Kaplan, L. E. Friedersdorf, P. C. Searson, Phys. Rev., **B45**, 13788 (1992)
[8] F. Koch, V. Petrova-Koch, T. Muschik, A. Nikolov, V. Gavrilenko, Mat. Res. Soc. Proc., **283** , 197 (1993)
[9] D. Kovalev, H. Heckler, M. Ben-Chorin, G. Polisski, M. Schwartzkopff and F. Koch, Phys. Rev. Lett., **81**, 2803 (1998)
[10] G. Fishman, R. Romestain and J. C. Vial, J. Lumin., **57**, 235 (1993)
[11] D. Kovalev, G. Polisski, M. Ben-Chorin, J. Diener and F. Koch, J. Appl. Phys., **80**, 5978 (1996)
[12] J. C. Merle, M. Capizzi, P. Fiorini and A. Frova, Phys. Rev., **B17**, 4821 (1978)
[13] Al. L. Efros, M. Rosen, M. Kuno, M. Nirmal, D. J. Norris and M. Bawendi, Phys. Rev., **B54**, 4843 (1996)
[14] G. Polisski, H. Heckler, D. Kovalev, M. Schwartzkopff and F. Koch, Appl. Phys. Lett., **73**, 1107 (1998)

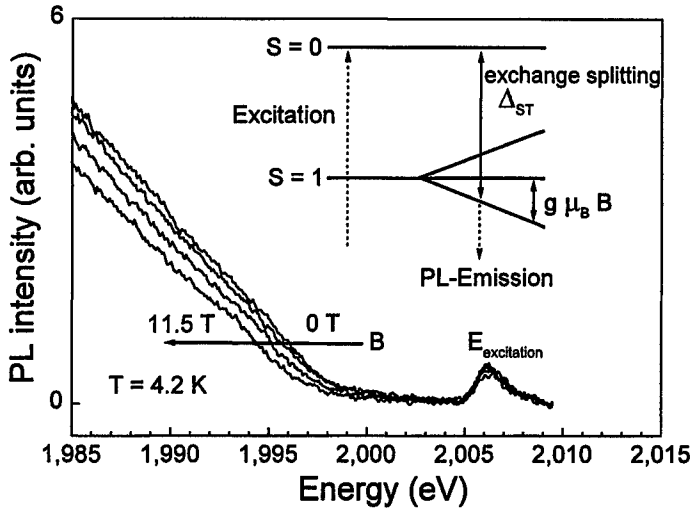


Figure 1: Onset of resonantly excited PL at different magnetic fields. From right to left the field strength was 0, 4, 8 and 11.5 T. For higher magnetic fields the PL onset shifts towards lower energy. Inset: The excitation creates the exciton in the upper lying, optically allowed spin-singlet state. After a fast spin-flip the PL emission occurs from the lowest possible triplet state, which shifts to lower energy due to the Zeeman-splitting.

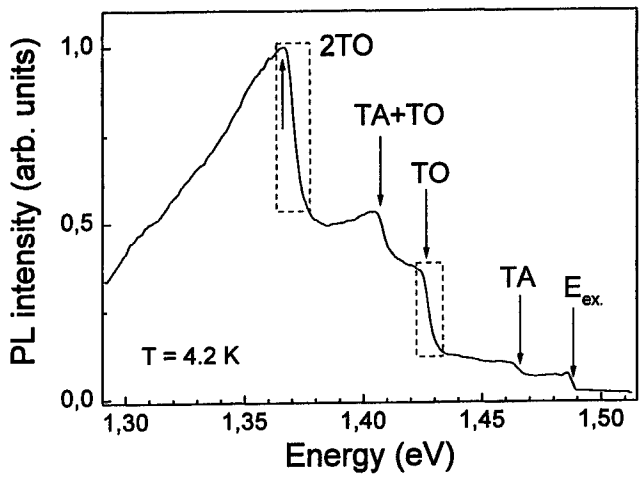


Figure 2: Resonant photoluminescence excited at the low energy end of the distribution of PL emission energies. Arrows show the spectral position of momentum conserving TO and TA phonon replicates. The sharpness of these features allows to trace a magnetic field shift of order 1 meV. The rectangularly marked features are shown enlarged in Fig. 3.

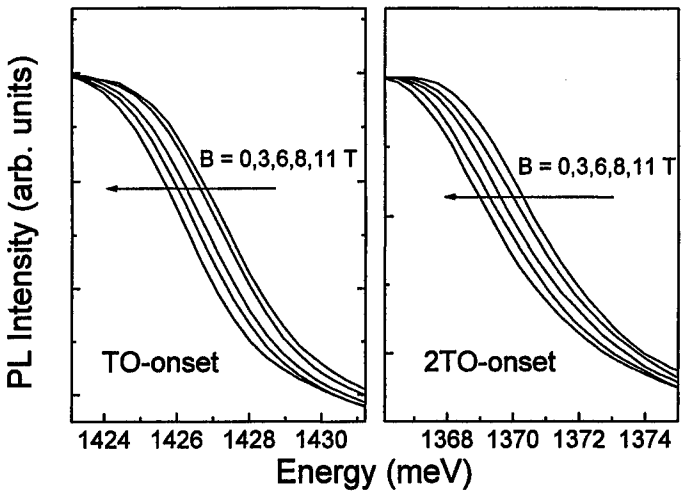


Figure 3: Magnification of the marked phonon features of Fig. 2 for magnetic fields between 0 and 11 T. Like seen for the PL onset in Fig. 1 both features are shifting towards lower energy with rising magnetic field.

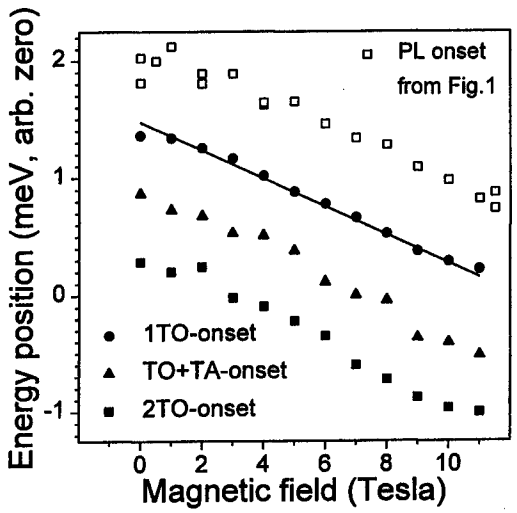


Figure 4: Analysis of the spectral position of the PL onset from Fig. 1 and the phonon features shown in Fig. 2 under magnetic field influence. All features are shifting linearly and parallel towards lower energy with rising magnetic field. The straight over the data of the 1TO feature has a slope of 120 μeV/T corresponding to a exciton-spin-g-factor of approx. 2.1.

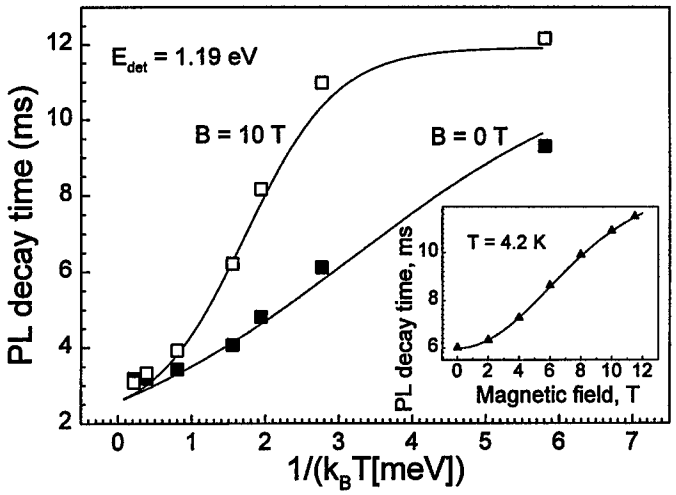


Figure 5: Dependence of the PL lifetime on temperature and for zero and 10 T magnetic field measured at 1.19 eV detection energy. The inset shows the PL lifetime at a constant temperature of 4.2 K and variable magnetic field. All solid lines are produced by one fit based on Boltzmann statistics assuming a singlet-triplet splitting of 0.5 meV and a strength of the Zeeman splitting of 110 μeV/T. The lifetimes of the singlet and the triplet state are 750 μs and 12 ms, respectively.

Porous Silicon

LIGHT EMITTING MICROPATTERNS OF POROUS SEMICONDUCTORS CREATED AT SURFACE DEFECTS

D.J. Lockwood[1], P. Schmuki[2], and L.E. Erickson[1]

1) Institute for Microstructural Sciences
National Research Council of Canada
Ottawa, Ontario, Canada K1A 0R6

2) Swiss Federal Institute of Technology
ETH/EPFL, Dept. of Materials Science, LC-DMX
CH-1015 Lausanne, Switzerland

ABSTRACT

We report a principle that allows writing visible light emitting semiconductor patterns of arbitrary shape down to the sub-micrometer scale. We demonstrate that porous semiconductor growth can be electrochemically initiated preferentially at surface defects created in an *n*-type substrate by Si^{++} focused ion beam bombardment. For *n*-type material in the dark, the electrochemical pore formation potential (Schottky barrier breakdown voltage) is significantly lower at the implanted locations than for an unimplanted surface. This difference in the threshold voltages is exploited to achieve the selectivity of the pore formation process. Visible light emitting patterns of porous Si and GaAs have been created in this way. At present, the size of the structures is limited only by the diameter of the writing ion beam, and pattern diameters in the 50–200-nm range are possible.

I. INTRODUCTION

Silicon is technologically the most important semiconductor material. However, applications in semiconductor photonics appeared unlikely due to its indirect electronic band gap [1]. Therefore, the discovery of electrochemically formed visible light emitting porous Si [2] has recently stimulated intense research activity [3]. The main reason for this tremendous interest is the prospect of light emitting devices (LEDs) made of porous Si [1,4].

Here we report a principle [5,6] that allows writing visible light emitting semiconductor patterns of arbitrary shape down to the sub-micrometer scale. Porous semiconductor growth can be electrochemically initiated preferentially at surface defects created in an *n*-type substrate by Si^{++} focused ion beam (FIB) bombardment. For *n*-type material in the dark, the electrochemical pore formation potential (Schottky barrier breakdown voltage) is significantly lower at the implanted locations than for an unimplanted surface. This difference in the threshold voltages is exploited to achieve the selectivity of the pore formation process.

Prior approaches to patterning porous Si include: Ga ion implantation followed by an anisotropic wet etch process [7]; a lithographic process using a silicon nitride mask and electrochemical polarization [8]; light induced carrier generation in *n*-type material together with electrochemical polarization [9]; an ion implantation process (both masked and maskless) to dope and amorphize silicon, which suppresses anodization (negative pattern) [10]; and by an ion milling process to create surface defects, which enhance the etch (or anodization) rate in the milled areas [8]. In contrast to these processes, we implant Si^{++} ions to avoid any doping effect in Si wafers, implant the ions at a sufficiently high energy to avoid surface sputtering effects, and use a maskless selective electrochemistry technique that produces porous Si only in the implanted regions.

II. EXPERIMENT

The ions were implanted into *n*-type Si and GaAs (100) wafers (doped with 5×10^{15} cm^{-3} As and 2.5×10^{17} cm^{-3} Si, respectively) at room temperature using a 100 kV JEOL 104UHV FIB system. Si^{++} ions at 200 keV were selected from the AuSi ion beam using an **E×B** mass filter. The nominal beam width was 100 nm. Patterns comprised of squares 50×50 μm^2 and alphabetic characters were implanted with ion doses from 3×10^{13} to 3×10^{16} ions/cm^2. The patterns could be observed in an optical microscope or a scanning electron microscope (SEM) after implantation, but before polarization, for doses exceeding 1×10^{15} ions/cm^2. This may be attributed to amorphization of the substrate and/or to defect-induced surface bulging.

The implanted samples were electrochemically polarized in 20% HF for Si and 1 M HCl for GaAs using a staircase potential sweep, in steps of 10 mV every 5 s (for Si) or every 2 s (for GaAs) in the anodic direction (further details can be found in Refs. 5, 6, and 11). The potentials were measured with respect to a saturated calomel electrode (SCE). This process was done in the dark to avoid light-induced carrier generation in the sample. Under these conditions (similar to the diode behaviour of a p–n junction under reverse bias), the holes (h^+) necessary in the case of Si for Si^0 oxidation and dissolution as $(SiF_6)^{2-}$, only become sufficiently available at the Si surface at

the potential where Schottky barrier breakdown occurs [5]. A similar process occurs in GaAs [12]. After the formation of the porous structures, the samples were intensively rinsed with deionized water, and then blown dry in an argon stream.

The room temperature photoluminescence (PL) of the samples was excited with 15 mW of 457.9-nm argon laser light, dispersed with a Spex 14018 double spectrometer, and detected with a cooled RCA 31034A GaAs photomultiplier. Scanning electron micrographs were acquired using a JEOL 840A SEM equipped with a Digiscan image-acquisition archiving system.

III. RESULTS

A. Pore formation

Figure 1 shows a polarization curve of an *n*-type GaAs (100) sample in 1 M HCl. The potential region with a blocking characteristic (low current flow), typical of *n*-type material/electrolyte junction in the dark, is obtained in the anodic direction up to a potential of approximately 3.1 V. At higher potentials a steep current increase is observed and previous investigations showed that at this potential the first pores are formed in the material [13]. Therefore, this potential value is called the pore formation potential (PFP).

Also included in Fig. 1 is a polarization curve of a sample that was scratched with a diamond scribe. The scratch is only several millimetres long, but a significant increase in the current—of more than a decade—is obtained at approximately 1.2 V; *i.e.*, this sample shows an initial PFP significantly lower than that of the intact sample. The inset in Fig. 1 shows an SEM image of the surface of a scratched sample polarized to 2.5 V (*i.e.*, below the PFP of an intact sample). The image reveals that pore formation took place only in the region of the scratch. The rest of the surface remained intact. Hence, dissolution processes occurred only locally at the scratch and the additional current flow, compared with an intact sample, must be attributed to this surface location. These very high local current densities indicate that Schottky barrier breakdown is facilitated at surface defects.

More controlled local defect generation can be achieved by using FIB implantation. This is shown, for example, in Fig. 2, which gives a typical current/voltage characteristic for a reference (nonimplanted) *n*-type Si sample in 20% HF. Starting from the open circuit potential, with an increasing potential the current increases up to a plateau region. In this region, the current is controlled by electrons that overcome the charge carrier depletion region (Schottky barrier) at the semiconductor/electrolyte interface by thermal activation. At a potential of approximately 3.8 V, the current steeply increases. In this region, local dissolution processes occur on the Si surface which, after extended polarization, lead to a porous surface. There are several

factors that influence the PFP such as the concentration of the anion in the electrolyte or the temperature. The predominant factors are, however, the conduction type and doping concentration of the substrate, as expected from the Schottky approach.

The defects created by the FIB have a drastic effect on the PFP. This is clear from the second curve included in Fig. 2, which shows a polarization curve acquired with a microelectrode pipette (ϕ=300 μm^2) that was placed on a 50×50-μm implanted square (dose of 3×10^{14} cm^{-2}). In this case, a first significant current increase appears at +0.25 V. Although the implanted area is only about 3% of the total area exposed to the electrolyte, the current density in the plateau region is more than a decade higher than for the reference sample. Hence, the effective current density in the implanted region is about 300 times higher than on the intact Si surface; *i.e.*, it becomes comparable to current densities observed with the reference sample above its PFP. Figure 3 shows an optical micrograph of a polarized sample where letters were written with the FIB at a dose of 3×10^{14} cm^{-2}. The letters show the typical porous Si interference colours ranging from red to green. The letter *R* was obtained with a single FIB scan, which resulted in a linewidth of approximately 200 nm. Figure 4(a) shows an SEM micrograph of a square implanted with the same dose (3×10^{14} cm^{-2}) and identically treated. From Fig. 4(b), it is apparent that porous Si has been formed within the square. The surrounding area is completely unattacked.

B. Photoluminescence

The PL spectrum shown in Fig. 5 was measured with an argon laser beam focused in the centre of the 50-μm square of Fig. 4. The PL spectrum peaks at 655 nm in the orange–red region of the spectrum and, in width and wavelength position, is typical of the PL response of porous Si [3]. The band shape shows irregularities that can be attributed to nanoscopic nonuniformities in the material porosity. Electrochemically treated areas next to the implanted patterns were investigated as a reference and, in every case, the unimplanted areas showed the spectral behaviour of a clean Si surface (no light emission in the visible range) as did implanted areas not yet electrochemically treated. This clearly indicates that the electrochemical formation of porous Si is responsible for the PL observed and not lattice defects or amorphization created by the implantation.

In Si, the highest PL intensity was observed from the sample implanted with a dose of 3×10^{14} cm^{-2} and polarized to 3.5 V (Fig. 5). Other conditions led to significantly lower PL intensities. The PL intensity and morphology of the samples were correlated, in that the sample with the highest amount of porosity, having feature sizes in the nanoscopic range, gave the highest PL intensity. This is consistent with a quantum confinement explanation for the red PL of porous Si [1,3].

In GaAs, similar results were obtained. Figure 6 shows a PL spectrum taken within the attacked square of a sample implanted with 1×10^{15} ions cm^{-2} and polarized to 3 V, and a reference spectrum of the GaAs (100) surface next to the square. For the

spectrum taken on the unimplanted part of the sample, an intense PL peak is observed at approximately 860 nm as expected for bulk GaAs (the sharp cutoff to higher wavelength is due to the photomultiplier response). The spectrum taken within the square shows an additional broad green–yellow band, peaked at approximately 540 nm. This spectral behaviour is consistent with previous work on porous GaAs [14]. For samples polarized to 1 and 2 V, no green PL peak was observed for any implantation dose. For a sample polarized to 3 V, the squares with dosages between 3×10^{14} ions cm^{-2} and 3×10^{15} ions cm^{-2} showed a significant green PL peak. The fact that for higher doses a nonuniform large-shape etching morphology occurred, which did not result in green PL, is consistent with an explanation for the visible PL in terms of a quantum confinement model, as postulated in earlier work [14,15].

At present, although visible to the eye, the PL intensity observed in both Si and GaAs is relatively weak when compared to the "bulk" porous material and, therefore, further optimization of the formation parameters is needed. However, it is noteworthy that this process has the potential to write nanostructures in the 50–200-nm range, depending on the diameter of the writing ion beam.

IV. CONCLUSIONS

In conclusion, we have shown how to produce laterally confined light-emitting Si or GaAs by a direct FIB writing process. We clearly demonstrate that a creation of surface defects followed by an electrochemical "development" treatment, tailored to trigger dissolution at defects, can be used to form visible light-emitting porous Si or GaAs selectively. At present, the size of the structures appears to be limited only by the diameter of the writing ion beam. Thus patterns in the 50–200-nm range seem quite possible.

Recently, electroluminescent devices based on large-scale porous Si structures have been reported [4]. The process described here could facilitate a drastic shrinkage in the dimensions of such devices and hence could be a basis for, or part of, a process leading to extremely high-resolution optoelectronic applications.

Additionally, the above findings show that surface lattice defects represent centres of enhanced dissolution, and hence represent the initiation site for pore formation, when conditions are established where Schottky barrier breakdown is the rate-determining step for the surface dissolution reaction.

ACKNOWLEDGEMENTS

We thank H.G. Champion, J.W. Fraser and H.J. Labbé for their meticulous help with the experiments and the Swiss National Science Foundation for financial support.

References

[1] D.J. Lockwood, Ed., *Light Emission in Silicon,* Academic Press, Boston (1997).

[2] L.T. Canham, *Appl. Phys. Lett.* **57**, 1046 (1990).

[3] See, for example, A.G. Cullis, L.T. Canham, and P.D.J. Calcott, *J. Appl. Phys.* **82**, 909 (1997).

[4] K.D. Hirschmann, L. Tsybeskov, S.P. Duttagupta, and P.M. Fauchet, *Nature* **384**, 338 (1996).

[5] P. Schmuki, L.E. Erickson, and D.J. Lockwood, *Phys. Rev. Lett.* **80**, 4060 (1998).

[6] P. Schmuki, L.E. Erickson, D.J. Lockwood, J.W. Fraser, G. Champion, and H.J. Labbé, *Appl. Phys. Lett.* **72**, 1039 (1998).

[7] J. Xu and A.J. Steckl, *Appl. Phys. Lett.* **65**, 2081 (1994).

[8] S.P. Duttagupta, C. Peng, P.M. Fauchet, S.K. Kurinec, and T.N. Blanton, *J. Vac. Sci. Technol. B* **13**, 1230 (1995).

[9] V.V. Doan and M.J. Sailor, *Science* **256**, 1791 (1992).

[10] J.C. Barbour, D. Dimos, T.R. Guilinger, M.J. Kelly, and S.S. Tsao, *Appl. Phys. Lett.* **59**, 2088 (1991).

[11] P. Schmuki, L.E. Erickson, D.J. Lockwood, J.W. Fraser, B.F. Mason, G. Champion, and H.J. Labbé, *J. Electrochem. Soc.* **146** (to be published in 1999).

[12] P. Schmuki, D.J. Lockwood, H.J. Labbé, J.W. Fraser, and M.J. Graham, in *Pits and Pores: Formation, Properties and Significance for Advanced Luminescent Materials,* edited by P. Schmuki, D.J. Lockwood, H.S. Isaacs, and A. Bsiesy (Electrochemical Soc., Pennington, NJ, 1997), p. 112.

[13] P. Schmuki, J. Fraser, C.M. Vitus, M.J. Graham, and H. Isaacs, *J. Electrochem. Soc.* **143**, 3316 (1996).

[14] P. Schmuki, D.J. Lockwood, H.J. Labbé, and J.W. Fraser, *Appl. Phys. Lett.* **69**, 1620 (1996).

[15] D.J. Lockwood, P. Schmuki, H.J. Labbé and J.W. Fraser, in *Pits and Pores: Formation, Properties and Significance for Advanced Luminescent Materials,* edited by P. Schmuki, D.J. Lockwood, H.S. Isaacs, and A. Bsiesy (Electrochemical Soc., Pennington, NJ, 1997), p. 447.

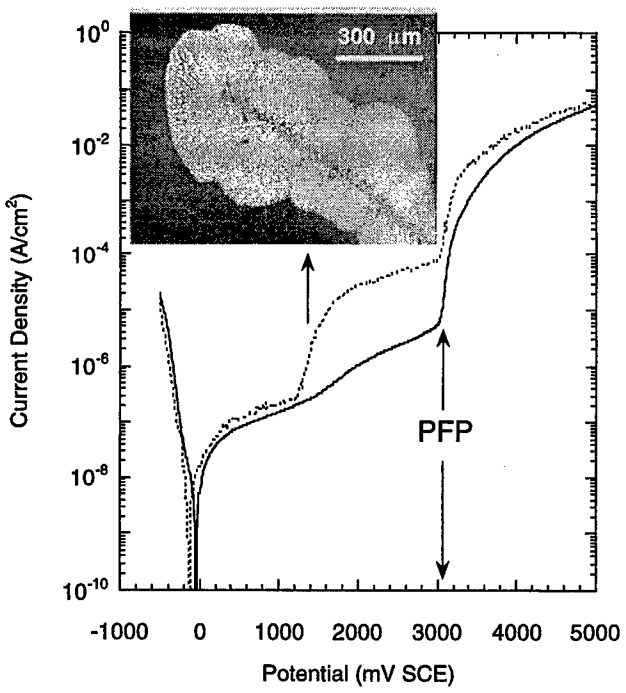


Figure 1. Current–voltage (polarization) curve of *n*-type GaAs (100) in 1 M HCl (solid line) and a polarization curve acquired with a sample that was intentionally scratched (dashed line). The curves were acquired in the dark. The inset shows the morphology of a scratched sample after polarization from -0.5 to 2.5 V.

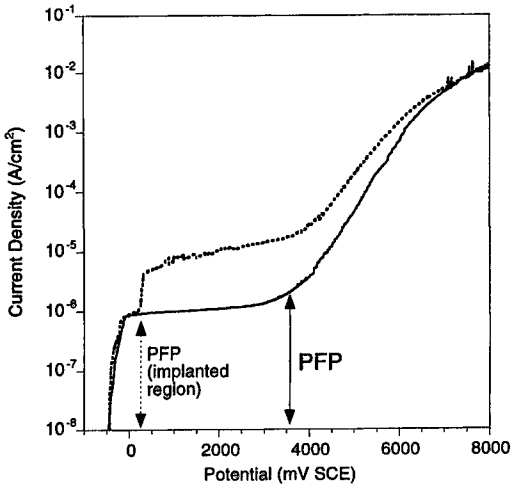


Figure 2. Current-voltage (polarization) curve of *n*-type Si (100) in 20% HF (solid line) and the polarization curve acquired with a ϕ=300 μm capillary electrode on a 50-μm square implanted with 3×10^{14} cm^{-2} Si^{++} (dashed line). The curves were acquired in the dark.

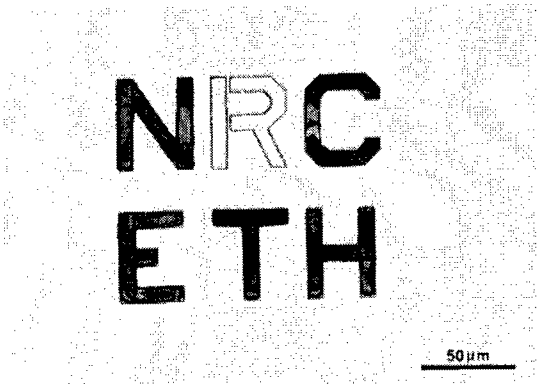


Figure 3. Optical micrograph of porous Si letters produced by 3×10^{14} cm^{-2} Si^{++} FIB implantation in *n*-type Si (100) and subsequent electrochemical polarization in 20% HF from -0.5 V to 3.5 V. The R in NRC was outlined with a single (100-nm-wide) FIB line; the rest of the letters were uniformly implanted. The letters show the green and red interference colours typical of porous Si.

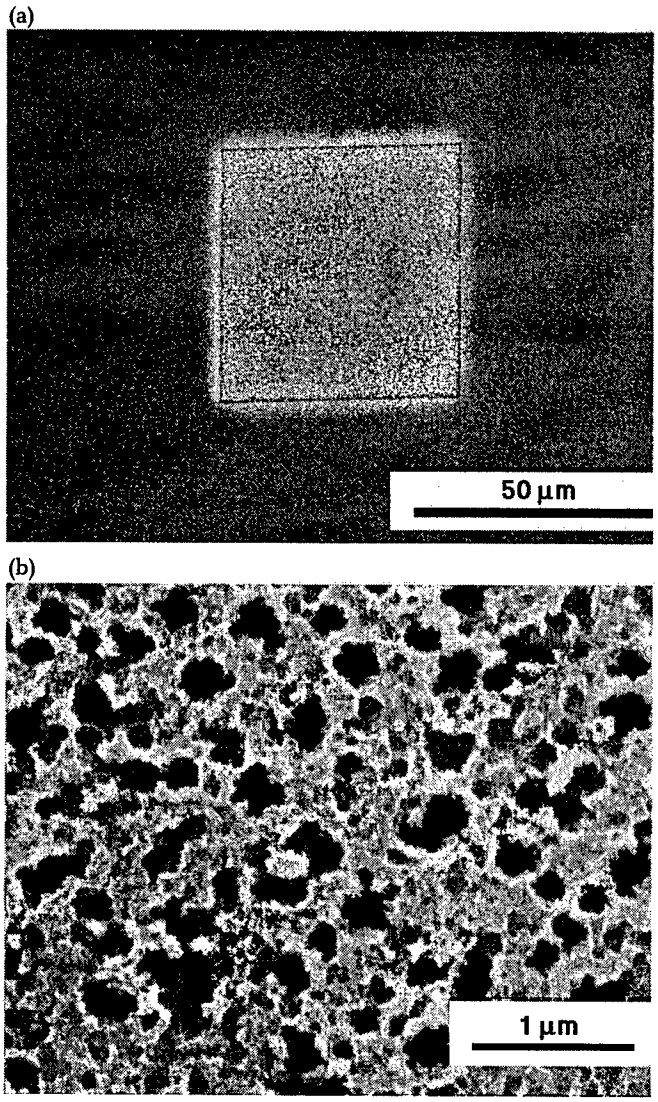


Figure 4. SEM image of a 50-μm square of Si implanted with 3×10^{14} cm^{-2} Si^{++} after polarization in 20% HF from -0.5 to 3.5 V. (b) Higher magnification of (a) within the square.

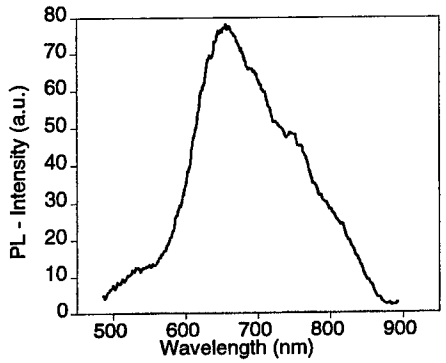


Figure 5. Room-temperature PL spectrum of porous Si acquired in the centre of the square shown in Fig. 4.

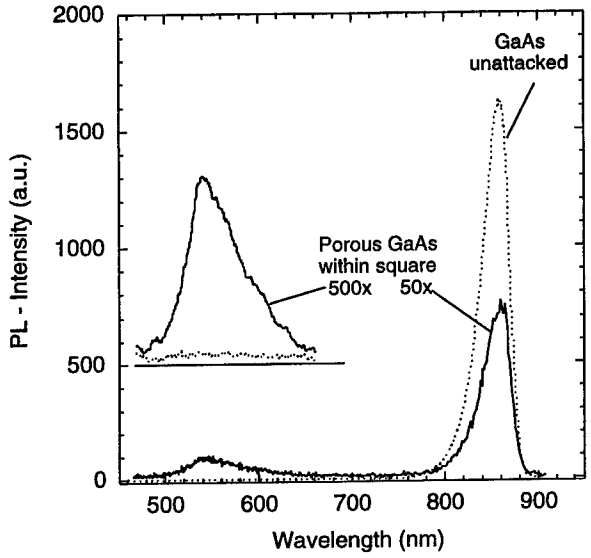


Figure 6. Room-temperature PL spectra acquired on a GaAs (100) sample implanted with 1×10^{15} cm^{-2} Si^{++} and polarized from -0.5 to 3.0 V. The solid line shows the response within the square and the dashed line from a surface location next to the square. The inset gives a magnification of the short wavelength region and is offset by 500 a.u.

QUENCHING OF RED PHOTOLUMINESCENCE OF POROUS SILICON WITH ADSORPTION OF ALCOHOLS

Michiko SHIMURA, Kouta KIYAMA, and Tsugunori OKUMURA
Course of Electric Engineering, Graduate School of Engineering
Tokyo Metropolitan University
Minami-osawa, Hachioji, Tokyo, 192-0397, Japan

E-mail: michi@eei.metro-u.ac.jp

Key words: porous silicon, red photoluminescence, quenching,
Stern-Volmer's relatlion.

ABSTRACT

Red photoluminescence (λ_{max}: 680 - 720 nm) of porous silicon was quenched in accordance with the density of adsorbed alcoholic OH groups on PS surface. The result agreed with Stern-Volmer's relation $PL/PL_{soln} = 1 + k_{NR\text{-}A}\tau(OH)$.

The rate constant of the nonradiative deactivation path produced with alcoholic OH groups, $k_{NR\text{-}A}$, was assumed considerably large and independent of temperature. On the other hand, the rate constant of the inherent non-radiative deactivation path, $k_{NR\text{-}T}$, was estimated to have an apparent activation energy of about 50 meV, from the slope of the linear plot of $\log[(PL_{100} - PL_T)/PL_{100}]$ vs. 1/T. Mechanism of non-radiative deactivation of excited electron with adsorbed alcoholic OH groups was proposed.

INTRODUCTION

At the anodic oxidation of porous silicon in ethylene glycol which is effective for the increase and stabilization of PL intensity [1, 2] we found that ethylene glycol conversely acted as a quencher for the PL when it remained on the surface of nanostructured silicon [3]. The quenching was found in other saturated alcohols [4]. However, under the irradiation of relatively high power N_2 laser (70 μJ/pulse, 1 pulse: 300 p sec, 10 Hz), the quenching was not observed. The latter phenomenon was considered due to the excess formation of excitated electrons under the irradiation of high power N_2 laser, since the number of the quenchable excited electrons were comparable to the adsorbants on the surface of PS and excess electrons were deactivated via radiative path.

Lifetime measurement showed that the lifetime was remarkably shortened in accordance with the numbers of the OH groups of the alcohols [4].

The rate constant $k_{NR\cdot A}$ of the nonradiative deactivation path, that was formed with the adsoption of alcohol OH groups, was assumed to be considerably large and thus independent of temperature. On the other hand, the rate constant $k_{NR\cdot T}$ of the inherently nonradiative temperature-depending deactivation path was estimated to have an apparent activation energy of about 25 ~ 50 meV from the slope of the linear plot of log $[(PL_{100} - PL_T/PL_{100}]$ vs. 1/T.

According to G. Allan et al [5], the excited electrons on nanostructured silicon recombine radiatively through self-trapped exciton state. We suppose that adsorbed alcoholic OH group forms non-radiative deactivation path through vibrational level via self-trapped exciton state.

There are serious problems that PL spectra (wavelength and intensity) are different each other for the PS samples prepared with the same condition. We investigated the problems in regard to the adsorption of chemical spesies such as saturated polyhydric alcohols.

II. EXPERIMENT

PS samples were prepared by the anodic etching of p-type Si(100) (14 ohm cm), of which the back side was evaporated with Au, at 120 mA/cm² for 5 min in hydrofluoric acid (49%) : H_2O = 1: 2 electrolytes and dried with N_2 gas flow. PL was measured under the illumination of 420 ~ 337nm light from a 150 W xenon lamp equipped with a fluorescence photometer (Hitachi F-4500), before and after orgnic solvents were adsorbed by dropping 1 μL on the surface of PS sample. The solvents used for adsorption were saturated alcohols such as 2-methyl-1-propanol (i-BuOH), ethylene glycol ($EG(OH)_2$), propylene glycol ($PG(OH)_2$), glycerol ($GL(OH)_3$) and n-hexane, n-pentane, and so on.

In order to investigate degree of quenching in accordance with the concentration of the alcohols, diluted alcohols (1 ~ 7.5 mol L^{-1} with n-hexane) were dropped by 1 μL on the surface of PS sample. We confirmed that n-hexane was practically ineffective for the PL quenching.

The temperature dependence of the PL intensity was measured between 300 and 100 K in He atmosphere.

Transmission FTIR measurements were carried out for the PS samples at three stages: immediately after the preparation, after adsorption of $EG(OH)_2$ for 5 min, and after rinsing with pure water.

III. RESULTS

It was confirmed that the same PL spectrum (λ_{max} :680 - 720 nm) was obtaind regardless of the excitation wavelengths between 420 and 337 nm from a 150 W xenon lamp for a given PS sample. This suggests that the photoexcited electrons in nanostructured silicon were

deactivated radiatively via the same recombination process. According to the consideration of G. Allan et al. [5], excited electrons (E level, as will be mentioned in Fig.10) in nanostructured silicon is deactivated radiatively to ground state (G) via the self-trapped exciton state (STE), where STE is higher than excited state (E') of large crystallites.

As previously mentioned [3, 4], the PL was quenched with the adsorption of saturated alcohols and that degree of the quenching differed with the kind of alcohols. Strong quenching was observed in the order of $GL(OH)_3$> $EG(OH)_2$> $PG(OH)_2$> i-BuOH> EtOH> MeOH. According to J. M. Lauerhass et al.[6], the quenching is induced with dipole moments of organic solvents. However, our results did not agree with such physical values (Fig. 1) but rather agreed with viscosities (Fig. 2) and boiling points of the organic solvents (Fig. 3). Better relationships with the latter physical values were considered due to the weakness of adsorption force of organic solvents on the nanostructured silicon and thus they were easily desorbed with the thermal energy at room temperature. In fact, transmission FTIR spectra showed reversible changes at wavenumbers of 2090 cm^{-1} (Si-H)[7], 2110 cm^{-1} ($Si-H_2$)[7], 2140 cm^{-1} ($Si-H_3$)[7] in accordance with the adsorption and the desorption of $EG(OH)_2$, but they did not show any change at the other regions (Fig. 4).

Figure 5 shows the relation between PL/PL_{solv} ratio and the concentration of i-BuOH in n-hexane, where the solution was dropped by 1 μL on the surface (0.28 cm^2) of as-prepared PS sample. The PL/PL_{solv} ratio vs. conc. of i-BuOH was introduced as follows.

$$PL = k_R/(k_R + k_{NR})$$

$$PL_{solv} = k_R/(k_R + k_{NR} + k_{NR\text{-}A}[OH])$$

$$PL/PL_{solv} = (k_R + k_{NR} + k_{NR\text{-}A}[OH])/(k_R + k_{NR})$$

$$= 1 + \{k_{NR\text{-}A}/(k_R + k_{NR})\}[OH] \qquad (1)$$

Here, k_R is the rate constant of radiative deactivation, and $k_{NR\text{-}A}$ and k_{NR} are the rate constants of nonradiative deactivation with alcoholic OH groups and others, respectively. n-Hexane was used as a solvent for the dilution of the saturated alcohols, since n- hexane was confirmed by us to be practically ineffective for the quenching. From Fig. 5 the concentration of i-BuOH that is effective for the quenching of the excited electrons on the nanostructured silicon was found in the range of 1 ~ 7.5 mol L^{-1}. This corresponds to 10^{18} molecules per flat Si (100) surface of 1 cm^2 (Si molecules of 6 x 10^{14}). Necessity of large amouts of i-BuOH molecules for the quenching suggests that real surface of nanostructured silicon is extremley large. The results indicated in Fig. 5 showed that PL/PL_{solv} ratios changed linearly with the concentration of i-BuOH and thus Stern-Volmer's equation was appliciable for them. This supports that alcohol ic OH groups interacted as a quencher for excited electron at STE state (see Fig. 10) of nanostructured silicon.

Figure 6 shows PL spectra of PS samples under 420 nm light irradiation from a 150 W

xenon lamp. For an as-prepared PS sample (Fig. 6-a), the PL intensity increased remarkably with decreasing temperature. This was caused by the supression of nonradiative deactivation path at low temperature, resulting in an increase of radiative deactivation path.

As for the nonradiative deactivation paths, the rate constants of which change with temperature, the following processes are taken into consideration: electron and hole capture on dangling bonds [8], collision with phonons [9], Auger recombination [10] and so on. Here, we group together such processes with the "temperature-dependent nonradiative process", and define the rate constant as $k_{NR\cdot T}$ ($k_{NR\cdot T} = A \exp(-\Delta E_{NR\cdot T}/k_B T)$, where, A is a constant, $\Delta E_{NR\cdot T}$ is the activation energy of the nonradiative deactivation path, k_B is Boltzmann constant and T is temperature at K). The overall rate constant k_0 for the recombination of the photoexcited electrons for the PS sample before alcohol adsorption can be expressed as

$$k_0 = k_R + k_{NR\cdot X} + k_{NR\cdot T} \qquad (2)$$

here, $k_{NR\cdot X}$ is the rate constant of the temperature-independent nonradiative deactivation path. From the fact that the PL intensity does not increase sufficiently with decreasing temperature for the PS sample with adsorbed alcohols, we introduced a new non-radiative deactivation path which is formed by the alcohols (rate constant $k_{NR\cdot A}$) and made the following correction:

$$k = k_R + k_{NR\cdot X} + k_{NR\cdot A} + k_{NR\cdot T} \qquad (3)$$

We tried to derive activation energy of nonradiative deactivation path from temperature dependence of the PL intensity at λ_{max} (680 nm). When the PL intensity increases to almost the maximum value at about 100 K, PL_{100} is regarded as the value when the temperature-dependent nonradiative deactivation path is suppressed to the lowest level (i.e., $k_{NR\cdot T} \rightarrow 0$), and thus the PL intensity can be expessed as

$$PL_{100} = k_R / (k_R + k_{NR\cdot X}) \qquad (4)$$

On the other hand, the PL intensities at T K can be expressed as

$$PL_T = k_R / (k_R + k_{NR\cdot X} + k_{NR\cdot T}) \qquad (5)$$

Since (PL_{100} - PL_T) implies values concerning nonradiative deactivation path, deviding (PL_{100} -PL_T) by PL_{100} yields equation (6). In the case of $(k_R + k_{NR\cdot X}) >> k_{NR\cdot T}$ (namely, when $k_{NR\cdot X} >> k_{NR\cdot T}$), equation (6) can be simplified as equation (7).

$$(PL_{100} - PL_T)/PL_{100} = k_{NR\cdot T}/(k_R + k_{NR\cdot X} + k_{NR\cdot T}) \qquad (6)$$

$$= B \exp(-\Delta E_{NR\cdot T}/k_B T) \qquad (7)$$

where $B = 1/(k_R + k_{NR\cdot X})$ = const and $\Delta E_{NR\cdot T}$: the activation energy for the nonradiative deactivation path.

Fig. 7 shows the plot of log $[(PL_{100} - PL_T)/PL_{100}]$ vs. 1/T for the as-prepared PS sample. From the slope of the straight line, $\Delta E_{NR\cdot T}$, activation energy for nonradiative deactivation was calculated as ca.50 meV. This value is close to the activation energy for the nonradiative deactivation path obtained by G. Amato et al. [11].

When the PS sample was adsorbed by $GL(OH)_3$, the PL intensity barely increased with decreasing temperature. The behavior suggests that $k_{NR\cdot A}$ is larger than $k_{NR\cdot T}$ and independent of temperature, that is, its activation energy or $\Delta E_{NR\cdot A}$ (i.e., $k_{NR\cdot A} = \exp(-\Delta E_{NR\cdot A}/ k_B T)$ is negligibly small.

Since $k_R + k_{NR\cdot X} + k_{NR\cdot A} >> k_{NR\cdot}$ is valid, the activation energy for the "nonradiative deactivation" path, $\Delta E_{NR\cdot T}$, can be derived from the log $[(PL_{100} - PL_T)/PL_{100}]$ vs. 1/T plot as in the followsing equation (11).

$$PL_{100} = k_R/(k_R + k_{NR\cdot X} + k_{NR\cdot A}) \quad (8)$$

$$PL_T = k_R/(k_R + k_{NR\cdot X} + k_{NR\cdot A} + k_{NR\cdot T}) \quad (9)$$

$$(PL_{100} - PL_T)/PL_{100} = k_{NR\cdot T}/[(k_R + k_{NR\cdot X} + k_{NR\cdot A}) + k_{NR\cdot T}] \quad (10)$$

$$= C k_{NR\cdot T} = C \exp(-\Delta E_{NR\cdot T}/k_B T) \quad (11)$$

where $C = 1/(k_R + k_{NR\cdot X} + k_{NR\cdot T})$.

Figure 8 shows the plot for log $[(PL_{100} - PL_T/PL_{100}]$ vs. 1/T for the PS sample with adsorbed $GL(OH)_3$. Although the PL was measured 10 min after the adsorption of $GL(OH)_3$, a line with multiple slopes was obtained, showing that $\Delta E_{NR\cdot T}$ = ca. 1.5 meV (at $0.003 \sim 0.004\ K^{-1}$) and ca. 30 meV (above $0.004\ K^{-1}$). The formation of multiple slopes was caused by an increase of the PS surface with adsorbed $GL\text{-}(OH)_3$, because viscous $GL\text{-}(OH)_3$ takes a long time to attain adsorption equilibrium.

Figures 9 (a) - (d) show the plots of log $[(PL_{100} - PL_T)/PL_{100}]$ vs. 1/T for PS samples with adsorbed Pr-OH, Bu-OH, $EG\text{-}(OH)_2$ and $PG\text{-}(OH)_2$. When the PS samples adsorbed viscous alcohols such as $EG(OH)_2$ and $PG(OH)_2$, they showed multiple slopes.

For the mechanism that saturated polyhydric alcohols weakly adsorbing on nanostructured silicon acts as quenchers for excited electron on nanostructured silicon, we propose a process as shown in Fig.10. While non-radiative deactivation of self-trapped exciton requires activation energy ΔE (point A), newly formed level by the adsorption of alcoholic OH groups is of lower activation energy having vibration levels.

IV. CONCLUSIONS

It was found that red PL intensity of porous silicon was substantially quenched with adsorption of saturared alcohols. The alcohols form a nonradiative deactivation path for

the excited electrons to the adsorbant molecules with life times of μsec, changing itself to nonradiative deactivation. The control of the surface condition of porous silicon is a prerequisite for obtaining reproducible PL.

Reference

[1] M. Shimura, M. Katsuma, and T. Okumura, *Jpn. J. Appl. Phys.*, **35**, 5730, (1996).

[2] M. Shimura, M. Katsuma, T. Chikuma, and T. Okumura, *J. Appl. Electrochem.* to be published.

[3] M. Shimura, M. Katsuma, T. Chikuma, and T. Okumura, *Abstracts of 190th Meeting of Electrochem. Soc.*, Vol. 96-2, pp.728 (1996).

[4] M. Shimura. T. Chikuma, and T. Okumura, *Proceedings of the 6th International Conference on "Luminescent Matterials"*, pp. 112 (1997).

[5] G. Allan, C. Delerue, and M. Lannoo, *Phys. Rev. Lett.*, **76**, 2961 (1996).

[6] J. M. Lauerhaas, G. M. Credo, J. L. Heinrich, M. J. Sailor, *J. Am. Chem. Soc.*, **114**, 1911 (1992).

[7] Y. Ogata, H. Niki, T. Sakka, and M. Iwasaki, *J. Electrochem. Soc.*, **142**, 195 (1995).

[8] C. Delerue, G. Allan, and M. Lannoo, *Phys. Rev. B*, **48**, 11024 (1993).

[9] T. Suemoto, K. Tanaka, A. Nakajima, and T. Itakura, *Phys. Rev. Lett.*, **70**, 3659 (1993).

[10] I. Mihalcescu, J. C. Vial, A. Bsiesy, F. Muller, R. Romestain, E. Martin, C. Delerue, M. Lannoo, and G. Allan, *Phys. Rev. B*, **51**, 17605 (1995).

[11] G. Amato, L. Boarino, N. Brunetto, A. M. Rossi, and A. Parisini, *Thin Solid Films*, **276**, 51 (1996).

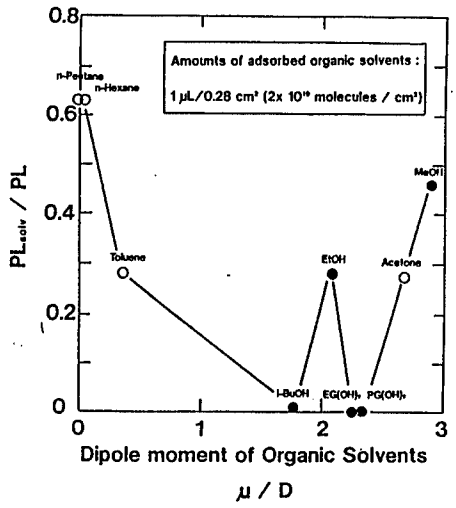


Fig. 1. Relation between PL_{solv}/PL ratio and dipole moment of organic solvents adsorbed on PS sample.

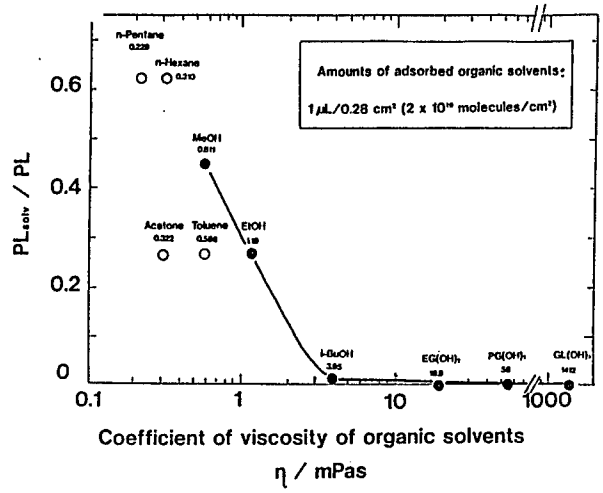


Fig. 2. Relation between PL_{solv}/PL ratio and coefficient of viscosity of organic solvents adsorbed on PS sample.

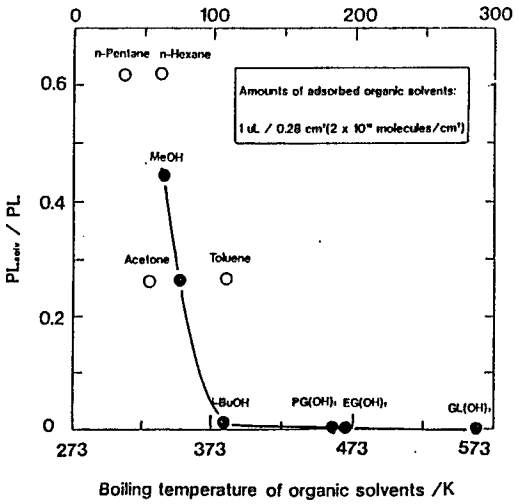


Fig. 3. Relation between PL_{sol}/PL ratio and boiling temperature of organic solvents adsorbed on PS sample, in normal condition.

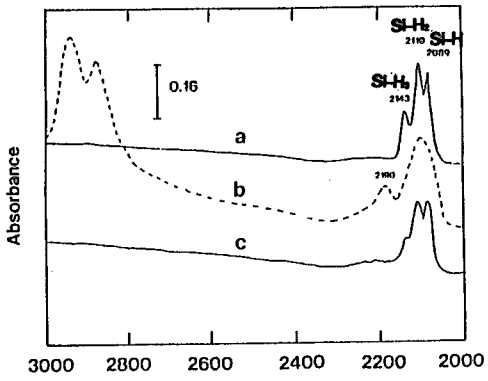


Fig. 4. Transmission FTIR spectra of PS sample. (a):as-prepared,(b): after 10 min EG(OH)₂ adsorption, (c): after 15 min rinsing with Pure water.

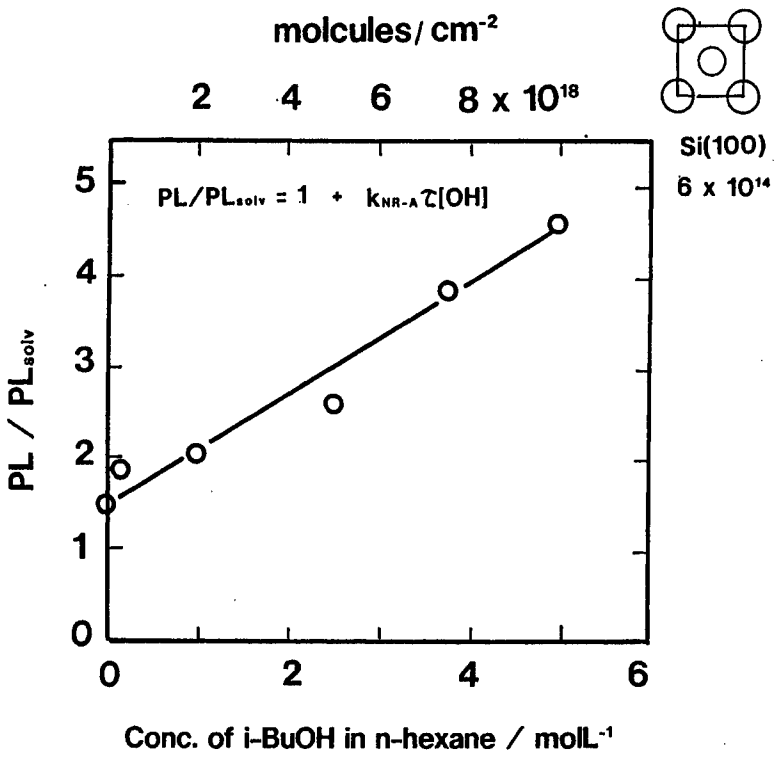


Fig. 5. Relation between PL/PL_{solv} and concentration of i-BuOH in n-hexane.

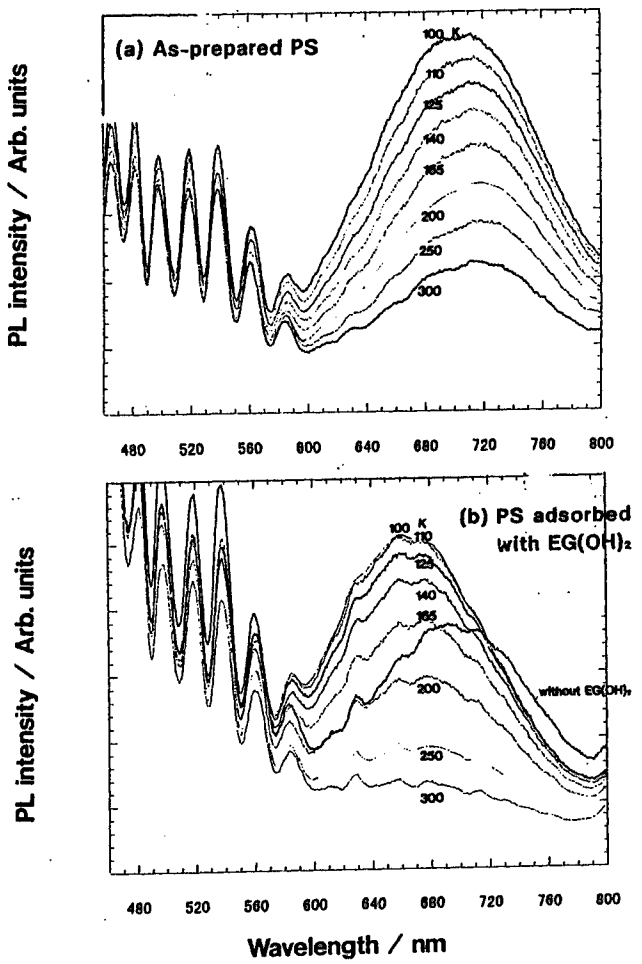


Fig. 6. Temperature dependence of PL spectra of PS sample under the irradiation of 420 nm light from 150 W xenon lamp. (a): as-prepared, (b): adsorbed with $EG(OH)_2$.

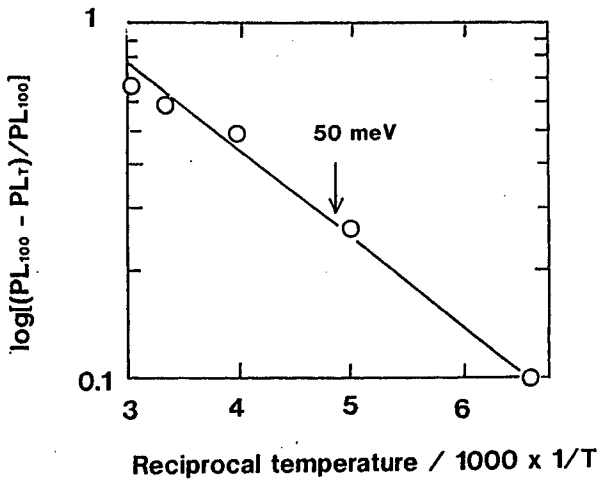


Fig. 7. Relation between $\log[(PL_{100}-PL_T)/PL_{100}]$ of as-prepared PS sample and reciprocal temperature.

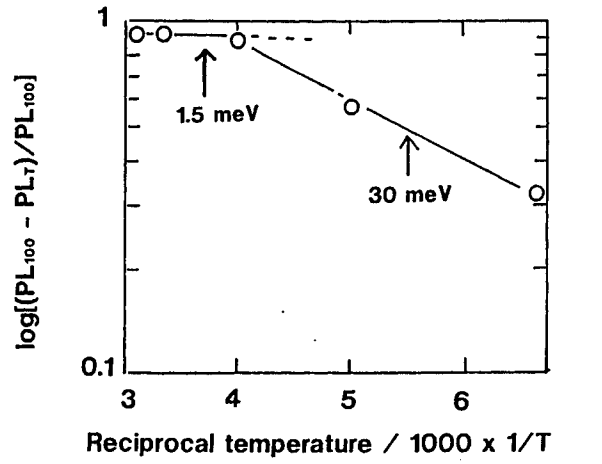


Fig. 8. Relation between $\log[(PL_{100}-PL_T)/PL_{100}]$ of PS sample adsorbed with $GL(OH)_3$ and reciprocal temperature.

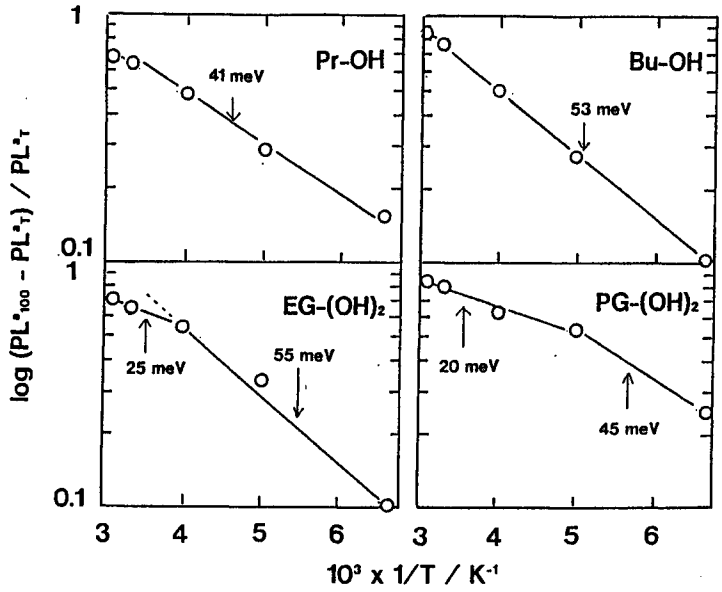


Fig. 9. Relation between $\log[(PL_{100} - PL_T)/PL_{100}]$ of PS samples adsorbed by (a): Pr(OH), (b): i-BuOH, (c): $EG(OH)_2$, (d): $PG(OH)_2$.

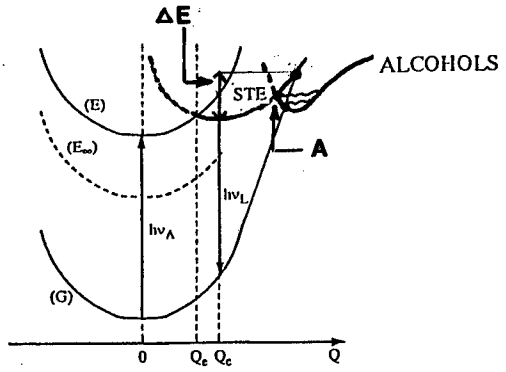


Fig.10. Proposed mechanism of quenching with adsorption of saturated polyhydric alcohols.

Quantum size controlled percolation effects on electron transport in nanoparticle thin films

J. Jacobs[a], B. Hamilton[a], D. Teehan[b] and L.T. Canham[c]

(a) Department of Physics, UMIST, Manchester M60 1QD, UK

(b) CLRC Daresbury Laboratory, Daresbury, Warrington WA4 4AD, UK

(c) DERA, Malvern, Worcs. WR14 3PS, UK

Abstract

In this paper we demonstrate that photo-electron emission excited by soft x-ray synchrotron radiation can be used as a "contactless" probe of the gross conduction processes in porous silicon. Moreover we demonstrate that this approach reveals an underlying conducting geometry which varies with temperature. We show that conduction porous silicon is to some degree controlled not only by the expected scattering and tunneling events, which exist at the microscopic level, but also by percolation phenomena. The evidence suggests that in order to pass vertically through a film, electrons must "find" a completely conducting route. We suggest that such routes are found within "percolating clusters" of nanoparticles which increase in size and density with increasing temperature. This percolation process controls the underlying geometry of the conducting network and hence plays a key role in determining the electrical properties of the film.

I. Introduction

One of the important remaining issues for the exploitation of porous silicon and other thin film systems, which are formed from interconnected nanoparticles, is the nature of electron transport in the material. In particular, the optimisation of any light emitting device requires a better understanding of how electrical energy can be coupled into the structure. This in turn demands more detailed information on the conduction

mechanisms and internal connectivity. Several reports exist on measurements of transport phenomena in porous silicon, e.g. [1], [2], [3], and these propose several mechanisms. In particular the role of band gap variation in disordered quantum wires, quantum size lowering of the local dielectric constant and deep surface traps have been examined. Transient conduction has also been measured and the percolation invoked as partial explanation of the data [4]. In this work, the contacts which are normally made to the film for transport measurement are not required, and we were able to explore a wider dynamic range of (average) conductivity than has been possible with traditional contact methods. This is because we are able to measure very small currents ($\approx$ p.A) which are typically observed at low temperatures in our work. Within this temperature range, we observe trends which support the idea that percolation plays an important role and that its effects may persist to room temperature and above for microporous silicon.

The presence percolation mechanisms dictates that, at a given temperature, some fraction of a given film is insulating, and we show by measuring the electron flow into the film which supplies the x-ray photo-emission current, the fraction of non-conducting material increases as temperature is reduced. It is also clear that, even at room temperature it is possible to have films which are only partly conducting, but which become significantly more conducting above 300K. This observation is significant for the understanding of room temperature LED performance, and is likely to be generally true for nanoparticle thin films.

Finally we present data which supports the notion that the fundamental conduction blocking process may be Coulomb Blockade, i.e. is size controlled. We interpret the "conducting sites" as the nanometre size fluctuations in the Si skeleton; at low temperatures the smallest nanostructures have a large Coulomb gap and will tend to block current flow which will break the continuous current paths. As the temperature is raised, the increased carrier thermal energy "de-blocks" the smaller sites and the un-blocked sites can cluster to form continuous conducting pathways through the film. Such a mechanism is also consistent with the observed effects of optical excitation on both totally insulating films at near liquid He temperatures or on partially conducting films at higher temperatures. In both cases, the supply of minority carriers can lead to de-blocking by removal of electrons from blocked sites via recombination.

II. Experimental data on conduction and photo-conduction in microporous Si.

The main experimental tool used in this work was the UK Synchrotron Radiation Source (Daresbury Laboratories). Measurements were made on the soft x-ray/VUV beamline 6.1. Samples were mounted on the tip of a He cryostat which had been modified to allow low noise electrical measurements whilst maintaining good temperature control. The whole assembly was held in a UHV chamber. Electrochemically processed microporous silicon was prepared in the standard way [5] using p^+ starting material. A variety of film thickness have been measured, but the data presented here relates to films

of several microns thickness. This is an important consideration because it ensures that the x-ray penetration depth is a small fraction of the total thickness, i.e. most of the film depth is not directly excited by the x-ray photon.

A schematic diagram of the experiment is shown in figure 1. The x-ray beam is used to excite photo-electrons; the precise mechanisms for electron ejection are complex, with some electrons being directly emitted due to interaction between the photon and a silicon inner shell electron and others resulting from Auger energy transfer as the hot core hole relaxes. In this work x-ray photon energies near the L_{23} edge of silicon (~100 eV) were used. Scanning through the Si-Si bond L_{23} resonance and fixing the energy at few volts above the resonant peak allowed us to ensure that x-ray interaction with the fully bonded Si nanostructures were dominating our measurements. The quantity measured was the current flowing into the Si substrate which compensates for the electrons lost by photoemission, this is usually referred to as the total electron yield (TEY). Usually, this replacement process is not limited by the transport of electrons to the film surface. Only when the material is insulating does the electron supply fail to meet the surface demand, and the structure charges; the surface charge then quenches electron emission and the TEY drops to zero.

The upper curve in figure 2. shows a typical measurement of TEY as a function of temperature for a porous film. The data were obtained by fixing the x-ray photon energy at 110 eV. i.e. above the L_{23} threshold; as the sample temperature is reduced the TEY signal drops monatonically (from its normalised value of 1 at room temperature). At the lowest temperature measured, the film has no measurable TEY signal and has become an effective insulator. The data are plotted in form which would reveal activation energies if any Arrhenius type behaviour. Although there are linear regions in the plot, it is clear that over the whole temperature range the variation in signal is much more complex than that predicted for straightforward thermally activated process. This is discussed below. It should be noted that high purity silicon wafer material shows the opposite trend: the TEY signal *increases* as temperature drops within the measured range despite the fact that the residual donors or acceptors are subject to freeze out. This comparison is important because it demonstrates that the TEY measurement is not, at least to first order, sensitive to the conductivity of the material. This can be understood by modeling the porous film as an interconnected set of nanoparticles which may individually be in a conducting or non conducting state. The nanoparticles in porous silicon must be understood to be fluctuations in the wire like Si skeleton; wide regions of the wires will represent low energy sites for electrons and are closely analogous to nanoparticles in the electrical sense.

In fact nanoparticles have a strong intrinsic mechanism for switching conduction properties with temperature viz. Coulomb Blockade [6]. In order for an electron to enter a nanoparticle an energy of $E_c = Q^2/2C$ (the Coulomb gap) must be supplied, where Q is the final charge held within the particle. The key parameter here is C, the self capacitance with particle diameter i.e. the Coulomb gap scales inversely with particle size. Thus, for very small particles the thermal energy may be insufficient to promote electron transfer; for the case of Si, Coulomb blockade is predicted to be an important

factor at room temperature for particles of sizes of around 2 nm. We can now picture, schematically what may occur in a nanoparticle film as it is cooled, and this is illustrated in Figure 3. At any particular temperature some nanoparticles will be blocked (i.e. those below a given size) and clusters of unblocked particles will remain. Those clusters which span the thickness of the film will contribute to the TEY, and are referred to as percolating clusters. Other clusters will not span the film and are referred to as non-percolating clusters. However, the precise magnitude of the contribution of a particular percolating cluster is defined by the area of the cluster which forms part of the physical (but discontinuous) surface. Thus the two percolating clusters illustrated, which have very different mass and which would be assigned radically different classical resistance, contribute about equally to the TEY because they have about the same surface area. Crucially this simple picture predicts that non conducting regions of the film exist, and it is the growth of these regions, as the temperature is lowered, which leads to the loss of TEY.

III. A model for percolation in a nanoparticle film

The notion that porous silicon becomes locally insulating at low temperatures, and that conducting pathways through the film increase in density and size as temperature is increased, is one which lends itself directly the framework of percolation theory. However in order to test the plausibility of these ideas we need to develop a percolation model which has built into it the key physics of the material system.

Percolation theory describes physical systems in terms of a percolation lattice in which lattice sites are either occupied or empty and which are inter-connected by bonds; here occupied and empty will signify conducting and non conducting respectively. Each site has some probability, P, of occupancy and if the P is above the percolation threshold, P_C, then clusters of occupied sites, so called fully percolating clusters, will exist which span the system. A percolating cluster in porous Si would therefore permit electron conduction through the film.

Two parameters are crucial to any percolation model; firstly the choice of percolation lattice (i.e. its geometry), and secondly the physics driving the probability occupancy of lattice sites. We have chose to investigate the Bethe lattice which has found many applications in condensed matter physics. This lattice has a tree-like structure and in spite of its apparent complexity, lends itself to simple algebraic solution. We do not suggest that the Bethe lattice mimics exactly the physical structure of microporous silicon, but it does preserve some important features. For example an electron moving through a Bethe lattice has no closed loops available and must find a unique 1-D route to the physical surface. The Bethe lattice used in this work was considered to have sites composed of the "nanoparticle" fluctuations in the Si quantum wires. The probability of site occupancy is dictated by the probability that an electron has the energy to overcome the Coulomb gap and enter the nanoparticle: an *occupied* site is then one which *is not blocked.* An *empty* site is one which *is blocked* due to

Coulomb Blockade. The bonds joining sites could be tunneling gaps or hopping channels in the physical structure, in a general sense they are regions of the structure which present no barrier to the electron.

The percolation threshold probability is easily calculated for a Bethe lattice with z bonds per site[7]:

$$P_c = \frac{1}{z-1} \qquad (1)$$

so for a lattice with 3 bonds per site (particle), P_c becomes 1/2, that is the electron has two choices of exit direction when leaving one nanoparticle and finding the next particle on its route through the film. For this case if $P < 1/2$, the film will not conduct. The key task now is to assign some credible value of P which must be a function of T and which will allow us to compare our percolation calculation with the experimental data. For porous silicon, we need to assign two probabilities to a lattice site. The first relates to the particle size distribution, which we shall take to be Gaussian (i.e. a normal error function), p_i:

$$p_i = \frac{1}{\sqrt{2\pi\sigma}} . e^{\frac{(x-\langle x \rangle)^2}{2\sigma^2}} \qquad (2)$$

This is the normalized probability that that one of the neighbouring particles will have a size have a size x.

The second is the probability that a particle of size x will be occupied, and this may be represented to a reasonable approximation by a Boltzmann occupation probability, p_j:

$$p_j = Ae^{\frac{-E_c(x)}{kT}} \qquad (3)$$

where E_c is the Coulomb gap energy and A is a constant. In assigning a value of E_c to a size x we have taken the experimental prediction of [6]. Both probabilities are normalised, and $p = p_i.p_j$ represents the probability that a neighbouring particle has a size x and that the size x will accept an electron. Thus, p is a distribution function which describes the probability of a particle within the original size distribution being an "occupied site" at a given temperature.. Since *any* "occupied" particle within p conducts and can contribute to a percolating cluster, the integral of p over all sizes is measure of P which is required for the percolation model. This method of assigning a site occupancy probability neglects localisation energies i.e. it assumes that Coulomb Blockade is the dominant barrier term. It is also worth noting that if a neighbouring nanoparticle is much larger than the particle from which the electron is emerging, then

there is no barrier; the large particle actually forms part of the bond system. In general the movement of an electron will be unrestricted as long as it is travelling through successively lower energy sites, but the above analysis applies when the electron is required to branch into higher energy sites. Thus not every nanoparticle forms a site on the Bethe lattice, this does not in any sense change the percolation lattice it simply implies that only a subset of the nanoparticles present are active sites.

An important outcome of percolation is that although the Boltzmann factor builds in an exponential temperature dependence to P, the predicted temperature evolution of the film conduction is much more complex than a simple thermal activation. This is because the conduction must reflect also the temperature dependency of the growth in size of a percolating cluster, and the size or strength of a percolating cluster on a Bethe lattice is not a linear function of P but is given by [7] for $P>P_c$:

$$S = P(1-\left[\frac{1-P}{P}\right]^3) \qquad (4)$$

We assume that the strength of the observed TEY signal varies linearly with S. Figure 4. shows a choice of size distribution p_i and the way in which the function becomes modified when the probability of an electron overcoming the Coulomb gap is included. It is clear that at low temperatures smaller particle sizes become excluded from the distribution function p, but that at very high temperatures the whole size distribution would be included i.e. the whole film would conduct equally.

By integrating p at each temperature it is now possible to calculate the strength of the percolating system S, which we take to be proportional to the TEY. This is plotted for a particle size distribution having a mean size of 4 nm., and is the lower curve in figure 2. Two comments should be made. Firstly the general shape of the prediction is similar to the experimental result, at least at lower temperatures. The slope is not a simple exponential but has a curvature on an Arrhenius plot which steepens as the film becomes completely insulating. We can now interpret this steepening of slope as the disappearance of a single percolating cluster, varying in strength with temperature, as it breaks up into smaller isolated percolating clusters. These clusters disappear as the sample becomes insulting at the percolation threshold. The second notable feature is the mean particle size which must be chosen for p_i in order to make the model predict (approximately) the same temperature for the percolation threshold, i.e. the departure of conduction from zero. The value of $\langle x \rangle$ shown is 9 nm, much larger than the size of nanoparticles that are known to contribute to the luminescence of porous silicon. This value of $\langle x \rangle$ is consistent with the idea that only a subset of the particle size distribution is optically active as luminescence centres.

The loss of conduction at low temperatures when $P<P_c$ is essentially a phase transition and it is not surprising that a description involving percolation theory is appropriate to describe the main effects. It has been demonstrated that the phase

transition can be reversed by optical pumping [8] which is consistent with idea that in the totally blocked state is a sign of stored volume charge, which can be redistributed with the aid of injected mobile charge.

Acknowledgements

The authors wish to acknowledge the support of the EPSRC for the financial support enabling us to use the Synchrotron Radiation Source and also for the provision of postgraduate Research studentships (JJ and DAH)

References

[1] Read A. J. *et. al. Phys. Rev. Lett.* **69**, 1232-1235 (1990)

[2] Tsu R. and Babic D., *Appl. Phys. Lett.* **64**, 1806-1808 (1994)

[3] Lehmann V., Hofman F., Moller F., and Gruning U., *Thin Film Solids*, **255**, 20-22 (1995)

[4] Lee P. A. *Physica B* **189**, 1-5 (1993)

[5] Hamilton B. *Semiconductor Science and Technology* **10**, 1187-1207 (1995)

[6] Ali D. and Ahmed H. *Appl. Phys. Lett.* **64**, 2119-2120 (1994)

[7] "Introduction to Perolation Theory", Stauffer D and Aharony A, Taylor and Francis, London (1994)

[8] B. Hamilton, J Jacobs, D A Hill, R F Pettifer D Teehan and L T Canham, Nature vol 393, 45

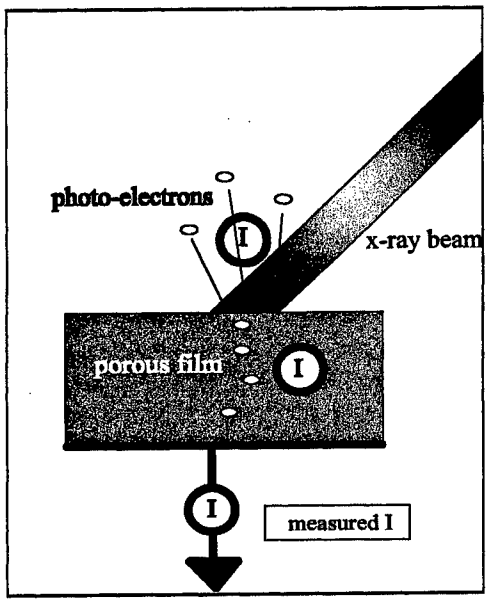


Figure 1: A schematic description of the experimental system used to detect current flow through the films. The quantity sensed is the current flowing into the substrate which is by charge conservation equal to the integrated electron loss from the surface (the TEY). If the transport through the film cannot match the surface loss rate then surface charging occurs and the TEY signal drops.

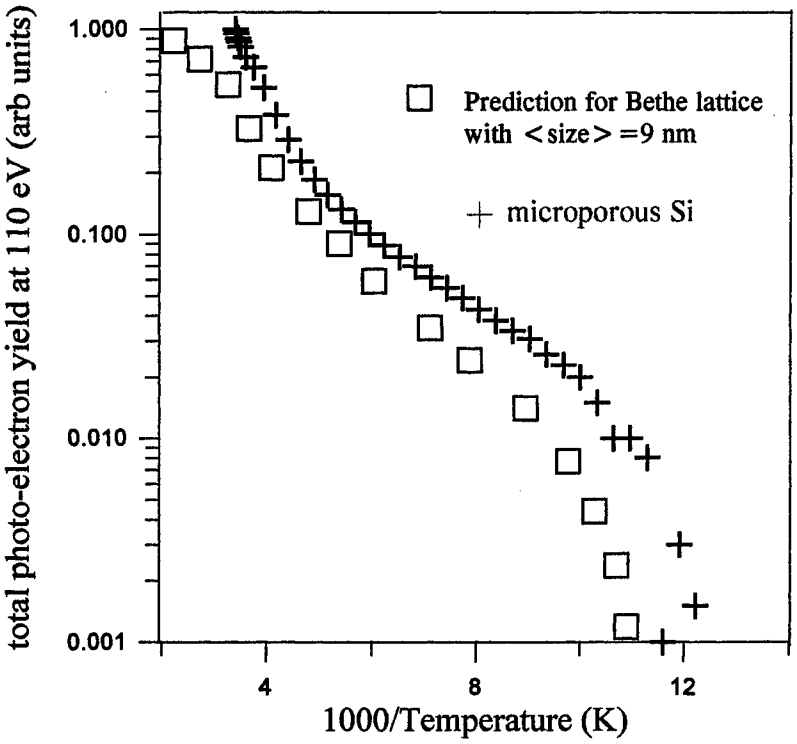


Figure 2: The variation of TEY with temperature for a microporous silicon film (85% porosity and 8 microns thick), as temperature is varied. Experimental data are plotted in the uper curve,+ and the prediction of percolation theory using a Bethe lattice with site switching controlled by Coulomb Blockade is shown in the lower curve,□

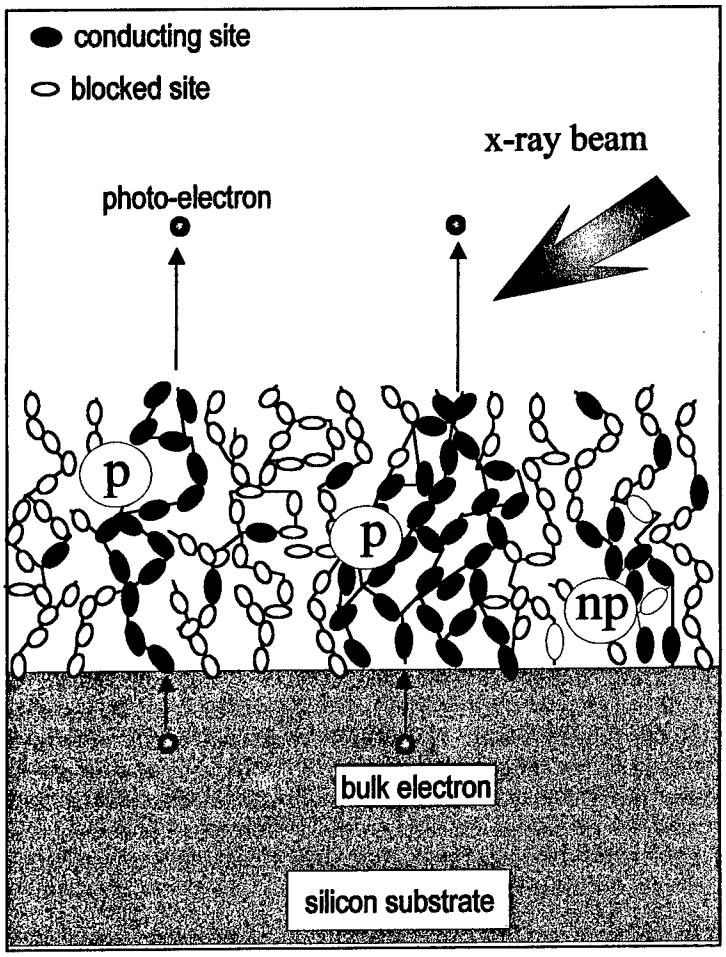


Figure 3: Illustrating the way in which a percolation controlled conduction can lead to a loss of TEY signal. The clusters shown a re either percolating (p) or non-percolating (np), but only the p clusters contribute to the measured signal.

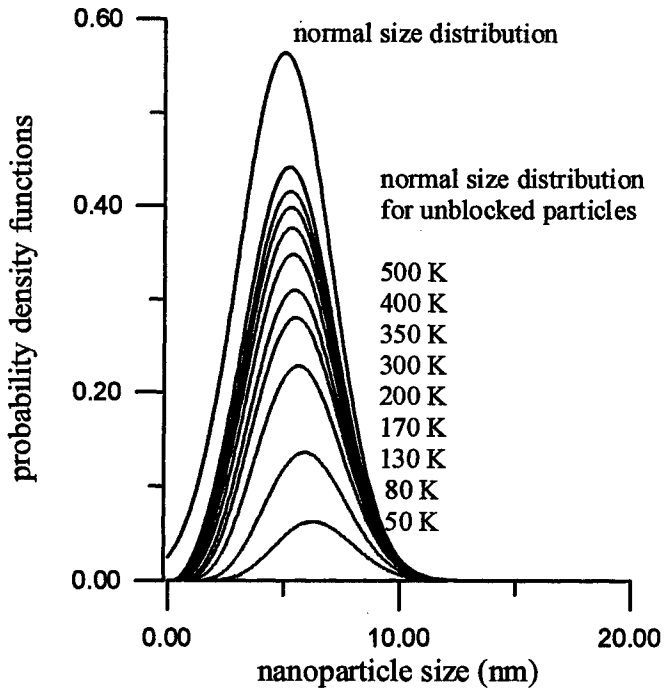


Figure 4: The distribution functions used to obtain a value for the probability P that an electron will move onto a neighbouring site on a Bethe lattice. The normal distribution shown here is for a mean particle size of 4 nm, and the family of functions nested within the size distribution show how the latter becomes modified as T is lowered and the probability of a thermally assisted transfer over the Coulomb gap is lowered.

Excitons in Nanostructures

Optical Properties of Semiconductor Nanocrystals Embedded in Dielectric Media

Al. L. Efros and M. Rosen
Nanostructure Optics Section
Naval Research Laboratory, Washington DC, 20975

ABSTRACT

The optical properties of 1 to 5 nm radius crystals embedded in various dielectric media are discussed. These properties are determined by transitions between electron and hole quantum size levels. An analytical theory of the QSLs within a spherical 8-band Pidgeon and Brown model has been developed This theory explicitly includes the coupling of conduction and valence bands, the 6-band structure of the valence band and naturally generalizes all previous multi-band considerations. The theory successfully describes the structure of the absorption spectra and transition oscillator strengths in narrow gap InAs nanocrystals using bulk band parameters. The interaction of electron and hole spins with the spins of paramagnetic centers is usually weak in bulk semiconductors because the interaction occurs via a contact potential. However, in nanosize quantum dots this interaction, which is proportional to the square of the electron and hole wave functions at the position of the para magnetic center, increases dramatically as the inverse of the volume of the quantum dot. As a result, the effective magnetic field of a paramagnetic center acting on electron spins is several orders of magnitude larger than in the bulk and can be as large as several hundred Tesla. This field should lead to a giant splitting of the spin sublevels of electrons and holes of as much as to several tens of meV and to giant Magnetic Circular Dichroism and Faraday effects whose magnitudes strongly depend on nanocrystal size.

1 Introduction

The optical properties of nanocrystal quantum dots have attracted the attention of many investigators because of their potential applications and for their funda-

mental scientific interest [1, 2, 3, 4]. These nanocrystals are embedded in dielectric matrices and have an almost ideal spherical shape. Current technology allows us to fabricate crystals in a controlled manner with radius from 10 to 100 angstroms. For purposes of clarity, we will discuss only the so called " strong quantization case", where the optical properties are determined by transitions between the quantum size levels of electron and holes and the Coulomb interaction shifts their energies only slightly to the red [5, 6]. This case is realized in small crystals.

2 Theory of the Quantum Size Levels

We have developed a theory for the quantum size levels that is valid for semiconductors having a cubic or zinc blende lattice structure and which have their band edge at the Γ-point of the Brillouin zone. Examples are GaAs, InP, InAs, InSb, CdTe, CdSe, and ZnSe.

In Fig. 1 we show the band structure of a typical zinc blende semiconductor. The conduction band is parabolic only at the bottom of the band. At the top of the valence band we have a four-fold degenerate Γ_8 subband, which describes the dispersion of the light and heavy hole branches at nonzero k and the spin- orbit split off subband Γ_7 which falls below the top of the valence band by the amount of the spin orbit splitting, Δ.

In wide gap semiconductors, hole and electron quantum size levels are described independently in the so called 6 band model [7]. This model has successfully described the optical spectra of CdSe nanocrystals [8, 9, 10, 11, 12]. It neglects, however, the coupling of the conduction and valence bands, which is important in narrow gap semiconductors such as InAs. For these nanocrystals we need the 8 band model, first proposed by Pidgeon and Brown [13].

Pidgeon and Brown model

The Pidgeon and Brown model takes into account exactly the coupling between the 6 valence and the 2 conduction bands, separated by an energy gap E_g between the bottom of the conduction and the top of the valence band. The magnitude of the coupling is determined by the Kane matrix element $V = -i < S|p_z|Z > /m_0$ taken between the Bloch functions of the conduction and valence bands, and m_0 is the free electron mass. The model also takes into account the contribution of the remote bands to the effective masses of electrons and holes: α, γ_1 and γ respectively. The electron effective mass at the bottom of the conduction band, m_e, can be written as the sum of remote band contributions plus a contribution

from the valence band:

$$\frac{1}{m_e} = \frac{1}{m_0}\left[\alpha + \frac{E_p}{3}\left(\frac{2}{E_g} + \frac{1}{E_g + \Delta}\right)\right] \quad , E_p = 2m_0V^2 \; . \tag{1}$$

The Luttinger parameters of the valence band:

$$\gamma^L = \gamma + \frac{E_p}{6E_g} \; , \quad \gamma_1^L = \gamma_1 + \frac{E_p}{3E_g} \; , \tag{2}$$

and the effective masses of the light, m_{lh}, and heavy holes, m_{hh}, can also be written as the sum of two similar contributions:

$$\frac{1}{m_{hh}} = \frac{\gamma_1^L - 2\gamma^L}{m_0} = \frac{\gamma_1 - 2\gamma}{m_0} \; , \quad \frac{1}{m_{lh}} = \frac{\gamma_1^L + 4\gamma^L}{m_0} = \frac{1}{m_0}\left(\gamma_1 + 4\gamma + \frac{E_p}{E_g}\right) \; . \tag{3}$$

The Pidgeon and Brown Hamiltonian [13] is a system of coupled second order differential equations and is quite complicated. However, for spherical nanocrystals we can simplify the problem considerably.

Case of zero spin-orbit splitting of the valence band

In spherical NCs each electron and hole state is characterized by a total angular momentum $j = l + J$, which is a sum of the envelope angular momentum, l, and the Bloch function angular momentum, J [14, 15]. Analytical equations for the quantum size level energies in QDs surrounded by an infinite barrier have been written for each j [15]. These equations are very complicated and we will only show them for the case where the spin-orbit splitting Δ, is zero. The energies of the electron levels, ΔE_e, in a nanocrystal with radius a surrounded by an infinite barrier are obtained from:

$$j_{j-1/2}(k_-a) = \frac{1}{2}\frac{\alpha}{|\alpha|}\sqrt{\frac{\Delta E_e(\gamma_1 + 4\gamma)}{(E_g + \Delta E_e)\alpha}}\left[(1 + \eta_j^+)j_{j+1/2}(k_-a) - (1 - \eta_j^+)j_{j-3/2}(k_-a)\right] \; , \tag{4}$$

where $j_n(x)$ is a spherical Bessel function, the momentum k_- is connected to the bulk dispersion energy of electrons, $\eta_j^+ = 1/2j$, and $j = 1/2,\ 3/2,\ ....$ Equating the right side of these equations to zero determines the positions of the uncoupled electron levels of wide band gap quantum dots.

The hole levels are obtained from two equations. For the odd hole states we have

$$j_{j-1/2}(k_h a) = 0 \; , \tag{5}$$

which is valid for all $j > 1/2$, and the momentum k_h is related to the hole energy, ΔE_h by the relationship: $\Delta E_h = (\gamma_1 - 2\gamma)k_h^2/2m_0$. For even hole states:

$$j_{j-3/2}(k_h a)j_{j+1/2}(k_- a) + \frac{1-\eta_j^+}{1+\eta_j^+} j_{j-3/2}(k_- a)j_{j+1/2}(k_h a)$$
$$= -\frac{\alpha}{|\alpha|}\sqrt{\frac{\Delta E_h \alpha}{(E_g + \Delta E_h)(\gamma_1 + 4\gamma)}} j_{j-1/2}(k_- a)\left[j_{j-3/2}(k_h a) - \frac{1-\eta_j^+}{1+\eta_j^+} j_{j+1/2}(k_h a)\right], \quad (6)$$

which is valid for all j starting from $j = 3/2$ and the momentum k_- is connected with the bulk dispersion energy of the light hole. Setting the right side of these equations to zero determines the positions of the uncoupled hole levels in wide gap nanocrystals.

The strength of the coupling is determined by the square root of the natural energy parameter: the ratio of the quantization energy to the energy gap, $\Delta E_{h,e}/(E_g + \Delta E_{h,e})$. It is clear that in narrow gap semiconductors the coupling is always strong because this parameter is then on the order of unity. But even in moderate gap semiconductors the square root dependence greatly magnifies the role of the coupling. An unexpected result is the sensitivity of the coupling to the ratio of the remote band contributions to the electron and light hole effective masses, $\alpha/(\gamma_1 + 4\gamma)$. The mixing of the conduction band in hole states is proportional to the square root of this ratio. But it is the inverse of this ratio that governs the valence band mixing in electron states. If it is weak for one carrier it is strong for the other. This ratio then could produce quite large an admixture even if the confinement energy were much smaller than the energy gap, or, conversely, considerably decrease the admixture even though $\Delta E_{h,e} > E_g$.

Fig.2 shows the size dependence of the lowest electron and hole levels calculated for parameters close to those of InP but taking $\Delta = 0$. In the upper panel we show the 1S(e) electron level calculated in parabolic approximation, taking nonparabolicity of the electron band into account, and finally the results of the calculation within the PB model using two different sets of parameters.

In parabolic approximation the hole ground $1P_{3/2}(h)$ state has p-type symmetry in InP. This state is a heavy hole state only and is not affected by the coupling. Selection rules however do not allow transitions from this state to the ground 1s electron state. The first $1S_{3/2}(h)$ hole state, from which transitions to the first electron level are allowed is shown here in parabolic approximation, taking nonparabolicity of the light holes into account and in the PB model for two sets of parameters. The first set of energy band parameters, with negative α, was determined for bulk InP ($E_g = 1.424\,\text{eV}$, $E_p = 20.6\,\text{eV}$, $\alpha = -1.2$, $\gamma = -0.51$, and $\gamma_1 = 0.41$); for the second set, with positive α, ($E_g = 1.424\,\text{eV}$, $E_p = 18.0\,\text{eV}$, $\alpha = 0.58$, $\gamma = -0.23$, and $\gamma_1 = 1.11$) we changed E_p by only 10%, but retained

the bulk InP values of the electron (m_e) and hole effective masses (m_{hh}, m_{lh}), described by Eqs. 1 and 3. Both calculations use the same electron and hole effective masses. You see how sensitive the spectra of the quantum size levels are to the parameters used.

Pseudopotentials and Multiband Effective Mass Approximation

Figure 2 is also useful for discussing the recent criticism by A. Zunger of the effective mass approximation. In several publications (see for example [16]) Zunger and colleagues compared the results of their pseudopotential calculations with the results of an inappropriate version of effective mass approximation and interpreted the disagreement as a failure of the latter.

It is important to remind the reader that: 1) pseudopotentials are not actual atomic potentials, and 2) parameters of these potentials are determined so as to reproduce the energy spectra around the critical points of the Brillouin zone of the bulk semiconductors (they are not unique). That is, pseudopotential calculations have similar limitations as the effective mass approximation. They do not describe "real" surfaces or heterointerfaces and do not work in small crystals.

Furthermore, and of particular importance, the pseudopotential Bloch functions depend on parameter selection and differ from the bulk ones. The pseudopotentials Zunger et al. use for InP may very well describe the effective masses of electrons and holes, but the Kane matrix element calculated with his Bloch functions is considerably smaller than that measured (E_p is only 15 eV in his calculations). In $\mathbf{k}\cdot\mathbf{p}$ theory this means that he underestimates the coupling strength and overestimates the effect of remote bands. Fig.2 shows the drastic effect of such a mistake [17].

Absorption Spectra of InAs Nanocrystals

The 8 band theory of the quantum size levels describes the size dependence of the absorption spectrum of narrow gap InAs nanocrystals. The bulk energy gap of InAs is only 0.42 eV. The nanocrystals studied are embedded in a polymer having an optical energy gap 4.5 eV. We modeled the InAs nanocrystals by a spherical potential well with conduction and valence band barrier offsets of 2 eV . For finite barriers the system of radial equations from ref. [15] have been solved numerically [18].

Fig.3 shows the photoluminescence excitation spectra (PLE) of samples of InAs nanocrystals with diameters between 25 and 68 Å. The PLE of these samples show up to 9 peaks corresponding to the transitions between a number of electron and hole quantum size levels.

Fig.4 shows the spectra plotted as a function of the ground state transition energy. The left panel compares the observed transitions with those calculated with the 8 band model using bulk values of the InAs energy band parameters ($E_g = 0.418\,\text{meV}$, $\Delta = 0.38\,\text{eV}$, $E_p = 21.6\,\text{eV}$, $\gamma_1^L = 19.7$, $\gamma^L = 8.9$, and $\alpha = 0.8$). The right hand panel shows the calculated relative oscillator strengths for the optically active transitions. The calculated level separations and their intensities closely reproduce the observed strong transitions. For example the calculations show that the second and the third transition to the $1S$ electron levels cross at an energy of 1.5 eV and their intensities exchange there. The observed E_3 PLE peak corresponds to one of these transitions for large dots and to the other for small dots. This explains why the E_3 peak does not appear to shift for small dots. The next two strongest transitions, E_5 and E_7 are each described by the two different transitions to the $1P$ electron level. The highest, weak excited states are ascribed to a combination of several of the transitions listed in the lower panel.

In conclusion, a theory of the quantum size levels in narrow gap semiconductor nanocrystals based on the spherical PB model has been developed. Analytical results show that conduction and valence band coupling may be important even in semiconductors with relatively wide gaps. The theory successfully describes the observed level structure and transition intensities of InAs nanocrystals embedded in polymers.

3 Giant Internal Magnetic Fields in Nanocrystals

The great enhancement of short range contact interactions is one of the most interesting properties of low dimensional semiconductor structures. These interactions may have different origins and completely different energy scales. The Hamiltonian of the spin-spin contact interaction can be generally written,

$$\hat{H}_{exch} = -v_0 \alpha_{exch} (\mathbf{S}_1 \cdot \mathbf{S}_2) \delta(\mathbf{r}_1 - \mathbf{r}_2) \,, \tag{7}$$

where v_0 is the volume of the primitive cell and the exchange constant α_{exch} is on the order of $10^{-3} - 10^{-2}$ meV for the electron-nucleus interactions, $\sim 200 - 500$ meV for electron-hole interactions and $\sim 1 - 3$ eV for electron or hole interactions with a magnetic ion.

The magnitude of the interaction strongly depends on the average distance between the interacting spins, $\mathbf{r}_1 - \mathbf{r}_2$. In fact it is inversely proportional to the cube of this distance. In bulk, it is on the order of the cube of the Bohr radius of the donor or exciton, a_B,

$$\langle \delta(\mathbf{r}_1 - \mathbf{r}_2) \rangle_{\text{bulk}} = \frac{1}{\pi a_B^3} \,; \tag{8}$$

in nanocrystals, it is on the order of the cube of the nanocrystal radius,

$$\langle \delta(\mathbf{r}_1 - \mathbf{r}_2) \rangle_{\rm NC} = \frac{\pi}{2a^3} \,. \tag{9}$$

The resulting enhancement of this interaction, $\langle \delta(\mathbf{r}_1 - \mathbf{r}_2) \rangle_{\rm NC} / \langle \delta(\mathbf{r}_1 - \mathbf{r}_2) \rangle_{\rm bulk} \sim 1.0 - 5.0 \times 10^3$, can be as much as three orders of magnitude in small nanocrystals.

Dark Exciton

It is a well known effect, that it is the enhancement of the electron-hole exchange interaction in nanocrystals that leads to the formation of the Dark Exciton. In bulk the electron-hole exchange interaction also splits the exciton into optically allowed and optically forbidden (Dark) exciton states. The magnitude of this splitting is only $\langle \hat{H}_{exch} \rangle \sim 0.01 - 0.1\,\text{meV}$. In nanocrystals, however, the splitting is on the order of 10-20 meV. This huge splitting strongly affects the photoluminescence and has been observed in CdSe[19, 20, 21], InP [22] and InAs [23] nanocrystals as well as in porous Si [24, 25].

Magnetic Fields of Nuclei in Nanocrystals

A huge increase occurs in the effective magnetic field acting on electrons arising from the nuclei in nanocrystals. This field can be written:

$$\mathbf{H} = (\mu_B g_e)^{-1} v_0 \sum_i \alpha^i_{exch} \mathbf{S}_i \Psi^2_e(\mathbf{r}_i) \,, \tag{10}$$

where $\Psi_e(\mathbf{r}_i)$ is the electron wave function at the i'th nucleus, g_e is the electron g-factor, and the sum goes over all nuclear positions.

At high temperature (almost any temperature, including Helium temperature, is high for nuclei if they are in equilibrium with the lattice), the average magnetic field is zero, because the nuclear spins are randomly oriented. However, the fluctuation of this magnetic field does not depend on temperature. The magnitude of this random magnetic field can be estimated from the square of the magnetic field:

$$\begin{aligned} \langle \mathbf{H}^2 \rangle &= (\mu_B g_e)^{-2} v_0 \sum_i (\alpha^i_{exch})^2 S_i(S_i+1) \int \Psi^4_e(\mathbf{r}) d^3r \\ &= \frac{0.67 (\mu_B g_e)^{-2} v_0 \sum_i (\alpha^i_{exch})^2 S_i(S_i+1)}{a^3} \,, \end{aligned} \tag{11}$$

where the sum goes over the nuclei in a primitive cell. The fluctuation of the effective magnetic field grows as $\sqrt{\langle \mathbf{H}^2 \rangle} \sim 1/a^{3/2}$ and reaches a value of 0.7 T in GaAs nanocrystals with 15Å radius. This fluctuation may be responsible for the homogeneous line width in small quantum dots.

At low temperatures of the nuclear system, which can only be attained as the result of dynamic cooling, alignment of the nuclei leads to the Overhauser effect and to polarized PL [26, 27].

The energy scale of all these effects is less than one meV but they become important when we discuss, for example, quantum computing or single electron transistors.

Giant Magnetic Field of Magnetic Ions

A completely different energy scale governs the enhancement of the interaction of electrons and holes with a magnetic ion. The effective magnetic field of a single magnetic ion acting on the electron can be written:

$$\mathbf{H} = (\mu_B g_e)^{-1} v_0 \alpha_{exch}^{ion} \mathbf{S} \Psi_e^2(\mathbf{r}) \,, \tag{12}$$

where $\Psi_e(\mathbf{r})$ is the electron wave function at the ion position, and α_{exch}^{ion} is on the order of several eV. One can see that the effective magnetic field is parallel to the ion spin direction, that its magnitude depends on the ion position in the nanocrystal, and that it grows as $1/a^3$. Calculations show that this field can reach thousands tesla and splits the electron spin sublevels by as much as 10–100 meV.

The effective magnetic field acting on a hole generally cannot be written in such a simple form, because of the strong spin-orbit interaction in the valence band. The effective magnetic field acting on a hole is not parallel to the spin direction of the magnetic ion and has a complicated dependence on the ion position in the nanocrystal [28]. Nevertheless it also grows as $1/a^3$, reaches thousands tesla and splits hole sublevels by as much as 100 meV.

The splitting of electron and hole spin sublevels exists in *zero* external magnetic fields. How is it evidenced? Because of the random orientations of the magnetic ion spins in an ensemble of nanocrystals, unpolarized and even circularly polarized light will excite transitions between all possible spin sublevels. As a result, a broadening occurs in the absorption spectrum of the allowed transitions in zero magnetic field instead of a splitting.

To observe the splitting, we need to apply an external magnetic field, B, which aligns all the ion spins along the direction of the field. In this case, circularly polarized light will excite appropriate individual components of the spin sublevels in accordance with the appropriate selection rules. A comparison of the absorption of right and left circularly polarized light gives the spin sublevel splitting. The degree of the magnetic ion spin alignment is determined by the Brillouin function, $B_S(x)$:

$$\langle S \rangle = S B_S \left(\frac{g \mu_B S B}{kT} \right) \,, \tag{13}$$

which is a function of the ratio of the magnetic energy, $g\mu_B SB$ to the temperature, T, and g is the magnetic ion g-factor. $B_S(x) = 1$ when $x \gg 1$, so that

at low temperature or high magnetic field one can reach a 100% alignment if the nanocrystals contain one magnetic ion. This allows us to measure the value of the sublevel splitting.

The maximum splitting occurs when the ion is at the center of the nanocrystal. Existing technology does not allow us to make such crystals at present; ions can occupy any possible metal site in the crystal. Assuming equal probability of all the ion positions, we obtain an average splitting of the electron and hole spin sublevels which is six times smaller than the maximum value:

$$\Delta E_{e,h} = \alpha^{ion}_{exch}(e,h) S \frac{3v_0}{16\pi a^3} \,. \tag{14}$$

This is the average splitting in nanocrystals containing a single magnetic ion. Isolation of the ions in a nanocrystal is important. Increasing the magnetic ion concentration in bulk leads to pairing and to a decrease in the effective magnetic field.

It is not a simple problem to avoid this effect without using special techniques. Statistically, even if we have one magnetic ion per crystal on the average, some nanocrystals contain no magnetic ion at all, and some have 2 magnetic ions per dot. For example in an ensemble of 16Å radius crystals with an average concentration of one magnetic ion per crystal on average, 38% of the nanocrystals are empty, 38% have one ion per dot and 20% have two magnetic ions per dot. This last group of crystals decreases the average effective magnetic field for the ensemble.

In conclusion, a giant enhancement of spin-spin contact interactions occurs in nanocrystals. Even the interaction with the nuclei becomes increasingly important with decreasing quantum dot size. The presence of a magnetic ion dopant results in a giant effective magnetic field which splits the electron and hole sublevels by as much as 100 meV in small nanocrystals. This field leads to a giant Faraday effect and Magneto Circular Dichroism. To maximize this field one should have one magnetic ion per crystal sitting at its center.

Aknowledgement

This work was supported by the Office of Naval Research.

References

[1] L. E. Brus, Appl. Phys. A **53**, 465 (1991).

[2] A. P. Alivisatos, Science **271**, 933 (1996).

[3] S. Schmitt-Rink, D. A. B. Miller, and D. C. Chemla, Phys. Rev. B **35**, 8113 (1987).

[4] P. Horan and W. Blau, Phase Transitions **24-26**, 605 (1990).

[5] Al. L. Efros and A. L. Efros, Sov. Phys. Semicond. **16**, 772 (1982).

[6] L. E. Brus, J. Chem. Phys. **79**, 5566 (1983).

[7] G. B. Grigoryan, E. Kazaryan, Al. L. Efros, and T. V. Yazeva, Sov. Phys. Solid State **32**, 1031 (1990).

[8] A. I. Ekimov, F. Hache, M. C. Schanne-Klein, D. Ricard, C. Flytzanis, I. A. Kudryavtsev, T. V. Yazeva, A. V. Rodina, and Al. L. Efros , J. Opt. Soc. Am. B **10**, 100 (1993).

[9] D. J. Norris, A. Sacra, C. B. Murray, and M. G. Bawendi, Phys. Rev. Lett. **72**, 2612 (1994).

[10] D. J. Norris and M. G. Bawendi, Phys. Rev. B **53**, 16338 (1996).

[11] A. I. Ekimov, Physica Scripta **39**, 217 (1991).

[12] P. A. M. Rodrigues, G. Tamulaitis, P. Y. Yu and S. H. Risbud, Solid State Commun. **94**, 583 (1995).

[13] C. R. Pidgeon and R. N. Brown, Phys. Rev. **146**, 575 (1966).

[14] P. C. Sercel and K. J. Vahala, Phys. Rev. B **42**, 3690 (1990); K. J. Vahala and P.C. Sercel, Phys. Rev. Lett. **65**, 239 (1990).

[15] Al. L. Efros and M. Rosen, Phys. Rev. B **58**, 7120 (1998).

[16] H. Fu, L.-W. Wang and A. Zunger, Appl. Phys. Lett. **71**, 3433 (1997).

[17] Al. L. Efros and M. Rosen, Appl. Phys. Lett. **73**, 1155 (1998).

[18] U. Banin, J. C. Lee, A. A. Guzelian, A. V. Kadavanich, A. P. Alivisatos, W. Jaskolski, G. Bryant, Al. L. Efros, and M. Rosen, J. Chem. Phys. **109**, 2036 (1998).

[19] M. Chamarro, C. Gourdon, P. Lavallard, and A. I. Ekimov, Jpn. J. Appl. Phys.**34**, Suppl.34-1, 12 (1995).

[20] M. Nirmal, D. J. Norris, M. Kuno, M. G. Bawendi, Al. L. Efros and M. Rosen, Phys. Rev. Lett. **75**, 3728 (1995); Al. L. Efros, M. Rosen, M. Kuno, M. Nirmal, D. J. Norris, and M. G. Bawendi, Phys. Rev. B **54**, 4843 (1996).

[21] M. Chamarro, C. Gourdon, P. Lavallard, O. Lublinskaya, and A. I. Ekimov, Phys. Rev. B **53**, 1 (1996).

[22] O. I. Micic, H. M. Cheong, H. Fu, A. Zunger, J. R. Sprague, A. Mascarenhas, and A. J. Nozik, J. Phys. Chem. B **101**, 4904 (1997).

[23] U. Banin, J. C. Lee, A. A. Guzelian, A. V. Kadavanich, and A. P. Alivisatos, Superlat. and Microstruct. **22**, 559 (1997).

[24] P. D. J. Calcott, K. J. Nash, L. T. Canham, M. J. Kane, and D. Brumhead, J. of Lumin. **57**, 257 (1993).

[25] D. Kovalev, H. Hecker, M. Ben-Chorim, G. Polisski, M. Schwrtzkopff, and F. Koch, Phys. Rev. Lett. **81**, 2803 (1998).

[26] S. W. Brown, T. A. Kennedy, D. Gammon, and E. S. Snow, Phys. Rev. B **54**, R17339 (1996).

[27] D. Gammon, S. W. Brown, E. S. Snow, T. A. Kennedy, D. S. Katzer, and D. Park, Science **277**, 85 (1997).

[28] Al. L. Efros and M. Rosen, to be published.

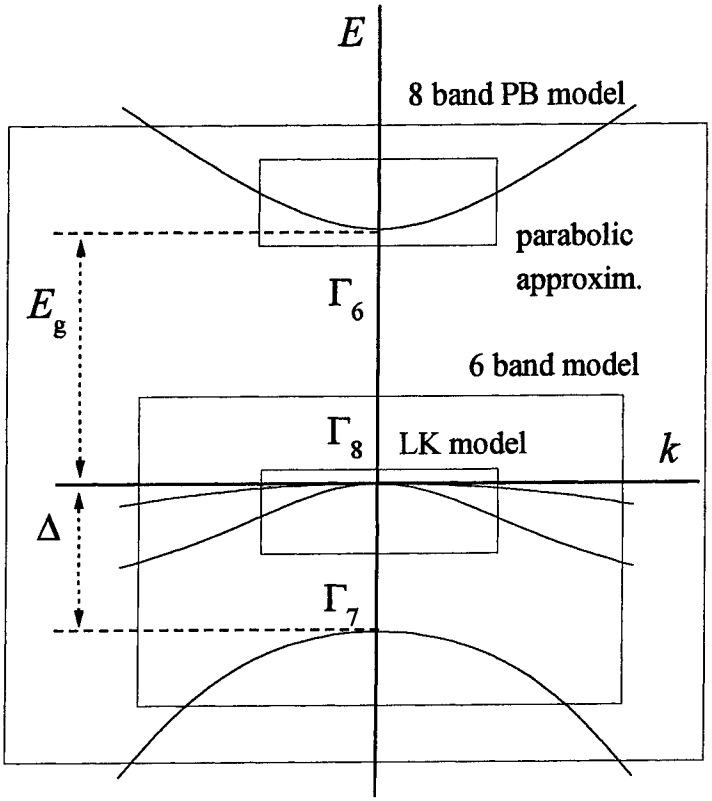


Figure 1: The bulk band structure of a typical direct gap semiconductor with cubic or zinc blende lattice structure and having its band edge at the Γ-point of the Brillouin zone. The boxes show the region of applicability of different effective mass approximation models used for the calculation of electron and hole QSLs.

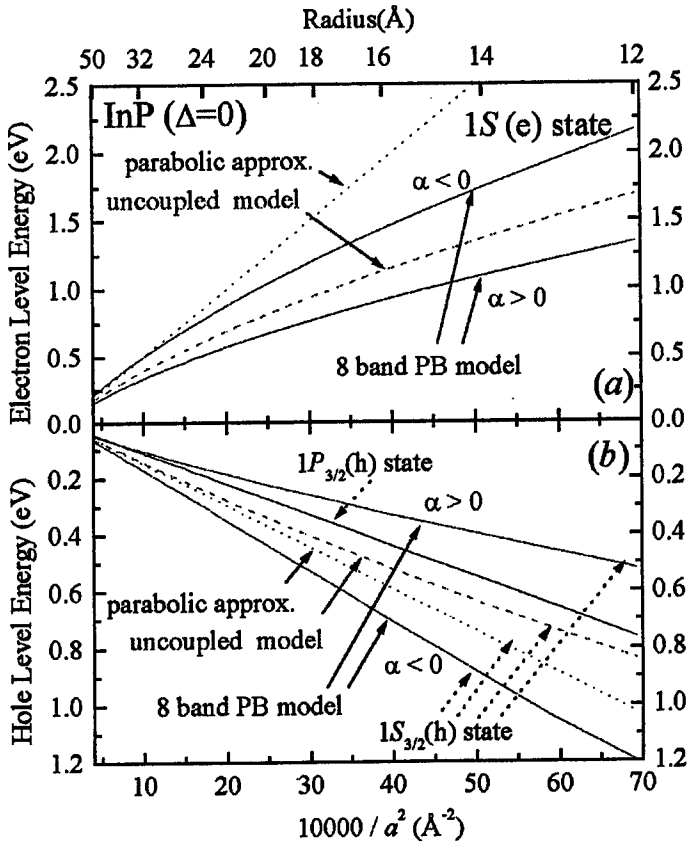


Figure 2: Size dependence of the lowest QSLs in InP nanocrystals, with $\Delta = 0$, calculated using different approximations: a) the $1S_e$ electron level and b) the $1P_{1/2}(h)$ and $1S_{3/2}(h)$ hole levels. Dotted lines show the results of calculations within the simple parabolic approximation for the conduction band and the Luttinger-Kohn parabolic approximation for the valence band. Dashed lines show the effect of the nonparabolicity of the electron and light hole spectra without taking the coupling of the conduction and valence bands into account. Solid lines show the results of the calculations done within the 8-band Pidgeon and Brown model for the set of energy band parameters discussed in the text for $\alpha > 0$ and $\alpha < 0$. The size dependence of the $1P_{3/2}(h)$ hole state is the same for all these models.

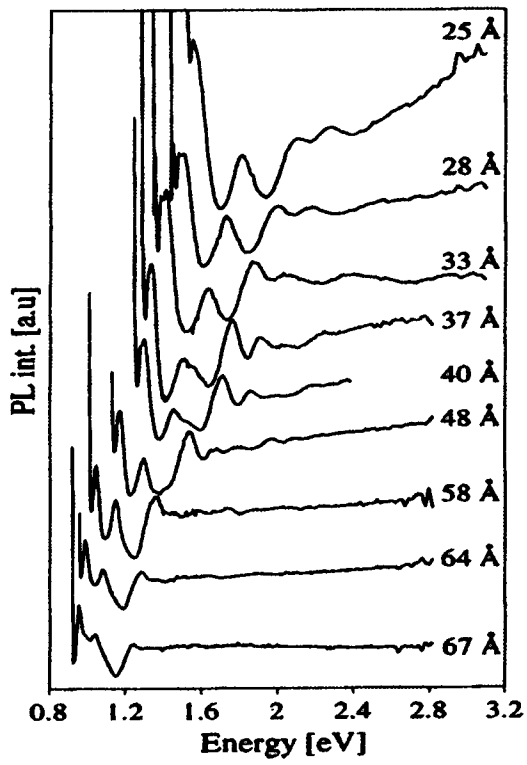


Figure 3: Size selected PLE spectra for InAs nanocrystals with diameters ranging between 25 and 67 Å (T=10 K).

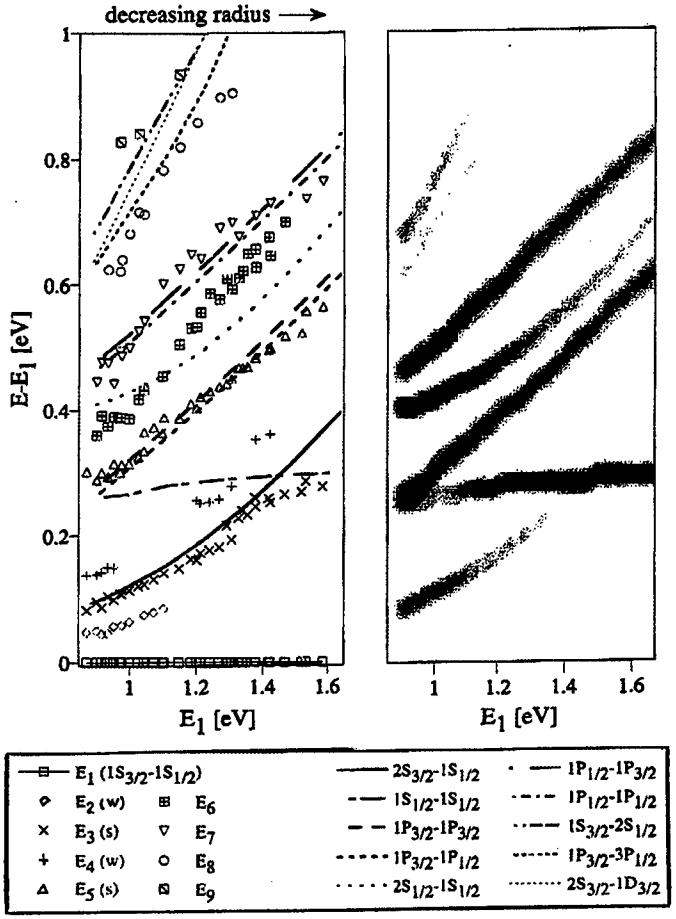


Figure 4: Map of the low lying levels of InAs nanocrystals extracted from the PLE experiments. Transition energies relative to the lowest transition are plotted versus the energy of the lowest transition. Left panel: The experimental results are compared with the levels calculated using the PB model. Right panel: Calculated oscillator strengths, represented by relative darkness, for the transitions in the left frame.

Excitonic Optical Nonlinearity and Exciton Dephasing in Quantum Dots

T. Takagahara
NTT Basic Research Laboratories, 3-1 Morinosato Wakamiya,
Atsugi, Kanagawa, 243-0198 JAPAN

ABSTRACT

The fundamental physics of multi-exciton states in semiconductor nanocrystals (quantum dots) are discussed focusing on the mesoscopic enhancement of the excitonic optical nonlinearity and the mechanism of their saturation with increase of the nanocrystal size. The weakly correlated exciton pair states are found to cause significant cancellation effect in the third-order nonlinear optical susceptibility at the exciton resonance, leading to saturation of the mesoscopic enhancement of the excitonic optical nonlinearity. The presence of the weakly correlated exciton pair states is confirmed convincingly from the good correspondence between theory and experiments on the induced absorption spectra from the exciton state in CuCl nanocrystals. Both dephasing and population relaxation of excitons localized in quantum dot-like islands in narrow GaAs quantum wells are investigated by using the three-pulse stimulated photon echo method. A direct comparison of these two closely related decay processes reveals the presence of pure dephasing that dominates excitonic dephasing at elevated temperatures. The pure dephasing contribution arises from coupling of excitonic states with a continuum of acoustic phonons and is enhanced by 3D quantum confinement. Both the magnitude and the temperature dependence of the dephasing rate can be described satisfactorily by a model that generalizes the Huang-Rhys theory of F-centers. We clarify the origin of qualitative difference in the temperature dependence of the excitonic dephasing rate for QDs with weak and strong quantum confinement.

I. Introduction

Optical properties of three-dimensionally confined electrons and holes in semiconductor nanocrystals (quantum dots) have been extensively studied in recent years from the interest in the fundamental physics of finite systems as well as in their potential use as efficient nonlinear optical and laser materials. The spatial confinement of electrons and holes leads to a discrete energy level structure with sharp absorption lines as in atoms. The concentration of the oscillator strength into well defined energies makes quantum dots (QDs) very attractive for electro-optic and nonlinear optical applications.

In addition to the spatial confinement, the Coulomb interaction between the excited electrons and holes also plays an important role in determining the excitation spectra of QDs. This is especially true in most of the currently studied crystallites of II-VI and I-VII semiconductors like CdS, CdSe, CuCl etc., owing to the large exciton binding energy in these materials. The formation of excitons and biexcitons in dots of radius (R) larger than several times the exciton Bohr radius (a_{ex}) leads to strong optical response at the exciton resonance. In fact, in this weak confinement regime ($R \gg a_{ex}$), the exciton oscillator strength is proportional to the volume of the quantum dot. Consequent superradiant decay of the exciton has been experimentally observed [1,2] with the lifetime decreasing inversely as the volume of the QD. But the deviation from this proportionality, i.e., the saturation of the excitonic radiative decay rate was observed at the large size region. The mesoscopic enhancement of the exciton oscillator strength would lead to, for example, a nonlinear optical susceptibility increasing with the size of the QD. The nonlinear response is, however, determined not only by the exciton states but also by multiexciton states and especially by the biexcitonic excitations. Recent experiments on CuCl QDs in the weak confinement regime have revealed many interesting features including enhanced nonlinear optical susceptibility with an intriguing size dependence [3], very large gain for biexcitonic lasing [4] and a blue shift of the excitonic absorption under a strong pump beam [5]. These observations indicate significance of the interplay of excitonic and biexcitonic states.

Recently, we discovered a weakly correlated (antibound) exciton pair state with a large oscillator strength, namely one of the excited biexciton states which provides important insights into various features of the experimental observations mentioned above [6,7]. We calculate the third-order nonlinear optical susceptibility at the exciton resonance and clarify the underlying physics of the observed saturation [3] of the mesoscopic enhancement which has so far eluded a satisfactory explanation. We also study the excited state absorption from the exciton ground state. From the comparison between the theory and experiments concerning the induced absorption spectra, i.e., the pump-and-probe spectroscopy, we obtain a convincing evidence for the presence of the weakly correlated exciton pair states

[8,9].

A resonant optical excitation creates an excited state population and also induces an optical polarization. Dynamics of this optical excitation is characterized by relaxation of the population as well as decay of the induced optical polarization. In lower dimensional semiconductors, electronic confinement leads to qualitative changes in population relaxation including spontaneous emission and exciton-phonon scattering, as shown in extensive recent studies[10]. These population relaxation processes are expected to contribute to dephasing with a dephasing rate given by $\Gamma_{\parallel}/2$ where $\Gamma_{\parallel}$ is the population decay rate. Pure dephasing processes that do not involve population or energy relaxation of excitons can also contribute to dephasing. Pure dephasing, which is a well-established concept for atomic systems, remains yet to be investigated in lower dimensional semiconductors due to a lack of direct comparison between dephasing and population relaxation and between theory and experiment. Understanding pure dephasing processes in lower dimensional semiconductors bridges our fundamental understanding of dephasing of atomic systems and of collective excitations in solids.

Narrow GaAs quantum wells(QWs) grown by molecular beam epitaxy(MBE) and with growth interruptions have provided a model system for investigating dephasing processes in lower dimensional semiconductors. In these narrow QWs, fluctuations at the interface between GaAs and AlGaAs lead to localization of excitons at monolayer-high islands. These localized states can be regarded effectively as weakly-confined quantum dot(QD)-like states. One dimension of the confinement is defined by the width of the QW, while the other two lateral dimensions are defined by the effective size of the islands. To avoid inhomogeneous broadening due to well-width and island-size fluctuations, earlier studies have used photoluminescence(PL) and PL excitation with high spatial resolution to probe excitons in individual islands[11-13]. As a result, a very narrow linewidth of about several tens of μeV was observed. The origin of this narrow linewidth is very interesting to study. Without additional information on population relaxation, it was suggested that at very low temperature dephasing of excitons in these structures is due to radiative recombination, while at elevated temperature dephasing is mainly due to thermal activation of excitons to higher excited states[13]. However, this interpretation is not complete since both of the suggested processes belong to the longitudinal decay processes and the dephasing rate is in general composed of half the longitudinal decay rate and the pure dephasing rate. In order to examine the presence of pure dephasing in this system, we carried out nonlinear optical measurements of the exciton dephasing based on the three-pulse stimulated photon echo method[14]. We clarified for the first time the presence of pure dephasing of excitons localized in QD-like islands and presented a theoretical model that can explain satisfactorily the magnitude as well as the temperature dependence of the dephasing rate.

II. Exciton and Biexciton Energy Levels

In order to discuss the excitonic optical nonlinearity, we have to know the energy spectra of excitons and biexcitons. In this section, we are mainly concerned with CuCl nanocrystals in which several beautiful experiments were carried out. In CuCl having the zincblende structure, the conduction band bottom at the Γ-point has the Γ_6 symmetry and is doubly degenerate due to the spin degree of freedom, whereas the valence band top at the Γ-point has the Γ_7 symmetry characterized by the spin-orbit combined angular momentum $j = l + s = 1/2$ and is doubly degenerate. This situation is caused by the negative sign of the spin-orbit interaction energy and is in striking contrast to the usual situation where the topmost valence band has the Γ_8 symmetry($j = 3/2$) and is four-fold degenerate. The four exciton states that can be formed from these doubly degenerate electron and hole states split into a non-degenerate state of Γ_2 symmetry and a triply degenerate state of Γ_5 symmetry. These states can be labeled by their total angular momentum, $I = 0$ and 1, respectively. The $I = 1$ state is triply degenerate and is a mixture of spin-singlet and spin-triplet electron-hole pair states. The $I = 0$ state is purely spin-triplet and has no exchange contribution to the energy. It is the $I = 1$ exciton state that is optically active since it contains the spin-singlet component.

Now we consider the biexciton states. They can be specified by the total angular momentum (J, M) of the Bloch function. From $I = 0$ and $I = 1$ exciton states, we may generate biexciton states with the Bloch function angular momentum $J = 0, 1$ or 2:

$$\begin{aligned} 0 \otimes 0 &= 0 \text{ or } \Gamma_2 \otimes \Gamma_2 = \Gamma_1 , \\ 1 \otimes 0 &= 1 \text{ or } \Gamma_5 \otimes \Gamma_2 = \Gamma_4 , \\ 1 \otimes 1 &= 0 \oplus 1 \oplus 2 \text{ or } \Gamma_5 \otimes \Gamma_5 = \Gamma_1 \oplus \Gamma_4 \oplus (\Gamma_3 \oplus \Gamma_5) . \end{aligned}$$

Thus an $I = 0$ exciton pair will get mixed with an $I = 1$ pair to give $J = 0$ biexciton states while $I = 1$ pairs will form $J = 2$ biexcitons and a pair made up of $I = 0$ and $I = 1$ excitons will mix with an $I = 1$ pair to give $J = 1$ biexcitons.

Only the Γ_5 ($I = 1$) excitons are optically excited from the ground state. As the Γ_5 exciton state is three-fold degenerate, subsequent excitation of the biexciton states will be dependent on the polarization of the exciton state. For the z-polarization, only the ($I = 1$, $I_z = 0$) exciton states can be excited by one-photon absorption from the ground state, while only the ($J = 0$, $J_z = 0$) and ($J = 2$, $J_z = 0$) biexciton states are excited by subsequent one-photon absorption. In Fig. 1, we plot the squared dipole moments for the exciton to biexciton transitions as a function of the transition energy for a few different values of the radius. The most interesting result is the existence of two nearly degenerate excited biexciton states at around twice the exciton energy with large oscillator strength. These states have oscillator strengths increasing proportional to the QD volume, and the sum

of their oscillator strengths approximately equals twice that of the exciton. Interestingly, we find that the wave functions of these states are well approximated by a product of two independent ground state exciton states, especially at larger sizes. In this sense, we can name these states " the weakly correlated exciton pair states". Because of their large oscillator strength, these states will dominate the excited state absorption as well as crucially influence the excitonic optical nonlinearity.

While the exciton oscillator strength is proportional to the volume of the crystallite, the oscillator strength of transition from the exciton state to the bound biexciton state tends towards a constant value in the bulk limit. This behavior can be understood by the following simple physical argument. The creation of a biexciton from an exciton state involves creation of a second exciton spatially close to the first one, within the volume of the biexciton. Thus in the bulk limit, the biexciton oscillator strength is of the order of the exciton oscillator strength corresponding to a coherence volume equal to the volume of the biexciton. This is a constant determined by the size of the biexciton.

III. Weakly Correlated Exciton Pair States

Let us consider the creation of a second exciton in a QD much larger in size than the exciton, when an exciton is already created. Such a process will be most efficient when the second exciton is created uncorrelated with the first one, as it then would have an oscillator strength of the same order as that of creating a single exciton. Such an uncorrelated exciton pair can be an approximate eigenstate of a large QD because the exciton-exciton interaction is short ranged (dipole-dipole like), unlike the electron-hole interaction in an exciton. We may, in fact, construct two such excited states with almost the same energy

$$\Phi^{\pm\pm}_{XX} = (1/\sqrt{2})\left(\phi^g_X(r_1,r_a)\phi^g_X(r_2,r_b) \pm \phi^g_X(r_1,r_b)\phi^g_X(r_2,r_a)\right) , \tag{1}$$

where ϕ^g_X is the envelope function of the exciton ground state.

In the limit of large R these two states (Φ^{++} and Φ^{--}) have a combined oscillator strength and energy twice those of the exciton ground state. The exchange interaction splits these into four states, two with $J = 0$, and one each with $J = 1$ and $J = 2$. The corresponding wave functions are given by

$$\Psi_{XX0} = \frac{\sqrt{3}}{2}\Phi^{++}_{XX}\chi^{00}_{00} - \frac{1}{2}\Phi^{--}_{XX}\chi^{11}_{00} , \tag{2}$$

$$\Psi_{XX0'} = \frac{1}{2}\Phi^{++}_{XX}\chi^{00}_{00} + \frac{\sqrt{3}}{2}\Phi^{--}_{XX}\chi^{11}_{00} , \tag{3}$$

$$\Psi_{XX1} = \Phi^{--}_{XX}\chi^{11}_{1M} , \tag{4}$$

$$\Psi_{XX2} = \Phi^{--}_{XX}\chi^{11}_{2M}\,, \tag{5}$$

where $\chi^{j_e j_h}_{JM}$ is the Bloch function for the total angular momentum (J, M) composed of two-electron and two-hole states with angular momentum j_e and j_h, respectively [7]. Only two of these, XX0 and XX2 (respectively with $J = 0$ and $J = 2$) are excited by two-step excitation via the $I = 1$ exciton ground state. The transition dipole moments for excitation of the states XX0 and XX2 from the exciton ground state are respectively equal to $\sqrt{2/3}$ and $\sqrt{4/3}$ times that of the exciton ground state. The larger oscillator strength for XX2 can be understood from the fact that the XX2 state consists of only the totally anti-symmetric envelope function so that the XX2 state is spatially more extended than the XX0 state, leading to the larger oscillator strength of transition from the exciton ground state. In the limit of large R, the states XX0 and XX2 have a combined oscillator strength of twice that of the exciton ground state.

It is interesting to note that the factor of two in the oscillator strength may also be understood as the bosonic enhancement factor corresponding to the creation of a second identical exciton. It would be interesting to extend this picture to creation of multiple exciton states in large QDs. We note that the independent boson picture implicit in this argument is reasonable as long as the QD is large enough to accommodate the excitons without considerable overlap. Further investigation of this aspect is left for future study.

IV. Nonlinear Optical Properties

IV.1 Size Dependence of the Third Order Nonlinear Susceptibility

As discussed above, the weakly correlated exciton pair states have a large oscillator strength. As the excitonic and two-excitonic contributions to the third order nonlinear susceptibility have opposite signs, the weakly correlated state would play a crucial role in determining the resonant excitonic nonlinearity in large QDs. We shall now investigate this in detail.

The third order nonlinear susceptibility, $\chi^{(3)}(-\omega;\omega,\omega,-\omega)$ can be obtained from the perturbation theory [15] as

$$\begin{aligned}\chi^{(3)}\ (-\omega;\omega,\omega,-\omega) &= \\ - \ iN\sum_{e,b}\frac{|\mu_{eg}|^2}{2\hbar^3\gamma^e_{||}}&\frac{\gamma_{eg}}{(\omega_{eg}-\omega)^2+\gamma^2_{eg}}\left[\frac{2|\mu_{eg}|^2}{i(\omega_{eg}-\omega)+\gamma_{eg}}-\frac{|\mu_{be}|^2}{i(\omega_{be}-\omega)+\gamma_{be}}\right] \\ - \ iN\sum_{e,b}\frac{|\mu_{eg}|^2|\mu_{be}|^2}{4\hbar^3}&\frac{1}{i(\omega_{eg}-\omega)+\gamma_{eg}}\frac{1}{i(\omega_{bg}-2\omega)+\gamma_{bg}}\end{aligned}$$

$$\times \quad \left[\frac{1}{i(\omega_{eg}-\omega)+\gamma_{eg}} - \frac{1}{i(\omega_{be}-\omega)+\gamma_{be}}\right], \tag{6}$$

where $\hbar\omega_{ij}$, μ_{ij} and γ_{ij}, respectively, denote the energy, dipole moment and dephasing rate corresponding to a transition between the states i and j. The subscripts g, e and b, denote the ground state, the exciton states and the biexciton states, respectively. $\gamma_{\|}^{e}$ denotes the exciton population decay rate and N is the number density of the quantum dots.

The first term in (6) arises from the saturation of the exciton population while the second term arises from the two photon coherence of the biexciton state. Thus there will be resonant enhancement of $\chi^{(3)}$ at the exciton to biexciton transition energy as well as at the exciton energy. In the weak confinement regime that we consider, the mesoscopically enhanced exciton oscillator strength would lead to mesoscopic enhancement of $\chi^{(3)}$ at the exciton resonance. On the other hand, the oscillator strength of transition from the exciton to the bound biexciton state saturates towards a constant value and no mesoscopic enhancement of $\chi^{(3)}$ would appear at the exciton to the bound biexciton transition energy. In fact, the resonant excitonic $\chi^{(3)}$ of CuCl QDs has been observed [3] to increase with the radius of the QD, exhibiting such a mesoscopic enhancement. But as R is increased to about 50Å (at 77K), $\chi^{(3)}$ was seen to saturate and then to decrease with further increase in R. This size dependence has never been explained satisfactorily. We shall see below that this saturation of the excitonic contribution to $\chi^{(3)}$ and the reversal of its size dependence arise from the competition between contributions from the weakly correlated exciton pair states and from the exciton ground state. The weakly correlated exciton pair states have mesoscopically enhanced oscillator strength in contrast to the bound biexciton states and a proper consideration of the size dependence of $\chi^{(3)}$ should include contribution from such states, as described by (6).

Now we consider the size dependence of the mesoscopically enhanced $\chi^{(3)}$ at the lowest exciton resonance. As there is considerable linear absorption at the exciton resonance it would be appropriate to consider the figure of merit defined by $|\chi^{(3)}|/\alpha\tau$ where α is the linear absorption coefficient and τ is the population lifetime of the exciton. This quantity has a meaning of the change in the absorption coefficient induced by an exciton in the unit volume [15]. Here τ includes the contribution from both the radiative and the non-radiative decay processes. Since theoretical estimate of the latter contribution cannot be very precise, we consider $\eta = |\chi^{(3)}|/\alpha$ instead of the above definition of the figure of merit.

In Fig. 2(a) we plot the maximum value of the $|\chi^{(3)}|/\alpha$ as a function of the radius for CuCl QD. In the size range considered, the peak value of $\chi^{(3)}$ occurs almost exactly at the exciton resonance frequency. Several values of γ_h are considered. For a small value of γ_h (less than a meV), η increases at small sizes sublinearly with R, the rate of increase slightly decreasing as R increases to $10a_{ex}$. But, as

γ_h is increased, this behavior dramatically changes. We find that at the radius for which γ_h becomes comparable to the energy difference $\delta E = E_{XX0} - 2E_X$ or $E_{XX2} - 2E_X$, where $E_X(E_{XX0}, E_{XX2})$ is the energy of exciton (weakly correlated exciton pair) state, the increase of $\chi^{(3)}$ tends to saturate and $\chi^{(3)}$ decreases with further increase in R. This correspondence between γ_h and the size dependence of the energy difference (δE) is illustrated in Fig. 2(b). For the case of $\gamma_h = 3$meV, the size at which $\delta E \approx \gamma_h$ is estimated to be $R = 68$Å and this value is in good agreement with the radius at which $\chi^{(3)}/\alpha$ shows a maximum in Fig. 2(a).

This behavior can be understood as arising from the cancellation between contributions from the exciton state and from the weakly correlated exciton pair states which occurs significantly around $\delta E \simeq \gamma_h$. In very small QDs where the electron-hole correlation is negligible, $\chi^{(3)}$ arises from the atomic-like level filling mechanism, while in the bulk semiconductor one would have excitons behaving like independent bosons strongly suppressing the excitonic contribution to $\chi^{(3)}$. The presence of the weakly correlated exciton pair states with nearly twice the exciton energy and with nearly twice the exciton oscillator strength that we have identified in large QDs implies approach to such a bulk-like behaviour.

In actual samples, there is also inhomogeneous broadening, probably due to size and shape inhomogeneities of the nanocrystals. In the absence of detailed information on the inhomogeneous broadening, we assume a phenomenological Gaussian inhomogeneous broadening with a common width γ_{ih} for all the one-photon transition frequencies, ω_{eg} and ω_{be}. Then the average over the inhomogeneous broadening is equivalent to that over the excitation photon energy and we have the average $\chi^{(3)}$ given by

$$\int \chi^{(3)}(-\omega';\omega',\omega',-\omega') \exp[-(\omega-\omega')^2/\gamma_{ih}^2]\, d\omega' . \qquad (7)$$

A similar averaging is done for α. In Fig. 3, we show the size dependence of $|\chi^{(3)}|/\alpha$ for different values of homogeneous and inhomogeneous broadening of the exciton and biexciton states. Increasing the inhomogeneous width causes the saturation radius to shift to lower values. We note that the experimentally measured value of $\gamma_h = 0.9$meV for $R > 50$Å is somewhat too small to cause the strong saturation observed around $R = 50$Å unless considerable inhomogeneous broadening is also present.

IV.2 Excited State Absorption from the Exciton Ground State

There is a growing interest in size selective spectroscopy of semiconductor crystallites. Recent progress in experiments has revealed the discrete energy level structures not only in the excitation spectrum [16,17] but also in the excited state

absorption spectra by resonant pump-probe technique [8,9]. Using the exciton and biexcitonic states calculated above, we can now predict the absorption spectra of excited crystallites in which one exciton has already been created.

We consider a pump-probe experiment in which a linearly polarized pump pulse excites a crystallite into the exciton ground state and a collinear probe pulse that follows probes the absorption spectra of this excited crystallite. We take the pump-probe propagation direction to be the x-axis and the pump-polarization to be along the z-axis, without loss of generality. The created exciton is in the $I = 1$ (Γ_5) state with $I_z = 0$. Subsequent absorption of a probe photon can then excite the ($J = 0$ and $J = 2$, $J_z = 0$) biexciton states if the probe is z-polarized, and the ($J = 1$ and $J = 2$, $J_z = \pm 1$) biexciton states if the probe is y-polarized.

The oscillator strength of transitions from the exciton ground state is plotted in Fig. 1. The lowest energy absorption peak red-shifted from the exciton energy corresponds to the biexciton ground state. There are a few weak transitions to the excited, but bound, biexciton states occurring below the exciton energy. The strong absorption peaks due to excitation of the $J = 0$ and $J = 2$ weakly correlated exciton pair states (denoted by • and *) occur blue-shifted from the exciton.

In Fig. 4, we plot the energies of a few dominant excited state absorption peaks as a function of the exciton ground state energy, i.e., the pump photon energy. It is interesting to note that the strongest excited state absorption to the $J = 2$ biexciton state shown by XX2 in Fig. 4 has a linear dependence on the exciton ground state energy. The linear proportionality of the induced absorption energy to the exciton confinement energy suggests that the exciton addition energy is primarily determined by the increase in the kinetic energy proportional to the inverse square of the nanocrystal radius and that the contribution from the changes in the Coulomb and exchange energies are subsidiary. In fact, it is illuminating to speculate, by invoking the center of mass confinement picture, that the weakly correlated exciton pair has an energy equal to that of two excitons confined independently in a region of half the volume of the nanocrystal. Such a picture gives the confinement kinetic energy of the weakly correlated exciton pair to be $2\sqrt[3]{4} = 3.174$ times that of a single exciton. Consequently, the corresponding excited state absorption energy is linearly dependent on the exciton energy with a slope of $2\sqrt[3]{4} - 1 \simeq 2.2$. The close agreement of this slope with experiments will be discussed in the next section.

IV.3 Experimental Observation of Weakly Correlated Exciton Pair States

Recently, Ikezawa et al. [8,9] succeeded in observing fine structures in the excited state absorption spectrum and the features in the observed spectrum agree well with those expected from the present calculation. In their pump-probe ex-

periments with the pump tuned to the exciton absorption energy, they observed a strong excited state absorption of the probe, blue shifted from the pump energy, in addition to the absorption peak to the biexciton ground state. The strength of the induced absorption to this excited biexciton state is found to be several times larger than that to the biexciton ground state as expected from the calculation.

Their experimental results are summarized in Fig. 5. The absorption spectrum shown by a solid line in Fig. 5(a) is very broad due to the inhomogeneous size distribution of nanocrystals. In order to eliminate the inhomogeneous broadening, they excited nanocrystals size-selectively using a spectrally narrow laser line and monitored the induced absorption. In Fig. 5(b), the differential absorption spectra are shown. The strongest peak is the main hole at the pump photon energy. On both sides of the main hole, there appear clear induced absorption peaks. These structures move with the pump photon energy confirming the size-selective excitation. The energy positions of these peaks are plotted in Fig. 6 as a function of the excitation photon energy. The solid dots represent the main hole at the pump photon energy and the dotted line has a slope of unity as a matter of course. The solid triangles denote the lower energy induced absorption peaks, whereas the open triangles depict the higher energy induced absorption peaks and the dashed line has a slope of 2.0. The theoretical results of the peak energies of induced absorption are already given in Fig. 4. The solid curve denoted by BX represents the induced absorption from the exciton ground state to the biexciton ground state. The induced absorption to the excited biexciton state with $J = 0(2)$ is indicated by XX0(XX2). In the experiment the pump and probe lights are orthogonally polarized so that the biexciton states with $J = 0$ cannot be excited in principle but the $J = 2$ states are excited strongly. The slope of the XX2 line is about 2.4 in qualitative agreement with the experimental value. From the overall good correspondence between theory and experiments, we can identify the lower energy peak as the induced absorption to the biexciton ground state and the higher energy peak as the induced absorption to the $J = 2$ weakly correlated exciton pair state. Thus we are convinced that the theoretically predicted $J = 2$ anti-bonding state of two excitons was observed experimentally.

V. Exciton Dephasing in GaAs Quantum Dots

V.1 General Aspects of Exciton Dephasing

The three-pulse stimulated photon-echo method enables the simultaneous measurement of the dephasing rate and the population decay rate[14]. The direct comparison between these decay rates revealed convincingly the presence of a pure dephasing process that dominates excitonic dephasing at elevated temperatures. The pure dephasing process arises from coupling of exciton states with a continuum

of acoustic phonons and is enhanced by 3D quantum confinement. The magnitude as well as the temperature dependence of the dephasing rate is described by a theoretical model that generalizes the Huang-Rhys theory of F-centers[18] to include mixing among excited exciton states through exciton-phonon interactions. The observed temperature dependence of the dephasing rate further indicates qualitative differences dependent on the strength of quantum confinement.

We used GaAs QW samples and experimental details are given elsewhere[14]. Figure 7 shows the observed temperature dependence of the dephasing and half the population decay rates for excitons at an energy 4 meV below the absorption line center. Similar temperature dependence has also been observed within the spectral range ($\sim$ 10 meV) of our measurements, suggesting the localization of excitons over the spectral range. The observed temperature dependence is in general agreement with an earlier study using PL with high spatial resolution[13]. However, our results show clearly the presence of the pure dephasing of the localized excitons in QWs. Note that the earlier study was done at a lower exciton energy where islands with comparable energies are spaced far apart such that discrete energy structures of a single island can be probed by using PLE with a small aperture. For the present study, islands with similar energies are spaced closer and as a result exciton migration among islands becomes more important.

We now discuss dephasing processes of excitons. Theoretically, contribution to dephasing from the population decay is half of its rate, namely $\Gamma_{\parallel}/2$. As can be seen in Fig. 7, at very low temperature the dephasing rate $\Gamma_{\perp}$ is very close to $\Gamma_{\parallel}/2$ suggesting that dephasing is caused mainly by the population decay. With increasing temperature the dephasing rate increases much faster than the population decay rate. At elevated temperatures (>30K), dephasing rates become much greater than $\Gamma_{\parallel}/2$, indicating a dominant contribution of pure dephasing. Note that for delocalized excitons in GaAs QWs, dephasing rates are much larger than those of localized excitons and increase linearly with temperature (below 50K), in contrast to the nonlinear temperature dependence in Fig. 7.

V.2 Theoretical Formulation of Excitonic Dephasing

The strong temperature dependence of the pure dephasing rate ($\Gamma_{\perp} - \Gamma_{\parallel}/2$) suggests that interactions between excitons and acoustic phonons play an essential role in the pure dephasing process. Dephasing or equivalently homogeneous linewidth of impurity states in solids due to electron-phonon interactions has been discussed by using models based on the Huang-Rhys theory [18]. These models, however, do not take into account the mixing of excitonic states through electron-phonon interactions. To understand pure dephasing for excitons localized in QD-like islands, we have developed a model to include mixing among excited electronic states. In this model, the Hamiltonian for the relevant ground and excited states

can be written, respectively, as

$$H_g = \sum_\alpha \hbar\omega_\alpha b_\alpha^\dagger b_\alpha \text{ and } H_e = H_e^0 + H_g + \sum_\alpha M_\alpha (b_\alpha + b_\alpha^\dagger)\,, \tag{8}$$

where $b_\alpha (b_\alpha^\dagger)$ is the annihilation (creation) operator of the acoustic phonon mode with index α, H_e^0 is the diagonal energy matrix of the excited state manifold for the QD-like island and matrix M_α has both diagonal and off-diagonal elements. The off-diagonal matrix elements induce mixing among the excited state manifold. Here the acoustic phonon modes are assumed to have continuous mode spectra as in the bulk since the elastic constants of the well material and the barrier material are not so much different. We take into account the electron-phonon interactions that are linear with respect to the phonon displacement. Even within this range, the well-known deformation potential coupling and the piezoelectric coupling are included. We note that in the elementary processes of the exciton-phonon interaction the crystal momentum conservation needs to be satisfied in directions where the translational invariance holds. The pure dephasing process becomes prominent in systems with 3D electronic confinement because the 3D confinement relaxes the crystal momentum conservation and also suppresses exciton population relaxation due to the exciton-phonon interactions.

The homogeneous linewidth of the exciton can be estimated from the half width at the half maximum of the optical absorption spectrum that is given by

$$I(\omega) = Re[\int_0^\infty dt\; e^{-i\omega t}\; \langle 0|e^{iH_e t/\hbar}\; e^{-iH_g t/\hbar}|0\rangle], \tag{9}$$

where $|0\rangle$ is the ground state of the system. This can be estimated by a diagrammatic expansion and is given by

$$I(\omega) = Re\; G(i\omega + \delta) \text{ with } G(s) = \frac{1}{s - iH_e^0/\hbar - \Sigma(s)}\,, \tag{10}$$

where δ indicates half the population decay rate caused by mechanisms other than phonon scattering. The self-energy part $\Sigma(s)$ in (10) can be expanded perturbatively with respect to the exciton-phonon coupling as

$$\Sigma(s) = \Sigma^{(2)}(s) + \Sigma^{(4)}(s) + \cdots\,. \tag{11}$$

In actual calculations, the self-energy is iteratively improved by replacing the propagators in Σ with Green's function G obtained in the last iteration and thus by summing an infinite series of a particular type of diagrams.

V.3 Temperature Dependence of Excitonic Dephasing Rate

The above is the framework of the theoretical formulation. In a more concrete

calculation, we have to specify a model for the QD-like island structure. Here we employ a quantum disk model whose height L_z is given by the thickness of the constituent QW and whose lateral dimensions are in general anisotropic. The lateral confinement potential for the electron (hole) is assumed to be Gaussian as

$$V_{e(h)}(x,y) = V^0_{e(h)} \exp[-(x/a)^2 - (y/b)^2] , \tag{12}$$

where the size parameters a and b can be fixed in principle from the TEM or STM images but are considered as adjustable. The potential depth $V^0_{e(h)}$ can be determined from the difference in the luminescence energy of QW islands with monolayer thickness fluctuations. For example, the exciton energy spectra are shown in Fig. 8 for the parameters of $L_z = 3$nm, $a = 20$nm, $b = 15$nm, $V^0_e = -6$meV and $V^0_h = -3$meV. There are optically active exciton states and optically forbidden (dark) exciton states. The latter are plotted by solid dots slightly above the horizontal axis of Fig. 8 to indicate their energy positions. The energy level spacings of the optically active exciton states are a few meV and correspond well to the PLE spectrum in [13]. In the calculation of the absorption spectrum given by (9), 13 levels in Fig. 8 are included and both of the deformation potential coupling and the piezoelectric coupling are taken into account. The calculated lineshape can be fitted by Lorentzian very well especially at low temperatures.

The calculated dephasing rate is plotted in Fig. 9 as a function of temperature with experimental data. The magnitude as well as the temperature dependence of the dephasing rate can be well reproduced by the model calculation. Furthermore, in the theory the contribution from the deformation potential coupling can be singled out. That contribution is denoted by "Def. pot." in the figure. The remaining part comes from the piezoelectric coupling and the interference between the two couplings but this part is simply denoted by "Piezo." in the figure. It is seen that the deformation potential coupling is dominantly contributing to the pure dephasing.

Generally speaking, pure dephasing means the decay of the dipole coherence without change in the state of the system. Any real transition to other states leads to the population decay. Thus the pure dephasing is caused by virtual processes which start from a relevant state and through some excursion in the intermediate states return to the same initial state. There are two kinds of such virtual processes which contribute to the pure dephasing. The first kind of processes are induced by the off-diagonal exciton-phonon interaction. Those processes start from the exciton ground state, pass through excited exciton states and return to the exciton ground state. The second kind of processes are induced by the diagonal exciton-phonon interaction and remain always within the exciton ground state. These processes are shown schematically in the inset of Fig. 10. The contribution to the pure dephasing from the second kind of processes can be singled out theoretically and is denoted by "Intra-exciton ground state" in Fig. 10. The remaining part

denoted as "Excited exciton states" comes from the first kind of processes and the interference between the two kinds of processes. It is seen that the "intra-exciton ground state" (diagonal) processes contribute significantly to the pure dephasing but the contribution from the off-diagonal processes is not negligible.

We have estimated also the dephasing rate of the excited exciton states. The results are shown in Fig. 11 for the first four optically active exciton states. In general, the dephasing rate is larger for the higher lying exciton states. However, the actual value of dephasing rate is dependent on details of the wavefunctions. In fact, the dephasing rate of the third exciton is smaller than that of the second exciton in Fig. 11.

V.4 Strength of Quantum Confinement and Temperature Dependence of Exciton Dephasing Rate

We have so far discussed the dephasing rate of excitons in GaAs QD-like islands. It is important to point out that the temperature dependence of dephasing rate can differ qualitatively for QDs with strong and weak 3D confinement. For QDs that have strong 3D confinement such as II-VI nanocrystals, a linear temperature dependence has been observed up to 200 K[19]. On the other hand, for CuCl nanocrystals belonging to the weak confinement regime, a temperature dependence similar to that in Fig. 7 was observed[20,21], although strongly nonlinear temperature dependence occurs above a higher temperature ($\sim$ 50 K). These different temperature dependences can be accounted for by the above model if we consider the different energy structures involved. For GaAs islands the energy separation between the ground and first excited exciton states is a few meV, whereas for CuCl nanocrystals with 4nm radius the energy separation is about several meV. In CdSe nanocrystals with radii smaller than 2nm, the relevant energy spacing is determined by the A- and B-exciton splitting($\sim$ 26meV).

In the case of strong confinement regime, the diagonal virtual processes dominate the pure dephasing in which the relevant state remains always within the exciton ground state and the electron-phonon interactions associated with small energy acoustic phonons are mainly contributing to the pure dephasing. Thus the high-temperature approximation for the phonon occupation number holds, leading to the linear temperature dependence of the dephasing rate up to the temperature corresponding to the energy spacing between the ground and first excited exciton states ($\sim$ 26meV in the case of CdSe nanocrystals). On the other hand, in the weak confinement regime, the off-diagonal virtual processes contribute significantly to the pure dephasing in which the virtual transition to excited exciton states occurs effectively when the thermal energy k_BT approaches the relevant energy level separation. In this case, acoustic phonons having the thermal energy contribute strongly to the dephasing rate at each temperature, leading to the nonlinear tem-

perature dependence.

Finally, the possible mechanisms of the population relaxation will be briefly discussed. Experimentally, two decay time constants were observed [14]. The slow time constant ($\sim$ 100 ps) is almost independent of temperature suggesting the radiative decay as its mechanism. The fast time constant ($\sim$ 30 ps) is weakly dependent on temperature. The likely mechanisms are the thermal activation to excited exciton states and the phonon-assisted migration to neighboring islands [22]. Detailed calculations [23] show that the former mechanism gives rise to the population decay rate about 10 to 20 μeV , whereas the population decay rate due to the latter mechanism is about several tens of μeV within the temperature range from 10 to 50 K. Thus we can identify the most likely mechanism of the population decay as the phonon-assisted exciton migration.

VI. Conclusions

We have investigated multi-exciton states in semiconductor QDs. The most important finding is the presence of weakly correlated exciton pair states with large oscillator strength of transition from the exciton state, which play a crucial role in determining the nonlinear optical properties of QDs in the weak confinement regime. These states are identified to consist of two weakly correlated ground state excitons (anti-bonding exciton pair states) and consequently have oscillator strengths, for excitation from the exciton ground state, increasing proportional to the volume of the QD. The discovery of these states provides the first consistent understanding of the experimentally observed size dependence of $\chi^{(3)}$ in CuCl QDs. Our theoretical prediction has been confirmed excellently by the recent measurement of excited state absorption spectra, giving a convincing evidence for the presence of the weakly correlated exciton pair states.

By comparing directly the dephasing and population relaxation of excitons in GaAs QD-like islands, we have identified the presence of pure dephasing process that dominates excitonic dephasing at elevated temperatures. The magnitude and temperature dependence of the dephasing rate can be described satisfactorily by a model that generalizes the Huang-Rhys theory of F-centers. The correlation between the strength of quantum confinement and the temperature dependence of the dephasing rate has been clarified and the observed qualitative differences in the temperature dependence has been described well.

Acknowledgment

The author would like to thank Dr. Selvakumar V. Nair and Prof. Hailin Wang for close collaboration and stimulating discussions.

References

[1] A. Nakamura, H. Yamada and T. Tokizaki, Phys. Rev. B **40**, 8585 (1989).

[2] T. Itoh, M. Furumiya and T. Ikehara, Solid State Commun. **73**, 271 (1990).

[3] T. Kataoka, T. Tokizaki and A. Nakamura, Phys. Rev. B **48**, 2815 (1993).

[4] Y. Masumoto, T. Kawamura and K. Era, Appl. Phys. Lett. **62**, 225 (1993).

[5] K. Edamatsu, S. Iwai, T. Itoh, S. Yano and T. Goto, Phys. Rev. B **51**, 11205 (1995).

[6] S. V. Nair and T. Takagahara, Phys. Rev. B **53**, R10516 (1996).

[7] S. V. Nair and T. Takagahara, Phys. Rev. B **55**, 5153 (1997).

[8] M. Ikezawa and Y. Masumoto, Jpn. J. Appl. Phys. **36**, 4191 (1997).

[9] M. Ikezawa, Y. Masumoto, T. Takagahara and S. V. Nair, Phys. Rev. Lett. **79**, 3522 (1997).

[10] See for example, L. C. Andreani, in *Confined Electrons and Photons, New Physics and Devices*, edited by E. Burstein and C. Weisbuch (Plenum, New York, 1995); D. S. Citrin, Phys. Rev. B **47**, 3832 (1993); H. Benisty et al., Phys. Rev. B **44**, 10945 (1991); U. Bockelmann et al., Phys. Rev. B **48**, 17637 (1993).

[11] H. F. Hess et al., Science **264**, 1740 (1994).

[12] K. Brunner et al., Phys. Rev. Lett., **73**, 1138 (1994).

[13] D. Gammon et al., Science **273**, 87 (1996); D. Gammon et al., Phys. Rev. Lett. **76**, 3005 (1996).

[14] Xudong Fan, T. Takagahara, J. E. Cunningham and Hailin Wang, Solid State Commun. (to be published)

[15] T. Takagahara, Phys. Rev. B **39**, 10206 (1989).

[16] M. G. Bawendi et al., Phys. Rev. Lett. **65**, 1623 (1990).

[17] D. J. Norris, A. Sacra, C. B. Murray and M. G. Bawendi, Phys. Rev. Lett. **72**, 2612 (1994).

[18] K. Huang and A. Rhys, Proc. Roy. Soc. (London) A **204**, 406 (1950).

[19] R. W. Schoenlein et al., Phys. Rev. Lett. **70**, 1014 (1993).

[20] T. Itoh and M. Furumiya, J. Lumin. **48 & 49**, 704 (1991).

[21] K. Inoue et al., OSA Technical Digest Series (CLEO'98) **6**, 266 (1998).

[22] T. Takagahara, Phys. Rev. B **32**, 7013 (1985); J. Lumin. **44**, 347 (1989).

[23] T. Takagahara, unpublished.

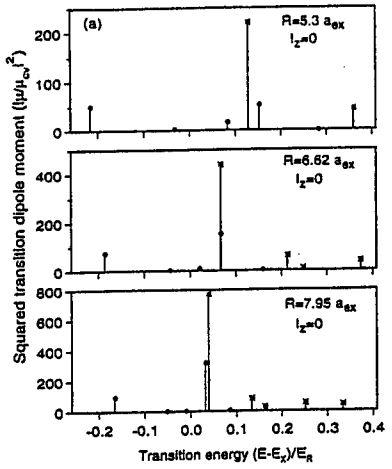


Figure 1: Squared transition dipole moments for transitions from the lowest $I = 1$, $I_z = 0$ exciton to the $J = 0$ and 2 biexciton states, respectively marked by • and $*$. The polarization of light is taken to be along the z-axis. (After [7])

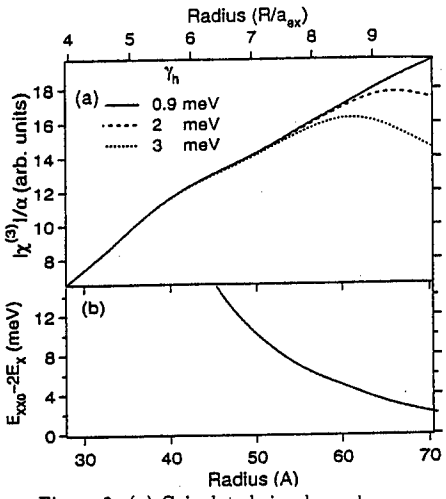


Figure 2: (a) Calculated size dependence of the peak value of $|\chi^{(3)}/\alpha|$ near the exciton resonance in CuCl QDs. All the curves are scaled to the same value at $R = 28$Å. (b) The size dependence of the energy difference between the weakly correlated exciton pair state (E_{XX0}) and twice the exciton ground state energy (E_X). (After [7])

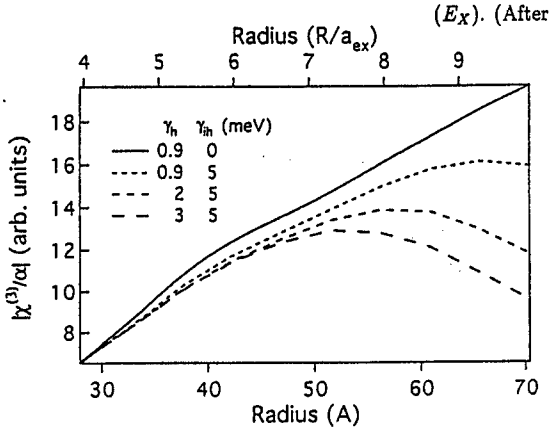


Figure 3: Same as Fig. 2(a), but with inhomogeneous broadening (γ_{ih}) included. (After [7])

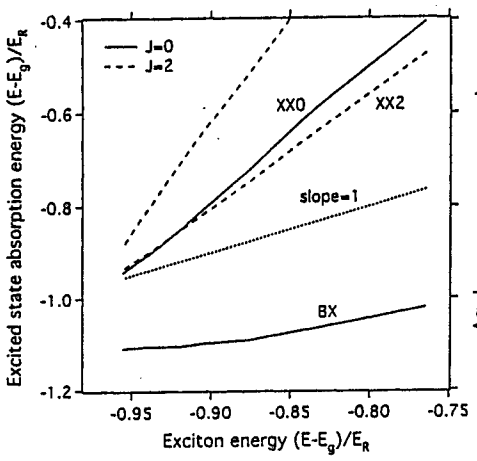


Figure 4: Energies of the dominant excited state absorption peaks are plotted as a function of the exciton ground state energy. BX, XX0 and XX2 denote transitions to the biexciton ground state and to the weakly correlated exciton pair states with $J = 0$ and 2, respectively. The dotted line is a line of slope 1 and is only shown for reference. (After [7])

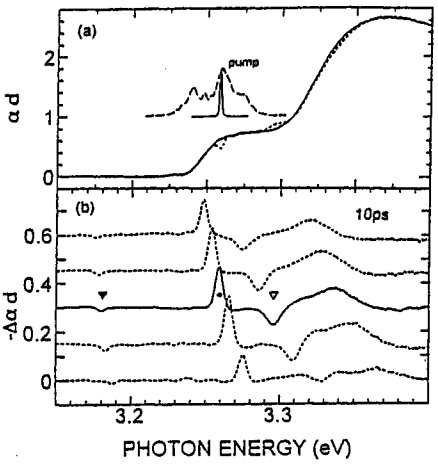


Figure 5: (a) A solid line and a dashed line show the absorption spectra of CuCl nanocrystals at 77K without and with a pump pulse, respectively. Inset: The spectrum of the pump pulse is shown by a solid curve, whereas the spectrally prefiltered second harmonic spectrum is depicted by a dashed curve. (b) Differential absorption spectra at 10ps after the pump are shown for various excitation energies. (After [8])

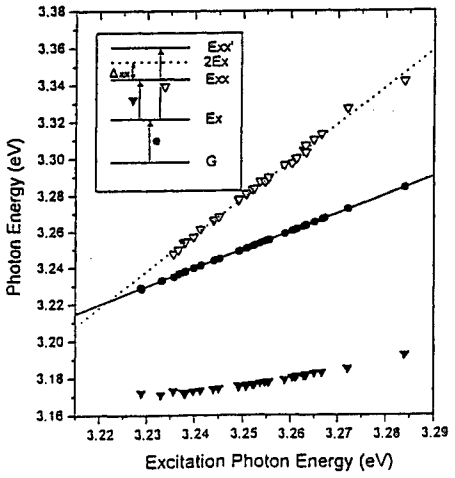


Figure 6: The energy positions of three prominent peaks in the differential absorption spectra are shown as a function of the excitation energy. ▽ :higher energy induced absorption. • :spectral hole at the excitation energy. ▼ :lower energy induced absorption. The slope of the dashed line is 2.0. The inset shows schematically the energy level diagram of excitons and biexcitons. (After [8])

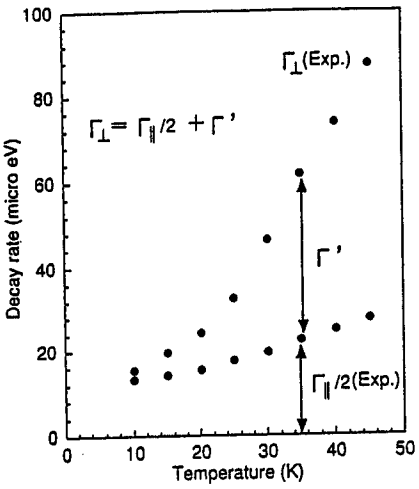


Figure 7: Dephasing rate $\Gamma_\perp$ and half the population decay rate $\Gamma_\parallel/2$ as a function of temperature. The difference between the two curves represents the pure dephasing rate.

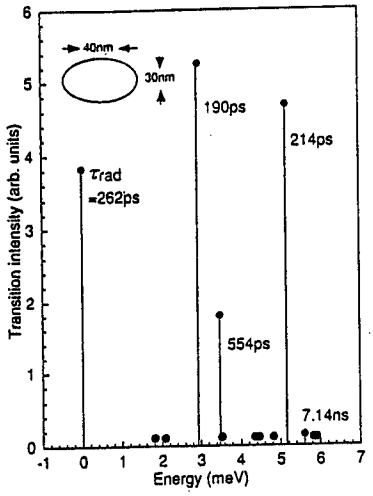


Figure 8: Exciton energy levels in a quantum disk with parameters of $a = 20$nm, $b = 15$nm, $L_z = 3$nm, $V_e^0 = -6$meV and $V_h^0 = -3$meV (see the text). The origin of energy is taken at the exciton ground state. The corresponding radiative lifetime is given for the optically active excitons. The energies of dark exciton states are indicated by dots slightly above the horizontal axis.

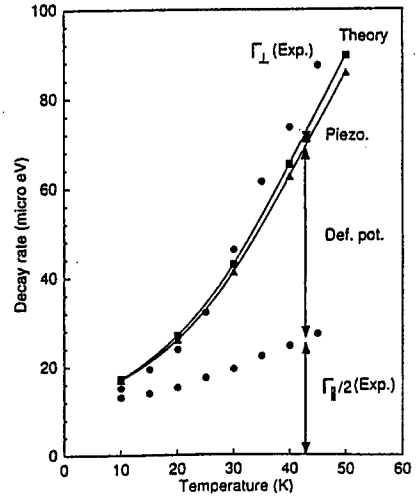


Figure 9: Calculated dephasing rates of the exciton ground state are shown with experimental data as a function of temperature. A quantum disk model is employed with the same parameters as in Fig. 8. The pure dephasing rate is decomposed into the contribution from the deformation potential coupling and that from the piezoelectric coupling and the interference term, denoted as, respectively, "Def. pot." and "Piezo.".

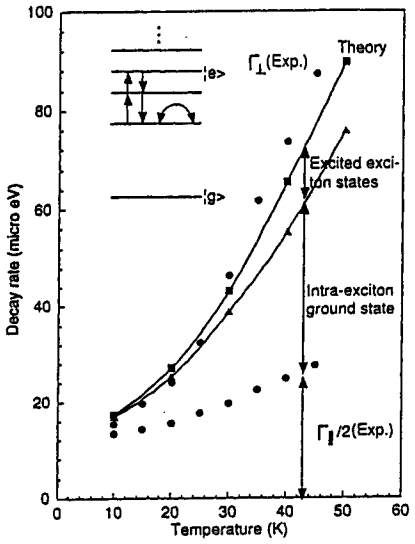


Figure 10: Calculated dephasing rates of the exciton ground state are shown with experimental data as a function of temperature. A quantum disk model is employed with the same parameters as in Fig. 8. The pure dephasing rate is decomposed into the contribution from the diagonal exciton-phonon interaction and that from the off-diagonal interaction and the interference term, denoted as, respectively, "Intra-exciton ground state" and "Excited exciton states".

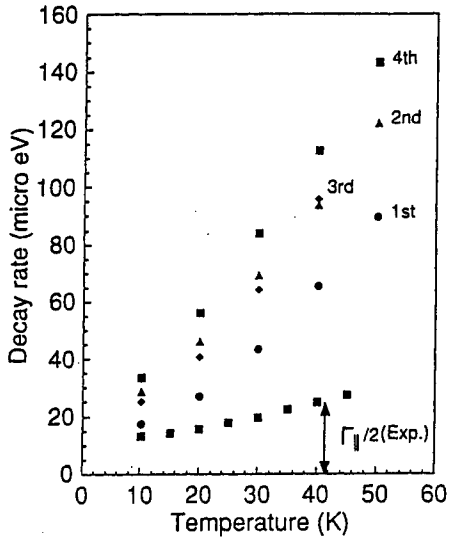


Figure 11: Calculated dephasing rates of the first four optically active exciton states are shown as a function of temperature for the same quantum disk as employed in Fig. 8.

OPTICAL PROPERTIES OF CHARGED InAs-QUANTUM DOTS

K.H. Schmidt[a,b], J. Garcia[b], G. Medeiros-Ribeiro[b], U. Kunze[a], and P.M. Petroff[b]

a) Werkstoffe der Elektrotechnik, Ruhr-Universität Bochum, D-44801 Bochum
b) QUEST and Materials Department, University of California, Santa Barbara, CA 93106

ABSTRACT

We used capacitance, photocurrent and photoluminescence spectroscopy to investigate the dynamics of optically excited electron-hole pairs in InAs self assembled quantum dots under different electric field and charging conditions. Since a change in the laser wavelength does not affect the position of the characteristic features in the photocurrent signal, we assume that the optically excited carriers relax into the quantum dot ground state before recombination processes or tunneling out of the quantum dot occur. The field range can be separated into a high field regime, where the carriers tunnel out of the quantum dot, and a low-field regime, where the exciton is trapped in the dot and recombines. When the quantum dots are loaded with electrons from the back contact, the ground state transition in the photoluminescence spectra shifts from E≈1.052eV down to E≈1.039eV and the full width at half maximum increases from 33meV to 38meV accompanied by a decrease in intensity by a factor of 2. In addition to the QD ground state a higher excited state transition appears at E≈1.11eV which is explained by a recombination process between an electron in the quantum dot d-shell and a hole in the s-shell. All the bias induced effects described above can be explained in terms of manybody interaction in charged QDs and are in excellent agreement with theory.

I. INTRODUCTION

In order to increase the packing density it is a goal of the semiconductor industry to reduce the size of devices. Within the last 45 years the size of DRAMs for example

decreased by three orders of magnitudes while the packing density increased by a factor of 10^6 [1]. However, for sizes below 100nm conventional lithography techniques gradually reach their limits. Additionally, quantum effects have to be taken into account.
Two dimensional quantum well structures are already used in High Electron Mobility Transistors (HEMT) [2]. The ultimate confinement, however, is given in quantum dots (QDs). Here, the carriers are confined in all three dimensions. The localization of the charge within a small volume allows one to control single electrons in transistors, memory devices or in an extremely sensitive electrometer [3-5]. Lasers or LEDs on Si-substrate with QDs in their active region might result in optic devices with improved performance [6,7]. However, QDs are not only interesting for applications but also for fundamental physics. The phonon bottleneck effect, for example, results in an enhancement of the carrier relaxation times in zero dimensional systems [8-10]. Additionally, Coulomb blockade and other charging effects can also be investigated due to the small sizes of these quantum boxes [3,11-14].
An easy way to fabricate such zero dimensional systems is the growth of InAs islands on GaAs substrate in the Stranski-Krastanow growth mode [15,16]. When 1 monolayer (ML) InAs is deposited by molecular beam epitaxy, a two dimensional wetting layer forms on the GaAs substrate. At an InAs coverage of ≈1.5ML the two dimensional growth characteristic transforms into a three dimensional one and small coherently strained InAs islands appear on top of the wetting layer. The radius of these islands is only ≈20nm and their height ≈4nm (when embedded in a GaAs matrix) [16]. The density and size of the islands increases with the amount of InAs deposited before dislocations are incorporated above a certain size limit. Since electron hole pairs recombine non-radiatively in such dislocated islands, the optical quality of the samples decreases for InAs coverages above ≈2.5ML [17]. However, coherently strained InAs-islands embedded in a GaAs-matrix show excellent optical and electrical properties [11-13,18,19]. Characteristic features of 0-dimensional systems - like the δ-function line shape of the density of states, Coulomb blockade effects and hints of the phonon bottleneck - have been already demonstrated in this system [18,20].
In this paper we report on the field induced dynamics of optically excited carriers and the optical properties of charged excitons in InAs QDs. Photoluminescence (PL) and Photocurrent (PC) spectroscopy are excellent techniques to study the optical properties while capacitance (CV) spectroscopy was used to investigate the electrical behavior of the dot system. With the latter technique it is even possible to determine the number of electrons (i.e. the charging conditions) in the dot.
In order to get information about the field induced dynamics of optically excited carriers we measured the PC-signal at certain well-defined energies of the pump laser versus the applied bias. Since the line shape of the PC-spectra does not significantly change with the excitation energy of the Ti-Sapphire laser, we assume that the resonantly excited carriers relax into the quantum dot ground state before they tunnel or recombine. The investigated field range can be divided into three regions. At low fields the optically excited carriers recombine in the QD. In this field regime the PC-signal is negligible and the PL-signal is maximum. In the intermediate field range the excitons are destroyed by

the internal field and the electrons as well as the holes tunnel out of the dot. However, the field is not strong enough for hole tunneling through the front barrier. Thus, the PC-signal is dominated by a displacement current. After the system has reached steady state conditions the additional carriers recombine in the dots and give rise to a PL-signal. At high reverse bias (i.e. high fields) the optically excited electron hole pairs tunnel out of the dots and both types of carriers reach their contact regions which results in a real (photo-) current flow. Since the carriers are extracted from the dot system the QD PL-signal decreases. This interpretation is confirmed by frequency and power dependent measurements.

The combination of PL and CV spectroscopy enables us to study the optical properties of charged quantum dots. A red shift of the QD ground state transition was observed in the PL spectra when a forward bias was applied to the sample and the QDs were loaded with electrons from the back contact. The energy shift is accompanied by a broadening of the QD ground state transition and a decrease of the PL intensity by a factor of 2. In addition, an excited state transition appears at high forward bias when the d-shell of the QDs is loaded with electrons. We attribute this feature to a recombination process between an electron in the d-shell and a hole in the s-shell of the QD. Due to Coulomb interaction, this transition becomes allowed at high charging conditions.

II. EXPERIMENT

The investigated sample was grown by molecular beam epitaxy (MBE) in a Varian Gen II system under an As pressure of $1 \cdot 10^{-5}$ Torr on semi-insulating (100) GaAs substrate. The growth temperature for all layers except for the InAs wetting layer and the quantum dots was 600°C. The back contact of the Schottky diode structure used in our experiments was formed by 20nm Si-doped GaAs ($n_D \approx 4 \cdot 10^{18}$ cm^{-3}). An intrinsic GaAs spacer layer of 25nm separates the InAs wetting layer from the back contact region. In order to achieve island formation 1.6ML of InAs were deposited at a substrate temperature of 530°C. The islands were covered with 30nm of undoped GaAs followed by 116nm of a GaAs/AlAs (2nm/2nm) short period superlattice and a GaAs cap layer of 4nm. We used a NiAuGe alloy annealed at 400°C to contact the n-doped material and a CrNiAu layer system for the Schottky contact. Details of the sample growth are discussed elsewhere [10,13]. Fig.1 shows a schematic band structure of the investigated sample.

All our data were measured with a dual phase Lock-In amplifier at T=10K.

In the PL- and PC-experiments we pumped the QDs resonantly from the rear with a tunable Ti-Sapphire laser. The position of the laser beam was controlled with a charged coupled device camera. The light emitted from the back side of our sample was dispersed by a 0.85m double monochromator (resolution 0.5 nm) and detected with a liquid nitrogen cooled Ge-detector.

In the capacitance experiments an AC-bias with an amplitude of 5mV and a modulation frequency of 500Hz was added to a variable DC bias.

III. RESULTS AND DISCUSSION

In order to get information about the field induced dynamics of electron hole pairs resonantly excited into QD levels we used PC spectroscopy. The inset of Fig.1 displays a schematic of the experimental setup. Due to the non transparent Schottky contact on top, we pumped the QDs through the GaAs substrate with a tunable Ti-Sapphire laser. For the laser energies used in our experiments the GaAs substrate is transparent and the electron hole pairs are resonantly pumped into excited QD levels. In order to get a PC signal the carriers have to be extracted out of the dot by the internal field. Measuring the PC current while the DC-bias between the Schottky and the n-doped back contact is changed it is possible to investigate the field induced carrier dynamics in our QD system. Only QDs in the contact region significantly contribute to the PC-signal. Therefore, the laser beam was chopped while the current flow between the Schottky gate and the back contact was measured in dependence of the applied DC-bias. The energy of the pump laser was kept constant.

Figure 2 depicts PC traces measured at three different laser energies. In order to get an idea about the QD levels pumped by the Ti-Sapphire laser we measured the PL signal of our sample excited with 200mW of an Ar^+-laser (inset of Fig.2). At $E\approx1.52$eV and $E\approx1.45$eV the GaAs band edge and the wetting layer (WL) transition are clearly observable. Below the WL feature several well defined peaks appear which we attribute to transitions between hole QD levels and electron QD levels with the same quantum number [10]. This interpretation is in good agreement with theoretical calculations based on lens shape QDs with a parabolic effective potential [21]. According to this model the transition at $E\approx1.05$eV (labeled 0 in the inset of Fig.2) reflects the recombination of an electron with a hole both in the QD ground state (s-shell). The PL feature at $E\approx1.12$eV occurs when an electron in the p-shell of the QD recombines with a p-shell hole. The arrows indicate the laser energies used in the field dependent PC-experiments. With increasing laser energy the carriers are excited into QD levels with reduced barrier height and width. Thus, smaller fields are necessary for tunneling out of higher excited states.

At $U\approx-0.6$V and $U\approx-0.15$V there are two well defined steps observable in the PC-spectra of Fig.2. However, no shift of the step like features is observable when the pump energy is changed from $E_{laser}=1.216$eV to $E_{laser}=1.340$eV. Thus, tunneling out of excited states can be excluded. We assume that the optically excited carriers relax into the QD ground state before they tunnel or recombine.

For $U<-0.15$V electrons as well as holes are able to leave the dot system. At high reverse bias ($U<-0.6$V) the field is even strong enough to observe subsequent hole tunneling through the front barrier which results in a real (photo-) current flow. Since almost no carriers recombine in the QD, the PL-signal is weak in this field regime [22]. The deviation of the curvature of the PC traces at high reverse bias is attributed to the Franz-Keldysh effect which becomes more pronounced at high pump energies [23].

For -0.6V<U<-0.15V the hole tunneling through the front barrier is blocked. The character of the PC-signal changes from a real current flow into a displacement current characteristic. As soon as the system has reached steady state additional carriers recombine in the dots. Thus, the PL-signal increases [22] and the PC decreases in intensity. At forward bias the optically excited excitons are trapped in the QDs and recombine. Consequently, the PC-signal is negligible in this field region. This model of the field induced carrier dynamics is confirmed by frequency [22] and power dependent measurements.

Figure 3 depicts the PC-signal versus the pump intensity of the Ti-Sapphire laser. At high fields (U=-2V) all carriers tunnel out of the QDs and contribute to the PC signal. The more carriers excited by the laser beam, the more PC-current is induced. Thus, the PC-intensity depends linearly on the laser power. For U≈-0.2V the PC signal is dominated by a displacement current. Holes are extracted from the dots and accumulate at the front barrier interface. This accumulation process causes band bending until the system has reached steady state and additional carriers radiatively recombine in the dots. Since the steady state conditions are almost independent from the pump intensity, a sublinear behavior is observed in the PC-trace of Fig.3 (U=-0.2V).

The PC-signal measured at U=0.5V shows also a sublinear power dependence. However, compared to the PC-trace measured at U=-2V the intensity of the PC-signal is reduced by three orders of magnitude at forward bias. Thus, tunneling is negligible in this field regime.

In conclusion the field induced carrier dynamics can be separated into two regimes. For U<0V electrons and holes leave the dots and contribute to a PC-signal. At forward bias the optically excited carriers remain in the dot and recombine. In this regime band bending caused by tunneling of optically excited carriers is negligible.

However, for U>0V the s-, p-, d-QD shells are charged with electrons from the back contact as is clearly observable in the dark CV trace shown in Fig.4. Coulomb blockade effects are also visible in Fig.4 [10-12]. Finally, electrons tunnel from the back contact into the 2-dimensional WL system and cause a strong increase in the capacitance trace for U>0.7V. Since optically excited carriers recombine in the dots for U>0V, the dark CV trace is still valid within certain limits even at high pump intensities (see also inset of Fig.3).

Thus, CV spectroscopy is very sensitive to charging effects while PL measurements allow the investigation of the optical properties. The combination of both techniques enables us to study the optical properties of charged InAs-QDs.

Figure 5 sketches the principle experimental setup for such investigations. The QDs are pumped resonantly from the rear with a Ti-Sapphire laser. The carriers relax and recombine. When a positive bias is applied to the Schottky diode, the QDs are loaded with electrons from the back contact. This charging process is monitored by CV measurements. Since we modulated the bias applied to the sample and not the laser beam, only the PL-signal originating from the charged QDs in the contact region was detected by the Lock-In amplifier [13].

Fig.6 displays two PL spectra taken at U=0V and U=1.2V, respectively. The data are normalized to the QD ground state transition. At U=0V only the ground state transition (labeled 0) is observable in the PL spectrum. For such an applied bias the QDs are neutral. Since all optically excited carriers relax into the QD ground state and recombine, no excited state transition appears at higher energies. We also conclude from Fig.6 that the pump intensity used for our investigation is not high enough to achieve saturation of the s-shell. Otherwise, higher excited state transitions should occur. When a positive bias is applied to the sample a red shift of the fundamental QD transition and an additional feature at high energies (labeled 1) is observed. Field effects can be excluded since no shift of the ground state PL-feature is detected at high fields [13,14]. We explain the bias induced change of the PL structure in terms of charging effects.
When the electron and hole are in the ground state of a neutral QD the transition energy $h\nu$ is described by the single particle energy E_{00} and the exciton binding energy E_X:

$$h\nu = E_{00} - E_X$$

In a charged QD, however, the Coulomb interaction between the optically excited electron-hole pair and the additional electrons ($E_{C,ee}$ and $E_{C,eh}$) as well as the exchange energy E_{ex} has to be taken into account. Thus, the transition energy of the ground state PL is given by:

$$h\nu' = E_{00} - E_X + E_{C,ee} - E_{C,eh} \pm E_{ex}$$

In a first approximation $E_{C,ee}$ and $E_{C,eh}$ are similar and the experimentally observed shift of the PL ground state transition is mainly due to exchange interaction. This interpretation is in good agreement with calculations published in Ref. [24]. In the gray scale graphic of Fig.7a the energetic position of the QD ground state transition is plotted versus the applied bias i.e. number of electrons in the dot. The charging conditions are checked by CV measurements (Fig.7b). The ground state transition gradually shifts from E≈1.052eV down to E≈1.039eV when the dots are loaded with electrons from the back contact region. In addition, the intensity of the peak decreases and the full width at half maximum (FWHM) increases from 33meV to 38meV with the number of electrons in the dots (Fig.8). At high forward bias an additional peak emerges at E≈1.11eV when the d-shell of the QD is loaded with electrons [see also ref. 13]. Such a PL feature appears in highly charged QDs when an electron in the d-shell (magnetic momentum m=0) recombines with a hole in the s-shell (m=0) [24]. In a neutral QD with parabolic potential, however, only transitions between QD levels with the same quantum number are allowed [21]. Even in charged QDs electrons and holes must have the same magnetic moment in order to recombine. Due to the short relaxation times holes are only available in the quantum dot ground state (m=0). The recombination of an electron in the p-shell (m=±1) with a hole in the s-shell (m=0) is forbidden. In the d-shell, however, the magnetic momentum of the Fock-Darwin states is m=0,±2 [21,24]. Thus, recombination between an electron in the d-shell with m=0 and a hole in the s-shell is possible in

charged QDs. This interpretation is confirmed by the data shown in Fig.9 where the relative intensity of the high energy peak is shown versus the applied bias (i.e. charging conditions). No excited state transition is observable when the s- and p-shell are loaded with electrons. However, as soon as electrons tunnel from the back contact into the QD d-shell a strong increase in PL signal at E≈1.11eV is observed. These findings are in excellent agreement with the theoretical predictions published in ref. 24.

IV. CONCLUSION

In conclusion we have investigated the dynamics of optically excited electron-hole pairs in InAs self assembled quantum dots under different electric field conditions. With a tunable Ti/Sapphire laser the carriers are pumped resonantly into the QD level. Since the voltage position of the characteristic PC structures are independent of the energy of the pump laser, we assume that the optically excited carriers relax into the QD ground state before they recombine or tunnel.

The field range can be separated into a low-field regime, where the exciton is trapped in the dot and recombines and a high field regime, where the carriers tunnel out of the QD ground state which results in a PC-signal. At high reverse bias (U<-0.6V) the internal electric field is strong enough to overcome the exciton binding energy and to separate the optically excited electron hole pairs. The electrons as well as the holes tunnel out of the QDs. Subsequent tunneling of the holes through the AlGaAs front barrier results in a real (photo-) current flow. In an intermediate range (-0.6V<U<-0.15V) the internal electric field is still strong enough to extract the electrons and holes out of the dots but tunneling through the front barrier is blocked. Thus the holes accumulate at the GaAs/AlGaAs interface and screen the field in the QD region until the system reaches steady state. The hole accumulation results in a displacement current characteristic of the PC signal. At low electric fields (U>0V) the holes as well as the electrons remain in the QD and recombine. Thus, the PC-signal vanishes.

Our interpretation of the field induced dynamics of optically excited carriers in InAs quantum dots is confirmed by frequency and power dependent PC spectra as well as by bias dependent PL-spectroscopy [13].

At low fields when the QDs are loaded with electrons band bending caused by optically excited carriers can be excluded. Thus, the dark capacitance trace is still valid within certain limits even under illumination. At forward bias charging of the QDs with electrons from the back contact region is clearly observable in the C-V spectra. With increasing number of electrons in the dot, the ground state transition in the PL spectra shifts from E≈1.052eV down to E≈1.039eV and the full width at half maximum increases by 5meV accompanied by a decrease in intensity by a factor of 2. In addition to the QD ground state a higher excited state transition appears at E≈1.11eV for U>0.55V. It gains in intensity with increasing forward bias. In this voltage regime the QD d-shell is loaded with electrons. Since electrons in the d-shell and holes in the s-shell have a magnetic momentum m=0, recombination between these types of carriers becomes allowed due to Coulomb interaction.

All the bias induced effects described above can be attributed to manybody interaction in charged QDs. Our findings are in excellent agreement with the theoretical predictions.

ACKNOWLEDGEMENT

One of the author (K.H.S.) would like to acknowledge fruitful discussions with P. Hawrylack, A. Wojs and C. Metzner. This work was financially supported by the Alexander von Humboldt Foundation (K.H.S.), the Center for Quantized Electronic Materials QUEST (K.H.S.) and the Brazilian agency CNPq (G.M.R.)

References

[1] N. Yokoyama, S. Muto, K. Imamura, M. Takatsu, T. Mori, Y. Sugiyama, Y. Sakuma, H. Nakao, and T. Adachihara, Soild State Electron. **40**, 505 (1996)

[2] E.F. Schubert, K. Ploog, H. Dämbkes, and K. Heime, Appl. Phys. A **33**, 63 (1984)

[3] M.A. Kasner, Rev. Mod. Phys. **64**, 849 (1992)

[4] K. Yano, T. Ishii, T. Hashimoto, T. Kobayashi, F. Murai, and K. Seki, IEEE Transactions on Electronic Devices **41**, 1628 (1994)

[5] L.W. Molenkamp, K. Flensberg, M. Kemerink, Phys. Rev. Lett. **75**, 4282 (1995)

[6] F. Heinrichsdorff, M.-H. Mao, N. Kirstädter, A. Krost, D. Bimberg, A.O. Kosogov, and P. Werner, Appl. Phys. Lett. **71**, 22 (1997)

[7] J.M. Gèrard, O. Cabrol, and Sermage, Appl. Phys. Lett. **68**, 3123 (1996)

[8] F. Adler, M. Geiger, A. Bauknecht, F. Scholz, H. Schweizer, M.H. Pilkuhn, B. Ohnesorge, A. Forchel, J. Appl. Phys. **80**, 4019 (1996)

[9] K. Mukai, N. Ohtsuka, H. Shoji, M. Sugawara, Phys. Rev. B **54**, R5243 (1996)

[10] K.H. Schmidt, G. Medeiros-Ribeiro, M. Oestreich, G.H. Döhler, and P.M. Petroff, Phys. Rev. B **54**, 11346 (1996)

[11] G. Medeiros-Ribeiro, F.G. Pikus, P.M. Petroff, A.L. Efros, Phys. Rev. B **55**, 1568 (1997)

[12] M. Fricke, A. Lorke, J.P. Kotthaus, G. Medeiros-Ribeiro, and P.M. Petroff, Europhys. Lett. **36**, 197 (1996)

[14] R.J. Warburton, C.S. Dürr, K. Karrai, J.P. Kotthaus, G. Medeiros-Ribeiro, and P.M. Petroff, Phys. Rev. Lett. **79**, 5282 (1997)

[13] K.H. Schmidt, G. Medeiros-Ribeiro, P.M. Petroff, Phys. Rev. B **58**, 3597 (1998)

[15] I.N. Stranski, and L. Krastanow, Akad. Wiss. Lit. Wien Math.-Natur. Kl. IIb **146**, 797, 1937

[16] D. Leonard, K. Pond, and P.M. Petroff, Phys. Rev. B **50**, 11687 (1994)

[17] K.H. Schmidt, G. Medeiros-Ribeiro, M. Cheng, and P.M. Petroff, Mat. Res. Soc. Symp. Proc. **452**, 275 (1997)

[18] M. Grundmann, J. Christen, N.N. Ledentsov, J. Böhrer, D. Bimberg, S.S. Ruminov, P. Werner, U. Richter, U. Gösele, J. Heydenreich, V.M. Ustinov, A. Yu. Egorov, A.E. Zhukov, P.S. Kop'ev, Zh. I. Alferov, Phys. Rev. Lett. **74**, 4043 (1995)

[19] H. Sakaki, G. Yusa, T. Someya, Y. Ohno, T. Noda, H. Akiyama, Y. Kadoya, and H. Noge, Appl. Phys. Lett. **67**, 3444 (1995)

[20] J.-Y. Marzin, J.-M. Gérard, A. Izrael, and D. Barrier, Phys. Rev. Lett. **73**, 716 (1994)

[21] A. Wojs, P. Hawrylak, S. Fafard, L. Jacak, Phys. Rev. B **54**, 5604 (1996)

[22] K.H. Schmidt, G. Medeiros-Ribeiro, J.M. Garcia, U. Kunze, P.Wellmann, and P.M. Petroff, Physica E 2, 627 (1998)

[23] N. Linder, W. El-Banna, U.D. Keil, K.H. Schmidt, G.H. Döhler, J.N. Miller, K.J. Ebeling, SPIE Proc. **1286**, 359-369 (1990)

[24] A. Wojs, and P. Hawrylak, Phys. Rev. B **55**, 13066 (1997)

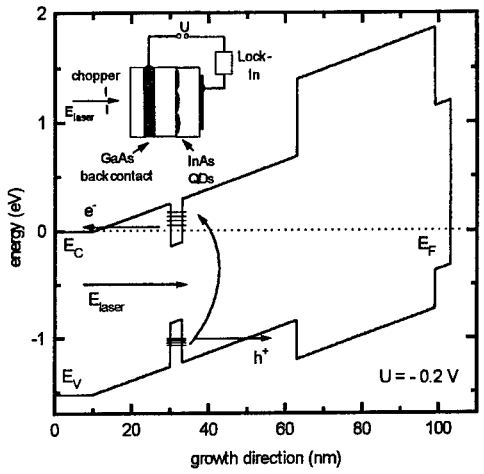


Figure1: Schematic band structure of the investigated sample sketched for an applied bias of U=-0.2V. The inset in the upper left corner depicts the principle experimental setup. Due to the non transparent Schottky contact on top the sample is illuminated from the back side through the GaAs substrate. The modulated Ti/Sapphire laser beam excites electron hole pairs resonantly into excited QD levels. When the carriers tunnel out of the dot a PC signal is measured with the Lock In amplifier. The tunnel efficiency is investigated by changing the applied bias U.

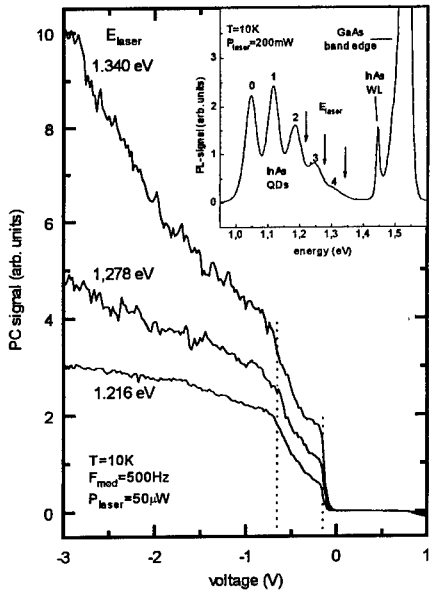


Figure 2: The PL spectrum shown in the inset was pumped with an Ar^+-laser and was measured at 10K. The GaAs band edge and the wetting layer transition are clearly observable. Due to the high pump intensity, not only the QD ground state (labeled 0) but several higher excited state transitions (labeled 1,2..) appear below the wetting layer feature. The arrows mark the pump energies E_{laser} of the Ti-Sapphire laser used to measure the PC-traces shown in the main frame. The laser power of 50μW was modulated at a chopper frequency of F_{mod}=500Hz. The data were taken at T=10K. No saturation of the PC-signal can be observed at high reverse bias for a laser beam energy of E_{laser}=1.34eV. This effect can be explained by Franz-Keldysh absorption in the i-GaAs material. At low fields (U>0V) the optically excited carriers recombine in the dot and the PC-signal vanishes.

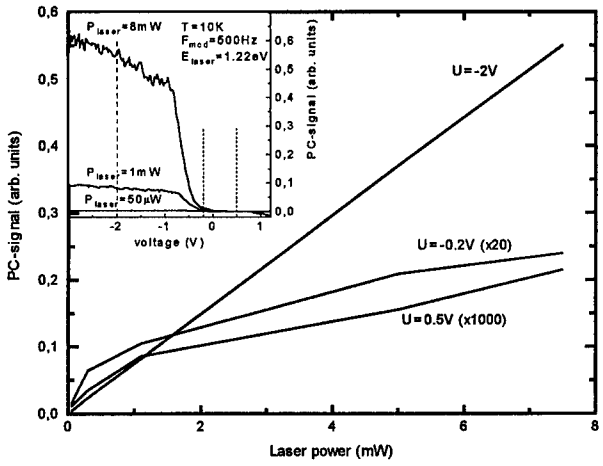


Figure 3: Power dependent PC-signal measured at U=-2V, U=-0.2V and U=0.5V. The spectra are multiplied by the number in brackets. The inset shows PC traces for three different pump intensities P_{laser}. The dashed lines mark the voltage positions used in the main frame. In all our measurements the sample was pumped with a laser energy of E_{laser}=1.22eV and a modulation frequency of F_{mod}=500Hz at T=10K.

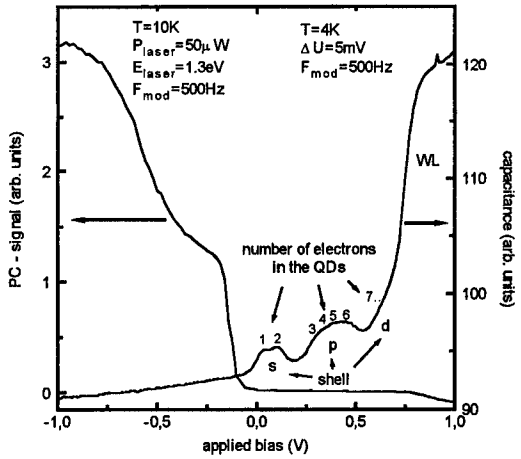


Figure 4: PC and CV signal versus applied bias. P_{laser}, E_{laser} and F_{mod} are the intensity, beam energy and modulation frequency of the pump laser used in the PC experiments. In order to measure the CV data, the sample was modulated with ΔU=5mV at F_{mod}=500Hz.

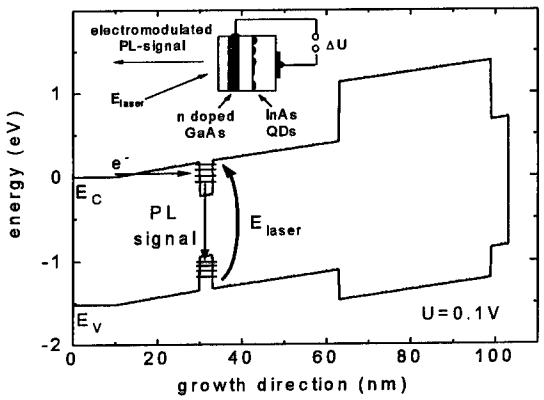


Figure 5: Experimental setup used in the voltage dependent PL experiments. The InAs QD system was pumped resonantly by a laser beam E_{laser}. The carriers relax in the QD and recombine. The PL signal was also measured from the rear. Applying a forward bias ΔU the QDs are charged with electrons from the back contact.

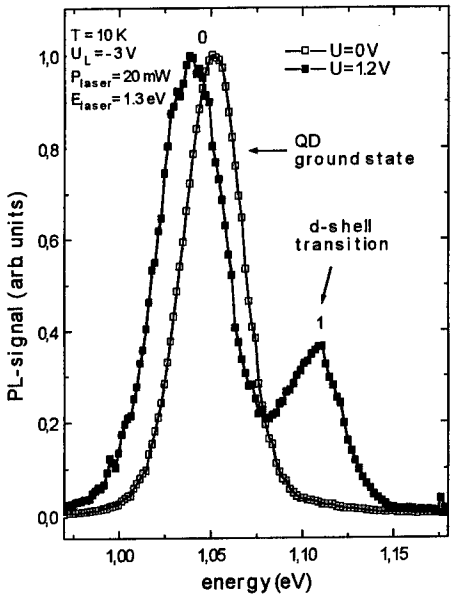


Figure 6: PL spectra measured at U=0V (neutral QDs) and U=1.2V (high charging conditions), respectively. The charge induced red shift of the QD ground state transition (labeled 0) is clearly observable. At U=1.2V an additional feature appears at E=1.11eV (labeled 1) which can be explained by recombination of an electron in the QD d-shell with a hole in the s-shell. This transition becomes allowed due to Coulomb effects. In order to measure only the charge induced variation of the PL signal, the applied bias was modulated between U_L and U. Since the optically excited carriers leave the dots at U_L=-3V, the PL signal is negligible for such high fields. The experiments were done at T=10K. The beam intensity of the Ti-Sapphire laser was P_{laser}=20mW and it's energy E_{laser}=1.3eV.

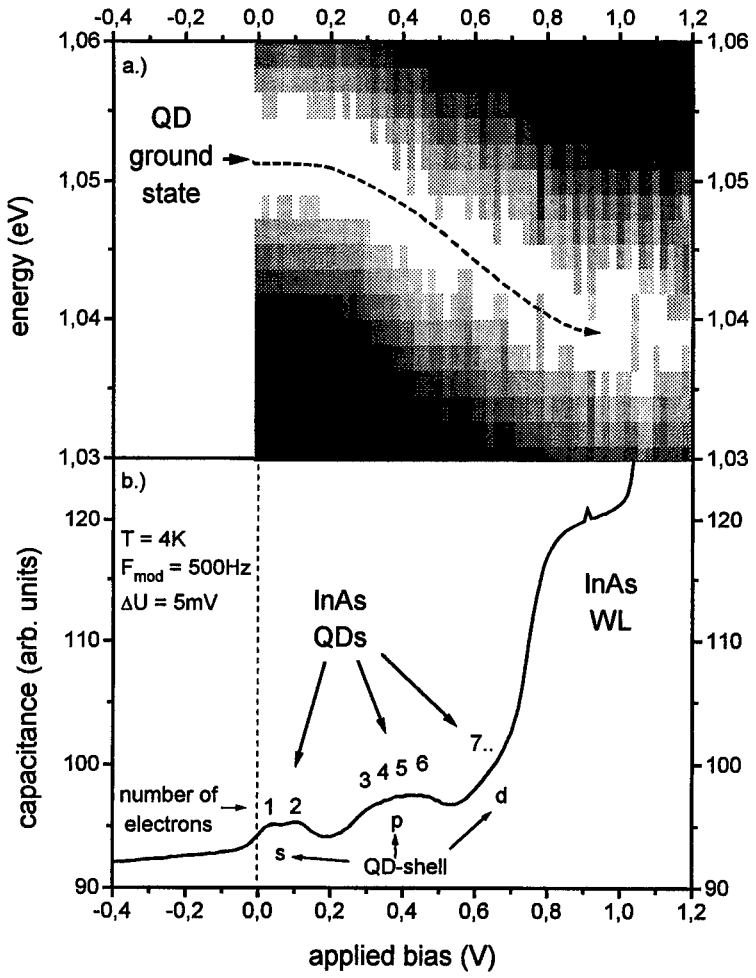


Figure 7: Intensity plot of the PL signal reflecting the energetic position of the QD ground state transition at high forward bias (a). The charge induced red shift is clearly observable. The dashed curve represents a guide line for the eyes. Fig. b depicts the dark capacitance trace at T=4K (see also Fig. 4). A peak appears in the CV trace when an electron tunnels from the back contact into a QD shell.

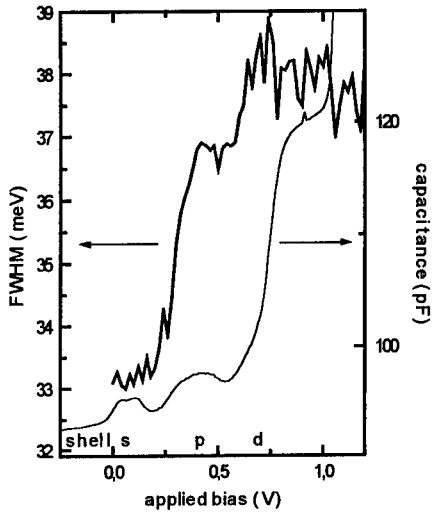


Figure 8: The full width at half maximum (FWHM) of the QD ground state transition increases when a forward bias U>0.3V is applied to the sample and the p-shell of the QD is loaded with electrons from the back contact. The charging process is observable in the CV-trace also shown in the figure.

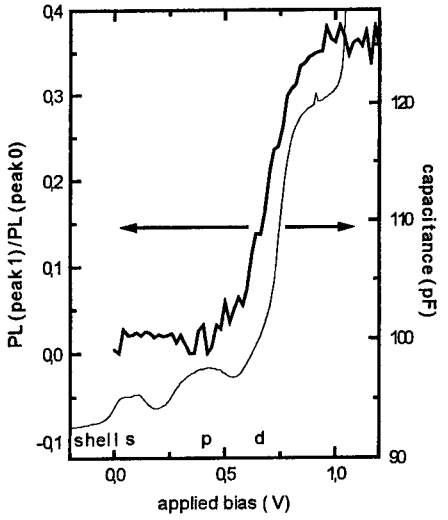


Figure 9: The peak intensity of the coulomb induced excited state transition (peak 1 in Fig.6) divided by the intensity of the ground state PL (peak 0 in Fig.6) is shown versus the applied bias. The charging conditions are detected with CV spectroscopy. When the d-shell of the QDs is loaded with electrons the relative intensity of the excited state transition increases. Thus, we attribute this transition to a recombination process between an electron in the d-shell (m=0) and a hole in the s-shell (m=0). This transition becomes allowed due to Coulomb interaction. Since the magnetic momentum of electrons in the p-shell is m=±1, the recombination process with an hole in the s-shell (m=0) is forbidden even in charged QDs.

INTERNAL TRANSITIONS OF NEUTRAL AND NEGATIVELY CHARGED MAGNETOEXCITONS IN GaAs NANOSTRUCTURES BY OPTICALLY DETECTED RESONANCE SPECTROSCOPY

B.D. McCombe†, H.A. Nickel†, G. Kioseoglou†, G.S. Herold†, T. Yeo†, H.D. Cheong†, A. Petrou†, A.B. Dzyubenko*, A.Yu. Sivachenko# and D. Broido‡

† Department of Physics and Center for Advanced Photonic and Electronic Materials University at Buffalo, State University of New York, Buffalo, NY 14260, USA
* General Physics Institute, Russian Academy of Sciences, Moscow 117942, Russia
# The Weizman Institute of Science, Rehovoth 76100, Israel
‡ Department of Physics, Boston College, Chestnut Hill, MA 02167, USA

ABSTRACT

Optically Detected Resonance (ODR) spectroscopy has been used to study resonances of electrons, holes, and their complexes in GaAs/AlGaAs quantum wells (QWs) in magnetic fields up to 15 T. The capability of observing electron and hole CR as well as several internal excitonic transitions (IETs) in a single sample is unique to ODR spectroscopy. In an undoped multiple-QW sample, in addition to an electron and two hole cyclotron resonances (CR), a $1s \rightarrow 2p_+$, and two $1s \rightarrow 2p$. IETs arising from two distinct neutral heavy hole magneto-excitons were observed. These measurements permitted verification of a predicted relationship resulting from the symmetry of the magneto-exciton Hamiltonian. Studies of negatively charged excitons in samples that showed both neutral (X) and negatively charged (X^-) exciton photoluminescence-lines were also made. Singlet and triplet transitions of X^- were observed, consistent with theoretical calculations that also reveal a hidden symmetry associated with this charged complex.

INTRODUCTION AND BACKGROUND

The Coulomb attraction between electrons and holes in semiconductors results in the formation of well-known correlated electron-hole complexes (excitons). In bulk GaAs due to the small masses of their constituents and the large dielectric constant, excitons are hydrogen-like with a Bohr radius of about 100 Å and a binding energy of about 5 meV. In quantum-well structures that confine the charge carriers strongly, a

series of excitons appears corresponding to the various interband transitions between confined electron and hole subbands; a quasi-2D exciton is associated with each of the allowed interband transitions. Such neutral excitons have been studied in a number of different materials systems for many years.

Recently there has been considerable interest in charged excitons in quasi-2-dimensional (2D) semiconductor systems since the initial observation of negatively charged excitons [1] in CdTe quantum wells. The evolution of the exciton system in quasi-2D as a function of excess electron concentration from isolated neutral excitons to "isolated" negatively charged excitons to a few-hole/many-electron plasma (the metal-insulator transition) and the effects of a magnetic field on these transitions have been a major focus of recent investigations. [2-4] In most of these studies the electron (or hole) density has been varied in a single quantum well by a gate voltage or by optical means while monitoring photoluminescence (PL) or absorption features. There are many similarities between the neutral and charged exciton systems and neutral and charged donors. However, in the case of X^-, there are also some fundamental differences in the basic physics and the allowed optical transitions. These derive from the free motion of the complex, and the continuum of final states of intra-excitonic transitions. Very recently, the interpretation of the PL feature attributed to X^- by a number of authors has been called into question.[5] These authors have suggested that it is associated with a neutral-donor (in the barrier) bound exciton (D^0-X_b), but there is no strong evidence favoring this interpretation.

A series of excited states exists for neutral excitons, and internal transitions satisfying the requisite electric-dipole selection rules are allowed, *e.g.*, s to np in the usual hydrogenic notation at zero magnetic field. At low magnetic fields these energy levels and transition energies are only slightly modified by the magnetic "perturbation", leading to the usual Zeeman splittings. At very high magnetic fields the magneto-exciton states are more easily understood by considering the Coulomb interaction as a perturbation on the high field free carrier (electron and hole) Landau oscillator states. In this limit the intra-excitonic transitions can be considered to be Coulomb-shifted electron cyclotron resonance (CR) (evolving from the $1s \rightarrow 2p_+$ low field transition) and Coulomb-shifted hole CR (evolving from the $1s \rightarrow 2p_-$ transition). Here the subscript $\pm$ denotes the quantum number ($m = \pm 1$) for projection of orbital angular momentum, and the spectroscopic notation has been used. The transition energy is blue-shifted from the corresponding bare CR energy in each case.

In QW systems with excess electrons in the well the negatively charged exciton (X^-), is the ground state. [1,2] Due to the additional binding energy of the second electron, the recombination energy of this complex is lowered (by about 11 cm^{-1} at zero field for a 20 nm GaAs QW) with respect to the neutral, heavy-hole exciton, hhX. Internal transitions of X^- are expected, somewhat analogous to the internal transitions of the shallow donor analog (D^-), which have been extensively studied. [6]

Study of the internal transitions offers an additional tool for understanding the excitonic state in the dilute situation and its evolution with excess electron density and magnetic field. For the high exciton density situation it may also provide the possibility to probe exciton-exciton interactions and the signature of an exciton condensate.

THEORETICAL BACKGROUND

The Hamiltonian for a two-dimensional neutral exciton in a magnetic field can be written

$$H = \frac{p_{rel}^2}{2m_r} + \frac{e^2B^2}{8m_rc^2} - \frac{e^2}{\varepsilon r} + \frac{1}{2}(\omega_{ce} - \omega_{ch})\hat{l}_z + \frac{e}{Mc}\vec{B} \bullet [\vec{r} \times \vec{K}], \qquad [1]$$

where m_r is the reduced electron-hole mass, $M = m_e + m_h$ with $m_{e(h)}$ the electron (hole) mass, l_z is the operator for projection of the relative angular momentum along the magnetic field direction, B is the magnetic induction, r is the relative coordinate in the plane perpendicular to B, ε is the background dielectric constant, and K is the momentum of the center of mass of the exciton. The last term in Eq. (1) is associated with the motion of the center of mass and describes the coupling between the center-of-mass motion and the relative motion.[7] We note that the magneto-PL lines are predominantly transitions with K = 0. At K = 0 the solutions are a set of discrete states that evolve from the usual hydrogenic states at low fields (1s, $2p_{\pm1,0}$, $3d_{\pm2,\pm1,0}$, etc. in the spectroscopic notation) to high field states associated with each electron (hole) Landau level (LL). In the high field case, the states can be labeled by the electron (hole) Landau quantum number, n_e (n_h), and $n_e - n_h$, the projection of relative angular momentum, m_z. Allowed electric-dipole transitions satisfy the selection rule $m_z = \pm 1$. It is easy to show [7] that as a result of the cylindrical symmetry leading to Eq. (1), for transitions labeled in the low-field notation the following important relationship is satisfied:

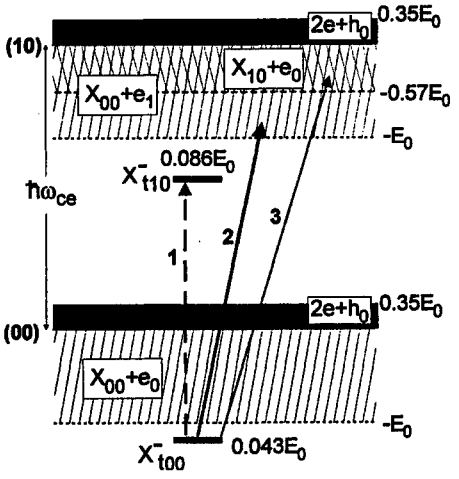


Fig. 1. Schematic diagram of the triplet energy states associated with the second electron in two electron-hole Landau levels for a strictly two-dimensional, high magnetic field limit. The notation is discussed in the text.

$E_{1s\to np+} - E_{1s\to np-} = \hbar(\omega_{ce} - \omega_{ch})$, where $\omega_{ce(h)}$ is the electron(hole) cyclotron resonance frequency, and $E_{1s\to np+(-)}$ is the transition energy from the ground state to an excited state (labeled for convenience and consistency with earlier work by the principle quantum number, n, and (in spectroscopic notation) by the projection of relative angular momentum quantum number $m_z = \pm 1$.

The situation for the three-particle problem of the negatively charged exciton is considerably more complex. We provide only a qualitative description here; a detailed quantitative description will be published elsewhere. [8] For the present purpose we consider a strictly-2D system in the limit of high magnetic fields (no Landau-level mixing). In this limit, in the zero LLs the only bound state is the X^--triplet, while there are no bound X^--singlet states. [9,10] This is in contrast to the B = 0 case, where the singlet is bound, while there are no bound triplet X^- states. The binding of X^- results from a delicate balance between the e-e repulsion and e-h attraction. As a result, the X^--triplet binding energy in the zero LLs is very small, 0.043 E_0. Here $E_0 = [\pi/2]^{1/2}[e^2/\varepsilon\ell]$, the characteristic Coulomb energy in 2D in high magnetic field with $\ell = [c\hbar/eB]^{1/2}$, the characteristic magnetic length.

The X^- states can be labeled by exact quantum numbers: the total spin of the electrons, singlet (S) or triplet (T), the total angular momentum projection M_z and, in the high field limit, the total electron (hole) LL quantum number $N_e(N_h)$ ($|N_e,N_h,M_z;S(T)>$). In a magnetic field the X^- states are macroscopically degenerate in M_z; this is just the LL degeneracy for the charged complex. For example, the degenerate bound X^- triplet states associated with the zero LLs are $|00,M_z;T>$, with $M_z = -1,-2,-3 \ldots$.

To understand internal X^- transitions, it is necessary to consider the eigenstates associated with higher LLs. In the next LL (one electron promoted to the first LL), there also exists only one bound triplet state, $|1,0,M_z;T>$ (also degenerate, $M_z = 0,-1,-2...$) and no bound X^--singlets. The binding energy of the $|1,0,M_z;T>$ state is 0.086 E_0, twice that of $|0,0,M_z;T>$. This is due to the fact that the two electrons in the excited triplet state can occupy the 1s (0 LL) and 2s (1 LL) single particle states, thus enhancing the e-h attraction relative to the ground triplet state in which the two electrons occupy an antisymmetric combination of the 1s (0 LL) and $2p_-$ (0 LL) single particle states.

There is a fundamental difference between the eigenspectra of the X^- states and D^- (negative donor ion) states in quasi-2D in a magnetic field. For the latter (and generally for any electron system in B) the eigenspectra are completely discrete, and all eigenstates are spatially localized. For the X^- (and generally for any electron-hole system in B) the spectra consist of discrete bound states and continua. The continua correspond to the motion of a neutral magneto-exciton as a whole. Therefore, for the quasi-2D D^- centers in a magnetic field all internal transitions are bound-to-bound, and there are no photoionizing transitions. For X^-, both bound-to-bound and photoionizing inter-LL transitions to the continuum are possible.

The far infrared spectra encompass both bound-to-bound and bound-to-continuum transitions. The bound-to-bound transition $|0,0,M_z;T> \rightarrow |1,0,M'_z;T>$ is allowed by the usual selection rules ($M_z \rightarrow M_z+1$ for σ^+ polarization, spin conserved); it lies below e-CR in energy. One might expect this to be the analog of the strong T^- transition for the D^- center.[11] As can be shown, however, this transition is forbidden for X^- by an additional selection rule, which is associated with the existence of translational invariance in B. [12] Final three-particle states in the first LL can also belong to a continuum which has a rich structure. This includes a band extending in energy from the first electron-hole LL minus E_0 to the first LL (corresponding to the 1s exciton plus a scattered electron in the first LL, labeled $X_{00}+e_1$), and another band beginning at the first electron-hole minus $0.57E_0$ and extending to the first LL (corresponding to a $2p_+$ exciton plus a scattered electron in the ground LL, labeled $X_{10}+e_0$). Moreover, there is a band above each free LL corresponding to the bound internal motion of the two electrons with the hole in a scattering state (labeled $2e+h_0$). This band is of almost no importance for FIR X^- transitions.

The FIR absorption spectra reflect this rich structure of the possible final states. The transitions to the $X_{00}+e_1$ continuum are dominated by a sharp onset at the edge indicated by transition 2, *i.e.*, at an energy = e-CR plus the $|0,0,M_z;T>$ binding energy. In addition, there is a broader and weaker peak corresponding to the transition to the lower edge of the $X_{01}+e_0$ magneto-exciton band indicated by arrow 3. The latter may be thought of as the 1s→2p+ internal transition of the magneto-exciton, which is shifted and broadened by the presence of the second electron. Thus the X^--triplet behaves physically in the FIR absorption as an exciton that very loosely binds an electron, and the two "parts" of the complex can absorb the FIR photon, to some extent, independently. Transition 2 corresponds to exciting the loosely bound electron to the next LL, while transition 3 corresponds approximately to exciting the "strongly bound" electron to an excited state within the X_{00} complex, while leaving the loosely bound electron in the lowest LL. At finite fields and confinement these qualitative features are preserved. Since there is no singlet bound state in the strictly 2D, high field limit, we reserve discussion of finite field, finite confinement results for these transitions to Section V.

EXPERIMENTAL DETAILS

A powerful technique that circumvents many limitations associated with magneto-PL, or far-infrared (FIR) transmission spectroscopy on undoped samples or samples with low carrier densities has recently been developed. It has been applied to the investigation of the electronic properties of semiconductors and semiconductor nanostructures, [13] in particular, to the study of internal excitonic transitions in type I multiple quantum wells (MQWs). [14, 15] Optically detected resonance spectroscopy combines the sensitivity of visible/near infrared (IR) photon detection with FIR

absorption. [13-15,16-18,19] In most implementations a sample is illuminated simultaneously by two laser beams, one visible and one FIR. The chopped FIR laser excites electronic transitions whose energies are tuned into resonance with the photon energy by an applied magnetic field. Resulting changes induced in the near IR PL simultaneously excited by a visible laser having photon energy greater than the effective bandgap of the structure under investigation are synchronously detected. These changes in intensity and shape of a particular band-edge photoluminescence (PL) feature, which are induced by resonant absorption of FIR radiation, are monitored. Among the major advantages of ODR spectroscopy are very high sensitivity and spectral specificity of both the absorption in the FIR and the near IR PL lines. The former permits studies of undoped materials and structures and detection of resonances involving very low densities of (photoexcited) free carriers and excitons, and impurities. The latter offers the possibility of obtaining detailed information about mechanisms of energy transfer from the various internal transitions excited by the FIR to the different recombination channels.

In the present low temperature experiments electrons, holes and excitons were continuously created in MQW samples by optical excitation with the 6328 Å line of a He-Ne laser via an optical fiber as shown in Fig. 2. The PL from the structure was collected with a second optical fiber, analyzed with a single, 0.75 m, grating-monochromator and detected with a Si photodiode or a thermoelectrically cooled photo-multiplier. A CO_2-pumped molecular-gas laser was used to generate FIR radiation at a number of wavelengths ranging from 70.1 to 513 μm. The chopped FIR radiation excites various transitions -- electron or hole CR, and internal excitonic transitions (IET) in the present case. The energies of these transitions are tuned into resonance by an applied magnetic field of up to 15 T. A lock-in amplifier referenced to the FIR laser chopper was used in conjunction with a dedicated personal computer to record the ODR signal (the difference in PL with the FIR laser on and off). The computer was also programmed to step the spectrometer drive to track the center of the peak of the selected PL feature as it shifted with magnetic field; spectrometer resolution was selected to incorporate the entire excitonic PL line. The sensitivity of this system corresponds to changes in the PL signal as small as 0.1%.

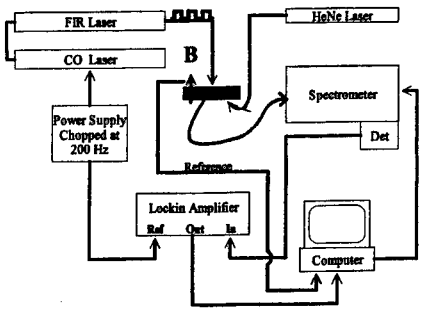


Fig. 2. Schematic diagram of the experimental setup for ODR. A particular PL feature selected by the monochromator is detected by a Si photo-diode or a photomultiplier and amplified by a lock-in amplifier referenced to the chopping frequency of the FIR laser. A dedicated PC records the signal as a function of magnetic field and also steps the spectrometer.

Table I: Characteristics of the GaAs/$Al_{0.3}Ga_{0.7}As$ MQW samples used in this study.

Sample Number	Layer Width Well/Barrier (nm)	Nominal Doping Well/Barrier (x 10^{10} cm^{-2})	Number of Repetitions
1	12.5/12.5	0/0	30
2	15/15	0/0	40
3	20/60	0/0	20
4	20/40	0/2	40

Four GaAs/$Al_xGa_{1-x}As$ multiple quantum well samples were studied in this work. The barrier composition was $x = 0.3$ in all cases, and Sample 4 was δ-doped with Si at the indicated sheet density. The other characteristics are given in Table I.

NEUTRAL MAGNETOEXCITONS

The results presented in this section extend earlier work on internal excitonic transitions by ODR spectroscopy. [14] The electronic states of two undoped GaAs/$Al_{0.3}Ga_{0.7}As$ MQW structures with well widths of 12.5 nm and 15 nm have been studied. The other sample characteristics are given in Table 1. With this powerful technique in a single series of experiments on individual samples, electron CR, hole CR, and several internal transitions of excitons were measured, thereby verifying and quantifying the predicted results of the symmetry inherent to such systems as discussed above.

The two principle hole CR transitions originating from the different spin states of the highest heavy-hole subband (hh1) Landau level ($|0,+3/2\rangle \rightarrow |1,+3/2\rangle$ and $|0,-3/2\rangle \rightarrow |1,-3/2\rangle$) are clearly identified from comparison with theoretical calculations described below. Here the hole states are labeled $|n_h\ m_J\rangle$, where $n_h = n' - m_J - 1/2$, with n' the harmonic oscillator index, and m_J the z-component of total angular momentum ($J = 3/2$). The hole wavefunction takes the closed form: $[F_{n'-2,\,3/2}, F_{n'-1,1/2}, F_{n',\,-1/2}, F_{n'+1,-3/2}]$. The following Luttinger parameters were used in the calculation: $\gamma_1 = 6.85$, $\gamma_2 = 2.1$, $\gamma_3 = 2.9$ and $\kappa = 1.2$.

An example of an ODR scan showing electron CR at 1.7 T, the $m_J = -3/2$ hole CR at 4.3 T and the $m_J = +3/2$ hole CR at 9.5 T is shown in the upper trace of Fig. 3. at an FIR laser energy of 23.1 cm^{-1} ($\lambda = 432.6$ μm). The predominantly negative-going ODR signals reflect a decrease in the PL associated with the free hhX caused by absorption of FIR radiation. The observed $m_J = +3/2$ hole CR occurs systematically about 2 cm^{-1} above the calculated position while the $m_J = -3/2$ hole CR agrees with the calculation to better than 1 cm^{-1}. The solid line through the electron CR data points is

the result of a three-band calculation of the non-parabolicity of the conduction band on the electron LLs. The calculation ignores the resonant magneto-polaron interaction of CR with the LO phonon at 296 cm^{-1} which depresses the CR energy measurably at magnetic fields above about 10 T. As discussed below, the simultaneous observation of electron and hole CR in low-dimensional structures along with the IETs allows the symmetry-derived relationship discussed previously to be verified, and the complex spectrum of IETs to be disentangled and individual transitions to be identified.

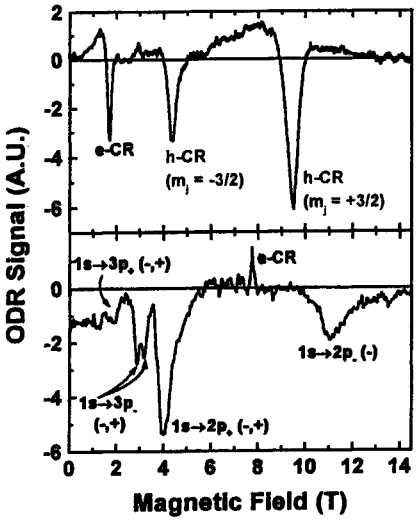


Fig. 3. ODR scans from Sample 1at 4.2 K as a function of magnetic field for FIR laser photon energies of (a) 23.1 cm^{-1}, and (b) 103.6 cm^{-1}. IETs in (b) are marked with (−) and/or (+) to indicate the electron and hole spin states of their constituents, *i.e.*, (+1/2, −3/2) or (−1/2, +3/2), respectively.

The lower trace in Fig. 3 shows several of the IETs as well as electron CR at 7.8 T at an FIR laser energy of 103.6 cm^{-1} (λ = 96.51 μm). The $1s\rightarrow2p_+$ IET, as well as *two* $1s\rightarrow2p_-$ IETs resulting from the [+1/2, −3/2] exciton (an exciton composed of an m_j = +1/2 electron and an m_J = −3/2 hole) and the [-1/2, +3/2] exciton are identified. A near degeneracy of the two $1s\rightarrow2p_+$ transitions (over this field region) prevents observation of two individual features. This assignment is supported by experimental observations, the known band structure of GaAs, and a physical understanding of the IETs in the high field limit. First, the measurements reflect the previously mentioned symmetry. Second, the slopes of the $1s\rightarrow2p_+$ and $m_J = \pm3/2$ $1s\rightarrow2p_-$ IETs at high magnetic fields are similar to those of electron and $m_J = \pm3/2$ hole CR, respectively. Third, ODR measurements with circularly polarized light at 84.2 cm^{-1} (λ = 118.8 μm) show that the nearly degenerate $1s\rightarrow2p_+$ features are stronger in the electron-CR-active polarization and the $1s\rightarrow2p_-$ features are stronger in the opposite polarization. Finally, in the high field limit the $1s\rightarrow2p_+$ transitions correspond to promotion of the electron from the lowest to the first LL. Since the energy difference between e-CR(+1/2) and e-CR(−1/2) is not measurable in this field range, the two corresponding allowed $1s\rightarrow2p_+$ features are also not distinguishable. On the other hand, the $1s\rightarrow2p_-$ transitions from the two different excitons correspond to promoting a hole from the lowest to the first hole LL. Since there is a large splitting between the ±3/2 h-CRs, there is a correspondingly large energy separation between the two $1s\rightarrow2p_-$ transitions.

The three highest energy excitonic features in the summary plot of Fig. 4 are tentatively identified as the $1s \rightarrow 3p_+$ transitions (nearly degenerate as in the $2p_+$ case), and the $1s \rightarrow 3p_-$ ($m_j = \pm 3/2$) transitions. These features can be seen in the lower trace of Fig. 3 at fields of 1.9, 2.8, and 3.2 T, respectively. Comparison of the energy difference between electron and hole CR with that of the $1s \rightarrow 3p_-$ to $1s \rightarrow 3p_+$ transitions is in agreement with this assignment. However, it is difficult to make this identification unambiguously due to the small number of data points and the weakness of the higher energy IETs. At 84.2 cm^{-1} the two $1s \rightarrow 3p_-$ transitions are not resolvable and appear as a single feature. More detailed measurements and calculations are needed to resolve this uncertainty.

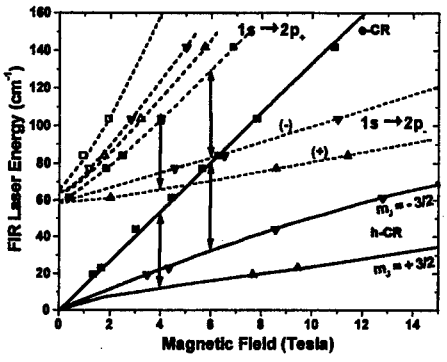


Fig. 4. Summary plot of the transition energies of the observed IETs and CR vs. magnetic field for Sample 1. Dashed lines are guides to the eye. Solid lines for e-CR and h-CR are calculations as described in the text. The open symbols are $1s \rightarrow 3p_\pm$ transitions. The lower arrows show the energy difference between e-CR and h-CR(+3/2) (at 4T) and h-CR(-3/2) (at 6T). The upper arrows are the lower arrows vertically displaced to originate on the $1s \rightarrow 2p_-(+)$ transition (at 4T) and the $1s \rightarrow 2p_-(-)$ transition (at 6T). Both terminate on the $1s \rightarrow 2p_-(\pm)$ IETs, as predicted from symmetry.

Figure 4 summarizes the observed internal excitonic transitions for different FIR laser energies for Sample 1. Lines are drawn as guides to the eye. Arrows are shown at magnetic fields of 4 and 6 T to display the electron/hole-CR, $1s \rightarrow np_\pm$ relationship. The length of the double-headed arrows represents the energy difference between electron CR and the appropriate hole CR measured from the data of Fig. 4. In the case of the $m_J = +3/2$ hole CR, a fit through the data points (parallel to the theoretically calculated line) was used. With the bottom of the arrow placed at the respective $1s \rightarrow np_-$ transition, the top of the arrow "predicts" the position of the $1s \rightarrow np_+$ transition. The CR energy difference is very close to the $1s$-$2p_\pm$ energy difference, and thus verifies the predicted symmetry-based relationship within experimental error.

In Fig. 5 ODR results from Sample 2 (15 nm well-width) are presented for several FIR laser lines. The general features are very similar to those obtained for Sample 1. At the longest wavelengths electron and hole CR are observed while at shorter wavelengths electron CR and internal transitions of neutral, heavy-hole excitons are seen.

A compilation of data from this sample is presented in Fig. 6. The various features are identified, and are compared with the data from Sample 1 (shown as the solid lines). As anticipated, the ODR features for the wider wells of Sample 2 occur at

systematically lower energies than the corresponding transitions from the narrower-well sample. Only one hole CR was observed in this sample ($m_J = +3/2$); so it is only possible to check the symmetry-derived relationship for this internal transition. The results in this case agree reasonably well with the prediction. There are two features that require additional explanation. There are two $1s \rightarrow 2p_-$ lines occurring rather close in energy (a much smaller splitting than calculated for the hole CR splitting), and two $1s \rightarrow 2p_+$ lines at fields above 4 T, where only one is expected. These pairs may be due to monolayer fluctuations in the well-widths, or one or more wells (out of the 40) that are narrower. The data for the 12.5 nm wells of Sample 1 extrapolate to a zero-field $1s \rightarrow 2p$ transition energy of 60 cm^{-1}, while the corresponding extrapolated zero-field energy for the 15 nm wells of Sample 2 is about 51 cm^{-1}, in reasonable agreement with calculations. [20] Data for a 20nm well-width sample (not shown) exhibit the expected qualitative trend to lower transition energies for weaker confinement; the extrapolated $1s \rightarrow 2p$ energy is 48cm^{-1}.

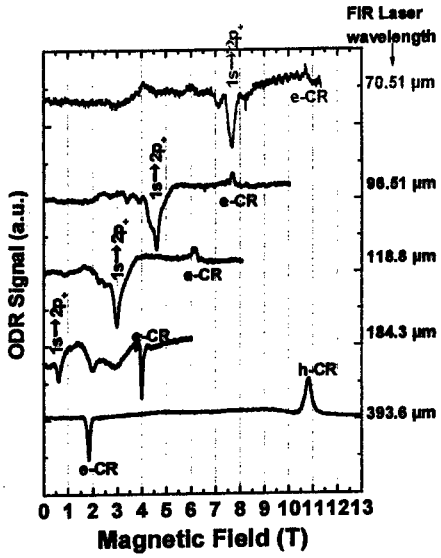


Fig. 5 ODR scans for Sample 2 (15 nm) at the indicated FIR laser wavelengths. Several transitions are labeled.

NEGATIVELY CHARGED MAGNETOEXCITONS

Figure 7 shows PL data obtained from Samples 3 (lower panel) and 4 (upper panel) at zero magnetic field. The separation of the two peaks labeled X and X^- is 10.5 cm^{-1}. The increase in the relative intensity of the X^- peak in Sample 4 results from the increased electron density in the wells due to

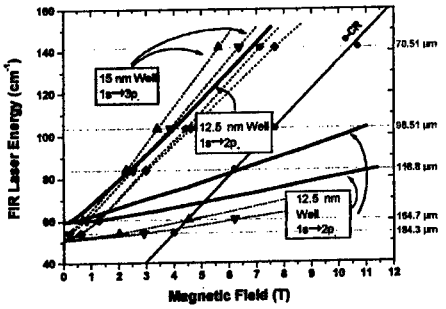


Fig. 6. Summary plot for Sample 2 (15 nm). Data for this sample are shown by the symbols connected by dotted lines. Electron CR is labeled, and the solid lines are the results for the lowest transitions (as indicated) of sample 1 (12.5 nm).

modulation-doping. Assignment of the lower energy peak to X^- is substantiated by magneto-PL measurements. These data show the characteristic small initial decrease in recombination energy with magnetic field (the final state of the recombination is the emitted photon plus an electron in the N=0 Landau level). An example of an ODR scan from each sample is presented in Fig. 8. The ODR signal obtained by tracking the X^- feature is plotted vs. magnetic field at a FIR photon energy of 85 cm^{-1} (very similar, but positive-going, ODR spectra are obtained by tracking the X-PL line). The sharp dip at 6.3 T is cyclotron resonance (CR). Essentially the same major features are observed in both samples, but certain of them are enhanced substantially in Sample 4 (particularly the features occurring just below e-CR and at about 3.7-3.8 T), indicating that these features are related to the excess electron density. The main feature in Sample 4 is the broad, strong minimum at 3.76 T; in sample 3 (undoped) this line is much weaker and occurs about 0.1 T higher in field. Another strong minimum in sample 4, asymmetrically broadened to low fields, appears just below e-CR; in Sample 3 this appears as a low-field shoulder. These features and the minimum at 4.75 T in sample 3 appear to be X^--related; the latter is also seen in sample 4 at slightly elevated temperatures.

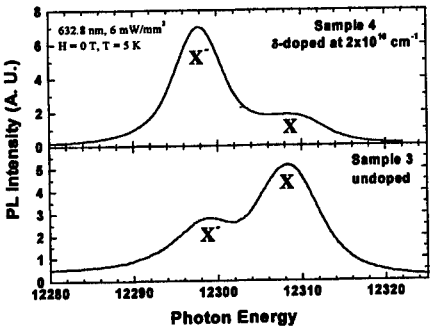


Fig. 7. Photoluminescence spectra at B = 0 for the two X^- samples discussed in the text. The neutral heavy-hole exciton (X) and the negatively charged exciton (X^-) features are indicated.

Assignments of the various features are based on the above qualitative trend, theoretical calculations in the high-field, strictly 2D limit, and numerical calculations for 20 nm wells at magnetic fields above 9T. Our experimental investigations of negative donor ions in quantum wells provide some guidance in assigning features; however, naïve comparisons are misleading in some cases due to the unusual behavior of X^- described in a previous section. Calculations, experiments and physical arguments for negative donor ions (D^-) all agree that the singlet transition is red-shifted from its one-electron $1s \rightarrow 2p^+$ neutral donor parent transition. Thus, naively, one might expect similar behavior for the X^--singlet. The features in Fig. 9 lying approximately 20 and 32 cm^{-1} above e-CR (open and solid triangles, respectively) are indeed lower in energy than the measured $1s \rightarrow 2p^+$ transition for X, except at the highest fields. The $1s \rightarrow 2p^+$ IET for hhX for a 20 nm well begins at an energy well-above either of these features at zero field, but has a smaller slope, and lies in the same region at high fields. The calculated $1s \rightarrow 2p$ transition energy at B = 0 is 49 cm^{-1}[20], and the extrapolated $1s \rightarrow 2p$ transition energy from experiments on internal transitions of neutral excitons for a 20 nm well-width sample yield a value of 48 cm^{-1}, both well-above the extrapolated values of any of the observed features in Samples 3 or 4. Numerical calculations for a 20 nm

well at 9T predict that the dominant X^--singlet transitions originate in a localized ground state associated with the zero LL (similar to that discussed in Section II for the triplet) but terminate in a continuum of states associated with the next LL (one electron promoted to the first excited LL). These transitions give rise to a broad, double peaked structure in the absorption spectrum; at 9 T the two peaks occur 24 and 42 cm^{-1} above e-CR, comparable to, but greater than, the positions of the measured features. Thus it is likely that the observed two lines are the singlet transitions. Other possible assignments [21] for the experimentally observed lines such as singlet transitions of (accidental) D^- ions in the wells can be excluded based on the measured energies in intentionally well-doped samples having the same well width. [13,22]

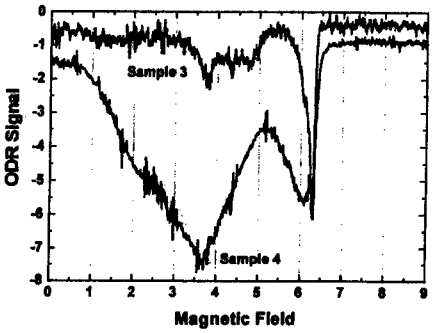


Fig. 8. A comparison of ODR Spectra for Samples 3 and 4 at a FIR laser wavelength of 117.7 μm. The various features are discussed in the text.

The line that lies just below e-CR in magnetic field (just above in energy) is assigned to a triplet (T^-) transition. The corresponding D^- transition is predicted to be blue-shifted and to lie very close to e-CR.[11] However, as discussed previously, although superficially very similar, the free motion of the center of mass of the excitons, and the continuum of scattering states involving the electron and a neutral exciton (the $X_{00} + e_l$ continuum in Fig. 1) lead to very different physics for X^-. All the oscillator strength for the X^--triplet internal transitions in the σ^+-polarization is shifted from the bound-to-bound transitions that dominate D^- to bound-to-continuum states lying below the first excited LL. For X^- the bound-to-bound transitions would be the $|0,0,M_z;T>$ to $|1,0,M_z+1;T>$ transitions (arrow 1 in Fig. 1), which have vanishing oscillator strength in 2D in a magnetic field. The dominant absorption features correspond to transitions to the edge of the X_{00}+e continuum with a tail of absorption to higher energies (as is observed in the experiments). For a 20 nm well,

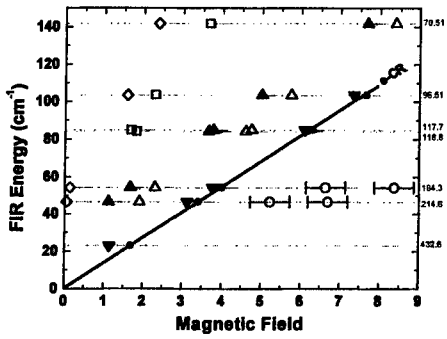


Fig. 9. A summary plot of E vs. B of the ODR lines for Sample 3 at several laser wavelengths (indicated). ▲ and Δ, possibly both singlet-related; ●, e-CR; ▼, bound-to-continuum triplet transition; o possible 1s - $2p_-$ -singlet transitions. □ and ◊, transitions to higher LLs.

numerical calculations give a peak in absorption about 5.5 cm^{-1} above e-CR. The experimental peaks lie approximately 3-4 cm^{-1} above e-CR, in fair agreement. From this comparison, we assign the broad feature with a peak just below e-CR in magnetic field and a tail to low fields (higher frequencies) to transitions to the $X_{00}+e_1$ continuum from the triplet ground state ($|0,0,M_z;T>$).

Finally, the broad and weak features at high fields and low photon energies (open circles with large error bars in Fig. 9) are somewhat perplexing. They are observed only in Sample 3. A possible assignment is $1S \rightarrow 2P_-$ transitions associated with the two different hole spin states, involving promoting a hole from the ground to the first Landau level. However, the absence of these transitions in Sample 4 seems to contradict this assignment. The weak features with large slopes in Fig. 9 appear to be higher excited state transitions.

In summary, we have presented evidence from ODR experiments for internal transitions of negatively charged excitons (X^-) in 20 nm $GaAs/Al_{0.3}Ga_{0.7}As$ MQWs. There are still a number of features that are not fully explained and which require further study. A definitive assignment of the various transitions awaits more detailed theoretical calculations at lower magnetic fields. [8]

CONCLUSIONS

The high sensitivity and general utility of the ODR technique are clear from the present results. The simultaneous detection of electron CR, $m_J = \pm 3/2$ hole CR, and several internal excitonic transitions has allowed a clear observation of the symmetry inherent in the electron and hole system, and verification of the predicted relationship between the energy differences between the np_+ and np_- internal transitions and the energy differences between e-CR and the two observed $m_J = \pm 3/2$ hole CRs. Calculations of the hole CR energies vs. B are in good agreement with the measurements.

Results on samples having excess electrons in the wells and exhibiting both X and X^- PL lines are interpreted in terms of internal transitions of X^- from localized, discrete ground states to a continuum of final states. In the case of the triplet-related transitions, this leads to the surprising result that the peak in the triplet resonance occurs above e-CR in contrast to analogous results for negative donor ions (D^-).

ACKNOWLEDGEMENT

The work at SUNY at Buffalo was supported in part by the National Science Foundation under grant DMR 9722625.

REFERENCES

[1] K. Kheng, R.T. Cox, Y.M. Daubigne *et al.*, *Phys. Rev. Lett.*, **71**, 1752 (1993).
[2] G. Finkelstein, H. Shtriktman and I. Bar-Josef, *Phys. Rev. Lett.*, **74**, 976 (1995).
[3] A.J. Shields, M. Pepper, D.A. Ritchie *et al.*, *Phys. Rev. B*, **51**, 18049 (1995).
[4] D. Gekhtman, E. Cohen, A. Ron *et al.*, *Phys. Rev. B*, **54**, 10320 (1996).
[5] O.V. Volkov, V.E. Zhitomirskii, I.V. Kukushkin *et al.*, *JETP Lett.*, **66**, 766 (1997).
[6] See *e.g.*, Z. X. Jiang, B. D. McCombe, Jia-Lin Zhu *et al.*, *Phys. Rev. B* **56**, R1692 (1997), and references therein.
[7] A.B. Dzyubenko, *JETP Lett*, **66**, 617 (1997).
[8] A.B. Dzyubenko and A.Yu. Sivachenko, to be published.
[9] J.J. Palacios, D. Yoshioka, and A.H. MacDonald, *Phys. Rev. B*, **54**, 2296 (1996).
[10] D.M. Whittaker and A.J. Shields, *Phys. Rev. B*, **56**, 15185 (1997).
[11] A.B. Dzyubenko and A. Yu. Sivachenko, *Phys. Rev. B*, **48**, 14690 (1993).
[12] A.B. Dzyubenko, to be published.
[13] J. Kono, S.T. Lee, M.S. Salib, *et al.*, *Phys. Rev. B*, **52**, R8654 (1995).
[14] M.S. Salib, H.A. Nickel, G.S. Herold *et al.*, *Phys. Rev. Lett.*, **77**, 1135 (1996).
[15] J. Černe, J. Kono, M.S. Sherwin *et al.*, *Phys. Rev. Lett.*, **77**, 1131 (1996).
[16] M.G. Wright, N. Ahmed, A. Koohian *et al.*, *Semicond. Sci. Techn.*, **5**, 438 (1990).
[17] S.J. Gubarev, A.A. Dremin, I.V. Kukushkin *et al.*, *JETP Lett.*, **54**, 355 (1991).
[18] R.J. Warburton, J.G. Michels, R.J. Nicholas *et al.*, *Phys. Rev. B*, **46**, 13394 (1992).
[19] G.S. Herold, H.A. Nickel, J.G. Tischler *et al.*, *Physica E*, **2**, 39 (1997).
[20] K.K. Bajaj, private communication.
[21] The possibility that the line represented by the solid triangles in Fig. 9 is related to $1s \rightarrow 2p^+$ absorption from neutral donors in the buffer/substrate cannot be completely excluded. Within experimental error the field dependent energies are the same. However, in ODR studies of many other samples we have not seen signals resulting from thermal coupling of resonant substrate absorption to the PL from the wells.
[22] S.N. Holmes, J.-P. Cheng, B.D. McCombe *et al.*, *Phys. Rev. Lett.*, **69**, 2571 (1992).

Optical Properties of Excitons in Semiconductor Quantum Wires.

V.Dneprovskii, E.Zhukov
M.V.Lomonosov Moscow State University,119899 Moscow, Russia
E.Mulyarov, S.Tikhodeev
Institute of General Physics, Russian Academy of Sciences, 117842 Moscow, Russia
Y.Masumoto
University of Tsukuba, Tsukuba, Ibaraki 305, Japan

Spectra of luminescence and linear and nonlinear absorption of semiconductor quantum wires crystallized in a transparent dielectric matrix have been investigated and interpreted in terms of excitonic transitions and filling of the exciton phase space. The calculated energies of excitonic transitions are in qualitative agreement with experimental data. The estimated values of exciton binding energies (>100 meV) in semiconductor quantum wires embedded in dielectric are a factor of several tens higher than in bulk semiconductors. The cause of this increase in the exciton's binding energy is not only dimensional quantization, but also the enhancement of Coulomb interaction, i.e. stronger attraction between electrons and holes owing to the large difference between dielectric constants of semiconductor filament and dielectric matrix.

Introduction

In recent years, researcher's attention has been attracted by quantum wires (QWRs), semiconductor nanostructures where carriers and excitons can move freely only in one direction, because they not only demonstrate interesting properties, but also show promise in view of their application to electronic and optoelectronic devices. In QWRs confinement reduces the distance between electron and hole in two dimensions and enhances their Coulomb interaction and therefore the exciton binding energy and its

oscillator strength. For the realistic QWRs (long filaments of small diameter $d \ll a_{ex}^{3D}$, where a_{ex}^{3D} is the effective radius of exciton in the bulk) the binding energy increases $\sim\left[\ln(d/a_{ex}^{3D})\right]^2$ and the effective length of exciton decreases: $a_{ex}^{1D} \sim \left|\ln(d/a_{ex}^{3D})\right|^{-1}$ [1]. The latter leads to the increase of the oscillator strength that is inversely the effective volume of exciton. The higher binding energy and oscillator strength of excitons in QWRs allowed to obtain effective laser emission even at room temperature [2,3]. Two-dimensional confinement increases the binding energy and oscillator strength of excitons, but only few times. The most important factor defining not high values of these parameters is the large dielectric constants ($\varepsilon_s > 10$) that are typical of semiconductors. In nanostructures, consisting of semiconductor and dielectric components, the Coulomb interaction between electron and hole inside the semiconductor layers or filaments may be considerably enhanced [4,5]. Qualitatively it can be explained resorting to the electric lines of forces that connect electron-hole pair. They propagate partially outside the semiconductor layer or filament in dielectric with the dielectric constant $\varepsilon_d << \varepsilon_s$. Thus it is possible to change the binding energy and the oscillator strength of excitons in QWRs constituting semiconductor filaments and dielectric matrix with different dielectric constants - realizing Coulomb interaction engineering [1].

This paper presents measurements of luminescence and linear absorption of InP, CdSe and GaAs QWRs crystallized in a transparent dielectric matrix and nonlinear absorption using powerful picosecond laser for excitation. The features observed in linear absorption and luminescence spectra can be interpreted in terms of excitonic transitions. The energies of excitonic transitions calculated using a variational procedure (with due account of image potentials and dimensional quantization of both electrons and holes) are in good accord with the measurements. Owing to the effect of dielectric enhancement [6-8], the exciton binding energies are very high (more than 100 meV). Physical processes leadiing to nonlinear effects in the absorption have been analyzed, in particular, filling of the exciton phase space, screening of excitons, renormalization and filling of

one-dimensional electron and hole bands when high-density plasma is generated in QWRs.

Experimental techniques and results

There are various techniques for fabrication of QWRs, namely, the molecular- beam epitaxy or metal-organic chemical vapor-phase deposition on preprocessed substrates, etching of two-dimensional semiconductor structures, and cleaving of a two-dimensional structure in a plane perpendicular to the surface with continued MBE process on the cleaved surface (fabrication of a T-shaped QWR), etc. These techniques, however, do not allow to produce samples in which the dimensions and density of QWRs are suitable to measure linear and nonlinear absorption spectra without an optical near-field microscope. We investigated samples manufactured using an alternative technique [9]: melted semiconductor material was injected in hollow nanometer size channels of crysotile asbestos tubes and crystallized. Given the large sample dimensions and density of crystalline QWRs, we could measure both linear and nonlinear absorption. The samples were densely packed regular structures of parallel crysotile asbestos nanotubes with an external diameter of about 30 nm containing InP, CdSe and GaAs crystalline QWRs The internal diameters of nanotubes were measured by a high-resolution microscope*. The samples in which semiconductor QWRs were grown contained nanotubes of two types: most of them had an internal diameter 4 - 4.8 nm, the rest had a diameter of about 5 - 6nm.

For nonlinear absorption measurements QWRs were excited by ultrashort pulses (with duration about 20 ps) of the second harmonic of a Nd:YAG mode-locked laser ($\hbar\omega$=2.33 eV). The pumping intensity was up to 100 MW/cm^2. The laser beam polarized in the direction parallel to the QWRs was incident normally on the sample surface and focused into a spot with a diameter of 200 μm. The central part of the excited spot was probed by a focused beam of "white" light (picosecond continuum). In

---

* These measurements were performed by N.A. Kiselev and D.N. Zakharov (Institute of Crystallography, Russian Academy of Sciences).

order to generate picosecond continuum, a fraction of laser light at the fundamental frequency was fed to a sell filled with heavy water. An optical delay line allowed us to delay the probing pulse and study the kinetic properties of the induced absorption. The spectrum of the probing pulse before and behind the sample was recorded using optical multichannel analyzer. In our experiments, we measured the differential transmission: $DT(\lambda)=[T(\lambda)-T_0(\lambda)]/T_0(\lambda)$ where $T(\lambda)$ and $T_0(\lambda)$ are the transmission spectra of the excited and nonexcited sample.

The spectra of linear absorption of InP, GaAs and CdSe QWRs grown inside crysotile asbestos nanotubes are given in Fig. 1, 2. Note the features in the linear absorption spectra, namely broad bands ("hills") peaking at the frequencies of exciton transitions in QWRs crystallized in dielectric matrix (see below) against the background of absorption increasing with decreasing wavelength. The position of the bleaching bands in the differential transmission spectra of GaAs [8] and InP QWRs coincided with these hills in the linear absorption spectra. The differential transmission spectra of CdSe QWRs crystallized in dielectric nanotubes (Fig.2) contain two bleaching bands: a short-wave band peaking at 1.98 eV and a long-wave band at about 1.8 eV. The positions of induced bleaching bands in the spectrum of differential transmission at zero delay between the pumping and probing pulses coincide with corresponding hills in the linear absorption spectrum.

The luminescence spectra of InP QWRs crystallized in crysotile asbestos nanotubes consist from two bands (Fig.3). The short-wave band peaked at 655 nm (4.2 K) and a long-wave band peaked at about 690 nm. The latter was detected only in some regions of the samples (the focused exciting laser beam was scanned across sample's surface). The full width at half maximum of luminescence band decreases at low temperature of the sample and in the case of recording the luminescence from the small area (Fig.4) using microscope.

The application of synchroscan technique and frequency-doubled mode-locked Ti-saphire laser for excitation has allowed to get the time-resolved spectra

of InP QWRs' luminescence (Fig.6).

The spectrum of InP QWRs' excitation (Fig.7) has been measured using Xe-lamp for pumping the samples and photon counting system for registration.

Theoretical model

Our theoretical description of the features in the linear absorption and luminescence spectra of QWRs is based on the model of Wannier-Mott exciton localized in a thin cylindrical semiconductor wire inside a dielectric matrix [6]. Given the large difference (a factor of five to six) between the dielectric constants of the semiconductor and matrix, image potentials play an essential role, alongside the dimensional quantization, which determines the quasi-one-dimensional character of excitons. These potentials lead to the effect of dielectric enhancement [4,5] (the exciton binding energy increases by a factor of several tens) and to renormalization of localizing potentials in QWRs owing to additional self-image potentials [7].

The separation between dimensional quantization levels in GaAs and InP (CdSe) QWRs varies between 100 meV for heavy holes (A and B valence subbands) to several hundreds of millielectronvolts for light holes and electrons. These values are comparable to or higher than the calculated exciton binding energies and much larger than the Coulomb correlation energy between dimensional quantization levels. This allows us to separate the carrier motion in the localizing potential perpendicular to the wire axis from the relative electron-hole motion along the QWR's axis. The complex spectrum of the valence band in InP, GaAs and CdSe and the hybridization of the light and heavy hole subbands (A and B subbands) under the localizing potential deserve a dedicated investigation (see, for example, Ref. [10]). Under the conditions of dimensional quantization, however, the valence band degeneracy (quasi-degeneracy in the case of CdSe QWRs is lifted and the hole subbands are split from one another (their effective masses remain anisotropic). The effects of band nonparabolicity in this case are suppressed, which allows us to neglect the hole mass renormalization when the subband splitting is large and use the hole effective masses [11] obtained at room temperature.

Thus, within our theoretical model we consider two types of excitons. In InP, GaAs we have e-hh excitons formed by holes which are light along the wire axis and heavy in the plane where the motion is confined, and e-lh excitons with holes that are heavy along the wire axis and light in the confinement plane. In CdSe, these are excitons formed by holes from A and B valence subbands.

Note that the two-dimensional localizing potentials acting on electrons and holes include, as in Ref. [7], the self-image potentials of charges. The self-image potentials essentially modify the quantum well shape by reducing its depth, which affects primarily the renormalized semiconductor band gap, hence the exciton peak position.

The exciton parameters, namely the binding energy, wave function, and dimension along the wire axis, are calculated using the variational technique [6] taking into account the contribution of image potentials to the energy of Coulomb interaction between electrons and holes averaged over wave functions of the transverse motion of carriers. The dependence of the exciton transition energies in InP QWRs upon the radius of QWR is presented in Fig.5 for different temperatures.

Discussion of results.

Unlike three- and two-dimensional semiconductor systems, optical properties of quasi-one-dimensional systems are largely controlled by excitonic transitions owing to the anomalously large concentration of oscillator strength at frequencies of excitonic transitions [12,13]. In linear absorption spectra of crysotile asbestos samples containing InP, GaAs and CdSe QWRs (Fig.1,2), we also observe absorption that monotonically grows with the photon energy. It seems that a fraction of the semiconductor material is crystallized between bunches of crysotile asbestos nanotubes in the form of relatively large microcrystalls. The interband absorption in the bulk semiconductor (microcrystalls unaffected by dimensional quantization) can contribute a monotonic component to the absorption spectrum.

This conjecture is confirmed by the spectra of the differential transmission of crysotile asbestos samples containing CdSe (Fig.2), which demonstrate, alongside the nonlinear absorption of CdSe QWRs, nonlinear changes near the bulk CdSe absorption edge

(about 700 nm) . The 1.79-eV band in differential transmission spectrum corresponds to transitions in bulk CdSe, and its blue shift and bleaching under high pumping excitation can be attributed to renormalization of the semiconductor band gap, filling of electron and hole bands, effects of Coulomb screening, and filling of the exciton phase space [14,15]. Differential absorption spectra of pumped samples allow us to separate the nonlinear absorption in QWRs due to "saturation" of excitonic transitions (see below). It seems that changes in the bulk absorption occur only in the band near the fundamental absorption edge after fast relaxation (in less than 10^{-11} s) of carriers to the band minimum, whereas the discrete bleaching band of CdSe (1.9-2.1 eV) arises due to changes in the absorption of nanostructures. Thus we can get rid of the background due to the bulk semiconductor by measuring differential transmission spectra.

In accordance with the suggested theoretical model, we attribute the peculiarities in the linear absorption spectra (Fig.1) and bleaching bands in differential transmission spectra of samples with InP, GaAs and CdSe QWRs to linear absorption by e-hh excitons in InP, e-hh and e-lh excitons in GaAs, linear and nonlinear absorption of A- and B-excitons in CdSe (Fig.2) QWRs with diameters 4-4.8 nm and with diameters exceeding 4.8 nm. The calculated energies of exciton transitions are shown by arrows in Fig.1,2. The great width of the excitonic absorption bands (Fig.1,2) and luminescence bands (Fig.3,4) is probably determined by the inhomogeneous broadening - mainly by size dispersion of QWRs. The energy of exciton transition in QWR, embedded in dielectric is very sensitive (Fig.5) to its lateral dimensions. The cooling of the samples with QWRs of InP allows to decrease the homogeneous broadening, while excitation of small area allows to exclude partly the inhomogeneous broadening of excitons luminescence bands (Fig.4).

The calculations of the exciton transitions that are in good agreement with measured linear absorption and luminescence also allow us to analyze features of the nonlinear spectra of QWRs. In the samples of CdSe QWRs the energies of transitions due to A- and B-excitons are close to each other (the separation between them is within the spectral line width) owing to the small difference between effective masses of A- and B-holes and initial small separation between these subbands, as a result, these pairs of

excitonic transitions form wide excitonic absorption bands (Fig.2). As the optical pumping intensity increases, different nonlinear processes in QWRs coexist and compete with one another, namely, the effect of filling of the phase space and screening of excitons, filling of electron and hole energy bands, and renormalization of the band gap in the one-dimensional semiconductor [16]. Generation of excitons and high density plasma leads to bleaching in the exciton absorption band (Fig.2) because the electron-hole interaction is moderated owing to screening effects and filling the phase space. The effect of phase space filling manifests because excitons are composed from electrons and holes, which are subject to Pauli's exclusion principle, whereas only electron-hole states unoccupied by electrons and holes can be involved in forming excitons. The screening leads to a spatial redistribution of electrons and holes. This process, which is usually suppressed in quasi-one-dimensional structures, can be essentially intensified in the presence of image charges. Both these effects - filling of the phase space and Coulomb screening - shift the exciton band to the short-wave side. On the other hand, the band gap renormalization taking place at high densities of photogenerated nonequilibrium carriers (it is up to 10^7 cm^{-1} in our experiments) leads to a long-wave shift of the exciton absorption line.

The decay of the intensity of InP QWRs' luminescence at the wavelength of e-hh exciton transition (655 nm at 2K and 660 nm at 300K) consists from fast and slow parts (Fig.6). The pumping intensity of Ti-saphire laser was too low to explain the kinetics of luminescence by any nonlinear process. The curves in Fig.6 can be approximated by two exponents ($I = A\exp(-t/\tau_1) + B\exp(-t/\tau_2)$) with τ_1=550 ps (2K), 400 ps (300K) and τ_2 =10 ns (2K), 4 ns (300K). The linear recombination at one and the same frequency with different relaxation times may be explained by the capture of part of excited carriers in surface localized states and their following slow recapture [17].

A new band in the vicinity of 590 nm has been registered in luminescence excitation spectrum of InP QWRs (Fig.7). The intensity of luminescence was measured at 650 nm with 1.5 nm gates. The increasing of the luminescence intensity in the case of tuning the

wavelength of the exciting beam from 570 to 600 nm may be explained by e-lh exciton absorption or by the peculiarities of quasi-one-dimensional interband absorption [13]. It is possible to estimate the e-hh exciton binding energy (200 meV) if the latter explanation is fair. This value corresponds to that calculated, using data in Fig.5.

Conclusions

Features of luminescence, linear and nonlinear absorption spectra of semiconductor quantum wires imbedded in dielectric nanotubes have been interpreted in terms of excitonic transitions and their saturation (filling of phase space and screening of excitons)

Owing to the effect of dielectric enhancement, a considerable increase (exceeding 100 meV) of the exciton binding energy has been observed in the studied samples. The theoretical estimates of exciton transition energies in quantum wires provide a fairly accurate description of features in linear absorption and luminescence spectra.

The enhancement of both the binding energy and the oscillator strength of excitons in semiconductor-dielectric quantum wires and the possibility to increase the strength of Coulomb interaction, responsible for the binding of electron-hole pairs to excitons, by combining semiconductor and dielectric materials with different values of dielectric constants open new possibilities for creation of excitonic devices operating at room temperature.

The work was supported by the Russian Fund for Basic Research (grants 96-02-17339, 97-02-17600), Physics of Solid-State Nanostructures program (grants 97-1083 and 97-1072), Single Quantum Dot Project, Erato (JST) and the project Materials for Electronic Techniques. We are indebted to V.V.Poborchii and S.G.Romanov for supplying the samples for our experiments, N.A.Kiselev and D.N.Zakharov for electronic microscope measurements, and to R.Zimmermann for constructive criticism.

References

[1] L.V.Keldish, phys.stat.sol.(a),**164**, 3 (1997)

[2] W.Weigscheider,l.n.Pfeiffer, M.M.Dignam, A.Pinczuk, K.W.West, S.L.McCall, R.Hull, Phys. Rev. Lett. **71**, 4071 (1993)

[3] E.Kapon, Proc.IEEE **80**, 398 (1992)

[4] N.S.Rytova, Dokl.Akad.Nauk SSSR **163**,1118 (1965)

[5] L.V.Keldysh, Pis'ma Zh.Eksp.Teor.Fiz. **29**, 716 (1979)

[6] E.A.Mulyarov, S.G.Tikhodeev, JETP **84**,151 (1997)

[7] E.A.Mulyarov, S.G.Tikhodeev,N.A.Gippius, T.Ishihara, Phys.Rev. B**51**,14370 (1995)

[8] V.S.Dneprovskii,E.A.Zhukov, E.A.Mulyarov, S.G.Tikhodeev, Zh.Eksp.Teor.Fiz. **113**, August(1998)

[9] V.V.Poborchii,M.S.Ivanova, I.A.Salamatina, Superlatt. and Microstr. **16**, 133 (1994)
V.N.Bogomolov, Usp.Fiz.Nauk **124**, 171 (1978)
V.Dneprovskii, N.Gushina, O.Pavlov, V.Poborchii, I.Salamatina, E.Zhukov, Phys.Lett. A **204**, 59 (1995)

[10] G.E.W.Bauer, T.Ando, Phys. Rev. B **38**, 6015 (1988)

[11] Landolt-Bornstein, New Series, Group III, Vol. 17, Springer-Verlag, Berlin (1982)

[12] T.Ogawa, T.Takagahara, Phys. Rev. B **43**, 14325 (1991); Phys. Rev. B **44**, 8138 (1991)

[13] S.Glutch, D.S.Chemla, Phys. Rev. B **53**, 15902 (1996)

[14] V.D.Egorov, Hoang Xuann Nguyen, R.Zimmermann, V.S.Dneprovskii, M.Kaschke,, D.S.Khechinashvili, phys. stat. sol. (b) **159**, 403 (1990)

[15] H.Haug, S.W.Koch, Quantum Theory and Electronic Properties of Semiconductors, World Scientific, Singapore (1990)

[16] S.Benner, H.Haug, Europhys. Lett. **16**, 579 (1991)

[17] M.G.Bawendi, P.J.Carroll, William L.Wilson, L.E.Brus, J.Cem.Phys. **96**, 946 (1992)

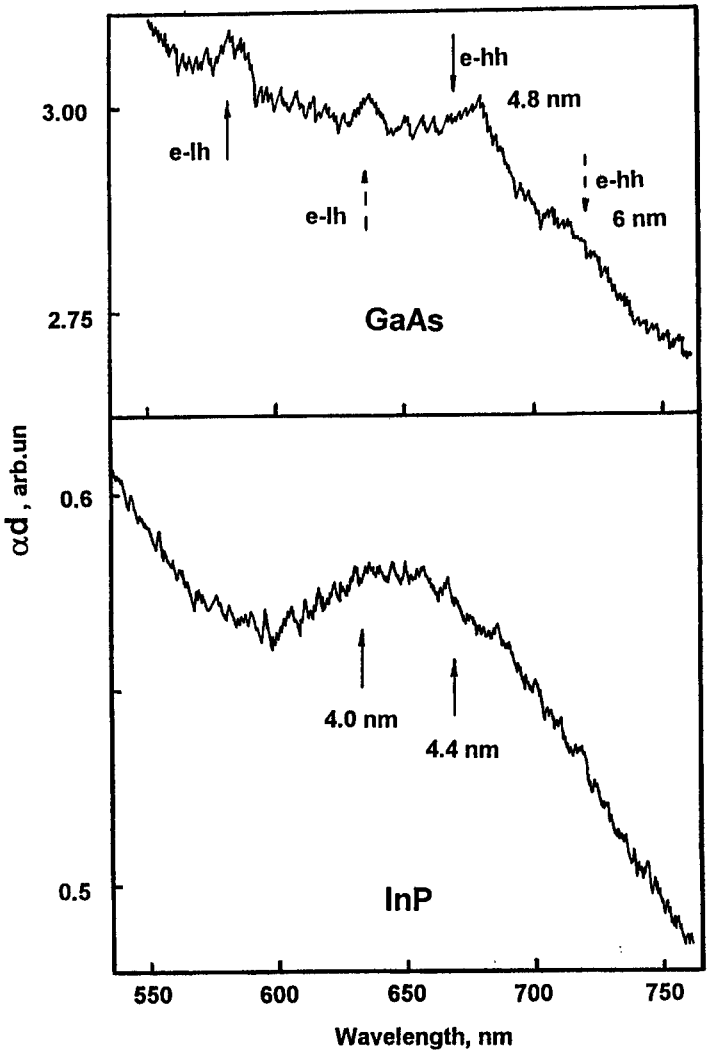


Fig. 1

The absorption spectra of GaAs and InP QWRs (T=300K). The calculated energies of exciton transitions of QWRs with different diametres are shown by arrows.

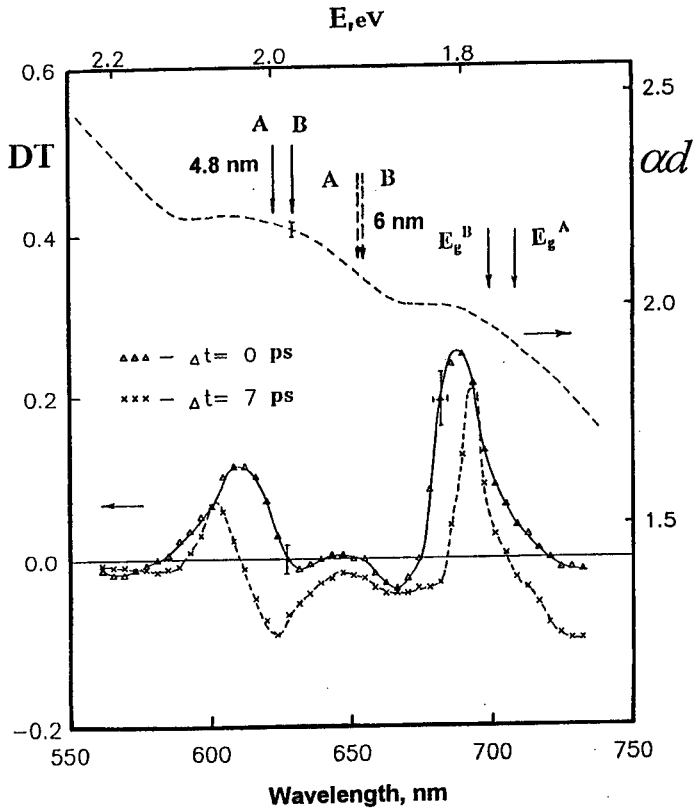


Fig. 2

The absorption and differential transmission spectra of CdSe QWRs. The calculated energies of exciton transitions and the energy gaps of the bulk CdSe are shown by arrows.

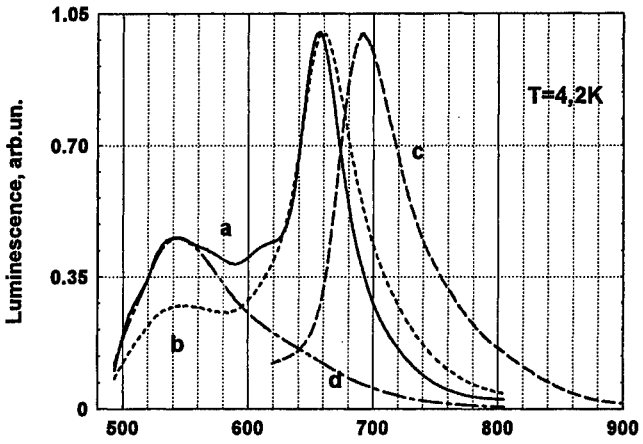


Fig. 3
The photoluminescence of InP QWRs for different regions of the sample (a-c) and for chrysotile asbestos (d)

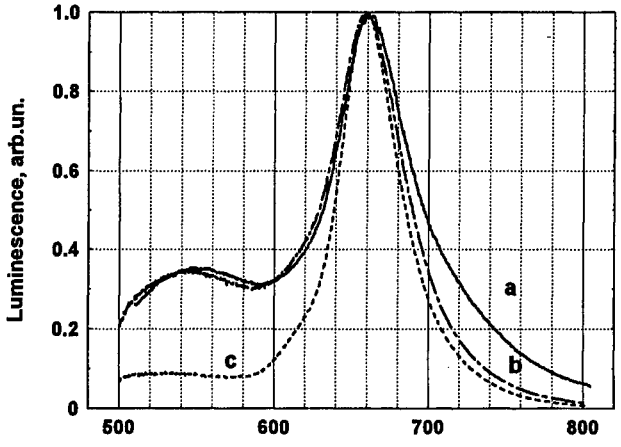


Fig. 4
The photoluminescence of InP QWRs a) T=300K, b), c) the luminescence is recorded from small area using microscope at different temperatures: T=300K (b), T=15K (c).

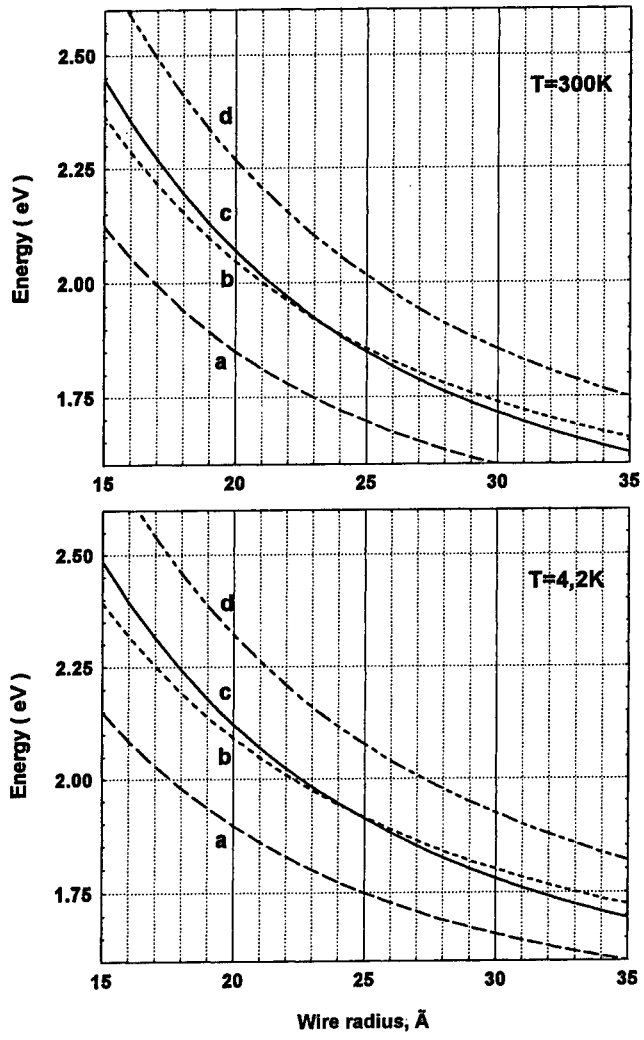


Fig. 5

The dependence of exciton transition energies and energy gaps of InP QWRs upon the wire radius: a)for e-hh-exciton, b) e-hh-gap, c) e-lh-exciton, d)e-lh-gap

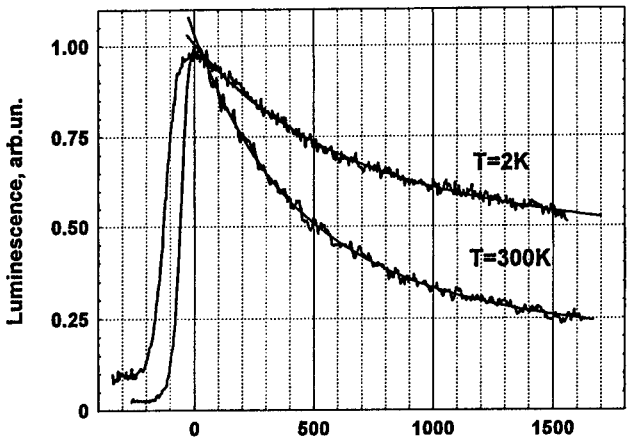


Fig. 6
Time-resolved luminescence of InP QWRs at λ=655 nm (2K) and λ=660 nm (300K)

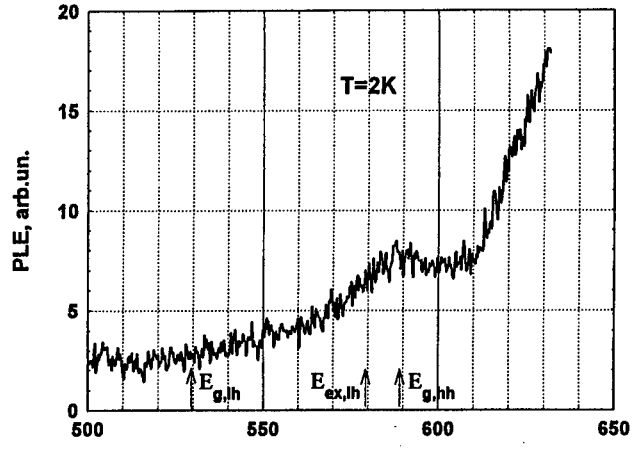


Fig. 7
The photoluminescence excitation spectrum of InP QWRs at λ=650 nm

Quantum Dot Structures

How to Describe the Electronic Structure of Semiconductor Quantum Dots

Alex Zunger

National Renewable Energy Laboratory, Golden Co 80401

ABSTRACT

I describe a new strategy for predicting the electronic properties of zero-dimensional semiconductor quantum dots, including the excitonic spectrum. This methodology was applied recently to both "free standing" (e.g. colloidal) and t semiconductor-embedded (e.g. self-assembled) dots.

1. Experimental advances in growth and characterization of semiconductor quantum dots call for theoretical methods capable of predicting the measured electronic structure as a function of the shape and size of the dot. The objectives of such an endeavor are to predict (a) the single-particle energy levels and their confinement energies, (b) the electron-hole Coulomb and exchange energies, (c) the ensuing two-particle excitonic spectrum and transition probabilities, (d) the energies needed to charge quantum dots ("Coulomb blocade") and (e) the nature of the electronic states in the system (e.g. s,p,d..., heavy hole-like, light-hole-like, Γ-like or X-like, etc).

2. For quantum-wells and superlattices (that are confined in only one dimension), there is a highly successful "standard model" for addressing the above theoretical requirements. This is the well-known effective-mass-approximation (EMA) k•p method. In this approach the wavefunctions of the nanostructure are expanded in terms of N_B Bloch states of the underlying bulk -periodic solid. This expansion is limited, however, only to Brillouin-zone center ("gamma") Bloch states. If $N_B = 1$ we have the "single band EMA" or "particle in the box". If we use the top of the valence band Γ_{15V} state to expand the wavefunction of the nanostructure then $N_B = 6$ (due to 3-fold spatial degeneracy of this p-state, times the 2-fold spin degeneracy). This approximation is called "6x6 k•p". If we add to the basis the bulk conduction band minimum Γ_{1C}, then $N_B = 8$ and the approximation is called "8x8 k•p". For quantum wells and superlatteces, the "8x8 k•p" model has provided a very good account of the electronic structure, using input ("Luttinger") parameters drawn

from the band structure of the bulk-periodic solid.

3. Quantum-dots lack translational periodicity in all 3 spatial directions, so they are conceptually more removed from the 3D bulk-periodic crystal than are the 2D periodic quantum wells. Would a bulk-crystal-derived formalism such as the EMA suffice for describing quantum dots? Mathematically, this question means "how many gamma-like 3D periodic bulk Bloch states does it take to capture the essential features of the wavefunctions of nD periodic nanostructure?" (n=0 for dots, n=1 for wires).

4. Until recently, the answer to the above question was unknown, since there wasn't any method capable of using an arbitrary number N_B of bulk basis functions for expressing the nanostructure wavefunctions. In fact, the success of the EMA was examined primarily by contrasting its predictions directly with experiments. This is usually an eminently reasonable way to test the validity of any theory. However, this is not the case if one uses adjustable parameters to fit the theory to experiment. This was often done in application of the EMA to quantum dots. Indeed, often the EMA parameters were adjusted to fit the experiments they claim to explain theoretically. For example, consider k•p calculations on CdSe dots: Norris and Bawendi [1] say, "We use standard nonlinear least-squares method to globally fit the experimental data...our fitting routine adjusts three parameters: the Luttinger band parameters $\gamma 1$ and $\gamma 2$ and the potential barrier for electrons." In another work, Efros et al. [2] say, "The position of the quantum size levels are very sensitive to the valence band energy parameter; those used for calculation...give the best description of the CdSe microcrystal absorption spectra." Wind et al. [3] say, "Fig. 1 shows the experimental values...the lines in fig. 1 have been calculated following a model including the valence mixing...The best correspondence could be obtained [by] choosing a Luttinger parameter $\gamma = 0.38$..." Since in such cases the EMA theory is explicitly fit to experiment, it cannot examine the legitimacy of either its successes or its failures. In these cases, good agreement with experiment does not necessarily imply good theory.

5. So how many gamma-like 3D-periodic bulk states *are* needed to expand a wavefunction of a nanostructure? The answer was recently given by Wood et. al [4-5] for AlAs/GaAs (001) superlatteces and quantum wells, by Wang and Zunger [6] for X-like states in bulk solids, and by Fu, Wang and Zunger [7,8] for quantum dots. These authors "projected" the pseudopotential-calculated wavefunctions of superlatteces, quantum wells and dots onto the gamma-like states of bulk-periodic solid, finding how many of the latter are needed for expanding the former. The unpleasant answer is that a reasonable description of even the *band* structure away from the Brillouin zone center requires as many as $N_B = 30$ gamma bands, (see figures 3 and 4 in Ref.6), while small quantum dots require a *few hundred* bulk bands for a

quantitative description.

6. So what happens if we disregard the above noted "mathematical warning" and go ahead using the EMA with a small number N_B of bands? Can we adjust the many parameters and still get away with this? The answer is that one can not do this with impunity. For example, the EMA with small N_B can even misrepresent the correct *physical symmetry* of the nanostructure, leading to qualitatively incorrect predictions. Here are a few examples:

● A film made of p monolayers of zincblende material can either have or lack reflection symmetry, depending on whether p is odd or even. Consequently, the energy levels of thin films oscillate [9] with the film thickness. The continuum-like EMA does not recognize reflection symmetry *and produces a monotonic dependence of the film energy levels on the film thickness.* Pseudopotential calculations [9] produce the expected odd-even oscillations.

● A spherical dot made of zincblende material (e.g., InP, AlAs) does not have spherical symmetry. Its physical T_d (tetrahedral) symmetry permits, in fact, mixing of s-like with p-like character in the wavefunctions. [10] The simple EMA, on the other hand views such dots as spherical with "s-like" or "p-like" states. This led to the expectation [11,12] that single-photon absorption experiments ("s→s" or "p→p") and two-photon ("s→p") experiments will reveal radically different spectra, reflecting "different level symmetries". In fact, the measured single-photon and two-photon spectra are virtually identical. This is the case for CuCl [11], CdSe [12] and InP dots. Analysis [10] of the real wavefunctions reveal indeed heavy mixing of s and p character, consistent with experiment.

● A square-based pyramidal dot made of zinc blend material (e.s, InAs) does not have C_{4v} symmetry [13]. Consequently, the two in-plane directions [110] and [$\bar{1}$10] are not equivalent. In contrast, the EMA k•p views the square-based pyramid as a classic pyramid, with 4-fold rotation symmetry. Consequently, the polarization ratio P[110] / P[$\bar{1}$10] for the lowest electron-hole transition in SK dots of InAs is ~ 1 in k•p. A realistic Pseudopotential calculation [14] gives a ratio of 1.3. The same problem exists in (001) superlatteces that lack a common atom, e.g. [15] InP/GaAs or InAs/GaSb: k•p leads to a polarization ratio of 1, while experiment and pseudo potential calculation give a "giant polarization".

7. Other difficulties when using the EMA:

● Sometimes quantum dots have X-derived or L-derived low-energy states that are missed by the Γ based EMA. Examples include: (a) Sufficiently small GaAs dots,

wires and films have an X_{1C}-like conduction band minimum [16,17,18] (b) The second bound electron state of InP dots is L_{1C}-derived [10] (c) Under hydrostatic pressure, InP dots [19] and GaAs-embedded-InAs dots[20] have X_{1C}-derived conduction band minium. (d) The Γ-X coupling matrix element in superlatteces and quantum dots[19,20] can be as large as the level spacings.

● Real surfaces (e.g. chemically-passivated, or reconstructed, or defects at surfaces) and real interfaces (e.g. coherently strained and/or inter diffused) can not be modeled by the EMA that is inherently "surfaceless".

● In strained quantum dots (e.g. InAs embedded in GaAs) the electronic levels shift and split due to strain, but EMA-based methods describe this coupling only via *linear* deformation potentials. Recent calculations [14] have shown that the linear approximation can lead to errors of a few hundred meV for strongly strained dots (e.g. InAs/GaAs, with its 7% strain).

8. Is there an easy way out?

One could add more basis functions to the conventional k•p, but this comes with an unpleasant rapid increase in mathematical complexity and in the number of fictitious adjustable parameters that are not "physical observables" which could be measured. It is likely that the inertia of the EMA for quantum dots, propelled by its many successes in higher-dimensional nanostructures (e.g. quantum wells) and its inherent simplicity and adjustability, will continue to promote its widespread use, especially among experimentalists, as proclaimed in this meeting by Ray Tsu. However, there is a possibility of moving forward, using a completely different approach, which we have recently developed [21-27]. It is not always an *easy* way out, but it overcomes *all* of the objections we have raised above, it provides all physical quantities listed in paragraph 1, and can be applied to dots, wires and films of almost any semiconductor, with any shape or strain profile.

9. So what is the basic idea?

Molecules, quantum dots and solids are made of atoms that can be characterized by approximately transferable atomic pseudopotentials $v_\alpha(r)$. The EMA does not recognize atoms or potentials. Instead, it describes the electronic structure via matrix elements over Bloch functions, retaining the "coarse", or "long-wavelength" characteristics of the molecule or dot, thus smoothing over its "fine", or "atomistic" structure. Not only does this remove sometimes the true physical symmetry of the molecule or dot, but it also results in a large number of parameters (=matrix elements) whose magnitude and coupling to strain are difficult to determine

as $N_B \to \infty$. Instead, we will treat a molecule, dot or solid as a linear combination of atomic pseudopotentials placed spatially where atoms are located. This immediately gives you the right symmetry of the object at hand, including the opportunity to model its surface or interface with atomic detail. Also, since such molecular potentials depend on the atomic positions within the molecule, and since "strain" is merely a collection of (displaced) atomic positions, this approach gives you in a natural way the full coupling of strain to the electronic structure. What we need to know is the screened atomic potential for each atomic type. The theory of construction of screened atomic psudopotentials that correctly reproduce a given set of measured bulk or molecular properties and *ab-initio* calculated wavefunction is described in refs [21,28] and will not be discussed here. The full informational content of the chemistry of our problem is encoded in the functions $V\alpha(r)$ for each atom type α.

Once we have constructed the molecular potential, we place each molecule/dot in a fictitious large unit cell and periodically repeat the cell so as to create (artificial) 3D periodicity. When studying 'free-standing" (e.g. colloidal) dots we surround each dot in a unit cell by a chemical passivation layer, followed by a thicker layer of vacuum, intended to separate the quantum dots. When studying matrix-embedded (e.g. InAs-in-GaAs "self assembled") dots, we surround each dot in a unit cell by its (usually strained) matrix material.

Now that we have a mathematically translationally periodic Hamiltionian, we can find its eigen solutions by employing much the same methods used in ordinary "band theory". We can expand the wavefunction of the dot as a linear combination of plane waves[22-27], or as a Linear Combination of Bloch bands (LCBB)[29]. The problem is that a dot has many more atoms per supercell (10^3-10^6) than an ordinary periodic solid ($\sim$10 atoms). Thus, the size of the Hamiltionian matrix for a dot is too large. Fortunately, however, the problem can be drastically simplified by realizing that the physics of quantum dots is often restricted to the energy levels in the vicinity of the band gap. For example, a dot made of 1000 Si atoms has 2000 occupied valence levels (assuming s+3p states for each atom), but all we care about is the 10-100 highest energy valence levels (plus a similar number of empty conduction states). We have invented a "Folded Spectrum Method" [22, 26] that permits us to find eigen solutions in a desired "energy window", without wasting computational effort on obtaining the remaining, less interesting states. Thus, the total computational effort rises only slowly (in fact, linearly) with the number of atoms N in the dot, rather than the N^3 scaling in common band structure methods.

Once we have found the energy levels and wavefunctions in the vicinity of the HOMO and LUMO, we can set-up a "configuration interaction" treatment [30,31] for describing the excitonic spectra beyond "mean field" theory. An excitonic state

is formed form a linear combination of products of a valence orbital times a conduction orbital. The expansion coefficients in this linear combination are found by seeking a variational solution. The hamiltonian matrix of this problem corresponds to both Coulomb and exchange electron-hole interactions that are computed explicitly from the orbitals. Solving the variational problem gives the two-particle excitonic levels and wavefunctions, thus the excitonic absorption spectrum.

10. Summary and references of what has been calculated so far with this method for free-standing (colloidal) dots:

- Band gap vs size for Si [26,32,33], InP [34], CdSe [35,36] and InAs [37] dots. The size scaling R^{-m} has $m \approx 1\text{-}1.5$ not $m=2$ as in EMA.

- Wavefunction analysis of InP dots, showing that the HOMO is s-like, not p-like as predicted by the EMA [8].

- The electron-hole Coulomb energies [38] of Si, InP and GaAs, showing that the EMA overestimates them by up to 40%. The size scaling R^{-n} has $n<1$.

- The electron-hole exchange energies [30] of Si, InP and CdSe showing that an hitherto neglected, long-range component exists, reflecting monopole-interactions. The size scaling R^{-p} has $p \sim 2$, not $p=3$ as previously assumed.

- The full excitonic spectrum of CdSe [36], InP [10] and InAs [37] dots.

- The effect of imperfect surface passivation (leading to cation and anion "dangling bonds") on the electronic structure, including the appearance of localized gap states capable of trapping carriers [34].

- Effects of pressure on direct-to-indirect transitions in InP dots [19].

- Effects of size on direct-to-indirect transitions in GaAs dots [16,17].

11. Summary and references of what has been calculated with this method so far for embedded ("self assembled") quantum dots:

- The prediction that while free-standing InP dots have a direct band gap, a GaP-embedded InP dot has an interface-localized "indirect" conduction band [39].

- The prediction that under pressure, the GaAs-embedded InAs dot will also have an interface-localized conduction band [20].

● The prediction [40] that a set of nested spheres ("Russian Doll") of GaAs/AlAs/GaAs/AlAs... can be made so that the hole wavefunction is localized on the central GaAs sphere, while the electron wavefunction is localized on an external shell, thus affecting charge-separation *on the same material.*

● The electronic structure of square-base InAs pyramid embedded in a GaAs matrix, showing [14,41,25] (a) splitting of the electron p state (b) strong in-plane anisotropy of the lowest excitonic transition (c) that as many as 5 confined electron levels exist and (d) that the hole states are so heavily intermixed that no (s, p, d...) nodal structure remains. All of these predictions are surprising in light of previous EMA calculations.

ACKNOWLEDGMENT

I would like to thank my collaborators in this project A. Franceschetti, H. Fu, J. Kim, L.W. Wang and A. Williamson. This work was supported by US DOE through OER-BES-DMS.

References

[1] D.J. Norris and M.G. Bawendi, *Phys. Rev B* **53**, 16338 (1996)

[2] A. Efros, V.A. Kharchenco and M. Rosen, *Solid State Commun.* **93,** 281 (1995)

[3] O. Wind, F. Gindele, and U. Woggon, *J. Lumin.* **72-74,** 300 (1997)

[4] D.M. Wood and A. Zunger, "Pseudopotential-based multiband k•p method for 250,000-atom nanostructure systems", *Phys. Rev B.* **53,** 7949 (1996)

[5] D.M. Wood, A. Zunger and D. Gershoni, "Origins of k•p errors for (001) GaAs/AlAs heterostructures", *Europhysics Letters* **33,** 383 (1996)

[6] L. W. Wang and A. Zunger, "Pseudopotentiall-based multiband k • p method for 250,000-atom nanostructure systems," *Phys. Rev. B.* **54**, 11417 (1996)

[7] H. Fu, L.W. Wang. and A. Zunger, "On the applicability of the k • p method to the electronic structure of quantum dots," *Phys. Rev. B.* **57**, 9971 (1998)

[8] H. Fu, L.W. Wang and A. Zunger, "Comparison of the k•p and the direct

diagnonalization approaches for describing the electronic structure of quantum dots," *Appl. Phys. Lett.* **71**, 3433-3435 (1997); H. Fu, L. W. Wang and A. Zunger, "Response to 'Comment on comparison of the k•p and the direct diagonalization approaches for describing the electronic structure of quantum dots,'" *Appl. Phys. Lett* **73**, 115 (1998)

[9] S.B. Zhang, and A. Zunger, "Prediction of Unusual Electronic Properties of Si Quantum Films," *Appl. Phys. Lett.* **63**, 1399 (1993); S. B. Zhang, C.Y. Yeh, and A. Zunger, "Electronic Structure of Semiconductor Quantum Films," *Phys. Rev. B* **48**, 11,204 (1993).

[10] H. Fu and A. Zunger, "Excitons in InP Quantum Dots," *Phys. Rev. B* ***Rapid Communication*** **57,** R15064 (1998).

[11] K. Edamatso, this conference.

[12] M.E. Schmidt, S.A. Blanton, M.A. Hines and P. Guyot-Sionnest, *Phys Rev. B.* **53,** 12629 (1996)

[13] C. Pryor, J. Kim, L.W. Wang, A. Williamson and A. Zunger, "Comparison of two methods for describing the strain profiles in quantum dots," *J. Appl. Phys.* **83**, 2548 (1998)

[14] L. W. Wang, J. Kim and A. Zunger, "Electronic structures of [110] faceted 'self-assembled' Pyrmidal InAs/GaAs quantum dots," *Phys. Rev. B* (In Press) (1999)

[15] R. Magri and S. Ossini, *Phys. Rev. B* **58,** R1742 (1998)

[16] A. Franceschetti and A.Zunger, "Free-standing vs. AlAs-embedded GaAs quantum dots, wires and films: the emergence of zero confinement state," *Appl. Phys. Lett.* **68**, 3455-3458 (1996).

[17] A. Franceschetti and A. Zunger, "Quantum Confinement - induced $\Gamma \rightarrow X$ transition in GaAs/GaAlAs quantum films, wires and dots," *Phys. Rev. B* **52**, 14,664 (1995).

[18] A. Franceschetti and A. Zunger, "GaAs quantum-structures: Comparison between direct pseudopotential and single-band truncated crystal calculations," *J.Chem.Phys.* **104**, 5572 (1996).

[19] H. Fu and A. Zunger, "Quantum-size effects on the pressure-induced direct-to-

indirect band gap transition in InP quantum dots," ***Physical Review Letters*** **80**, 5397 (1998)

[20] A. J. Williamson and A. Zunger, "Effect of interfacial states on the binding energies of electrons and holes in InAs/GaAs quantum dots," *Phys. Rev. B* **58,** 6724 (1998)

[21] L.W. Wang and A. Zunger, "LDA-Derived Empirical Pseudopotentials". *Phys. Rev. B,* **51,** 17398 (1995); A. Zunger, "First-Principles and Second Principles Pseudopotentials" in "Physics of Real Materials" edited by J.R. Chelikowsky and S.G. Louie, Kluger Academic Publishers, Boston 173-187 (1996)

[22] L.W. Wang, and A. Zunger, "Solving Schrodinger's Equation Around a Desired Energy: Application to Si Quantum Dots," *J. Chem. Phys.* **100**, 2394 (1994)

[23] A. Zunger and L. W. Wang, "Theory of Silicon Nanostructures," *Appl. Surface Science*, **102**, 350 (1996).

[24] A. Zunger, C. Y. Yeh, L. W. Wang, and S. B. Zhang, "Electronic Structure of Silicon Quantum Films, Wires and Dots: How Good Is the Effective Mass Approximation?" *Int. Conf. Phys. Semicond.* (Vancouver, Canada) p. 1763 (1994).

[25] A. Zunger, "Electronic Structure Theory of Semiconductor Quantum Dots," *MRS Bulletin* **23**, 35 (1998).

[26] L.W. Wang and A. Zunger, "Pseudopotential Theory of Nanometer Silicon Quantum Dots," Chapter in *Studies in Surface Science and Catalysis*, Eds. P. V. Kamat and D. Meisel, Elsevier Science Vol. 103, p. 161-207 (1996).

[27] A. Zunger, "Pseudopotential Theory of Semiconductor Quantum Dots, Wires, and Films," in *23rd Conference on the Physics of Semiconductors*, Edited by M. Scheffler and R. Zimmermann, World Science, Singapore, Vol. 2, p.1341-1348 (1996).

[28] H. Fu and A. Zunger, "Local-density-derived Semiempirical Nonlocal Pseudopotentials for InP with Applications to Large Quantum Dots," *Phys. Rev. B.* **55**, 1642 (1997).

[29] L.W. Wang, A. Franceschtti and a. Zunger "Million-Atom Pseudopotential calculation of Γ-X Mixing in GaAs/AlAs Superlltices and Quantum dots", ***Phys***

Rev. Letters **78,** 2819 (1997)

[30] A. Franceschetti, L.W. Wang, H. Fu and A. Zunger, "Short-range versus long-range electron-hole exchange interactions in semiconductor quantum dots," *Physical Review* ***Rapid Communication*** **58,** R13367 (1998)

[31] A. Franceschetti, H. Fu, L.W. Wang and A. Zunger "Many-body pseudopotential theory of excitons in InP and CdSe quantum dots" (submitted for publication).

[32] L.W. Wang, and A. Zunger, "Electronic Structure Pseudopotential Calculations of Large (~1000 atoms) Si Quantum Dots," *J. Phys. Chem.* **98,** 2158 (1994).

[33] C.Y. Yeh, S.B. Zhang, and A. Zunger, "Confinement, Surface and Chemisorption Effects on the Optical Properties of Si Quantum Wires," *Phys. Rev. B* **50,** 14405 (1994).

[34] H. Fu and A. Zunger, "InP Quantum Dots: Electronic Structure, Surface Effects, and the Redshifted Emission," *Phys. Rev. B* **56,** 1496 (1997).

[35] L. W. Wang and A. Zunger, "Pseudopotential Calculations of Nanoscale CdSe Quantum Dots," *Phys. Rev. B.* **53,** 9579 (1996).

[36] L.W. Wang and A. Zunger, "High Energy Excitonic Transitions in CdSe Quantum Dots," *J. Phys. Chem.* (Letter section) **102** 6449 (1998).

[37] A.J. Williamson and A. Zunger "A pseudopotential study of electron-hole excitations in free-standing InAs quantum dots", (submitted for publication)

[38] A. Franceschetti and A. Zunger, "Direct Pseudopotential Calculation of Exciton Coulomb and Exchange Energies in Semiconductor Quantum Dots," ***Physical Review Letters*** **78,** 915-918 (1997).

[39] A.J. Williamson A. Zunger, and A. Canning, "Prediction of a strain-induced conduction-band minimum in embedded quantum dots," *Phys. Rev. B.* ***Rapid Communications*** **57,** R4253 (1998).

[40] J. Kim, L.W. Wang and A. Zunger, "Prediction of charge separation in GaAs/AlAs 'Russian Doll' nanostructures," *Phys. Rev.* ***Rapid Communications*** **56** R15541 (1998).

[41] J. Kim, L.W. Wang and A. Zunger, "Comparison of the electronic structure of InAs/GaAs pyramidal quantum dots with different facet orientations," *Phys. Rev. **B Rapid Communications*** **57**, R9408 (1998).

SPECTROSCOPY OF FEW ELECTRON LATERAL DOTS

C.Gould[1,2], A.S.Sachrajda[1], P.Hawrylak[1], P.Zawadzki[1], Y.Feng[1] and Z.Wasilewski[1]

[1]Institute For Microstructural Sciences, National Research Council, Canada, K1A 0R6
[2]Département de Physique and CRPS, Université de Sherbrooke, Sherbrooke, Québec, Canada J1K 2R1

ABSTRACT

Small lateral quantum dots have been fabricated. The number of electrons in these dots was varied from 5 to 20 by the application of voltages to a series of electrostatic gates. Both ground state and excitation level spectroscopy were performed using single electron techniques. Measurements were made as a function of magnetic field. In this paper a brief description is given of some of the effects which have been observed in these dots.

INTRODUCTION

Quantum dots have often been compared to artificial atoms, in which the nucleus of the atom is replaced by the quantum dot confining potential. The properties of each quantum dot element are governed by several factors including the exchange, Coulomb, Zeeman and kinetic energies. The application of a magnetic field alters the relative strength of these energies and leads to a variety of interesting phenomena such as spin flips[1,2] and a predicted density reconstruction[3] of the spin polarized quantum dot at high magnetic fields. Single electron transport spectroscopy, developed originally for larger lateral electrostatically defined quantum dots enables spectroscopic measurements to be performed on *single* quantum dots. Both ground state [4] and excitation level [5] transport spectroscopic techniques

have been developed. Although originally developed for lateral dots the same techniques have recently been applied with great success to gated vertically etched dots[6] in the few electron limit. Capacitance spectroscopy[7] has also been performed on vertical dots. Intrinsic features of lateral dots had, however, always restricted them to the many electron regime (typically 50 to 100 electrons). Lateral dots defined electrostatically in a two dimensional electron gas (2DEG) have potentially very useful features for these type of spectroscopic measurements. Firstly, the source and drain reservoirs to the dots consist of the well understood and behaved 2DEG material. For example we have found that at even moderate magnetic fields edge state transport in the 2DEG results in the injection of only spin down electrons allowing us to differentiate between spin down and spin up tunneling events. In addition since the electrons enter and exit the dot at the edge additional spatial spectroscopic information can be obtained. The major disadvantage of lateral dots is that the dots cannot be completely emptied so that techniques need to be developed to identify the number of electrons in the dot. We demonstrate below that this counting problem can be overcome in our dots. It was clear that the fabrication of few electron quantum dots was desirable.

Recently we have overcome the limitations [8] mentioned above and have managed to fabricate lateral quantum dots which contained as few as 5 electrons. The inset in figure 1 shows one such design. The dot comprises of four electrostatic gates which form an approximate equilateral triangle. Three of the gates are used to define entrance and exit tunneling barriers while the fourth at the apex of the triangle is used as a plunger gate to vary number of electrons in the dot. The gates are placed above a high mobility 2DEG in a AlGaAs/GaAs heterstructure. Although the density of the bulk 2DEG was 1.7×10^{15} m^{-2} we were able to ascertain that the density in our dots was be below 0.67×10^{15} m^{-2}. This conclusion was reached from an analysis of the well understood ballistic magnetic focusing features observed on a larger square quantum dot [9] defined on material from the same wafer[ref].

Figure 1 is a greyscale showing the low field behavior (gate voltage position) of four of the peaks observed in one of the dots we have measured from zero field (B=0) to the magnetic field at which the first spin flip occurs. The trace covers the regime from 13 electrons to 17 electrons. The peaks

correspond to the gate voltages at which the electron number in the dot changes by one (i.e. these are the Coulomb blockade peaks). In this particular dot the lowest number of electrons achieved at zero field was 8. Several spectroscopic features can be seen in the Fig. 1.. The same features were also observed for other traces containing different peaks corresponding to different electron numbers. Each peak has several sharp features at low magnetic fields which are due to level crossings. It is important to note here that the peaks correspond to a dot with a fixed number of electrons and levels. This is confirmed by looking at peaks 1 and 2 which move out of phase at low fields. While these peaks move out of phase peaks 2 and 3 move in phase. In fact at very low fields we find that pairs of peaks have similar magnetic field trends (e.g. peaks 2 and 3 in the figure). This is a consequence of the fact that at zero magnetic field there exists a level degeneracy due to the spin quantum number. At the feature marked (a) in peaks 3 and 4 a clear departure from the parallel behavior of peaks 2 and 3 can be seen. This is related to the effect of coulomb and exchange interactions on the ground state level spectrum. This effect, similar to the Hund's rule effect at zero magnetic field, has also been observed in vertical dots [10]. The arrows in figure 1 refer to the onset of $\nu = 2$ i.e. the spin unpolarized droplet. At the onset of $\nu = 2$ for peaks 1 and 3 there is a sharp rise in the peak position followed by a steep slope downwards to the first spin flip regime. For peaks 2 and 4, however, there is a small rise followed by a shallow slope. The same behavior is observed on different dots. We believe that this behavior is related to the difference at $\nu = 2$ between dots with an even number of electrons which are totally spin unpolarized and those dots with an odd number of electrons which always have one spin left over. More details of this will be published elsewhere. Figure 1 also reveals amplitude modulation which is related to the spatial sensitivity of single electron tunneling in lateral dot measurements. The amplitude modulation occurs primarily at the sharp features in the data which correspond to ground state level crossings, i.e. the amplitude modulation contains information about the spatial arrangement of the wavefunctions of the different levels. It is important to note, however, that this technique measures addition energies and not individual levels. This behavior is currently being investigated in more detail.

We are able to identify the number of electrons in the dot by counting the number of spin flips between the spin unpolarized droplet at $\nu = 2$ and the spin polarized droplet at $\nu = 1$. The number of electrons is equal to twice the number of spin flips. This appears not to be possible in vertical dots because spin flips are not as clear in that geometry [11]. To illustrate just how clear the spin flips are in our lateral dots we plot in figure 2 the position of six peaks in between $\nu = 2$ and $\nu = 1$ for a second dot. Each 'step' in the peak position is due to a 'spin-flip' process. The amplitude drops during the upward part of each step. As one moves down the figure one spin-flip event is lost for every two traces confirming that these are indeed the spin flip events. Based on this electron number allocation, it was found that the lower field spectrum for the dot in figure 1 was similar to that obtained for vertical dots (nb. the comparison was made for dots containing between 13 and 19 electrons). This is quite surprising since the electrons in these two types of dots are in quite different environments. From a careful temperature dependence analysis of the spin flip regime and a comparison with exact diagonalization calculations we were able to show that these spin flips are complex events and that even Hartree-Fock calculations were incapable of explaining the data. Correlations were found to be crucial in explaining the results[2]. A simplified picture for the spin flip process is the following.. In our experiments we were able to distinguish between spin up (low amplitude) and spin down (high amplitude) tunneling events for two reasons; firstly we were only injecting spin down electrons from a spin resolved edge state in the bulk 2DEG and secondly close to $\nu = 1$ the spin up electrons were located near the center of the dot but far from the tunneling barriers. A spin flip involves the removal of a spin up electron near the center of the dot and its placement near the edge of the dot as a spin down electron. This process lowers the exchange and coulomb energies. On the way to the edge, however, the spin up electron depolarises the dot by flipping some of the spin down electrons. The resulting low lying spin texture (or quantum dot skyrmion) excitations explain why the observed amplitude modulation at the spin flips was only a very low temperature effect.

The last spin flip is not, however, the end of the structure in the traces of the peak position of the individual levels in the dot. The dot continues to shrink as the magnetic field is raised. This increases the coulomb energy. At

some point the dot reconstructs either through a density reconstruction or through a spin texture. There have been several observations of structure beyond $\nu = 1$ which has been linked to such processes [7,1,12]. In figure 3 we plot the peak position at fields beyond $\nu = 1$ in our lateral dots. Additional structure is observed on every peak. It is found to have a much smaller field dependence on electron number than the spin flips. The structures persist to much higher temperatures than the spin flips. We are currently investigating this regime in more detail.

We are also able to perform excitation level spectroscopy on the dot at different magnetic fields. Some examples are given in figure 4. More details of all these regimes will be given elsewhere. Figure 4(a) shows three peaks at an excitation of 650μV at $\nu = 2$. The peak asymmetry is independent of the direction of applied gate voltage. A comparison with calculations performed using exact diagonalization technique reveal that the origin of the periodic structure on the peaks are collective charge edge excitations. The peak amplitude asymmetry is also reproduced in the calculations and is due to an intrinsic electron hole asymmetry in lateral devices in which it is easier to add electrons to an edge than to remove them from the center of the dot. Figure 4(b) shows some traces taken at 500μV at a spin flip event. Such behavior is reproduced at other spin flips. Again an asymmetry can be seen in the behavior at the two edges of the dot. In this case the behavior is closely related to the spin textures mentioned above and will be described in detail elsewhere. Finally in figure 4(c) we plot a trace at 500μV through a step in the reconstruction. The width of the peak under such circumstances is related to a parameter, α, linking the applied plunger gate voltage to the energy scale. If the dot reconstructs then one might expect a sudden change in this parameter. In our case, in contrast to what is observed in vertical dots [12] we have not observed dramatic changes in the width of the peak at the step. An analysis of Coulomb diamonds before and after the first step in the reconstruction yields a change in area of the dot of about 7% for dots containing 10 electrons, in reasonable agreement with the 1/N behavior expected based on a single empty orbital reconstruction.

In summary we have fabricated the first few lateral electron dots. We are able to deduce the number of electrons by both counting the number of spin flips between $\nu = 1$ and $\nu = 2$ and by comparing the low magnetic field

spectrum with published data from vertical dots. We have performed both ground state and excitation level spectroscopy in a variety of magnetic field regimes. We have observed a variety of correlation phenomena by making use of the spatial information that is unique to lateral devices.

References

[1] O.Klein et al. Phys. Rev. Lett. 74 785 (1995), D.G.Austing et al. submitted to Jap. J. Appl. Phys. (1998)

[2] P.Hawrylak et al. submitted to Phys. Rev B. (1998).

[3] P. Hawrylak Phys. Rev. Lett. 71, 3347 (1993), Phys. Rev. B51 17 708 (1995), C.de C.Channon and X.G.Wen Phys. Rev. B49 8227 (1994), S.R.-E Yang et al, Phys. Rev. Lett. 71 3194 (1993), M.Ferconi and G.Vignale Phys. Rev. B56 12108(1997), P. Hawrylak, A. Wojs, and J. A. Brum, Phys. Rev. B54 11397 (1996), A. Wojs and P. Hawrylak , Phys. Rev. B bf 56 13227 (1997)

[4] P.L.McEuen et al., Phys. Rev. B45 11419 (1992)

[5] J. Weis J, R.J. Haug., K. von Klitzing and K.Ploog Phys. Rev. Lett. 71 4019

[6] S.Tarucha et al., Phys. Rev. Lett. 77 3613 (1996)

[7] R.Ashoori et al., Phys. Rev. Lett. 71 613 (1993)

[8] A.S.Sachrajda, C.Gould, P.Hawrylak, Y.Feng, Z.Wasilewski, to be published in Physica Scripta

[9] I.V.Zozoulenko et al. Semicond. Sci. and Tech. 13 (1998) A7-A10

[10] Private Communication D.G.Austing.

[11] D.G.Austing et al., submitted to Jap. J.Appl. Phys. (1998)

[12] T.H.Osterkamp et al., cond-mat/9810159.

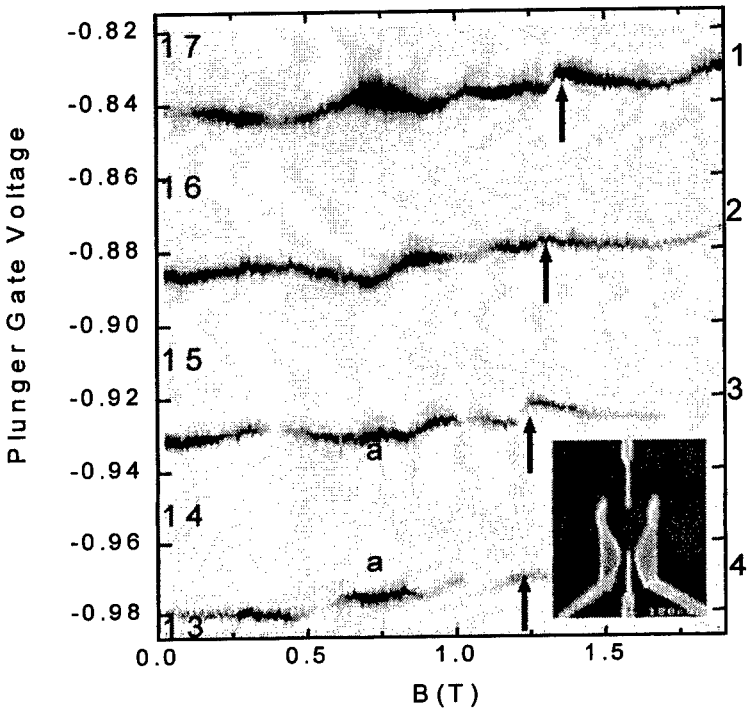


Figure 1: The position of four Coulomb blockade peaks as a function of magnetic field. The numbers (1 to 4) refer to the peak label in the text The numbers between peaks (13 through 17) refer to the number of electrons in the dot. The feature 'a' is explained in the text. The arrows correspond to the transition to $\nu = 2$. The inset illustrates one design of dot used.

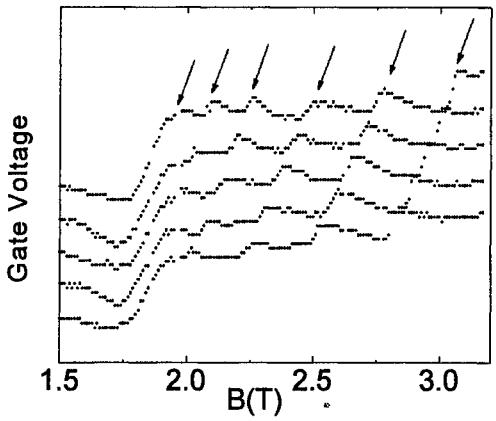


Figure 2: The peak position of five peaks in the spin flip regime. The peaks have been shifted for clarity. The arrows illustrate the spin flip positions. The graph illustrates how the number of spin flips changes by 1 every 2 levels as expected. Around 1.75T the field trend is different for even and odd numbers of electrons.

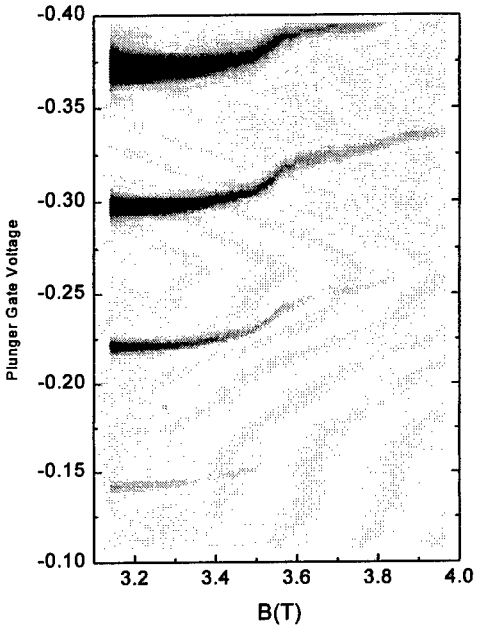


Figure 3: The peak position of four peaks at magnetic fields higher than the last spin flip. The reconstruction step and features are visible (see text for details)

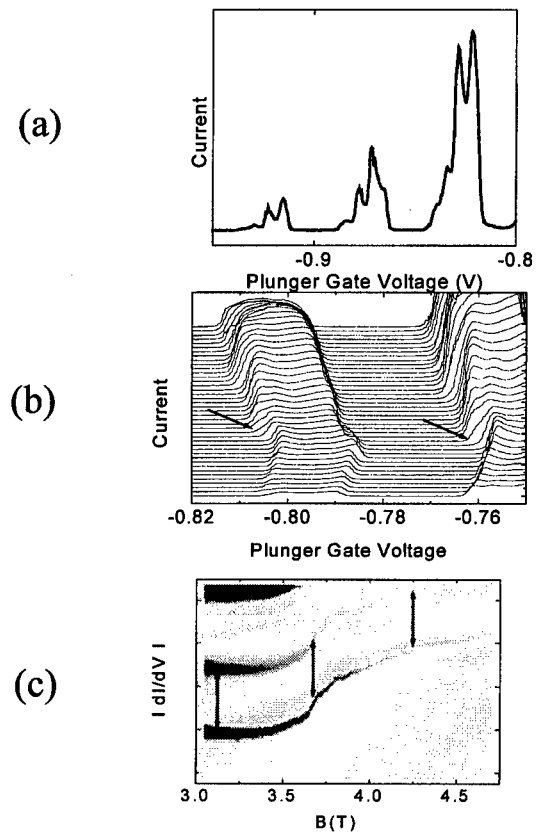


Figure 4: Examples of excitation spectroscopy. (a) at $\nu = 2$
(b) at a spin flip and (c) at a reconstruction step (nb. the absolute value of the derivative is being plotted – the arrows illustrate the width of the peak)

STARK SPECTROSCOPY INVESTIGATION OF SPECTRAL DIFFUSION IN SINGLE CdSe QUANTUM DOTS

K. Shimizu, S. A. Empedocles, R. Neuhauser, M.G. Bawendi
Department of Chemistry
Massachusetts Institute of Technology, Cambridge, MA 02139

ABSTRACT

Photoluminescence spectroscopy of single CdSe nanocrystallite quantum dots reveals the atomic-like nature of the emitting state by removing inhomogeneous broadening. However, spectral diffusion is found to be a dynamic source of spectral line-broadening. We investigate the origins of spectral diffusion and conclude that changing local electric fields produce a Stark effect that results in these spectral shifts.

INTRODUCTION

Through advancements in the colloidal synthesis of quantum dots (QD) [1], tunable size dependent optical features predicted by theory [2] have been realized. CdSe QDs, with diameters ranging from 10 ~100 Å [1], have a band gap that spans the visible range of light; hence, CdSe is an ideal system for studying optical quantum confinement effects. Furthermore, the photostability of these dots (overcoated with a ZnS shell) in a multitude of environments opens the door to engineering applications for CdSe QDs. Applications in light emitting displays, lasers, optical modulators, optical data storage, and biological tagging become possible because these QDs can be dispersed in a variety of polymers, incorporated in other semiconductor thin films [3], dissolved in a number of organic and aqueous solvents, and assembled into three-dimensional arrays of quantum dots [4].

Ensemble studies into the photophysics of QDs, however, are limited by inhomogeneities in the structure and environments of a given sample; often, details of spectra are lost due to ensemble averaging over the distribution of energy levels. Even size-selective procedures like fluorescence line narrowing (FLN) have been unable to realize the narrow line widths predicted by theory [5].

We present recent results of single CdSe nanocrystallite QD spectroscopy, using epi-fluorescence microscopy techniques similar to single molecule spectroscopy. Using single QD spectroscopy, the ensemble averaging due to the distribution of dot size and shape are eliminated, revealing new information about CdSe QD fluorescence.

EXPERIMENT

Sample Preparation

The CdSe QDs were synthesized using the methods of ref [2] and later overcoated with a ZnS layer [6,7]. The ZnS is nearly epitaxial and an increase in the room temperature quantum yield is observed. The nanocrystallites were diluted in hexane and spin cast in a 200 Å layer of poly(methyl methacrylate) on a crystalline quartz substrate. In the Stark experiments, electric fields were applied within the sample plane using interdigitated electrodes with 5 μm spacings that were lithographically fabricated on the crystalline quartz substrates.

Imaging and Spectral Analysis

Single QD images and spectra were taken with a far-field epi-fluorescence imaging microscope. The details of the setup are discussed in ref [8]. A 514 nm Ar^+ excitation source was used for all the images and spectra described here. As an advantage of epi-fluorescence microscopy over confocal microscopy, we can acquire data in parallel from multiple dots simultaneously. For the Stark experiments, the electrodes were connected to a DC voltage source to apply the electric fields across the dots.

RESULTS

A typical image of nanocrystallites at 10 K and the same dots spectrally resolved are shown in figure (1a) and (1b), respectively. Each bright spot in the image mode represents a single QD; the dots are dispersed at <1 dot/μm^2, well above the resolution limit of the far-field optics. On the time scale of a single image (0.5 s), the fluorescence from individual dots is often seen to blink on and off, a feature termed fluorescence intermittency [9]. The blinking pattern varies from dot to dot and is highly dependent on the excitation intensity. This binary fluorescent blinking is strong evidence that the individual spots are single nanocrystallites; otherwise, incoherent blinking of multiple dots would result in a stepwise or continuous dimming of the emission.

Figure (1c) shows a comparison between a representative sample of single dot spectra and the corresponding ensemble spectrum from the same sample. All single dot spectra show similar spectral characteristics including narrow peaks and a longitudinal optical (LO) phonon progression with peak spacing comparable to the bulk LO phonon frequency. Differences in phonon coupling are seen amongst the dots with an average value equal to the ensemble-measured FLN value. As expected, the ensemble emission spectrum is reproduced after convoluting the average single dot spectrum with the distribution of zero-phonon energies measured in the sample [Figure (1d)]. The fit of the single dot data to the ensemble measured data attests that what is measured on the single QD level is representative of the ensemble distribution.

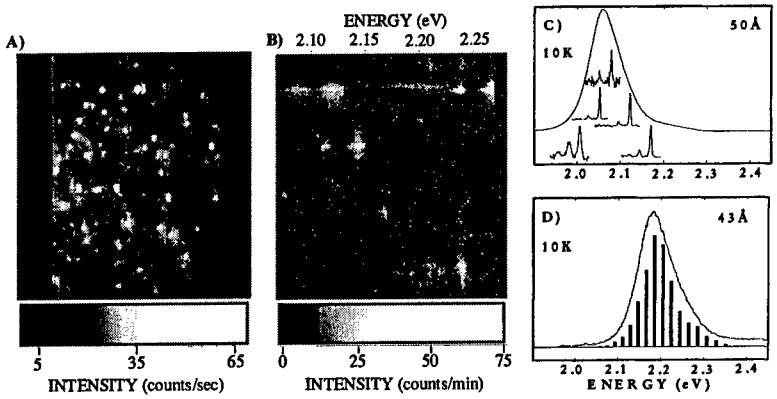


FIG. 1. (a) Typical image of CdSe dots at 10 K with a 0.5 sec integration time and 150 W/cm^2 excitation intensity. (b) Spectrally dispersed image of nanocrystallites shown within dotted lines in (a). (c) Ensemble spectrum with a representative set of single dot spectra obtained from the same 50 Å diameter sample. (d) Ensemble spectrum with histogram of energies of 513 single dot spectra obtained from the same 43 Å diameter sample.

While narrower than FLN spectra, the single dot luminescence appears to be broadened by spectral diffusion (a random shifting of the emission energy with time). Figure (2) shows such an example. The single dot spectrum taken with a 10 second integration time shown in figure (2a) appears much different than the 0.1 second single dot spectra shown in figure (2b). The line width and the spectral energy are very different in figures (2a) and (2b). In figure (2b), the single dot zero phonon line (ZPL) peak is shifting in time while the figure (2a) spectrum takes the time-averaged ZPL peak. Hence, the time scale of the shifting with respect to the integration time determines the final line shape and spectral position. Moreover, the time scale of a spectral shift is sometimes faster than 0.1 seconds and multiple peaks are observed, as in spectrum 6 of figure (2b).

To verify that the time averaged spectrum incorporates the individual ZPL peaks shifting, figure (2c) shows a histogram of 150 consecutive ZPL peak positions for the single dot in (a) with a 0.1 sec integration time. The comparison between figure (2a) and (2c) clearly shows distinct similarities.

Although line widths that depend on integration time have been reported in single molecule spectroscopy [10], observing spectral diffusion in single quantum dots was somewhat of a surprise. Single molecule electronic states are very sensitive to the environment of the molecule, but QDs should have little interaction with the environment due to the enclosure of the exciton within the nanocrystal. In addition, the energies of the delocalized exciton in CdSe nanocrystallites appear insensitive

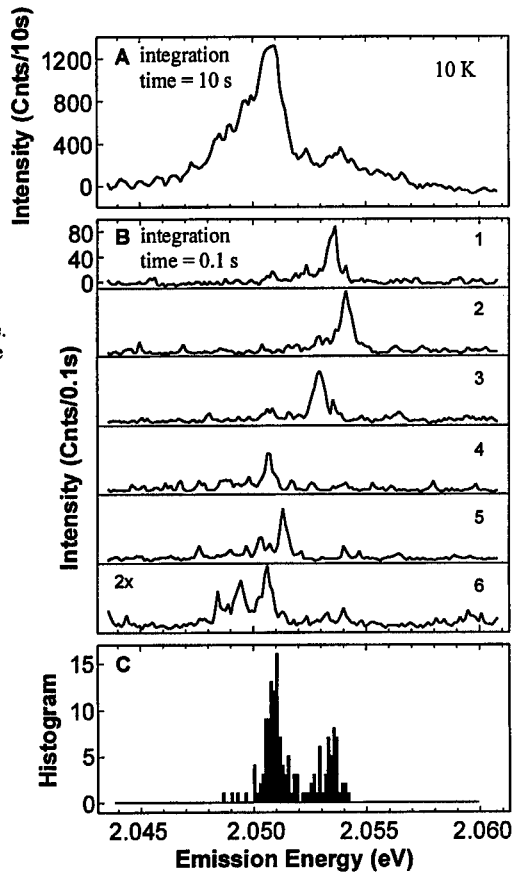


FIG. 2. (a) Single dot spectrum taken with 10 sec integration time. (b) Six single dot spectra from the same QD as in (a) taken with 0.1 sec integration time. (c) Histogram of 150 consecutive single dot ZPL peaks taken with 0.1 sec integration time.

to the chemical nature of the nanocrystallite surface [11]. As such, the perturbing force required to produce the observed spectral shifts must be quite large. Upon closer examination of spectral diffusion, we found that the spectral characteristics are similar to those observed in ensemble Stark experiments [12]: the phonon coupling increases and the band edge fluorescence intensity decreases as the ZPL shifts to the red. To further investigate the correlation between spectral diffusion and Stark shifts, single QDs were studied in the presence of an applied electric field [13]. Figure (4a) and (4b) show a comparison between two spectra where the shifts in emission are due

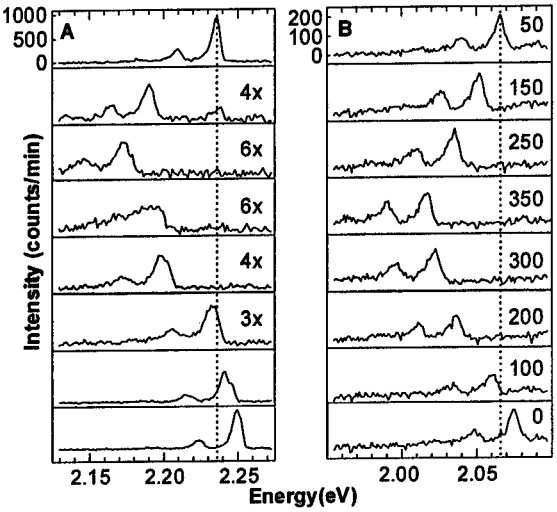


FIG. 4. Stark shift versus spectral diffusion. (a) Eight sequential 1 min emission spectra of a single QD shifting as a result of spontaneous spectral diffusion in the absence of an applied electric field. Frames indicate a magnification of the y-axis in each spectrum (b) Stark series for a single QD. Frames indicate applied field in kilovolts per centimeter.

to spectral diffusion and externally applied fields, respectively. The similarities, not only in the ZPL shifting, but also in the changes in phonon coupling suggest that spectral diffusion is an extrinsic effect caused by changing local electric fields. Such high fields would be consistent with free carriers residing near the surface of the QD. In addition, Stark spectroscopy analysis determined that the CdSe QD lowest excited state is highly polarizable (~ 10^5 Å^3) with a dynamic dipolar character induced by changing local electric fields. As an example of the dynamic nature of this induced dipole, figure (5) shows a stark series of the same QD before (a) and after (b) a spectral diffusion shift. Although the polarizability does not change, the induced dipole changes

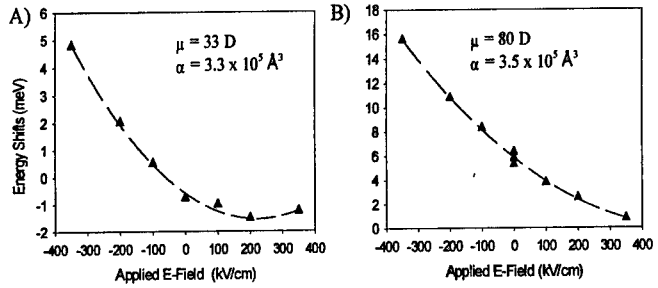


FIG. 5. Stark shift of a single ZnS overcoated QD emission spectrum (a) before spectral diffusion and (b) after spectral diffusion. The line indicates a fit to the sum of a linear and quadratic shift as a function of field. μ and α refer to the measured excited state dipole and polarizibility respectively.

by more than a factor of 2. This is consistent with the conclusion that spectral diffusion is the result of changing local electric fields.

CONCLUSION

Although single nanocrystallite spectroscopy has shown that by removing spectral inhomegeneities, narrow line widths are observable for CdSe QDs, light-driven spectral diffusion was found to introduce a dynamic source of line broadening. For CdSe QDs, changing local electric fields appear to be the cause of spectral diffusion by creating Stark shifts in single QD spectra.

REFERENCES

1. C. B. Murray, D. J. Norris, M. G. Bawendi, J.Am. Chem. Soc. **115**, 8706 (1993).
2. Al. L. Efros and A. L. Efros, Sov. Phys. Semicond. **16**, 772 (1982).
3. M. Danek, K. F. Jensen, C. B. Murray, M. G. Bawendi, J. Cryst. Growth **145**, 714 (1994).
4. C. B. Murray, C. R. Kagan, M. G. Bawendi, Science **270**, 1335 (1995).
5. A. P. Alivisatos *et al.*, J. Chem. Phys. **90**, 3463 (1989).
6. M. A. Hines and P. Guyot-Sionnest, J. Phys. Chem. **100**, 468 (1996).
7. B. O. Dabbousi *et al.*, J. Phys. Chem. B. **101**, 9463 (1997).
8. S. A. Empedocles and M. G. Bawendi, Phys Rev Lett. **77**, 3873 (1996).
9. M. Nirmal *et al.*, Nature **383**, 802 (1996).
10. J. K. Trautman, J. J. Macklin, L. E. Brus, E. Betzig, Nature **369** 40 (1997).
11. M. Kuno, J. K. Lee, B. O. Dabboussi, F. Mikulec, M. G. Bawendi, J Phys Chem, **106**, 9869 (1997).
12. A. Sacra, thesis, Massachusetts Institute of Technology (1996).
13. S. A. Empedocles and M. G. Bawendi, Science **278**, 2114 (1997).

CARRIER RELAXATION IN THERMAL ANNEALED InGaAs/GaAs QUANTUM DOTS

N. Perret[a], D. Morris[a] and R. Leon[b]

(a) Centre de Recherche en Physique du Solide, Département de physique, Universite de Sherbrooke, (Quebec) Canada J1K 2R1
(b) Jet Propulsion Laboratory, California Institute of Technology, Pasadena, CA 91109-8099

ABSTRACT

Carrier relaxation times in a series of thermal annealed self-assembled InGaAs/GaAs quantum dots have been measured by means of time-resolved photoluminescence experiments. Further investigation on the nature of the relaxation mechanisms has been conducted by looking at the temperature and excitation density dependence of the luminescence rise times of the quantum dot ground state transitions. Different mechanisms are involved in the as-grown and the intermixed samples according to the comparison of their intersublevel energy spacing with respect to the phonon energy. Auger type processes are dominant in our as-grown sample whereas multiphonon processes play an increasing role with greater compositional interdiffusion.

INTRODUCTION

Recent experimental studies have shown that quantum dots (QDs) intermixing can be used to blue-shift the photoluminescence transitions [1] and to tune the intersublevel energy spacing [2]. Based on theoretical works [3, 4], this is expected to change drastically the carrier relaxation time since scattering rates with single LO-phonon and multiphonon depend critically on this energy spacing. A recent experimental work showed some evidence that carrier capture and relaxation in QDs is more efficient in intermixed samples [5]. This result is not consistent with the expected level spacing dependence of the single LO-phonon scattering rate. However, mechanisms like Auger-type processes [6, 7] or defect-assisted phonon emission [8] may well explain this increased carrier relaxation efficiency. On the other hand, time-resolved experiments done by Ohnesorge et al. [9] on smaller QDs indicate that multiphonon processes are the dominant relaxation mechanisms at low excitation densities while Auger processes

become dominant at high carrier densities. More experimental results have to be obtained in order to understand the influence of both the QD structures and the experimental conditions on the carrier relaxation time. In this work, we report on a systematic study of the PL rise time of the QD ground state optical transition as a function of the thermal annealing time (which control the intersublevel spacing), the excitation density and the temperature.

EXPERIMENT

The sample structure consists of a four-layer stack of buried self-assembled $In_{0.6}Ga_{0.4}As/GaAs$ quantum dots grown by MOCVD under optimized conditions [1]. The QD layers are separated by 50nm GaAs barriers. All layers were grown at 550 °C on (100) GaAs substrate. The as-grown sample contains a concentration of 3.6 x $10^{10}/cm^2$ InGaAs QD with 29.5 nm average diameter. Post-growth rapid thermal annealing (RTA) of samples was carried out using a SiO_2 capping layer, under a nitrogen ambient, at 900 °C for various times ranging from (1x) 30 s to (5x) 30 s.

The photoluminescence (PL) spectra were obtained using the 514 nm continuous-wave (cw) output of an ion Argon laser for excitation and a cooled Ge detector or GaAs photomultiplier tube for signal detection. The time-resolved (TR) measurements were obtained using a Ti:sapphire laser (100 fs, 82 MHz) as the excitation source. For these experiments the excitation energy has to be tuned above (1.675 eV), in resonance (1.517 eV) or below (1.442 eV) the GaAs bandgap. An up-conversion detection technique with sub-picosecond resolution and a GaAs photomultiplier tube were used for the TRPL measurements.

RESULTS AND DISCUSSION

Rapid thermal annealing induces compositional disordering at the barrier/dot interface which results in large blue-shifts of the PL transitions and a significant linewidth reduction as illustrated in Fig. 1 [1-2]. As observed previously [11], the broad Gaussian shape of the QD luminescence peak corresponds to an ensemble of sharp single-dot lines where QDs have slightly different sizes. The blue-shift of the QD emission line increases gradually as a function of annealing time from 1.225 eV (as-grown sample) up to 1.417 eV (annealed sample for 5 x 30 s). This large energy shift (192 meV) shows the efficiency of the intermixing process. Simultaneously a significant linewidth reduction of the QD luminescence is observed from 68 meV (as-grown sample) to 37 meV (annealed sample for 5 x 30 s). This behavior appears to be general and it is observed to varying extents in different types of III-V quantum dots [10]. The reasons for this inhomogeneous line narrowing are still under study.

The time-resolved photoluminescence spectra shown in Figure 2 give similar information of the energy position of the QD levels. However under high laser pulsed-excitation density (> 5 W/cm^2), the number of carriers occupying the excited QD levels is high enough to see, for the as-grown sample, the individual optical transitions associated with these levels (n = 1, 2 and 3) together with the emission coming from the GaAs barriers (at 1.515 eV). The absence of the wetting layer peak (very thin quantum well from which the QDs are formed) suggests that carrier capture by the QDs is very efficient under our experimental conditions. This result is somehow expected because the QD surface coverage is very high in our samples. Hence the average interdot spacing is smaller than the carrier diffusion length in the wetting layer, so there is no recombination from wetting layer states [12]. Note also in this figure that it is not possible to distinguish the individual QD transitions in the PL spectra of the annealed samples when the intersublevel energy spacing decreases. We can estimate the energy between the QD levels from the difference in energy between the PL features, by making crude approximations. Thus assuming a parabolic confining potential and a ratio of electron to heavy-hole confinement energy of 0.8, we find for the as-grown sample intersublevel energies of ≈ 29 meV (for electron) and ≈ 7 meV (for heavy-holes). Considering the PL linewidth reduction after annealing, we estimate for the (5 x 30s)-annealed sample intersublevel energies of ≈ 15 meV (for electron) and ≈ 4 meV (for heavy-holes).

Figures 3a and 3b show the time-resolved PL signal of the QD ground state transitions. Decay times are deduced from the exponential behavior at the longer times (Fig. 3a). The PL rise times are obtained from the fit of the experimental data (Fig. 3b) using the following function describing the photoluminescence intensity :

$$I_{PL}(t) \propto \left(e^{-t/\tau_d} - e^{-t/\tau_r} \right) / (\tau_d - \tau_r)$$

where τ_d and τ_r are respectively the decay and the rise time of the PL emission.

The behavior of the PL decay time as a function of temperature is presented in figure 4. At 20K, the deduced decay time is 670 ps for the as-grown sample and it goes below 500 ps for all the annealed samples. Also, the decay times drop quickly above 100 K for all samples. Carrier thermal emission and subsequent non-radiative recombination in the barrier is probably responsible for the reduced PL decay times at higher temperatures. The correlation between the confining potential (which decreases with the annealing time) and the QD PL decay time tends to reinforce this interpretation. The slight increase of the PL decay time between 20 K and 80 K might be due to the non negligible exciton radiative recombination rate (at low temperatures) and its temperature dependence [13].

The PL rise time results as a function of temperature is presented in figure 5 while its laser excitation density dependence is shown in figure 6. Results obtained by pumping above or below the GaAs bandgap energy are also shown in Figure 6. Let's start by analyzing the results obtained for the as-grown sample. It is found that the PL rise time is nearly constant ($\approx$ 12 ps) as a function of temperature (see Fig. 5) while it decreases slightly as function of the excitation density (see Fig. 6). Besides the PL rise time of the QD ground state transition increases when we pumped below the energy of the confining barriers. In this case, the electron and hole plasma densities in the barriers (which could act as effective carrier scattering sources) decreases drastically. All these results suggest that Auger processes are the dominant relaxation mechanisms in these particular QDs, within our investigated excitation density regime. Our results did not allow us to discriminate between the single capture Auger process or the sequential Auger process involving capture and intersublevel relaxation mechanisms. The minor role played by the phonon emission mechanisms is consistent with the fact that both electron and hole intersublevel energies are smaller than the LO-phonon energy but sufficiently high (>> 1 meV) for neglecting the scattering rate mediated by the emission of acoustical phonons [4].

The PL rise time for the annealed sample (see Fig. 6) decreases significantly with increasing excitation density dependence : it is about 38 ps at 0.5 W/cm^2 and 7 ps at 250 W/cm^2. Again, these results suggest dominant Auger relaxation mechanisms at high excitation levels. However, a drastic change in the PL rise time behavior as a function of temperature (see Fig. 5) is observed for the annealed samples : the PL rise time of the 5 x 30 s annealed sample decreases from 24 ps at 20 K to 3 ps at 150 K. These temperature and excitation density dependencies combined with the fact the low-temperature (20 K) PL rise times increases with the thermal annealing time (intersublevel spacing getting smaller), indicate that intermixing decreases the efficiency of the Auger-processes while it increases the contribution of the multiphonon emission or the defect-mediated processes. The increasing role played by phonon emissions results from the fact that new relaxation channel opens up as the separation between the QD levels decreases; carriers are also more sensitive to surface states in that case. The influence of the thermal annealing process on the efficiency of the Auger relaxation mechanisms is still under study.

CONCLUSION

The systematic study of the QD PL rise times as a function of temperature and excitation density have shown that the intermixing process affects significantly the carrier recombination and relaxation times. Decreasing the intersublevel energy spacing and the confining potential tend to decrease both the recombination time and the carrier relaxation time (at high temperatures, for T > 100 K). The carrier relaxation efficiency

is very high in these QDs . Auger processes seem to be the dominant relaxation processes in as-grown sample whereas multiphonon scattering may play a major role in intermixed QDs.

ACKNOWLEDGEMENT

This work is supported by the Centre de Recherche en Physique du Solide de l'Université de Sherbrooke.

REFERENCES

[1] R. Leon, Y. Kim, C. Jagadish, M. Gal, J. Zou and D. J. H. Cockayne., Appl. Phys. Lett. **69**, 1888 (1996)

[2] R. Leon, S. Fafard, P. G. Piva, S. Ruvimov and Z. Liliental-Weber, Phys. Rev. B**48**, R4262 (1998)

[3] U. Bockelmann, Phys. Rev. B**48**, 17637 (1993)

[4] T. Inoshita and H. Sakaki, Phys. Rev. B**46**, 7260 (1992)

[5] S. Marcinkevicius and R. Leon, Phys. Stat. Sol. (b), Vol. **204**, 290 (1997)

[6] U. Bockelmann and T. Egeler, Phys. Rev. B**46**, 15574 (1992)

[7] A.L. Efros, V.A. Kharchenko and M. Rosen, Solid State Comm., Vol. **93**, 281 (1995)

[8] P. C. Sercel, Phys. Rev. B**51**, 14532 (1995)

[9] B. Ohnesorge, M. Albrecht, J. Oshinowo, A. Forchel and Y. Arakawa, Phys. Rev. B**54**, 11532 (1996)

[10] C. Lobo, R. Leon, S. Fafard and P. G. Piva, Appl. Phys. Lett. **72**, 2850 (1998)

[11] S. Fafard, R. Leon, D. Leonard, J. L. Merz and P. M. Petroff, Phys. Rev. B**50**, 8086 (1994)

[12] R. Leon and S. Fafard, Phys. Rev. B58, R1726 (1998)

[13] D.S. Citrin, Superlattices and Microstructures, Vol. 13, p. 303 (1993)

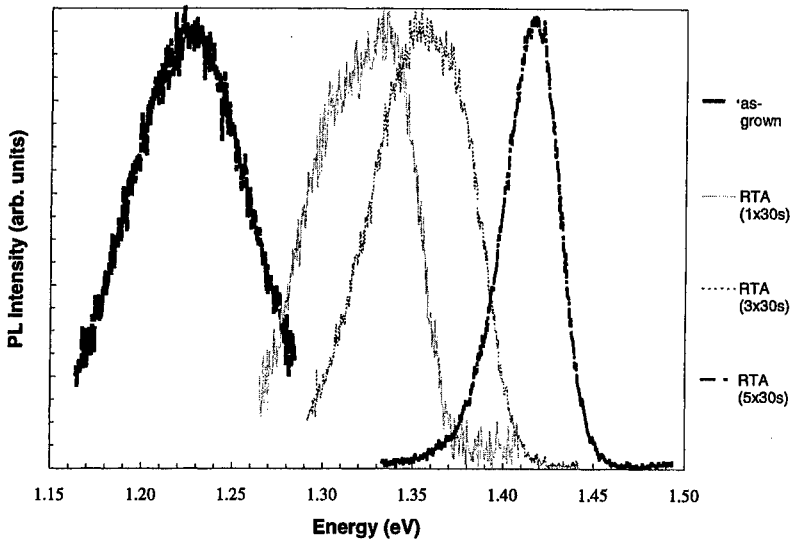


Figure 1 : Photoluminescence spectra of the different samples (as-grown and rapid thermal annealed ones) obtained at T = 15 K under continuous-wave laser excitation. The excitation density and energy are respectively 75 W/cm^2 and 2.409 eV.

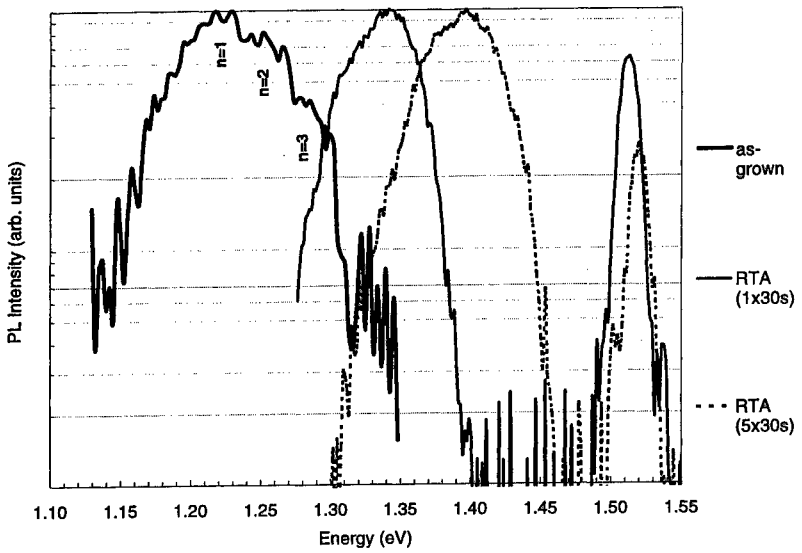


Figure 2 : Time-resolved photoluminescence spectra measured at 100 ps after a pulsed laser excitation. The temperature is 20 K, the photon excitation energy is 1.675 eV and the excitation density is 5 W/cm^2.

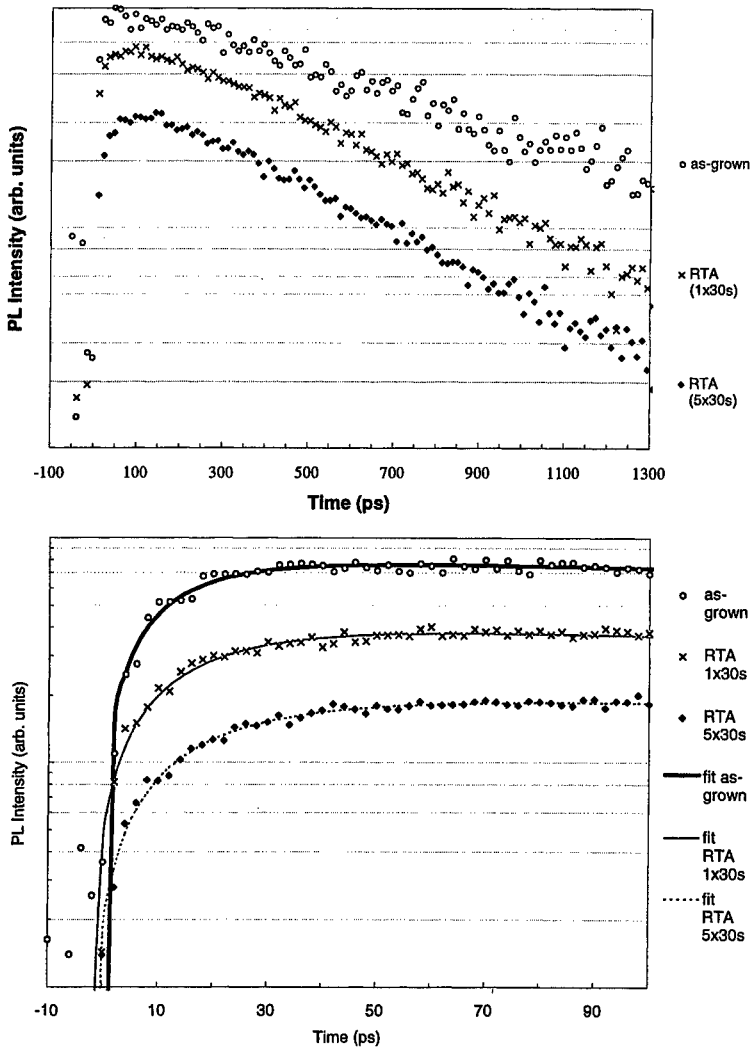


Figure 3: Time-resolved PL intensity detected at the energy of the corresponding QD ground state transition. $E_{exc.}$= 1.675 eV and T = 20 K. Fig. 3a and 3b were used to deduce the PL decay and rise times (τ_d and τ_r).

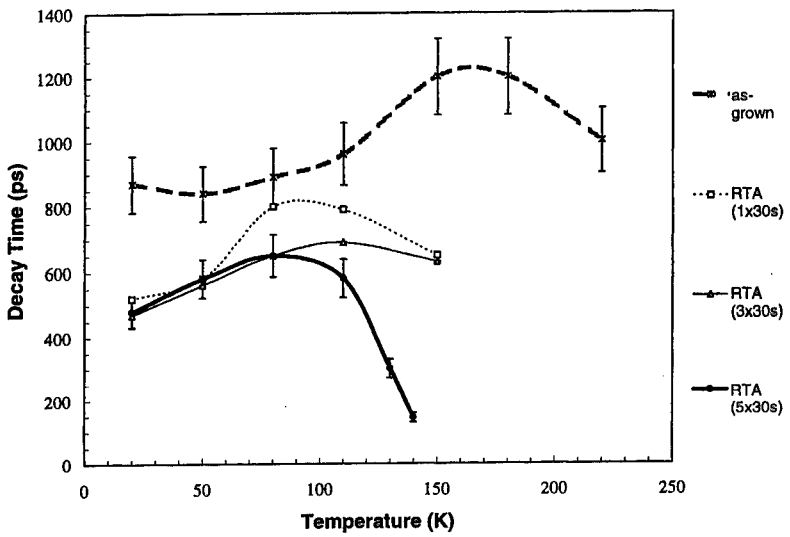


Figure 4 : PL decay time of the QD ground state transition measured for the different thermal annealed samples. $E_{exc.}$= 1.675 eV and P = 5 W/cm^2. The error bars correspond to the uncertainties resulting from the fitting procedure (it is about 10 %).

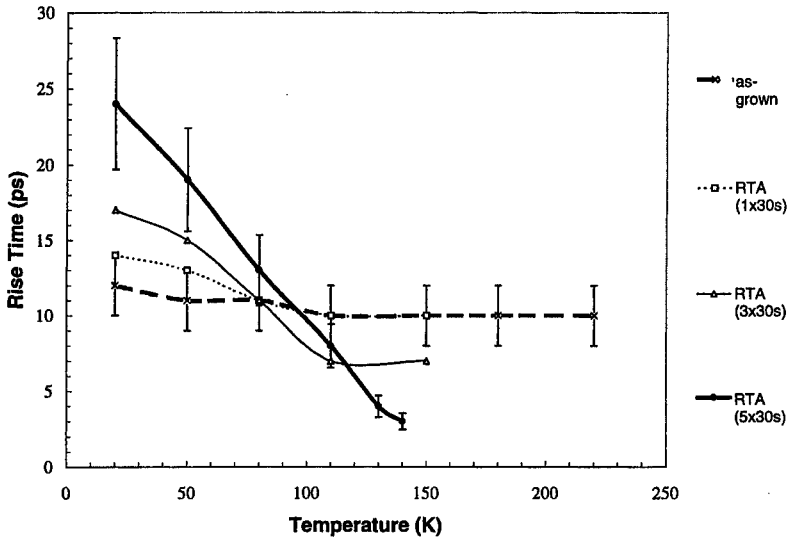


Figure 5 : PL rise time of the QD ground state transition measured for the different annealed samples. $E_{exc.}$= 1.675 eV and P = 5 W/cm^2. The error bars correspond to the uncertainties resulting from the fitting procedure (it is about 10%).

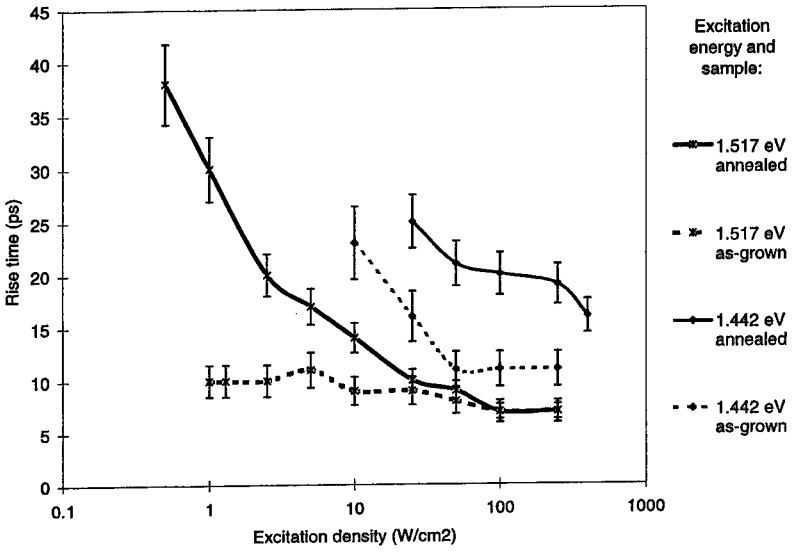


Figure 6 : PL rise time of the QD ground state transition measured for the as-grown sample and for one annealed sample (4 x 30 s) using two different photon excitation energies at T = 20 K. Note that the number of photocarriers per pulse and per dot depends on the excitation energy : for comparable laser excitation density, the carrier density per dot is in fact much smaller when the photon excitation energy is below the GaAs bandgap.

Engineering of the Ferro-Magnetic and Ferro-Electric Properties of Strained Quantum Dots

Jacob B. Khurgin and Feng Jin
Department of Electrical and Computer Engineering
The Johns Hopkins University
Baltimore MD 21218

Abstract

Multiple quantum dot structures with ferrimagnetic and/or ferroelectric properties are proposed. Curie temperatures are estimated for InGaAs/InAlAs quantum dot for ferrimagnetic arrangement and InGaAs/InP quantum dots for ferroelectric arrangement on InP substrate. Potential applications in information processing and storage are also considered.

1 Introduction

Advances in the growth of semiconductor materials have allowed to apply methods of bandgap engineering [1] to develop structures with novel electronic and optical properties. Recently attentions have been gradually shifting from 2-dimensional structures to lower-dimensional ones such as the self-organized quantum dots (QDs) [2]. QDs, being essentially large scale models of individual atoms or molecules, allow ultimate flexibility in the design of materials with pre-determined physical properties and a number of proposals have been put forward promising to utilize QDs for information processing [3, 4].

As for the magnetic properties, research had been conducted mostly on the low-dimensional structures made from either ferromagnetic or diluted paramagnetic materials [5, 6]. Experiments on spin-polarized transport and tunneling have led to the proposal for spin-transistors [7], laying a foundation for a new field of magneto-electronics. To make the magneto-electronic devices practical, they must be compatible with conventional VLSI technology, yet nowadays the research has been conducted with materials that are magnetic even in the absence of confinement, and for the most part incompatible with the Si or GaAs technology [8]. Confinement in one or more dimensions does modify magnetic properties, but the changes mostly have quantitative character.

In general, rather weak magnetic field is difficult to detect, and it might be far more desirable to have devices exploiting the electric properties of QDs. Bakshi et

al [3, 9] had proposed using arrays of spontaneously polarized anti-ferroelectric elongated QDs ("quantum dashes") for information processing. This concept had been further explored by Chaplik and Govorov [10, 11], who had shown that depending on the arrangement of QDs in the array, one can obtain both ferroelectric and anti-ferroelectric arrangement. From the practical point of view, ferroelectric arrangement is preferable since the macroscopic polarization greatly facilitates input and output via dipole-dipole interactions, yet the "triangular" arrangement of QDs in plane [10], required for ferro-electricity, is far beyond the capability of present fabrication techniques. As shown by Landauer [12], there also exists a very strong limitation on the size of such arrays imposed by the depolarization force of the array itself. An arrangement of four coupled QDs has been suggested [13, 14] for the so-called cellular automata. The four-dot cell is, however, a quadrupole, and in order to read information one has to directly detect the charge on each dot [15, 16], i.e. the QDs have to be capacitatively-coupled to input-output circuit which makes the access more difficult. Thus it appears to be preferable to get hold of a material with sizable macroscopic dipole moment which can be remotely sensed and switched. The information can be then written upon or read from such material remotely - using an external field sensor that does not have to make physical contact with the medium. Alternatively, one can incorporate this artificial ferroelectric material into the field effect transistors (FETs) in order to create non-volatile recording medium.

In this paper, two strained quantum dot structures are proposed. The first one, an array of QD subject to compressive and tensile strain, is shown to lead ferrimagnetic arrangement of magnetic moments, while the second one, consisting of alternating strained and unstrained QDs, possesses spontaneous polarization. In section 2, analysis of ferrimagnetic arrangement is presented and an example of strained $In_{1-x}Ga_xAs/InAlAs$ QDs grown on InP substrate is used to estimate to Curie temperature. In section 3, ferroelectric arrangement is discussed, and Curie temperature and spontaneous polarization are calculated for the case of $In_{1-x}Ga_xAs/InP$ QDs grown on InP. Improvements and potential applications are discussed in section 4.

2 Engineering of Ferri-magnetic Properties

In semiconductors, Coulomb repulsion forces are strong enough to make it feasible to keep a single carrier per QD [17]. One can then imagine an array of QDs each having a single carrier that has gotten there by either doping or applying potential to a gate. The exchange interaction will always be negative ($J_{ex} < 0$), yielding the system's ground state with an anti-ferromagnetic (AFM) alignment of spins, as predicted by Hubbard [18]. It has been proposed in [19] and [20] that AFM-arranged QDs can be used in order to construct single-electron quantum computers that would hold a number of advantages over the "anti-ferroelectric" QD computers [4], and the stability

of the AFM alignment has been examined in [21]. There are two basic problems with AFM QD computing and memory - the input/output is extremely difficult, because there is no long-range magnetic field and each QD needs to be accessed individually, and constant bias magnetic field is always required for the system to settle in a well-defined state. Obviously, the arrangement of spins with macroscopic magnetic moment is highly desirable.

AFM alignment of the spins does not preclude the possibility of having a net macroscopic magnetic moment as long as the magnetic moments on neighboring sites do not cancel each other exactly, as in ferrimagnetic (FiM) materials. But where can this dissimilarity of magnetic moments come from in the case of QDs? Not from the conduction band, where at low doping density electrons occupy the states with zero orbital momentum. No matter what material is used, the magnetic moment is equal to $\mu_z = -g_s\mu_B\hbar^{-1}S_z$, where $\mu_B = e\hbar/2m$ is Bohr magneton and $g_s \approx 2$ is the gyromagnetic ratio. The situation is quite different near the top of valence band. where the magnetic moment μ_z is a function of not only its spin S_z, but also its orbital momentum L_z, or $\mu_z = -g_J\mu_B\hbar^{-1}J_z$, where g_J is a Lande splitting factor that is equal to 4/3 for the states near the top of valence band - ${}^2P_{\frac{3}{2}}$.

In order to create a FiM QD we thus need to combine QDs populated by holes with different values of L_z and J_z. In III-V and group IV semiconductors the top of the valence band is four-fold degenerate with heavy holes (HHs) described by Bloch functions $u_{h,\pm\frac{3}{2}} = |J = \frac{3}{2}\hbar, J_z = \pm\frac{3}{2}\hbar >$, and light holes (LHs) described by $u_{l,\pm\frac{1}{2}} = |J = \frac{3}{2}\hbar, J_z = \pm\frac{1}{2}\hbar >$. It is clear that HHs have projection of the magnetic moment on axis z equal to $\mu_{z,hh} = \pm 2\mu_B$ and the LHs $\mu_{z,lh} = \pm\frac{2}{3}\mu_B$. If a QD with a single LH is placed next to a QD with a single HH (Fig. 1), then the Heisenberg Exchange Hamiltonian can be introduced as $\mathcal{H}_{ex} = \mathcal{J}_{ex}\hbar^{-2}\mathbf{J_{hh}} \cdot \mathbf{J_{lh}}$, The exchange integral $\mathcal{J}_{ex}$ is, of course, negative, and favors the anti-parallel alignment of moments, $J_{z,hh} = \pm\frac{3\hbar}{2}$ and $J_{z,lh} = \mp\frac{\hbar}{2}$. The magnetic moment of this state, however, is not 0, but is equal to $\mu_z = \pm\mu_{z,hh} \mp \mu_{z,lh} = \pm\frac{4}{3}\mu_B$. Expanding to an array with two sub-lattices of QDs - one with LHs and one with HHs we can create a FiM with Curie temperature of the order of $T_c \sim \mathcal{J}_{ex}/k_BT$.

This approximation shall be refined further on, but for now, the crucial question is how to obtain array of alternating LHs and HHs? The answer lies in the use of strain that splits the degeneracy of the LHs and HHs. The presence of the shear component of strain causes the energies of the HH and LH bands to split near the Γ - point by $\delta E_{sh} = E_{lh}(k = 0) - E_{hh}(k = 0)$ which can be as large as $100meV$. Now, if one considers the situation in Fig. 1, there are two QDs grown on InP substrate. The composition of QD_1 is $In_{1-x}Ga_xAs$; $x > 0.47$ hence QD_1 is under biaxial tension and the LH, $J_z = \pm\frac{1}{2}$ is above the HH $J_z = \pm\frac{3}{2}$, while in the QD_2, grown from $In_{1-y}Ga_yAs$; $y \leq 0.47$ the situation is reversed. The QDs are separated and surrounded by a lattice-matched $In_{0.52}Al_{0.48}As$ barrier. By properly choosing the

dimensions of QDs it is not difficult to achieve a near resonance between $E_{lh,1}$ and $E_{hh,2}$. Magnetic properties of the structure do not rely upon the resonant tunneling, and thus the structure is relatively tolerant to size disorder, which can be as large of 10% according to our calculation.

To find $\mathcal{J}_{ex}$ let us consider a simple Hubbard model for two QDs with six Pauli-allowed two-hole states:

- $\Phi_1 = |\Psi_{1,\frac{1}{2}}, \Psi_{1,-\frac{1}{2}}>$ and $\Phi_2 = |\Psi_{2,\frac{3}{2}}, \Psi_{2,-\frac{3}{2}}>$ - $J_{z,t} = 0$ - both holes are on QD_1 or QD_2 respectively;
- $\Phi_3 = |\Psi_{1,\frac{1}{2}}, \Psi_{2,\frac{3}{2}}>$ and $\Phi_4 = |\Psi_{1,-\frac{1}{2}}, \Psi_{2,-\frac{3}{2}}>$ - $J_{z,t} = \pm 2\hbar$ - two "ferromagnetic" states with orbital moments of QD_1 and QD_2 parallel to each other;
- $\Phi_5 = |\Psi_{1,\frac{1}{2}}, \Psi_{2,-\frac{3}{2}}>$ and $\Phi_6 = |\Psi_{1,-\frac{1}{2}}, \Psi_{2,\frac{3}{2}}>$ - $J_{zt} = \mp\hbar$ - two "FiM" states with orbital moments of QD_1 and QD_2 anti-parallel to each other;

The one-hole states Ψ_{i,J_z} here are the products of the envelope wavefunction f_{i,J_z} and one of the Bloch wave-functions $u_{l(h),J_z}$.

Hubbard Hamiltonian [22, 23] can now be written as

$$\mathcal{H}_{Hub} = \begin{pmatrix} E_0+U_1 & 0 & T_2 & T_2 & T_1 & T_1 \\ 0 & E_0+U_2 & T_2 & T_2 & T_1 & T_1 \\ T_2 & T_2 & E_0 & 0 & 0 & 0 \\ T_2 & T_2 & 0 & E_0 & 0 & 0 \\ T_1 & T_1 & 0 & 0 & E_0 & 0 \\ T_1 & T_1 & 0 & 0 & 0 & E_0 \end{pmatrix}, \quad (1)$$

where $E_0 = E_{1,lh} = E_{2,lh}$, $T_1 =< \Psi_{1,\frac{1}{2}}, \Psi_{1,-\frac{1}{2}}|H|\Psi_{1,\frac{1}{2}}, \Psi_{2,-\frac{3}{2}} >\sim< u_{l,\frac{1}{2}}|u_{h,\frac{3}{2}} >$ is the probability of hole tunneling between QD_1 and QD_2 with change in angular momentum $\Delta J_z = \pm\hbar$, $T_2 =< \Psi_{1,\frac{1}{2}}, \Psi_{1,-\frac{1}{2}}|H|\Psi_{1,\frac{1}{2}}, \Psi_{2,\frac{3}{2}} >\sim< u_{l,\frac{1}{2}}|u_{h,-\frac{3}{2}} >$ is a probability of hole tunneling between QD_1 and QD_2 with change in angular momentum $\Delta J_z = \pm 2\hbar$, and U_1 and U_2 are Coulomb interactions between the two holes in the same dot. These tunneling probabilities are not zero since a fair amount of band-mixing takes place in small QDs. Indeed, using 4X4 Luttinger-Kohn [24] Hamiltonian it is not difficult to show that the coupling of heavy-to-light holes in two QDs is much stronger if $\Delta J_z = \pm\hbar$ than if $\Delta J_z = \pm 2\hbar$, i.e. $T_1 \gg T_2$. Substituting $T_2 \approx 0$ into Hubbard Hamiltonian (1) we obtain splitting the $J_{1,z} + J_{2,z} = \pm\hbar$ and $J_{1,z} + J_{2,z} = 2\hbar$ states by $\delta = -4T_1^2/\bar{U}$, where $\bar{U}^{-1} = (U_1^{-1} + U_2^{-1})/2$ and formally introduce the Heisenberg exchange integral into

$$\mathcal{J}_{ex} = -\frac{2}{3}\frac{4T_1^2}{\bar{U}} \quad (2)$$

and then follow mean field theory [25] to obtain the spontaneous magnetization in the absence of external field $\mathcal{H}$ at the Curie temperature

$$T_c = \frac{1}{2} \cdot \frac{3}{2} |\mathcal{J}_{ex}| / k_B = \frac{2T_1^2}{\bar{U} k_B} \tag{3}$$

Calculations based on diagonalization of Hubbard Hamiltonian (1) are performed with matrix elements determined by diagonalization of the Luttinger-Kohn Hamiltonian for a variety of one-dimensional QD arrays with a number of variable parameters. All the investigated structures consist of alternating a narrow square unstrained $In_{0.53}Ga_{0.47}As$ QD and a wider strained $In_{1-x}Ga_xAs(x > 0.47)$ QD separated by unstrained $In_{0.52}Al_{0.48}As$ barriers. For each set of the parameters for the strained QD_1, the thickness of the unstrained QD_2 has to be adjusted to assure the resonance between $E_{lh,1}$ and $E_{hh,2}$ prior to evaluation of the T_c.

In Fig. 2 the dependence of T_c on the thickness of QD_1 is plotted for four different compositions of the strained QD_1. The general trend of the T_c is to increase with the decrease in the thickness of the QDs and their separation - quite a natural result of the increase in coupling energy T_1, but eventually the delocalization takes place and spontaneous magnetization disappears resulting in maximum T_c of about $25K$.

If QDs are arranged in a two-dimensional superlattice, with four or more nearest neighbors, T_c would be of the order of $100K$, and it would be a true Curie temperature, i.e. one indeed could expect phase transition at temperature close to T_c. But the growth of QDs of different compositions in the same plane appears to be out of reach of today's methods. As for 1-dimensional pillar-like structure (Fig. 3), it is well known [26] that no long-range (i.e. $N_{QD} \to \infty$) order can exist there and thus there is no spontaneous magnetization. But for a limited number of QDs we can expect the system to maintain spontaneous polarization as long as $T \ll T_c/lnN_{QD}$. So, for a small number of QDs lined-up in a polymer-like chain, one can expect the magnetic order to be maintained in the absence of external field, albeit at temperatures less than $25K$. These FiM pillars can be accessed by an STM tip (Fig. 3) or, conceivably, electrically using current loops.

3 Engineering of Ferro-Electric Properties

Ferro-electric properties of quantum dots are achieved in a similar way. The proposed structure, which can be grown on a InP substrate, as shown in Fig. 4, consists of a number of unit cells, each made up of two "dashes", each "dash" being a pair of coupled QDs (CQDs). The first pair of CQDs is made up of $In_{0.53}Ga_{0.47}As$ and thus is unstrained, while the other one, made up of $In_{1-x}Ga_xAs(x < 0.47)$ material, is compressively strained. We assume here the barrier material to be InP, although InAlAs

can also be used. The two QDs of the same pair are placed close so that holes can tunnel through the barrier t_b between them. On the other hand, the distance between pairs l is made larger than t_b in order to prevent tunneling. The valence band discontinuity of $In_{1-x}Ga_xAs(x < 0.47)/InP$ is larger than that of $In_{0.53}Ga_{0.47}As/InP$, so that the inter-dot hole tunneling in the strained CQD pair is weaker than that in unstrained CQD pair for the same barrier thickness. Therefore, in the strained pair, the energy split between the ground (symmetric) and the first excited (anti-symmetric) states is smaller and, consequently, it is easier for the Coulombic force exerted by the adjacent CQD pair to move the center of the positive charge away from the center of the pair. Thus, when one hole is placed in each pair, the strained CQD pair acquires a larger dipole moment than the unstrained one, and the net polarization results.

The dimensions of CQDs are chosen in such a way that the ground state energies of unstrained and strained pairs are nearly equal. Typical sizes are $70 \times 70 \times 160\mathring{A}^3$ for the unstrained and $55 \times 55 \times 160\mathring{A}^3$ for the strained CQDs.

It is important to note that the ferroelectricity of the proposed structure depends mostly on the interactions between the adjacent CQDs along the direction of growth, where all the dimensions can be precisely controlled. Therefore, in principle, one can think about the individual "ferroelectric pillars" if the CQDs are widely separated in the lateral plane. Bringing the "pillars" together will result in two- or three- dimensional ferroelectric domains, but the longitudinal dipole-dipole interaction always dominates the lateral interaction.

We have performed computer simulation of the proposed structure in order to determine the value of macroscopic polarization d_x and Curie temperature T_c by iteratively solving the following the Schrödinger equation of the ionized acceptor ions.

$$\hat{H}(\vec{r}_1, \vec{r}_2) \mid \Phi_1(\vec{r}_1), \Phi_2(\vec{r}_2)\rangle = E \mid \Phi_1(\vec{r}_1), \Phi_2(\vec{r}_2)\rangle \tag{4}$$

where $\mid \Phi_1(\vec{r}_1)\rangle$ and $\mid \Phi_2(\vec{r}_2)\rangle$ are wave-functions of holes in unstrained and strained pairs respectively, and the Hamiltonian is

$$\hat{H}(\vec{r}_1, \vec{r}_2) = -\frac{\hbar^2}{2m_1^*}\nabla_1^2 - \frac{\hbar^2}{2m_2^*}\nabla_2^2 + V_1(\vec{r}_1) + V_2(\vec{r}_2) + \frac{e^2}{4\pi\epsilon \mid \vec{r}_1 - \vec{r}_2 \mid} \tag{5}$$

where $V_1(\vec{r}_1)$ and $V_2(\vec{r}_2)$ may include the potential due to background charges, and the exchange interaction between the pairs is neglected due to the negligibly small overlap between $\Phi_1(\vec{r}_1)$ and $\Phi_2(\vec{r}_2)$. The per-pair net dipole moment can then be evaluated as

$$d_x = e\int x|\Phi_1(\vec{r}_1)|^2 d\vec{r}_1 + e\int x|\Phi_2(\vec{r}_2)|^2 d\vec{r}_2 \tag{6}$$

while the Curie temperature is found as

$$T_c \approx N\frac{E_0 - E}{k_B} \tag{7}$$

where N is the number of nearest neighbors, which is 2 in our case, k_B is the Boltzmann's constant, and E_0 is the energy of unpolarized state, i.e. the state in which both holes are in the symmetric states in their respective CQDs.

In Fig. 5, T_c and net dipole moment d_x versus the thickness of the CQD barrier t_b are shown for two values of compressive strain, 0.2% and 0.4% (corresponding to x=0.439 and 0.410 respectively). The distance between the CQD pairs l is kept at a constant value of $150\mathring{A}$. As the barrier thickness increases, the symmetric-antisymmetric energy split decreases, so that Coulomb interaction is capable of localizing the holes "diagonally" which results in larger T_c. While the individual dipole moments of CQD pairs increase, they become nearly equal to their respective maxima and hence the net dipole moment decreases and converges to a fixed value, determined by the sizes of the cell.

Both Curie temperature T_c and the dipole moment d_x can be optimized, as shown in Fig. 6 and 7, where both l and t_b are varied while l is kept at least $10\mathring{A}$ larger than t_b. The reason for existence of the maxima is the fact that two competing processes - tunneling within each CQD pair which tends to de-localize holes and Coulomb repulsion that tends to localize them, depend on the t_b. But these dependencies are quite different - roughly inverse exponential in case of tunneling and a much weaker one in case of Coulomb repulsion. Therefore, there is always an optimum t_d for which the net localizing force is the strongest. The maximum of T_c is about 27K, which, while far below the boiling point of liquid nitrogen, is still significantly higher than that in triangular array in [10] and does not depend on the exact arrangement of QDs in the lateral plane.

The net dipole moment of each cell at this temperature is about $8e\mathring{A}$, which, for a three-dimensional material, corresponds to the spontaneous polarization density of $10^{-5}C/m^2$. Such spontaneous polarization can generate electrostatic fields of the order of $10^3 - 10^4 V/cm$ in the vicinity of the artificial ferroelectric - more than enough to be "picked up" by a external sensor or enough to cause the depletion of the channel of FET if it is placed between the gate and channel.

4 Discussions

The main reason for such low Curie temperatures is that in QDs Coulomb interactions responsible for magnetic alignment are scaled down in comparison to conventional materials due to large dot-to-dot distances and larger dielectric constant. The order of this reduction is comparable to scaling down of the Rydberg energy in the material. Therefore, in the wider-bandgap materials, such as GaN-based, one can expect the increase of the T_c by as much as an order of magnitude. On the other hand, going to the lower-bandgap materials, such as InSb, with their large effective Lande factors would allow one to increase the magnetization . These structures could be then used

as memory cells or, possibly switching elements.

For ferro-electric structures, the predicted low Curie temperature is caused by both the low effective mass and the high dielectric constant of the InGaAs and InP. Therefore, one can envision that by employing wider-bandgap semiconductors, such as, nitride or II-VI materials, one may succeeding raising the Curie temperature above 77K.

In conclusion, we have proposed a method of engineering one-, two-, and three- dimensional QD arrays that possess ferrimagnetic and/or ferroelectric properties which are insensitive to the lateral arrangement of the QDs. We estimated the Curie temperature for the artificial ferrimagnetic to be of the order of $25K$, while for the artificial ferroelectric the Curie temperature is found to be of the order of $20K$, and the spontaneous polarization of the order of $10^{-5}C/m^2$. The proposed structures can find applications in information storage and processing.

This work is supported by NSF and AFOSR.

References

[1] F. Capasso and A. Y. Cho, Surface Science **299**, 878 (1994).

[2] P. M. Petroff and S. P. DenBaars, Superlattices and Microstructures **15**, 15, (1994).

[3] P. Bakshi, D.A. Broido, and K. Kempa, J. Appl. Phys. **70**, 5150 (1991).

[4] C. S. Lent, P. D. Tougaw, W. Porod, and C. H. Bernstein, Nanotechnology **4**, 49 (1993).

[5] S. Gider, D. D. Awchalom, T. Douglas, S. Mann, and M. Chaparala, Science **268**, 77 (1995).

[6] S. A. Crooker, D. D. Awschalom, and N. Samarth, IEEE J. on Selected Topics in Quantum Electronics **1**, 1082 (1995).

[7] M. Johnson and R. Silsbee, Phys. Rev. **B 35**, 4959 (1987).

[8] J. Shi, J. M. Kikkawa, R. Proksch, T. Schaff, and D. D. Awschalom, Nature **377**, 707 (1995).

[9] K. Kempa, D. A. Broide, and P. Bakshi, Physical Review B **43**, 9343 (1991).

[10] A. O. Govorov and A. V. Chaplik, J. Phys.:Condens. Matter **6**, 6507 (1994).

[11] A. V. Chaplik and A. O. Govorov, J. Phys.:Condens. Matter **8**, 4071 (1996).

[12] R. Landauer, Solid State Commun. **95**, 7 (1995).

[13] C. S. Lent, P. D. Tougaw, and W. Porod, Appl. Phys. Lett. **62**, 714 (1993).

[14] Craig S. Lent and P. D. Tougaw, J. Appl. Phys. **75**, 4077 (1994).

[15] I. Amlani, A. O. Orlov, G. L. Snider, C. S. Lent, and G. H. Bernstein, Appl. Phys. Lett. **71**, 1730 (1997).

[16] I. Amlani, A. O. Orlov, G. L. Snider, C. S. Lent, and G. H. Bernstein, Appl. Phys. Lett. **72**, 2179 (1998).

[17] J. H. F. Scottt-Thomas, S. B. Field, M. A. Kastner, H. I. Smith, and D. A. Antoniadis, Phys. Rev. Lett. **62**, 583 (1989).

[18] J. Hubbard, Proc. Roy. Soc. **A276**, 238 (1963).

[19] S. Bandyopadhyay, B. Das, and A. E. Miller, Nanotechnology **6**, 113 (1994).

[20] S. Bandyopadhyay, A. Balandin, V. P. Roychowdhury, and F. Vatan, Superlattices and Microstructures **23**, 445 (1998) and references therein.

[21] V. V. Kostyuchenko, Russian Microelectronics **25**, 327 (1996).

[22] P. W. Anderson, *Magnetism* (G. T. Rado and H. Suhl, eds.), (Academic Press, NY, 1963), Vol.1, p.25.

[23] J. Calloway, *Quantum Theory of the Solid State* (Academic Press, San Diego, 1991), p.272-276.

[24] J. W. Luttinger and W. Kohn, Phys. Rev. **97**, 869 (1955).

[25] J. S. Smart, *Effective field theories of magnetism* (Saunders, Philadelphia 1966).

[26] T. D. Schultz, D. C. Mattis, and E.H. Lieb, Rev. Mod. Phys. **36**, 856 (1964).

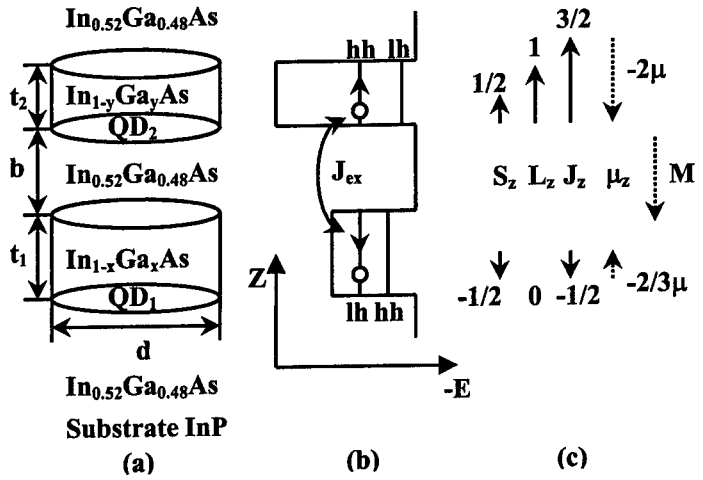


Figure 1: One period of the ferrimagnetic QD array.
a) geometry
b) valence-band alignment
c) directions of mechanical and magnetic momenta.

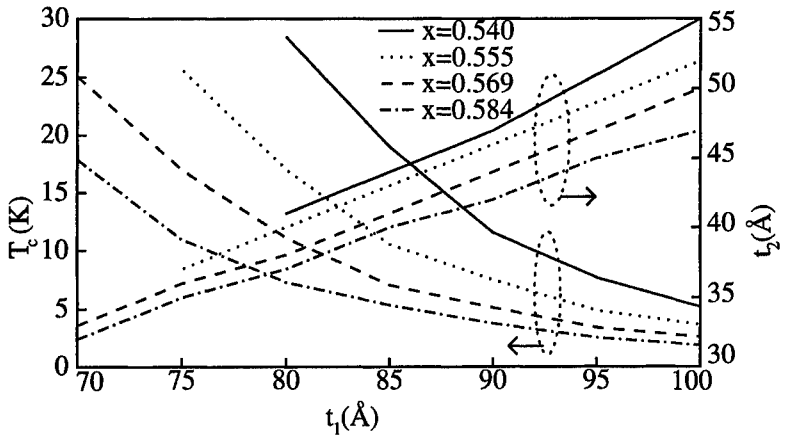


Figure 2: Curie temperature T_c and the thickness of unstrained QD_2 - t_2 as functions of the thickness of strained QD_1 - t_1 for different compositions x of strained $In_{1-x}Ga_xAs$ QD_1. The lateral size $d = 120\mathring{A}$. The barrier thickness $t_b = 20\mathring{A}$.

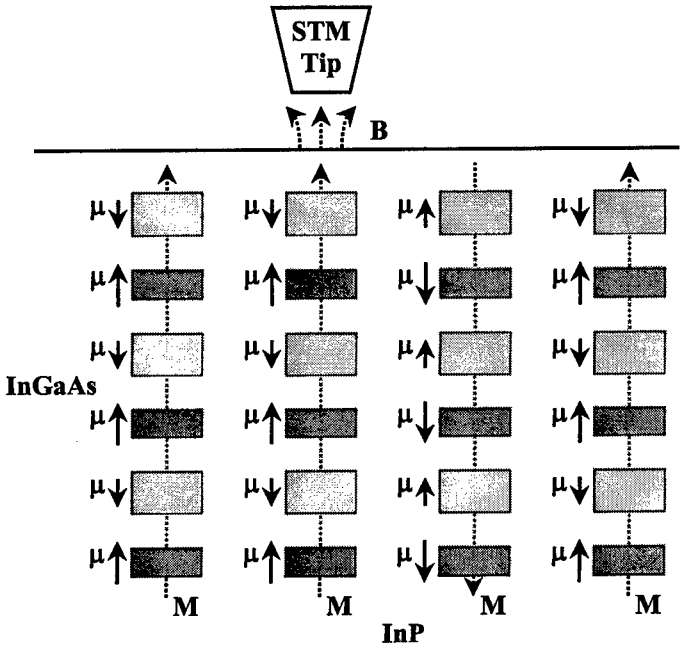


Figure 3: Ferrimagnetic pillars accessed by STM.

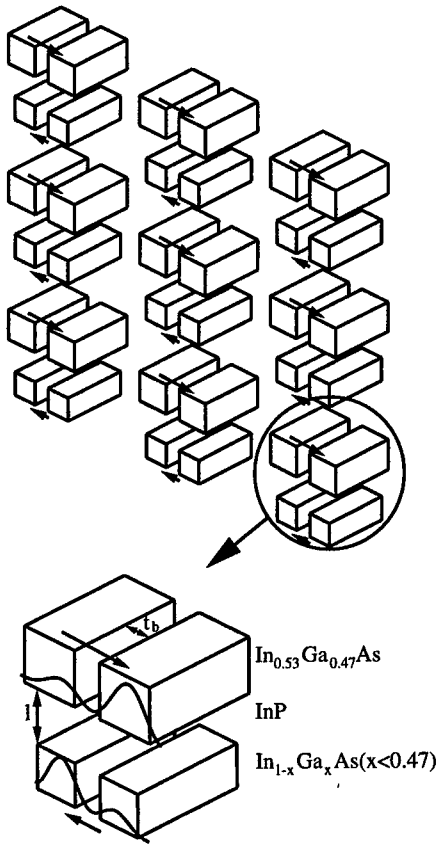


Figure 4: Array of ferroelectric coupled QDs.

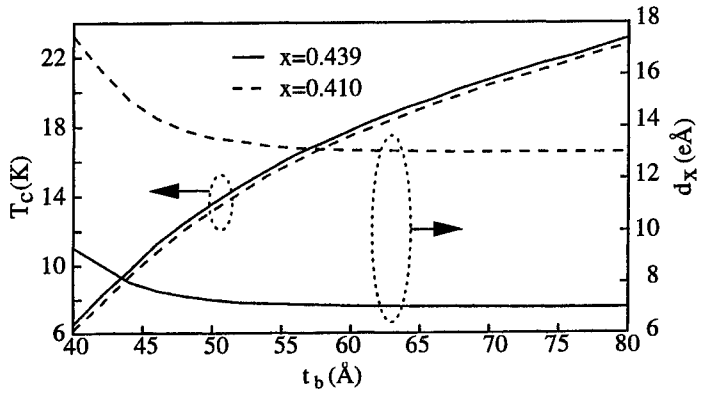


Figure 5: Curie temperature and per-unit-cell dipole moment vs the barrier thickness of the CQD t_b. l is equal to 150$\AA$.

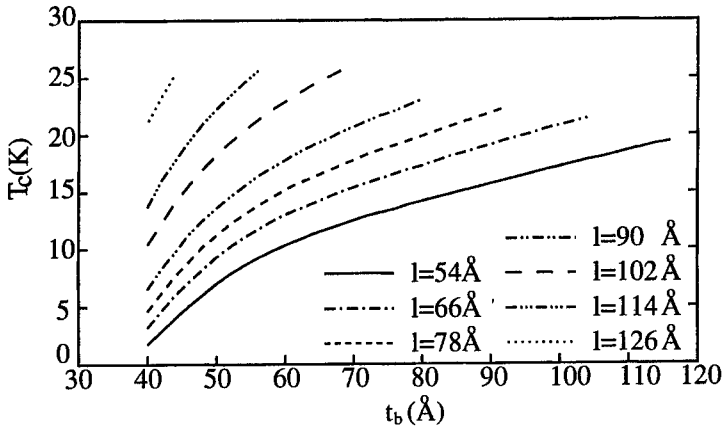


Figure 6: Curie temperature as a function of t_b and l. x=0.439 in $In_{1-x}Ga_xAs(x < 0.47)$.

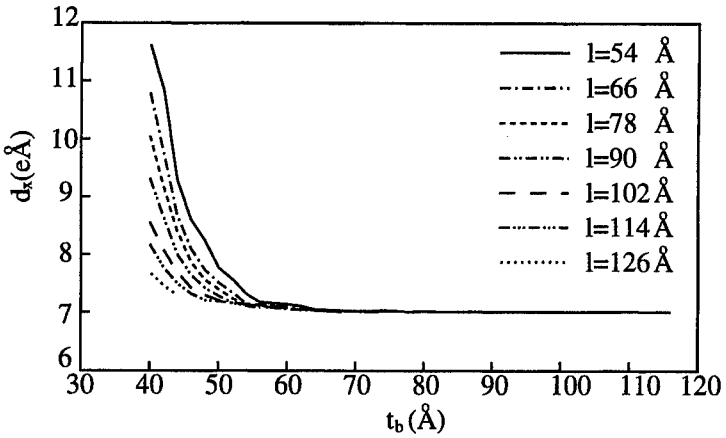


Figure 7: Dipole moment per unit cell as a function of t_b and l. x=0.439 in $In_{1-x}Ga_xAs(x < 0.47)$.

OPTICAL PROPERTIES OF ZnSe/CdSe-BASED QD STRUCTURES

A.D. Andreev, R.P. Seisyan, R.M Datsiev, S.V. Ivanov
A.F.Ioffe Physical-Technical Institute
26 Polytekhnicheskaya, St.-Petersburg 194021, Russia
Fax: +7-812-247-1017; Phone: +7-812-247-9994
E-mail: andreev@theory.ioffe.rssi.ru

ABSTRACT

Optical properties of planar arrays of CdSe QDs in Zn(S)Se matrix have been investigated both theoretically and experimentally. Structures with different nominal thickness of the CdSe QD-like insertions have been studied. Real absorption spectra of CdSe QDs extracted from the transmission and reflection spectra have been obtained. It is shown that when the nominal thickness of CdSe increases, the optical density spectrum peak, which corresponds to the absorption by QDs, shifts to lower energies and becomes more pronounced. Strain distribution, carrier spectrum and exciton binding energy in disk-like QDs which form a periodic array have been calculated. The results of calculations are used to interpreter the obtained experimental data. The calculated positions of the QD absorption maximum are in good agreement with experimental ones.

I.INTRODUCTION

The quantum dot (QD) structures have potential advantage over conventionl QW structures, which is due to their 0D density of states properties. First laser structures with CdSe planar QDs in ZnSe-based matrix have been fabricated recently and laser light radiation has been successfully obtained [1]. Howéver, it was demonstrated both theoretically and experimentally [2, 3] that in some cases planar CdSe QDs do not provide proper carrier localization and therefore the advantages of 0D structures do not realize.

The aim of this paper is to carry out thorough analysis of optical properties of ZnSe/CdSe-based heterostructures with QDs as perspective candidates for the creation of blue lasers. In particular, the following problems are studied: (1) calculation

of the strain distribution and carrier energy spectrum in the QD structure; (2) determination of the optimal structure parameters when proper carrier localization exists, which is accompanied by realization of 0D structure advantages.

II.EXPERIMENT

The structures studied in this paper were grown by MBE and contain 20 CdSe 2D insertions (planar QDs) equally spaced by 30 Å and inserted in $ZnS_{0.07}Se_{0.93}$ or ZnSe matrix, were grown by MBE on GaAs(001) substrate. Growth conditions and alloy composition control technique have been reported elsewhere [4]. The thin ($\sim$ 200 Å) ZnMgSSe barriers on both sides of the CdSe/ZnSSe or CdSe/ZnSe submonolayer superlattice were grown to provide a proper carrier confinement. The nominal thickness of the CdSe insertions, ξ is estimated from growth calibrations and X-ray measurements to be from $\xi \sim 0.55$ to $\xi \sim 1$ monolayers for different samples.

For optical studies the substrate was completely removed. The optical transmission and reflection spectra as well as photoluminescence spectra have been obtained at helium temperature. Real absorption spectra of the samples were extracted from the transmission and reflection ones (see Fig.1). Taking account of properties of light propagation through relatively transparent plate we can exclude all interference picture hindrance and reconstruct true absorption (see for example [5]). Figure 2 shows the absorption spectra obtained for three samples with nominal thickness of CdSe equal to $\xi_1 = 1.0$; $\xi_2 = 0.6$ and $\xi_3 = 0.55$. Features due to the exciton transitions corresponding to the carrier states in QDs can be clearly observed at the lower energy part of the absorption spectra. Respective transition energies, E_i^{ex} are listed in Table I. For the structures with larger nominal thickness ξ the height of the CdSe QD is larger, the carrier localisation is stronger and corresponding absorption maxima becomes very clear. For the structures with relatively small ξ these maxima are very close to the quasi-bulk continuum absorption corresponding to the bulk-like superlattice of QDs (see curve 3 on Fig. 2). For all three structures the QD absorption is accompanied by strong photoluminescence maximum with Stokes shifts of 28, 25 and 15 meV for samples 1, 2 and 3 respectively. Strong maxima on the absorption spectra at higher energy part around $E \approx 2.84$ eV correspond to the absorption of ZnSe or ZnSSe matrix and buffer layers.

III.THEORY

To model the optical properties of the structures we assume that: (i) the CdSe QDs have a shape of flat cylinder with diameter D and height h; (ii) the QDs form a 3D periodic structure with in-plane period $d_{||}$ and with the period d_z in the growth direction.

Since the CdSe/ZnSe-based QD structure is a strongly lattice mismatched system, detailed calculation of the strain field is required for further modelling of the electronic and optical properties. For calculation of the strain distribution in the QD structure we have used Green's tensor formalism which takes account of elastic anisotropy of cubic crystals [3, 8]. For simplicity we assume that the elastic constants of the QD and the matrix materials are equal. The main advantage of our method is that it allows to obtain analytical expression for the strain distribution in the periodic QD structure. First we obtain the analytical formulae for the Green's tensor [6] for the elastic equations for the infinite media of cubic symmetry. Then using Eshelby's method of inclusions [7] we found the analytical expression for the Fourier transform of the strain tensor [8]. These expression were used for further calculations of the carrier spectrum. Figure 2 shows the calculated strain tensor components in the CdSe/ZnSe-based structure. In the (x, y) plane perpendicular to the growth direction z the strain decrease rather rapidly outside the dot; on the distances of order of 1 nm the strain tensor components nearly vanish. Along the growth direction the strain in matrix is relatively high, which provides effective compensation of strain. This means that using QDs it is possible to achieve strain relaxation in defect-free structures and therefore such structures is a perspective candidate for the creation of long-living lasers.

Due to specific QD structure under study, in calculation of the energy spectra in CdSe-based QDs it is important to take account the following points: (i) the QDs form the 3D superlattice and therefore tunnelling processes between the dots are crucial; (ii) QDs are rather thin (several monolayers) and, consequently, the case of finite value of the barrier heights both for electrons and holes should be considered; (iii) full account of 3D strain distribution is necessary in order to obtain the actual potential profile for the carriers in QD. All these three effects are taken into account in the present paper. As shown in the previous section, the strain is rather large in our case and therefore the splitting between light and heavy hole states in the QD is enough to consider these states separately neglecting light-heavy hole mixing. For wide band-gap semiconductors the conduction band can also be considered completely decoupled from the valence band. Thus, it is possible to use simple effective-mass model taking account of calculated strain distribution. We employ plane-wave expansion method to find the carrier spectrum and wave functions. In was found out that the degree of the carrier localisation in QDs strongly depends on the structures parameters: QDs height h and distances between nearest QD in the growth direction, d_z, and in the lateral direction, $d_{||}$, and on the barrier composition. Using two-parameter variational technique and obtained wave functions of the carriers in QD structure we have calculated the exciton binding energy and oscillator strength. The position of the calculated exciton absorption peak and oscillator strength turn out to be in good agreement with experiment (see Table I) proving that the developed theoretical model describe properly the optical properties of the studied samples.

sample	ξ_i	E_i^{ex}, eV	E_{ex}^{theor}, eV
1	1.0	2.658	2.650
2	0.60	2.709	2.701
3	0.55	2.770	2.765

Table I. Theoretical and experimental energies E_i^{ex} of the transitions corresponding to the exciton states in QD structures with different nominal thickness ξ of CdSe insertion. Experimental values are extracted from measured absorption spectra as indicated on Fig.2.

IV. CONCLUSIONS

In this paper we have measured the optical absorption and photoluminescence spectra of CdSe planar QDs in ZnSSe matrix. It is demonstrated that the absorption maximum due to exciton states in QDs is shifted to lower energies as the QD height increased (i.e. nominal thickness ξ is increased). To interpret the obtained experimental results and perform gain modelling of the lasers based on the studied structures we have developed a theoretical model assuming that the QD are flat cylinders with characteristic diameter of $D \sim 4$ - 5 nm. Calculation of the strain distribution in the studied structures with strong lattice mismatch demonstrated that the matrix becomes partly strained providing enough smooth strain relaxation and small amount of intrinsic structure defects. Therefore high quality QD-based structures are perspective candidates for the creation of long-living lasers. Calculated energy positions of the QD absorption maxima are in good agreement with experimental values. We found that in structures with thin QDs (like sample 3) the carrier localisation is poor and QD advantages do not realise in full degree. Increasing the QD height by increasing the nominal thickness of the CdSe insertion leads to partial in-plane carrier localisation accompanied in larger exciton binding energy and oscillator strength. In experiment this fact is expressed in more pronounced exciton maximum on the absorption spectrum (sample 1, see Fig.2).

References

[1] N.N. Ledentsov, I.L. Krestnikov, M.V. Maximov, S.V. Ivanov, S.V. Sorokin, Zh.I. Alferov, D. Dimberg, C.M. Sotomayor Torres, Appl. Phys. Lett., **96** (10), 1343-1345 (1996).

[2] A.D. Andreev, G.N. Aliev, R.M. Datsiev, S.V. Ivanov, I.L. Krestnikov, R.P. Seisyan, Phys. Stat. Sol. (a), 164, 449 (1997)

[3] A.D. Andreev, *in "In plane Semiconductor Lasers: from Ultraviolet to mid-infrared II"*, Ed. by H. Choi and P. Zory, Proc. SPIE, **3284**, pp. 151 (1998)

[4] S. V. Ivanov, S. V.Sorokin, P. S. Kop'ev, J. R. Kim, H. D. Jung, H. S. Park, J. Crystal Growth, **16**, (1996), 159

[5] D.S. Gerber, G.N. Maracas, IEEE J. of Quan. Elec., **29**, (1993), 2589

[6] I.M. Lifshits, L.N. Rosentsverg, Zhurnal Exper. and Teor. Phiziki, v. 17, N. 9 (1947) (in russian)

[7] J.D. Eshelby, Proc. R. Soc. London, Ser. A, **241**, 376 (1957)

[8] A.Andreev, J. Downes, D. Faux and E. O'Reilly, submitted to J. of Appl. Phys. (1998)

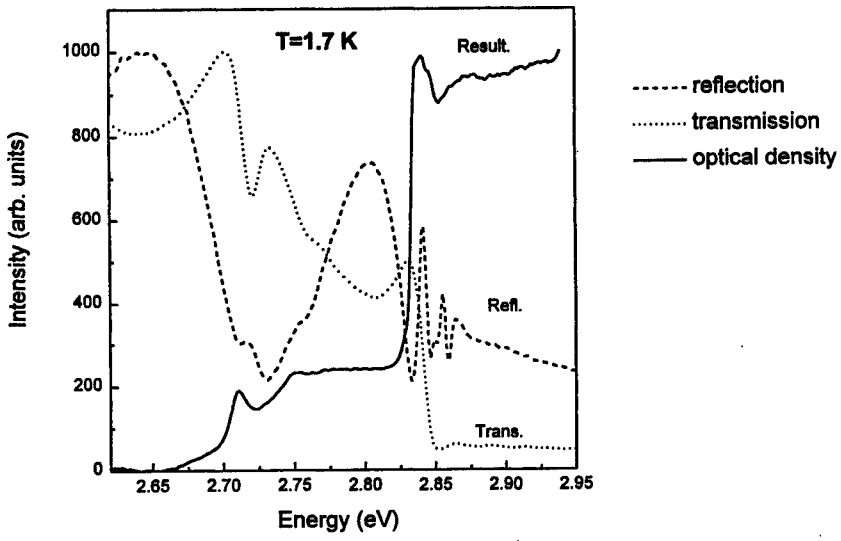


Fig. 1. Transmission, reflection and absorption spectra for CdSe Qds in ZnSe matrix. The nominal thickness of CdSe is 0.6 ML

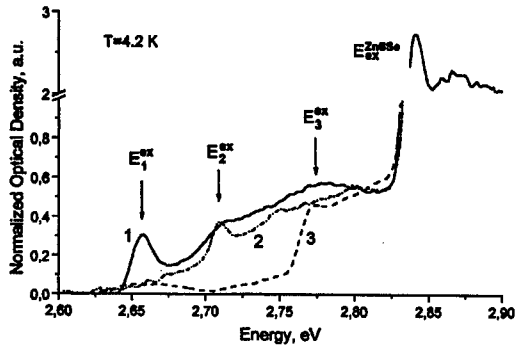


Fig. 2. Normalised optical density versus energy for three samples with different nominal CdSe thickness ξ. Arrows indicate energy positions E_i^{ex} of the exciton maxima corresponding to the states in the QDs for these three samples.

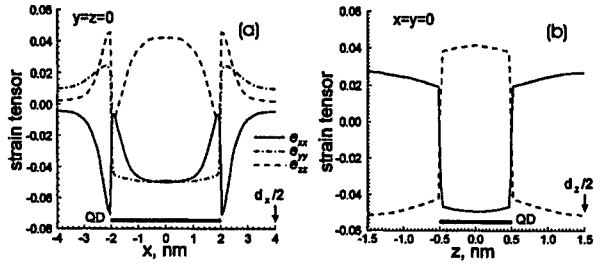


Fig. 3. Variation of elastic tensor components along x (a) and z (b) axises for the following structure parameters: $h = 1$ nm, $D = 4$ nm, $d_x = d_y = 8$ nm, $d_z = 3$ nm. The origin of the co-ordinate system (x, y, z) is in the QD centre, axis z is directed along the growth direction, axises x and y are directed to the center of the nearest QD in the plane. Bold horizontal lines show the boundaries of the QD. Because of symmetry e_{xx} and e_{yy} are equal along z axis and therefore only e_{xx} is shown on the figure (b).

EFFECT OF CARRIER RELAXATON AND EMISSION ON PHOTOLUMINESCENCE OF INAS QUANTUM DOTS

Haijun Zhu, Z.M.Wang, B.Q.Sun, S.L.Feng, D.S.Jiang, and H.Z.Zheng
National Laboratory for Superlattices & Microstructures, Institute of semiconductors, Chinese Academy of Sciences, P.O.BOX 912, Beijing 100083, China

I. INTRODUCTION

Some theoretical studies have proposed that the "phonon bottleneck effects" [1] have bad effects on realizing lasing of QDs. The "bottleneck effects" could be mediated by an alternative rapid relaxation process, such as multi-phonon effects [2] and Auger recombination [3]. In this paper, we report the dependence of PL on temperature at very low excitation density to explore relaxation mechanisms in QDs.

II. EXPERIMENTS AND DISCUSSION

The samples were fabricated by MBE on (100)GaAs substrate. A 0.5μm GaAs buffer layer was deposited first at 600°C, following by a single InAs layer with thickness of 1.7 to 2.5ML, 60s growth interruption and a 20nm GaAs cap layer at 450°C. The QDs nucleation was observed directly by RHEED. Fig. 1 show the PL spectra at several temperatures of a 1.7ML InAs QD sample. All spectra are dominated by a strong luminescence from the InAs QDs. By elimination of the effect of temperature on the band-gap of InAs (Inlet of Fig. 1), it can be found that, the edge of PL at high energy decrease, while the edge of PL at low energy almost does not change. So the red shift of peak position should be considered thermal exciting of excitons from small island with low exciting energy [4] besides the variation of band gap of InAs with temperature. This is consistent with the strong dependence of PL intensity(Fig. 2), peak energy and FWHM(Fig. 3) with the increasing of temperature from 70K to 200K.

However, an anomalous increase of PL intensity was detected with a temperature raising up to 70K as shown in Fig. 2. Other samples also exhibit similar temperature-dependent behaviors. As we know, quantum dots have a temperature-independent recombination lifetime τ [4] of excitons. So, the rate equation of the temperature-related distribution of excitons in steady state, $f(E,T)$, can be written as: $\frac{df(E,T)}{dt} = Cg(E,0) - \frac{f(E,T)}{\tau_w}\exp(\frac{E-E_b}{kT}) - \frac{f(E,T)}{\tau} = 0$, in which $C = C_0/(\tau_c + \tau_r)$ and $g(E,0)$ is used to model the energy distribution of QD states. C_0 is proportional to the excitation power density by the laser, τ_c and τ_r is the carrier capture time from the GaAs barrier into the high-lying energy levels in QDs and that from excited to ground levels in QDs, respectively. For the phonon relaxation process, the relaxation process inside the QDs is slow due to the "bottleneck effects" and reveals a stronger temperature dependence which is determined by a Bose distribution function of longitudinal-acoustic (LA) phonons $n_B = [\exp(\varepsilon/kT) - 1]^{-1}$, following the form $\tau_r = \tau_r^0 \times (n_B + 1)^{-1}$. ε and τ_r^0 denote the threshold LA-phonon energy and the relaxation time for T=0K. τ_{sc} and E_b denote the effective scattering time from the QD ground state into the barrier states and the energy barrier for the thermal emission of carriers, respectively. Our study of the thermal activation process demonstrated that the InAs wetting layer acts as a barrier for the thermal emission of carriers in QDs. Follows from the analysis of the above rate equations The distribution of excitons $f(E,T)$ can be written as:

$$f(E,T) = \frac{\lambda g(E,0)}{[1 + \alpha - \alpha \exp(-\frac{\varepsilon}{kT})][1 + \beta \exp(\frac{E - E_b}{kT})]}$$

where $\lambda = C_0\tau/\tau_c$, $\alpha = \tau_r^0/\tau_c$ and $\beta = \tau/\tau_w$. To avoid Auger process induced carrier scattering, a very low excitation power of 0.2W/cm^2 was used in our experiments, and the corresponding carrier density is estimated to be not larger than $\sim 6\times10^8 cm^{-2}$, i.e. in average less than 0.01 electron-hole pairs per dot. Under a low excitation, the capture time was 25~35ps, while the relaxation time was 30~60ps [5]. It is reasonable to assume $\alpha = 1$. $g(E,0)$ is determined by the low temperature PL spectra and the

energy barrier of the InAs wetting layer with 1.42eV[6] was used for E_b. Considering the InAs QD height about 2.5nm obtained from AFM images, we obtain $\varepsilon = 3.0meV$ [5]. Using the equation (2) to fit the temperature dependence of PL intensity yields $\beta \approx 10^7$, the value being the same order as that obtained by other group [7]. Considering the excitonic lifetime of 1ns, the effective scattering time is ~0.1fs, which is apparently shorter than the value obtained in InGaAs/GaAs quantum wells [8]. Further study is needed to make clear the physics origin. The agreement between the fit and experimental results (Fig. 2) indicates that the phonon-related processes are important for carrier relaxation in InAs QDs. The carrier relaxation is accelerated by the temperature increase due to the enhanced Bose function of LA phonons, which results in a distinct increase of the PL intensity at low temperature range. Using the same set of parameters, we have calculated the temperature behaviors of the peak energy and the FWHM, which is qualitatively in good agreement with the experimental results as shown in Fig. 3. This demonstrates that the thermal emission of carriers out of the QDs is the dominant mechanism leading to the fast red-shift of PL energy and U-shaped dependence of FWHM with increasing temperature. The difference of magnitude partly results from the inter-dot tunneling transfer and the re-trapping of thermal emitted carriers by lower energy QDs which can not be neglected in a given temperature range.

III. CONCLUSION

In summary, the enhancement of the PL intensity with increasing temperature up to 70K was detected under low excitation power, thus suggesting multi-phonon processes play a significant role for carrier relaxation in InAs/GaAs QD structures. Then the strong temperature dependence of PL peak energy and line-width could be well understood.

REFERENCES

1.H.Bensty, C.M.Sotomayor-Torres, and C.Weisbuch, Phys. Rev. B44, R10945 (1991).
2.T.Inoshita and H.Sakaki, Phys. Rev. B46, 7260 (1992).
3.Al.L.Efros, V.A.Kharchenko, and M.Rosen, Solid State Commun. 93, 281 (1995).
4.G.Wang, S.Fafard, D.Leonard, J.E.Bowers, J.L.Merz, and P.M.Petroff, Appl. Phys. Lett. 64, 1815 (1996).
5.B.Ohnesorge, M.Albrecht, J.Oshinowo, A.Forchel, and Y.Arakawa, Phys. Rev. B54, 11532 (1996).
6.S.Sauvage, P.Boucaud, F.H.Julien, J.-M. Gerard, and J.-Y.Marzin, J. Appl. Phys. 82, 3396 (1996).
7.R.Leon, D.R.M.Williams, J.Krueger, E.R.Weber, and M.R.Melloch, Phys. Rev. B56, R4336 (1997).
8.G.Bacher, H.Schweizer, J.Kovac. A.Forchel, H.Nickel, W.Schlapp and R.Losch, Phys. Rev, B43, 9312 (1991).

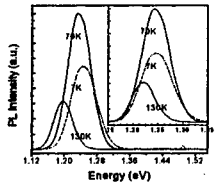


Fig.1 7K, 70K and 130K PL spectra of 1.7ML InAs/GaAs structure. In the inset, the luminescence from InAs QDs at 70K and 130K were energy offset to account for the InAs band-gap variation with temperature.

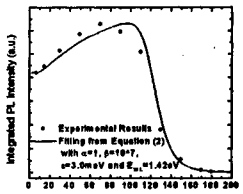


Fig.2 Temperature dependence of the integrated PL intensity of 1.7ML InAs QDs.

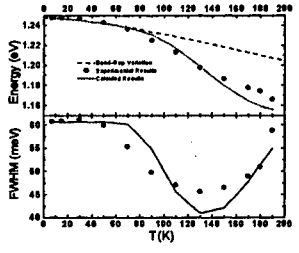


Fig.3 Temperature dependence of the PL peak energy (a) and the PL FWHM (b) of 1.7ML InAs QDs.

DYNAMIC AND SPECTRAL PROPERTIES OF QUANTUM DOT LASERS AT VARIOUS OPERATING CONDITIONS

D. Bhattacharyya, E.A. Avrutin, A.C. Bryce, J.M.Gray, J.H. Marsh,
Dept. of Electronics & Electrical Engineering, University of Glasgow, G12 8LT Scotland, UK

D. Bimberg, F. Heinrichsdorff
Institute of Solid-state Physics, Technical University of Berlin, D-10623, Germany

V.M.Ustinov, S.V.Zaitsev, N.N.Ledentsov and Zh.I. Alferov
A.F. Ioffe Physico-Technical Institute, St.Petersburg 194021, Russia

A.I. Onishchenko, E.P. O'Reilly
Dept. of Physics, Uniersity of Surrey, Guildford GU2 5XH, England, UK

ABSTRACT

The spectral and dynamic properties of InAs/GaAs MOCVD-grown vertically stacked quantum dot lasers are studied experimentally. A strong mode grouping effect (quasiperiodic modulation of the lasing spectrum) is observed and interpreted as a result of wavelength-dependent losses in the laser waveguide associated with substrate leakage and reflection. In relaxation oscillation pulse trains, a substructure is observed which we believe to be a dynamic manifestation of the mode grouping; a preliminary rate-equation simulation supports this interpretation.

1. INTRODUCTION

Self-organized growth using the Stranski-Krastanow mechanism is considered to be the most promising technique for in-situ fabrication of quantum dot arrays as a semiconductor laser gain medium [1,3]. Quantum dot (QD) lasers are expected to exhibit superior lasing properties such as low threshold current density, high temperature stability of the threshold current, high differential gain, wide modulation bandwidth and chirpfree operation under direct current modulation, as compared to quantum well lasers [4,6]. The introduction of vertically coupled QD layers has improved the lasing performance at room temperature by overcoming the gain saturation effect and so increasing the modal gain [7,8]. Some recent studies [9], however, suggest that an important limitation to the high frequency behaviour may be posed by the relatively slow carrier capture processes due to the phonon bottleneck problem [10]. Preliminary studies of relaxation oscillation behaviour at various temperatures [9,11] have demonstrated relaxation frequencies of the order of 5-10 GHz for vertically stacked QD lasers at modest excitation levels, implying that the differential gain values are in the range of 10^{-14}-10^{-12} cm^2. Further characterisation and optimisation of the high frequency response of the QD lasers are, therefore, important tasks for understanding the underlying physical properties and for assessing applications in the high speed regime. Spectral properties of QD lasers have also been extensively studied. The lasing spectra measured in these devices tend to be much broader than those usually observed in quantum well and bulk active media. Several groups [14,15] also observed an effect of mode grouping, i.e. a strong periodic or quasi-periodic modulation of the

spectral shape. However, to the best of our knowledge, the relation between the dynamics and spectra of QD lasers has not received much attention to date.

In this paper we present room-temperature measurements of spectral behaviour and relaxation transients in five-fold stacked InAs/GaAs QD lasers with 4 nm separation layer thickness grown by metalorganic chemical vapour phase deposition (MOCVD). The interrelation between dynamic and spectral properties of the QD laser emission is discussed. An explanation for the mode grouping observed in the laser spectra is given in terms of waveguiding phenomena, and a simple rate-equation model is used to interpret the observed dynamics.

2. STRUCTURE GROWTH AND CHARACTERISATION

The vertically stacked quantum dot laser heterostructure was grown by MOCVD using TMIn, TMGa, TMAl, DMZn, SiH_4 (2% in H_2) and pure AsH_3 as source materials on exactly (001) ± 0.1 ° oriented GaAs substrates at 20 mbar total reactor pressure. The growth temperature was 640 °C for the buffer layer and 485 °C for the dot and cap layers. The growth was interrupted for 8 s after InAs deposition to allow the dots to form. Then, a GaAs cap layer was deposited. The growth rate for the QD layer was 1-2 monolayers (MLs) per second. The cap layer growth was interrupted for 10s following 4 nm of GaAs deposition and the consecutive dot layers were grown. The optimum V-III flux ratio during InAs deposition is 40. The separate confinement heterostructure (SCH) was achieved by a five-fold QD stack embedded in a 140 nm thick GaAs waveguide core sandwiched between two 1 μm thick $Al_{0.5}Ga_{0.5}As$ cladding layers. The upper barriers and cladding layers were grown at the relatively low growth temperatures of 485 °C and 600°C respectively, to avoid degradation of the dots due to thermally induced intermixing with the GaAs matrix. On top of the cladding layer, a Zn-doped GaAs contact layer of 600 nm thickness was grown at 600 °C.

Plan-view and cross-section TEM images of the QD samples (taken with JEOL JEM1000 (1 MV) and JEOL JEM4000 (400 kV) microscopes) are shown in Fig. 1. The image in Fig.1(a) shows a dot density around 4×10^{10} cm^{-2} with dots having a lateral size of 15-18 nm. The dot bases are nearly square-shaped, oriented along <100> and with a slight elongation along one of the <110> directions. The increased lateral size of the stacked QDs can be clearly observed in the dark field cross-section image, Fig.1(b). The lower InAs sheet indicates only small thickness variations that develop into vertically aligned QDs in the second and subsequent layers. The small dots in the first InAs sheet do not corrugate the wetting layer of the second sheet significantly. Thus the effect of vertical alignment can be attributed to the attractive local strain field of the small dots in the first sheet enhancing the QD nucleation probability [12]. In contrast, the deposition of second and third dot layers leads to a bending of the surface by 1-2 nm on top of each QD column. This effect leads to pronounced bending of the AlGaAs layer (white contrast) 25 nm above the topmost dot sheet as shown in Fig.1(b). This very slow smoothing of the growth surface is in clear contrast to observations for the MBE case, where efficient smoothing of the growth surface has been achieved [13].

Photoluminescence (PL) measurements were carried out with the 514 nm line of an Argon-ion laser in the temperature range of 8 K to 300 K. The luminescence was detected using a liquid nitrogen cooled germanium pin diode. Room temperature photoluminescence for this heterostructure is shown in Figure 2. The PL peak is at 1.075 eV with a linewidth (FWHM) around 95 meV. This reflects the non-uniformity in dot size and shape.

3. LASER FABRICATION AND CHARACTERISATION

Ridge waveguide lasers were fabricated from vertically stacked QD SCH layers, using standard photolithography, $SiCl_4$ dry etching, SiO_2 lift-off process and metallisation. The ridge waveguide is 4 μm wide and dry etched to a depth of 1.46 μm. The sample was thinned to approximately 180 μm and Ti/Pd/Au p-type, and Au/Ge/Au/Ni/Au n-type contacts were deposited by electron beam evaporation. The samples were cleaved to give device lengths ranging from 500 μm to 1.5mm. The lasers were characterised using a current source with 400 ns long pulses and a 0.04% duty cycle. The devices showed a turn-voltage of 1.3V and forward resistance of 6-10Ω. The light-current characteristics in Figure 3 show a relatively high threshold current density of 4.4kA/cm^2 for a 1350 μm long device at room temperature. The internal quantum efficiency η_i was calculated from the plot of laser cavity length (L) against the inverse of the external quantum efficiency η_{ex} as described by the widely used formula [see, e.g., 11]:

$$\frac{1}{\eta_{ex}} = \frac{1}{\eta_i} - L\left[\frac{\alpha}{\eta_i \ln R}\right] \qquad (1)$$

The slope of the graph yields an internal quantum efficiency of 60-80 % and an internal optical loss α = 10 cm^{-1}, assuming a reflection coefficient R=0.3 at the facets. The low dot density as well as low temperature growth of GaAs barrier and AlGaAs cladding layers may cause carrier evaporation at higher temperature, thus leading to an increase of the threshold current and a decrease in internal efficiency in these yet unoptimised structures [6]; current spreading is another probable reason for an increase in the threshold current.

4. SPECTRAL PROPERTIES OF THE LASERS

4.1. Experimental

Figure 4 shows the spectral characteristics of a 1000 μm long laser sample. The emission occurs in the higher energy side of the PL peak (at λ=1076 nm, i.e. E≈1.15 eV). This indicates that excited dot states can be contributing to room temperature lasing process (although other effects, such as the wavelength dependence of the mode confinement factor, may also contribute to the wavelength difference between the PL peak and the lasing line). The spectra contain several groups of longitudinal modes which are separated by approximately 2 nm (i.e. about 7 intermodal intervals) and are excited one by one with increasing bias current (note that in Fig.4, the groups are seen as broadened "modes" due to the resolution of the spectrum analyser). Other workers have reported similar behaviour [14,15]. A strong modulation was also observed in the spectrum of a 1350 μm long laser, but with a less regular structure.

4.2. Discussion

We believe the most probable origin of the mode grouping effect [16,17] lies in the waveguide peculiarities of the GaAs/InGaAs lasers. The effect was first studied for the case of quantum-well lasers [17]; it may be explained as follows [16]:

The waveguide transverse mode decays exponentially in the semi-infinite cladding layers of the laser waveguide (Fig. 5). A typical cladding layer thickness in a semiconductor laser, (d_c~1-

2 μm, 1 μm in our structure) is sufficiently wide to form a good waveguide mode, almost identical to that of an ideal waveguide. Nevertheless, the waveguide mode has a finite magnitude, ~exp(-pd_c) at the edge of the cladding layer, where p is the inverse decay length (p~ 5 μm^{-1} in the laser structure studied here). A small fraction of the mode will then leak out of the cladding, propagating as $C\exp(iqx)$ through the transparent substrate of thickness h_s (Fig.5). Part of this leaking mode is reflected back from the bottom of the substrate, returning towards the cladding with an amplitude $D\exp(-iqx)$, where $|D|=r|C|$, r being an effective reflection coefficient assigned to the substrate bottom [17]. The net loss, $\Delta\alpha_s$, associated with leakage into the substrate is then proportional to $|C|^2 - |D|^2$. By assuming continuity of the mode profile and its derivative, Arzhanov et al. [17] showed that

$$\Delta\alpha_s(\lambda) = \Delta\alpha_o \frac{\exp(-2pd_c)(1-r^2)}{1+r^2-2r\cos(\psi-\varphi(\lambda))} \qquad (2)$$

where $\varphi(\lambda) = 2qh_s + \varphi_0$, $\exp(i\psi) = (p+iq)/(p-iq)$, and φ_0 is the effective phase shift due to reflection from the substrate bottom. The prefactor, $\Delta\alpha_0$, is of order $1/d_{eff}$, d_{eff} being the effective transverse size of the mode. As d_{eff} is typically ~ 1 μm in a GaAs/AlGaAs laser, this gives $\Delta\alpha_0 \sim 10^4$ cm^{-1}. We see from (2) that the leakage-related loss is modulated as the substrate pathlength, $\varphi(\lambda)$, changes. This results in a modulation in the net modal gain $g_m(\lambda) \approx \Gamma g - \Delta\alpha_s - \alpha_o$, where Γ is the optical confinement factor, g is the material gain and α_o denotes other losses in the cavity. The loss modulation depth, $\delta\alpha_s = \Delta\alpha_s^{max} - \Delta\alpha_s^{min}$, is given by

$$\delta\alpha_s = \Delta\alpha_s^{max} - \Delta\alpha_s^{min} = \frac{4r\Delta\alpha_o \exp(-2pd_c)}{1-r^2} \qquad (3)$$

For simple "three-layer" waveguides of the type shown in Fig.5, analytical results obtained using eqs. (2-3) are in excellent agreement (to within a relative accuracy < 0.01) with a numerical calculation using a transfer matrix approach [18]. We therefore used the numerical model to calculate the loss modulation in our somewhat more complicated structures. We also pointed out in [16] that, in addition to the wavelength-dependent *loss* term, the substrate leakage and interference result in a modulation $\Delta\Gamma = \Gamma - \Gamma_0$ of the optical confinement, Γ_0 being the value calculated without leakage. This effect, which increases with substrate thickness, was not considered in [17] but can be clearly understood: as the intensity of the field increases in the substrate, the field intensity and hence Γ must decrease in the active region. Our numerical simulations show that the resulting modal gain modulation $\Delta\Gamma g$ (g being the material gain at threshold) is approximately proportional, and of comparable magnitude, to $\Delta\alpha$ for a typical structure of the type discussed above (Fig.6). The total modal gain modulation is $\Delta g_m(\lambda) \approx \Delta\Gamma g - \Delta\alpha_s$; the amplitude values of 0.2 cm^{-1} (Fig.6) constitute about 1% of the total cavity loss (about 20 cm^{-1} for the laser structure studied here). It is well known in the theory of semiconductor lasers [18] that a net gain modulation as small as < 0.1% of the threshold loss translates into very significant modulation of the CW output spectra; therefore, the magnitude of the observed effect is sufficient to cause the mode grouping seen in the experiments. As regards the modal gain modulation period $\Delta\lambda$, it easily follows from Eqs. (2)-(3) that it is inversely proportional to the substrate thickness h_s: $\Delta\lambda = \pi\lambda/qh_s$. With the material and waveguide parameters used in this

work, a modulation period of 2-3 nm corresponds to a substrate 200-300 μm thick, in agreement with what is commonly obtained by substrate thinning.

Although modal gain modulation due to substrate leakage has been observed [17] in InGaAs/AlGaAs *quantum well* lasers, the mode grouping in these lasers is not very pronounced; instead, nearly single-mode spectra with some mode hopping have been observed. However, we can expect the problem to be more marked in InGaAs/AlGaAs quantum dot lasers. Indeed, in general, two main effects may contribute to the onset of lasing in an increasingly large number of longitudinal modes. The first effect is short-scale *spatial* hole burning, caused by depletion of population inversion in the antinodes of the standing wave(s) corresponding to the longitudinal mode(s) lasing initially. For bulk and quantum well semiconductor lasers, the effect is known to be relatively weak because of the diffusion smoothing of the resulting carrier density modulation. However, in quantum dot lasers, where carriers are spatially localised and diffusion insignificant, hole burning may be expected to be very strong - in common with solid-state lasers and in contrast to other semiconductor active media. Asryan and Suris [19] have recently developed a quantitative theory of this effect and estimated that for realistic laser parameters, the second longitudinal mode may be expected to lase at currents exceeding the threshold value by less than 1%. The second effect governing multimode emission is *spectral* hole burning, caused by depletion of population inversion in those dots whose electron-hole level separation is resonant with the lasing mode energy. This effect, too, may be expected to be several orders of magnitude stronger in quantum dots than it is in bulk or QW semiconductor media because of the absence of fast energy relaxation of localised carriers.

It follows from the discussion above that the inter-group modulation can be eliminated by increasing the cladding layer thickness. Indeed, experimentally, we observed no mode grouping in lasers with cladding layers 1.8 μm thick.

We note also that the non-ideal periodicity of modulation of the modal gain was attributed in [17] to uncontrollable variations of the substrate thickness. This is consistent with the fact that in our measurements, the shorter 1000 μm laser demonstrates the effect of mode grouping very clearly, whereas in the longer 1350 μm laser (where the effect of the variation of substrate thickness may be expected to be stronger) we observe a less regular mode group structure.

5. DYNAMIC PROPERTIES

5.1. Experimental

Large-signal relaxation oscillations were studied at room temperature in a 1350 μm-long laser. The sample was driven by 3 ns long pulses with a rise time of 450ps at a repetition frequency of 1.17 MHz. The temporal output was observed using a Hamamatsu streak camera with a time resolution of 2ps. The relaxation transients, for increasing injection currents above threshold, are shown in Figure 7. We note that even at low currents, relaxation peaks have a clear sub-structure as if two relaxation processes have been superimposed on each other. This makes clear determination of the repetition frequency from the relaxation oscillation train difficult, particularly at higher pumping currents where the substructure becomes so pronounced that it virtually obscures the relaxation process as such, resulting in a very smeared aperiodic structure.

Close to threshold, an estimate of the distance between the clearly pronounced peaks gives a relaxation frequency around 1 GHz.

5.2. Simplified Model and Interpretation

A full theoretical description of a ridge- stripe quantum dot laser dynamics would need to describe the dynamics of a large number of longitudinal modes and more than one lateral mode, with an adequate account for the wavelength-dependent waveguide properties as described above. It would also require an accurate account to be taken of the processes of carrier capture, energy and coherence relaxation, including excited state filling, as well as spectral and spatial hole burning. While such a complex model is currently being developed, here we have used a simplified, semi-qualitative rate equation model to gain some insight and help interpret the results. We take into account the presence of the experimentally observed mode grouping effect by considering two "modes", with intensities S_1, S_2 each of them corresponding to one of the experimentally observed mode groups. Moreover, we allow each of these modes to be associated mainly with a group of dots ("carriers") with densities N_1 N_2 respectively. Then, we write a set of ordinary differential equations for $N_{1,2}$ and $S_{1,2}$:

$$\frac{dN_{1,2}}{dt} = \frac{J_{1,2}}{ed} - \frac{N_{1,2}}{\tau} - A_{1,2}(N_{1,2} - N_t)\frac{S_{1,2}}{1+\varepsilon_s S_{1,2} + \varepsilon_x S_{2,1}} + \frac{N_{2,1} - N_{1,2}}{\tau_{rel}} \tag{4a}$$

$$\frac{dS_{1,2}}{dt} = \beta\frac{N_{1,2}}{\tau} + \left(\frac{\Gamma_{1,2}A_{1,2}(N_{1,2} - N_t)}{1+\varepsilon_s S_{1,2} + \varepsilon_x S_{2,1}} - \frac{1}{\tau_{ph}}\right)S_{1,2} \tag{4b}$$

Eq. (4) are identical to those usually applied to modelling semiconductor lasers (see e.g. [18]) apart from the last term in (4a) that contains a phenomenologically introduced time of energy relaxation between dots τ_{rel}. The other notations above have their standard meaning, J standing for the pumping current, d for the thickness of the active (dot-containing) layer, N_t for the transparency carrier density, ε_s and ε_x for the self-and cross-saturation coefficients (we assume ε_x <<< ε_s, as may be expected with hole burning nonlinearities). The time constants τ and τ_{ph} are the carrier and photon lifetimes respectively. The exact physical nature of the two groups of dots is not specified in this model; there are, in principle, two ways in which these groups may be distinct from each other. Firstly, because of the wavelengh separation, it is clear that they are separated in *dot energy*. Secondly, earlier experimental studies that exhibited the mode grouping effect [14] also showed that different groups of longitudinal modes tend to have different lateral (in-plane) mode composition, which means that the dots interacting with different groups are separated at least partly in *space*. Therefore, in (4), the values Γ_1=0.02×0.8; Γ_2=0.02×0.7 have been used for the coefficients of the mode overlap with the dot-containing region, i.e. it has been assumed that the groups of longitudinal modes belong to the same transverse mode, but different lateral modes. Other important parameters include carrier lifetimes τ=2 ns and the gain cross sections A_1=A_2=$(c/n)\cdot 1\cdot 10^{-13}$ cm^2. The phenomenologically introduced time of energy relaxation between dots τ_{rel} was treated as a free parameter.

Typical simulation results are shown in Figure 8(a) and 8(b). Both cases show the transient response of a laser pumped by a 3 ns long pumping pulse with an amplitude 1.6 times above

threshold. The difference between the two cases is that to simulate the process shown in Fig.8a, the relaxation time was set as τ_{rel}=30 ps, meaning that the two groups of modes compete for essentially the same carrier density (as is the case for longitudinal modes in a standard narrow-stripe laser), whereas Fig. 8b was calculated with τ_{rel}=3 ns, meaning that the groups of modes are coupled with significantly different groups of dots ("carriers") which are essentially isolated from each other. It can be seen from Fig. 8 that the experimentally observed substructure in the relaxation oscillation train is completely inconsistent with the simulation shown in Fig. 8(a) yet is reasonably similar to that shown in Fig. 8(b). In principle, the time of interaction between the two groups of dots of the order of $\tau_{rel} > 1$ ns may be associated with the energy level separation between the dots in the two groups (then the time τ_{rel} is the characteristic time of interaction between dots, either through tunnelling or escape and recapture). Alternatively, the long relaxation time may be due to spatial separation because of the predominant interaction with different *lateral* modes in different mode groups (the time τ_{rel} being the time of diffusion of free carriers in the material surrounding the dots across the stripe). Further experiments are necessary to determine which of the two effects is more important.

6. DISCUSSION AND CONCLUSIONS

A comparison of the spectral and dynamical properties of the laser shows that mode grouping significantly degrades the high-frequency performance of a QD laser and should be eliminated in any laser intended for any high-frequency applications. Analysis suggests that this could be achieved relatively easily by careful optimisation of the waveguide structure (mainly by ensuring that the cladding layers are sufficiently thick). On the other hand, control of waveguide selectivity in a quantum-dot laser could be both put to practical use (for engineering the spectral shape) and used as an investigation tool, e.g. to quantify the effects of spectral and spatial hole burning in quantum dot lasers and extract the relevant parameters.

ACKNOWLEDGEMENTS

The authors would like to thank K. Schatke for expert technical assistance during the MOCVD growth. This work was funded in parts by the Deutsche Forschungsgemeinschaft (SFB 296), the UK Engineering and Physical Sciences Research Council and INTAS. D. Bhattacharyya is supported by Overseas Research Awards (ORS) Scheme, UK.

REFERENCES

1. L. Goldstein, F. Glas, J.Y. Marzin, M.N. Charasse, G. Leroux, Appl. Phys. Lett., **47**, p.1099, 1985.

2. D. Leonard, M. Krishnamurthy, C.M. Reaves, S.P. Denbaars, P.M.Petroff, Appl. Phys. Lett., **63**, 23, p.3203, 1993.

3. N. Kirstaedter, N.N. Ledentsov, M.Grundmann, D.Bimberg, V.M Ustinov, S.S. Ruvimov, M.V. Maximov. P.S. Kop'ev, Zh.I. Alferov, U. Richter, P.Werner, U.Gösele, J. Heydenreich, Electr.Lett. 30, 1416 (1994)

4. Y. Arakawa, H. Sakaki, Appl. Phys. Lett., 40, p.939, 1982.

5. M.Asada, Y. Miyamoto, Y. Suematsu, IEEE J. Quantum Electron., **QE-22**, p.1915, 1986.

6. D. Bimberg, N. Kirstaedter, N.N. Ledentsov, Zh.I. Alferov, P.S. Kop'ev, V.M. Ustinov, IEEE J. Selected Topics in Quantum Electron., **3**, 2, 1997.

7. Q. Xie, A. Madhukar, P. Chen, N.P. Kobayashi, Phys. Rev. Lett., **75**, p.2542, 1995.

8. O.G. Schmidt, N. Kirstaedter, N.N. Ledentsov, M.H. Mao, D. Bimberg, V.M. Ustinov, A.E. Egorov, A.E. Zhukov, M.V. MAximov, P.S. Kop'ev, Zh.I. Alferov, Electron. Lett., **32**, p.1302, 1996.

9. D.Klotzkin, K.Kamath, P. Bhattacharya, IEEE Photon. Technol. Lett., **9**, p.1301, 1997.

10. H. Benisty, C.M. Sotomayor-Torres, C. Weisbuch, Phys. Rev. B, **44**, 10945, 1991.

11. M.H. Mao, F. Heinrichsdorff, A. Krost, D. Bimberg, Electron. Lett., **33**, p.1641, 1997.

12. J. Tersoff, C. Teichert, M. G. Lagally, Phys. Rev. Lett., **76**, p.1675, 1996.

13. F. Heinrichdorff, A. Krost, N.Kirstaedter, M.H. Mao, M. Grundmann, D. Bimberg, A.O. Kosogov, P. Werner, Jap.J. Appl. Phys., **36**, p. 1129, 1997.

14. N.Yu.Gordeev, A.M.Georgievski, V.I.Kopchatov, S.V.Zaitzev, A.Yu.Egorov, A.R.Kovsh, V.M.Ustinov, A.E.Zhukov, P.S. Kop'ev, Proceedings of the International Symposium on "Nanostructures: Physics and Technology", St.Petersburg, Russia, 1997, pp.183-186

15. L.Harris, D.J.Mowbray, M.S.Skolnick, M.Hopkinson and G.Hill, in: CMMP'97 conference, December 1997, Exeter, UK.

16. . E. O'Reilly, A.Onishchenko, E.Avrutin, D.Bhattacharyya, J.H.Marsh, Electron. Lett., **34**, 1998 (accepted for publication)

17. E.V.Arzhanov, A.P.Bogatov. V.P.Konyaev, O.M.Nikitina, V.I. Shveikin, Quantum Electronics, **24**, p.581, 1994

18. See e.g. T. P. Lee, C. A. Burrus, J. A. Copeland, A.G. Dentai, D. Marcuse , IEEE J. Quant.Electron., **18**,.p.1101, 1982

19. L.Asryan, R.A.Suris, Proceedings of the International Symposium on "Nanostructures: Physics and Technology", St.Petersburg, Russia, June 1998, pp. 390-393

FIGURES:

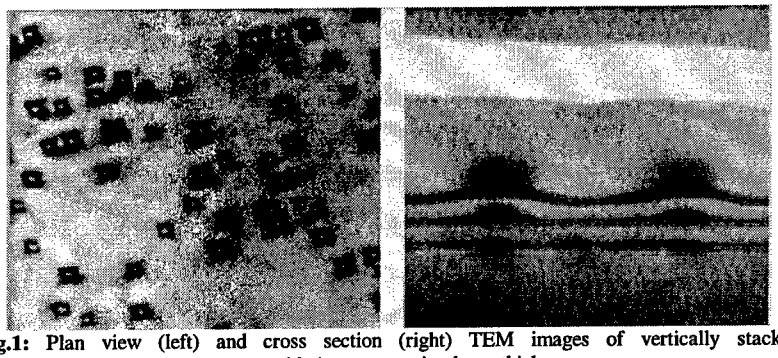


Fig.1: Plan view (left) and cross section (right) TEM images of vertically stacked InAs/GaAs quantum dot structure with 4 nm separation layer thickness.

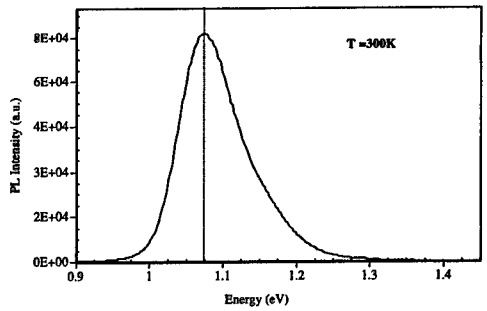


Fig.2: Room temperature photoluminescence spectrum of InAs/GaAs stacked QDs.

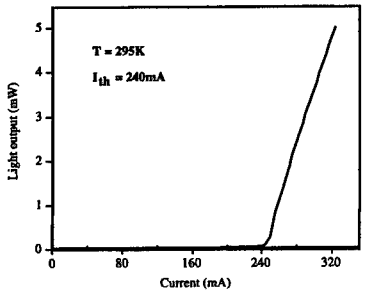


Fig.3: Light-current characteristics of 1.35 mm long and 4 μm wide QD ridge waveguide laser at room temperature.

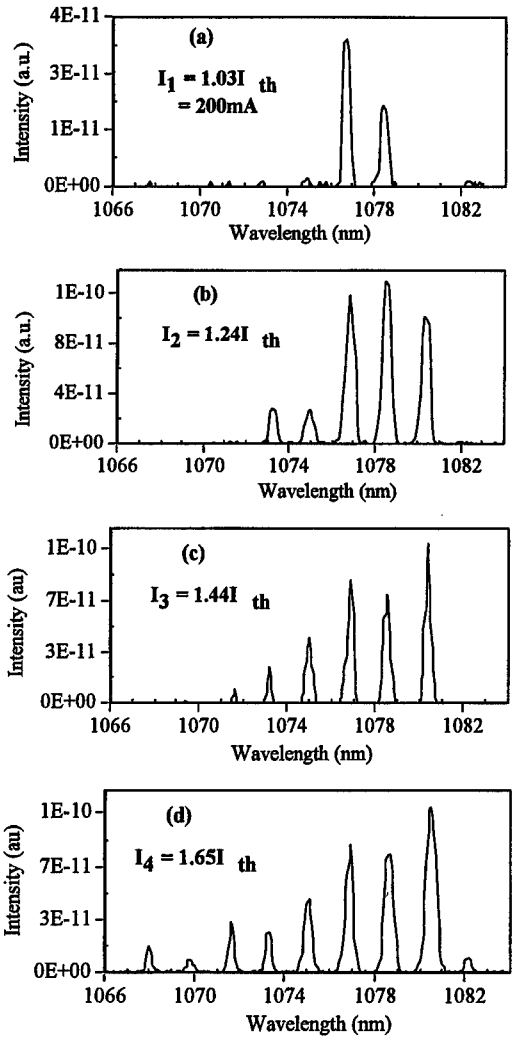


Fig.4: Pulsed spectrum of 1000 μm long and 4 μm wide QD ridge waveguide QD laser with increasing bias current at room temperature.

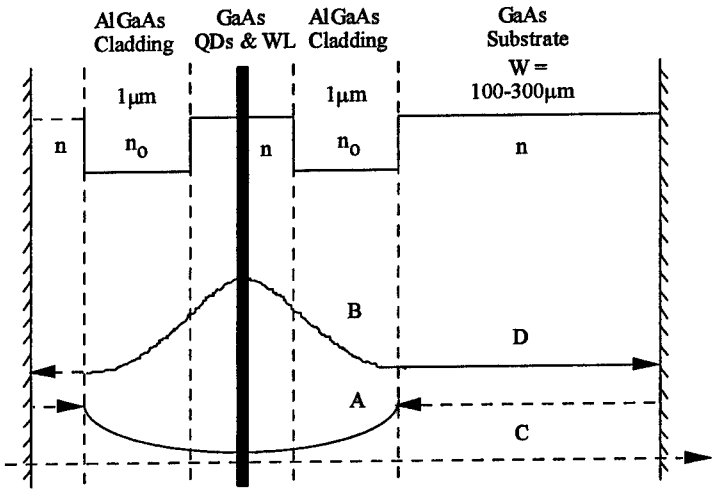


Fig.5: Illustration of mode selectivity by substrate leakage and reflection in a laser waveguide;

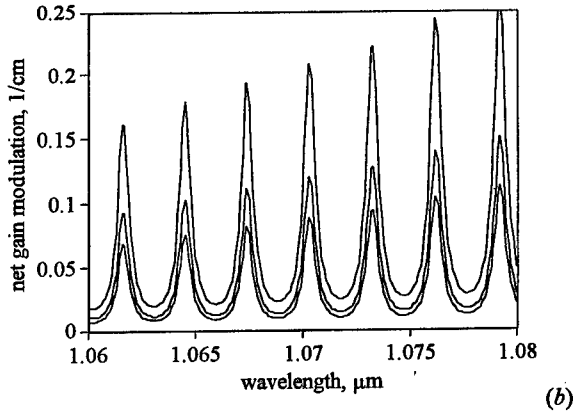


Fig.6: Calculated contributions of leakage loss and confinement factor modulation to total net gain modulation in a quantum-dot laser. Top line: total net gain modulation; bottom line: leakage loss contribution; middle line : confinement modulation contribution.

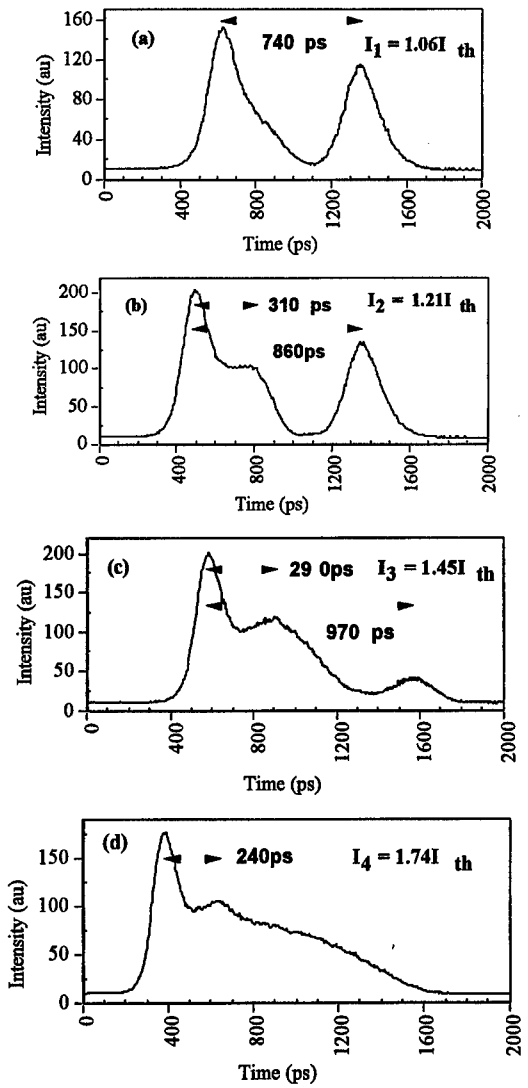


Fig.7: Measured temporal response of 1350 μm long and 4 μm wide QD ridge waveguide laser with increasing injection current at room temperature (observed by streak camera)

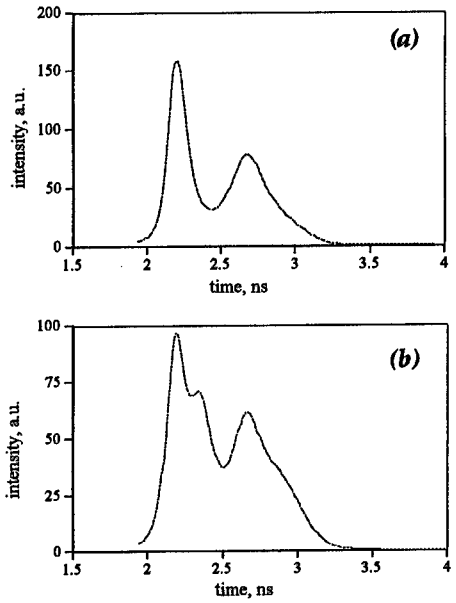


Fig.8: Simulated temporal response of a laser measured in Fig.6, pumped by a 3 ns long current pulse with an amplitude 1.6 times threshold current. Relaxation time between groups of dots 30 ps (a), 3 ns (b).

Self-Ordered Nanostructures

SIZE-CONTROLLABLE NANOSTRUCTURE ARRAY FABRICATION WITH SELF-ASSEMBLY

Chiseki Haginoya, Masayoshi Ishibashi, and Kazuyuki Koike
Advanced Research Laboratory, Hitachi, Ltd.,
2520 Akanuma, Hatoyama, 350-0395, JAPAN

ABSTRACT

Periodic array structures consisting of 100-nm-scale and 200-nm-scale in Si substrates can be fabricated by combining the self-assembly of polystyrene spheres with reactive ion etching. We show here that the period and hole size can be determined independently. This relatively low cost and easy to use fabrication method is applicable in many areas of science and technology.

INTRODUCTION

Nanoscale periodic structures have many potential applications not only in technological area, such as high-density magnetic recording [1,2], arrays of field emitters for flat panel display [3,4], biotechnology [5,6], but also in scientific areas such as electron confinement [7,8]. Electron beam lithography is commonly used [1,9] to obtain nano-scale periodic structures, and ion-beam lithography [10,11], X-ray lithography [12], and electron holographic lithography [13] can also be used. These methods can be used to fabricate periodic structures of arbitrary sizes and covering relatively wide areas, but the equipment required is huge and expensive. Laser interference lithography is a remarkable method for making nanoscale structures covering wide areas [14,15,16,17] but it is subject to a size limitation determined by the wavelength of the light.

Some fabrication techniques exploiting self assembly have been proposed. For instance, nanochannel array grass [18], self-assembled colloidal particles [19,20,21], anodic alumina [22], and so on are available. Though they are relatively easy to use and their costs are low,

their application range has been limited because the geometric parameters of the arrays they produce can not be altered in a controlled way. Although a distinctive improvement of anodic alumina is proposed [23] to add them a controllability, they need a electron beam lithography system to obtain a original mold. In this paper we describe a size-controllable nanostructure array fabrication process exploiting the self-assembly of polystyrene spheres.

APPROACH AND RESULTS

Figure 1 shows schematic top and cross-sectional views illustrating the fabrication process. Because an orderly arrangement of spheres can not be obtained unless the substrate surface is hydrophilic and clean [20], the Si substrate is first washed in acetone and pure water using ultrasonic agitation. Polystyrene spheres are then arranged on the substrate by pouring on a colloidal suspension diluted with pure water (Fig. 1(a)). The aligned polystyrene spheres are then thinned by oxygen reactive ion etching (RIE). Since oxygen ions react with organic substances more than inorganic substances, the polystyrene spheres are etched selectively and the substrate remains almost unetched (Fig. 1(b)). Metal is then sputter-evaporated onto the surface (Fig. 1(c)), and the metal-covered spheres are removed to form a mask for making holes (Fig. 1(d)). Then the sample is etched with mixture of carbon fluoride and oxygen gasses, which form a nanohole array by selectively etching the substrate (Fig. 1(e)).

The period of the array is obviously determined by the original diameter of the sphere, and the depth of the holes is determined by the time of carbon fluoride RIE. Because the hole diameter depends on the size of the thinned polystyrene spheres, it can be controlled by changing the oxygen RIE condition.

Assuming that the vertical etching rate is independent of surface position on the polystyrene sphere, we can easily evaluate the relation between the diameter of the thinned sphere and degree of the oxygen etching. Figure 2 shows the model of oxygen RIE. In Fig. 2(b) the upper surface of the etched sphere is represented by the surface of a sphere obtained by moving the original sphere downwards by distance a corresponding to the etched thickness. Denoting the initial radius of the sphere as r_0, the radius of the thinned spheres as r, and the angle between a horizontal line and the line connecting the center of the original sphere and the outermost edge of the thinned sphere as θ, we can

write the relation between r and a as

$$r = r_0 \cos(\arcsin(a/2r_0)) . \quad (1)$$

Although the value of a depends on the many etching condition, it is reasonable to assume that a is proportional to the etching time t when the other conditions are fixed. Thus

$$a = v\,t,$$

where v is the etching velocity for the given etching conditions. Consequently, we can obtain

$$r = r_0 \cos(\arcsin(v\,t/2r_0)) , \quad (2)$$

which means that the hole diameter can be controlled by changing the oxygen RIE time.

To substantiate this, we used polystyrene spheres 200 nm in diameter to fabricate nano-hole arrays with holes of different diameters [24]. Scanning electron microscope (SEM) images (not of the same area) of each process step are shown in Fig. 3 [24]. Figure 3(a) shows the polystyrene spheres arranged in a close-packed hexagonal array, and Fig. 3(b) shows the spheres after they were thinned by RIE with oxygen 160 mW/cm^2, 5 Pa, 90 s. This etching resulted in spheres with an average diameter of 82 nm. Onto this surface, Pd-Pt alloy was sputter-evaporated to a thickness of 5 nm. The spheres were then removed by rubbing the sample surface with an acetone-soaked cotton bud (Fig. 3(c)), and the sample was etched by RIE with a mixture of CF_4 and oxygen gas 80 mW/cm^2, 2 Pa, 300 s. This resulted in an array the period of which was 200 nm (2.8 G holes/cm^2) and in which the average diameter of the holes was 83 nm. Figure 3(e) is a cross sectional view of the hole array. It shows that hole depth is 57 nm, the side walls are nearly vertical, and the bottoms of the holes are flat.

Figure 4 shows a hole array fabricated by using the same process, except that the oxygen RIE time had changed from 90 s to 60 s [24]. The period was the same, but the average hole diameter was 157 nm .

To find out weather Eq. (2) represents the etching process well, we fitted the experimental results showing in Figs. 3 and 4 with v as a fitting parameter. Figure 5 shows the fitted result for the relation between oxygen RIE time and thinned sphere diameter [24]. As shown by the line, Eq. (2) reproduces the experimental data well when v = 4.0 nm/s. The

value of v depends on the oxygen RIE condition, such as temperature, gas pressure, and incident power.

To obtain smaller holes and a more dense periodic structure, we tried to fabricate by using smaller spheres. Figure 6 shows the SEM images (not of the same area) of the sample at various steps in a fabrication process starting with 100-nm-diameter polystyrene spheres. Fabrication steps in Figs. 6 (a)-(d) corresponds to those in Figs. 3 (a)-(d). The initial sphere array on the Si substrate (Fig. 6(a)) was etched with oxygen RIE at 80 mW/cm^2, 5 Pa, for 60 s (Fig. 6(b)). Pt-Pd was sputter-evaporated onto the surface, and thinned spheres were removed (Fig. 6(c)). CF_4 RIE resulted in a hole array the period of which was 100 nm (11.5 G holes/cm^2) and in which the average hole diameter was 45 nm (Fig. 6(d)). By changing the oxygen RIE time, we could obtain an array of thinned spheres with different average diameter array (Fig. 6(e)).

Figure 6(d) shows that the diameter of the hole is not uniform, and this irregularity can be attributed to the variation of initial diameter of the polystyrene spheres. For the spheres available commercially, the smaller the diameter, the larger the relative standard deviation of the sphere diameter. In our experiment, the relative nominal standard deviations were 5% for 200-nm spheres and 10% for 100-nm spheres. Thus the ranges of the initial diameter of nominally 200-nm and 100-nm spheres were 190-210 nm and 90-110 nm. Figure 7 shows the relation, calculated from Eq. (2), between oxygen RIE time and diameter for spheres with initial diameters in the upper , middle, and lower parts of these ranges. The line for 100-nm-diameter spheres in Fig. 7(a) was calculated for v = 3.0, which was obtained by the fit to the average sphere diameters in Figs. 6(a) and (b). Although we tried to keep the same RIE condition for the samples shown in Figs. 2(b) and 6(b), the v= 3.0 nm/s obtained for Fig. 6(b) is a little smaller than the v = 4.0 nm/s obtained for Fig. 2(b). The discrepancy might be due to a difference in temperature, which we did not control. The v = 3.0 nm/s was also used for the calculation of the RIE time dependences of spheres 90 nm and 110 nm in diameter, and the results are shown by lines in Fig 7(a). The v = 4.0 nm/s was used for the calculation of the RIE time dependences of spheres 190 nm and 210 nm in diameter, and the results are shown together with the result for 200-nm spheres by lines in Fig 7(b). In Fig. 7(a) it can be seen that the diameters of spheres etched for 60 s ranged from 14 nm to 65 nm. This range of the diameters coincides well with the experimental result, 17-62 nm, in Fig.

6(b). As shown in Fig. 7(b), the diameters of 200-nm spheres etched for 90 s should range from 57 nm to 106 nm. The range measured from Fig. 3(b), however, is smaller than this. One explanation of this discrepancy might be that the initial variation was actually smaller than the nominal value of 5%. From Fig. 7 we can see that the relative variation of hole size becomes larger when r/r_0 is smaller.

The use of 100-nm-diameter spheres for fabricating hole array causes more lattice defects, some of which are seen in Fig. 6, than does the use of 200-nm-diameter spheres. The cause of the defects is thought to be larger dispersion of diameters of 100-nm spheres. Applying an electric field might reduce the number of defects as shown by Trau et al [25], even for larger dispersion of the spheres diameters.

From the discussion above, we can see that spheres with uniform diameters are necessary for obtaining arrays of holes the same size. The required standard deviation of sphere diameter depends on required dispersion of the hole diameter and the area of ordered array.

SUMMARY

We have developed a fabrication technique combining the self assembly of polystyrene spheres and reactive ion etching and have demonstrated the fabrication on silicon substrates of hole arrays with period of 100 nm (11.5 G holes/cm^2) and 200 nm (2.8 G holes/cm^2). This method enables the array period and hole size to be adjusted independently and therefore would be applicable in many areas of science and technology. Hole diameter, however, varies as a result of the variation of the size of the original spheres. To obtain highly ordered arrays of holes that are the same size, we therefore need initial polystyrene spheres of uniform size.

ACKNOWLEDGMENTS

The authors would like to thank Drs. M. Mitsuya, H. Takei, M. Kato, H. Nishida, Y. Sasaki, T. Shinomura, K. Uchida, S. Fukuzono, and S. Umemura at Advanced Research Laboratory for their valuable and stimulating discussions during the course of this work.

REFERENCES

[1] S. Y. Chou, M. S. Wei, P. R. Krauss, and P. B. Fischer, J. Appl. Phys. **76**, 6673 (1994)

[2] R. H. M. New, R. F. W. Pease, and R. L. White, J. Vac. Sci. Technol. B **12**, 3196 (1994)

[3] Z. Huang, N. E. McGruer, and K. Warner, IEEE Electron Device Lett. **14**, 121 (1993)

[4] C. O. Bozlar, C. T. Harris, S. Rabe, and D. D. Rathman, J. Vac. Sci. Technol. B **12**, 629 (1994)

[5] R. V. Parthasarathy and C. R. Martin, Nature **369**, 298 (1994)

[6] C. R. Musil, D. Jeggle, H. W. Lehmann, L. Scandella, J. Gobrecht, and M. Dobeli, J. Vac. Sci. Thchnnol. B **13**, 2781 (1995)

[7] H. Fang, R. Zeller, and P. J. Stiles, Appl. Phys. Lett. **55**, 1433 (1989)

[8] M. Green, M. Garcia-Parajo, and F. Khaleque, Appl. Phys. Lett. **62**, 264 (1993)

[9] W. Chen and H. Ahmed, Appl. Phys. Lett. **63**, 1116 (1993)

[10] R. L. Kubena, J. W. Ward, F. P. Stratton, R. J. Joyce, and G. A. Atkinson, J. Vac. Sci. Technol. B **9**, 3079 (1991)

[11] J. C. Wolfe, S. V. Pendharkar, P. Ruchhoeft, S. Sen, M. D. Morgan, W. E. Horne, R. C. Tiberio, and J. N. Randall, J. Vac. Sci. Technol. B **14**, 3896 (1996)

[12] F. Rousseaux, D. Decanini, F. Carcenac, E. Cambril, and M. F. Raver, J. Vac. Sci. Technol. B **13**, 2787 (1995)

[13] K. Ogai, Y. Kimura, R. Shimizu, J. Fujita, and S. Matsui, Appl. Phys. Lett. **66**, 1560 (1995)

[14] T. A. Savas, S. N. Shah, M. L. Schattenburg, J. M. Carter, and H. I. Smith, J. Vac. Sci. Technol. B **13**, 2732 (1995)

[15] M. Farhoud, M. Hwang, H. I. Smith, M. L. Schattenburg, J. M. Bea, K. Youcef-Toumi, and C. A. Ross, IEEE Trans. Magn. **34**, 1087 (1998)

[16] M. Thielen, S. Kirsch, H. Weinforth, A. Carl, and E. F. Wassermann, IEEE Trans. Magn. **34**, 1009 (1998)

[17] M. A. H. Hasst, J. R. Schuuruis, L. Abelmann, J. C. Lodder, and T. J. Popma, IEEE Trans. Magn. **34**, 1006 (1998)

[18] R. J. Tonucci, B. L. Justus, A. J. Campillo, and C. E. Ford, Science **258**, 783 (1992)

[19] H. W. Deckman and J. H. Dunsmuir, Appl. Phys. Lett. **41**, 377 (1982)

[20] R. Micheletto, H. Fukuda, and M. Ohtsu, Langmuir **11**, 3333 (1995)

[21] J. C. Hulteen and R. P. V. Duyne, J. Vac. Sci. Technol. A **13**, 1553 (1995)

[22] H. Masuda, H. Yamada, M. Satoh, H. Asoh, M. Nakao, and T. Tamamura, Appl. Phys, Lett. **71**, 2770 (1997)

[23] H. Masuda and K. Fukuda, Science **268**, 1466 (1995)

[24] C. Haginoya, M. Ishibashi, and K. Koike, Appl. Phys. Lett. **71**, 2934 (1997)

[25] M. Trau, D. A. Saville, and I. A. Aksay, Science **272**, 706 (1996)

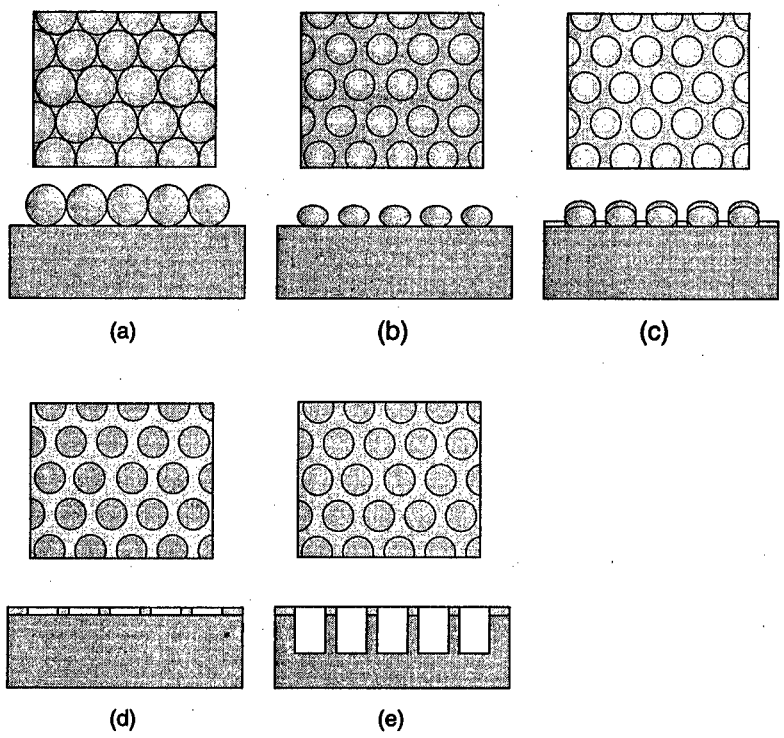


Figure 1: Schematic diagram of the fabrication process (top and cross-sectional view). (a) Arrangement of polystyrene spheres. (b) Thinning of spheres by reactive ion etching (RIE) with oxygen. (c) Sputter-evaporation of metal. (d) After removal of spheres. (e) hole array formed by CF_4 RIE.

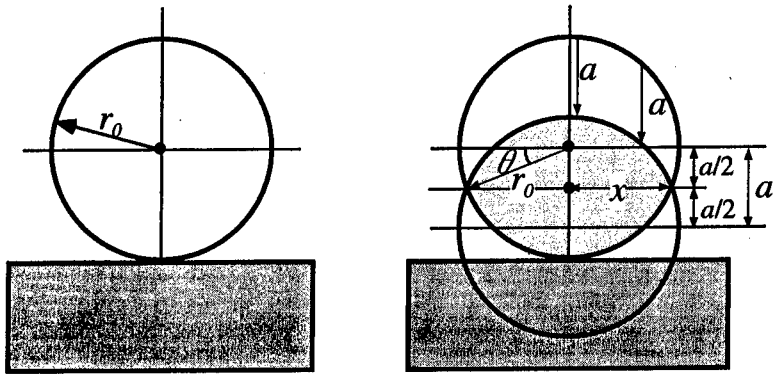


Figure 2: Schematic side view of simplified model assuming that vertical etching rate is independent of surface position: (a) Before RIE . (b) After RIE.

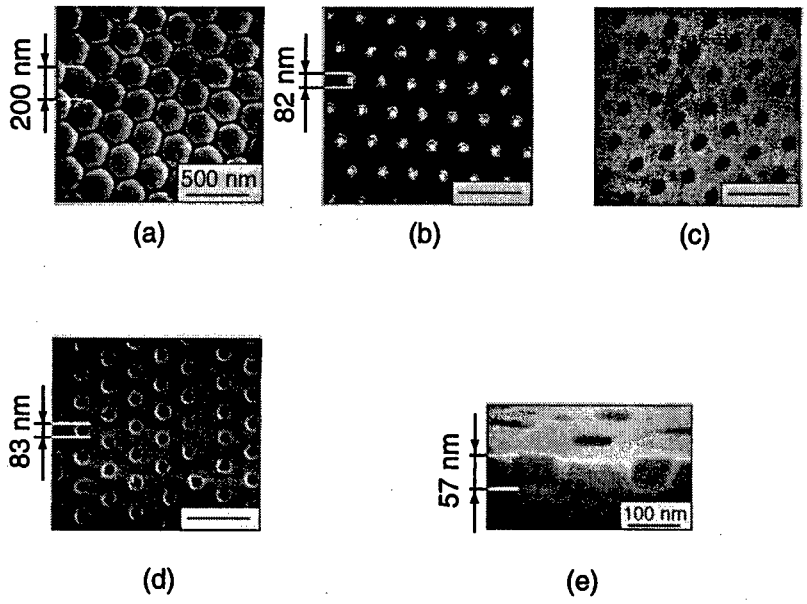


Figure 3: SEM images of the sample at each fabrication process step: (a) Arrangement of polystyrene spheres (original sphere diameter is 200 nm.) (b) Sphere array after oxygen RIE for 90 s. (c) After removal of the thinned spheres. (d) Holes array of with an average diameter of 83 nm after CF_4 RIE. (e) Cross-section of the cleaved array.

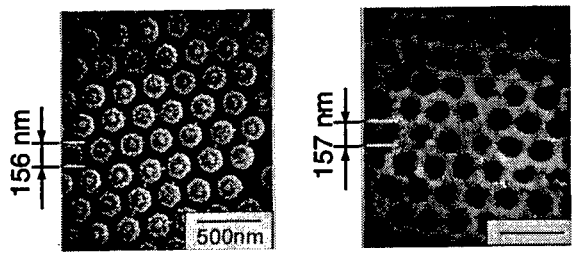


Figure 4: SEM images of the sample at selected steps in another fabrication process using spheres diameter with an original of 200 nm: (a) array of thinned spheres with an average diameter of 156 nm after oxygen RIE for 60 s. (b) Array of holes with an average diameter of 157 nm after CF_4 RIE.

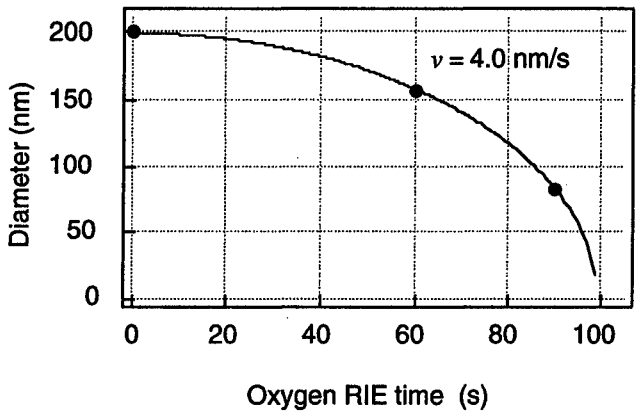


Figure 5: Relation between oxygen RIE time and the diameter of thinned sphere. The black dots are experimental data from Figs. 3(b) and 4(a). The solid line was calculated using equation (2).

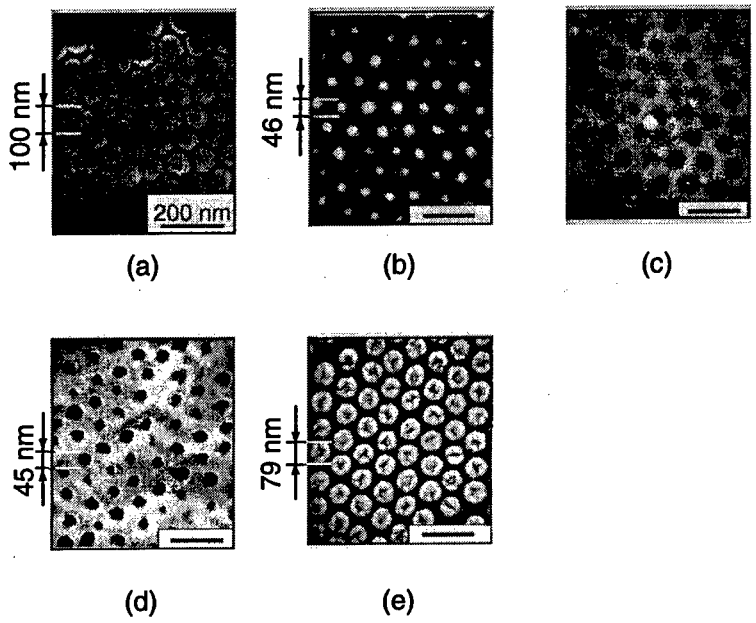


Figure 6: SEM images of the sample at each fabrication process step when the original sphere diameter was 100 nm. (a) Arrangement of polystyrene spheres. (b) Sphere array after oxygen RIE 160 mW /cm^2, 5 Pa, 60 s. (c) After removal of spheres. (d) Array of holes with an average diameter of 45 nm after CF_4 RIE for 160 mW /cm^2, 5 Pa, 60 s. (e) Another sample fabricated using different oxygen RIE conditions for 80 W/cm^2, 5 Pa, 30 s.

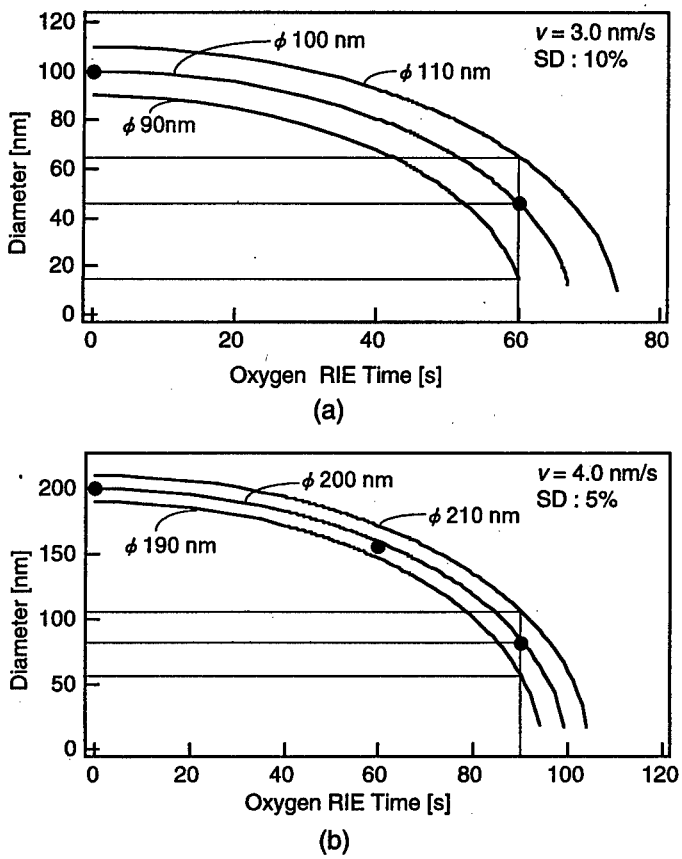


Figure 7: Relation between O_2 RIE time and thinned diameter for spheres with initial nominal diameters of (a) 100 nm and (b) 200 nm. The circles are experimental data and the solid lines are results calculated using Eq. (2). Since the standard deviation were 5% for the 200-nm spheres and 10% for the 100-nm spheres, the actual diameter ranged from 190 to 210 nm and from 90 to 110 nm. The results calculated for these spheres are also shown.

CARRIER DYNAMICS IN STACKED SELF-ASSEMBLED InAs/GaAs QUANTUM DOTS

D. Morris[a] and S. Fafard[b]

(a) Centre de Recherche en Physique du Solide, Département de physique, Université de Sherbrooke, (Québec), Canada J1K 2R1
(b) Institute for Microstructural Sciences, National Research Council, Ottawa, Ontario, Canada K1A OR6

ABSTRACT

Carrier relaxation and recombination processes in self-assembled InAs/GaAs quantum dots are investigated by means of time-resolved photoluminescence spectroscopy. We discuss the physical mechanisms involved in these processes by studying the dependence of the rise and decay times of the barriers and the quantum dots optical transitions as a function of the temperature and the excitation density. The strong photoluminescence signals of our dots result from fast capture and relaxation times. Carrier-carrier scattering processes are found to be responsible for these efficient relaxation mechanisms.

INTRODUCTION

Energy relaxation in zero-dimensional systems has attracted considerable attention from both fundamental and application point of view. Recent experimental studies [1–3] show that carrier relaxation times are shorter than theoretical values predicted for single LO-phonon scattering. Auger processes [4,5] and multiphonon scattering mechanisms [6,7] have been proposed to provide such an efficient relaxation. Further experimental studies have to be obtained in order to confirm the nature of the dominant relaxation mechanisms and to establish the regime (temperature and carrier densities) where each of these processes becomes important.

EXPERIMENTS

In this work, we have studied stacked self-assembled InAs/GaAs QDs grown by molecular beam epitaxy (MBE) with optimized conditions [9] in order to minimize the particle size distribution. The QDs were grown at a substrate temperature of 520°C on (100) GaAs. The structure consists of a stack of 50 QD layers separated by 30nm GaAs barriers. A modulation doping in the barrier is used in order to introduce electrons in

the QDs (the first electron QD states should be filled). The lens shaped dots have an average diameter of 20nm while the average QD density is about $5x10^9$ cm^{-2}.

The PL spectra were obtained using the 514nm continuous-wave (c-w) output of an ion Argon laser for excitation and a cooled Ge detector for signal detection. The time-resolved measurements were obtained using a Ti:sapphire laser (740 nm, 100 fs, 82 MHz) as the excitation source. An up-conversion detection technique with sub-picosecond resolution and a GaAs photomultiplier tube were used for signal detection.

RESULTS AND DISCUSSION

Figure 1 shows the c-w PL spectra temperature dependence of our sample. At low-temperature (14K) several well resolved PL features could be identified. We clearly see the signature of the individual QD optical transitions (those associated with the first four quantum levels) together with the wetting layer (WL) and the GaAs PL peaks. The strong PL signals obtained even at room temperature and the quite narrow QD peaks show the excellent optical properties of our sample. These observations indicate efficient carrier capture in the dots combined with reduced nonradiative channels and particle size distribution. It is seen that the relative importance of the barrier (WL and GaAs) PL signals as compared to the QD intensities decreases when the temperature increases. Also, the QD optical transitions associated with the higher excited levels tend to disappear at high temperature. These behaviors might be due to the combined increasing rate of carrier thermal excitation above the confining potential and the increasing rates of carrier capture and intersublevel relaxation with temperature.

Recombination from the excited confined electron and hole levels are even more prominent under high laser excitation density, as seen in the TRPL spectra of figure 2. This can be explained by band-filling effect of the lowest QD states, which is observed at short delay times (< 100 ps) after the pulsed excitation. The GaAs PL signal decreases as a function of time while the PL intensity of the QD transitions increases at short times. The temporal evolution of these spectra indicates that carriers relax efficiently from the source (the GaAs barriers) to the 2D states of the WL and finally to the QD energy levels.

To investigation of the energy carrier dynamics further, the kinetics of the PL signals at different energies has been studied. The long-time (-100 to 1300 ps) and the short-time (-10 to 100 ps) behaviors of PL signal measured at three specific energies are plotted in Figure 3a) and b). Decay times are deduced from the exponential behavior at the longer times (Fig. 3a). A value of about 1.1ns has been found for the QD transition associated with recombination from the lowest confined electron and hole levels (n=1). This shows that the carrier recombination time is quite long (≥ 1ns) in our sample. The PL decay times increase for the higher energy transitions since new relaxation channels

open up for carrier occupying higher energy states. The PL decay time of GaAs barrier signal is about 45 ps. Note that photocarriers excited in the GaAs substrate (which also contribute to the PL signal) will recombine after a characteristic time much longer than the carrier capture time in the wetting layer. Therefore, we are measuring from the GaAs PL decay behavior an effective relaxation time that overestimates the capture time. For determining the PL rise times, we used the following function, which corresponds to the solution of the population rate equations for a three- level model :

$$I_{PL}(t) \propto \left(e^{-t/\tau_d} - e^{-t/\tau_r} \right) / \left(\tau_d - \tau_r \right)$$

where τ_d and τ_r correspond respectively to the decay and the rise times. The PL rise time of the QD transition associated with recombination from the lowest confined electron and hole levels is found to be < 20 ps. This small value indicates that both capture and QD intersublevel relaxation processes are rapid.

The nature of the dominant relaxation processes has been investigated by looking at the variations of the PL rise and decay times as a function of the excitation density. These results are presented in figures 4 and 5. The PL decay times (Fig. 4) show only a slight increase with the excitation density for the QD transitions that is attributed to band filling effects. These effects tend to increase the effective recombination time at high excitation densities. Note that we can not extract directly the carrier capture time from the decay times of the WL and the GaAs PL signals. The contribution of the radiative emission coming from the GaAs substrate and the filling of the lower QD states complicates the situation. However, information on the relaxation times (capture + intersublevel relaxation) can be extracted from the QD PL rise times (Fig. 5). The fact that QD PL rise time is smaller for the lower energy transitions combined with the fact their corresponding decay times are longer (compare Fig. 4 and 5) show that there is a sequential filling of the QD states from the bottom level to the highest energy levels. Again, this results from efficient relaxation mechanisms between these QD states. Note that the doping level of our sample is such that the first electron QD levels are completely filled. Therefore, our measured PL rise time corresponds to the effective hole relaxation time which is ≈25ps at low excitation density and ≈11ps at the highest density. This excitation density dependence suggests that carrier-carrier scattering and Auger-like processes play a dominant role in the relaxation dynamics in this excitation regime (the estimated number of photocarriers per dot varies between 5 and 20).

Figure 6 and 7 show the temperature dependence of the PL rise and decay times. It is found that PL decay times (see Fig. 6) for the n=1 to n=3 QD transitions are almost constant as a function of temperature. Thermal activation of the carriers and nonradiative recombination in the barriers are not very probable under our experimental conditions because recapture of those carriers is very efficient. The strong room temperature QD PL signal is also an indication of this fast recapture time. It is

found that the decay time of the GaAs barrier reduces from 80 ps to 25 ps as the temperature increases from 18K to 125K. This behavior indicated that carrier capture is more efficient at higher temperature. As explained before, the PL rise time of the QD transition, associated with recombination from the lowest confined electron and hole levels, gives a better estimate of the carrier relaxation time. Figure 7 shows that the QD PL rise time is nearly constant as a function of temperature. In the limit of our excitation regime, this suggests that multiphonon emissions play a minor role in the carrier relaxation mechanism in QDs. However, this behavior is consistent with dominant Auger processes. Note that the doping level of our sample is an other factor which favors Auger processes; the confined carriers in the dots will interact with an increasing electron plasma density.

CONCLUSIONS

The strong QD PL intensities and the short decay times of the GaAs and the WL PL signals (<100ps) indicate efficient QD carrier capture. The sequential filling of the QD states and the very fast (<20ps) PL rise time show that carriers relax quickly from the excited states down to the QD lowest states. The laser excitation dependence and the nearly independent temperature PL rise time of the QD transition associated with recombination from the lowest confined electron and hole levels, suggests that carrier-carrier scattering processes play a dominant role in the relaxation mechanisms in quantum dots, under high excitation densities.

AKNOWLEDGMENTS

This work is supported by the Centre de Recherche en Physique du Solide (CRPS) de l'Université de Sherbrooke and by NSERC of Canada.

REFERENCES

[1] B. Ohnesorge, M. Albrecht, J. Oshinowo, and A. Forchel, Phys. Rev. B**54**, 11532 (1996)

[2] S. Raymond, S. Fafard, S. Charbonneau, R. Leon, D. Leonard, P.M. Petroff and J.L. Merz, Phys. Rev. B**52**, 17238 (1995)

[3] V. Klimov, P. Haring and H. Kurz, Phys. Rev. B**53**, 1463 (1996)

[4] U. Bockelmann and T. Egeler, Phys. Rev. B**46**, 15574 (1992)

[5] Al. L. Efros, V.A. Kharchenko and M.Rosen, Solid State Comm. **93**, 281 (1995)

[6] T. Inoshita and H. Sakaki, Phys. Rev. B**46**, 7260 (1992)

[7] P. C. Sercel, Phys. Rev. B**51**, 14 532 (1995)

[8] S. Fafard, Z. R. Wasilewski, C. Ni. Allen, D. Picard, P.G. Piva, J.P. McCaffrey, accepted in Superlattices and Microstructures (1998).

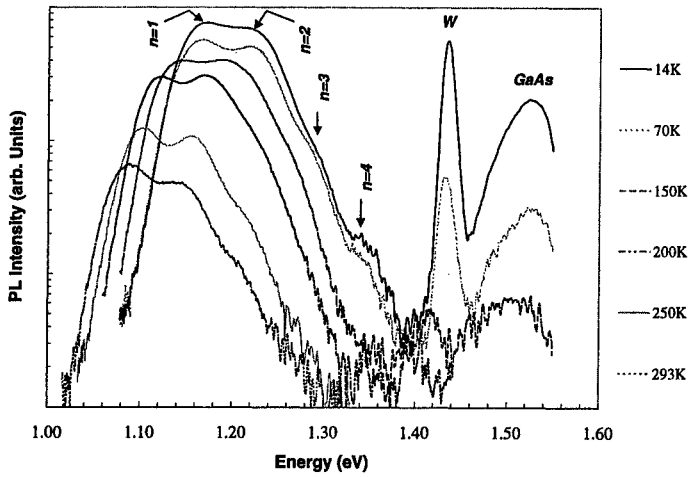


Figure 1 : Photoluminescence spectra obtained at different temperatures under cw laser excitation. The excitation density and energy are respectively 50W/cm^2 and 2.409eV.

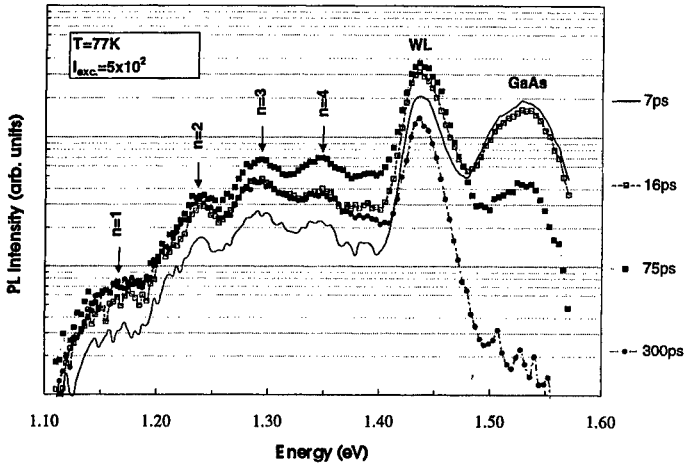


Figure 2 : Time-resolved photoluminescence spectra obtained at different delay times under high excitation density (500W/cm^2) at 1.675eV. The different transitions (QD levels, WL and GaAs) are clearly identified.

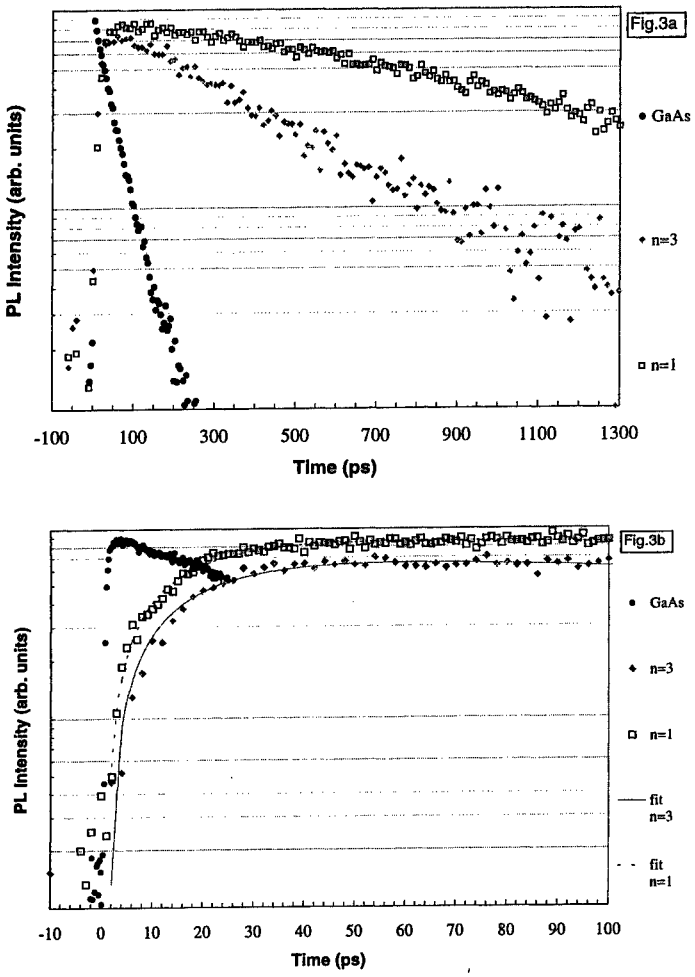


Figure 3: Time-resolved PL intensity detected at three energies corresponding to the maximum of the GaAs, the n=1 and the n=3 peaks. Figures a) and b) are used for the determination of the PL decay and rise times respectively. $E_{exc.}$=1.675eV, $P_{exc.}$≈50W/cm^2 and T=77K.

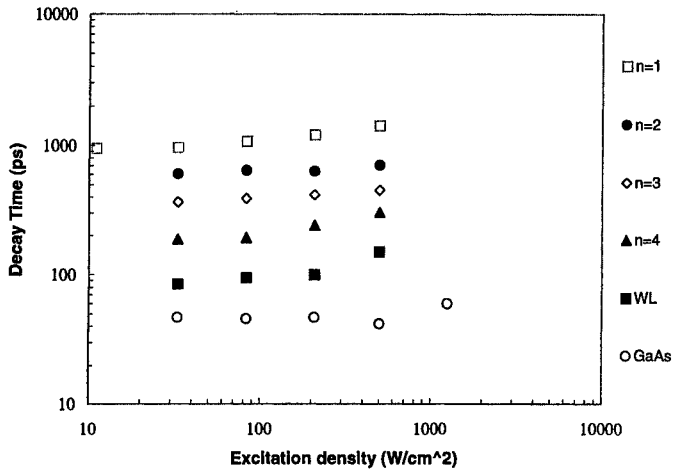


Figure 4: Decay time of the different PL structures versus the excitation density. $E_{exc.}$=1.675eV and T=77K. The uncertainties resulting from the fitting procedure correspond approximately to 5%.

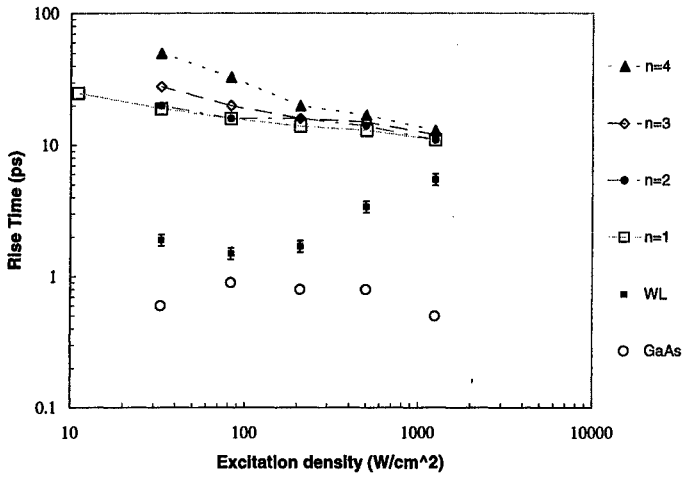


Figure 5: Rise time of the different PL structures versus the laser excitation density. $E_{exc.}$=1.675eV and T=77K. The uncertainties resulting from the fitting procedure correspond approximately to 10%.

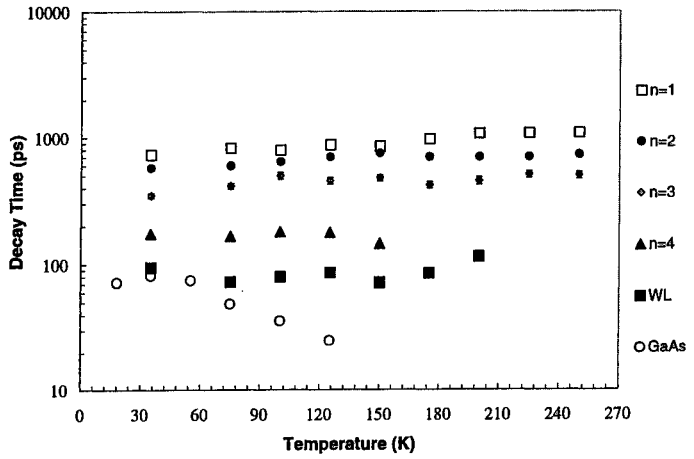


Figure 6 : Decay time of the different PL structures versus the temperature. $E_{exc.}$=1.675eV and $P_{exc.}$≈50W/cm^2. The uncertainties resulting from the fitting procedure correspond approximately to 5%.

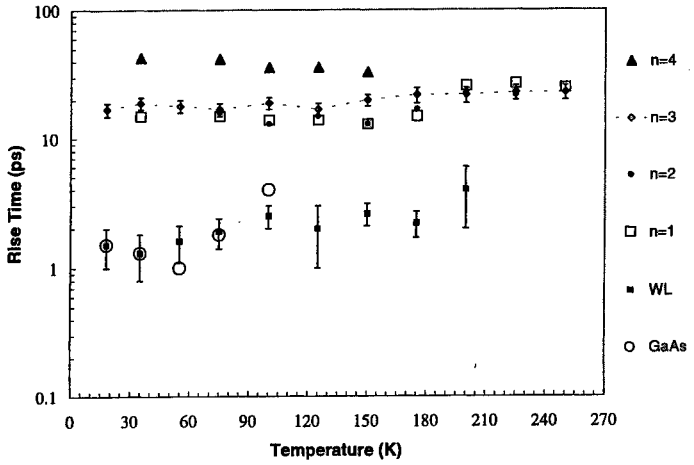


Figure 7 : Rise time of the PL structures versus the temperature. $E_{exc.}$=1.675eV and $P_{exc.}$≈50W/cm^2. The uncertainties resulting from the fitting procedure is about 10% and reach 50% for very short rise times (<2ps).

INTRABAND EXCITED STATES AND RELAXATION TIME IN InAs/GaAs SELF-ASSEMBLED QUANTUM DOTS

S. Sauvage, and P. Boucaud
Institut d'Electronique Fondamentale, Bât. 220,
Université Paris-Sud, 91405 Orsay, France.

F. Glotin, R. Prazeres, and J. M. Ortega
CLIO/LURE, Bât. 209 D,
Université Paris-Sud, 91405 Orsay, France.

A. Lemaître, and J.-M. Gérard
France Telecom, CNET Bagneux,
196 Av. H. Ravera, 92225 Bagneux, France.

V. Thierry-Mieg
L2M-CNRS
196 Av. H. Ravera, 92225 Bagneux, France.

ABSTRACT

We have investigated the confined states and the intradot relaxation time in InAs/GaAs self-assembled quantum dots using mid-infrared absorption between the confined levels. The intraband absorption is observed in both *n*-doped and *p*-doped quantum dots. The transition energy and the polarization selection rules of the intraband absorptions are correlated to those predicted by a three-dimensional numerical resolution of the Schrödinger equation for a lens-shaped quantum dot geometry. The intradot relaxation time is investigated by the saturation of the intraband absorption and time-resolved pump-probe experiments in the mid-infrared. Relaxation times of 3 ps and 1.5 ps are measured in the conduction and in the valence band respectively.

INTRODUCTION

Self-assembled semiconductor quantum dots are presently intensively studied both for their fundamental properties and their potential applications for optoelectronic devices [1]. A prerequisite for a comprehensive study of the quantum dot properties is a good knowledge of the energy diagram. Confined states in self-assembled quantum dots have been investigated experimentally by several techniques including photoluminescence spectroscopy at low and high-pump intensity [2], photoluminescence excitation [3], interband absorption [4], capacitance measurements [5]... The energy diagram of the quantum dots can also be directly investigated by looking at optical transitions between the confined

states in the conduction band or in the valence band. Such optical transitions are referred to as intraband or intersublevel absorption [6]. In InAs/GaAs self-assembled quantum dots, the first observation of intraband absorption has been reported in 1994 [7]. We have recently shown that intraband absorption in quantum dots can be observed in the valence and conduction band using a photoinduced absorption spectroscopy technique [8]. Direct observation of intraband absorption in doped self-assembled quantum dots has also been reported [9]. It is worth noticing that the existence of intraband absorption in the quantum dots has led to first demonstrations of mid-infrared photoconductive detectors [10,11].

In this article, we show that the study of intraband absorption can bring valuable information on the excited states in quantum dots. The energy diagram as deduced from the intraband experiments is found in agreement with the theoretical one deduced from the three-dimensional resolution of the Schrödinger equation. We further show that the study of intraband absorption under high pump regime gives access to the intradot relaxation times between the confined states in the conduction and in the valence band.

INFRARED ABSORPTION

The InAs/GaAs self-assembled quantum dots investigated in this work were grown by molecular beam epitaxy. The growth of the quantum dots is performed at 520 °C under As_4 beam pressure [8]. The doped samples are modulation-doped with a δ-doping (6×10^{10} cm^{-2}) lying 2 nm from the wetting layer. In all doped samples, only the ground state of the quantum dots is populated. The quantum dot multistacking typically consists of 20 InAs quantum dot layers separated by 50 nm thick GaAs barriers. To increase the interaction length with the mid-infrared light, two quantum dot multilayers were embedded in a mid-infrared waveguide. The mid-infrared waveguide, grown on a heavily doped (2×10^{18} cm^{-3}) GaAs substrate, consists of a $Al_{0.9}Ga_{0.1}As$ 5 μm thick cladding layer followed by a 2 μm thick GaAs layer, the active region and a 2.5 μm GaAs top layer. Cross section transmission electronic microscopy images of quantum dot samples grown in similar conditions show that the quantum dots have a lens-shape geometry with an average dot base diameter ≈25 nm and an height ≈2.5 nm [12]. The areal dot density is estimated around 4×10^{10} cm^{-2}.

The infrared absorption measurements were performed with a Fourier transform infrared spectrometer. The quantum dot waveguide characterizations were achieved with a mid-infrared microscope coupled to the spectrometer. The samples without waveguide were polished in a multipass geometry with 45° facets. Details of the photoinduced absorption measurements can be found in Ref. 8.

Figure 1 shows the influence of the average size of the dots on the mid-infrared electronic absorption. The samples are *n*-doped and the room-temperature infrared absorption is attributed to a bound-to-continuum transition as previously reported [9]. The absorption is polarized along the *z* growth axis of

the quantum dots. For the *n*-doped samples, the absorption cross section for one dot layer plane is estimated to be 3 x 10^{-15} cm^2. The striking feature reported in Fig. 1 is that the absorption shifts to lower energy as the average size of the quantum dots is decreased. The difference of average sizes is directly observed on the photoluminescence energy maximum (1.23 eV for the small dots and 1.17 eV for the large dots at low temperature). As will be shown in the next section, the red-shift of the absorption as the dot size decreases is explained by the increase of the quantum confinement of the ground electron state while the energy of the hybridized wetting layer states is hardly modified. It is important to note that the energy of the intraband absorption can be accurately controlled with the size of the dots. Such feature will be useful for the design of quantum dot infrared photodetectors.

The comparison between the infrared absorption of *n*-doped and *p*-doped self-assembled quantum dots is reported in Fig. 2. For both samples, the quantum dot layers are embedded in a mid-infrared waveguide. In both cases, the absorption is dominated by the absorption polarized along the *z* growth axis of the quantum dots. The infrared absorption of the *n*-doped sample is similar to the one reported in Fig. 1 and characteristic of a bound-to-continuum transition. In the case of the *p*-doped sample, the absorption exhibits a narrower linewidth. This reduced linewidth is explained by the fact that the absorption occurs between two confined hole states h_{000} and h_{001}. The absorption cross section for this transition is 10^{-15} cm^2. The broadening of the transition stems from the inhomogeneous broadening of the dot sizes and from the subsequent variation of the intraband energy. For the *p*-doped sample, a small bound-to-continuum absorption can also be observed with a maximum at around 350 meV.

ENERGY LEVELS CALCULATION

The confined energy levels in the lens-shaped quantum dots have been calculated by numerically solving the three-dimensional Schrödinger equation in the effective-mass approximation [13]. In the conduction band, the effective mass in the InAs layer is taken isotropic ($m^* = 0.04\ m_0$ where m_0 is the free-electron mass). In the valence band, the effective mass is taken anisotropic and decoupled between the *z* growth axis and the layer plane ($m_z = 0.59\ m_0$ and $m_{x,y} = 0.07\ m_0$.) The electronic (hole) confined levels are denoted $e_{n_x,n_y,n_z}(h)$ where the subscripts n_x,n_y,n_z correspond to the number of nodes of the envelope wavefunctions along the *x*, *y*, and *z* directions respectively of the corresponding wavefunctions in a parellelepipedic quantum dot.

The electronic energy structure as a function of the quantum dot height is presented in Fig. 3. A fixed aspect ratio (height/base diameter) of 0.1 has been considered in the calculations, as observed by cross section transmission electron microscopy images of the lens-shaped quantum dots. The number of confined electronic states is naturally found dependent on the size of the quantum dots. The states with a confinement energy larger than 560 meV are hybridized with the two-dimensional wetting layer states. The first excited state is doubly degenerate. The confined states exhibit a strong dependence *vs* the quantum dot size. It

explains the large broadening of the bound-to-continuum absorption which occurs from the ground state to the hybridized wetting layer states. This transition is predicted to occur around 120 meV for a 2 nm height quantum dot and around 250 meV for a 3 nm height quantum dot. These transition energies are in agreement with the values reported in Fig. 1 and 2. It is worth noticing that the e_{000}-e_{100} intraband transition has a very large dipole ($\approx$ 3 nm for a 2.5 nm height quantum dot) and that this transition is in-plane polarized. However, this transition has not been observed experimentally because it occurs below the detector cutoff energy. On the contrary, the transition e_{000}-e_{110}, which would be forbidden in a cubic quantum box with infinite potential confinement, has a much weaker dipole (0.15 nm) and is polarized along the *z* growth axis.

The energy of the first confined states in the valence band as a function of the quantum dot height is shown in Fig. 4. Due to the heavier mass, the confinement energy is much lower than in the conduction band. The largest dipole length is associated with the h_{000}-h_{100} intraband transition (3.1 nm for a 2.5 nm height quantum dot). Like in the case of the conduction band, this transition is in-plane polarized. The dipole matrix elements for the h_{000}-h_{110} and h_{000}-h_{001} transitions are 0.21 nm and 0.52 nm respectively. These transitions are predicted to be polarized along the *z* growth axis, as observed experimentally. A comparison between the experimental and calculated transition energies shows that the energy of the hole intraband transitions is overestimated by the calculation. However, the values of the dipole length are correctly predicted : 0.35 nm (experimental) for the h_{000}-h_{001} intraband transition reported in Fig. 2 as compared to the 0.52 nm theoretical value [14]. Moreover, the broadening of the h_{000}-h_{001} transition is well reproduced if we account for the size dispersion of the dots, as observed by photoluminescence, and the size dependence of the intraband transition energy, as reported in Fig. 4.

The polarization selection rules of the intraband transitions can be directly visualized by looking at the envelope wave functions of the confined states. The envelope functions of the first 4 confined hole states are shown in Fig. 5. The ground hole state is *s* type while the first excited state is *p* type. We see that the transition from the ground state to the first excited state will correspond to a transfer of charge in the layer plane and explains that the transition is in-plane polarized. On the contrary, the transitions to the second and third excited states will correspond to a transfer of charge along the *z* axis, as observed experimentally. For these two last transitions, the theoretical dipole in the layer plane direction is zero.

EXPERIMENTAL ENERGY DIAGRAM

The study of infrared absorption in doped samples allows an unambiguous assignment of the intraband transitions. However, the observation of small infrared absorptions requires a very high signal-to-noise ratio, which is difficult to achieve in direct measurements. Very weak absorptions can nonetheless be observed using a photoinduced absorption spectroscopy technique [8]. Figure 6 shows an example of photoinduced infrared absorption in undoped self-assembled

InAs/GaAs quantum dots [13]. The absorption spectra are reported in *p* and *s* polarizations and for two different temperatures. The h_{000}-h_{001} hole transitions along with the e_{000}-continuum transitions which are similar to those reported in doped samples (see Fig. 2) can be easily observed. A careful look at the absorption spectra shows that several other transitions can also be distinguished, in particular the in-plane polarized absorption from the electronic state to the continuum states above the GaAs barriers. Similar photoinduced experiments have been performed on samples with different quantum dot average sizes [13]. An experimental energy diagram as deduced from the intraband absorption measurements is shown in Fig. 7. Each transition reported in Fig. 7 has been experimentally observed. It demonstrates that intersublevel absorption is a sound spectroscopy technique to disentangle the energy diagram of self-assembled quantum dots. Note that the intersublevel absorption spectra can be correlated to the interband photoluminescence spectra, as reported in Ref. [15].

An important feature reported in Fig. 7 is the polarization selection rules of the transitions. In the mid-infrared spectral range (i.e. above 90 meV), the absorption is clearly dominated by *z*-polarized transitions. However, weak in-plane polarized transitions with absorption cross sections as low as 10^{-16} cm^2 can be observed. The in-plane polarized transitions to the continuum states above the GaAs barrier, either in the conduction or in the valence band, can be suitable for normal-incidence infrared photodetection even if their oscillator strength is weak. It explains the recent demonstration of a 5.5 μm quantum dot infrared photodetector operating at normal incidence but characterized by a low detectivity ($D^* = 4.7 \times 10^7$ cm $Hz^{1/2}$ /W) [11].

SATURATION OF ABSORPTION AND INTRADOT RELAXATION TIME

The knowledge of the carrier relaxation time between confined states in self-assembled quantum dots remains a very important issue. The carrier relaxation in quantum dots has been predicted to be slowed down because of the difficulty to conserve the energy following an inelastic phonon scattering [16]. It has been shown that different mechanisms like multiphonon scattering [17] or Auger assisted relaxations [18] allow carrier relaxation between the confined states. However, the values of intradot relaxation time reported in the literature vary considerably, going from 0.6 ps [19] to 40 ps [20] for intradot carrier relaxation time in the valence band. In order to disentangle this problem, we have investigated the intradot carrier relaxation time in our samples using the intraband absorption. The experiments have been performed using the CLIO picosecond free-electron laser which is available in Orsay.

The first experiments aimed at the demonstration of the saturation of the intraband absorption. A typical result for a *n*-doped quantum dot sample is presented in Fig. 8 [21]. The investigated sample is the *n*-type waveguide sample whose mid-infrared absorption is shown in Fig. 2. The saturation of the absorption is measured at room temperature for a 8 μm pump wavelength which corresponds to the wavelength of maximum absorption. Fig. 8 depicts the

transmission of the 8 μm pump wavelength as a function of the pump intensity. The saturation of the absorption is clearly observed along with the complete bleaching of the intraband absorption above 10 MW.cm^{-2}. A saturation intensity of 600 kW.cm^{-2} is deduced from the experiments [21]. Similar results have also been obtained for the *p*-doped quantum dot sample. The estimation of the intradot carrier relaxation time from the intraband saturation intensity is however not straightforward. We have therefore performed time-resolved pump-probe experiments to extract the intradot carrier relaxation time.

In the time-resolved experiments, the pump was set in TM-polarization (polarization along the *z* growth axis) while the probe was set at 45° between TE (polarization in the layer plane) and TM polarizations. The variation of transmission in TE polarization as a function of the time delay between the pump and the probe is reported at 300K in Fig. 9. The pump wavelength is 8 μm and the pump intensity is around 1 MW.cm^{-2}. The investigated sample is the *n*-type quantum dot sample as reported above. As seen, the transmission of the probe is modified when the pump and probe are coincident. The absorption recovers its value(1/e of maximum) after a 3 ps relaxation time. It is worth noticing that this relaxation time which corresponds to the relaxation of the carriers from the wetting layer states to the electronic ground state is relatively short. Similar values of short electron relaxation times have also been reported using time-resolved differential transmission spectroscopy experiments in InGaAs quantum dots [19].

Time-resolved pump-probe experiments have also been performed using the hole intraband absorption. The investigated sample corresponds in this case to the *p*-type waveguide sample whose absorption is reported in Fig. 2. For this sample, the intraband absorption is associated with two confined hole states (h_{000}-h_{001}) and does not involve the wetting layer states like for the *n*-type quantum dot sample. The result of the pump-probe experiment is reported at room temperature in Fig. 10. The wavelength of the free-electron laser was set in this experiment at 12.5 μm which corresponds to the absorption maximum. The intradot carrier relaxation time (h_{001} towards h_{000}) is also found very short in this experiment and typically corresponds to a 1.5 ps hole relaxation time.

CONCLUSION

In conclusion, we have reported on the mid-infrared intraband absorption in InAs/GaAs self-assembled quantum dots. We have shown that the study of the intraband absorption allows the investigation of the confined states in the quantum dots and the determination of the energy diagram of the dots. The features associated with the intraband absorption (energy and broadening of transitions, polarization selection rules) are found in agreement with those predicted by a three-dimensional resolution of the Schrödinger equation in the lens-shaped quantum dots. The saturation of the intraband absorption has been demonstrated for the first time. We have finally measured the electron and hole intradot relaxation times by time-resolved pump-probe experiments using a free-electron laser.

ACKNOWLEDGEMENT

This work is supported by DGA under contract 97062/DSP.

References

[1] See e.g. MRS Bulletin, 23 February 1998.

[2] M. Grundmann, N. N. Ledentsov, O. Stier, D. Bimberg, V. M. Ustinov, P. S. Kop'ev, and Zh. I. Alferov, Appl. Phys. Lett. **68**, 979 (1996).

[3] L. R. Wilson, D. J. Mowbray, M. S. Skolnick, M. Morifuji, M. J. Steer, I. A. Larkin, and M. Hopkinson, Phys. Rev. B **57**, R2073 (1998).

[4] K. H. Schmidt, G. Medeiros-Ribeiro, M. Oestreich, P. M. Petroff, and G. H. Döhler, Phys. Rev. B **54**, 11346 (1996).

[5] G. Medeiros-Ribeiro, D. Leonard, and P. M. Petroff, Appl. Phys. Lett. **66**, 1767 (1995).

[6] The absorption between the confined states in the conduction or valence band is differently denoted in the literature. By opposition to the interband absorption, this absorption is often denominated as intraband absorption since it occurs between confined states lying in the same band (conduction or valence band). However, the denomination "intraband" can be somewhat misleading since it suggests that some bands are involved like for bulk semiconductors, which is not the case due to the δ-like density of states in self-assembled quantum dots. Some authors have therefore chosen to call the "intraband absorption" the intersublevel or interlevel absorption since it is more appropriate for quantum dots. Both denominations can be used. However, the denomination intersubband absorption, as often reported in the literature, should be avoided. In quantum wells, the subbands have a physical existence and the term intersubband is appropriate. In quantum dots, there are no subbands and the use of the "intersubband" denomination does not make sense.

[7] H. Drexler, D. Leonard, W. Hansen, J. P. Kotthaus, and P. M. Petroff, Phys. Rev. Lett. **73**, 2252 (1994).

[8] S. Sauvage, P. Boucaud, F. H. Julien, J. M. Gérard, and J. Y. Marzin, J. Appl. Phys. **82**, 3396 (1997).

[9] S. Sauvage, P. Boucaud, F. H. Julien, J. M. Gérard, and V. Thierry-Mieg, Appl. Phys. Lett. **71**, 2785 (1997).

[10] S. Maimon, E. Finkman, G. Bahir, S. E. Schacham, J. M. Garcia, and P. M. Petroff, Appl. Phys. Lett. **73**, 2003 (1998).

[11] S. Kim, H. Mohseni, M. Erdtmann, E. Michel, C. Jelen, and M. Razeghi, Appl. Phys. Lett. **73**, 963 (1998).

[12] J. M. Gérard, J. Y. Marzin, G. Zimmermann, A. Ponchet, O. Cabrol, D. Barrier, B. Jusserand, and B. Sermage, Solid-Sate Electronics, **40**, 807 (1996).

[13] S. Sauvage, P. Boucaud, J.-M. Gérard, and V. Thierry-Mieg, Phys. Rev. B **58**, 10256 1998).

[14] S. Sauvage, P. Boucaud, F. Glotin, R. Prazeres, J. M. Ortega, A. Lemaître, J. M. Gérard, and V. Thierry-Mieg, submitted.

[15] S. Sauvage, P. Boucaud, J. M. Gérard, and V. Thierry-Mieg, J. Appl. Phys. **84**, 4356 (1998).

[16] H. Benisty, C. M. Sottomayor-Torres, and C. Weisbuch, Phys. Rev. B **44**, 10945 (1991).

[17] T. Inoshita, and H. Sakaki, Phys. Rev. B **46**, 7260 (1992).

[18] U. Bockelmann, and T. Egeler, Phys. Rev. B **46**, 15574 (1992).

[19] T. S. Sosnowski, T. B. Norris, H. Jiang, J. Singh, K. Kamath, and P. Bhattacharya, Phys. Rev. B **57**, R9423 (1998).

[20] R. Heitz, A. Kalburge, Q. Xie, M. Grundmann, P. Chen, A. Hoffman, A. Madhukar, and D. Bimberg, Phys. Rev. B **57**, 9050 (1998).

[21] S. Sauvage, P. Boucaud, F. Glotin, R. Prazeres, J. M. Ortega, A. Lemaître, J. M. Gérard, and V. Thierry-Mieg, submitted to Appl. Phys. Lett., manuscript L-5794.

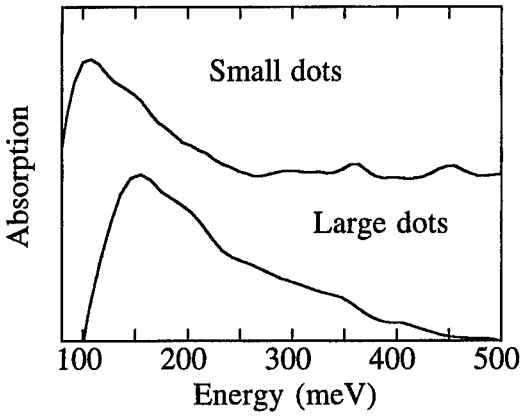


Figure 1: Room-temperature infrared absorption for different average sizes of *n*-doped InAs/GaAs self-assembled quantum dots: large dots : low-temperature photoluminescence maximum ≈ 1.17 eV. Small dots : low-temperature photoluminescence maximum ≈ 1.23 eV. The absorption is polarized along the *z* growth axis.

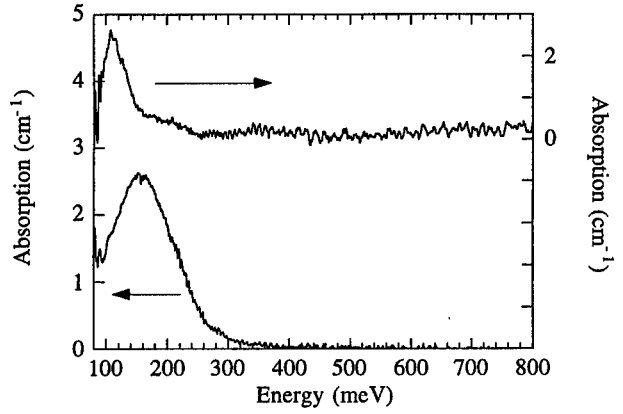


Figure 2 : Infrared absorption of *n*-doped quantum dots (bottom curve) and *p*-doped quantum dots (top curve). The quantum dots are inserted in a mid-infrared waveguide.

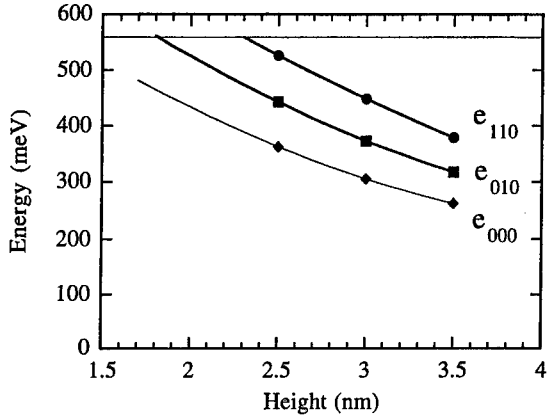


Figure 3 : Electronic energy levels in lens-shaped self-assembled quantum dots. The aspect ratio (height/base diameter) is 0.1. The origin of the energy is taken at the bottom of the InAs conduction band. The onset of the wetting layer states is 560 meV.

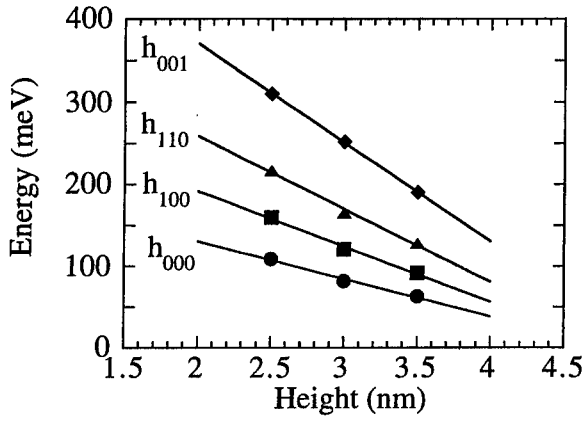


Figure 4 : First confined energy levels in the valence band in lens-shaped self-assembled quantum dots. The aspect ratio (height/base diameter) is 0.1. The origin of the energy is taken at the bottom of the InAs valence band. The h_{100} level is doubly degenerate.

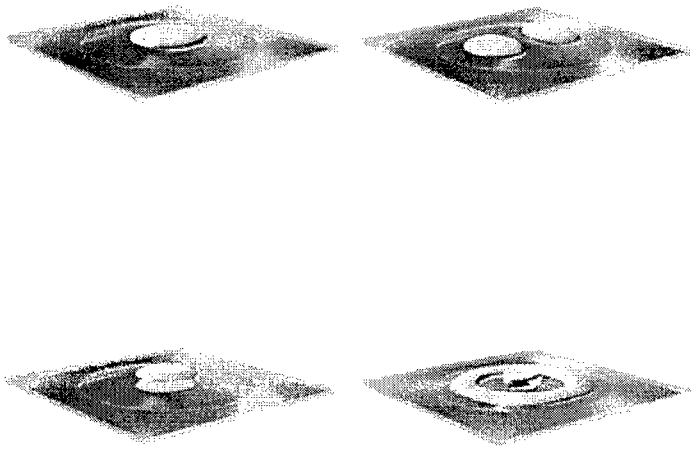


Figure 5 : Surfaces of isoprobability for the h_{000}, h_{100}, h_{110} and h_{001} levels (from left top clockwise) in a lens-shaped quantum dot. The probability of finding the carrier within the volume is 2/3.

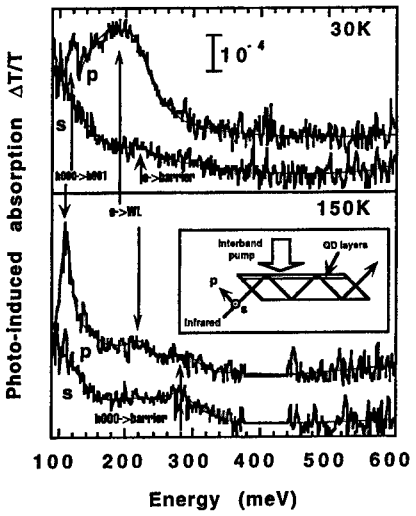


Figure 6 : Photoinduced infrared absorption of undoped self-assembled quantum dots in *p* and *s* polarizations. The inset shows a schematic description of the experimental setup. WL stands for wetting layer.

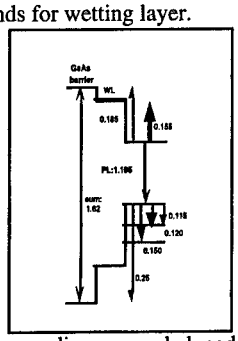


Figure 7 : Experimental energy diagram as deduced from the intersublevel absorption (120K). The thickness of the lines is proportional to the oscillator strength of the transitions. The grey arrows correspond to in-plane polarized absorptions.

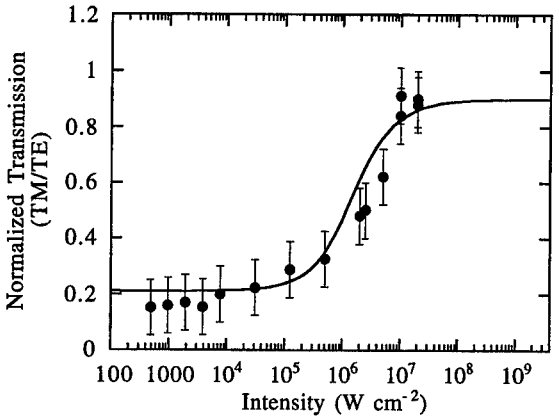


Figure 8 : Room temperature 8 μm transmission as a function of the pump intensity in a *n*-type quantum dot sample. The absorption spectrum of the quantum dots is reported in Fig. 2.

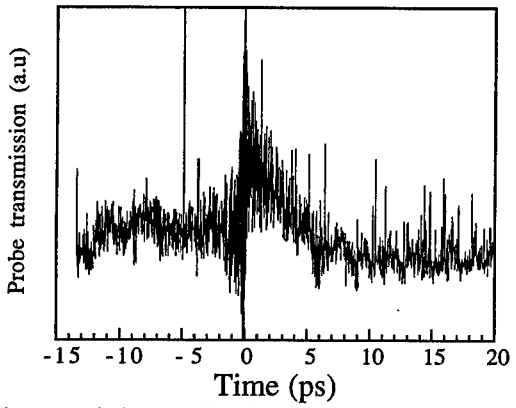


Figure 9 : Probe transmission as a function of the time delay between pump and probe at 300K. The pump wavelength is set at 8 μm. The quantum dots are *n*-doped.

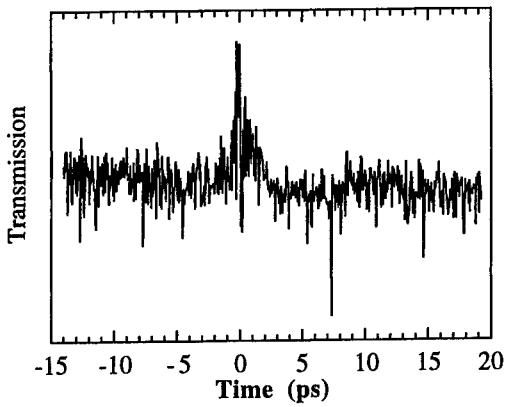


Figure 10: Probe transmission as a function of the time delay between pump and probe. The pump is set at 12.5 μm. The absorption spectrum of the *p*-doped quantum dots is reported in Fig. 2. The experiment is performed at room-temperature.

Electronic bistability in an electrochemically self-assembled array of semiconductor quantum dots

S. Bandyopadhyay[(a)]*, N. Kouklin[(a)], L. Menon[(a)], A. Balandin[(a)]†
D. Zaretsky[(b)], A. Varfolomeev[(b)] and S. Tereshin[(b)]

[(a)] *Department of Electrical Engineering*
University of Nebraska
Lincoln, Nebraska 68588-0511

[(b)] *Kurchatov Institute*
Kurchatov Square
Moscow, Russia

Abstract

A novel electronic bistability has been observed in a two-dimensional array of electrochemically self-assembled CdS quantum dots dispersed in alumina. The dots are produced by electrodepositing CdS in 100 Å-sized self-organized pores in a nanoporous alumina film produced by the anodization of an aluminum foil in sulfuric acid. The current-voltage characteristic of the array shows two distinct conductance states. The system switches from one conductance state to another if the dc bias is taken past a threshold voltage. This bistable behavior is perfectly repeatable. If the system is left in one conductance state, it remains there indefinitely until switched to the other state by the application of an external dc bias. A speculative model is proposed which may explain this behavior. Such an effect may find applications in extremely dense static random access memory.

*Corresponding author. E-mail: bandy@quantum1.unl.edu
†Current affiliation: Dept. of Electrical Engr., University of California-Los Angeles.

1 Introduction

There is significant current interest in self-assembled quantum dots for optical applications [1], magnetic storage media [2, 3] and non-linear optics [4]. In spite of their impressive success in these applications, most self-assembled arrays however have found limited use in electronics. In this paper, we report a novel phenomenon that may have an electronic use, namely in static random access memory.

2 Self-assembled quantum dots: sample preparation

A well-regimented two-dimensional array of CdS quantum dots is aself-assembled by electrochemical synthesis [5]. A 0.1 mm thick foil of 99.9999% pure aluminum is first electropolished in a solution of 62 cc of perchloric acid, 700 cc of ethanol, 100 cc of butyl cellusolve and 137 cc of distilled water for 30 seconds at 60 volts. The film is then washed in distilled water and dc-anodized in 15% sulfuric acid at room temperature with a current density of 40 mA/cm^2. This produces a thin nanoporous film of alumina on the surface of the foil with a quasi-regimented array of pores [5]. The average pore diameter is 100 Å with a 10% standard deviation and the average separation between pores (center-to-center) is 400 Å with a 4% standard deviation. Bright field transmission electron micrographs of the pore arrangement can be seen in ref. [5].

The pores are then slightly enlarged and "rounded" by dissolving part of the surrounding alumina walls in sulfuric acid. Next, it is washed to remove debris and dried. The porous film (still on the aluminum foil) is then ac electrolysed in sulfuric acid for 10 seconds with an ac current source operating at a frequency of 200 Hz and a rms current density of 40 mA/cm^2 which leaves behind the S^{--}

ions in the pores. Selective deposition of S^{--} in the pores occurs since the pores offer the least impedance path for the ac current. Finally, the film is immersed in boiling deionized water containing a 10% solution of $CdSO_4$. The Cd^{++} ions in the solution reacts with the S^{--} in the pores to form CdS in the pores. The duration of immersion determines to what depth the pores are filled. In the experiments described in this paper, the immersion time was 7 seconds. Cross-section transmission electron microscopy has revealed that usually this will lead to the bottom 100-150 Å of the pores to be filled up.

CdS dots produced by this technique have been directly imaged in the past by transmission electron microscopy, field emission scanning electron microscopy, and characterized by Raman spectroscopy, photoluminescence, absorption spectroscopy, ellipsometry, energy-dispersive analysis of x-ray, Auger depth profiling, ESCA, etc. High resolution TEM has shown that the dots are polycrystalline. Optical probing has revealed strong signatures of quantum confinement [5].

Variable angle spectroscopic ellipsomtery was used to probe the shapes of the dots. Although this method lacks sufficient accuracy, we found that we can fit the ellipsometric data best if we assume that the shapes of the dots are rotational ellipsoids. In the present experiment, the CdS dots are expected to resemble rotational ellipsoids (the shape of a football) with major axis $\approx$ 150 Å and the minor axis $\approx$ 100 Å. Cross-section TEM shows similar shapes.

Before the experiment, the presence of CdS in the pores was again established with x-ray emission spectroscopy using electron beam excitation. In addition to the lines associated with Cd and S, intense blue-white cathodoluminescence was observed from the CdS dots

3 Current-voltage characteristics

To measure the dc current-voltage characteristic of the dot array, two large-area gold contact pads (0.1mm × 0.1mm cross-section and thickness 300 Å) were first deposited on the surface of the array by resistive evaporation. These were used as current and voltage probes. Measurements were carried out with a voltage source.

In Fig. 1, we show the measured current-voltage (I-V) characteristic. The I-V characteristic is linear indicating ohmic conduction. It is surprising that the conductance is so high given that the alumina walls separating adjacent CdS quantum dots are insulating and that the average thickness of these walls is 300 Å. Indeed, if the experiment is repeated without the prior step of electron beam excitation, we see no measurable conduction at all. We therefore surmise that electron beam irradiation introduces a very high density of traps and gap states in the alumina that may form impurity bands which allow significant conduction.

If the irradiated array is initially in the low conductance state of 1 mS, it remains in that state till the applied dc bias exceeds $\sim$ 10 volts. Thereupon, it switches to the high conductance state of 20 mS. The current doubles while the voltage falls to one-tenth of its value before switching.

In the high conductance state, another switching occurs when the voltage is swept past 2.5 V. The array returns to the low conductance state. The current falls from 50 mA to 4 mA and the voltage increases to 4 V. This process can be repeated over and over again. If the array is left in any of the two conductance states, it remains there indefinitely till it is switched.

The above conductance bistability can be exploited to realize *non-volatile* or static binary memory. The low conductance state could encode, say, binary bit 0 and the high conductance state binary bit 1. To "read" the stored bit, one could probe the conductance with a small ac bias. The "writing" strategy is the following.

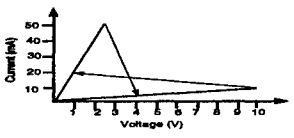


Figure 1: The current versus voltage characteristic of a self-assembled CdS quantum dot array dispersed in alumina. These measurements were made at room temperature.

Precede the write cycle with a read cycle. If the stored bit is already the desired bit, do nothing. Otherwise, apply a dc bias past the threshold for switching. This will switch the array to the desired state and thus write the desired bit.

4 Possible origins

It is fairly evident that the conduction is assisted by traps introduced during electron beam irradiation. We propose the following speculative model to explain the bistability.

Assume that the array is in the high conductance state. As the dc bias is increased, electrons from the CdS tunnel into the traps in the alumina and get trapped. All the traps get saturated and completely filled. The sudden fall in the free (untrapped) electron concentration then causes the conductance to drop

discretely.

Once in the low conductance state, the system persists in that state until the bias exceeds a value when the quasi-Fermi level at the traps dips below the trap band. The traps then empty and emit the trapped electrons. The original free carrier concentration is restored and the conductance reverts to the high value. This explains the bistability. A somewhat similar mechanism can give rise to negative differential resistance in gold-doped Germanium [6].

The bistability can also be viewed as a combination of an N-type and an S-type non-linearity. It is well-known that the first type is associated with the formation of high field domains, whereas the latter results in the formation of current filaments [7]. Our present research efforts are directed towards an attempt to observe these domains using electrostatic force microscopy.

Acknowledgement This work was supported by the U.S. Army Research Office under grant DAAG55-98-1-0015 and partially by the Defense Advanced Research Projects Agency under the ULTRA program contract 35918-OH.

References

[1] D. Bimberg, M. Grundmann and N. Ledentsov, *Quantum Dot Heterostructures*, (John Wiley & Sons, New York, 1998).

[2] C. A. Huber, T. E. Huber, Mqio Sad, J. A. Lubin. S. Manalis and C. B. Prater, *Science*, **263**, 800 (1994).

[3] S. Bandyopadhyay, L. Menon, N. Kouklin, H. Zeng and D. J. Sellmyer, to appear in *J. Elect. Mat.: Special Issue on Quantum Dots, April 1999.*

[4] A. Balandin. S. Bandyopadhyay, P. G. Snyder, S. Stefanovich, A. Varfolomeev, D. Zaretsky, G. Banerjee and A. E. Miller, *Phys. Low Dim. Struct.*, **11/12**, 155 (1997).

[5] S. Bandyopadhyay, A. E. Miller, H-C Chang, G. Banerjee, V. Yuzhakov, D-F Yue, R. E. Ricker. S. Jones, J. A. Eastman, E. Baugher and M. Chandrasekhar, Nanotechnology, Vol. 7, (1996) 360.

[6] B. K. Ridley and R. G. Pratt, *Phys. Lett.*, **4**, 300 (1963).

[7] B. K. Ridley, *Proc. Phys. Soc.*, **82**, 954 (1963).

Clusters and Other Nanostructures

MAGNETO-OPTICAL PROPERTIES OF II-VI SEMICONDUCTOR NANOPARTICLES, EITHER EMBEDDED IN GLASS MATRIX OR COVERED BY EPITAXIAL CAPPING

E. Lifshitz, H. Porteanu, I. Litvin and A. Glozman, Department of Chemistry and Solid State Institute, Technion, Haifa 32000, Israel

ABSTRACT

The magneto-optical properties of CdS embedded in phosphate glasses or capped by epitaxial shells (e.g. CdS/HgS/CdS) were examined by the utilization of optically detected magnetic resonance spectroscopy. The results showed that the magneto-optical properties of the aforementioned structures are governed by the existence of surface and interface defects, which cause trapping of photogenerated carriers. Furthermore, these carriers act as unpaired spins that undergo magnetic resonance transitions at the excited state, revealing information about the mechanism of recombination and identification of the trapping sites.

INTRODUCTION

Semiconductor nanoparticles offer the opportunity to tune the energy of electronic states and optical transitions, with variation in the particle's size [1-5]. This makes them potentially useful in new and emerging technologies, such as optical switches [4], efficient lasers [4], light emitting diodes [6], biological markers [7,8], single-electron transistors [9], photo-voltaic cells [10-12] and catalysis devices [13]. The discussed research is concern with the investigation of II-VI semiconductor nanoparticles, either embedded in glass or polymer media, or capped with epitaxial shell. These nanoparticles are prepared by chemical reactions with a high degree of reproducibility, controlled diameters of < 10 nm, relatively narrow size distribution (<5-15%) and uniform shape. Nevertheless, they still exhibit crystalline mismatch with the surrounding, dangling bonds, stoichiometric defects, and external adatoms at surface/interface sites. The dependence of the electronic properties on size (the quantum size effect) has already been studied extensively [2, 3,14-18]. However there is very little knowledge about the role of the surfaces/interfaces.

Recent single-nanoparticle measurements of CdSe, CdS, and InAs showed that the exciton emission undergoes bright/dark periods during the time of acquisition. The dark periods can last between millisecond to a second. At the current moment there are two major explanations for the occurrence of this intermittence, associated either with surface trapping [19] or Auger process [19]. The studies of single nanoparticles also showed periodic spectral diffusion during the bright time, shifting as much as 60 meV [19,20]. This can be due to a self-induced Stark effect created by the trapped carrier local electric field at the surface or in the medium [21]. Thus, the single nanoparticles measurements emphasize prosper need to identify the surface/interface trapping sites. Therefore, the present work investigated the influence of surface and interface states on

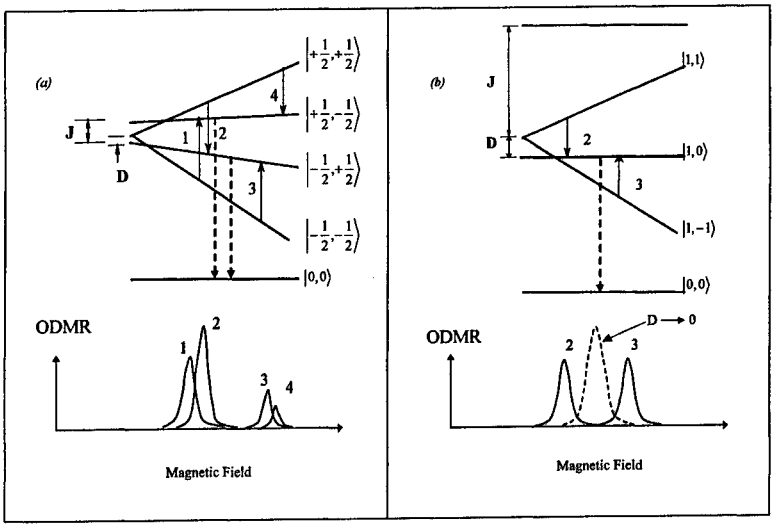


Figure 1: *(a) Schematic diagram of the spin energy states of recombining electron and hole. The notations in the diagram are explained in the text. (b) Anticipated ODMR spectrum for a big J value, with isotropic g-factors of the recombining sites, for an unthermalized case.*

the optical properties of the materials, by the utilization of an optically detected magnetic resonance (ODMR) spectroscopy. This method supplies static and dynamic information regarding structural uniformity (core versus surface), localization of photogenerated carriers, exchange interactions between carriers, and the interaction of a carrier with the lattice. In addition, it enables to follow radiative and non-radiative recombination mechanisms at the surface/interface. The principals of the latter methods are explained in the following section.

Optically detected magnetic resonance spectroscopy

In the ODMR method, one measures the change in luminescence intensity due to a magnetic resonance event at the excited state. Although it resembles a conventional electron spin resonance spectroscopy, the sensitivity is larger by 5 orders of magnitude due to the detection of electric dipole instead of magnetic dipole transitions. The contour shape of an ODMR event, associated with recombination between trapped electron (e) and hole (h), depends on the e-h mutual interactions [22,23], and can be explained according to the diagram shown in figure 1. This figure presents a case with spin quantum number S=1/2, for the electrons and holes. In a case of weak e-h interaction, the excited state consists of fourfold spin state (diagram 1a), associated with the electron [$m_S(e)=\pm 1/2$] and hole [$m_S(h)=\pm 1/2$] spin projections on the external magnetic field direction. The spin resonance transitions are shown by the small arrow and the numbers

1-4, while the optical transition are given by the dashed lines. J corresponds to an isotropic e-h exchange interaction, while D to the anisotropic interaction (or zero field splitting). The zero-angular momentum optical transitions take place from the |+1/2,-1/2> and |-1/2,+1/2> sub-levels. Then, if thermal distribution of the spin states population does not occur, the magnetic resonance transitions, will enhance the intensity of the optical transitions. The anticipated ODMR spectrum is shown below the diagram. It consists of two doublets, each is associated with flipping of the electron (transitions 1 & 2) and hole (transitions 3 & 4) projection direction. The separation within a doublet corresponds to J, while the separation between the doublets is associated with the Zeeman interaction of each carrier with the external magnetic field. Upon thermal distribution among the spin states, some of the resonance transitions may reverse their direction (shown by the arrows in the diagram). The latter will lead to a quenching of the optical transitions, and appearance of negative signals in the ODMR spectra (one resonance in each doublet in figure 1a will be negative).

For J>> βgB, the |+1/2, -1/2> spin state is pushed to higher energy, creating singlet (S=0) and triplet (S=1) spin states, as shown schematically in diagram 1b. Then, the zero-angular momentum optical transition originates from the triplet |0,0> state and the magnetic resonance transitions 1 and 4 are eliminated. Thus, the anticipated spectrum, drown below the diagram, consists of resonance signals (2 and 3) corresponding to the transitions among a triplet manifold, with mutual separation which is equal to D. It should be noted that the positions of resonance signals 2 and 3, in the latter case, might be exchanged, if the sign of D is negative. Moreover, when $D \rightarrow 0$ the ODMR spectrum will coalesce into a single broad resonance, as presented by the dashed line in spectrum 1b.

In any event, an ODMR spectrum of recombined e-h pairs, can be simulated by the utilization of the following spin Hamiltonian:

$$H_S = \beta S_e g_e H_0 + \beta S_h g_h H_0 + S_e D S_h + J S_e S_h \qquad [1]$$

where the first two terms correspond to the effective Zeeman interaction of an electron and hole, the third term corresponds to the zero field splitting, while the last term to the isotropic exchange interactions. It should be noted that the hyperfine interaction has been neglected in the present case, due to the random distribution of the nanoparticles within the matrix.

EXPERIMENTAL

Material preparation

The preparation of II-VI nanoparticles in various matrices were performed according to the following procedures:

(1) Nanoparticles embedded in glass media were prepared in-situ, during a phosphate glass formation [24,25]. The glass solution was composed of P_2O_5-Na_2O-ZnO-AlF_3-Ga_2O_3 and was prepared at 1200°C. The semiconductor ions, Cd^{+2}, S^{-2}, of 0.8-1.2 wt%, were added to the glass solution at the initial stage. Then, the

nanoparticles of CdSe were grown by a process of diffusion controlled phase decomposition, utilizing post-annealing treatment of the glass films at moderate temperatures (430-470°C) for duration of 10-90 minutes.

(2) The synthesis of the CdS core, with an average size of 5.5 nm, was carried out in a colloidal solution. $Cd(ClO_4)_2$ and H_2S were used as the preliminary precursors, while sodium polyphosphate and NaOH acted as a stabilizer and a pH agent, respectively. The core-shell CdS/HgS nanoparticles were prepared by an addition of $Hg(ClO_4)_2$ solution, leading to a displacement of Cd^{+2} ions and the creation of a stoichiometric monolayer (0.3 nm) of HgS. The cladding layer was prepared by a drop-wise addition of H_2S/water solution. The reaction with S^{2-} led to re-precipitation of the Cd^{2+} ions over the surface of the particles. The thickening of the HgS layer was simply achieved by repeating the displacement and re-precipitation reactions. Following the discussed sequence of steps resulted in the formation of the colloidal particles, consisting of a CdS core (cubic, $E_{g,bulk}$=2.5 eV, lattice parameter a=5.818 Å), surrounded by 1-3 monolayers of β-HgS (cubic, $E_{g,bulk}$=0.5 eV, a=5.851 Å), and 1-3 outer cladding layers of CdS. A detailed description of the CdS/HgS/CdS nanoparticles synthesis is given in previous publications [26].

The shape and size of the various nanoparticles were determined by transmission electron microscopy (TEM), while electron diffraction or X-ray diffraction determined the crystallographic structure.

Instrumental

The PL and ODMR measurements were carried out by immersing the samples in a cryogenic dewar (at 1.4K) and exciting them with continuous Ar^+ laser. The emitted light was passed through a holographic grating monochromator and detected by Si, or Ge detectors. The ODMR spectra were recorded by placing the sample on a special sample probe, at the centered of a high-Q resonance cavity, coupled to a microwave (mw) source (9 GHz), and surrounded by a superconducting magnet (B). These spectra were obtained by measuring the change in luminescence intensity of the non-excitonic PL band, induced by a magnetic resonance event at the excited state. This change was plotted versus the strength of the external magnetic field, B, leading to magnetic resonance-like spectra. The non-excitonic luminescence was isolated by appropriate cut-off color filters, while the emitted beam was detected in either of the following directions: (a) parallel to the external magnetic field (Faraday configuration), or (b) perpendicular to it (Voight configuration). A change in the emission circular-polarization component was also detected in the Faraday configuration.

RESULTS AND DISCUSSION

CdS nanoparticles embedded in phosphate glasses

A non-excitonic band (not shown) dominates the photoluminescence (PL) spectra of CdS nanoparticles embedded in phosphate glasses [27]. A change in their intensity was measured due to a magnetic resonance transition at the excited state, and produced

the ODMR spectra. Representative spectra of nanoparticles' sample with mean size of 5.7 nm, 4.2 nm and 3.2 nm, are shown in figure 2. The latter were recorded at the Voight (k_{em} H_0) configuration. The ODMR spectrum of the 5.7 nm sample consist of a major band (labeled II) and two additional weak shoulders (labeled I and III). The ODMR spectrum of the 4.2 nm sample is similar to that of the 5.7 nm sample, however, shoulders I and III have lower intensity and the III resonance is slightly negative. Then, the II resonance in the latter spectrum seems to be narrower.

The ODMR spectrum of the 3.2 nm sample, is dominated by the I and III resonances, however resonance II is essentially missing. Thus, the representative spectra indicate that the ODMR transitions of the various samples are similar, however their relative intensities vary from sample to sample. ODMR spectra, recorded at the Faraday

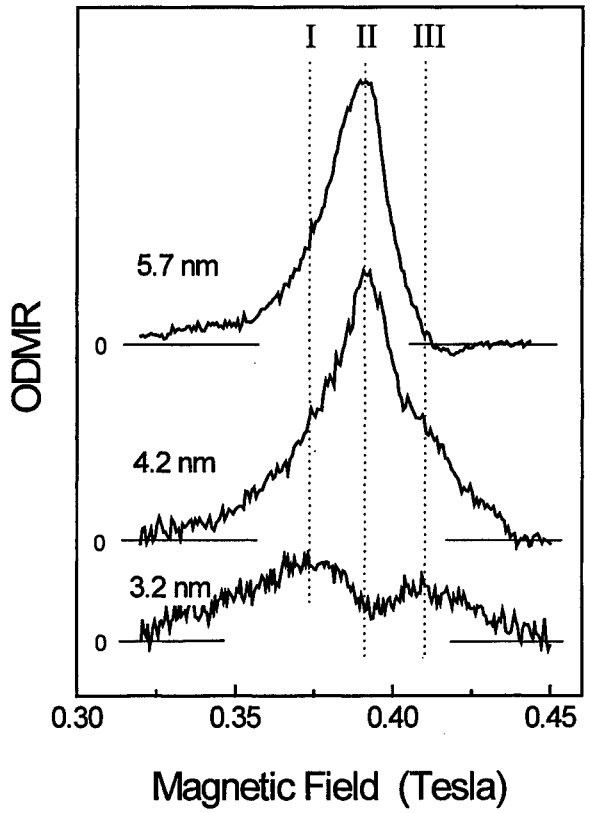


Figure 2: *Representative ODMR spectra of CdS nanoparticles for three different samples, with mean size, as indicated in the figure. The experimental conditions are given in the text.*

configuration ($k_{em}||H_0$), appeared to be identical to that observed under the Voight configuration. The right (σ+) and left (σ-) circular polarization components of ODMR in the latter configuration showed identical spectrum.

The spin Hamiltonian was utilized, in order to simulate each one of the resonance events. The simulation of resonances I and III of the various samples showed that they are associated with relatively weakly interacting (small J) electron and hole pairs, with J=0.03 meV, D=0 and g_e=1.95 and g_h=2.08. Moreover, it was essential to consider anisotropic g-factor and distribution of values for the exchange coupling J. The simulation of resonances I and III are shown by the solid lines in figure 3. The simulation of resonance II required the consideration of trapped electron-hole recombination, with relatively strong isotropic exchange interaction ($J>>g\beta H_0$) and $D<<J$. The small D value leads to coalescence of the resonance into a single band with

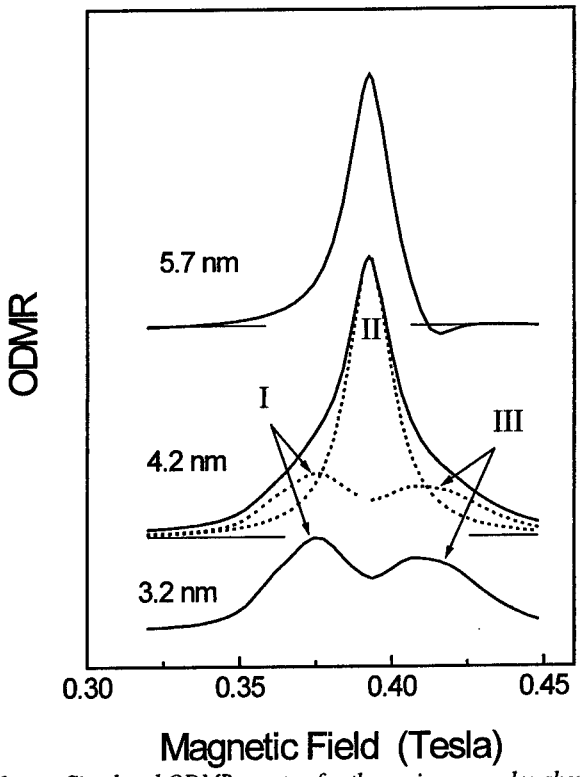


Figure 3: *Simulated ODMR spectra for the various samples shown in figure 2. The dashed lines correspond to the simulations of the individual resonances, while the solid lines show the sum of the entire resonance transitions.*

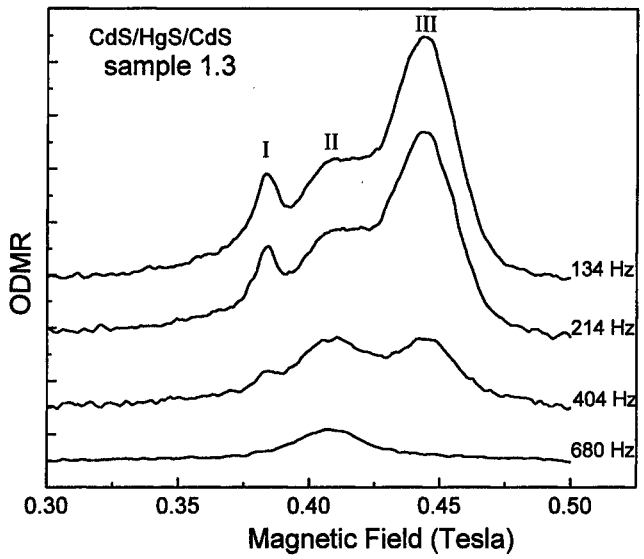


Figure 4: *The ODMR spectra of the 1.3 sample, recorded at different microwave modulation frequencies.*

average g-factor $g_{avr}=(g_e+g_h)/2$, as shown by the dashed line in figure 3.

The anisotropy of the trapping sites, associated with resonances I and III excludes the possibility of their location at the core of an hexagonal particle and instead, suggests localization at the surface. Accordingly, the distribution of exchange interaction values can be due to the existence of ensemble of e-h pair distances, more-likely, around the periphery of a nanoparticle. Based on the experimental observations, it is presumed that resonance II is associated with different chemical imperfections. Its nearly isotropic behavior (D~0, g~2.00) suggests a location of the corresponding trapping sites in the core of the nanoparticles. Indeed, it is seen in figure 2 that ODMR spectrum of a sample with the smallest average nanoparticles size, is dominated by recombination at surface sites and is missing the resonance of the core defects. On the contrary, the ODMR spectrum of the largest average size sample, is dominated by recombination from core defect centers. It should be noted that the random orientation of the particles within the matrix, avoided the possibility to identify any local crystallographic axis of the trapping sites, however, several suggestions regarding the chemical nature of the trapping sites can be raised. Previous studies [28] suggested that deep states, in particles with nanometer dimensions, are mainly associated with surface defects. They can be associated with Cd^{+2} and S^{-2} vacancies (stoichiometric defects), dangling bonds or external adatoms (like oxygen) [23,29]. Stoichiometric defects may exist at the core of the nanoparticles as well. Furthermore, the relative softness of the phosphate glass matrix, avoids particular stress on the nanoparticles and consequently eliminate diffusion of the core defects to the surface of the particles.

The diminuation in intensity of resonance I and the change in sign of resonance III in the ODMR spectrum of the 3.2 nm sample, is associated with a competing effect

between e-h recombination and spin lattice relaxation times. This demands the consideration of thermalization effects (Bolzmann distribution among the spin states), in combination with the spin Hamiltonian parameters, leading to a best fitted spectrum for the 3.2 nm sample, as shown in figure 3.

CdS/HgS/CdS nanoparticles

The PL spectra of CdS/HgS/CdS samples, excited above the core-CdS band-gap energy and recorded at 1.4K (not shown) consist of an exciton band, predominantly tunable with the thickness of the internal HgS layer, and an additional broad band at lower energies. The latter is mainly pronounced in the samples with a HgS monolayer. The ODMR phenomenon was examined mainly at the lower energy PL band. Representative spectra of a sample that contains one monolayer of HgS and three cladding layers of CdS (denoted as 1.3), and recorded at different modulation frequencies of the microwave source, are shown in figure 4.

Careful observation of this figure suggests that the resonance signals III and I alter simultaneously, while resonance II behaves differently. This suggests that the ODMR spectra consist of two overlapping magnetic resonance events, and more likely, resonance III and I correspond to a common incident. Examination of the microwave modulation frequency and laser power dependence of the ODMR spectra of samples 1.2 and 2.1 shows a similar behavior to that described for the 1.3 sample. The Hamiltonian given in equation 1 was utilized in order to simulate each one of the resonance events. Resonance signals III & I resemble a case of spin singlet transitions with a relatively weak exchange interaction. Thus, in the first stage we simulated a situation with a relatively small J and D and isotropic g-factor. It showed a narrow and symmetric resonance signal, in contradiction with the experimental spectra. Incorporation of anisotropy in the g-factor led to an asymmetric broadening or singularities in the resonance signals. In order to make a best-fit with the experimental spectra, additional broadening associated with the distribution of J values was essential. The last broadening was, more or less, sufficient for the simulation of resonance III however, it did not predict the sharpness of resonance I and the relative intensities between resonance I & III. This sharpness could be simulated when an additional thermal distribution parameter had been considered. Observation of resonance II suggests that it is associated with e-h pair recombination with relatively strong isotropic exchange interaction ($J>>g\beta H_0$) and $D<<J$. The small D value leads to coalescence of the resonance into a single band with an average g-factor $g_{avr}=(g_e+g_h)/2$. Thus, the summation of the simulations associated with I & III and II led to the best-fit of the experimental spectrum as shown in figure 5.

The g(I)=1.9 and g(II)=1.7 values of the different resonance signals deviate substantially from those of the valence and conduction band [30] and thereupon, suggest that the ODMR phenomenon corresponds to a recombination between states with wavefunctions that are not necessarily associated with CdS or HgS band edges. The J= 0.04 eV of resonance I & III is smaller than the exchange interaction of a typical exciton in II-VI nanoparticles (~0.3 eV in CdSe nanoparticles [3]), supporting the non-excitonic character of the studied recombination emission.

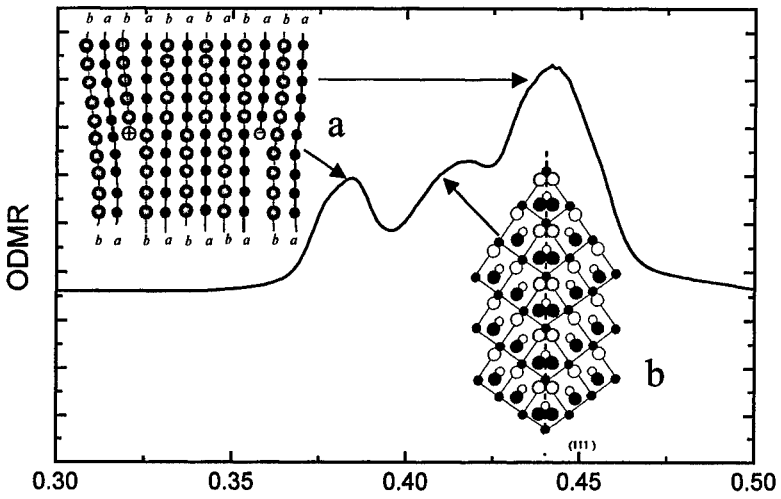


***Figure 5**: The simulation ODMR spectra. In the inset: possible suggestions of the trapping sites: (a) particle dislocations in AB - compounds (b) twin grain boundary.*

The anisotropy of the trapping sites, associated with resonance I & III excludes the possibility of their location at substitution or interstitial sites within a cubic zinc blende nanoparticles. Instead, it suggests localization at an interface or surface. Several suggestions regarding the chemical nature of the trapping sites can be raised. Mews et.al showed the crystallization of CdS/HgS/CdS nanoparitcles have tetrahedral shapes with (111) facets. They also indicated the possibility of twin grain boundaries between the HgS and the CdS cladding layer (as shown schematically at the inset of figure 5). Such a boundary causes the appearance of that acts as traps for carriers. Furthermore, in the zinc blende crystallographic unit, with three atomic layers (ABC), these vacancies can be either in the metal (Cd, Hg) or in the S atomic layer. Cd^{+2} vacancies and S^{0} vacancies act as double acceptors. However, trapping of a single hole alone leads to the creation of paramagnetic centers that can be detected by the ODMR method. Cd^{0} and S^{-2} vacancies act as double donors, and in a similar manner, the trapping of one electron will be detected by the ODMR method. In other words, photo-generated electrons and holes can be trapped at vacancy defects that are created at the twin grain boundaries in CdS/HgS/CdS structures. The unique principal axis, (the spectroscopic g-factor) is considered to be normal to the boundary while the other axes are tangential to it. Accordingly, the distribution of exchange interaction values can be due to the existence of an ensemble of e-h pair distances, more likely, around the periphery of an interface. The twin grain boundaries can very well describe the resonance signals in the ODMR spectra. The occurrence of a vacancy on any second atom at the twin boundary, lead to a condensed distribution of trapped electrons and holes that consequently causes a strong exchange interaction, associated with resonance signal II. However, larger spatial

distribution of trapped electron and hole along the twin boundary may lead to a weaker exchange interaction and to the origin of I & III resonance signals.

Alternatively, Mews and Eychmüller showed that the growth of a monolayer is not perfect [31] and it can be terminated by an edge dislocation, shown as an inset in figure 5. In a similar manner to the described vacancies, such terminations have unsaturated chemical bonds, creating electron and hole trapping sites. Likewise, these edges have asymmetric local chemical bonds, reflected in an asymmetric g-factor. Since these edge dislocations are distributed randomly, more likely, they will be spaced apart from more than two-chemical bonds and thereupon, the exchange interaction of carriers trapped in those sites will be relatively small. Hence, the edge dislocations can be associated with trapped e-h pairs that produce the resonance signals III & I in the studied ODMR spectra.

SUMMARY

Nanoparticles of CdS embedded in phosphate glasses were prepared under diffusion control process. The particles of CdS/HgS/CdS were prepared in colloidal solution include substitution reaction of the ions at the surface. In both cases the materials includes interface positions, either between the particle and the medium or with the epitaxial cover. Utilization of the ODMR method was found to be useful for the study of the influence of the discussed interface properties on the magneto-optical properties of the materials. The results showed that the optical events are associated with trapping of photogenerated carriers at interface sites. For example, CdS/HgS/CdS nanoparticles exhibit twin boundaries or edge dislocations. The latter defects include vacancies of metal or ligand that offer the opportunity for electron and hole trapping.

ACKNOWLEDGMENTS

This research was supported by the Israel Ministry of Science contract no. 5839-2-96. I. L. expresses his gratitude to the Eshkol graduate student fellowship, given by the Israeli Ministry of Science and H. P. acknowledges the fellowship of Israeli Council for Higher Education.

REFERENCES

1 A. P. Alivisatos, *J. Phys. Chem.*, **100**, 13266 (1996) and references therein.

2 Al. L. Efros, M. Rosen, M. Kuno, M. Nirmal, D. J. Norris and M. G. Bawendi, *Phys. Rev. B*, **53**, 4843 (1996).

3 M. Nirmal, D. J. Norris, M. Kuno, M. G. Bawendi, Al. L. Efros and M. Rosen, *Phys. Rev. Lett.*, **75**, 3728 (1995).

4 S. Schmitt-Rink, D. A. B. Miller and D. S. Chemla, *Phys. Rev. B*, **35**, 8113 (1987).

5 (a) L. E. Brus, *J. Phys. Chem.*, **80**, (1984) 4403. (b) L. E. Brus, *IEEE J. Quantum Electronics*, **QE-22**, 1909 (1986). (c) L. E. Brus, *J. Phys. Chem.*, **90**, 2555 (1986).

6 V. L. Colvin, M. C. Schlamp and A. P. Alivisatos, *Nature*, **370**, 354 (1994).

7 A. P. Alivisatos, *MRS-Conference Proceedings*, Boston (1998) (in press).

8 C.J. Murphy, E.B. Brauns, L.Gearheart, *MRS-Conference Proceedings*, Boston (1997) p.597.

9 D. L. Klein, R. Roth, A. Lim, A. P. Alivisatos and P. L. McEuen, *Nature*, **389**, 679 (1997).

10 N. C. Greenham, X. Peng, A. P. Alivisatos, *Synthetic Metals*, **84**, 545 (1997).

11 G. Hodes, *Isr. J. Chem.*, **33**, 95 (1993).

12 H. Weller, A. Eyechmuller, R. Vogel, L. Katsikas, A. Hasselbarth and M. Giersig, *Isr. J. Chem.*, **33**, 107 (1993).

13 D. W. Bahnemann, *Isr. J. Chem.*, **33**, 115 (1993).

14 A. J. Nozik, O. I. Micic, *Luminescence*, **70** (1-6), 95 (1996).

15 H. Giessen, B. Fluegel, G. Mohs, and N. Peyghambarian, J. Sprague, O. I. Micic and A. J. Nozik, *Appl. Phys. Lett.*, **68** (3), 304 (1996).

16 T. D. Krauss and F. W. Wise, *Phys. Rev. Lett.*, **79**, 5102 (1997).

17 T. D. Krauss and F. W. Wise, *Phys. Rev. Lett.*, **76**, 1376 (1996).

18 J. Valenta, A. I. Ekimov, P. Gilliot, B. Honerlage, R. Levy, *Luminescence*, **72-74**, 406 (1997).

19 J. Tittel, W. Gohde, F. Koberling, Alf Mews, A. Kornowski, H. Weller, A. Eychmüller, Th. Basche, *Ber. Bunsenges. Phys. Chem.*, **101**, 1626 (1997).

20 M. Nirmal.; B. O. Dabbousi; M. G. Bawendi; J. J. Macklin; J. K. Trautman; T. D. Harris; L. E. Brus, *Nature*, **383**, 802 (1996).

21 S. P. Empedocles; M. G. Bawendi, *Science,* **278**, 2114 (1997).

22. E. Lifshitz, I. Dag, I. Litvin, G. Hodes, *J. Phys. Chem. B*, **102**, 9245 (1998).

23. E. Lifshitz, L. Bykov, M. Yassen and Z. Chen-Esterlit, *Chem. Phys. Lett.*, **273**, 381 (1997).

24. E.V. Kolobkova, A.A. Lipovskii, N.V. Nikonorov, V.D. Petrikov, A.A. Sitnikova and I.E. Jakovlev, *J. Non-crystalline Solids*, **221**, 18 (1997).

25. E.V. Kolobkova, A.A. Lipovskii, N.V. Nikonorov and A.A. Sitnikova, *Phys. Status Solidi A*, **147**, K65 (1995).

26. A. Eychmüller, A. Mews, H. Weller, *Chem. Phys. Lett.*, **208** (1), 59 (1993).

27. E. Lifshitz, H. Porteanu, I. D. Litvin and A.A. Lipovskii, *Chem. Phys. Lett.*, **295**, 249 (1998).

28. E. Lifshitz, I. Dag, I. Litvin, S. Hodes, G. Gorer, R. Reisfeld, M. Zelner and H. Minti, *Chem. Phys. Lett.*, **288**, 188 (1998).

29. I. Dag, E. Lifshitz, *J. Phys. Chem.*, **100**, (1996) 8962.

30. J. J. Hopfield and D. J. Tomas, *Phys. Rev. B*, **122**, 35 (1961).

31. A. Mews, A. V. Kadanovich, U. Banin, A. P. Alivisatos, *Phys. Rev. B*, **53** (20), 13242 (1996).

PHOTOLUMINESCENCE OF NANOCRYSTALLINE ZnO PARTICLES

A. van Dijken[a], E.A. Meulenkamp[b],
D. Vanmaekelbergh[a], A. Meijerink[a]

[a]Debye Institute, Utrecht University,
P.O. Box 80.000, 3508 TA Utrecht, The Netherlands
[b]Philips Research Laboratories Eindhoven,
Prof. Holstlaan 4, 5656 AA Eindhoven, The Netherlands

ABSTRACT

The optical properties of colloidal suspensions of nanocrystalline ZnO particles in 2-propanol were investigated. It was observed that, with increasing particle size, the quantum efficiency of the emission decreases. Study of the evolution of the luminescence properties during particle growth, combined with decay measurements, leads to more insight into the radiative processes that take place in ZnO particles after excitation. The characteristic blue-green emission band is probably due to the transition of a photogenerated electron from the conduction band to a deeper lying state. This interpretation can be corroborated by the fact that charging of the ZnO particles leads to a quenching of this particular emission.

INTRODUCTION

In the past decade nanocrystalline semiconductor particles have been the subject of extensive studies. In particular the sulfides (CdS and ZnS) and selenides (CdSe) have received considerable attention [1]. Less research has been devoted to nanocrystalline ZnO particles although its bulk properties are well known. Both bulk and nanocrystalline ZnO show two emission bands upon photoexcitation. The maximum of the first emission band coincides with the bandgap energy (exciton emission). The second emission band has its maximum at lower energy which means that electronic levels in the bandgap have to be involved in the recombination process (trap emission). In spite of numerous studies the origin of the trap emission is still not clear. For example, for bulk ZnO it has been shown that firing in an oxygen or hydrogen atmosphere quenches the trap emission [2, 3]. The interpretation of these results is complicated by the influence of the width of the depletion layer on the luminescence intensity [3].

In the present study crystalline ZnO particles with a mean diameter of about 50Å and smaller are investigated. These particles have a size similar to that of the exciton in ZnO (⌀~40Å) and depletion layer effects will not play a role. The aim of this work is twofold : first to study both the exciton and trap emission as a function of the particle size; second to examine the nature of the trap emission.

RESULTS AND DISCUSSION

A suspension of nanocrystalline ZnO particles in 2-propanol can be prepared by slowly adding 25 ml 0.02 M NaOH to 225 ml 0.001 M $Zn(CH_3COO)_2 \cdot 2H_2O$ [4]. A rapid formation of extremely small ZnO particles is followed by a relatively slow growth of the particles. The rate of particle growth is mainly determined by the temperature. For instance, at 65 °C the particles have reached their final size after two hours while at 0 °C the same process takes weeks to complete. This enables one to study nanocrystalline ZnO particles with different sizes by doing measurements at various times during the growth process. Fig. 1 shows a collection of emission spectra taken at different times during particle growth at room temperature. Two emission bands are clearly visible and their maxima shift to lower energies upon particle growth. The relatively narrow emission band at higher energies (UV) is due to band-band recombination (exciton emission), while the more intense broad emission band

in the visible part of the spectrum is assigned to trap emission. For the exciton emission the shift to higher energies for small particles is well known and is explained by quantum confinement [1,5]. The trap emission band is also at higher energies for the smaller particles. This will be discussed in more detail below. Decay measurements have shown that the lifetime of the exciton emission is at least more than two orders of magnitude shorter than the lifetime of the trap emission. As the intensity of the trap emission is much higher than that of the exciton emission, there must be a very fast - perhaps non-radiative - process that competes with the exciton emission process.

As the ZnO particles grow bigger, the intensity of the trap emission band decreases, while that of the exciton emission band increases. The intensity of the two emission bands as a function of particle size depends on changes in both the radiative and non-radiative recombination rates. The increase of the intensity of the exciton emission band with increasing particle size shows that the exciton recombination rate increases relative to the trap recombination rate and the non-radiative decay rate. The decrease of the trap emission intensity show that the opposite is true for the trap recombination rate. From Fig. 1, it is also clear that the total integrated emission intensity decreases upon particle growth. With a solution of Coumarin 153 as a reference, it is possible to determine quantum efficiencies. Using results that are available from the literature [5], one can determine the mean particle size from extrapolating the steep part of the absorption spectrum. Fig. 2 shows the quantum efficiences plotted versus the mean particle radius. While the absolute values of the quantum efficiencies depend on the preparation method, the decrease in quantum efficiency upon particle growth is always observed. The present results are in agreement with results obtained by Bhargava et al. [6] who observed an increase in the quantum efficiency of the Mn^{2+} emission in nanocrystalline $ZnS:Mn^{2+}$, which was explained by faster trapping of charge carriers in nanosized particles.

When the energy of the maximum of the trap emission band is plotted versus that of the maximum of the exciton emission band, at different stages during the particle growth as obtained from Fig. 1, there seems to exist a linear dependence (see Fig. 3). When these points are fitted by a straight line, a slope of 0.58 is obtained. A linear relation between the two emission maxima can be explained by a model as shown schematically in Fig. 4. The energetic position of the conduction band edge (e) is given by $E_e=E_{g,bulk} + C/m_e^*R^2$ and that of the valence band edge (h) by $E_h=-C/m_h^*R^2$, in which C is a constant, m_e^* and m_h^* the effective masses of the electron and hole

respectively (in units m_e), and R the radius of the particle. At very small particle sizes the increase in exciton binding energy due to enhanced Coulomb interaction ($\sim R^{-1}$) is negligible compared to the widening of the bandgap due to quantum confinement effects ($\sim R^{-2}$). The energetic position of the electron in the trap is assumed to be independent of particle size since it is determined by the local structure of the trap. The maximum of the exciton emission band as well as that of the trap emission band can be calculated as a function of R. Plotting the calculated maximum of the trap emission band versus that of the exciton emission band, gives a straight line for both models. The slope of this line however, is different for both cases. When the trap emission involves the edge of the conduction band (A), a slope of μ/m_e^* is calculated (μ is the reduced mass of the exciton, in units m_e). If the valence band plays a role (B), the calculated slope has the value μ/m_h^*. For ZnO, this means a slope of 0.64 for model A, and a slope of 0.36 for model B. The value predicted by model A is in fair agreement with the experimentally obtained value. This indicates that the sub-bandgap emission is due to the transition of a photogenerated electron from the conduction band to a deeper lying state.

Fig. 5 shows the results of decay measurements performed at the maximum of the trap emission band, both at an early stage of particle growth and on fully aged ZnO particles. It is clear that the decay curves consist of multiple μs-components. Bi-exponential fits gave good results. The decay time for the fastest component, which comprises more than 90% of the total signal, could be determined quite accurately. At early stages of particle growth, a decay time of 0.9 μs is obtained while the aged particles exhibit a decay time of 1.3 μs. Thus, as the ZnO particles grow bigger, the quantum efficiency of the trap emission decreases while the decay time increases.

A striking feature of the trap emission of nanocrystalline ZnO particles is the observation that it can be quenched by illumination with UV light, after the suspension has been saturated with an inert gas (e.g. nitrogen) [4]. This behaviour has been linked to the removal of oxygen from the system. First, bubbling with nitrogen removes the oxygen molecules from the suspension. At this point, the trap emission still has the same intensity as before. Illumination with UV light leads to a photodesorption of the oxygen molecules that are adsorbed on the particle surface and cannot be removed by simply bubbling with an inert gas [4]. When these adsorbed oxygen molecules are removed, the trap emission is quenched. To explain the quenching of the trap emission it has been proposed that trap filling occurs via adsorbed oxygen on the ZnO particle surface as an electron shuttle [4]. Removal of

adsorbed oxygen by UV illumination would thus quench the trap emission. In Fig. 6 the intensity of the trap emission is shown for an oxygen-free suspension of ZnO particles in 2-propanol. Initially, the emission intensity slowly decreases, which is due to the slow removal of chemisorbed oxygen under UV illumination. After a few minutes in the dark, the emission signal recovers to its initial value, but now the signal decreases rapidly under UV illumination. This observation is not in agreement with an electron shuttle mechanism via chemisorbed oxygen. In that case, there would be no difference in quenching rates after the emission signal has fully recovered. Also, the trap emission process most probably does not involve surface traps, as bulk ZnO exhibits the same characteristic emission.

Instead, we ascribe the quenching of the trap emission to the creation of excess electrons on the ZnO particles. In the absence of oxygen, which tends to trap electrons, the ZnO particles will be charged upon illumination as the holes can still be scavenged by the 2-propanol molecules. As a result, the Fermi level inside the semiconductor particle will be raised above the level of the trap involved in the emission process. For instance, it is known that in ZnO a positive monovalent oxygen vacancy ($V_O^{\bullet}$) gives a defect level that lies about 2 eV below the edge of the conduction band [7]. If the nanoparticles are charged with electrons, these centers will no longer exist as they are converted to $V_O^{\times}$ centers (neutral oxygen vacancies), whose position is about 0.05 eV below the conduction band [7]. If the $V_O^{\bullet}$ levels were involved in the trap emission process, this emission will be quenched when the particles are charged. For example, $V_O^{\bullet}$ centers could be involved in fast trapping of holes, forming $V_O^{\bullet\bullet}$ centers, followed by radiative recombination of a conduction band electron with the trapped hole, yielding a visible trap emission. The rate of the quenching process is dependent on the UV intensity and the ability of the solvent molecules to scavenge holes from the particles. Keeping the suspension in the dark for a period of time leads to a discharge of the particles. The influence of electron storage on the fluorescence properties of colloidal ZnO films has been investigated before [8], with observations similar to the ones described here.

It is clear that when the trap emission quenches, the intensity of the exciton emission increases. At the same time, the maxima of both emission bands shift (ΔE=0.03 eV). The trap emission band shifts to higher energy, while the exciton emission band does the opposite. Admission of oxygen restores the original situation. The slight shift of the emission bands upon UV illumination may be explained by assuming that only the trap emission from the larger particles in the suspension is

quenched. Consequently, the intensity of the exciton emission from the larger particles increases resulting in a shift of the maximum of the exciton emission band to lower energies. The remaining trap emission originates only from the smallest particles and therefore lies at a higher energy.

CONCLUSION

Emission and decay measurements were performed on suspensions of nanocrystalline ZnO particles with various sizes. Quantum efficiency measurements show an increase of the efficiency for smaller particles. At the same time the decay time of the trap emission decreases. Both the exciton and the trap emission band shift to higher energies with decreasing particle size. From the linear relationship (with a slope of 0.6) between the maxima of both emission bands, it can be derived that the trap emission probably involves the recombination of an electron with a deeply trapped hole. Finally, the quenching behaviour of the ZnO trap emission under UV illumination in an oxygen-free 2-propanol suspension is explained by a charging of the particles.

REFERENCES

[1] A. Henglein, Top. Curr. Chem., **143**, 113 (1988).

[2] T. Sekiguchi, N. Ohashi, Y. Terada, Jpn. J. Appl. Phys., **36**, L289 (1997).

[3] K. Vanheusden, W.L. Warren, C.H. Seager, D.R. Tallant, J.A. Voigt, B.E. Gnade, J. Appl. Phys., **79**, 7983 (1996).

[4] D.W. Bahnemann, C. Kormann, M.R. Hoffmann, J. Phys. Chem., **91**, 3789 (1987).

[5] M. Haase, H. Weller, A. Henglein, J. Phys. Chem., **92**, 482 (1988).

[6] R.N. Bhargava, D. Gallagher, X. Hong, A. Nurmikko, Phys. Rev. Lett., **72**, 416 (1994).

[7] F.A. Kröger, The Chemistry of Imperfect Crystals, North-Holland Publishing Company, Amsterdam 1964, First Edition, p. 691.

[8] P. Hoyer, H. Weller, J. Phys. Chem., **99**, 14096 (1995).

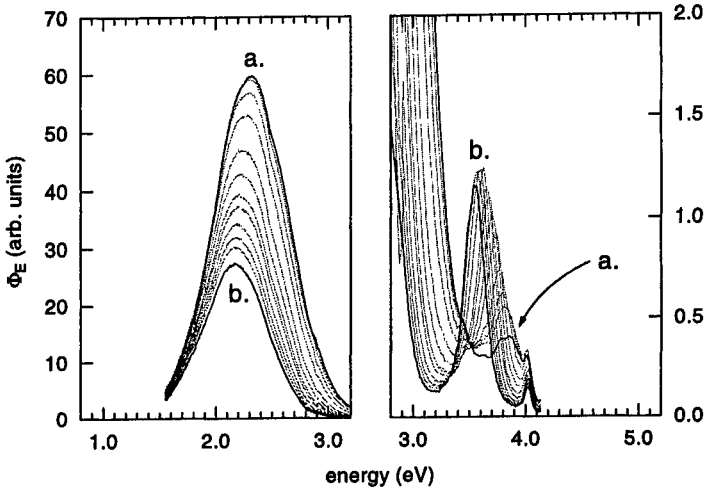


Figure 1 : Emission spectra of a suspension of ZnO particles in 2-propanol at different stages of the particle growth at room temperature. The first emission spectrum (a.) is taken after 15 min. and the last spectrum (b.) after 420 min. of particle growth. The spectra are taken at room temperature upon excitation with 4.45 eV.

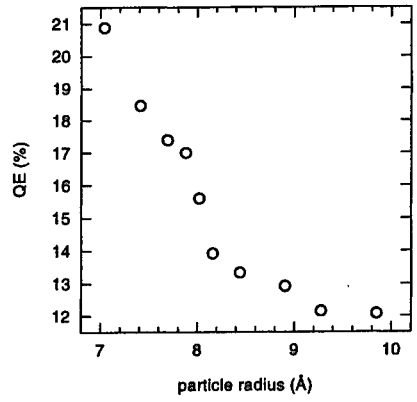


Figure 2 : Quantum efficiencies (relative to Coumarin 153) versus particle radius.

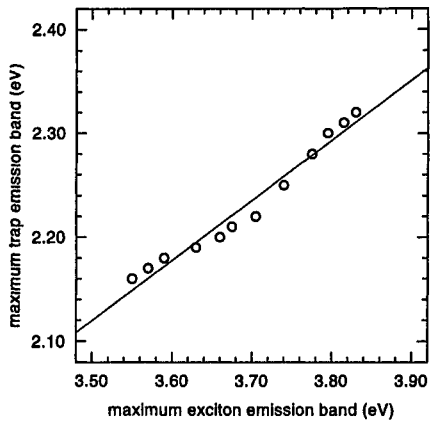


Figure 3 : The maxima of the trap emission band plotted versus the maxima of the exciton emission band, as obtained from the emission spectra from Fig. 1. The straight line is a linear fit to the experimental points.

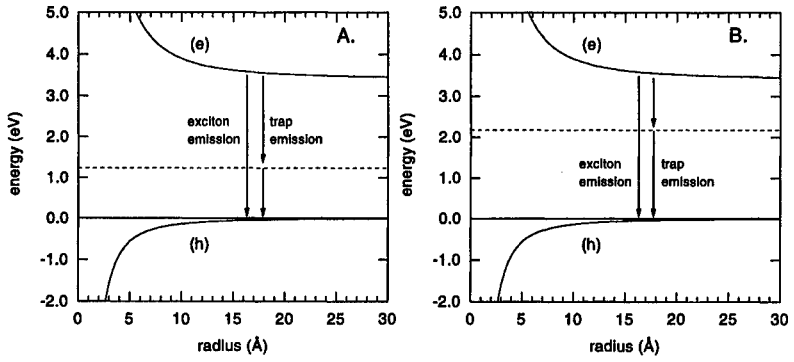


Figure 4 : Schematic pictures of two models that describe the origin of the trap emission band and the exciton emission band of nanocrystalline ZnO particles. It is assumed that the energetic position of a trapped charge carrier is independent of particle size (= dashed line). It is also assumed that the trap emission involves one of the band edges.

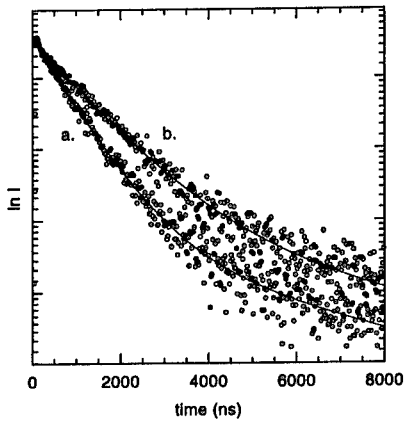


Figure 5 : Decay measurements performed on a suspension of ZnO particles at an early stage of particle growth (a) and on fully grown particles (b). The emission was monitored at the maximum of the trap emission band (a: 2.53 eV, b: 2.32 eV). Excitation took place with 4.03 eV from a pulsed XeCl excimer laser. The straight lines are bi-exponential fits to the data points.

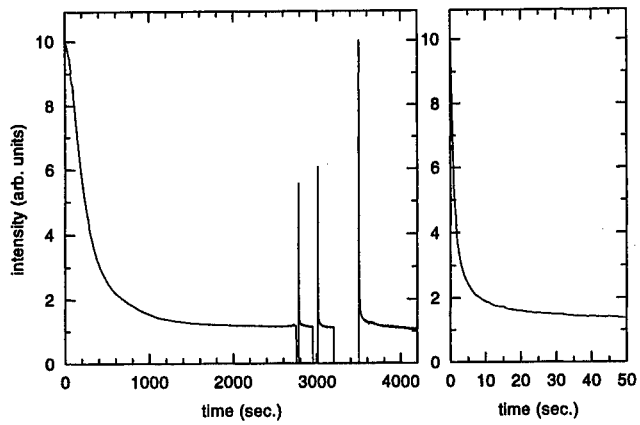


Figure 6 : Intensity of the trap emission of a suspension of nanocrystalline ZnO particles in 2-propanol during illumination with UV light. The suspension has first been saturated with nitrogen. The graph on the right shows the fast quenching of the trap emission in more detail.

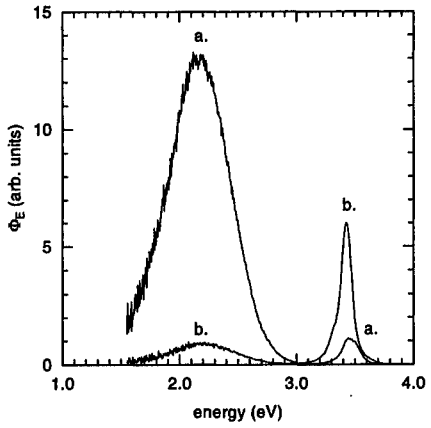


Figure 7 : Emission spectra of a suspension of nanocrystalline ZnO particles in 2-propanol upon excitiation with 4.96 eV (Φ_E is the photon flux per constant energy interval). Spectrum a was taken under normal conditions while for spectrum b the suspension was first saturated with nitrogen and illuminated with UV light.

PHOTO-INDUCED NANO-PATTERNS ON THE SURFACE OF C_{60} SINGLE CRYSTALS

Lei Jiang*, Yousoo Kim#, Tomokatsu Iyoda*, Jin Li#, Koichi Kitazawa#,
Akira Fujishima*,# Kazuhito Hashimoto*,##
*Kanagawa Academy of Science and Technology,
KAST Laboratory, 1583 Iiyama, Atsugi-shi, Kanagawa, Japan.
#Department of Applied Chemistry. Faculty of Engineering,
University of Tokyo, Hongo, Bunkyo-ku, Tokyo 113, Japan.
##Research Center for Advanced Science and Technology,
University of Tokyo, Komaba, Meguro-ku, Tokyo 153, Japan

ABSTRACT

Atomic force microscopy (AFM) studies have demonstrated that surface reconstructions on the (111) and (100) faces of C60 single crystal are generated and controlled by exciton band (1.6 ~ 2.2 eV) excitation. The surface reconstruction is a kind of partial dislocation, similar to that on inorganic materials. These photo-generated surface structures appear as different nano-patterns depending on light intensity and polarization as well as lattice symmetry, suggesting that the cooperative interaction between photon excitation process and anisotropic lattice symmetry of the surface molecules accounts for the surface reconstruction.

I. INTRODUCTION

Surface reconstructions have been widely studied on metals and semiconductors [1-4], since the creation of these structures is often accompanied with interesting physical phenomena. Generally, surface reconstructions are attributed to the lack of symmetry of surface atoms in comparison with bulk atoms. In a certain parameter range the reconstructed surface structures are usually minimal in energy and appear to be metastable structures, e.g., they have been generated by thermal treatment [1,2], electrochemical potential [3], and the presence of adsorbates [4]. Here, we report the first example of photo-induced surface reconstruction, which was observed on the (111) and (100) faces of C_{60} single crystals by using an atomic force microscopy (AFM). These photo-induced structures appear as different nano-patterns depending

on light intensity and polarization as well as lattice symmetry, suggesting that the cooperative interaction between photon excitation process and anisotropic lattice symmetry of the surface molecules accounts for the reconstruction.

Our strategy for exploring photo-induced surface reconstruction system is as the following two-fold: (I) To search a metastable surface phase in which the energy difference between the metastable phase and stable phase is relatively small. This may allow the existence of the metastable phase or coexistence of the two phases on the surface. (II) To select the excitation within the Urbach-Martiensen (U-M) tail of the lowest exciton absorption band, where strong electron-lattice coupling is expected [5,6]. For a suitable system, the exciton-lattice coupling constant (g) should be greater than 1 [6]. These prerequisites are met in the case of C_{60}. It has been reported that C_{60} may condense into both face-centered cubic (fcc) and hexagonal-close-packed (hcp) phases at room temperature [7]. The hcp phase is a metastable one, and the cohesive-energy difference between hcp phase and fcc phase is as small as ΔE=0.9 kcal/mol [7] and surface reconstruction (coexistence of the two phases) has been observed on C_{60} thin films [8,9]. The UV-visible absorption spectrum of solid C_{60} shows a band gap at 2.3 eV, and a U-M tail in the range of 2.0 ~ 1.6 eV [10] corresponding to Frenkel exciton band [11]. Furthermore, the g factor is reported to be 3.7 [12] which is much larger than those of the other typical molecular systems [6]. Therefore, C_{60} single crystal is a good candidate for the demonstration of photo-induced surface reconstruction.

II. Experimental

The laser beam incident perpendicularly to the crystal surface. Light intensity was controlled by applying neutral density filters or adjusting the size of the laser beam. For the observations of photo-induced surface reconstruction, a commercial AFM setup was used (Seiko SPA3700 instrument) under ambient conditions. All the images shown in the present work were obtained in constant height mode, while precise height information was obtained from simultaneous constant force mode images. A triangular-shaped Si_3N_4 cantilever with a spring constant of 0.02 N/m was used to acquire images in contact mode. The applied force was typically 0.1 nN.

III. RESULTS

A semiconductor laser with photon energy of 1.85 eV and power of 50 μW was used as the light source to excite the exciton band in the range of 2.0 ~ 1.6 eV. High quality fcc single crystals were prepared via a vapor transport technique [13]. As-grown crystals with large (111) and (100) surfaces were imaged by AFM. Figure 1a shows an AFM image of the (111) surface of C_{60} crystal before illumination. The surface consists of multilayer steps and molecularly flat terraces. After illumination (1.1×10^4 photons/nm^2·s), arrays of dislocation line (DL) were observed along the three equivalent [112] directions creating a reconstructed surface (Fig. 1b). DLs in the

three equivalent [112] directions cross each other forming triangular nano-patterns. These DLs are typical partial dislocation [14] corresponding to one dimensional domain walls between fcc and hcp stacking regions. In the dislocation region, the molecules occupy bridge site instead of hollow site of the lower layer molecules (as shown in Fig. 2a) and look higher in the AFM image. The nearest-neighbor distance between parallel DLs is in the range of 90~110 nm and the corrugation difference of the DLs is about 0.3 nm. Similar structures were also observed on surface of C_{60} thin films [8,9] and C_{70} single crystal [15]. In the lower right part of the image (represented by "S"), which was in the shadow of the AFM tip and cantilever, no reconstruction appeared. The clear boundary between the reconstructed and unreconstructed areas suggests that reconstruction is not created via a thermal process, but via a photo-induced process. This is further confirmed by the calculation of photo-induced temperature increase which is only 10-15 K under the present illumination conditions and experimental result that the reconstruction can not be generated when the sample temperature is higher than 90 °C. To eliminate the possibility of adsorbate induced effect [4], we also illuminated the surface under ultra high vacuum (UHV) condition (3×10^{-10} Torr), and observed the same phenomena. On the other hand, the reconstructed surface structure disappeared after heating the crystal under N_2 atmosphere (in absence of O_2) at about 300 °C. This implies that the reconstructed surface is a metastable state and can be relaxed thermally.

Remarkably, surface reconstruction does not depend on the light intensity linearly. Fig. 3 represent plot of the density of the DL as a function of incident light intensity. It is apparent that surface reconstruction is initiated at a threshold light intensity value of ca. 3.6×10^3 photons/nm^2·s , maximizing at a value of ca. 1×10^4 photons/nm^2·s. Thereafter, DL density decreases with increasing light intensity. This is probably due to a near surface reconstruction which may occur in several layers at these higher light intensities.

Furthermore, we illuminated the C_{60} single crystal surface at different photon energies with normalized light intensity. The results are summarized as following: (I) under super-band gap (2.3 eV) illumination with photon energy of 3.81 eV, 2.78 eV or 2.41 eV, cracked surfaces were generated which were reported to be due to a photochemical reaction [16], and (II) under sub-band gap (Frenkel-exciton) illumination with photon energy of 1.96 eV or 1.85 eV, reconstructed surfaces were generated. IR and Raman measurements of the C_{60} thin films show no spectroscopic change after the illumination and indicating that no photochemical reactions occur with photon energy of either 1.96 eV or 1.85 eV [17]. It is considered from these observations that excitation of the Frenkel exciton is responsible for photo-induced surface reconstruction on C_{60} single crystal.

Upon photon absorption in the 1.6 ~ 2.2 eV range, Frenkel excitons are generated from a strong exciton-lattice coupling effect ($g = 3.7$) in solid C_{60} [12]. These excitons are found hopping between the nearest neighbor molecules [18], i. e., anisotropic hopping along the three equivalent [110] directions on the (111) surface or two equivalent [011] directions on (100) face. The electron-lattice coupling occurs during the exciton relaxation, such as self-trapping and annihilation process [10]. Considering

the situation of resonance vibronic coupling [19,20] at higher light intensity, collective molecular displacement is induced on the surface of the crystal which results in a large scale surface molecular rearrangement. In a highly ordered system the collective displacement of the molecules are confined in specific directions according to the lattice symmetry [14]. On the (111) surface, the collective displacement is along the three equivalent [110] directions (top of Fig. 4a), therefore the DLs are created in perpendicular [112] directions forming a triangular pattern (Fig. 4a). On the (100) surface, the collective displacement is along two equivalent [011] directions (top of Fig. 4b) and may generate the DLs in perpendicular [011] directions. Accordingly, we can also predict a cubic nano-pattern on the (100) face of the crystal. The experimental result indeed shows the cubic nano-pattern on the (100) face of single crystal (Fig. 4b). These observations indicate that under unpolarized light illumination the DLs appear in all possible symmetric directions of the crystal lattice.

Considering the general interaction of a photon with a molecule, the major force operating on the electrons in consequence of a passing light wave is due to the undulating electric field. Additionally, the direction of photo-induced dipole is always parallel to the direction of the electric field [21]. Therefore, the orientation of the DLs is expected to be controlled by linear polarized light. We used polarized light with the electric field parallel to one of the [110] direction to illuminate the (111) surface. After illumination (Fig. 4c), the DLs are oriented in only one [112] direction which is perpendicular to the direction of the electric field indicating a collective molecular displacement along the [110] direction (top of Fig. 4c). In this case, the excitons hopping mainly occur in this [110] direction, resulting in a stronger lattice vibration along this direction. Likewise, the DL arrays were also generated in the other [112] directions by turning light polarization direction in a perpendicular [110] direction. It should be noted that the present photo-induced reconstruction is different from pulsed laser induced periodic damage structure on inorganic materials in which periodic arrays were also generated in a perpendicular direction of the light polarization [22]. The latter has no relation with the surface lattice symmetry of the crystals.

IV. CONCLUSIONS

Above all, a C_{60} single crystal was used as an ideal model to demonstrate a photo-induced surface reconstruction. Both lattice symmetry and light polarization dependent reconstruction effects suggest that the surface reconstruction is due to the cooperative interaction between the photo-induced collective molecular displacement and the anisotropic lattice structure of the crystals. Moreover, photo-induced surface reconstruction can be understood as a general phenomenon and may occur on a wide variety of molecular crystals, e.g., by using the same strategy, we have recently realized photoinduced phase transition on the surface of anthracene single crystals.

ACKNOWLEDGEMENT

The authors thank Drs. R. Wang and P. Sawunyama for inspiring discussions. We

would also like to thank Dr. Yamaguchi for the help of UHV measurements.

References

[1] For example, K. Takayanagi, Y. Tanishiro, K. Yagi, K. Kobayashi, G. Honjo, Surf. Sci. 1988, 205, 637-651. and the reference therein.

[2] J.V. Barth H. Brune, G. Ertl, R. Behm, J. Phys. Rev. 1990, B42, 9307-9318.

[3] A.S. Dakkouri, Solid State Ionics, 1997, 94, 99-114, and the reference therein.

[4] S. Titmuss, A. Wander, D.A. King, Chem. Rev. 1996, 96, 1291-1305,

[5] H. Sumi, Y. Toyzawa, J. Phys. Soc. Japan 1971, 31, 342-358.

[6] K. Mizuno, A. Matsui, G. J. Sloan, Chem. Phys. 1989, 131, 423-433.

[7] Y. Guo, N. Karasawa, III.W.A. Goddard, Nature 1991, 351, 464-467.

[8] W. Krakow, N.M. Rivera, R.A. Roy, R.S. Ruoff, J.J. Cuomo. J. Mater. Res. 1992, 7, 784-787.

[9] Y. Kim, L. Jiang, T. Iyoda, K. Hashimoto, A. Fujishima, Surf. Sci. 1997, 385, L945-L951.

[10] D. Sarkar, N. J. Halas, Solid State Commun. 1994, 90, 261-265 and the reference therein.

[11] R.W. Lof, M.A. van Veenendaal, B. Koopmans, H.T. Jonkman, G.A. Sawatzky, Phys. Rev. Lett. 1992, 68, 3924-3927.

[12] K.C. Chiu, J.S. Wang, C.Y. Lin, J. Appl. Phys. 1996, 79, 1784-1787.

[13] J. Li, T. Mitsuki, M. Ozawa, H. Horiuchi, K. Kitazawa, Y. Achiba, J. Crystal Growth 1994, 143, 58-65.

[14] J.P. Hirth, J. Lothe, Theory of dislocations, Edited 2nd (Wiley, New York, 1982).

[15] L. Jiang, T. Iyoda, N. Kino, K. Kitazawa, K. Hashimoto, A. Fujishima, Surf. Sci. 1996, 349, L101-L106.

[16] M. Haluska, H. Kuzmany, M. Vybornov, P. Rogl, P. Fejdi, Appl. Phys. 1993,A56,161-167.

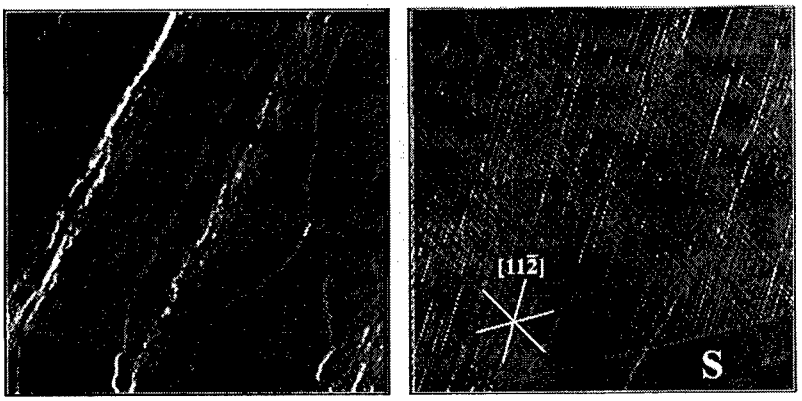
[17] Y. Kim, L. Jiang, T. Iyoda, T. Araki, K. Hashimoto, A. Fujishima, To be submited to J. Phys. Chem.
[18] A.M. Janner, R. Eder, H.T. Koopmans, H.T. Jonkman, G.A. Sawatzky, Phys. Rev. 1995, B52, 17158-17164.

[19] W.T. Simpson, D.L. Peterson, J. Chem. Phys. 1957, 26, 588-593.

[20] D. Fox, S. Yatsiv, Phys. Rev. 1957, 108, 938-945.

[21] N.J. Turro, Modern Molecular Photochemistry, 1978, 76.

[22] J. F. Young, J. S. Preston, H. M. van Driel, J. E. Sipe, Phys. Rev. 1983, B27, 1155-1172.



(a) (b)

Figure 1: AFM images (10 μm x 10 μm) of the C_{60} (111) surface (a) before and (b) after laser illumination for I hr. The nearest-neighbor distance between parallel DLs is in the range of 90~110 nm and the corrugation difference of the DLs is about 0.3 nm.

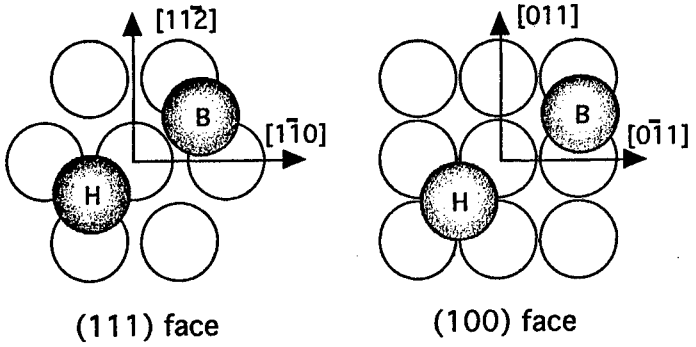


Figure 2 : Plane view of the (111) and (100) face of C_{60} single crystal showing the definition of azimuthal directions and bridge site (labeled as B) and hollow site (labeled as H) on these faces. Filled circles represent the top layer molecules.

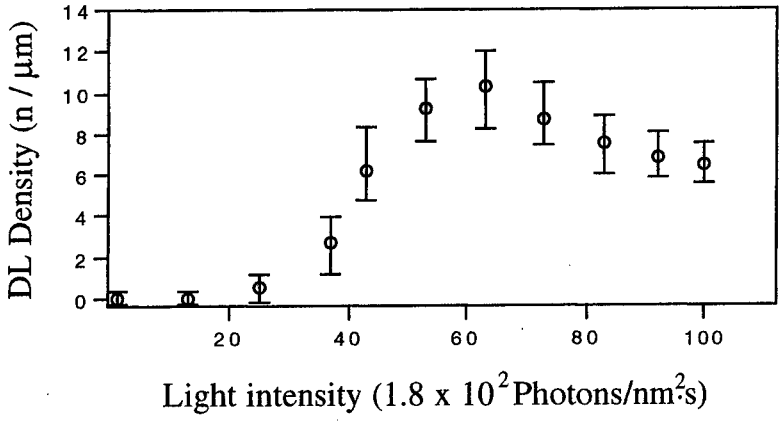


Fig. 3 The light intensity dependence of the number of DL density (n/μm) in [110] direction on the (111) face of C_{60} single crystal. Illumination time was 1 hour at every data point.

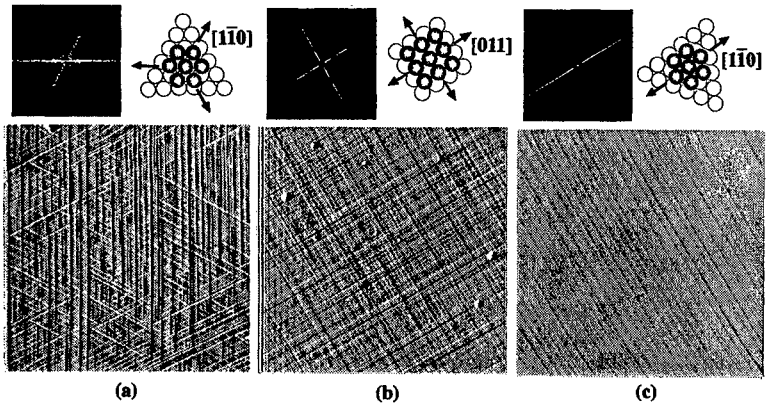


Figure 4 : AFM image of (a) the triangular and (b) cubic nano-patterns which were generated by using unpolarized light (1 hour illumination with the intensity of 1.8 x 10^4 photons/nm^2·s) on the (111) face and (100) face of C_{60} single crystal, respectively. (c) The dislocation array was generated in one of the individual [110] directions by illuminating with linear polarized light (1 hour illumination with the intensity of 1.5 x 10^4 photons/nm^2·s) on the (111) face of the C_{60} single crystal. The scales of images are 10 μm x 10 μm, respectively. On top of the images, fast Fourier tansform (FFT) and two layer molecular models of the collective molecular displacement under different conditions are shown. In molecular models, the top layer molecules are represented by filled circles. The collective molecular displacement directions of the top layer molecules are indicated by the arrows, which are just parallel to the FFT patterns.

PHOTORESPONSE OF SPRAY- PYROLYTICALLY SYNTHESIZED NANOCRYSTALLINE n-Fe_2O_3 THIN FILM ELECTRODES TOWARDS THE WATER-SPLITTING REACTION

by

Shahed U. M. Khan and Jun Akikusa
Department of Chemistry and Biochemistry
Duquesne University
Pittsburgh, PA 15282

ABSTRACT

Semiconducting nanocrystalline thin films of n-Fe_2O_3 were synthesized by spray-pyrolytic method and their photoresponse towards water-splitting reaction was studied. The photoresponse of these films was found to depend on the spray time, substrate temperature, solvent composition in the spray solution and as well as on the concentration of the spray solution. The maximum photocurrent density of 3.7 mA cm^{-2} at 0.7 V/SCE was obtained at the n-Fe_2O_3 film synthesized using the optimum condition of substrate temperature of 350°C, the spray time of 60 sec and the spray solution of 0.11 M $FeCl_3$ in 100% ethanol. The bandgap energy of this film was found to be 2.05 eV. The flatband potential of –0.74 V/SCE and the donor density of 2.2 x 10^{20} cm^{-3} was found from the Mott-Schottky plots at the AC frequency of 1000 Hz. The n-Fe_2O_3 films synthesized using the optimum conditions gave rise to a conversion efficiency of 4.7 % and a practical conversion efficiency of 1.8 % at an applied potential of 0.2 V/SCE at pH 14.

INTRODUCTION

As a photoelectrode, n-Fe_2O_3 has an advantage of having small bandgap energy of about 2.0 eV which corresponds to the wavelength of 620 nm (1, 2) and as a result it can absorb most of photons of AM 1 illumination. n-Fe_2O_3 is naturally abundant in the earth's crust. n-Fe_2O_3 films were investigated by several researchers (1-8). For example, n-Fe_2O_3 films were synthesized by sputtering method (4), and by pressing powders of Fe_2O_3 (5-7). The n-Fe_2O_3 films were also synthesized using the spray pyrolysis method (1, 2) on a conducting SnO_2 coated glass substrate. Although the photoresponse of n-Fe_2O_3 towards water splitting to hydrogen and oxygen gases was improved by doping with iodine (2), the

optimum reaction conditions of the spray-pyrolytic synthesis of n-Fe_2O_3 films have not been investigated.

In this work we focused on the optimization of spray-pyrolytic synthesis of nanocrystalline n-Fe_2O_3 films in terms of spray-time, solvent composition in the spray-solution, concentration of the spray-solution and the substrate temperature for the efficient photoelectrochemical splitting of water. Various physical properties such as quantum efficiency, flatband potential, bandgap energy and the doping density of such nanocrystalline films were also determined. .

EXPERIMENTAL

Synthesis of n-Fe_2O_3 Thin Films by Spray-Pyrolysis:

An n-Fe_2O_3 Photoanode was prepared by the spray-pyrolysis method and it was described in detail in the earlier reports (9-12). Tin oxide glass sheet (60 Ω cm^2, 1/8 inch thickness pyrex glass, Swift Glass Company, NY) was used as a substrate for the spray-pyrolytic deposition of nanocrystalline n-Fe_2O_3 thin films.

A small area of the tin oxide glass was covered by aluminum foil to prevent the deposition of n-Fe_2O_3 so that this area can be used for the electrical contact. An area of 1.0 cm^2 of tin oxide surface was exposed to the spray solution of $FeCl_3.6H_2O$ in ethanol. The concentration of spray-solution of $FeCl_3.6H_2O$ was varied from 0 .01 M to 0.11 M and the temperature of the substrate on the hot plate were changed from 310 to 410°C for the spray-pyrolytic synthesis of n-Fe_2O_3 films. The duration of each spray was 10 sec with a 5 min interval to maintain a constant substrate temperature. The electrical contact was made by connecting the uncoated area of the tin oxide surface with an alligator clip connector.

Photoelectrochemical Measurerments:

The photoelectrochemical measurements were performed in a glass cell having a flat pyrex glass window to facilitate the transmittance of light to the photelectrode surface. The three-electrode glass cell was used for the photoelectrochemical measurements. The working iron oxide thin film had a surface area of 1.0 cm^2, while a Pt wire and Ag/AgCl electrodes were used as the counter and the reference electrodes respectively. A constant intensity of 50.0 watt cm^{-2} of light from the Xenon lamp (Kratos Model LH 150/1) was maintained taking into account of the loss through the pyrex glass window. The intensity of light was measured with a digital radiometer (model IL 1350). A monochromator (kratos model GM 100) was used to generate the light of a particular wavelength. The

electrolyte solution used for the water-splitting reaction was 1.0 M NaOH. A scanning potentiostat (EG & G Princeton Applied Research, Model 362) was used for the measurement of photocurrent under an applied potential. The Photocurrent - potential dependence was recorded on an X-Y recorder, Houston Model RE 0092. A Keithley multimeter was also used to monitor the photocurrent.

AC Impedance Measurements:

The AC impedance of n-Fe_2O_3 films was measured using an EG & G Two-Phase Lock in Analyzer Model 5208 equipped with EG & G potentiostat/ Galvanostat Model 273. These instruments were computer controlled by EG & G software model 378 that automatically adjusted the phase angle during each measurement. AC amplitude of 10 mV was used for all the measurements. A Pt mesh electrode was used as the counter electrode and the n-Fe_2O_3 films were used as the working electrode. These measurements were carried out in the dark at 1.0 M NaOH solution.

The capacitance, C was calculated using the following expression of impedance, Z, for a series capacitor- resistor model

$$Z = Z' + iZ'' \qquad (1)$$

where Z′ is the real part of the impedance and Z″ is the imaginary part of the impedance from which the capacitance, C can be obtained using $Z'' = -i/\omega C$, with $\omega = 2\pi f$, $i = (-1)^{1/2}$, and f is the AC frequency in Hertz.

RESULTS AND DISCUSSION

Photocurrent Density - Applied Potential Dependence:

Fig. 1 shows the dependence of photocurrent density on the applied potential at spray-pyrolytically synthesized n-Fe_2O_3 films. A highest photocurrent density of 3.7 mA cm^{-2} at 0.7 V/SCE was observed at the n-Fe_2O_3 film synthesized using 60 sec spray-time at the substrate temperature of 310°C. Fig. 1 also includes the results of photocurrent density at n-Fe_2O_3 synthesized earlier (2) by spray-pyrolysis method including iodine in the spray-solution which consisted of 80% EtOH and 20% of 1.0 M HCl in 0.1 M $FeCl_3$ solution..

It is important to note that the n-Fe_2O_3 films synthesized in the present work gave rise to a much higher photoresponse compared to those of earlier studies (1, 2). Furthermore, the n-Fe_2O_3 films synthesized in this work showed a higher photoresponse compared to

those prepared by the compression of n-Fe_2O_3 powder or by the thermal oxidation of iron metal sheets (18-20).

Effect of Solvent Composition in the Spray Solution:

In order to improve the photoresponse of n-Fe_2O_3 films the solvent composition in the spray solution was varied. Fig. 2 shows the dependence of the photocurrent density on the solvent composition in the spray-solution at an applied potential of 0.6 V/SCE. A moderate dependence of the photocurrent density on the composition of the solvent was observed, and the highest photoresponse was found when the solvent in the spray solution was 100 % EtOH.

The difference of the photoresponse on the solvent composition in the spray solution can be attributed to the difference in the heat of vaporization; ΔH_{vap} which is 35.21 kJ/mol for MeOH and 38.36 kJ/mol for EtOH (13). We also observed that the use of HCl acid in the spray solution decreased the photoresponse to a considerable extent.

Effect of Concentration of the Spray Solution:

The effect of concentration of the spray solution on the photocurrent density is plotted in Fig. 3. The maximum photocurrent density was observed when the concentration of spray solution was 0.11 M $FeCl_3$ in 100% ethanol. This result indicates that at low concentration of spray-solution the thickness of the iron oxide film becomes too thin to absorb enough light and consequently photocurrent decreases. At high concentration of spray solution the films become thick enough to have higher resistance and as a result photocurrent also decreases.

The effect of Substrate Temperature:

The substrate temperature for the spray-pyrolytic deposition is dependent on the semiconductor material. The dependence of photocurrent density on substrate temperature during the spray-pyrolytic deposition of n-Fe_2O_3 thin film is shown in Fig. 4. It is observed that the photocurrent density becomes limiting when the substrate temperature is about 370°C. It also shows that with the decrease of substrate temperature, the photoresponse of n-Fe_2O_3 decreases remarkably. This can be attributed to the fact that at low substrate temperature the quality of the nanocrystals became poor by producing dislocations and kink sites. These dislocations and kink sites act as the recombination centers for the photogenerated electron-hole pairs and consequently reduce the photoresponse of these films.

Reproducibility of Spray-Pyrolytic Synthesis of n-Fe_2O_3 Thin Films:

It is important to test the reproducibility of the synthesis of n-Fe_2O_3 thin films by spray-pyrolysis method. The reproducibility was tested for the n-Fe_2O_3 films synthesized at optimum substrate temperature of 370°C for 60 sec using the spray-solution of 0.11 M $FeCl_3$ in 100% ethanol.

Fig. 5 shows the photocurrent (j_p) - potential (E) dependence of several n-Fe_2O_3 films prepared at the optimum synthesis condition as mentioned above. It is observed that the open circuit potential did not change and stayed at -0.45 V/SCE ± 0.03 V. The magnitude of the photocurrent density was affected especially at the middle of the S-curve and less affected near 0.60 V/SCE. The average photocurrent density of 3.06 mA cm^{-2} (3.0, 3.0, 3.1, 3.15 mA cm^{-2}) was found at 0.6 V/SCE for these samples. These data correspond to a standard deviation, σ of 0.065 mA cm^{-2} which indicates a good reproducibility of the spray-pyrolytically synthesized n-Fe_2O_3 films in this work.

Onset Potential from j_p^2 – Potential (E) Plots:

. Fig. 6 shows j_p^2 – potential (E) dependence of n-Fe_2O_3 films. A straight line was observed with an intercept at 0.0 V/SCE. This potential of 0.0 V/SCE represents the onset potential for the generation of photocurrent density in the milli amperes range in 1.0 M NaOH electrolyte solution of pH 14.

Quantum Efficiency:

The quantum efficiency under monochromatic light illumination, $\eta(\lambda)$ was calculated using the following relation (22),

$$\eta(\lambda) = j_p(\lambda) / e_o I_o(\lambda) \qquad (2)$$

where $j_p(\lambda)$ is monochromatic photocurrent density, e_o is electronic charge, and $I_o(\lambda)$ is the flux of incident photon at wavelength, λ.

The quantum efficiency of n-Fe_2O_3 films was calculated using Eq. (2), and the results are shown in Fig. 7. The quantum efficiency starts to increase near 600 nm having energy of 2.07 eV. The maximum quantum efficiency of 22.5 % was obtained at 370 nm. This value of low quantum efficiency indicates higher recombination of photo-generated holes in the n-Fe_2O_3 film prior to reaction with the OH^- in the electrolyte solution.

Bandgap Energy:

The bandgap of semiconducting TiO_2 films can be determined using the following equation (23-24),

$$\eta(\lambda)h\nu = A(h\nu - E_g)^n \qquad (3)$$

where A is a constant, n equals either 0.5 for allowed direct transition or 2 for allowed indirect transitions. The allowed direct transition of an electron from the valence band to the conduction band by light energy, hν is not phonon assisted since such a transition does not need any change in momentum (momentum is conserved). For the indirect bandgap the transition of an electron is phonon assisted since such a transition involves change in both energy and momentum. In the case of the indirect transition, momentum is conserved via a phonon interaction, because light photons cannot provide a change in momentum (24). Furthermore, Eq. (3) is most appropriate to use when the applied potential is far from the flatband potential, so that the transport of photogenerated carriers inside the semiconductor becomes the rate determining step (25).

The bandgap of n-Fe_2O_3 film was determined using Eq. (3). Fig. 8 shows the plot of $(\eta h\nu)^{1/2}$ versus hν. A straight line was observed and an intercept was obtained at 2.05 eV which corresponds to the bandgap energy of the n-Fe_2O_3 film. Several values of optically measured bandgap of n-Fe_2O_3 were reported, such as 2.3 eV (1) and 1.97 eV (2). The bandgap of 2.05 eV is close to earlier reported of 2.10 eV which was determined from the constants of ionization energy and the electron affinity (26).

Flatband Potential from Mott-Schottky plots:

It is well known that the flatband potential (E_{fb}) of a semiconductor can be obtained from the intercept of Mott-Schottky plot using the relation,

$$1/C^2 = (2/e_o\varepsilon\varepsilon_o N_d)(E_{app} - E_{fb} - kT/e_o) \qquad (4)$$

where ε is the dielectric constant of the semiconductor, ε_o is the permitivity of the vacuum, N_d is the donor density, E_{app} is the applied potential and kT/e_o is the temperature dependent term in the Mott-Schottky equation.

Fig. 9 shows the Mott-Schottky plot for the n-Fe_2O_3 film at various AC frequencies in the electrolyte solution of 1.0 M NaOH in the dark. In Fig. 9 straight lines are observed at all the AC frequencies used for the measurement of impedance.

For n-Fe_2O_3, film a single intercept was obtained at -0.71 V/SCE for the AC frequencies between 100 Hz and 1000 Hz giving a flatband potential of -0.74 V/SCE which included the kT/e_o term. However, at higher AC frequencies of 2500 Hz and 5000 Hz, the flatband potentials shifted to -0.82 V/SCE and -0.92 V/SCE respectively (see Table 1.).

Effect of pH of the Electrolyte Solution on Flatband Potential:

Fig. 10 shows the Mott-Schottky plots for the n-Fe_2O_3 films in two electrolyte solutions, one having pH = 0 (0.5 M H_2SO_4) and another having pH = 14 (1.0 M NaOH). The AC frequency of 1000 Hz was used for the measurement of impedance. A parallel shift of the plot toward positive potential was observed without any change in the slopes when the pH was changed from 14.0 to 0.0. The intercept of the lines in 0.5 M H_2SO_4 and 1 M NaOH were found to be at 0.18 V/SCE and at – 0.70 V/SCE respectively. This potential shift (ΔE) of –0.88 V corresponds approximately to change of potential by -0.06 V per pH.

Donor Density in n-Fe_2O_3 Films:

The donor density in n-Fe_2O_3 films was determined from the slope of the Mott-Schottky plot in Fig. 9. Dielectric constant of n-Fe_2O_3 film was used as 12 (13). Since the slopes of these plots changed with the AC frequency, the donor density also changed. Table 1 shows that the AC frequency dependence of the donor density of n-Fe_2O_3 was relatively small giving a donor density range from 1.6×10^{20} cm^{-3} to 3.6×10^{20} cm^{-3} in the frequency range between 100 Hz and 5000 Hz. The donor density at the AC frequency of 1000 Hz was found to be 2.2×10^{20} cm^{-3}. For a comparison, the donor density of n-Fe_2O_3 prepared by the compression of Fe_2O_3 powder with subsequent sintering was reported earlier to be 7×10^{19} cm^{-3} measured at AC frequency of 1000 Hz (27).

Conversion Efficiency

The conversion efficiency of light and electrical energy to chemical energy at a semiconductor photoelectrode in the presence of an external applied potential under illumination can be expressed as (1),

$$\% \varepsilon_{eff} = [(\text{power output})/(\text{total power input})] \times 100$$

$$= [(j_p E^{\circ}_{rev})/(I_o + j_p E_{app})] \times 100 \quad (5)$$

where

$$\text{total power input} = (\text{light power input} + \text{electrical power input})$$
$$= (I_o + j_p E_{app}) \quad (6)$$

j_p is the photocurrent density which corresponds to the rate of photo-assisted water-splitting reaction, E°_{rev} is the standard reversible potential which is 1.23 V/NHE for the water splitting reaction at pH = 0, I_o is the light intensity in mW cm^{-2} (25) and E_{app} is the appplied potential at the semiconducting n-Fe_2O_3 electrode. Using I_o = 50 mW cm^{-2} and j_p = 2.0 mA cm^{-2} at E_{app} = 0.2 V/SCE at pH = 14 (which is equal to1.27 V/NHE at pH = 0) in eq. 5 the conversion efficiency was found to be 4.7 %.

However, the practical conversion efficiency of light energy to chemical energy in the presence of an applied potential can be expressed as (28),

$$\% \varepsilon_{eff}(\text{practical}) = [(\text{power output} - \text{electrical power input})/(\text{total power input})] \times 100$$

$$= [j_p(E_{onset} - E_{app})/(I_o + j_p E_{app})] \times 100 \qquad (7)$$

where $E_{onset} = (E^{\circ}_{rev} + E_{overvoltage})$ is the practical onset potential needed to split water which includes the overvoltage, $E_{overvoltage}$ for the water-splitting at a Pt electrode.

Using I_o = 50 mW cm^{-2}, j_p = 2.0 mA cm^{-2} at an applied potential, E_{app} = 0.2 V/SCE at pH 14 (= 1.27 V/NHE at pH 0.0) and E_{onset} = 1.73 V/NHE (for $E_{overvoltage}$ = 0.5 V/NHE) in Eq. 7, the practical conversion efficiency was found to be 1.8 %.

In conclusion, it should be pointed out that the spray-pyrolytically synthesized nanocrystalline iron oxide thin films of optimum thickness, crystal structure and doping density can serve as an inexpensive and stable photoanode for the efficient photo-assisted water-splitting reaction.

REFERENCES

1. S. A. Majumder, and S. U. M. Khan, *Int. J. Hydrogen Energy*, **19**, 881 (1994).
2. S. U. M. Khan, and Z. Y. Zhou, *J. Electroanal. Chem.*, **357**, 407 (1993).
3. V. Battaglia, J. Newman,*J. Electrochem. Soc.* ,**142**, 1423 (1995).
4. S. Virtanen, P. Schmuki, H. Böhni, P. Vuoristo, T. Mäntylä, *J. Electrochem. Soc.* ,**142**, 3067 (1995).
5. P. Schmuki, M. Büchler, S. Virtanen, H. Böhni, R. Muller, L. J. Gauckler, *J. Electrochem. Soc.* ,**142**, 3336 (1995).
6 K. G. McGregor, M. Calvin, J. W. Otvos, *J. Appl. Phys.*, **50**, 369 (1979).
7. M. M. Khader, N. N. Lichtin, G. H. Vurens, M. Salmeron, G. A. Somorjai, *Langmuir*, **3**, 303 (1987).
8 N. S. McAlpine, R. A. Fredlein, *J. Electroanal. Chem.*, **272**, 101 (1989).

9. K. L. Chopra, R. C. Kainthla, D. K. Pandya, and A. P. Thakoor, *Physics of Thin Films*, **12**, 165 (1982).
10 E. Shanthi, A. Banerjee, and K. L. Chopra, *Thin Solid, Films*, **88**, 93 (1982).
11. E. Shanthi, V. Dutta, A. Banerjee, and K. L. Chopra, *J. Appl. Phys.*, **51**, 6243 (1981).
12 J. Kane, H. P. Schweizer, And W. Kern, *J. Electrochem. Soc.*, **123**, 270 (1976).
13. D. R. Lide, Editor-in-Chief, Handbook of Chemistry and Physics, 74th Edition, CRC Press, (1994).
14. H. H. Kung, H. S. Jarrett, A.W. Sleight, and A. Ferretti, *J. Appl. Phys.*, **48**, 1914, (1977).
15. J. Augustynski, J. Hinden, and C. Stalder, *J. Electrochem. Soc.*, **124**, 1063 (1977).
16. C. Stalder, J. Augustynski, *J. Electrochem. Soc.*, **126**, 2007 (1979).
17. A. Monnier, and J. Augustynski, *J. Electrochem. Soc.* ,**127**, 1576 (1980).
.18 C. Leygraf, M. Hendewerk, and G. A. Somorjai, *J. Phys. Chem.* **86**, 4484 (1982).
19. J. H. Kennedy, M. Anderman, *J. Electrochem.Soc.* **131**, 848 (1983).
20. J. H. Kennedy, K. W. Frese, Jr, *J. Electrochem.Soc.* **125**, 709 (1978)
21. F. T. Liou, C. Y. Yang, and S. N. Levine, *J. Electrochem.Soc.* **129**, 342 (1974).
22. J. O'M. Bockris, M. Szklarczyk, A. Q. Contractor and S.U.M. Khan, *Int. J. Hydrogen Energy*, **9**, 741 (1984).
23. P. C. Searrson and R.M. Latanision, *J. Electrochem. Soc.*, **135**, 1358 (1988)
24. J. I. Pankove, Optical Processes in Semiconductor, Dover Pub., Chapter 3, New York, 1971.
25. J. O'M. Bockris and S. U. M. Khan, Surface Electrochemistry, Chapter 5, Plenum Press, New York, 1993.
26. G. V. Samsonov, "The Oxide Handbook." IFI/Plenum Data corp., New York, 1978.
27. J. H. Kennedy, and K.W. Frese, Jr., *J. Electrochem. Soc.*, **125**, 723 (1978).
28. S. U. M. Khan and S. A. Majumder, *Int. J. Hydrogen Energy, 14, 653 (1989)*

Table 1. Dependence of flatband potential and donor density of n-Fe_2O_3 on the frequency of Mott-Schottky plot in 1.0 M NaOH.

Frequency (Hz)	Flatband potential (V/SCE)	Donor density (cm^{-3})
100	- 0.74	3.6×10^{20}
500	- 0.74	2.7×10^{20}
1000	- 0.74	2.2×10^{20}
2500	- 0.82	1.9×10^{20}
5000	- 0.92	1.6×10^{20}

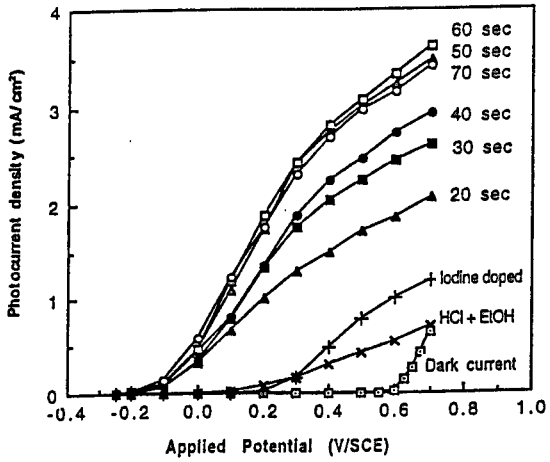


Fig. 1. Photocurrent density - applied potential characteristics of n-Fe_2O_3 synthesized by the spray pyrolysis method. The concentration of the spray solution was 0.11 M $FeCl_3$. Spray solvent: 100% EtOH, spray time: 60 sec, pyrolysis temperature: 370 °C. The n-Fe_2O_3 cells with "iodine doped" and "HCl + EtOH" in figure were made according to ref. 30, 31. Light intensity of Xe: 50 $mWcm^{-2}$, solution: 1.0 M NaOH.

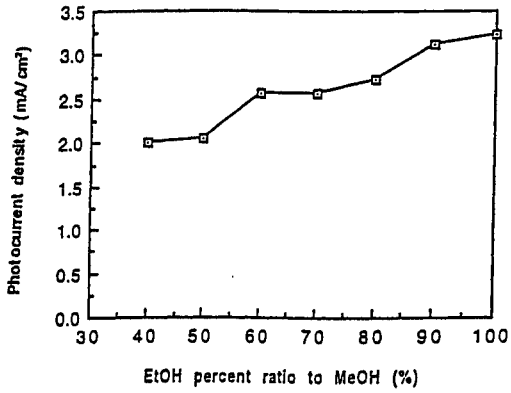


Fig. 2. Dependence of photocurrent density on EtOH / MeOH ratio of solvent for the synthesis of n-Fe_2O_3. The concentration of the spray solution was 0.11 M $FeCl_3$. Spray time: 60 sec, pyrolysis temperature: 370 °C. Applied potential: 0.60 V/SCE, light intensity of Xe: 50 $mWcm^{-2}$, solution: 1.0 M NaOH.

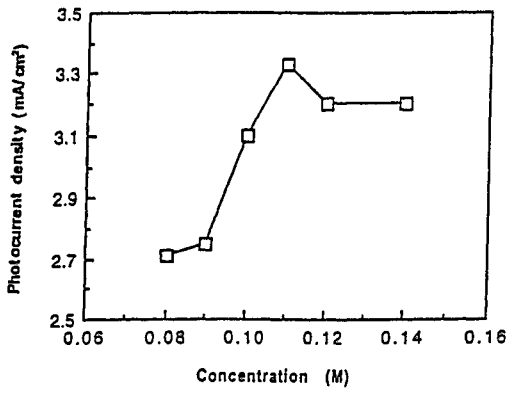


Fig. 3. Dependence of photocurrent density on concentration of $FeCl_3$ solution. Spray solvent: 100% EtOH, spray time: 60 sec, pyrolysis temperature: 370 °C. Applied potential: 0.60 V/SCE, light intensity of Xe: 50 $mWcm^{-2}$, solution: 1.0 M NaOH.

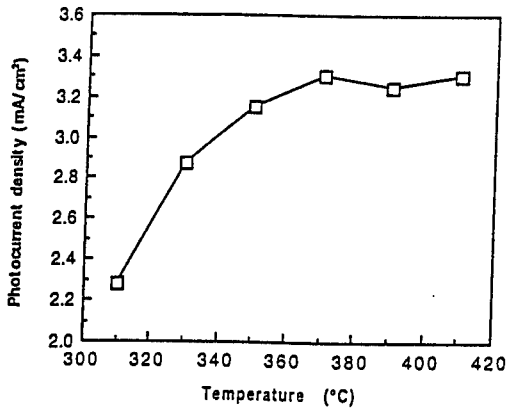


Fig. 4. Dependence of photocurrent density on the pyrolysis temperature of the synthesis of n-Fe_2O_3. Spray solution concentration: 0.11 M $FeCl_3$, spray solvent: 100% EtOH, spray time: 60 sec. Applied potential: 0.60 V/SCE, light intensity of Xe: 50 $mWcm^{-2}$, solution: 1.0 M NaOH.

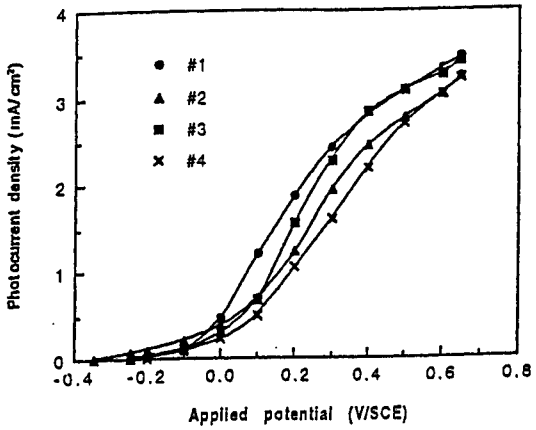


Fig. 5. Reproducibility of the synthesis of n-Fe_2O_3 for the photocurrent-potential characteristics. The n-Fe_2O_3 film was synthesized by the spray pyrolysis method. Spray solution of n-Fe_2O_3 synthesis: 0.11 M $FeCl_3$, spray solvent: 100% EtOH, spray time: 60 sec, pyrolysis temperature: 370 °C. Electrolyte solution 1.0 M NaOH, light intensity of Xe: 50 $mWcm^{-2}$.

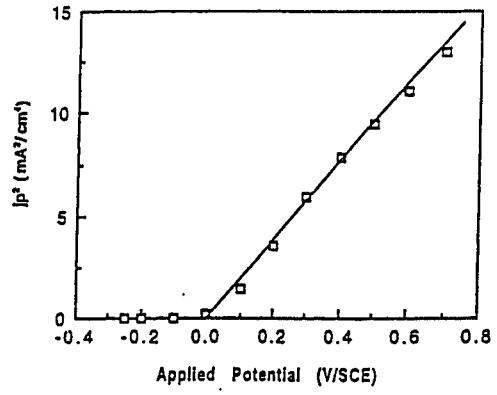


Fig. 6. Onset - potential determination from j_p^2 - V plot for n-Fe_2O_3. Spray solution concentration: 0.11 M $FeCl_3$, spray solvent: 100% EtOH, spray time: 60 sec, pyrolysis temperature: 370 °C. In solution of 1.0 M NaOH.

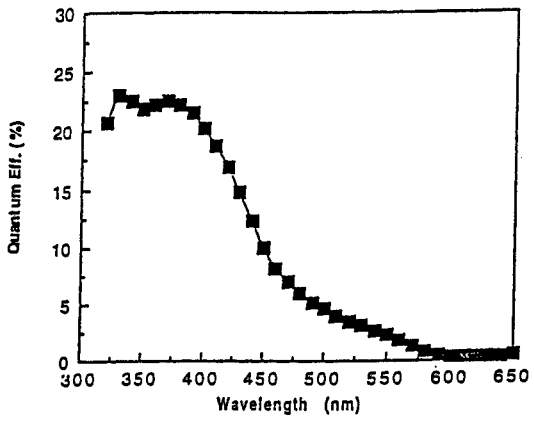


Fig. 7. Quantum efficiency of n-Fe_2O_3 synthesized at 370 °C. Spray solution concentration: 0.11 M $FeCl_3$, spray solvent: 100% EtOH, spray time: 60 sec. Applied potential: 0.60 V/SCE, solution: 1.0 M NaOH.

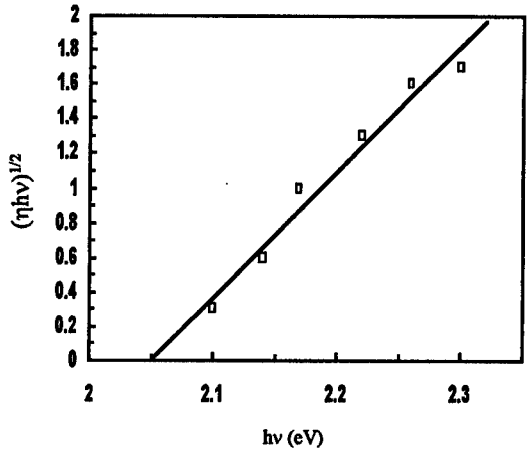


Fig. 8. Bandgap determination of n-Fe_2O_3 from $(\eta h\nu)^{1/2}$ vs. $h\nu$ plot. Spray solution concentration: 0.11 M $FeCl_3$, Spray solvent: 100% EtOH, Spray time: 60 sec, Pyrolysis temperature: 370°C. Applied potential: 0.60 V/SCE, Electrolyte solution: 1.0 M NaOH

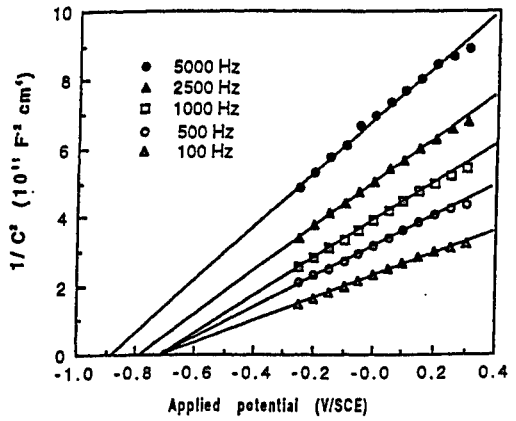


Fig. 9. Mott-Schottky plot of n-Fe_2O_3 film measured at various frequencies. Solution: 1.0 M NaOH, AC amplitude: 10 mV, measured in the dark condition. Dielectric constant of Fe_2O_3: 12. Spray solution of n-Fe_2O_3 synthesis: 0.11 M $FeCl_3$, spray solvent: 100% EtOH, spray time: 60 sec, pyrolysis temperature: 370 °C.

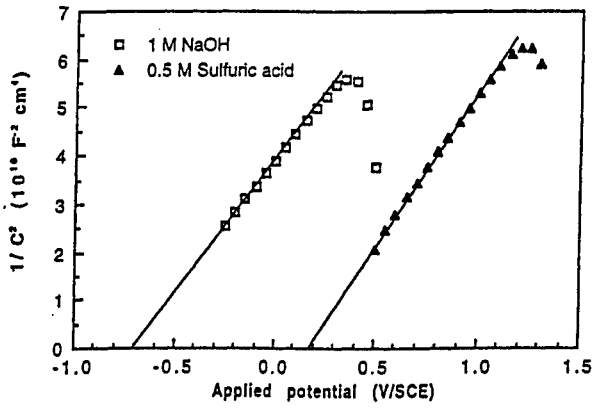


Fig. 10. Dependence of Mott-Schottky plot on pH of the solution for n-Fe_2O_3 film. The pH of 1.0 M NaOH was 14.0, the pH of 0.50 M H_2SO_4 was 0.0. AC frequency : 1000 Hz, AC amplitude: 10 mV, measured in the dark condition. Spray solution of n-Fe_2O_3 synthesis: 0.11 M $FeCl_3$, spray solvent: 100% EtOH, spray time: 60 sec, pyrolysis temperature: 370 °C.

Modification of One Phonon Emission Rates Due to Finite Size Effects in Y_2O_3:Eu^{3+} nanocrystals

Ho-Soon Yang, R. S. Meltzer and W. M. Dennis

Department of Physics and Astronomy, University of Georgia, Athens, GA 30602-2451, USA

S. P. Feofilov

A. F. Ioffe Physical-Technical Institute, St. Petersburg,Russia 194021

Brian M. Tissue

Department of Chemistry, Virginia Polytechnic Institute and State University, Blacksburg, VA 24061-0212, USA

Abstract

In this paper, we investigate changes in the nonradiative relaxation rates of electronic levels due to finite size effects in nanoparticles. Nonradiative relaxation processes are expected to be inhibited since the phonon density of states becomes sparse with a low frequency cut off in nanoscale materials. The results of time resolved measurements on Y_2O_3:Eu^{3+} nanoparticles are compared with those on 1 μm sized particles of Y_2O_3:Eu^{3+} with the same crystal structure. The temperature dependence of the nonradiative relaxation rates is measured in the temperature range 1.5 K – 10 K.

I. INTRODUCTION

The phonon density of states at low frequencies in bulk systems is known to be well described by the Debye model which predicts that the phonon density of states is a continuous function with an ω^2 dependence. However, the density of states in nanocrystalline materials is modified due to the finite particle size. For isolated nanoparticles the phonon spectrum is expected to become discrete with a gap opening up at very low frequencies.

The Y_2O_3:Eu^{3+} nanoparticles used in this study are in the form of a white powder with particle sizes in the range 7 to 25 nm. Particles with this size distribution are sufficiently small that they are unable to able to support acoustic phonons with energies of the order of a few wavenumbers.

In this paper, we measure fluorescence transients from three electronic levels with narrow energy separations (3 cm^{-1} and 7 cm^{-1}) in order to investigate the effect of the modified phonon spectrum on the direct process relaxation of electronic levels in nanocrystalline materials.

We have calculated the vibrational spectrum for Y_2O_3 spheres with 7, 11 and 20 nm diameters to obtain model phonon spectra for nanocrystals with sizes in the range 7 – 25 nm. We have used the numerical technique of Visscher and coworkers [1] to calculate the normal modes of elastic objects under stress free boundary conditions. We point out that the numerical calculation of the nanoparticle vibrational spectrum has an advantage over an analytic calculation in that it is equally appropriate for less symmetric nanoparticle shapes.

For these calculations it was necessary to use the elastic constants for cubic Y_2O_3 as we were unable to find values for elastic constants for monoclinic Y_2O_3. The results of these calculations are presented in Fig. 1. The calculations indicate that 3 cm^{-1} and 7 cm^{-1} phonons in nanoparticles with this size distribution lie either below the cutoff frequency or in a region where phonon modes are very sparse. We therefore anticipate that electronic relaxation by one phonon emission will be either absent or slowed down in these materials.

We compare our measurements in the nanoparticles with similar measurements in 1 μm

Y_2O_3:Eu^{3+} crystals with the same monoclinic structure. The phonon properties of the 1 μm materials are expected to be very similar to those of the bulk crystal. We observe that the form of the time resolved emission from the upper levels of the $^5D_1$ manifold in nanocrystals is qualitatively different from that observed in the 1 μm crystals.

II. EXPERIMENTAL CONSIDERATIONS

A gas phase condensation technique using CO_2 laser heating of ceramic pellets was used to prepare the Y_2O_3:Eu^{3+} nanocrystals used in this study. The source materials were sputtered under 400 Torr of Nitrogen gas and collected on a cold finger held at 60 °C. The particle size and phase of the nanocrystalline powders are characterized by transmission electron microscopy and powder X-ray diffraction, respectively. [2] The Y_2O_3:Eu^{3+} nanocrystals grown using these parameters have diameters in the range 7 - 23 nm. Nanocrystals prepared in this way crystallize in a monoclinic phase which possesses three crystallographically distinct cation sites (denoted A, B, and C). [3], [4]

The emission from Eu^{3+} ions at the A site is very weak due to energy transfer processes and is not discussed further in this paper. For Eu^{3+} ions situated at the B site, the level separations of the second and third levels from the lowest level of the $^5D_1$ manifold are 25 cm^{-1} and 39 cm^{-1} respectively. In contrast, Eu^{3+} ions situated in the C site have energy separations from the lowest level of $^5D_1$ manifold of 3 cm^{-1} and 7 cm^{-1} respectively.

Both nanocrystals and micron sized materials were mounted in small wells which were machined into a brass sample holder. The samples were held in place by a glass window which provided optical access. For the lowest temperature measurements the samples were immersed in superfluid liquid helium which was held at 1.5 K. Measurements above 2.1 K were performed by cooling the samples with cold helium gas.

Fig. 2 shows the excitation spectra for Eu^{3+} ions at the B and C sites of Y_2O_3 nanocrystals. The excitation spectrum for Eu^{3+} ions at the C site reveals the three closely separated electronic levels which we use to study the one phonon relaxation process.

III. RESULTS AND DISCUSSION

Fluorescence transients for Eu^{3+} ions situated at the C site were measured for both the micron sized and nanocrystalline materials and are shown in the upper and lower panels of Fig. 3, respectively.

These measurements were obtained by monitoring the fluorescence from the lowest, second, and third levels of the $^5D_1$ manifold to the lowest level of the $^7F_3$ manifold and are labelled (a), (b), and (c), respectively. All transients presented in this paper were fit (solid lines) using a double exponential fitting function.

For micron sized materials, the fluorescent transient for the lowest level, (a) was found to have a single exponential decay with a lifetime of 137 μs in good agreement with the value of 138 μs observed previously [2]. The transients for the second (b) and third (c) levels both exhibit a rapid initial decay on a 100 ns timescale (not shown) followed by long tails of 134 μs and 132 μs, respectively. This behavior is consistent with rapid direct process relaxation.

As can be seen from the lower panel of Fig. 3, in the nanocrystalline material, the fluorescence from the lowest level of the $^5D_1$ manifold, (a), is predominantly single exponential with a lifetime of 131 μs. However, the emission from the second level, (b), was fit to a double exponential and with decay times of 27 μs and 113 μs, while the emission from the third level, (c), yielded decay times of 7 μs and 101 μs. i.e. the nonradiative relaxation of the second and third levels is much slower than that observed in the bulk.

The nonradiative lifetimes described above were found to be independent of temperature in the range between 1.5 K and 10 K, indicating that the electronic relaxation in the nanoscale materials was dominated by neither the Orbach nor the Raman relaxation process. The exact mechanism by which electronic relaxation occurs in these nanoparticles has not been determined at this time.

Finally we point out that the emission from the upper two levels of the $^5D_1$ manifold for Eu^{3+} ions at the B site was extremely weak, indicating that the nonradiative relaxation rate for these levels was considerably faster than that for Eu^{3+} ions at the C site. The energies

of these levels 25 cm^{-1} and 39 cm^{-1} above the $^5D_1(I)$ are sufficiently high that electronic relaxation by one phonon emission process is no longer expected to be absent.

IV. CONCLUSIONS

We have investigated the effect of a finite size modified phonon spectrum on the electronic relaxation in Y_2O_3:Eu^{3+} nanocrystals. The nonradiative decay rates observed in the nanoparticles are dramatically reduced by up to two orders of magnitude compared to those observed in micron sized materials. The mechanisms responsible for the electronic relaxation in the nanoscale materials are the subject of a continuing investigation.

ACKNOWLEDGMENTS

This work was supported by the National Science Foundation (CAREER award CHE-9502460) and by a Research Corporation Cottrell Scholars Award.

REFERENCES

[1] William M. Visscher, Albert Migliori, Thomas M. Bell, and Robert A. Reinert, J. Acoust. Soc. Am. **90**, No. 4, Pt. 1, 2154 (1991).

[2] Bipin Bihari, Hergen Eilers, and Brian M. Tissue, J. Lumin. **75**, 1 (1997).

[3] Harry L. Yakel, Acta Crystallogr. B **35**, 564 (1979).

[4] H. T. Hintzen, and H. M. van Noort, J. Phys. Chem. Solids **49**, 873 (1988).

FIGURES

FIG. 1. Vibrational spectra for Y_2O_3 spheres with diameters of 7, 11, and 20 nm. Elastic constants for cubic Y_2O_3 were used in these calculations.

FIG. 2. Excitation spectra for Eu^{3+} ions situated at the B (upper panel) and C (lower panel) sites of monoclinic Y_2O_3. The crystal field splittings are much smaller for Eu^{3+} ions situated at the C site.

FIG. 3. Fluorescence transients for the three levels of the $^5D_1$ manifold in micron sized and nanoscaled Y_2O_3:Eu^{3+} crystals at the upper and lower figures, respectively. The bold lines are single exponential fits to the data for micron sized material and multiexponential fits to the data for nanoscale materials. The dashed line is the fit to fluorescence transient of the lowest level scaled down to those of the upper levels for comparison. (a) $^5D_1$(I), (b) $^5D_1$(II) and (c) $^5D_1$(III).

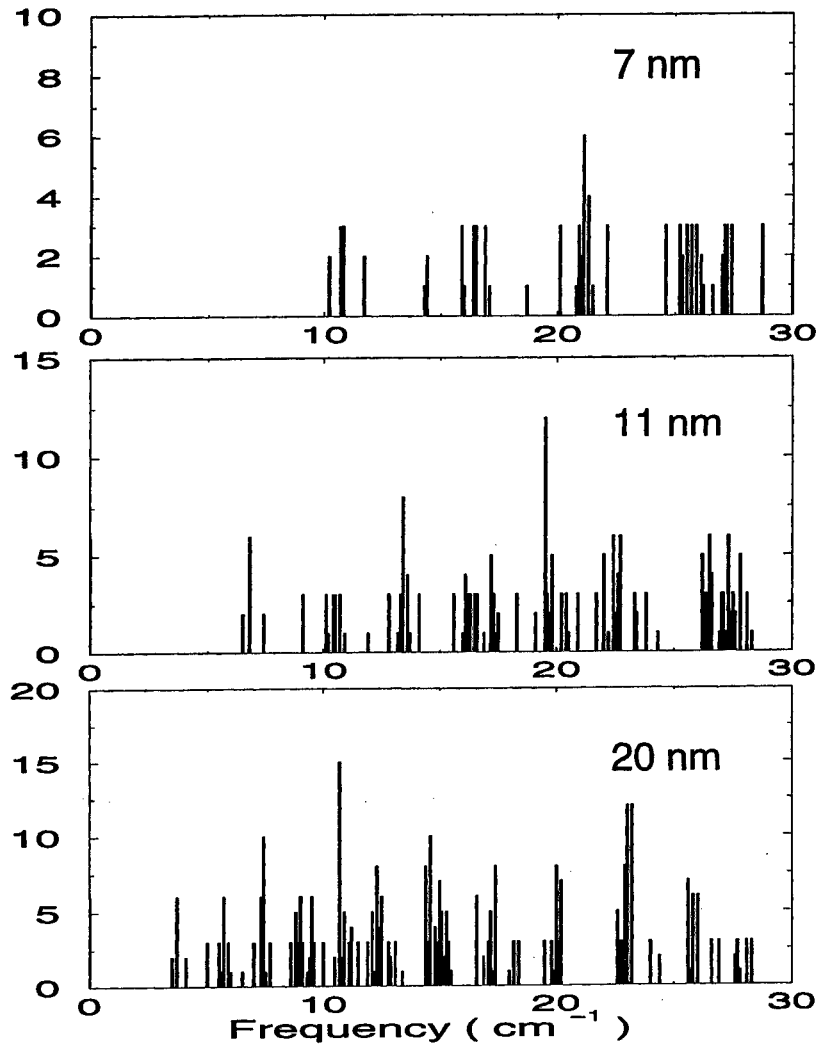


Figure 1

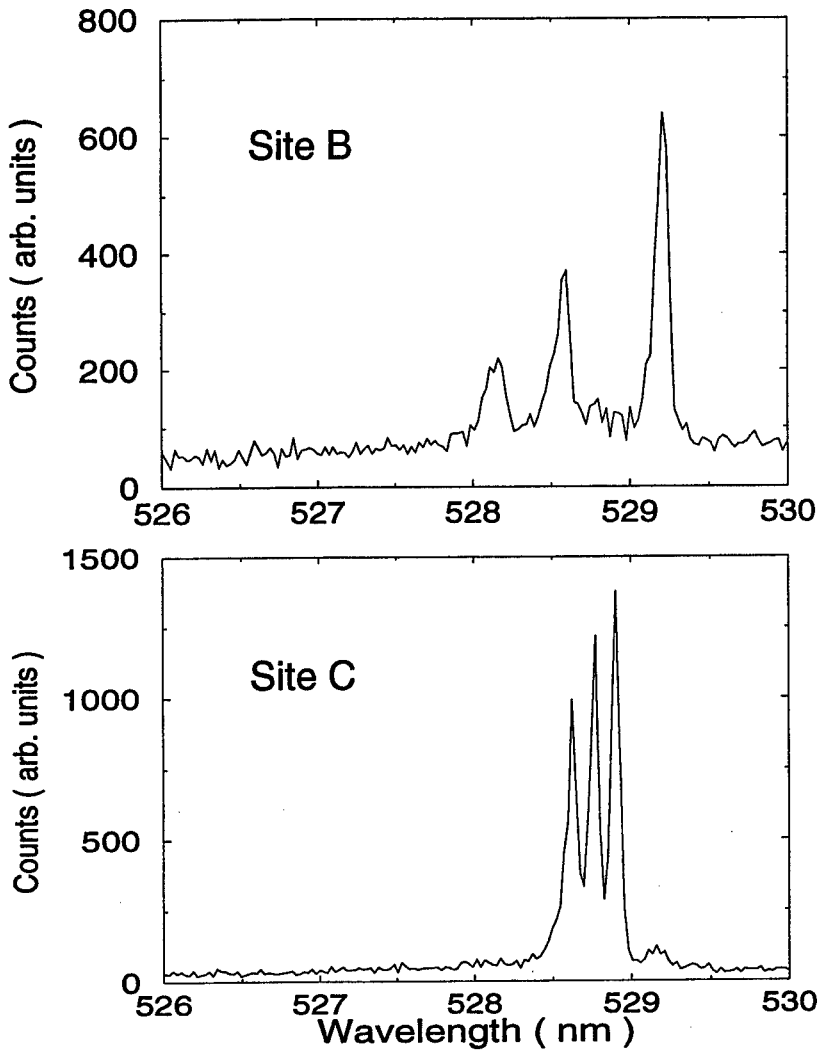

800
600
400
200
0
Counts (arb. units)
Site B
526
527
528
529
530
1500
1000
500
0
Counts (arb. units)
Site C
526
527
528
529
530
Wavelength (nm)

Figure 2.

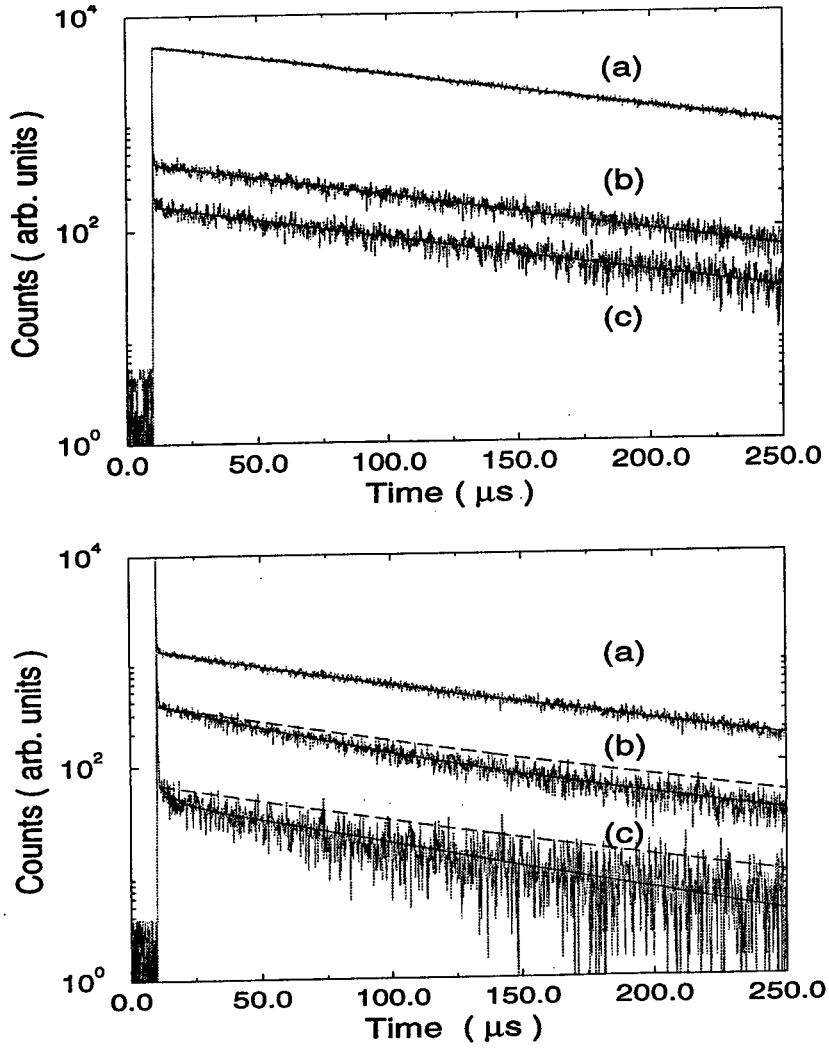

10⁴
10²
10⁰
Counts (arb. units)
(a)
(b)
(c)
0.0
50.0
100.0
150.0
200.0
250.0
Time (μs)
10⁴
10²
10⁰
Counts (arb. units)
(a)
(b)
(c)
0.0
50.0
100.0
150.0
200.0
250.0
Time (μs)

Figure 3.

OPTICAL PROPERTIES OF Au NANOCRYSTALS CONFINED IN POROUS VYCOR GLASS:
Effects of Thermal Annealing and Pulsed Laser Irradiation

R. Mu, A. Ueda, M.H. Wu and D.O. Henderson
Chemical Physics lab, Department of Physics
Fisk University, Nashville TN 37208

K. Malone and G. Mills
Department of Chemistry
Auburn University, Auburn AL 36849

A. Meldrum
Solid State Division
Oak Ridge National Labs, Oak Ridge, TN 37831

ABSTRACT

Au particles were generated inside porous Vycor by photoreduction of $AuCl4^-$ ions present in the channels of the glasses. The as-prepared Au-Vycor has blue color. Both optical and TEM studies suggest that the Au nanocrystals in Vycor is very small in size and the presence of atomic Au possible. Thermal annealing below 600 °C was not high enough to cause the Au to diffuse in Vycor. At the temperature above 600 °C, more and more Au nanoparticles are formed. The blue color faded away and a red color appeared. At a temperature above 1000 °C, there is a dramatic increase in the surface plasmon intensity and the pore network of the Vycor began to collapse. At 1100 °C, long time annealing can lead to loss of Au in Vycor suggesting the rate of pore collapsing was not fast enough to encapsulate the Au in pores. In addition, the surface plasmon absorption band is broadened, which consists of two peaks indicating the presence of elongated Au nanoparticles.

Pulsed laser irradiation at 8 mJ/cm^2 at 532 nm with a pulse width of 30 ps can lead to a size reduction of the Au in pores. The size reduction of the Au nanoparticles may not support thermal evaporation mechanism. The optical field induced fragmentation and optical irradiation pressure may be the plausible mechanisms. At higher fluences, *i.e.*, 12 mJ/cm^2, elongated Au nanoparticles are also observed.

INTRODUCTION

Metallic nanocrystals embedded in glassy and single crystal host materials have shown many unusual electronic and optical (linear and nonlinear) properties with respect to their bulk counterparts although the physical structure of the basic building blocks forming these

nanocrystals is virtually identical to that of the bulk materials. Both electronic and optical properties of metallic nanoparticles result from the extreme spatial localization of the *free* electron gas inside the particles. The constrains in the physical dimension including the size and the shape of the nanocrystals themselves and the non-zero amplitude of the wavefunction outside of the nanoparticles of the confined small number of *free* electrons dictates that the optical properties of the nanoparticles can be strongly influenced by both size, shape of the nanoparticles and their confining media.

Driven by an understanding of fundamental principles underlying the linear and nonlinear optical properties and the potential of creating all optical switching and optical computing devices,[1,2] there has been an explosion of research activities in nanoparticle fabrication techniques. Metallic nanocrystals have been produced both from chemical synthesis, organometallic vapor deposition, chemical reduction from solution, sol-gel techniques and by physical means, such as pulsed laser deposition, ion implantation, sputtering *etc.* [3-6] Among these, much of the effort has been devoted to the precise control of the particle size and shape and to the production of the nano-composite materials in the optically transparent dielectrics.

In this paper, we have reported new experimental approaches using porous glass with well defined pores as a host material and using photochemical reduction of a solution containing $AuCl_4^-$ ions as the means to generate Au nano-particles in the optically transparent media. Both the size and the shape of the Au particles can be controlled, to a certain extent, by the pore structure of the host and the thermal annealing conditions. Pulsed laser irradiation experiments were also conducted to explore the potential for re-sizing the nanoparticle that reside in the pores of the host material.

EXPERIMENTAL

I. Sample Preparation:

Porous Vycor glass from Corning has an average pore size of 4 nm in diameter. The total average pore volume is 28%. The internal surface area is ~ 250 m^2/g. The chemical compositions are: > 96% SiO_2, ~3% B_2O_3 and ~ 1% of other trace of oxides such as, Na_2O, Al_2O_3 and ZrO_2.

Au particles were generated inside porous Vycor by photoreduction of $AuCl4^-$ ions present in the channels of the glasses. The first step was to immerse the glass samples (either 1 x 1 cm or 0.7 x 1 cm) for 10 min into methanol solutions containing 1 x 10^{-2} M $NaAuCl_4$. The glasses were removed from the solutions followed by drying their external surfaces. At this point the samples were light yellow due to the presence of the metal complexes in the channels of the glasses. It was found that evaporation of methanol from the glass channels was very slow, which allowed for illuminating the glasses in the absence of external solutions of Au precursors. This, in turn, minimized formation and/or precipitation of Au crystallites on the outside of the Vycor samples. Exposure times of about 1 h were possible before severe solvent loss caused fogging of the glasses.

Photoreduction of the Au complexes was achieved by placing the Vycor samples inside closed glass containers and exposing them to 350 nm photons from a Rayonet illuminator.

Spectrophotometric determinations at wavelengths above 500 nm were used to follow the reaction progress. The photochemical, actinometric, XRD and UV-Vis measurements were performed as described previously [3].

The loading mass of Au into porous Vycor glass was estimated from the vacuum dried total mass change of the sample before and after the sample preparation. The volume filling fraction of Au in pores was ~0.8% by assuming that Vycor has 28% pore space over its total volume.

II. Thermal Annealing:

Two samples (Sample #3 and #4) were chosen for a series thermal treatment. Each sample was cut into quarters. Each quarter of the sample was thermally annealed in a tube furnace at a fixed temperature. The annealing temperatures were from 400 to 1100 °C with an interval of 100 °C. The annealing atmosphere was N5 Ar gas. A reducing annealing environment (90%Ar + 10% H_2) was also used for last stage of the annealing experiment for some samples. The 500 °C annealed sample was also further annealed at 1200 °C for a total of 1 hr annealing time. Each sample quarter was first annealed at preset temperature for 15 min. Optical absorption spectra were collected after each annealing treatments. No additional annealing was performed when the optical spectra indicated no change in these absorption curves. The overall annealing time was determined by a close examination of optical absorption spectra. That is, an annealing experiment was terminated if no further absorption spectrum change between the adjacent spectra with annealing time interval of hours.

III. Pulsed Laser Irradiation:

The 2nd harmonic at 532 nm of 30 ps Nd:YAG laser (PY61C-10) was used for pulsed laser irradiation experiments. This laser has been further upgraded with the temperature controllers to all the crystals and optical bench in PY61C-10 to ensure its shot-to-shot and long term stability. The fluence used in the current experiment was 4 - 12 mJ/cm^2. The profile intensity variation (or spikes) deviating from a Gaussian beam was estimated to be less than a factor of 3. The sample was irradiated with the laser ranging from 100 to 1000 shots.

IV. Sample Characterization:

All eight sample quarters were characterized with a Hitachi 3501 UV-Vis-NIR spectrophotometer before and after each thermal and/or laser treatments. Optical absorption spectra were made possible with the help of an integrating sphere accessary. All spectra were collected with 1 nm spectral resolution in the region of 2500 - 200 nm (~0.5 - 6.2 eV).

Transmission electron microscopic (TEM) analysis was carried out on 3 samples and in five different regions. They are: a 400 °C annealed sample quarter for 16 hrs, a 1000 °C annealed sample quarter for 4 hrs with laser irradiated and non-irradiated regions and a 1200 °C annealed sample quarter for 15 min with laser irradiated and non-irradiated regions. EDS analysis was also conducted to provide the chemical composition information.

RESULTS AND DISCUSSION

Photoreduced Au in Vycor samples have a dark blue color. As illustrated in Fig. 1, the Au surface plasmon absorption band is very broad with full width at half maximum (FWHM) ~ 200 nm and the center peak position is ~ 600 nm. The different absorption intensities for each samples is due to the different loading masses of Au in each Vycor substrate. Fig. 2 shows the thermal annealing effect on Au in Vycor at 500 °C under Ar. As the annealing time increases, the Au surface plasmon absorption peak increases and the linewidth FWHM narrows. After 60 min isothermal annealing, no further intensity increase was observed. The final linewidth FWHM is ~120 nm and the surface plasmon absorption peak is blue-shifted to 540 nm from 600 nm. Another feature observed during the 60 min annealing was what was appeared to be a change in the slope of the baseline. This change was attributed to a small amount of organic contaminants adsorbed in the porous Vycor. When the organic contaminated Vycor was annealed at the temperature above 350 °C, the decomposition of the organic molecules leads to certain level of carbon deposited on the walls of the porous Vycor glass. Residual of carbon in pores absorb the incident light through out the UV-Vis region. This phenomenon has been observed in number of cases, which has been confirmed by annealing a virgin Vycor sample. Fig. 3 is the thermal annealing effect of Au in Vycor at 800 °C. At this temperature, the absorption intensity of the surface plasmon resonance continuously increases and the linewidth FWHM gradually narrows as a function of time. After 18 hrs annealing, the surface plasmon absorption is shifted to 522 nm and the linewidth FWHM is ~ 75 nm. Fig. 4 shows the thermal annealing effect of Au in Vycor at 1100 °C under an Ar atmosphere. The drastic surface plasmon absorption increase was observed from 15 to 60 min thermal annealing. The center peak position is at ~ 522 nm and the linewidth FWHM becomes ~55 nm. When the annealing time was longer than 60 min the absorption peak was broadened and the center position of the absorption peak is red-shifted from 522 to 541 nm. The spectral line-shape is also changed. In addition, the total absorption intensity is also decreased with annealing time.

Fig. 5 provides the summary of the absorption spectra which have the highest absorption intensity at various temperatures. Below 600 °C, the surface plasmon absorption peak is at ~540 nm. In the temperature range of 600 - 900 °C, the surface plasmon absorption peak is at ~522 nm. When the temperature is above 900 °C, the surface plasmon absorption peak is at ~541 nm and the spectral lineshape is also changed. As we will demonstrate later, there are two absorption peaks overlapping with each other which is the consequence of the line-shape change. Fig. 6 is the optical absorption spectra of pulsed laser irradiation effects on Au in Vycor and the thermal reversibility test. Clearly, 1000 shots of the pulsed laser irradiation at 532 nm and the fluence of 8 mJ/cm^2 have dramatically changed the color of the optical absorption spectrum of the Au in Vycor which has been annealed at 1000 °C. After 1000 shots of irradiation, the surface plasmon absorption band is broadened towards the longer wavelength region and the surface plasmon resonance peak is shifted to the red by ~ 5 nm. The most important feature is that the spectral change due to the laser irradiation can be recovered by annealing the sample at 1000 °C under Ar for 15 min. The recovered spectrum is virtually identical to the spectrum before the laser

irradiation.

Figs. 7 - 9 are TEM images of 400, 1000 and 1200 °C annealed samples together with the laser irradiated areas in the samples. Fig. 7 is the TEM images of as-prepared and a focused electron beam irradiated areas. For the as-prepared area, fig. 7a, the TEM image shows small dark patches long the pore walls in the sample. In the electron irradiated area, the pore structure was collapsed and gold nanocrystals were formed. The particle size can be very large depending upon the size of the electron irradiated area. In addition, a new metastable phase of Au_2Si was also found under focused electron irradiation. Fig. 8 shows a 1000 °C annealed sample in pink (non-irradiated) and blue (laser irradiated) regions. In the pink region, fig. 8a, the image contains many more patches visiblly dispersed around the sample. A few large and twined gold particles could also be observed. In the blue region, on the other hand, fig. 8b, it was very hard to find any particles. In some regions, there exist areas of dark contrast. Fig. 9 illustrates the TEM images of 1200 °C annealed sample in both laser irradiated (blue) and non-irradiated (pink) regions. In the non-irradiated region, fig. 9a, there are a lot of small gold particles with an average particle size of 3-4 nm. In the blue region, some elongated cigar-like and some island-like particles were also observed and the spherical particles can be found between. A few oval particles appear to be aggregates.

As discussed in a great detail by Weaver *et al.* [6], illumination of solutions containing $AuCl_4^-$ electron donors induces a reduction of the metal complex. A similar chemical process may also be expected to be the same for the solution in Vycor as in the methanol-swollen poly(DADMAC). With UV light irradiation, the color of the sample changes from yellowish to light blue. The light blue deepens as a function of irradiation time. No red color was observed suggesting no large gold nanocrystals were formed inside of Vycor. The thermal annealing experiments below 600 °C did not lead to a red color formation. The absorption spectra in the gold surface plasmon resonance region of these samples are still broad although they were somewhat narrowed as illustrated in figs. 2 & 5. It is also known that the linewidth of the surface plasmon resonance should be broadened when the Drude-like electrons in these particles experience size limited scattering [7,8]. The observed broad absorption band observed in the 500 - 700 nm region for the as-prepared and the thermally annealed below 600 °C can be attributed to very small gold particle absorption. The TEM images of 500 °C annealed sample also supports this hypothesis. It is also possible that very small gold clusters (or molecules) and even neutral gold atoms may also deposit on the pore walls as it is indicated in the TEM image of fig. 7a. There are traces of dark lines running along the pore walls. As suggested by Schaaff *et al.*, [9] very small gold particles fail to exhibit a surface plasmon resonance absorption. They observed an inflection upward at a wavelength shorter than ~775 nm (1.6 eV), which is corresponding to the interband transition edge. As illustrated in fig. 5, the 400 and 500 °C annealed and as-prepared samples show more steep absorption below 500 nm. Certainly, it is arguable that the low temperature thermal annealing does not cause the gold clusters to diffuse along the pore surface that allows to the formation of bigger gold particles that cause the red color in the Vycor.

When the annealing temperature was increased above 600 and below 1000 °C, the blue

color started to fade away and red color started to be dominant. This suggests that the thermal energy is high enough to cause the gold clusters or atoms to diffuse along the surface. As larger particles are formed, the surface plasmon absorption becomes more evident. As shown in figs. 2 - 3, after 18 hrs of thermal annealing, no further spectral changes were observed suggesting the system has reached the thermal equilibrium. That is, the very small gold particles or atoms have diffused into their nearby bigger particles. This suggests that the separation of these bigger gold particles is larger than the thermal diffusion length of these ultrasmall particles or atoms.

When the annealing temperature is above 1000 °C, there are two physical changes in the Au-Vycor system: *a*) the pores of the Vycor start to collapse. The densification of the Vycor will lead to an increase of the gold particle density per unit volume. That is, the average particle separation is also decreased; *b*) gold nanoparticles are expected to be in molten phase. It is known that the melting point of the bulk gold is 1065 °C. The melting point of the gold nanoparticles is expected to be well below its bulk melting point due to the large surface to volume ratio [9]. At 1000 °C, diffusion of the gold clusters or atoms was fast enough to reach dynamic thermal equilibrium of the diffusion and growth process in about 60 min. The annealing time longer than 60 min did not result in an increase of the surface plasmon absorption. TEM images, shown in fig. 8 suggest that the gold particles are still very small. A few bigger nanoparticles $\leq$ 4 nm could be occasionally observed. At 1100 °C, the gold in Vycor became so mobile that longer annealing time ($t > 60$ min) suggests there is a loss of gold from the sample. The densification rate of the pores was not sufficiently fast enough to enclose the gold before diffusing out. At 1200 °C, the rate of the pore collapsing is fast enough to encapsulate the gold in pores. As shown in fig. 9, the gold nanoparticles were formed in a much mono-dispersed manner and the average particle size is the same as the average pore size.

Although the pore size in Vycor has very narrow distribution with an interconnected network, the variation in pore size can be considered as a throat-pore configuration. That is, the large openings are pores and the small openings which connect the large ones are throats. At high temperature, all the throats will be first closed. Under this condition, the gold is trapped inside these isolated pores. As these pores shrinks, more and more gold inside pores will further diffuse together until the total space of these pores are filled with gold. Thus, the pore size has served as a upper limit of the final size of the gold nanocrystals. It is, therefore not surprising to see an average of 4 nm gold particles being formed.

Perhaps the most interesting aspect of this report is the pulsed laser irradiation effect on gold nanoparticles residing inside the pores of Vycor. The pulsed laser irradiation of the Au-Vycor system which has been annealed at 1000 °C with fluence of 8 mJ/cm^2 per pulse at 532 nm and a pulse with of 30 ps can convert red colored Vycor gradually into blue. The conversion rate depends on shot number. Thermal annealing experiments at 1000 °C for 15 min of the laser irradiated sample suggest that the color change from red to blue due to laser irradiation is reversible. This experiment has been repeated three times. The TEM images in fig. 8a and 8b show two different regions of dark contrast. Namely, the irradiated area has lighter contrast than that of the unirradiated area. The optical spectrum of the

irradiated area shows that the surface plasmon resonance peak intensity decreased and the linewidth FWHM is broader than that of the unirradiated area suggesting that pulsed laser irradiation causes the gold particle to reduce in size. The lighter contrast in the TEM image seems also to support this argument. However, we can not rule out that aggregation may also occur. The irregular shape of the gold particles can also lead to surface plasmon modes decoupling which in turn can cause the broadening of the absorption spectra. However, TEM results do not seem to support the later case.

One of the more challenging aspects of this investigation is to understand the mechanism(s) leading to the laser induced color change in the Au-Vycor samples. Studies of the surface plasmon relaxation dynamics of gold colloids has shown that the excited electrons in gold nanocrystals thermallize into the electron gas in $\leq$ 1 ps via electron-electron and electron-phonon scattering [12,13]. The electron-lattice relaxation time is estimated to be a few ps. The energy dissipation into the matrix from the gold nanocrystals is usually several hundreds ps. Therefore, it can be argued that during one pulse (30 ps), there is no energy flowing into the matrix. All the absorbed energy is converted into the heat. Our calculation from the experimental data shows that the expected temperature rise was not more than 75 °C . Unlike the work reported by Kurita *et al.*, the change of the optical absorption may not be due to gold evaporation and redeposition process [4]. It is also hard to imagine any other possible solution chemistry related coagulation, and dissolution [10, 11] since the 1000 or 1200 °C thermal annealing is high enough to remove all the residuals of solute species. It is also high enough to decompose Au chlorine related complex.

There are two possible mechanisms responsible for the laser induced color change. The first possible mechanism is related to an electrical field induced fragmentation process of the gold nanoparticles. Under an intense laser field irradiation, the field strength is high enough to cause the ionization of Au nanoparticles by the ejection of the electrons from the gold particles. The repulsive force due to the positive charges on the Au nanoparticles can result in the breaking of the interatomic bonds or overcoming the cohesive energy potential of the nanocrystals. Some of the gold atoms or clusters could be fragmented away from the parent gold particles and redeposit on to the pore walls nearby. To a certain degree, the mechanism is analogous to the mechanism of laser ablation of insulator materials [14]. The second possibility is laser induced gold colloid aggregation. Under a high fluence, the gold particles reside on the walls of the pores can be knocked off by irradiation pressure and the absorption of the photons. These free gold particles inside the pores then will be repeatedly knocked around which can lead to the loosely packed aggregated. These aggregates in turn can also cause the broadening of the optical absorption spectrum of the gold surface plasmon. However, we intend to believe the first interpretation should be the dominant effect in the present case.

As the illumination fluence increases, at 12 mJ/cm^2 a much more dramatic optical spectral change results. The TEM images for laser irradiated region also show the elongated cigar-like particles or aggregates. The observation may support in part the second mechanism as discussed above. These aggregates can be diffuse together under high laser fluence. This hypothesis may be hold in the area of laser hot spikes under high fluence.

More detailed analysis on pulsed laser irradiation on Au-Vycor system will be reported in a upcoming paper. The current experimental observation opens a new aspect of how to control the metal nanocrystals in solid hosts.

CONCLUSION

It has demonstrated that it is possible to generate Au nanoparticles in porous Vycor glass via photoreduction of Au complex in solution. A proper control of the load mass of the metals in pores and of thermal annealing temperatures can help to control the metal nanocrystal size and shape. Pulsed laser irradiation can change the Au nanoparticle size and size distribution. The preliminary results also suggest new laser - nanoparticle mechanism(s) operative.

ACKNOWLEDGMENTS

Authors at Fisk University would like to acknowledge the supports from NASA Lewis under CARET grant NCC3-575 and from DOE grant DE-FG02-94ER45521. Work at Auburn was supported by the NSF EPSCoR Program. Electron microscopy was done at the ShaRE Facility, ORNL.

REFERENCES

[1] R. F. Haglund, Jr "*Handbook of Optical Properties*" Vol. II, Chap. 8, pp 181- 231, CRC Press Inc. (1997).

[2] U. Kreibig and M. Vollmer, "*Optical Properties of Metal Clusters*" Springer-Verlag (1995).

[3] S. Weaver, D. Taylor, W. Gale and G. Mills, Langmuir 12, 4618 (1996).

[4] H. Kurita, A. Takami and S. Koda, Appl Phys. Lett 72, 789 (1998).

[5] K. Fukumi, A. Chayahara, K. Kadono, T. Sakaguchi and Y. Horino, J. Appl. Phys. 75, 3075 (1994).

[6] D.O. Henderson *et al.* J. Vac. Sci. Technol. B13, 1198 (1995); J. Vac. Sci. Technol. 14, 1199 (1996); Nucl. Instru. and Meth. Phys. Research B141, 261 (1998) (and refs there in).

[7] L. Genzel, T.P. Martin and U. Kreibig, Z. Phys. B 21, 339 (1975).

[8] J.A.A.J. Perenboom and P. Wyder, Phys. Rep. 78, 173 (1981).

[9] P. Buffat and J.P. Borel, Phys. Rev. B 13, 2287 (1976).

[10] P.V. Kamat, M. Flumiani and G. Hartland, J. Phys. Chem. B102, 3123 (1998).

[11] H. Fujiwara, S. Yanagida and P.V. Kamat, J. Chem. Soc. Chem. Comm. (In print, 1998).

[12] M. Perner, P. Bost, U. Lemmer, G.V. Plessen and J. Feldmann, Phys. Rev. Lett. 78, 2192 (1997).

[13] C. Suarez, W.E. Bron and T. Juhasz, Phys. Rev. Lett. 75, 4536 (1995).

[14] R.F. Haglund, Jr, "*Laser Ablation and Desorption*" ed. by J.C. Miller and R.F. Haglund Chap. 2, pp 15-138, Academic Press (1998).

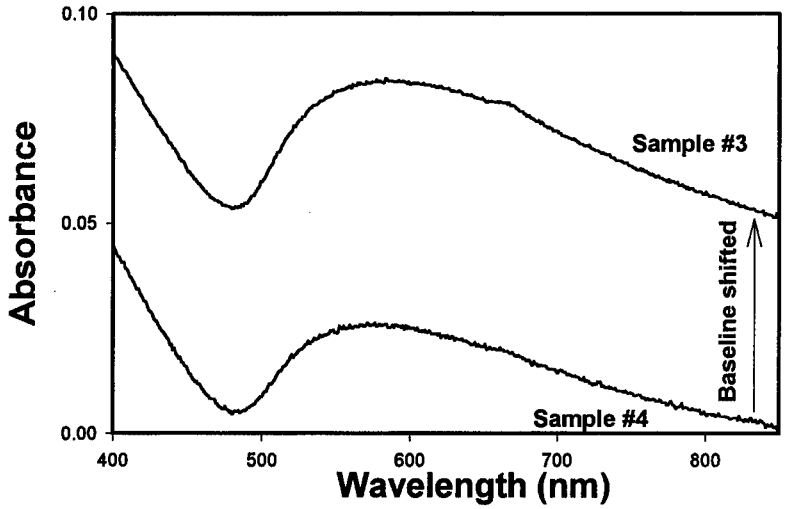


Fig. 1 Optical absorption spectra of as-prepared samples (samples #3 and #4 as mensioned in the text).

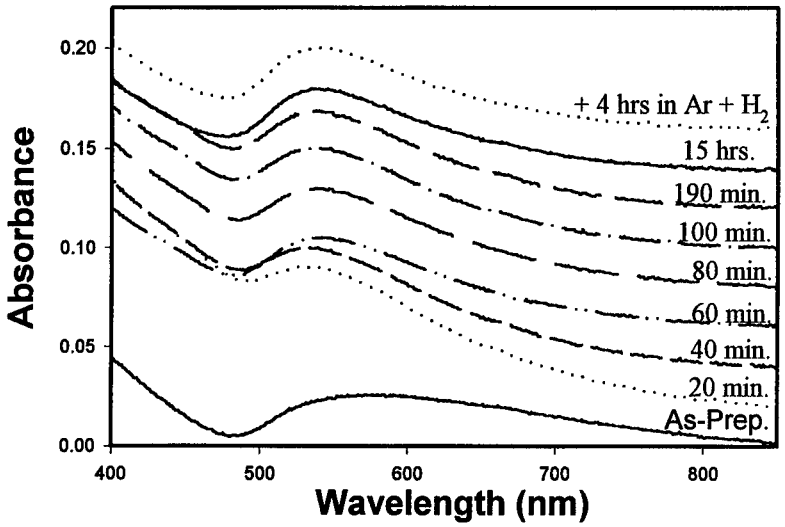


Fig. 2 Optical absorption spectra of Au in Vycor annealed at 500 °C under Ar atmosphere as a function of annealing time.

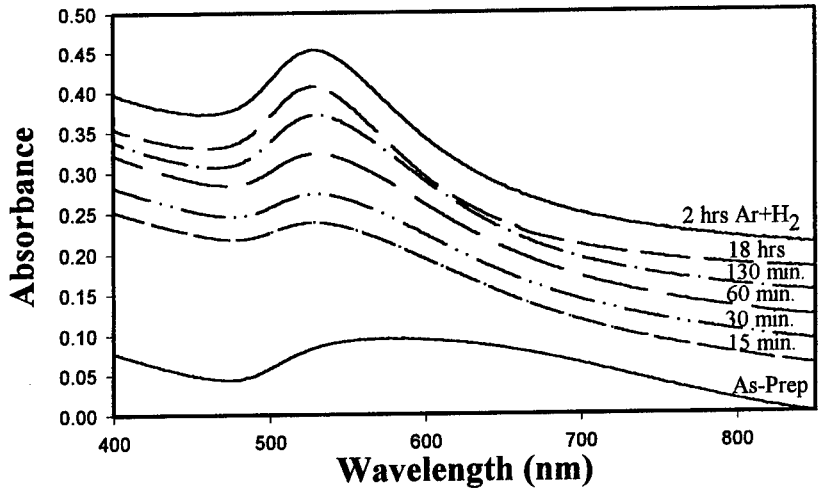


Fig. 3 Optical absorption spectra of Au in Vycor annealed at 800 °C under Ar atmosphere as a function of annealing time.

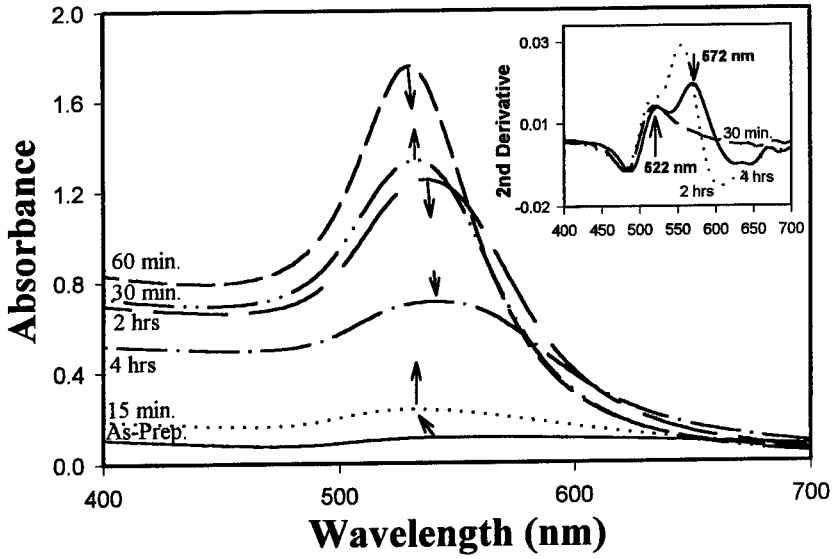


Fig. 4 Optical absorption spectra of Au in Vycor annealed at 1100 °C under Ar atmosphere as a function of annealing time.

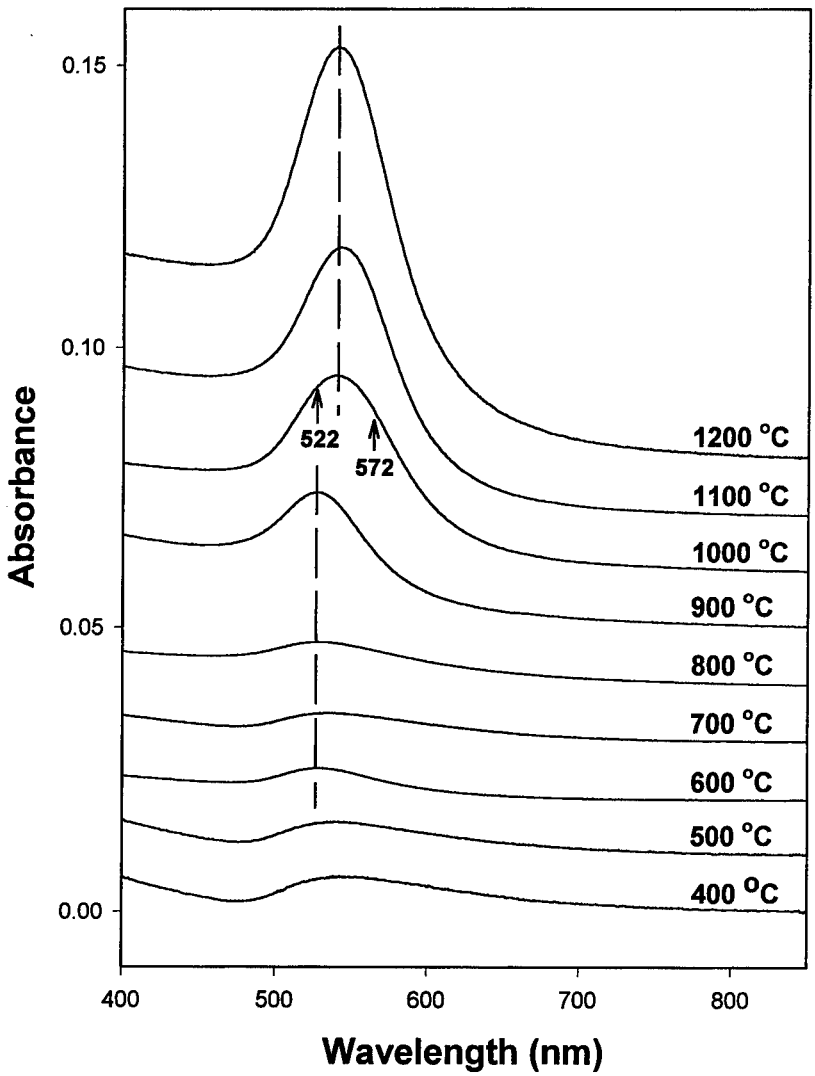


Fig. 5 Optical spectra of Au in Vycor as a function of annealing temperatures under Ar Atmosphere.

Fig. 6 Optical absorption spectra of as-annealed, laser irradiated with 1000 pulses and annealed after the laser irradiation at 1000 °C for 15 min.

Fig. 7 TEM images of Au in Vycor annealed at 400 C for 18 hrs. a) As-prepared sample and b) focused electron beam irradiated area.

Fig. 8 TEM images of pulsed laser irradiated Au in Vycor annealed at 1000 C for 15 min. a) Before laser irradiation and b) after laser irradiation. (pulse width : 30 ps, wavelength: 532 nm, fluence: 8 mJ/cm2 and 1000 pulses).

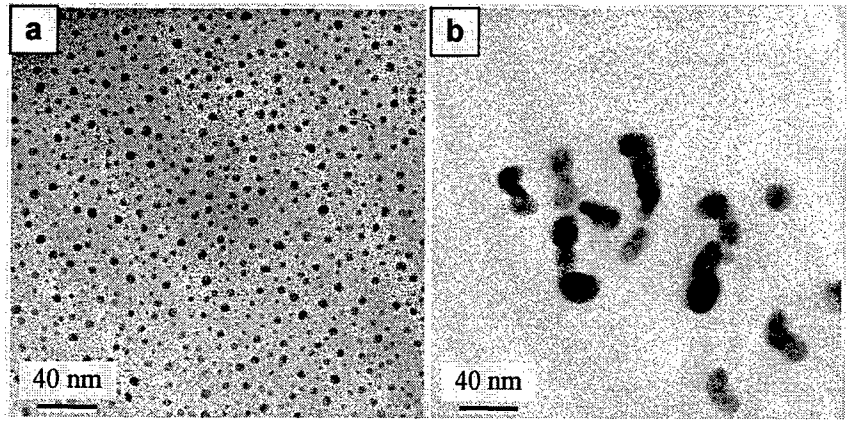


Fig. 9 TEM images of laser irradiated Au in Vycor annealed at 1200 C for 15 min. before laser irradiation. a) Before laser irradiation and b) after laser irradiation (pulse width: 30 ps, wavelength: 532 nm, fluence: 12 mJ/cm^2 and 1000 pulses).

Copper doped CdSe nanocrystalline thin films

Nirmala Chandrasekharan, Sasha Gorer and Gary Hodes
The Weizmann Institute of Science, Rehovot, 76100 Israel

ABSTRACT

The energy level structure of semiconductor quantum dots changes gradually from the band structure of the bulk semiconductor to an atomic-like structure as the quantum dot size decreases. This results in an increase in the effective optical band gap as a function of crystal size. Apart from the inherent flexibility in tailoring quantum dot properties, it is of interest to see how doping affects these properties further. In this work, copper doped QDs and larger nanocrystals, from 3 nm to several tens of nm, were deposited by chemical solution deposition and their morphological and optical properties compared with similarly-deposited undoped CdSe. Crystal size was measured by XRD and by TEM imaging. Optical and photoelectrochemical spectral response measurements were made and correlated with the doping.

I. INTRODUCTION

In semiconductor Quantum Dots (QDs) , a gradual transition from solid state to molecular structure occurs as the particle size decreases. Consequently there is a change in the energy band structure expressed in the increasing effective optical band gap and a change from continuum to discrete quantized energy levels. To obtain the desired electrical properties, semiconductors are normally doped. For quantum dots in the size range investigated by us, a single dopant atom would drastically change the properties of the dots and therefore doping might be expected to affect the semiconductor properties in a different manner than it does for the bulk semiconductors. We have studied copper doped CdSe quantum dots deposited by chemical solution deposition and compared their properties to those of undoped CdSe quantum dot films.

II. EXPERIMENTAL

Synthesis : Copper Doped CdSe and the corresponding undoped samples were deposited by chemical solution deposition onto substrates of glass or SnO_2 conducting glass [1]. A 10ml aqueous solution containing 80mM $CdSO_4$, and 110-160 mM potassium nitrilotriacetate(K_3NTA) was made up to pH 7 by the addition of NaOH. An aqueous solution of Na_2SeSO_3 (80 mM) was then added and the solution made up to pH 10. For the Cu-doped films, 0.8 mM CuCl (1% of the Cd concentration) dissolved in potassium nitrilotriacetate was also added before the addition of the selenosulfate.

The films were deposited at two different temperatures (5°C and 80°C) and were ca. 50-70 nm thick, consisting of aggregated nanocrystals. Typically, the low temperature films deposited within 8 hours to 2 days. The high temperature films took about 30 minutes to 1 hour for deposition. The films deposited on the lower side of the substrate were used for the measurements. The deposition on the other side was removed with a cotton swab dipped in dilute HCl.

XRD : Powder X-ray diffraction was performed on the deposited films. Since the glass substrate diffracts strongly in the region of the main peaks between 2θ=15-30°, the less intense peaks between 35-55° were used for particle size measurement using the Scherrer formula.

Transmission Electron Microscopy/Electron Diffraction (TEM): TEM was carried out by removing the films from the glass substrate, using dilute HF and lifting them onto carbon-coated copper grids.

Photelectrochemical measurements : Photoelectrochemical spectral response measurements were made using a Xe light source through a double monochromator and lock-in detection. The electrolyte was 0.2M Se in 0.5M Na_2SO_3 (Na_2SeSO_3).

Optical characterization : Optical absorption spectra of the samples were recorded after correcting for reflectance in the 400-900 nm range.

III. RESULTS

Xray Diffraction (XRD) : Fig. 1 shows the particle sizes of four samples: undoped CdSe at the two different temperatures, 5°C and 80°C and the corresponding 1% copper-doped samples, obtained from XRD using the Scherrer formula. The low temperature undoped film has a particle size of 3.2 nm similar to that obtained for the corresponding doped sample. The 5°C samples were indexed in the cubic symmetry. The high temperature 80°C samples exhibit larger particle sizes as expected, compared to the low temperature samples, with the doped sample showing a particle size of 10.3 nm and the undoped, 6 nm. Fig. 2 shows a wider range of 2θ from 20-55° (after subtracting for the glass signal) for the 80°C samples. The doped film deposited at 80°C shows a hexagonal symmetry unlike the corresponding CdSe which is cubic. The three peaks of the hexagonal phase at ca. 25° are not well resolved although all three can be seen.

Transmission electron microscopy(TEM): Fig. 3 shows the bright field imaging of the undoped (Fig. 3a) and doped (Fig. 3b) CdSe deposited at 5°C. The electron diffraction (ED) (Fig. 3c) for the two samples was similar and revealed a cubic zinc blende structure. The sample in Fig. 3a consists of very small particles, uniformly distributed with isolated spherical agglomerations of the quantum dots. The high temperature 80°C samples show a significant change between the doped and undoped films (Fig. 4). The ED of the undoped 80° CdSe is similar to that obtained for the 5°C CdSe. The doped sample, in contrast, shows extremely large twinned particles (Fig. 4c). The ED shows highly oriented crystals (spots in diffraction) and the hexagonal symmetry can be clearly seen (Fig.4d).

The copper-doped 5°C samples show an average particle size obtained from TEM, of 3.1 nm (Fig. 5b), similar to that obtained from XRD.and a wider particle size, with particle sizes ranging from 2 to 6 nm. The undoped CdSe (Fig. 5a) shows an average particle size of 3.6 nm which is slightly larger than that obtained from XRD. For the 80°C samples, the undoped film shows an average particle size of 6.3 nm (Fig. 5c) comparable to that obtained from XRD. Particle size distributions range from 4-10 nm. In the case of the doped sample, the average size is 84 nm , with a very wide particle size distribution ranging from 10-100s of nm, very different from that obtained from XRD data. (Fig. 5d)

Photoelectrochemical spectroscopy(PEC): Photoelectrochemical spectra for the low temperature 5°C samples are presented in Fig 6a and 6b for the 5°C and 80°C films respectively. There is a broad sub-band gap tail present in the doped sample (solid line Fig. 6a) not present in the undoped one (solid line). The photocurrent onset at 550 nm parallels that obtained in the optical spectrum shown in Fig. 7a (dotted line). The onset is relatively sharp. The tailing behavior and sub-band gap absorption is also clearly seen for the doped film in the absorption spectrum (solid line in fig. 7a). In order to address the question of whether copper is present on the surface or in the bulk, we treated the sample with very dilute KCN (0.05 M) for 20 seconds. KCN is known to remove surface copper by complexing with copper to form the cyanide species. There was a considerable difference in the signal compared to the as-deposited sample. The sub-band gap (tail) disappeared (Fig. 6a dotted-dashed line) and the signal onset became sharp near the band gap region. The similarity to the undoped CdSe signal was striking. These features can also be seen in the absorption spectrum (Fig. 7a dotted dashed line). Another important point to note is the quantum efficiency (QE) of the signals involved. The doped sample shows a relatively small QE compared to the undoped one. On treatment with KCN, the efficiency is enhanced. These studies were also performed for the samples at 80°C (Fig. 6b). The PEC spectra for the undoped, copper doped and the KCN-treated doped films are seen as dotted, solid line and dotted-dashed respectively. The corresponding absorption spectra of the samples are seen in Fig. 7b. The spectra are red-shifted compared to the low temperature samples, which is expected, from the larger particle sizes (quantum size effect). The magnitude of the quantum efficiency is much higher (orders of magnitude) compared to the 5°C films. If we compare the doped samples, we see similar tailing behaviour. However, the KCN treatment reveals a different behaviour in the high temperature doped films. Dipping the sample in the KCN solution, even for 1-2 minutes does not remove the sub-band gap tail completely. Prolonged treatment with KCN causes the film to peel.

IV. CONCLUSIONS

The morphological and spectroscopic studies reveal that for the undoped CdSe, increasing the temperature (and hence the size) causes no change in the crystal structure. The particle size distribution is fairly narrow with slight broadening in the high temperature sample.

The copper doped samples, however, show much larger changes with temperature. The size distribution in general increases on doping although the size of the doped sample is slightly smaller compared to the undoped one at 5°C and enhanced dramatically in the 80°C doped sample, accompanied by a phase change from cubic to hexagonal. In the low temperature sample the copper is located on the surface (as evidenced from PEC and optical measurements) and is hence completely removed when exposed to KCN. In the 80°C sample the copper is distributed both on the surface and in the bulk. Only the surface copper (roughly half the total) is removed on treatment with KCN. The bulk copper (possibly present at the twin boundaries) remains. For the 5°C QDs the comparatively smaller size implies small grains and therefore more grain boundaries for the same given thickness.The electrons and holes have a greater chance of recombinations which cause lowering of the quantum efficiency. This results in the low temperature samples having much lower Q.E. as compared to the high temperature samples. The copper doped films have lower Q.E. in comparison to the undoped samples. In the doped films the copper which is probably present as $Cu_{2-x}Se$ (XPS shows Cu in the +1 state) is present in high concentration and can act as charge traps, which enhances recombination thus lowering the Q.E. as compared to undoped sample. This decrease is more in the 5°C samples because all the copper is present on the surface and is present in higher concentration.

ACKNOWLEDGEMENT

This research was supported by the Israel Ministry of Science and the United States-Israel Binational Science foundation(BSF), Jerusalem, Israel.

References

[1] Sasha Gorer and Gary Hodes J. Phys, Chem. **98**, 5338,(1994)

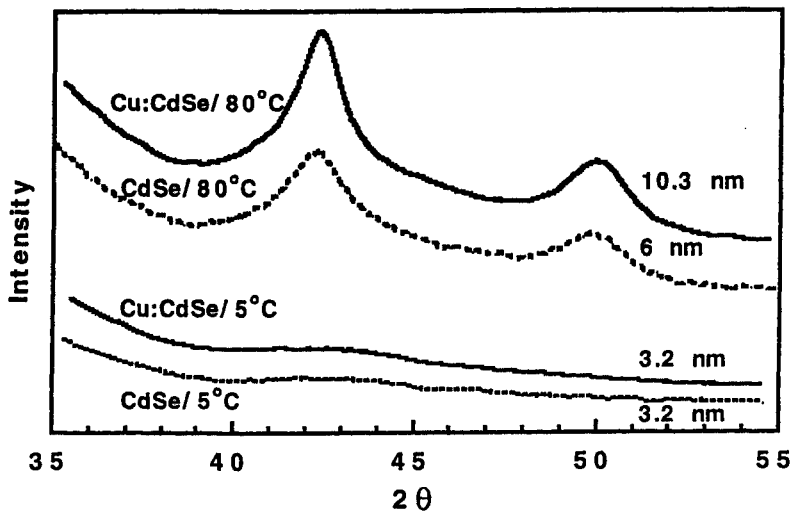


Fig. 1. X-ray diffraction pattern of the copper doped and undoped CdSe at two different deposition temperatures, 5°C and 80°C.

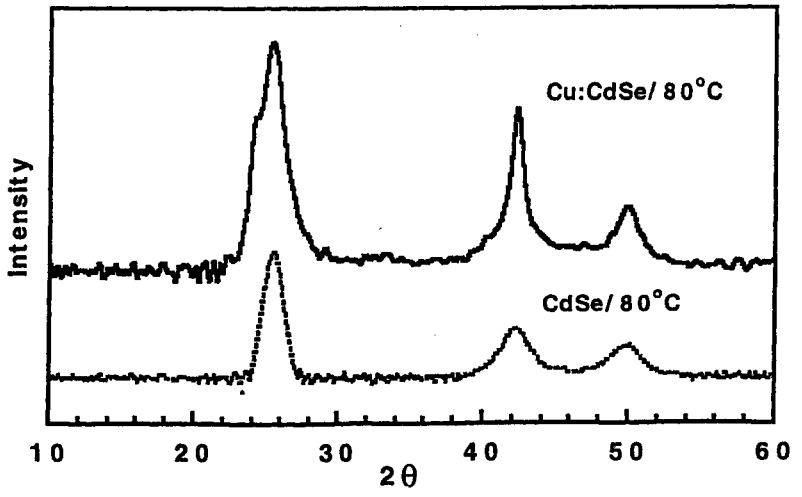


Fig. 2. Wide range X-ray diffraction pattern for the doped and undoped CdSe deposited at 80°C.

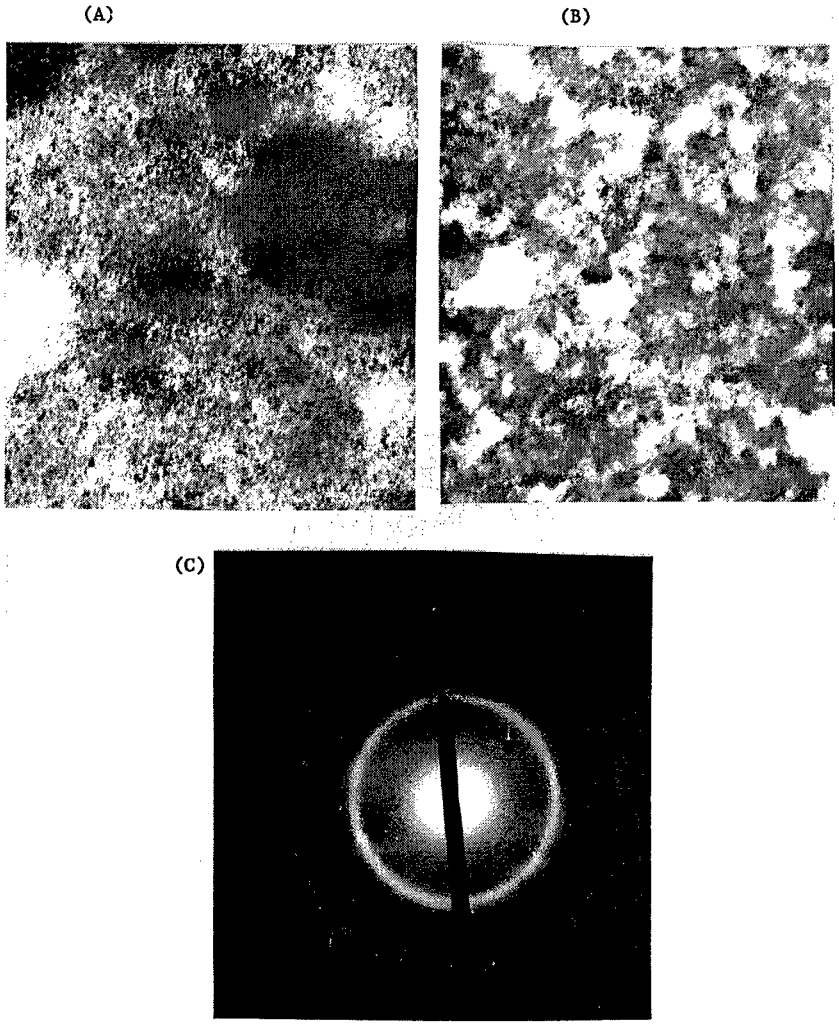


Fig 3 a) Bright field image of undoped CdSe deposited at 5°C b) the bright field image for the copper doped CdSe deposited at 5°C c) The electron diffraction for the samples deposited at 5°C.

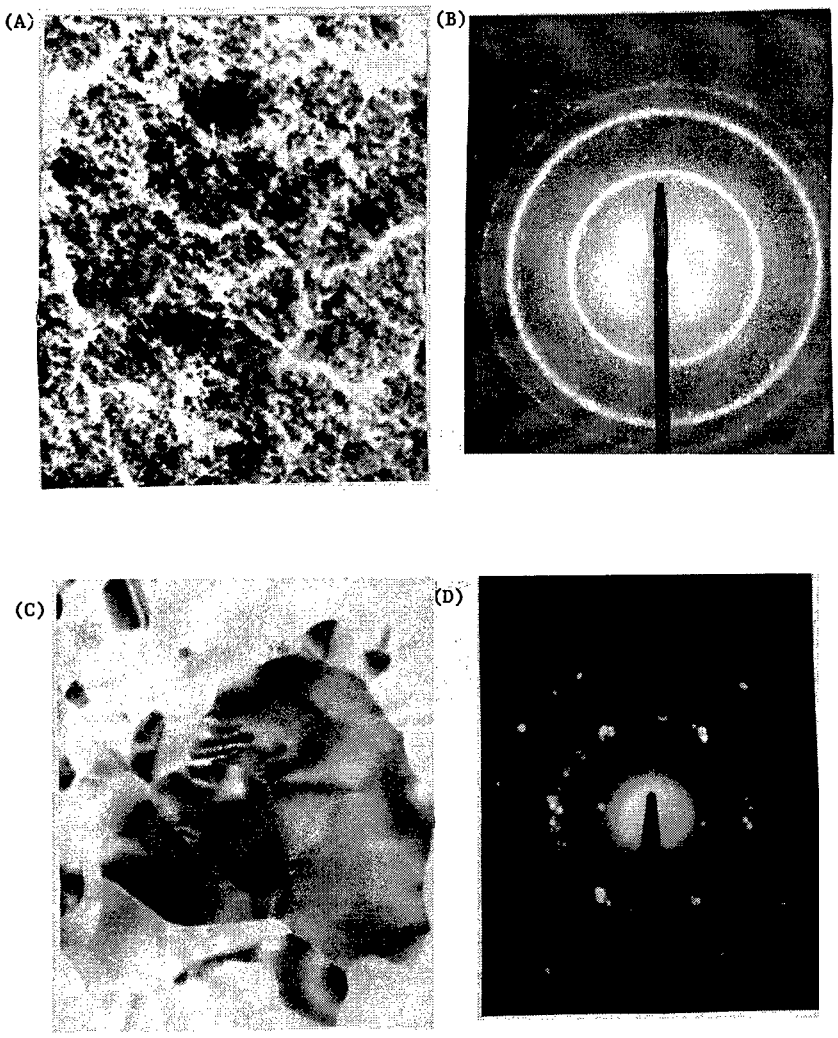


Fig 4 a) The bright field image of the undoped CdSe deposited at 80°C b) the electron diffraction image of the sample in a. c) the bright field image of the copper doped CdSe deposited at 80°C d) the electron diffraction image of the sample in c.

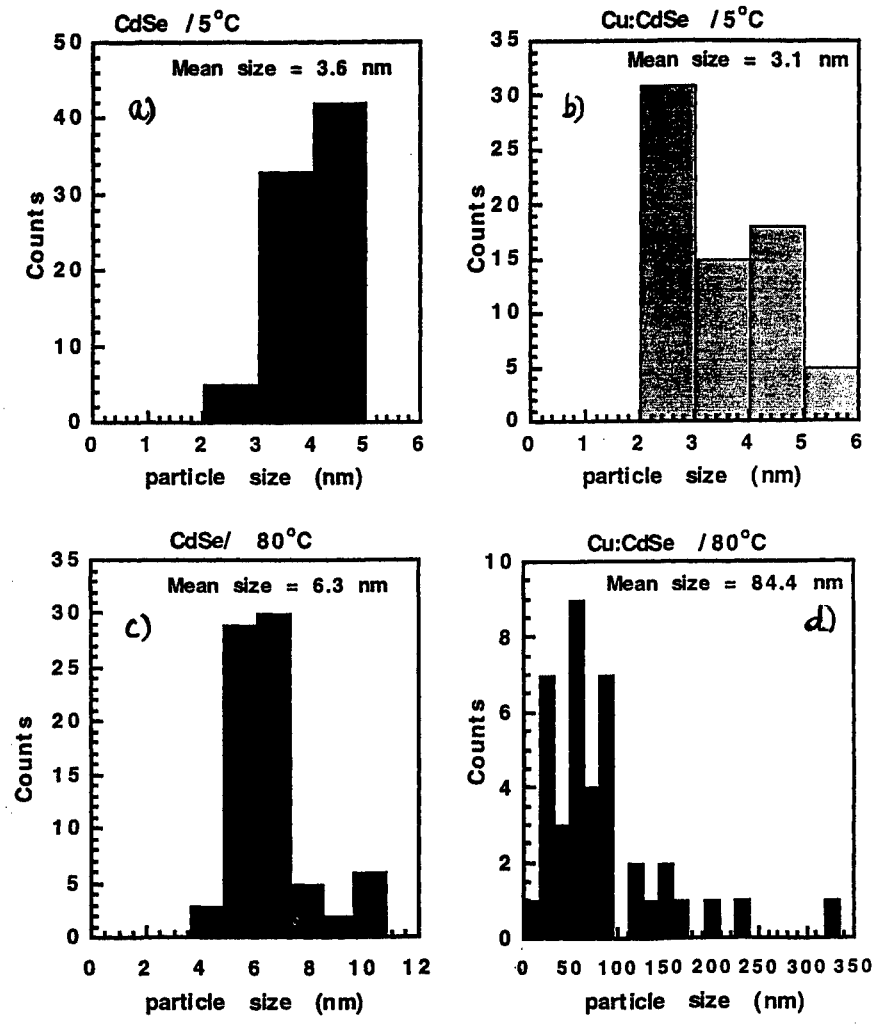


Fig. 5. Particle size distribution from TEM for a) deposited at 5°C b) 1% Cu:CdSe deposited at 5°C c) CdSe deposited at 80°C; d) 1% Cu:CdSe deposited at 80°C.

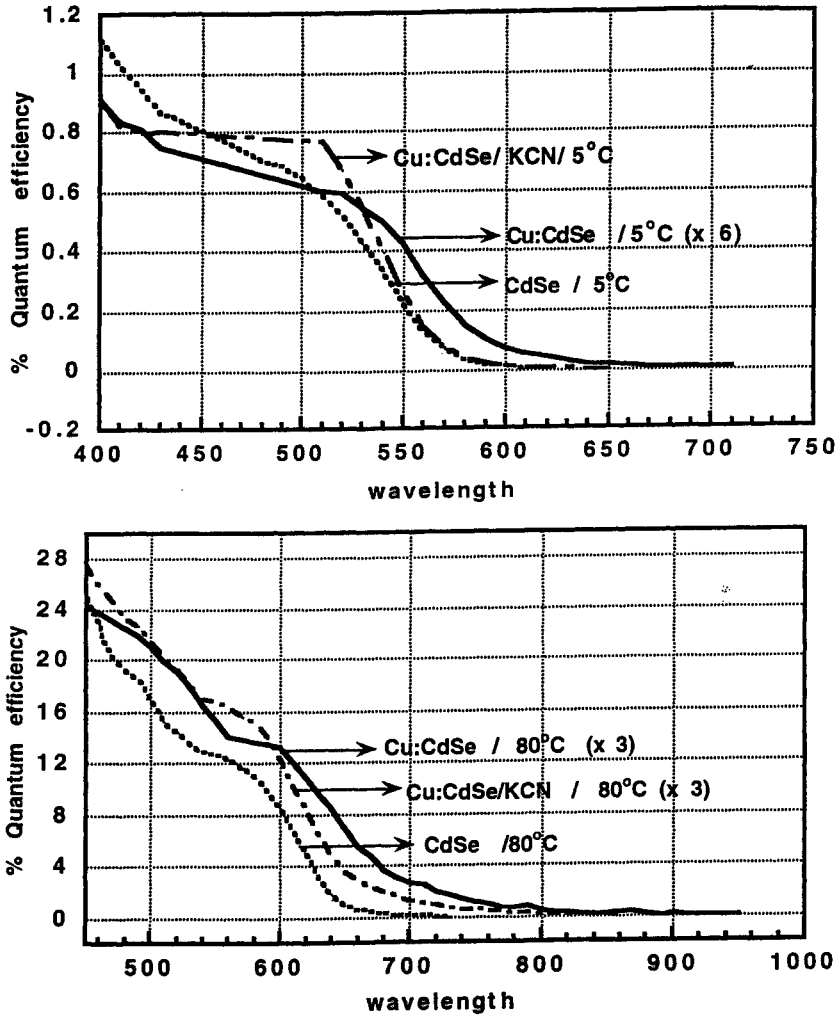
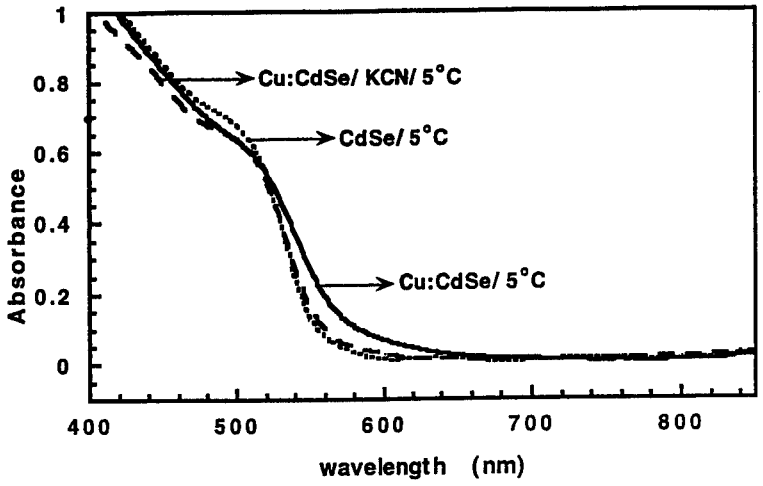


Fig 6. a) Photoelectrochemical spectral response of the copper doped, undoped CdSe and the doped sample treated with KCN. (Deposition temperature 5°C) b) as a), but deposited at 80°C.



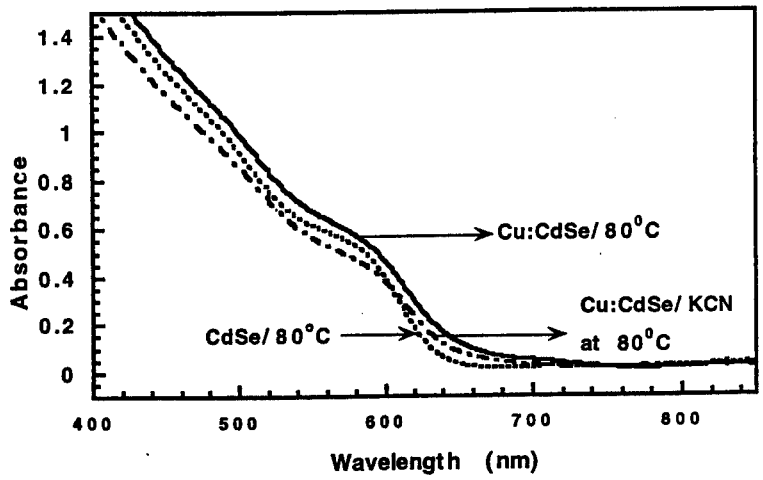


Fig. 7 a) Absorbance spectra of the copper doped CdSe , undoped CdSe and the copper doped CdSe treated with aqueous KCN. The deposition temperature of the sample was 5°C. b) Absorbance spectra of the copper doped CdSe , undoped CdSe and the copper doped CdSe treated with aqueous KCN. The deposition temperature of the sample was 80°C.

CALCULATION OF STRUCTURE AND PROPERTIES OF SEMICONDUCTOR CLUSTERS: IMFLUENCE OF EXTENDED DEFECTS

K. Masuda-Jindo
Department of Materials Science and Engineering, Tokyo Institute of Technology Nagatsuta, Midori-ku, Yokohama 226, Japan

M. Menon, K.R. Subbaswamy
Department of Physics and Astronomy, University of Kentucky, Lexington Kentucky 40506, U.S.A.,

and M. Aoki
Faculty of Engineering, Gifu University,
1-1 Yanagido, Gifu 501-11, Japan

ABSTRACT

The atomistic properties of lattice defects in the nano-scale semiconductor crystallites are studied using the nonorthogonal tight-binding molecular-dynamics (TBMD) method. This nonorthogonal TB theory, with only three adjustable parameters gives values of the energies and bonding distances which are in excellent agreement with the ab initio results for small semiconductor clusters. We apply this type of MD scheme for the calculations of lattice defects (dislocations) and γ-surface in the small semiconductor crystallites with the atomic size of N~200. For comparison, we have also used bond order potential (BOP) method for some of the calculations. We have found that there are marked differences in the properties of lattice defects between those in the bulk and those in the nano-scale crystallites.

INTRODUCTION

Recently, there has been a great interest in the study of nano-scale materials since they provide us a wide variety of academic problems as well as the technological applications [1-3]. In particular, the important experimental findings in this field are the

discovery of carbon nanotubes and the discovery of superconductivity in the alkali-metal doped C_{60} system. The properties of clusters and fine particles are generally quite different from those of the bulk materials, e.g., in magnetism, catalytic activities, elastic properties and optical properties. It has also been observed that the mechanical properties of materials exhibit a strong dependence on the size of the sample, small specimens appear to be stronger than larger ones [4]. In general, the junctions between contacting solids are small, then their mechanical properties are drastically changed from those of the same materials in the bulk. In addition, it has been pointed out that continuum mechanics is not fully applicable as the scale of the materials bodies and the characteristic dimensions of the specimens are reduced.

It is the purpose of the present study to investigate the atomistic properties of nano-scale semiconductor clusters by using the TB type of electronic theory. We calculate the atomic configurations and electronic states of dislocations in C and Si clusters using the TB molecular dynamics method [4-8]. Summarizing the calculated results of the lattice defects, we discuss the atomistic properties of the lattice defects and the related mechanical properties of the nono-scale crystallites, in comparison with those of bulk materials.

APPROACH

The total energy of the system is given by the sum of two terms [6–8]

$$U = U_{el} + U_{rep} = \sum_k \varepsilon_k + (1/2)\sum_{ij} \phi(r_{ij}), \qquad (1)$$

where U_{el} is the sum of the one-electron energies ε_k for the occupied states, and U_{rep} represents the remaining repulsive energy contribution. Here r_{ij} is the separation of atoms i and j. The repulsive potential $\phi(r)$ is taken to be short ranged and varies exponentially with the interatomic distance. To fix absolute energies either a constant or a coordination dependent energy term is added to eq.(1).

In the nonorthogonal TB scheme the characteristic equation is written, in matrix form, as

$$(H - E_n S)C^n = 0, \qquad (2)$$

where C^n is a column vector or LCAO coefficients. **H** is the Hamiltonian matrix and **S** the overlap matrix of the LCAO basis set.

The Hellmann-Feynman theorem for obtaining the electronic part of the force can be obtained from

$$\partial E_n / \partial x = C^{n*}[\partial H / \partial x - E_n \partial S / \partial x]\ C^n / C^{n*} S C^n \qquad (3)$$

where C^n vectors are normalized so that

$$C^* S C = 1. \qquad (6)$$

In the conventional TB (orthogonal) approach, the basis set is presumed to be an orthogonal set $S_{ij}=\delta_{ij}$. In the Slater-Koster scheme the Hamiltonian matrix elements are given in the two-center forms, which are assumed to decrease exponentially with the interatomic distance r_{ij}.

The eigenvalues of a system with nonorthogonal basis set can then be obtained from

$$\det | H_{ij} - E S_{ij} | = 0. \qquad (7)$$

Evaluation of (7) is expedited by the use of the well known Cholesky factorization in which **S** is factored into

$$S = BB^+. \qquad (8)$$

This factorization is always possible provided **S** is positive definite.

The present non-orthogonal basis TB theory involves six parameters, atomic energy terms E_s and E_p, the covalent radius (d_0), the interaction falloff rate α, the nonorthogonality constant K and the repulsive coefficient χ_0. Of these, E_s, E_p, d_0, and two center integrals $V_{\lambda\lambda'\mu}$ are set a priori from Harrison's universal TB scheme. Thus, in the present scheme, there are only three adjustable parameters, α, K and χ_0. These parameters can quite simply be fitted to the related experimental values.

For comparison, we have also used the bond order potential (BOP) method [9], (i, e., TBMD method of orthogonal basis) for some of the calculations of atomic clusters, containing more than ~50 atoms. Within the BOP scheme, the band structure contribution can be estimated by using the formula

$$U_{bond}^{ij} = 2\sum_{\alpha,\beta} H_{i\alpha,j\beta}\Theta_{i\beta,i\alpha}, \qquad (9)$$

$$\Theta_{i\alpha,j\beta}(E_F) = \sum_{n=0}^{\infty} \frac{1}{2}\left[\Gamma_{i\alpha}^n(E_F) + \Gamma_{j\beta}^n(E_F)\right] \xi_{i\alpha,j\beta}^{n+1} \qquad (10)$$

$$\Gamma_{i\alpha}^{n}(E_F) = -\frac{2}{\pi} Im \int_{-\infty}^{E_F} \frac{\partial G_{i\alpha i\alpha}(E+i0)}{\partial \mu_{i\alpha}^{n}} dE, \qquad (11)$$

where the interference terms $\zeta_{i\alpha,j\beta}^{n+1}$ is defined by

$$\zeta_{i\alpha,j\beta}^{n+1} = \langle i\alpha | H^{n} | j\beta \rangle \ . \qquad (12)$$

This type of TB scheme provides us an efficient calculational method that the computational time required for the atomistic simulation is proportional to the number of atoms in the system. This calculational scheme is called as the order of N [O(N)] method.

RESULTS

The discovery of carbon nanotubes with unusual geometric and electronic properties has generated considerable interest [3]. These tubes can be visualized as graphitic sheets rolled up into cylinders giving rise to quasi-one dimensional structures. Firstly, we briefly summarize the MD calculatious for carbon-related materials [5,6].

There are two kinds of carbon nanotubes, with type *A* and type *B* structures. The tube of type *A* is constructed by taking two layers of carbon atoms forming the equatorial belt structure resulting in a hollow tube. The ends of the tube are then terminated by placing the polar caps of C_{70}, resulting in a D_{5h} structure. Tube B can be obtained by rotating the hexagons forming the hollow of tube A by 90° and terminating the ends by placing a polar cap with threefold rotation symmetry, resulting in a D_{3h} structure. In this tube there are a series of carbon-carbon bonds parallel to the tube axis. Tube A showed no appreciable Jahn-Teller distortions or relaxation using our molecular dynamics method. The relaxed structure was found to be metallic with no gap between the highest occupied molecular orbital (LUMO). Tube *B*, however, showed considerable symmetry lowering Jahn-Teller distortions. The relaxed structure was found to be semiconducting, with a gap of 0.7 eV. Tube *B*, was found to be slightly more stable than tube *A* (by 0.5 eV).

We next consider the graphite sheet. Graphite is a prototype sp^2 covalent solid, with two atoms in the unit cell, with nearest-neighbor bond length less than the sum of the covalent radii of the carbon atoms. We obtain a nearest-neighbor bond length of 1.42 Å. The computed band structure is good agreement with accepted band structure calculations. The dynamical matrix for graphite is calculated by special point averaging in the irreducible two-dimensional zone, to be 1588 cm^{-1} for the E_{2g} mode, in excellent agreement with the experimental value of 1582 cm^{-1}. For the A_{2u} mode, we calculate a value of 695 cm^{-1}, in

reasonable agreement with the experimental value of 868 cm^{-1}.

We now turn to the discussions of structural defects in nano-scale materials. In Fig.1, we present the calculated atomic configurations of edge dislocation in two-dimensional (2D) planar C_{70}, C_{92} and C_{142} carbon clusters. The core structure of the edge dislocation is characterized by the five- and seven-memvered rings in the 2D carbon clusters. The excess energies due to introduction of the edge dislocation are also estimated by comparing the energies of carbon clusters with and without the edge dislocations. In Fig. 2, we show the relative stability (excess energies) of the carbon clusters, as a function of the size of the clusters N (number of atoms). The energy is given in unit of eV/atom, relative to that of C_{142} cluster without edge dislocations. One can see in Fig.2 that there are no marked differences in the stability between the clusters with and without edge dislocations. We have also checked that this tendency is also true when we use the BOP method [9], i. e., orthogonal TBMD scheme.

This indicates that the self-energy of the edge dislocation is very small and may become even negative for the certain clusters. Then, we come to the conclusion that the dislocation can be generated spontaneously without sizeable activation energy in the small semiconductor clusters. In other words, the semiconductor clusters can be mechanically deformed more easily compared to the corresponding bulk materials. It may be interesting to check that the similar behavior also occurs in the metallic clusters. The continuum elasticity theory also predicts that the elastic distortion energy of lattice defects depends on the exsistence of the free surfaces due to the so-called image effect [10], compared to those in the infinite crystals. However, the above mentioned cluster size dependence of the self-energy of the dislocation can not be explained within the continuum elasticity theary.

The more detailed information on the glide behavior of the edge dislocation of graphite or 2D carbon clusters can be obtained from the γ-surface calculations [11]. In Fig.3, we present some of the atomic configurations which are formed during the rigid body translation between the upper- and lower-half crystallites, both for (11) and (10) planes. The γ-surface calculations have been performed for larger carbon clusters ~C_{142} and the results of energy barriers as a function of the rigid body translation R_{sh} are shown in Fig.4. Due to the geometry of the clusters, the period of the potential barriers on the (11) and (10) planes are different, and they are $\sqrt{3}/2$ and 3.0, respectively, in unit of the nearest-neighbour distance d_0. One can see in Fig.4 that the rigid body translation on (11) plane occurs more easily compared to that on (10) plane, indicating the easy (11) glide plane.

We now discuss the properties of dislocations in Si clusters, in comparison with the

lattice dislocation in diamond cubic Si crystal [12–14]. Before discussing on the defects in the Si clusters, we briefly summarize the atomic of structures silicon clusters. In Fig.5, we compare the atomic structures of small Si clusters, $Si_7 \sim Si_{10}$, calculated by non-orthogonal TBMD (upper figures) and orthogonal TBMD (lower figures) schemes. In general, two methods predict similar structures. For instance, both TBMD methods predict pentagonal bipyramid for Si_7 cluster. As shown in Fig. 5, however, they give slightly different structures for Si_8 and Si_9 clusters, as shown in Fig.5. In the case of the Si_8 cluster, calculated by non-orthogonal TB the energy minimum corresponds to *a* distorted bicapped octahedron with C_{2h} symmetry, 0.554eV lower than the undistorted D_{3h} bicapped octahedron (Fig.8a of Ref.15). This is consistent with the ab initio calculations, which predicted an energy difference of 0.56eV between the two structures. For Si_9 cluster, C_{2v} distorted tricapped trigonal prism and the C_{3v} tricapped octahedron structures are found to be almost equal energy, in agreement with the LDA calculations .

We now discuss the atomistic properties of larger Si clusters than Si_{10}.

In Fig.6, we present the atomic configurations of Si_{84} cluster both for the unrelaxed (Fig.6a) and relaxed structures(Fig.6b). One notices in Fig.6 that the volume of the Si crystallite decreases drastically during the relaxation process, ~20% reduction compared to those of the unrelaxed structures. This indicates that the overlap between the atomic orbitals increases due to the shrinkage of the crystallite, and it is required to treat the non-orthogonality of the localized orbitals more accurately.

In a diamond cubic crystal, the important dislocations are the 60°, screw and 90° (edge) perfect dislocations [10-12]. The first one dissociates into a 30° and 90° partial dislocations while the others splits into a pair of 30° and 60° partial dislocations, respectively. All the partials are separated by intrinsic stacking faults. These partials, which have line directions along <110> are believed to be reconstructed into a structure with no dangling bonds.

The atomic configurations of 30° partial dislocations in Si_{150} cluster and in bulk Si crystal are shown in Figs. 7a and 7b, respectively. In Fig. 7a, the reconstruction defects "solitons" can be seen near the center of the crystallite. These point singuralities "solitons" in the small crystallites are formed by the atomic reconstruction, which is initiated at the surfaces and then propagate into the interior region of the crystallite. Therefore, depending on the size of the cluster, e.g., for odd number of core atoms(five core atoms in Fig.7a), there remains isolated single point singularity "soliton". In contrast, for the clusters with even number of core atoms, there arises no point singularity along the dislocation line.

The core structure of the dislocation in bulk crystal is calculated as follows: In order to save computational CPU time for the simulation of dislocations in the bulk crystal, the

initial atomic configuration is chosen to be the artificial reconstructed structure. Therefore, in the calculations of dislocations in bulk crystals, no point singularities appear spontaneously in the process of the MD computer simulations. It is noted that in real crystals such point-like singularities do exist as thermodynamical defects, like vacancies in the crystals at finite temperatures. In this respect, the appearance of the soliton in the dislocation line is different in nature from that in the small crystallite.

The kinks on the dislocation line can be modelled by breaking and forming bonds in such a way that the stacking fault is advanced to the next Peierls valley. The kinks A and B as shown in Fig. 7(b), are formed by the side-wide motion of the indivisual kinks after the smallest double kink formation: This type of the double kink nucleation occurs as a thermally activated process and can not be simulated by the computer experiments. Figure 7(b) shows the kink pair structure along the 30 ° partial dislocation in the bulk Si crystal. It is noted that there are two types of kinks along the 30 ° partial. Two five-membered rings are placed through the formation of the double kink by a four- and six-membered ring at A and by a five- and six-membered ring at A and by a five- and six-membered ring at B. The kinks along the 90 ° partial have identical structures and can be described as a trasfer of two six-membered rings to a five-and a seven-membered ring. The kinks are fully coordinated and have the same local geometry for trailing and leading partials. We have found that no gap states associated with the kinks appear in the core of 30°and 90°partial dislocations. This is due to the fact that there are compressed and stretched bonds around the kink sites and compensation occurs for the local electronic states.

CONCLUSION

We have employed a minimal parameter generalized tight-binding molecular dynamics scheme for the calculations of the lattice defects in the semiconductor clusters. It has been shown that inclusion of nonorthogonality in tight-binding theory in conjunction with a judicious choice of parameters can provide results in good agreement with experiment. The scheme is considerably faster than *ab initio* or LDA methods. This has been achieved by incorporationg very few parameters and a simple scaling with distance of the parameters.

In the present study, we have used minimal-basis TBMD scheme, and investigated the properties of lattice defects in the small semiconductor clusters. It has been shown that there are marked differences in the properties of lattice defects in the clusters and those in the bulk crystals. The excess energies of dislocations in the small clusters are very small and often take negative values. The core reconstruction of the dislocation in the small

crystallites occurs in a different manner compared to those in the bulk crystals. These theoretical findings can suggest that the deformation behavior and mechanical properties of the small clusters depend strongly on the size of the clusters and are quite different from those of the bulk materials.

References

[1] H.W. Kroto, J.R. Heath, S'.C. O'Brien, R.F. Curl and R.E. Smally, Nature **318**, p.162 (1985).

[2] W. Kratschmer, L.D. Lamb, K. Fostiropoulos and D.R. Huffman, Nature **347**, p.354 (1990).

[3] S.Iijima, Nature **354**, p.56 (1991).

[4] U. Landman, W. D. Luedtke, N. A. Buruham, and R. J. Colton, Science 248, P454 (1990)

[5] K.Laasonen and R.M. Nieminen, J. Phys: Condens. Mater. **2**, p.1509 (1990).

[6] P. O. Ordejon, D. Lebedenko and M. Menon, Phys. Rev. B50, p.5645 (1994).

[7] M. Menon, and K. R. Subbaswamy, Phys. Rev. **B50**, p.11577 (1994).

[8] M. Menon, E. Richerter and K. R. Subbaswamy, J. Chem. Phys. **104**, p.5875 (1996).

[9] M. Aoki, Phys. Rev. Lett., **71**, p.3842 (1993).

[10] J.P. Hirth and J. Lothe, "Theory of Dislocations" , (McGraw Hill, New York, 1968).

[11] V Vitek, Cryst. Lattice Defects **5**, P. 1 (1975); Prog-Mater. Sci. **36**, p.1 (1992)

[12] H. Alexander and H. Teichler, Mater. Sci. and Tech. **4**, p.249 (1991).

[13] K. Masuda-Jindo, Solid State Phenomena, **37-38**, p.125 (1994).

[14] K. Masuda-Jindo, Superlattices and Microstructures **16**, p.359 (1994); ibid., **20**, p.117 (1996).

[15] K. Raghavachari and C. M. Rohlfing, J. Chem. Phys. **89**, p.2219 (1988).

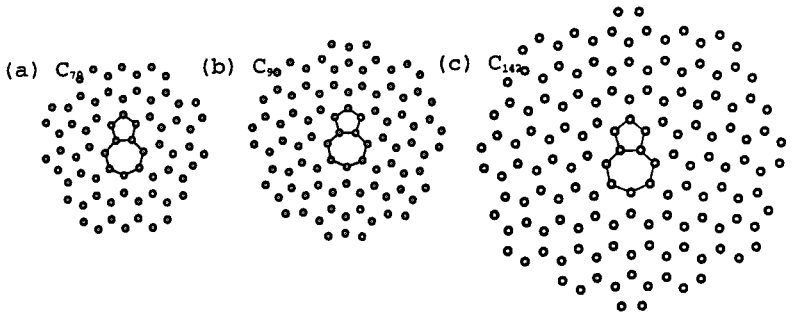


Figure 1: Atomic configurations of edge dislocations in C_{70}, C_{92} and C_{142} clusters.

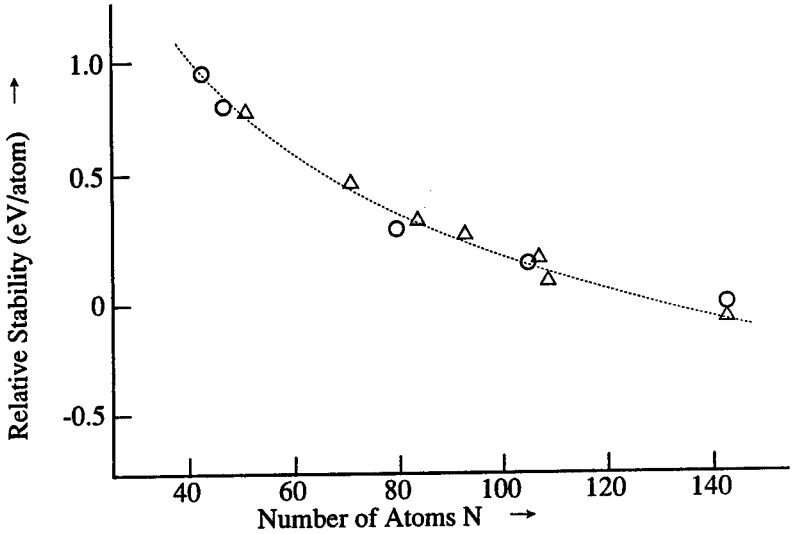


Figure 2: Relative stabilities of carbon clusters with and without edge dislocations are shown by symbols △ and ○, respectively. The energy is given in unit of eV/atom, and the origin is taken to be that of C_{142} cluster without edge dislocation.

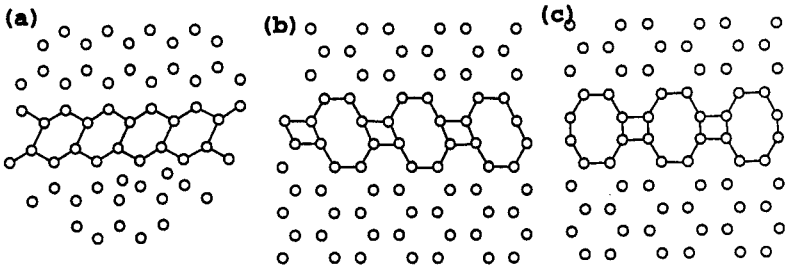


Figure 3: Atomic configurations formed during the rigid body translation: (a) is for (11) plane, while (b) and (c) for (10) plane.

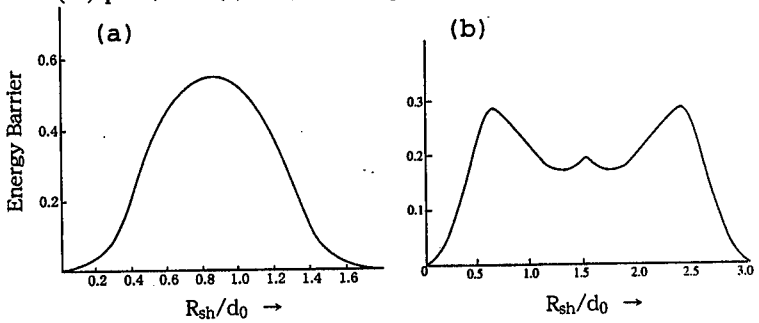


Figure 4: Energy barriers (arbitrary unit) for the rigid body translation on (11) and (10) planes in 2D planar carbon clusters.

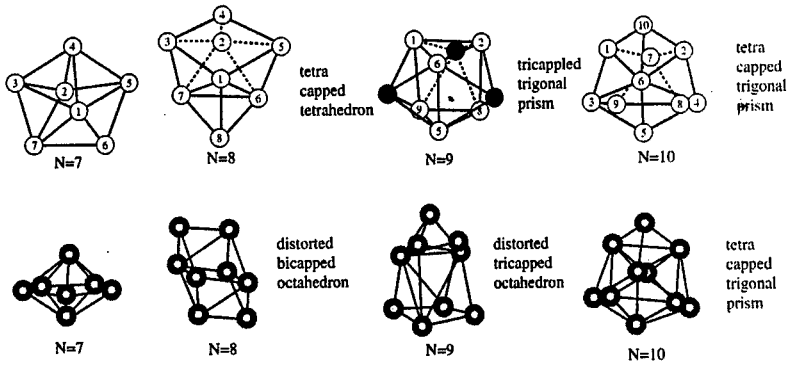


Figure 5: Atomic configurations of small Si clusters, $Si_7 \sim Si_{10}$. Upper (lower) clusters are obtained by orthogonal (non-orthogonal) TBMD.

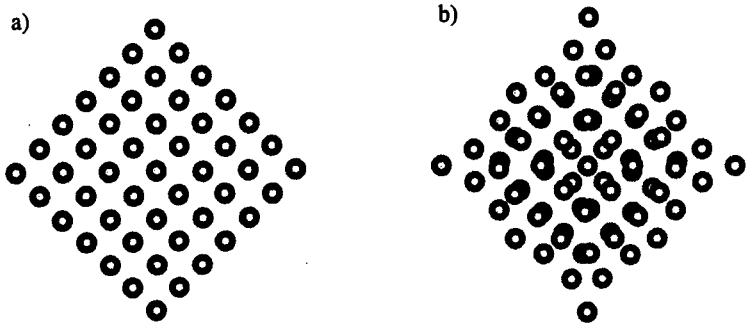


Figure 6: Atomic configuration of Si_{84} cluster: unrelaxed (a) and relaxed structures (b)

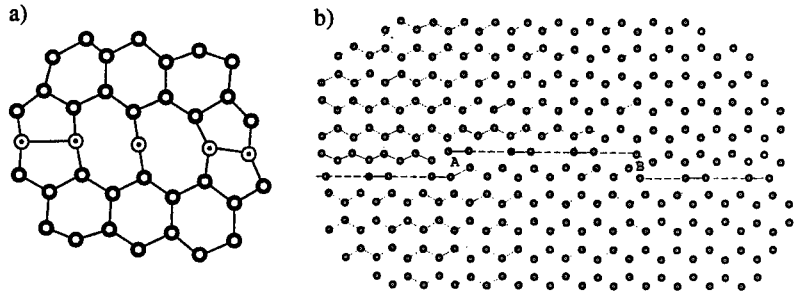


Figure 7: Core structure of 30° partial dislocations in Si cluster (a) and bulk Si crystal (b). Soliton like defect can be seen in a) and double kink A and B in b). In figure a), "core atoms" are shown by symbols ⊙.

COMPUTER SIMULATION STUDY OF THE PROPERTIES OF STRAINED LAYER SUPERLATTTICES BY TBMD AND PPM

K. Masuda-Jindo[a] and R. Kikuchi[b]

[a] Department of Materials Science and Engineering,
Tokyo Institute of Technology,
Nagatsuta, Midoriku, Yokohama 226-8503, Japan
[b] Materials Science and Mineral Engineering,
UC, Berkeley, CA 94720-1760, U. S. A.

ABSTRACT

The atomic and electronic structures of semiconductor heterostructures including steps, misfit dislocations and interface disorder are studied by using the tight-binding molecular dynamics (MD) simulation. Atomic structures of misfit dislocations both edge type 1/2<110>(001) and 60° dislocations in the semiconductor heterostructures, like ZnSe/GaAs(001) and GaAs/Si(001) systems are calculated by using order of N [O(n)] calculational method. It is shown that the deep gap states associated with the misfit dislocations depend strongly on the atomistic configurations of the interface. The path probability method in the statistical physics is used to study the influence of the interface disorder on the electronic properties of the semiconductor heterostructures. It is shown that even for the very early stage of the junction relaxation, the interface electronic properties are strongly influened by the interface disorder.

INTRODUCTION

Recently, considerable attention has been paid to the study of surfaces, interfaces, superlattices, quantum wells and quantum dots because of their relevance to modern device and materials applications [1-6]. Accordingly, the need to work with large lattice mismatched systems becomes increasingly important. However, little is known about the atomistic mechanisms of strained layer epitaxial growth, e.g., thin film growth on semiconductor substrate by molecular beam epitaxy (MBE) [4].

In the present study, we investigate the atomic configurations and electronic states of the semiconductor heterostructures, including steps, misfit dislocations and interface disorder using the TB molecular dynamics method and the recursion method with minimal basis sp^3s^* functions. We report self-consistent calculations of the atomistic and electronic structures of the misfit dislocations, i,e., Lomer edge dislocations and 60° dislocations lying in the plane of interface. The path probability method (PPM) is also used to study the influence of interface disorder on the electronic properties of the semiconductor heterostructures [7,8].

MISFIT DISLOCATION

An experimental investigation of the misfit dislocation networks has been carried out by transmission electron microscopy (TEM) in the GaAlAsP/GaAs, GaAlAsSb/GaSb, InGaAsP/InP, SiGe/Si and Ge/GaAs heterostructures grown on the (001)-oriented substrates [9-11]. Pure edge misfit dislocations in a form of curved lines leaving the interface and greatly deforming misfit dislocation network are frequently observed.

The misfit dislocations are usually named as type-I and type-II dislocations. Type-I dislocations are ideal edge dislocations with Burgers vector 1/2[110] and the line vector [110] or vice versa. Type-I dislocations are "beneficial" because they effectively relax the mismatch stress, but do not degrade the film. However, type-II dislocations, having their Burgers vector 1/2[101], 1/2[$10\bar{1}$], 1/2[011], or 1/2[$01\bar{1}$], and line vectors [110] or [$1\bar{1}0$], lie in the {111} planes and very probably propagate to the film surface as complete dislocations or by dissociating into partial dislocations. If the dissociation of type-II dislocations happens, one partial is left at the interface, but the other partial propagates to the film surface. The areas between these two partials are stacking faults. Furthermore, type-II dislocations have only 70% of the total Burgers vectors in the misfit plane so that they are not so effective to release the strain. Therefore, the occurence of type-II dislocations should be minimized because it is harmful to the film quantity. The former type-I misfit dislocations are introduced either by the reaction of two 60° dislocations or during island growth and are effectively sessile. The critical issue on heteroepitaxy technology is to look for an efficient way to release the misfit strain by predominately type-I dislocations or to suppress type-II dislocations as much as possible.

APPROACH

We use TBMD method to simulate atomic configurations of semiconductor heterostructures and core structures of misfit dislocation. The total energy of the system can be given by [12,13]

$$H = p_i^2/2m + 2\sum_k \varepsilon_n(\mathbf{k}) + U_{rep}\,, \qquad (1)$$

where the first term represents the ionic motion energy and $\varepsilon_n(\mathbf{k})$ are the single-particle TB energies (band structure energy) of the occupied states. The last term U_{rep} is a quantum mechanical repulsion which can be written as $U_{rep} = E_{ii} - E_{ee}$, where E_{ee} describes the electron-electron interaction and corrects the double counting of the electron-electron interactions in E_{bs} and E_{ii} is the Coulomb interaction among bare cores.

Following the conclusions by Majewski and Vogl for the isotropic expansion of crystalline sp-bonded materials [12,13], it has been proposed that an useful expansion for E_{pot} in the above eq.(1) is given by

$$E_{pot} = E_{bs} + \{\Phi_1 \exp\{-(r_{ij}-r_0)/a\} + \Phi_2\, r_0/r_{ij}\}\,, \qquad (2)$$

where the first band structure energy term is calculated by a minimal sp^3s^* basis set with nearest-neighbour interactions and two-centre approximation [12]. The matrix elements are scaled upon the interatomic distance as r_{ij}^{-2} according to Harrison's rule. The orbital-overlap repulsive potential is written in the Born-Mayer form where r_0 is the equilibrium interatomic distance. Only nearest-neighbour interactions are taken into account. The last term describes the charge transfer effects, which include both the intra-site repulsion and the intersite Coulomb attraction: the sum of such contributions results into a repulsive potential of the form of eq.(2).

The atomic relaxation calculation is performed by using the quenched molecular dynamics method, i.e., by integrating the Newtonian equation of motion with the central difference algorithm [5,6]. The path probability method is also applied to study the interface disorder due to interdiffusion at the semiconductor heterostructures [7,8]. It is known that cationic intermixing at the interface takes place during the growth process, and this influences quite significantly on the vibrational properties of ultra thin superlattices and Raman spectroscopy has been used to investigate the interface quality [14, 15]

RESULTS

Heterostructure including misfit dislocation

The atomistic irregularities, such as misfit dislocations, threading dislocations, steps and interface disorder of constituent atoms are important factors in discussing the quality of the semiconductor interfaces. Steps and interface disorder exist at the semiconductor interfaces, and their control is quite important in semiconductor heteroepitaxy technology. For instance, it has been reported that the predominant occurrence of the misfit dislocation depends strongly on the condition of the substrate surface, i.e., flat or stepped surfaces. On the other hand, it is known that the interface disorder (due to cationic diffusion) has important consequences for the vibrational properties of ultra thin superlattices [16-18].

In Fig.1(a), we present the atomic configurations of misfit dislocations in ZnSe/GaAs(001) semiconductor heterostructures, with double stepped interfaces. Also shown in Fig.1(b) represents the core structure of 60° shuffle set dislocation located at the interface of the ZnSe/GaAs(001) heterostructure. The details of the calculation method of the core structure of the misfit dislocations has been presented in our previous study [5,6].

In the present calculation, the valence band discontinuities ΔE_v at heterostructures are estimated by using the simplified local charge-neutrality condition [19-20]. Within this scheme, the charge transfers are restricted to the interface atom pairs and the net electron transfer $[=_N_1(\Delta)+\delta N_2(\Delta)]$ vanishes for the self-consistent treatment of compound semiconductors. We have also used this scheme with minor modification for the calculation of ΔE_v of ZnSe/GaAs(001), ZnTe/GaAs(001) and GaAs/Si(001) heterojunctions, both flat and stepped interface configurations. In Fig-2(a), we present the electronic DOS of perfect ZnSe(A,B) and ZnTe (C,D) crystals, calculated by using the recursion method with sp^3*-basic functions.

Within the TB recursion theory, the dislocation-induced bound electron states can be detected in the density of states (DOS) by additional sharp spectral lines in the band gap region. The present recursion method of the sp^3s^* basis function [5,6] can reproduce correctly the structures in the DOS curves of the perfect compound semiconductors like ZnSe and ZnTe (compared to those calculated by the k-space tetrahedron method). In Fig.2(b), A and B show the local DOS of a Zn-site at the first layer of the ZnSe/GaAs heterojunctions, with flat and stepped interfaces, respectively. In Fig.2(b), C and D show the corresponding results for the second layer Se-sites. We have performed similar calculations for ZnTe/GaAs(001) heterostructures. Also shown by dashed curves in A-D

of Fig.2(b) are the electronic states associated with the type I edge dislocations in the ZnTe/GaAs(001) heterostructures. We have found a single bound state associated with the misfit dislocation in ZnTe/GaAs, in contrast to the two prominent deep levels D_1 and D_2 in ZnSe/GaAs(001) systems [5,6]. In these electronic structure calculations, it is remarkable that a prominent deep gap states disappears when the misfit dislocation is located at the double step position, as shown in C and D of Fig.2(b) both for ZnSe/GaAs(001) and ZnTe/GaAs(001) systems. The disappearance of the deep gap states at the step position can be considered to arise from the facts that (i) the atomic species of the nearest-neighbours are different from those of the flat surface, and (ii) the valence band discontinuity becomes slightly changed (larger) at the step position.

In Fig.3, we present the local DOS in the core region of the 60° shuffle set dislocation located at the interface of ZnSe/GaAs(001) heterostructure: Figures a, b, c, d, e, f, and g are the DOS on the corresponding atoms A~G depicted in the inset of the figure. One can see in Fig.3 that prominent deep levels appear in B, E, F and G sites depending on the relative position of the core of 60 ° shuffle set dislocations. In view of the fact that the 60° dislocation lies on the {111} plane, it is expected to tend to propagate to the film surface, and behaves as threading dislocations: We have found that this type of threading dislocations produces the deep gap states, and is harmful for the electronic and optical device applications.

In view of the fact that the degradation of ZnSe/GaAs(001) heterostructures is enhanced strongly due to the presence of the misfit dislocations [4], the above mentioned theoretical findings are of great significance. The present theoretical findings can suggest that by controlling the atomic geometry of the semiconductor heterostructures (flat or intentionally tilted step-rich interfaces), one can design more efficient semiconductor heterostructures with desired properties using the "step technology".

Interface Disorder

Atomic species disorder at the interface is also an important ingredient in discussing the properties of the semiconductor heterostructures. It is noted that the semiconductor heterostructures are always not in equilibrium, and therefore the junction profile can be changed by thermal means or by elastic stresses, as schematically shown in Fig. 4. The atomic relaxation at the semiconductor heterostructures can be discussed using the non-equilibrium irreversible statistical mechanical approach, path probability method (PPM) [7,8]. In contrast to the continuum theories, the PPM takes into account the local correlations of atoms, which are significant when the concentration gradient is large. We apply the pair approximation of PPM to the junction relaxation of the semiconductor

heterostructures.

We work with a binary compound with vacancies, i = 0, 1 and 2 are used to designate a vacancy, an A atom and a B atom, respectively. We use two classes of variables, the state variables and the path variables, which are defined as follows: The variables which specify the state of the system at time t are called the state variables, and we use point variable $x_n(i;t)$ and pair variable $y_v(i,j;t)$, where i and j are 0, 1 or 2, $x_n(i;t)$ is the probability of finding a species i at an n-th lattice point at time t, where as $y_v(i,j;t)$ is the probability of finding i on an n point and j on an adjacent $(n+1)$ point at time t. There are geometrical relations among these variables

$$\sum_j y_{v-1}(j,i;t) = x_n(i;t) = \sum_j y_v(i,j;t) \ . \tag{3}$$

The normalizations of these probability functions are given by

$$1 = \sum_i x_n(i;t) = \sum_i \sum_j y_v(i,j;t) \ . \tag{4}$$

We now introduce path variables. In the pair approximation, we use the point path variables, X's, and the pair path variables Y's, which are written in the upper case letters to be distinguished from the state variables. The meaning of $X_n(i;0)_R$ is the probability of finding such an n lattice point that was occupied by an i atom at time t and becomes vacant (0) at $t+\Delta t$ with the i atom having moved to the right. The subscript L is when the atom moves to the left. For the sake of brevity, we do not write t and $t+\Delta t$ explicitly below, unless needed. Then, It can be shown that between x's and X's variables,

$$x_n(i;t) = X_n(i;i) + 2\left(X_n(i;0)_L + X_n(i;0)_R\right) \qquad \text{for } i \neq 0 \tag{5-a}$$

$$x_n(i;t+\Delta t) = X_n(i;i) + 2\left(X_n(i;0)_L + X_n(0;i)_R\right) \tag{5-b}$$

$$x_n(0;t) = X_n(0;0) + 2\sum_{i\neq 0}\left(X_n(0;i)_L + X_n(0;i)_R\right) \tag{6-a}$$

$$x_n(0;t+\Delta t) = X_n(0;0) + 2\sum_{i\neq 0}\left(X_n(0;i)_L + X_n(0;i)_R\right) \tag{6-b}$$

In the PPM procedure, the path probability function (PPF) is given in terms of the path variables, and then we maximize the PPF to derive the most probable path relations, to obtain the differential equations to describe how the system changes in time. Usually the step of writing the PPF is skipped, because the most probable path relations can be written down based on intuitive interpretation. In the present calculation, we take

into account the energy levels after an atomic jump as well as those before the jump. Secondly, we impose an additional new constraint to the path variables.

The PPF P is made of three factors, which we write P_1, P_2 and P_3. Here often, N is referred to as the number of lattice points on a plane parallel to the boundary, and $2N$ is the number of bonds for each ν position. The first factor P_1 is for the unit jump probabilities :

$$\ln P_1(t,t+\Delta t) = 2N\sum_{\nu}\sum_{i}\left(Y_V(i0;0i)_R + Y_V(0i;i0)_L\right)\ln(\Delta t\Theta_i) \tag{7}$$

In the last factor, we used

$$\Theta_1 \equiv \theta_1 \exp(-\beta U_i), \tag{8}$$

where θ_i is the oscillation frequency, which we may also call the attempt frequency, of an i atom, and U_i is the activation energy for an i atom to jump into a neighboring vacancy. We assume these are independent of the variables, since this assumption is appropriate at this level of the theory.

The second factor P_2 is for the activation energy to be supplied from the heat bath P_2 can be given in the following form:

$$P_2(t,t+\Delta t) = \exp\left(-\beta\Delta E_{\text{supplied}}\right), \tag{9}$$

where $\Delta E_{\text{supplied}}$ denotes the energy to be supplied to break bounds. Specifically, we write be supplied to break an i-j bond as ε_{ij} (>0), so that

$$\Delta E_{\text{supplied}} = 2N\sum_{\nu}\sum_{ij}\varepsilon_{ij}\left(\left(2Y_V(ij;0j)_L + Y_V(ij;0j)_R\right) + \left(Y_V(ij;i0)_L + 2Y_V(ij;i0)_R\right)\right) \tag{10}$$

The third factor P_3 is the degeneracy number, and is derived from the CVM pair expression for the coordination 4. We write it for an ensemble of M systems as:

$$\left(P_3(t,t+\Delta t)\right)^M = \prod_{\text{nor }\nu}\left(\frac{\left(\{\text{Point at n}\}_M\right)^3}{\left(\{\text{Pair at v}\}_M\right)^2 (M!)}\right)^N, \tag{11}$$

where { } is the standard CVM notation to represent a product of factorials. In rewriting P_3 in the logarithmic form using Stirling's approximation, we use the $L(x)$ function defined as

$$L(x) \equiv x \ln x - x. \tag{12}$$

The explicit expression of the logarithm of (11) is

$$N^{-1} \ln P_3(t, t+\Delta t) = 3\sum_n \left(Ln(X_n)\ \text{TERMS}\right) - 2\sum_v \left(Ln(Y_v)\ \text{TERMS}\right) + \sum_n 1. \tag{13}$$

Note that the last term, the sum over 1, cancels other terms resulting from -x in eq. (12). The first sum in eq. (13) is

$$\begin{aligned}\left(Ln(X_n)\ \text{TERMS}\right) \equiv \sum_i L(X_n(i;i)) + 2\sum_{i\neq 0}\left(L(X_n(i;0)_L) + L(X_n(i;0)_R)\right) \\ +2\sum_{i\neq 0}\left(L(X_n(0;i)_L) + L(X_n(0;i)_R)\right)\end{aligned} \tag{14}$$

Note that in this expression all X variables are summed. We may write X's in terms of the exchange variables. Considering that eq. (13) is summed over n, we can rewrite (14) as

$$\left(Ln(X_n)\ \text{TERMS}\right) \equiv \sum_i L(X_n(i;i)) + 4\sum_{i\neq 0}\left(L(Y_v(0i;i0)_L) + L(Y_v(i0;0i)_R)\right) \tag{15}$$

The second term of eq. (13) becomes

$$\begin{aligned}\left(Ln(Y_v)\ \text{TERMS}\right) \equiv \sum_{i;j} L(Y_v(ij;ij)) + \sum_{i\neq 0}\left(L(Y_v(0i;i0)_L) + L(Y_v(i0;0i)_R)\right) \\ + \sum_{i\neq 0,\, j\neq 0}\left(L(Y_v(ij;i0)_L) + 2L(Y_v(ij;i0)_R) + 2L(Y_v(ij;0j)_L) + L(Y_v(ij;0j)_R)\right) \\ + \sum_{i\neq 0,\, j\neq 0}\left(2L(Y_v(i0;ij)_L) + L(Y_v(i0;ij)_R) + 2L(Y_v(i0;00)_L) + L(Y_v(i0;00)_R)\right) \\ + \sum_{i\neq 0,\, j\neq 0}\left(L(Y_v(0i;ji)_L) + 2L(Y_v(0i;ji)_R) + L(Y_v(0i;00)_L) + 2L(Y_v(0i;00)_R)\right) \\ + \sum_{i\neq 0}\left(L(Y_v(00;i0)_L) + 2L(Y_v(00;i0)_R) + 2L(Y_v(00;0i)_L) + L(Y_v(00;0i)_R)\right).\end{aligned} \tag{16}$$

In writing the PPF P, we expect that we maximize it to derive the most probable path. We differentiate with respect to all the exchange and the side-exchange variables. Since they are not independent, the constraint requirement among them are taken into account by adding the Lagrange multipliers $C_{\lambda\gamma}$ to P. We have listed all necessary expressions to write in P, which, however, is lengthy and its total expression is not written here.

Different from the CVM treatment, we do not normalize the path variables to unity. Instead, the conditions we have for the path variables are that their projections to time t are

equal to the given state variables at t. These constraints are used to make the *stationary* path variables as dependent on the rest of Y's. Namely, we have for i≠0 and j≠0

$$Y_V(ij;ij) = y_V(ij;t) - Y_V(ij;i0)_L - 2Y_V(ij;i0)_R - 2Y_V(ij;0j)_L - Y_V(ij;0j)_R \quad (17)$$

$$Y_V(i0;i0) = y_V(i0;t) - \sum_{j\neq 0}\left(2Y_V(i0;ij)_L + Y_V(i0;ij)_R - Y_V(i0;0i)_R - 2Y_V(i0;00)_L - Y_V(i0;00)_R\right) \quad (18)$$

$$Y_V(0i;i0) = y_V(0i;t) - \sum_{j\neq 0}\left(Y_V(0i;ji)_L + 2Y_V(0i;ji)_R - Y_V(0i;i0)_L - Y_V(0i;00)_L - 2Y_V(0i;00)_R\right) \quad (19)$$

$$Y_V(00;00) = y_V(00;t) - \sum_{i\neq 0}\left(2Y_V(00;0i)_L + Y_V(00;0i)_R + Y_V(00;i0)_L + 2Y_V(00;i0)_R\right) \quad (20)$$

Also one can dirive the following relations:

$$X_n(i;i) = x_n(i;t) - 2\left(Y_{V-1}(0i;i0)_L + Y_V(i0;0i)_R\right) \qquad \text{for } i \neq 0 \quad (21)$$

$$X_n(0;0) = x_n(0;t) - 2\sum_{i\neq 0}\left(Y_V(0i;i0)_L + Y_{V-1}(i0;0i)_R\right) \quad (22)$$

The path probability function (PPF) is the variational function from which the most probable path is derived, in the sense as the free energy is the variational function from which the equilibrium state in derived. The PPF, derived in the first step of the formulation, contains not only for the most probable path but also for fluctuated path. Then, the PPF is maximized to derive the most probable path, which describes the macroscopically observed direction of change of the system. The most probable path leads to the set of kinetic equations to describe the evolution of the system.

The important problem in the calculation of the junction relaxation is to find the driving force for the atomic flux: The composition gradient or chemical potential term $\Delta\mu_n/\Delta n$ may not always be interpreted as the driving force for the atomic flux. In order to understand the driving force, one must consider the kinetic equation. For instance, the atomic flux through the specific bond $\nu = 1.5$ is written as

$$J_v(1)_R = Y_v(1)_R - Y_v(1)_L \quad (23)$$

where $Y_v(1)_R$ is the probability of a species #1 to jump from an n = 1 point to an adjacent n = 2 point towards right through the $\nu = 1.5$ bond, and $Y_v(1)_L$ is the reverse jump towards left. The most probable path in the pair approximation of PPM leads to the following expressions

$$Y_v(1)_R = \Delta t \Theta_1 y_v(10;t)\, B\{v-1,n,v;t\}\, G\{v,n+1,v+1;t\} \quad (24)$$

$$Y_v(1)_L = \Delta t \Theta_1 y_v(01;t)\, G\{v-1,n,v;t\}\, B\{v,n+1,v+1;t\} \quad (25)$$

where Θ_1 is the attempt frequency factor including the activation energy contribution. The bond-breaking contribution $B\{v-1,n,v;t\}$ and the bond-forming contribution $G\{v-1,n,v;t\}$ depend on the pair variables $y_{v-1}(ij;t)$, $y_n(ij;t)$, $y_v(ij;t)$ and $x_a(i;t)$ as indicated by the arguments [7,8].

One of the example calculations of the relaxation of semiconductor heterojunction is presented in Fig.5. We have found the following characteristic features:

(i) At the initial stage of relaxation of a sharp profile, overshooting of the profile occurs.

(ii) Near a sharp junction profile, the atom flux changes sign during relaxation.

(iii) Near the junction, the chemical potential gradient becomes zero at a different time t* from that of the atom flux. There is a time period in which atoms do not flow downhill along the chemical potential gradient.

(iv) The local chemical potential gradient in non-equilibrium state depends not only on the density gradient but also on atomic pair correlation.

(v) While the overshooting is occurring, the free energy of the entire system monotonically decreases.

(vi) The overshooting can be understood by a kinetic reasoning as due to the repulsion of atoms.

Even for the very early stage of the junction relaxation, i.e., after ~ 100 time steps, the electronic states associated with the misfit dislocations are influenced quite significantly by the interface disorder compared with those located at the sharp interface. We have found that when one of the atoms in the core of the misfit dislocation is changed by interface relaxation, the dislocation induced gap state is drastically altered, it even leads to the disappearance of the gap states. Therefore, the appearance of electronic bound states of the misfit dislocations must be discussed by using the precise knowledge of atomic species in the core region of the misfit dislocations.

In the present study, we have considered semiconductor heterostructures with ideal interfaces as well as those with interface disorder, by allowing cationic intermixing, which very likely takes place during the growth process. We have found that the interface disorder influences quite significantly the electronic properties of the semiconductor heterostrucutres. The present atomistic simulation is also of significance in view of the

recent experimental results that the interface disorder is much larger in (113) heterostructures than in (001) ones.

REFERENCES

[1] Semiconductors and Semimetals, edited by R.K. Willardson and A.C. Beer (Academic, New York, 1987), Vol.24.

[2] Proceedings of PCSI [J. Vac. Sci. Technol. **5**, p.922 (1987)].

[3] A.-B. Chen, Y.-M. Lai-Hsu and W. Chen, Phys. Rev. **B39**, p.923 (1989).

[4] W. Bala, M. Drozdowski and M. Kozielski, phys. stat. sol., **130a**, K195 (1992).

[5] K. Masuda-Jindo, Mater. Sci. Forum, **143-147**, p.549 (1994).

[6] K. Masuda-Jindo, Microstructures and Superlattices **20**, p.117 (1995).

[7] L.-Q. Chen and R. Kikuchi, Scripta Metall. et Mater., **30**, p.53 (1994).

[8] R. Kikuchi and H. Sato, J. Chem. Phys. **53**, p.2702 (1970).

[9] R. Beanland, D.J. Dunstan and P.J. Goodhew, Adv. Phys. **45**, p.87 (1996).

[10] K. W. Schwarz, Phys. Rev. Lett., **78**, p.4785 (1997).

[11] A.E. Romanov, W. Pompe, G. Beltz and J.S. Speck, phys. stat. sol., **198(b)**, p.599 (1996).

[12] J.A. Majewski and P. Vogl, "The Structure of Binary Compounds", North Holland, Amsterdam, p.287 (1989).

[13] C. Molteni, L. Colombo and L. Miglio, Europhys. Lett., **24**, p.659 (1993).

[14] B. Jusser and, F. Alexandre, D. Paquet and G. Le Roux, Appl. Phys. Lett., **47**, p. 301 (1985) E.P. O'Reilly and J. Robertson, Phys. Rev. **B34**, p.8684 (1986).

[15] J. Melendeg, A. Mazuelas, P. S. Dominguez, M. Garria, M. I. Alonso, G. Armelles, L. Tapfer, and F. Briones, Appl. Phys. Lett., **62**, P. 1000 (1993)

[16] P. Castrillo, L. Colombo and G. Armelles, Phys. Rev. **B49**, p.10362 (1994)

[17] R. Fisher et al., J. Appl. Phys. **60**, p.1640 (1986).

[18] Y.H. Lo, M.C. Wu, H. Lee and S. Wang, Appl. Phys. Lett., **52**, p.1386 (1988).

[19] C. Priester, G. Allan and M. Lannoo, Phys. Rev. **B33**, p.7386 (1986).

[20] L. Lefegre, M. Lannoo, C. Priester, G. Allan and C. Delerue, Phys. Rev. **B36**, p.1336 (1987).

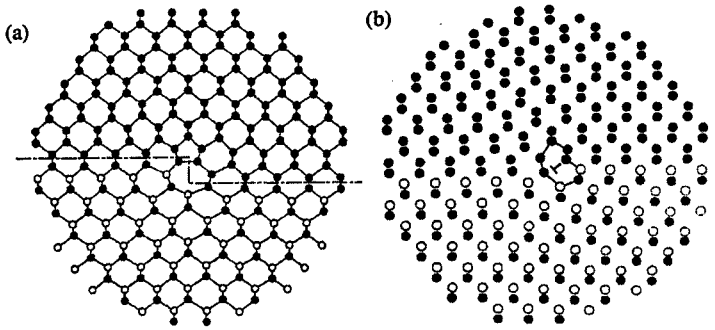


Figure 1: Atomic configurations of semiconductor heterostructures at a (001) interface of a zincblende crystal. (a) misfit dislocation at a double step, (b) 60° dislocation at the interface.

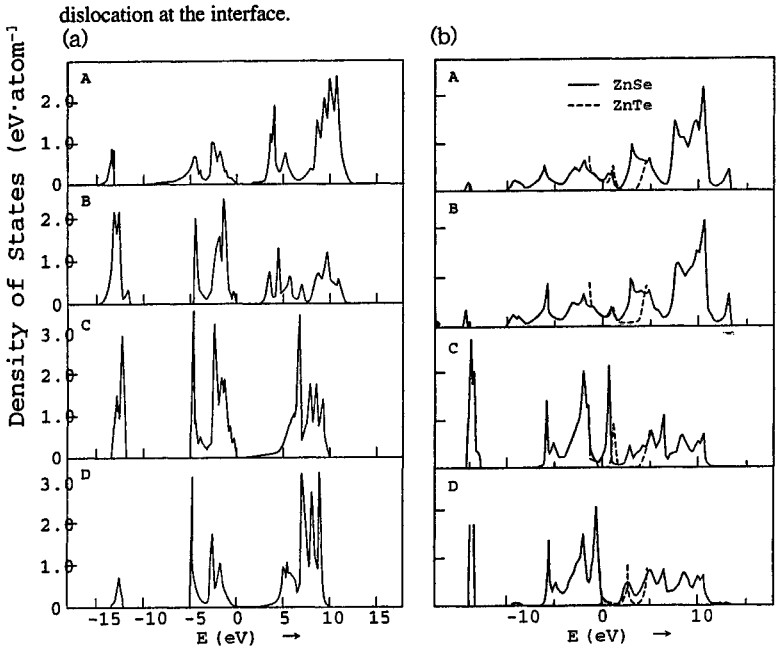


Figure 2: (a): Electronic DOS of perfect ZnSe and ZnTe crystals, A and B are Zn and Se, and C and D are Zn and Te in ZnSe and ZnTe, respectively. (b): Local electronic DOS in the core of type I edge dislocation, shown in Fig.1(a).

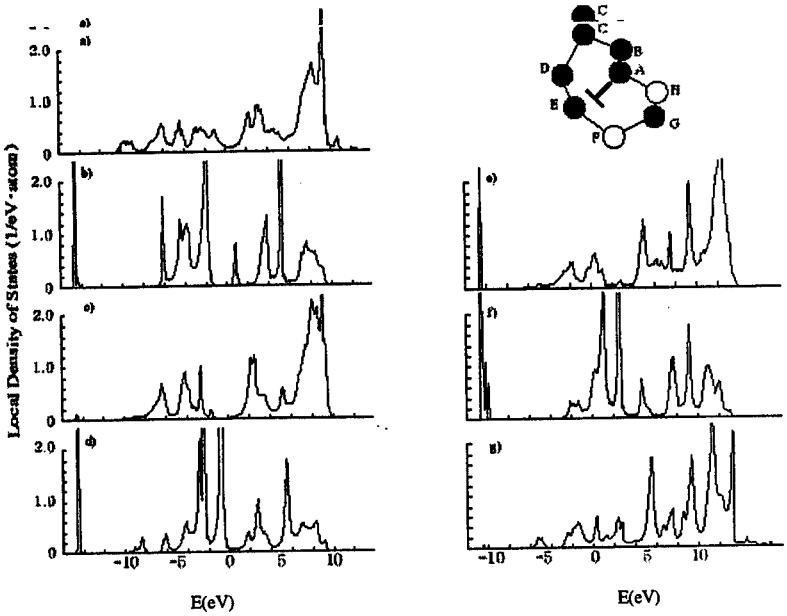


Figure 3: Local electronic DOS in the core of shuffle-set 60° dislocation in a ZnSe/GaAs(001) heterostructure. a, b, c, d, e, f and g represent local DOS of the corresponding sites (A~G) shown in the inset.

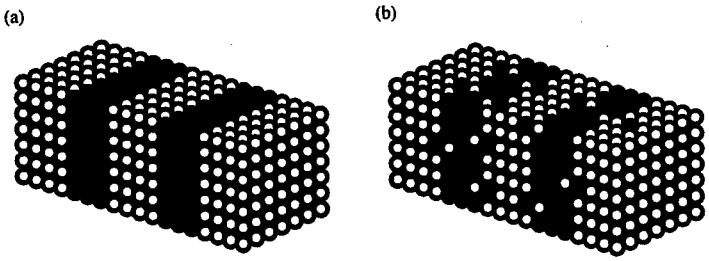


Figure 4: Schematic drawings of semiconductor superlattices ; (a) sharp interface and (b) diffuse interface.

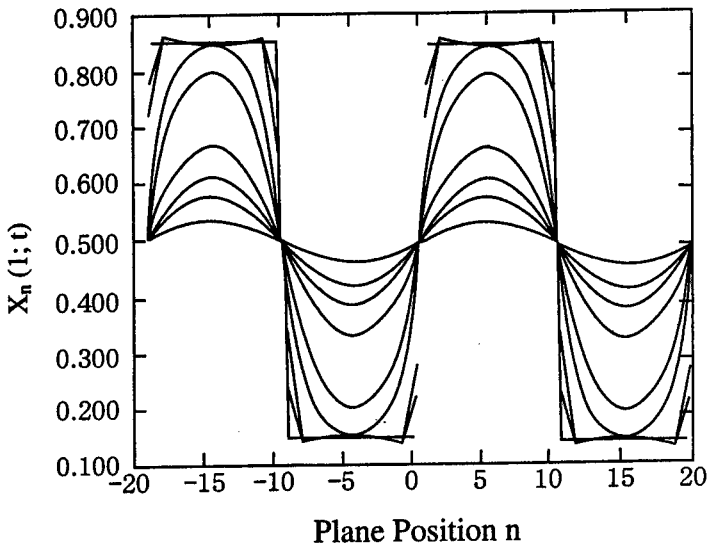


Figure 5: Relaxation of composition profile obtained by integration. The initial composition is taken to be $x_n(1)=0.15$ at the flat bottom, and 0.85 at the flat top. Other curves are at the time steps 450, 1000, 10000, 30000, 100000, 150000 and 30000 in an arbitrary time interval.

INTERFACE LIGHT ABSORPTION IN NANOSTRUCTURES

L. Braginsky
Institute of Semiconductor Physics
630090 Novosibirsk, Russia

and V. Shklover
Laboratory of Crystallography, ETH Zentrum
CH-8092 Zürich, Switzerland

ABSTRACT

Light absorption at the semiconductor boundary is analized. It is found that the posibility of the electron momentum nonconservation at the interface can lead to essential enhancement of absorption. Influence of the interface roughness is considered. The size dependence of the absorption is estimated.

I. INTRODUCTION

It is well known that the direct interband electron transitions is the main mechanism of light absorption in pure semiconductors. These transitions are direct owing to the momentum conservation low for the excited electron. The momentum, which this electron obtains from the light wave ($\sim \pi\hbar/\lambda_0$, where λ_0 is the wavelength of the light), is small in comparison with the electron momentum in the crystal ($\sim \pi\hbar/a$, where a is the lattice constant). It is clear, however, that the momentum is not conserveing if the absorption takes place at the crystal boundary or at the interface between two crystals. The possibility of indirect electron transitions at the interface can result in enhancement of the absorption. This means that the considerable enhancement of light absorption has to be observed in porous and microcrystalline semiconductors where the share of the interface atoms is sufficiently large.

This interface mechanism of light absorption becomes most important if indirect electron transitions are more preferable than the direct ones. This happens, first, in indirect-band-gap semiconductors where the electron transition to the side

valley in the bulk should be accompanied by the electron-phonon or electron-impurity interaction. This happens also in direct-band-gap semiconductors if the density of electron states in one of the bands (valence or conduction) essentially exceeds the density of states in another band.

Both possibilities are considered in this paper. We consider the frequency dependence of the absorption at the fundamental absorption edge and estimate the relative value of the interface absorption.

I. THE MODEL

We consider the light absorption at the surface of the semiconductor quantum dot or the microcrystallite embedded in an insulator media. For definiteness, suppose that this microcrystallite is a cylinder, and assume each size of this cylinder to be large in comparison with the lattice constant. On this assumption the envelope function approximation is valid. Moreover, this assumption allows us to consider the light absorption as the inelastic scattering of the electron at the interface if the electron wavelength is sufficiently small. We introduce the Cartesian coordinate system, where the z axis coincides with the axis of the cylinder, and assume that semiconductor occupies the region $z < 0$.

The probability for the photon to be absorbed in the crystallite is

$$\eta = \frac{(2\pi\hbar)^2 e^2}{m_e^2 c\omega n S} \sum_{\mathbf{p},\,\mathbf{q}} \left| < f|\frac{\partial}{\partial z}|i > \right|^2 \delta(\varepsilon_c - \varepsilon_v - \hbar\omega), \tag{1}$$

where $\hbar$, e, m_e, and c are the fundamental constants, ω is the photon frequency, n is the refraction index, S is the area of the crystallite side $z = 0$ where the absorption is considered, $\mathbf{p}$ and $\mathbf{q}$ are the electron momenta, p and q are their z components, $\varepsilon_c(\mathbf{q})$ and $\varepsilon_v(\mathbf{p})$ are the energies of the electron in the conduction and valence bands. The electric field of the light is directed along the z axis; $i >$ and $f >$ are the wave functions of the electron before the excitation (in the valence band) and after it (in the conduction band) correspondingly. Wave functions $i >$ and $f >$ depends on the band structure of the crystallite and the boundary conditions for the envelope wave functions at the interface between the crystallite and the insulator.

To consider the Coulomb interaction, which occurs between the exited electron and the hole in the valence band, within the framework of our model, we have to input the weight factor $\Phi(\gamma) = \pi\gamma \exp \pi\gamma/(\sinh \pi\gamma)$ [where $\gamma = (qa_B/\hbar)^{-1}$, and a_B is the effective Bohr radius] into the sum (1) [1].

It is possible to change summation in Eq. (1) by integration over the electron

energy and parallel-to-the-interface components of the momentum $\mathbf{q}_{||}$. We obtain

$$\eta = \frac{e^2 m_c m_h a^2}{(2\pi)^2 \hbar^4 m_e^2 \omega c n} \int \frac{\Phi(\gamma)|\mathcal{P}_{vc}|^2 \, d\varepsilon_c \, d^2 q_{||}}{\sqrt{2m_h(\hbar\omega - \varepsilon_c) - q_{||}^2}\sqrt{2m_c(\varepsilon_c - E_g) - q_{||}^2}}, \qquad (2)$$

where $\mathcal{P}_{vc} = -i\frac{N}{N_s} < f|\frac{\partial}{\partial z}|i >,$

m_c and m_h are the effective masses of the electron in the conduction and valence bands respectively, a is the lattice constant, N and N_s are the numbers of atoms in the crystallite and at the interface, and E_g is the gap. The limits of integration are determined by the region where the expressions under the square roots in the integrand are positive. Note that η value is independent of the crystallite length.

III. BOUNDARY CONDITIONS FOR THE ENVELOPE WAVE FUNCTION AT THE SHARP INTERFACE OF MATERIALS WITH A DIFFERENT CRYSTAL SYMMETRY

Let $z = 0$ be the interface between two crystals. The electron spectrum in each crystal could be degenerate. This means that a few states for the electron with the same energy E can exist. These states correspond to the different valleys or bands of the spectrum. Let M^l be the degeneracy degree in the left crystal, and M^r be that in the right crystal. The wave function of the electron in this system is

$$\Psi(\mathbf{r}) = \begin{cases} \sum\limits_{i=1}^{M^l} \psi_i^l(\mathbf{r})\varphi_{k_i}^l(\mathbf{r}) & \text{in the left crystal,} \\ \sum\limits_{i=1}^{M^r} \psi_i^r(\mathbf{r})\varphi_{k_i}^r(\mathbf{r}), & \text{in the right crystal.} \end{cases} \qquad (3)$$

Where $\varphi_{k_i}^{l,r}(\mathbf{r})$ are the Bloch wave function of the electron in the left and right crystals correspondingly, and $\psi_i^{l,r}(\mathbf{r})$ are the envelopes. The subscript i enumerates the different states of the electron with the energy E, and $\mathbf{k}_i$ are the wave vectors. The envelopes $\psi_i^{l,r}(\mathbf{r})$ should be smooth, so that they do not appreciably change on the scale of the lattice constant.

The envelopes should be matched at the interface. In the effective mass approximation the boundary conditions at the interface $z = 0$ are of the form [2]

$$\psi_i^r(\mathbf{r}_i) = \sum_{j=1}^{M^l} b_{i,j}^l \psi_j^l(\mathbf{r}_j), \qquad i = 1, \ ..., \ M^r \qquad (4)$$

$$\psi_i^l(\mathbf{r}_i) = \sum_{j=1}^{M^r} b_{ij}^r \psi_j^r(\mathbf{r}_j), \qquad i = 1, \ ..., \ M^l.$$

Where $b_{ij}^{l,r}$ are the parameters of the boundary conditions, which relate the envelopes at the different sites $\mathbf{r}_i$ of each crystal lattice. It is important that these sites are close to the interface, so that $|\mathbf{r}_i - \mathbf{r}_j| \sim a$, and $a\nabla\psi_i^{l,r} \sim a/\lambda \ll 1$ (here λ is the electron wavelength). When it is possible to expand the envelopes at the interface and rewrite Eq. (4) as follows:

$$\begin{aligned}
\psi_i^r + \tau_{i0}^r \nabla\psi_i^r &= \sum_{j=1}^{M^l} (b_{ij}^l \psi_j^l + \tau_{ij}^l \nabla\psi_j^l) \quad i = 1, \ \ldots, \ M^r, \\
\psi_i^l + \tau_{i0}^l \nabla\psi_i^l &= \sum_{j=1}^{M^r} (b_{ij}^r \psi_j^r + \tau_{ij}^r \nabla\psi_j^r) \quad i = 1, \ \ldots, \ M^l.
\end{aligned} \tag{5}$$

Where $b_{ij}^{l,r}$ and $\tau_{ij}^{l,r}$ are the real values which are independent of the electron energy. The vectors $\tau_{ij}^{l,r}$ can be directed along the normal to the interface; $|\tau_{ij}^{l,r}| \sim a$, so that $|\tau_{ij}^{l,r}\nabla\psi_j^{l,r}| \sim a/\lambda \ll 1$.

In the simplest case of the contact of nondegenerate semiconductors ($M^l = M^r = 1$) the boundary conditions (5) can be rewritten in the form:

$$\begin{pmatrix} \Psi_r \\ \Psi_r' \end{pmatrix} = \hat{T} \begin{pmatrix} \Psi_l \\ \Psi_l' \end{pmatrix}, \tag{6}$$

where $\hat{T}$ is the 2×2 matrix with the real components $\|t_{ik}\|$. Their values can be written in terms of b_{ik} and τ_{ik}. They are independent of the electron energy and can be used as the fenomenological parameters.

Nonlocal boundary conditions (4) can be used to obtain the boundary conditions for the envelope wave function at the rough interface. We consider the special form of a rough interface that is presented on Fig. 1. The interface looks like an array of the plane areas of the same crystallographic orientation. The random function $z = \xi(\boldsymbol{\tau})$ of the coordinates in XY plane determines the positions of these areas relative to $z = 0$.

We assume the average height of roughnesses σ to be small in comparison with the electron wavelength. Then it is possible to describe the rough interface by means of the correlation function $W(\mathbf{r}', \mathbf{r}'') = \overline{\xi(\mathbf{r}')\xi(\mathbf{r}'')}$. For the homogeneous rough interface $W(\mathbf{r}', \mathbf{r}'') = W(\mathbf{r}' - \mathbf{r}'')$, i.e., the correlation function becomes the function of one variable: $\boldsymbol{\rho} = \mathbf{r}' - \mathbf{r}''$. There are two parameters which are most important when the statistical properties of a rough interface is considered: $\sigma^2 = W(0)$ and the correlation length l — the mean attenuation length of the correlation function. In our model the correlation length l can be associated with

the mean size of the plane area (Fig. 1). We shall analyze the relation between the light absorption and parameters σ and l.

The special form of the rough interface (Fig. 1) allows us to apply the boundary conditions that are applicable for a plane interface at each plane $z = \xi$. It is important that these boundary conditions are not applicable at the vicinity of the corner points (like point 1 on Fig. 1). We assume the mean size of the plane areas to be large in comparison with the lattice constant, so that the relative number of the corner points is small.

To obtain the boundary conditions at the rough interface, it is necessary to expand the envelopes in Eq. (4) at $z = \xi(\mathbf{r})$, instead of $z = 0$. This means that the values of $\boldsymbol{\tau}$ in Eq. (5) should be replaced by $\boldsymbol{\tau} + \xi$, so that the matrix of the boundary conditions $\hat{T}$ becomes of the form

$$\hat{T} = \begin{pmatrix} t_{11} + t_{21}\xi & t_{12} + (t_{11} + t_{22})\xi + t_{21}\xi^2 \\ t_{21} & t_{22} + t_{21}\xi \end{pmatrix}, \tag{7}$$

where t_{ik} are the components of the boundary conditions matrix (6) at the plane interface.

It is important that now the boundary conditions matrix depends on $\boldsymbol{\rho}$. This results in the diffuse components of the wave functions. We write the envelopes as the sum of their average $\Phi_{l,r}$ and diffuse $\varphi_{l,r}$ components

$$\Psi_{l,r} = \Phi_{l,r} + \varphi_{l,r}, \text{ where } \overline{\Psi_{l,r}} = \Phi_{l,r}, \quad \overline{\varphi_{l,r}} = 0. \tag{8}$$

The boundary conditions for the average components are of the form of Eq. (6), where

$$\begin{aligned} \tilde{t}_{11} &= t_{11} + it_{21} \int k_z \tilde{W}(\mathbf{k} - \mathbf{k}_0)\, d^2\mathbf{k}, \\ \tilde{t}_{12} &= t_{12} + i(t_{11} + t_{22}) \int k_z \tilde{W}(\mathbf{k} - \mathbf{k}_0)\, d^2\mathbf{k}, \\ \tilde{t}_{21} &= t_{21} \left[1 + \int k_z^2 \tilde{W}(\mathbf{k} - \mathbf{k}_0)\, d^2\mathbf{k}\right], \\ \tilde{t}_{22} &= t_{22} + it_{21} \int k_z \tilde{W}(\mathbf{k} - \mathbf{k}_0)\, d^2\mathbf{k}, \end{aligned} \tag{9}$$

are the effective parameters of the boundary conditions, $W(\boldsymbol{\rho}) = \overline{\xi(\boldsymbol{\tau} + \boldsymbol{\rho})\xi(\boldsymbol{\tau})}$ is the correlation function of the rough interface, and $\tilde{W}$ is its Fourier transform

$$\tilde{W}(\mathbf{k}) = \int W(\boldsymbol{\rho}) e^{-i\mathbf{k}\boldsymbol{\rho}}\, d^2\boldsymbol{\rho}.$$

For the diffuse component of the envelope $\varphi(\mathbf{r})$ we obtain

$$\varphi(\mathbf{r}) = -\frac{2iq}{(2\pi)^2} \int A(k_z)\xi(\mathbf{k} - \mathbf{q}_{\|}) e^{i(k\rho - k_z z)}\, d^2\mathbf{k}, \text{ where} \tag{10}$$

$$A(k_z) = i\frac{k_z t_{21}(\tilde{t}_{22} - ip\tilde{t}_{12}) - (\tilde{t}_{21} - ip\tilde{t}_{11})[k_z(t_{11}+t_{22}) + it_{21}]}{[t_{21} - ik_z(t_{11}+t_{22}) - k_z^2 t_{12}][\tilde{t}_{21} - ip\tilde{t}_{11} - ikq\tilde{t}_{22} - pq\tilde{t}_{12}]},$$
$$k_z = \sqrt{2m_c\varepsilon_c - k^2}.$$

We should emphasize the two-fold influence of the interface roughness. First, the roughness of the interface results in the diffuse component of the scattered wave. This component is always small for the long wavelength electrons and vanished when $\lambda \to \infty$. Second, the effective parameters of the boundary conditions depend on the interface roughness. This effect depends on the relation between the electron wavelength and the correlate length of the rough interface. Indeed, if $\lambda \ll l$ then we can assume $\tilde{W}(\mathbf{k} - \mathbf{q}_{||}) \sim \sigma^2\delta(\mathbf{k} - \mathbf{q}_{||})$. The corrections to the effective boundary conditions parameters (9), coursed by the roughnesses, become proportional to $\sigma^2/(l\lambda)$.

Corrections to t_{ik} become independent of λ then $\lambda \gg l$. This is clear from Eq. (9) because in this case $|\mathbf{q}_{||}| \ll |\mathbf{k}|$. It is easy to understand the reason. Formally, the roughnesses each size of which is less then the electron wavelength could be taken into account when the boundary conditions parameters b_{ik} and τ_{ik} are obtained. In that consideration the roughnesses affect the value of these parameters but don't make them dependent on λ [2]. It follows from Eq. (9) that λ dependent corrections to $\tilde{t}_{ik}$ are of the order of $(l/\lambda)^2$; this is in agreement with estimations Ref.[2].

IV. INTERFACE LIGHT ABSORPTION IN INDIRECT-BAND-GAP SEMICONDUCTORS

The band structure of the semiconductor is presented on Fig. 2. For simplicity, we assume the nondegenerate valence band. There are two valleys in the conduction band: the central valley with the minimum at the center of Brillouin zone, and the side valley at the edge of it. It is important that the side valley is situated in the direction of the normal to the base of the cylinder.

We can write the electron wave functions as follows:

$$i >= \frac{1}{\sqrt{N}} \begin{cases} [v(\mathbf{r})e^{ipz} + Rv^*(\mathbf{r})e^{-ipz}]\, e^{i\boldsymbol{p}_{||}\boldsymbol{\rho}}, & z < 0, \\ T_v e^{-\gamma_v z + i\boldsymbol{p}_{||}\boldsymbol{\rho}}, & z > 0, \end{cases}$$
$$f >= \frac{1}{\sqrt{N}} \begin{cases} \left[Au_0(\mathbf{r})e^{\kappa z} + Bu_q^*(\mathbf{r})e^{i(q-\frac{\pi}{a})z} + u_q(\mathbf{r})e^{-i(q-\frac{\pi}{a})z}\right] e^{i\boldsymbol{q}_{||}\boldsymbol{\rho}}, & z < 0, \\ T_c e^{-\gamma_c z + i\boldsymbol{q}_{||}\boldsymbol{\rho}}, & z > 0. \end{cases} \quad (11)$$

Where $\gamma_{c,v}$ are decaying factors of the wave functions apart from the crystallite, v, u_0, and u_q are the Bloch amplitudes in the valent band, the central and side

valleys of the conductive band; p, κ, and q are z components of the wave numbers in these valleys, $\mathbf{p}_{\|}$ and $\mathbf{q}_{\|}$ are their components that are parallel to the interface, and $\boldsymbol{\rho}$ is the radius vector in this direction. The semiconductor occupies the region $z < 0$, so that the wave functions decay when $z > 0$. The coefficients R, T_v, A, B, and T_c can be determined from the boundary conditions for the envelopes (5). We obtain

$$
\begin{aligned}
R &\simeq -1 - \frac{2ip\,(t^v_{21}\tau^v_{11} - \tau^v_{20})}{t^v_{11}t^v_{21} - 1 - ip\,(t^v_{21}\tau^v_{11} - \tau^v_{20})}, \\
A &\simeq -\frac{2iqt^c_{21}\,(\tau^c_{12} - t^c_{12}\tau^c_{30})}{1 - t^c_{12}t^c_{31} - t^c_{11}t^c_{21} - iq\,(t^c_{31}\tau^c_{12} + t^c_{11}t^c_{21}\tau^c_{30} - \tau^c_{30})}, \\
B &\simeq -1 - \frac{2iq\,(t^c_{31}\tau^c_{12} + t^c_{11}t^c_{21}\tau^c_{30} - \tau^c_{30})}{1 - t^c_{12}t^c_{31} - t^c_{11}t^c_{21} - iq\,(t^c_{31}\tau^c_{12} + t^c_{11}t^c_{21}\tau^c_{30} - \tau^c_{30})}.
\end{aligned}
\tag{12}
$$

Where t^v_{ij}, τ^v_{ij} t^c_{ij},, and τ^c_{ij} are the parameters of the boundary conditions (5) for the valence and conductive bands correspondingly.

The inequalities $|p\tau| \ll 1$ and $|q\tau| \ll 1$ should be satisfied for the electron which has been exited from the top of the valence band to the bottom of the conductive band. This point had been taken into account when Eq. (12) was obtained.

It is difficult to obtain the parameters of the boundary conditions (5). Nevertheless, we can relate them to the positions of the energy levels that are separated from the conduction and valence bands at the interface. Positions of these interface levels are determined by the poles of Eq. (12). Thus,

$$
1 + R = -\frac{2ip}{\kappa_v - ip}, \quad A = -\frac{2iq}{\kappa_c - iq} \cdot \frac{t^c_{21}\,(\tau^c_{12} - t^c_{12}\tau^c_{30})}{(t^c_{31}\tau^c_{12} + t^c_{11}t^c_{21}\tau^c_{30} - \tau^c_{30})}, \quad 1 + B = -\frac{2iq}{\kappa_c - iq},
\tag{13}
$$

where $\kappa_v = \sqrt{2m_h E_v}$, $\kappa_c = \sqrt{2m_c(E_g - E_c)}$; κ_v^{-1}, and κ_c^{-1} are the decay factors of the electron wave functions of the interface states; E_v and E_c are the energies of the interface levels separated from the valence and conduction bands respectively; m_h and m_c are the effective masses of the electron in these bands. We assume that energies are measured from the top of the valence band.

The probability of the photon absorption in the crystallite is determined by Eq. (2), where

$$
\begin{aligned}
\mathcal{P}_{vc} &= \frac{A^* P_c}{a}\left(\frac{1}{\kappa + ip} + \frac{R}{\kappa - ip}\right) + \frac{1}{2}P_s(1 + B^*)(1 + R), \\
P_c &= -i\hbar \int_{\Omega_0} u_0^* \frac{\partial v}{\partial z}\, d^3r, \quad P_s = -i\hbar \int_{\Omega_0} u_q^* \frac{\partial v}{\partial z}\, d^3r,
\end{aligned}
\tag{14}
$$

ε_c and ε_v are the electron energies in the conductive and valence bands respectively, and Ω_0 is the unit cell.

We see that the frequency dependence of η is determined by the momentum dependence of $\mathcal{P}_{vc}$ which, in turn, essentially depends on the relation between κ_v, κ_c and the corresponding momenta p, q, i.e., on the interface levels, whether they are close to the bottom of the corresponding bands. If we assume the Coulomb factor $\Phi(\gamma)$ as independent of q then the result of integration Eq. (2) can be written as follows:

$$\eta \propto (\hbar\omega - E_g)^\nu \left[|P_s|^2 + \beta\frac{|P_c|^2}{(\kappa a)^2}\right], \text{ where} \tag{15}$$

$$\nu = \begin{cases} 3 & \text{if } \hbar\omega - E_g \ll \min(E_v,\ E_g - E_c), \\ 2 & \text{if } \min(E_v, E_g - E_c) \ll \hbar\omega - E_g \ll \max(E_v, E_c), \\ 1 & \text{if } \hbar\omega - E_g \gg \max(E_v,\ E_g - E_c). \end{cases}$$

where β is the dimensionless parameter, which has been aroused from the first term of the expression (14). Two terms in the square brackets of Eq. (15) can be interpreted as follows: the first one corresponds to the immediate transition of the electron to the side valley at the interface, second term corresponds to the excitation of the electron to the virtual interface state of the central valley subsequented by conversion to the side valley, it prevails if the valleys minima are close ($\kappa a \ll 1$).

In fact, $\Phi(\gamma)$ is independent of q if $qa_B \gg \hbar$. Otherwise, if $qa_B \ll \hbar$, it is proportional to q^{-1}; in this case the exponent ν changes, so that $\nu \to \nu - 1/2$ when $\hbar\omega - E_g \ll \mu e^4/(2\epsilon^2\hbar^2)$ (where $\mu^{-1} = m_c^{-1} + m_h^{-1}$, $\epsilon = n^2$).

Thus, the frequency dependence of the absorption at the fundamental absorption edge essentially depends on the conditions at the interface. Namely, whether or not the interface electron levels are close to the corresponding bands extrema.

V. INTERFACE LIGHT ABSORPTION IN DIRECT-BAND-GAP SEMICONDUCTORS

Let us consider the interface light absorption in semiconductor the band structure of which is presented on Fig. 3. We suppose the effective mass approximation to be valid in each band and assume that the effective mass in the conduction band m_c essentially exceeds the effective mass in the valence band m_h, ($m_h \ll m_c$). Such a situation occurs in the TiO_2 band structure in $\Gamma - M$ direction.

We can write the wave functions as follows:

$$i>= \frac{1}{\sqrt{N}} \begin{cases} [v_p(\mathbf{r})e^{ipz} + R_v v_p^*(\mathbf{r})e^{-ipz}]e^{i\mathbf{p}_\parallel\rho}, & z < 0 \\ T_v e^{-\gamma_v z + i\mathbf{p}_\parallel\rho}, & z > 0, \end{cases}$$

$$f>= \frac{1}{\sqrt{N}} \begin{cases} [u_q^*(\mathbf{r})e^{-iqz} + R_c u_q(\mathbf{r})e^{iqz}]e^{i\mathbf{q}_\parallel\rho}, & z < 0 \\ T_c e^{-\gamma_c z + i\mathbf{q}_\parallel\rho}, & z > 0. \end{cases} \tag{16}$$

Where $u_q(\mathbf{r})$ and $v_p(\mathbf{r})$ are the Bloch amplitudes in the conduction and valence band respectively; R_v, R_c, T_v, and T_c are the reflection and transmission coefficients. It is possible to relate these values with positions of the interface levels. Then we obtain

$$1 + R_v = -\frac{2ip}{\kappa_v - ip}, \quad 1 + R_c = \frac{2iq}{\kappa_c + iq}, \tag{17}$$

where $\kappa_v = \sqrt{2m_h E_v}$, $\kappa_c = \sqrt{2m_c(E_g - E_c)}$.

The value of interband matrix element $\mathcal{P}_{vc}$ is of the form:

$$|\mathcal{P}_{vc}|^2 = 4U_1^2 \frac{(\kappa_c + \kappa_v)^2(\omega - \varepsilon_c)}{2m_c(\varepsilon_c - E_c)(\omega - \varepsilon_c + E_v)} \delta_{p_\parallel, q_\parallel}, \text{ where} \tag{18}$$

$$U_1 = \int_{\Omega_0} u_0 v_0 \, d^3\mathbf{r}.$$

If we assume the Coulomb factor $\Phi(\gamma)$ as independent of q, then the result of integration (2) can be written as follows:

$$\eta \propto (\hbar\omega - E_g)^\nu, \text{ where} \tag{19}$$

$$\nu = \begin{cases} 2 & \text{if } \hbar\omega - E_g \ll \min(E_v,\ E_g - E_c), \\ 1 & \text{if } \min(E_v, E_g - E_c) \ll \hbar\omega - E_g \ll \max(E_v, E_c), \\ 0 & \text{if } \hbar\omega - E_g \gg \max(E_v,\ E_g - E_c). \end{cases}$$

In direct-forbidden-band-gap semiconductors $u_0(\mathbf{r}) = 0$. We assume $u_q(\mathbf{r}) = 2i\sin(qa/2)\, w_q(\mathbf{r})$, where $w_q(\mathbf{r})$ is the periodic function of $\mathbf{r}$ that is not vanished at $q = 0$. Then for $\mathcal{P}_{vc}$ value we obtain

$$|\mathcal{P}_{vc}|^2 = 4U_2^2 \frac{(\varepsilon_c - E_g)(\omega - \varepsilon_c)}{(\varepsilon_c - E_c)(\omega - \varepsilon_c + E_v)} \delta_{p_\parallel, q_\parallel}, \text{ where} \tag{20}$$

$$U_2 = \int_{\Omega_0} w_0 \frac{\partial v_0}{\partial z} \, d^3\mathbf{r},$$

Integration of Eq. (2) yields

$$\eta \propto (\hbar\omega - E_g)^\nu, \text{ where} \tag{21}$$

$$\nu = \begin{cases} 3 & \text{if } \hbar\omega - E_g \ll \min(E_v,\ E_g - E_c), \\ 2 & \text{if } \min(E_v, E_g - E_c) \ll \hbar\omega - E_g \ll \max(E_v, E_c), \\ 1 & \text{if } \hbar\omega - E_g \gg \max(E_v,\ E_g - E_c). \end{cases}$$

Strictly speaking, Eq. (21) valids only then $\hbar\omega - E_g \ll W_c$, where W_c is the conduction band width. This value is small in TiO_2. For that reason it is interesting to consider the opposite limiting case $W_c \ll \hbar\omega - E_g \ll W_v$, where W_v is the valence band width. In this case ε_c can be considered as independent of q, so that it is possible to assume $\varepsilon_c = E_g$ in Eq. (1). Then for ν value we find

$$\nu = \begin{cases} 3/2 & \text{if } \hbar\omega - E_g \ll E_v, \\ 1/2 & \text{if } \hbar\omega - E_g \gg E_v. \end{cases} \tag{22}$$

VI. LIGHT ABSORPTION AT A ROUGH INTERFACE

To obtain the roughnesses influence on the interface absorption we should use the boundary conditions at a rough interface which has been obtained in Sec. III. When for the average squared module of the matrix element $\mathcal{P}_{vc}$ in Eq. (2) we obtain

$$\begin{aligned}
&\overline{|\mathcal{P}_{vc}|^2} = |\mathcal{P}_{vc}^{(1)}|^2 + \overline{|\mathcal{P}_{vc}^{(2)}|^2} + \mathcal{P}_{vc}^{(1)}\overline{\mathcal{P}_{vc}^{(3)*}} + \mathcal{P}_{vc}^{(1)*}\overline{\mathcal{P}_{vc}^{(3)}}, \\
&\text{where} \quad \mathcal{P}_{vc}^{(1)} = (1+R_v)(1+R_c^*)U_2\,\delta_{\mathbf{p}_\parallel,\mathbf{q}_\parallel}, \qquad (23) \\
&\overline{|\mathcal{P}_{vc}^{(2)}|^2} = \frac{4U}{S}W(\mathbf{p}_\parallel - \mathbf{q}_\parallel)\left|p(1+R_c^*)A^c - q(1+R_v)A^{v*}\right|^2, \\
&\overline{\mathcal{P}_{vc}^{(3)}} = 4ipqU\delta_{\mathbf{p}_\parallel,\mathbf{q}_\parallel}\int A^c A^{v*} W(\mathbf{k}_\parallel - \mathbf{q}_\parallel)\,d^2\mathbf{k}.
\end{aligned}$$

The expressions (23) allow to estimate influence of the roughness on the value and the frequency dependence of light absorption. Note that the $\mathcal{P}_{vc}^{(1)}$ value is of the same form as that for the plane interface Eq. (18). This value determines an influence of the shift of the interface levels owing to the interface roughness. Expressions for $\mathcal{P}_{vc}^{(2)}$ and $\mathcal{P}_{vc}^{(3)}$ in Eqs. (23) determine an influence of the diffuse components of the scattered waves on the absorption; the values of these components are as small as σ/λ. On the contrary, this small parameter is absent in the expression for $\mathcal{P}_{vc}^{(1)}$. However, $\mathcal{P}_{vc}^{(1)}$ is proportional to $(1+R_v)(1+R_c^*)$. This value is small if the interface electron levels are not close to any band. Then the values of $\mathcal{P}_{vc}^{(2)}$ and $\mathcal{P}_{vc}^{(3)}$ may be of the same order or even exceed $\mathcal{P}_{vc}^{(1)}$.

The correlation length l of the rough interface is also important for the light absorption. If the correlation length is small, $l \ll \lambda$, then the roughness influence is determined by the terms $\mathcal{P}^{(1)}$ and $\mathcal{P}^{(3)}$. In this case enhancement of the absorption arises due to an increase of the number of the interface atoms $N_s \to N_s\sigma/a$ in vicinity of which the interband absorption with the momentum nonconservation occurs. The shift of the interface levels also affects the absorption.

In the opposite limit, $l \gg \lambda$, we can assume $\tilde{W}(\mathbf{k}) = \sigma^2\delta(\mathbf{k})$. It can be shown that $\overline{|\mathcal{P}_{vc}^{(2)}|^2} + \mathcal{P}_{vc}^{(1)}\overline{\mathcal{P}_{vc}^{(3)*}} + \mathcal{P}_{vc}^{(1)*}\overline{\mathcal{P}_{vc}^{(3)}} = 0$, i.e., $\overline{|\mathcal{P}_{vc}|^2} = |\mathcal{P}_{vc}^{(1)}|^2$ in this case. It is easy to understand the reason: roughnesses, the mean length of which essentially exceeds the electron wavelength, could't affect the electron properties of the interface.

The interesting situation arises then $l \sim \lambda$. In this case the diffuse scattering that is described by the term $\overline{|\mathcal{P}_{vc}^{(2)}|^2} \sim \kappa_c^2\sigma^2 l^2[2m_{c\parallel}(\hbar\omega - E_g)]|\mathcal{P}_{vc}^{(1)}|^2$ leads to the change in the frequency dependence of the absorption, where $m_{c\parallel}$ is mean parallel component of the effective mass. This means the more rapid increase of the absorption at the low frequencies then $2m_{c\parallel}(\hbar\omega - E_g)l^2 \le \hbar^2$, so that the exponent ν changes its value $\nu \to \nu + 1$.

We should emphasize tree-fold influence of the interface roughnesses on the light absorption. First, they lead to the effective increase of the number of the interface atoms in vicinity of which the indirect interband absorption occurs. Second, they lead to the shift of the interface levels. Third, at the rough interface not only the normal-to-the-interface component of the electron momentum but also all of it components can be nonconservative. This affects the frequency dependence of the absorption when $l \sim \lambda$.

VII. DISCUSSION

We considered the light absorption at the interface and found that the absorption value and its frequency dependence at the fundamental absorption edge are sensitive to the conditions at the interface. Namely, to the interface electron levels, whether or not they exist in vicinity of the bands extrema. To estimate the value of interface absorption, we have to compare the absorption of the microcrystalline solid composed from the crystallites under considereation, $\alpha = \eta/L \sim a/L$ (where L is the main size of the crystallite), with the light absorption in the bulk semiconductor. The small value a/L characterizes the ratio of the number of the atoms at the interface to the number of atoms in the whole of solid.

In order to the interface absorption becomes important in Ge and indirect-band-gap semiconductors of $A_{III}B_V$ group this small value should exceed the small parameter of electron-phonon interaction g (this value is about 10^{-3}–10^{-2}). In these semiconductors the interface absorption essentially increases due to the intervalley conversion, which is determined by the second term in Eq. (15). That is possible if $a/L(\kappa a)^{-1} \geq g$.

The main mechanism of light absorption in bulk Si is the impurity absorption. In order to the interface absorption becomes significant in this material, the number of the interface atoms should exceed the number of impurities.

The essential difference in the effective masses of the valence and conduction band also can lead to the enhancement of light absorption in direct-band-gap semiconductors. It is easy to understand the reason of this enhancement. The interband absorption in the bulk semiconductors happens due to the direct electron transitions $1 \rightarrow 2$ (Fig. 3). The additional small parameter arises in direct-forbidden-gap semiconductors because the points 1 and 2 are close to the bands extremums. Nevertheless, the indirect transitions $3 \rightarrow 4$ become possible at the same photon energy near the interface where the normal-to-the-interface component of the electron momentum is not conservative.

Such situation is characteristic for TiO_2. The conduction band in this material composed mainly of d orbitals of Ti. These orbitals are stringly localized. For this reason the conduction band in TiO_2 is narrow and become even flat in Γ-M direction. It is important that direct interband electron transition is dipole-

forbidden in this material. There is two-fold advantage from indirect transitions. First, they are allowed, i.e., the dipole matrix element of the indirect transitions is not small. Second advantage arises due to the large density of states for the electron in the conduction band.

Let us compare the interband transitions in the bulk of semiconductor $1 \rightarrow 2$ and at the interface $3 \rightarrow 4$. The absorption is proportional to the density of electron states in each band. The density of states in the conduction band of TiO_2 essentially exceeds that in the valence band. Nevertheless, it is the density of electron states in the valence band which determines the absorption in the bulk of crystal. This happens because of the momentum conservation law, which makes the electron states with the large momentums inaccessible for the exited electrons. On the contrary, indirect electron transitions make such states accessible.

Both advantages are not significant in vicinity of the absorption edge then the points 2 and 4 are close, but they become significant at the larger photon energy. That is the reason why the rapid increase of the absorption takes place at low ($\hbar\omega < E_g + W_c$) photon energies (Fig. 4). The electron transitions to any point of the conduction band become possible when $\hbar\omega = E_g + W_c$. Further enhancement of the absorption occurs only due to an increase of the electron density of states in the valence band. For this reason the slope of the $\eta(\hbar\omega)$ curve decreases then $\hbar\omega > E_g + W_c$. Results of our analyzes confirm these qualitative arguments.

We can use Eq. (21) to estimate the value of absorption coefficient of the microcrystalline direct-forbidden-band-gap semiconductor:

$$\frac{\alpha}{\alpha_0} \sim \frac{a}{L}\left(\frac{m_c}{m_h}\right)^2 \sim \frac{a}{L}\left(\frac{W_v}{W_c}\right)^2$$

where α_0 is the absorption coefficient of the bulk monocrystal, W_c and W_v are width of the conduction and valence bands respectively. $W_c \sim 10\,\text{meV}$ and $W_v \simeq 1\,\text{eV}$ [3] for TiO_2. Thus, the interface mechanism of the absorption becomes comparable with the bulk one for the microcrystalline TiO_2 the mean size of the crystallite in which is $L \leq a(W_v/W_c)^2 \sim 100\,\text{nm}$.

Large difference between the effective masses of the electron in the conduction and heavy hole valence bands takes place also in some other semiconductors. To estimate the interface absorption in this case, we can use Eq. (19). Then we find

$$\frac{\alpha}{\alpha_0} \sim \frac{a}{L}\left(\frac{m_h}{m_c}\right)^2.$$

In conclusion, we show that the possibility of the momentum nonconservation at the interface can lead to enhancement of light absorption in small crystallites. The effect increases at a rough interface where the share of the interface atoms is larger.

ACKNOWLEDGEMENT

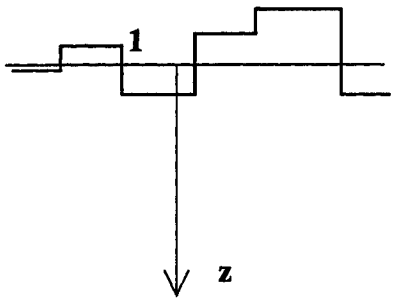
The authors would like to thank Prof. E. Ivchenko, Prof. V. Volkov, and Prof. M. Entin for helpful discussions. This work was supported by the Swiss National Science Foundation, Project No. 7SUPJ048573, and the Russian Foundation for the Fundamental Investigations, Grant No. 96-02-19028.

References

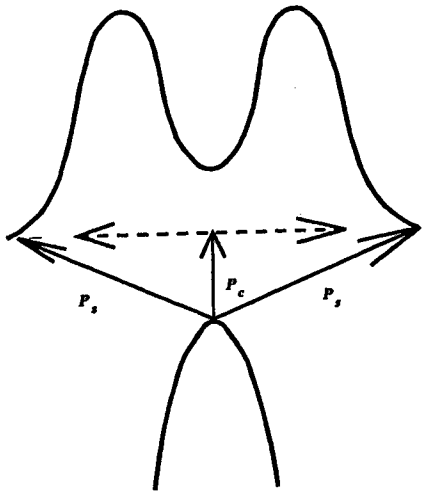
[1] Elliot R. J., Phys. Rev., Vol. 108, p. 1384 (1957).

[2] L. Braginsky, Phys. Rev. B, Vol. 57, p. R6870 (1998); L. Braginsky, cond-mat/9705004 (unpublished).

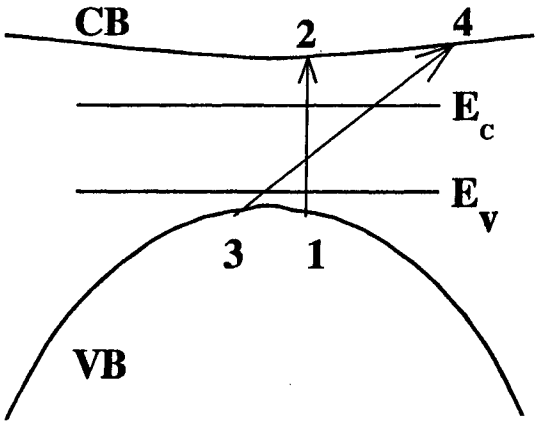
[3] K. Glassford and J. Chelikowsky, Phys. Rev. B, Vol. 46, p. 1284 (1992); F. Cora et al, J. Phys. Chem. B, Vol. 101, p. 3945 (1997).



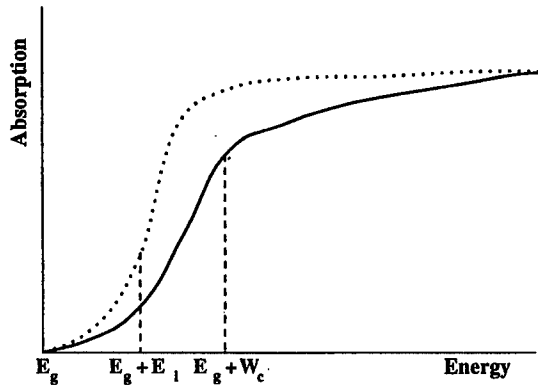
1. The model of the rough interface. Side view.



2. The two ways of the light absorption at the indirect-band-gap semiconductor interface: the immediate electron transition to the side valley P_s, and the vertical transition P_c followed by the conversion to the side valley (dotted arrow).



3. Schematic band structure of the crystallite. Here E_v and E_c are the interface levels. Arrows indicate two ways that light absorption takes place: direct electron transition $1 \rightarrow 2$, and indirect $3 \rightarrow 4$ that occurs at the interface.



4. Interband light absorption at the fundamental absorption edge in the crystallite. The dotted line indicates the influence of the interface roughness. Here $E_l = \hbar^2(2m_{c\|}l^2)^{-1}$.

Quantum Devices, Architectures, and Circuits

ROLE OF SMALL DIMENSIONS AND QUANTUM CONFINEMENT IN SMALL SILICON MEMORIES

Sandip Tiwari*, Farhan Rana#, Arvind Kumar*, J. J. Welser* and C. T. Black*

**IBM Research Division, T. J. Watson Research Center, Yorktown Heights, NY, 10598*

#Department of EE & CS, Massachusetts Institute of Technology, Cambridge, MA, 02139

ABSTRACT

Memories that utilize single electron effects are an attempt at combining the discreteness observable in transport of electrons on to very small capacitances (~10^{-18} F), and into three-dimensionally quantum-confined states with the reproducibility, architecture and integration of the field-effect devices. We discuss the implications of size and electrostatics on variability, acceptability and reproducibility of properties desired; of barriers on speed; and of random variations and of tunneling on limits in the use of the field-effect. We show that in silicon-on-insulator based structures silicon and back-insulator thicknesses matter through the linear variations introduced in the electrostatic potential and quadratic variations introduced in the sub-bands, the quantum-dots and nano-crystals matter secondarily through the electrostatics and the linear dependence of capacitance on size and the quadratic dependence of the allowed eigen-energies on size. We also discuss the implications of tunneling on time constants of charging of the confined states and in between the source and the drain for the ultimate structure size limit. We end with a discussion of limits to usefulness of discrete numbers of electrons in the context of variability that they endanger.

INTRODUCTION

For field-effect devices, one of the most significant effects of scaling of critical dimensions to the ~10 nm range is a reduction in collective effects whose reproducibility has been so profitably applied over the last many decades. Examples of such collective phenomena are the number of electrons flowing through the channel, the number of electrons transferred during a CMOS switching event, and the number of dopants used to control the threshold voltage. A larger number of electrons flowing in the channel leads to smaller fluctuations in the current, a larger number of electrons transferred during switching leads to smaller fluctuations in the switching voltage levels, and a larger number of dopants leads to smaller fluctuations in the threshold voltage. The scaling of device dimensions has been driven by higher function and

lower cost gained from an increase of device density and performance, a lowering of power density, and mixing of logic and memory technologies. Logic and memory have to co-exist at such small dimensions, and the various forms of memories have to be capable of providing a range of performance from high speed to low power and non-volatility.

Nano-crystal and Quantum-dot memories [1-3], examples of flash memories, are small dimension structures that utilize quantum-dot(s) between the gate and the channel of a field-effect transistor to store small numbers of electrons, which screen the mobile charge in the channel and thus induce a change in the threshold-voltage or conductivity of the channel. These quantum-dots are transmissively coupled to the channel and isolated from the gate. Their reduced dimension and confinement brings forth two important features that are absent in the conventional silicon field-effect transistors and floating gate memories: a reduced density of states which restricts the states available for electrons and holes to tunnel to and from, and the Coulomb blockade effect, arising from a larger electrostatic energy associated with placing a charged particle onto a smaller capacitance. The consequence of these two effects is a reduction of the number of charged carriers used in the operation of the device - a reduction in the "collective phenomena." These effects - in size and transmission - need to be harnessed even as we control the consequences of semi-classical effects - of electrostatics resulting from dopants and barriers, of density of states, and of single electron charging energy. Does this lead to a decrease in noise margin or other significant consequences which make these devices impractical?

We discuss the properties of this reduced dimension system and will focus on three aspects. The first will be a description of the capacitances of such structures, while including the quantum-effects, and we will deduce their influence on the operation. The second will be life-time in the storage quantum-dot and the writing and erasing of such structures modeled using a rate equation derived from the equation of motion of the density matrix. This gives a reasonable description of the coupling between the three-dimensionally confined quantum-dot and one-dimensionally confined inversion layer (the writing process) or the unconfined system (the erasure process) and elucidates the role of barriers and the size of the quantum-dot. We will also derive from this the fluctuations in charge, threshold voltage shifts, and hence the noise to be expected during operation. The third will be the role of random defects at small dimensions and their influence on the variance in threshold voltage of the devices. For nano-crystal memories, we will also relate the storage of electrons to the percolation transport in the silicon channel.

I. STRUCTURE AND OPERATION

In constructing single electron effect sensitive devices, such as the quantum-dot and nano-crystal memories which couple single electron and quantum effects to the field-effect, we must solve a number of the same practical problems that CMOS has to solve. Also, because they use an overlapping and common technology with CMOS, it is realistic to expect that these single electron devices will also help in the progress of CMOS through simplification in technology and lowering of power - attributes that are useful for systems on a chip. Nano-crystal and quantum-dot memories are floating gate memory structures where the dimension of the storage node has been scaled to very small dimensions. Fig. 1

and 2 show example cross-sections of these structures together with the voltage dependent quasi-stable hysteresis effect. When the gate energy is lowered w.r.t. that of the source and the drain, electrons transfer to the floating gate storage nodes. For nano-crystal memories, these are small single-crystal silicon islands (nano-crystals of an areal density in the 10^{11} cm^{-2} range) that are deposited by chemical vapor deposition on the tunneling oxide. For the quantum-dot memory, this is a poly-crystalline island patterned at the intersection of the gate and the channel line.

Electrons stored on the island screen the charge in the channel and hence lead to less channel charge for the same applied gate-to-channel potential. This is effectively a change in the threshold voltage as seen in the Figures 1 and 2. The biggest implication of the scaling of the floating gate region is that the number of electrons used in the device structure are discrete and small. But, this discreteness, or quantization, is not used directly in the device operation. Instead, it is coupled to the channel of the device. That is, these electrons trapped on the islands influence the conduction of a channel underneath them, and thus the conduction of the channel is a measure of the storage of the electrons. Barriers, used for storage of the electrons are thus important to the write, erase, and the refresh conditions. But, reading of the device, and the amount of signal delivered by the device, are related to field-effect. The limits of the device operation are due to field-effect. The single electron, or the quantum effects, provide a perturbation to it that are detected through the influence of immobile charge on mobile charge. The device behaves as a gain cell.

For a nano-crystal density of v_{nxt} of size t_{nxt}, a tunneling injection oxide of t_{inj}, a control oxide of t_{cntl}, and $\bar{v}$ average number of electrons per nano-crystal, the threshold-voltage is approximately given by:

$$\Delta V_T = \frac{e\bar{v}n_{nxt}}{\varepsilon_{ox}}\left(t_{cntl} + \frac{1}{2}\frac{\varepsilon_{ox}}{\varepsilon_{nxt}}t_{nxt}\right)$$

The spacing between the nano-crystals should be less than the screening length in order to minimize percolative transport in the channel underneath. Fig. 1 shows, at low currents, evidence of this percolation. The oxide in between the nano-crystals is kept large enough to suppress transport directly between the nano-crystals since leakage and subsequent loss to source and drain regions is one of the major methods for loss of charge in floating gate structures. The control oxide is designed to be thick enough (7-15 nm) so that the only path for electron transport to and from the nano-crystals is from the silicon underneath - inversion channel region during injection and depletion region during ejection. The barrier height of Si/SiO_2 interface is large (~3.15 eV). Oxide thicknesses in the 1-10 nm range controls the transmission efficiency over nearly 20 decades. This allows the memories to

be made volatile and high speed (small injection oxide thickness) to non-volatile and slower speed.

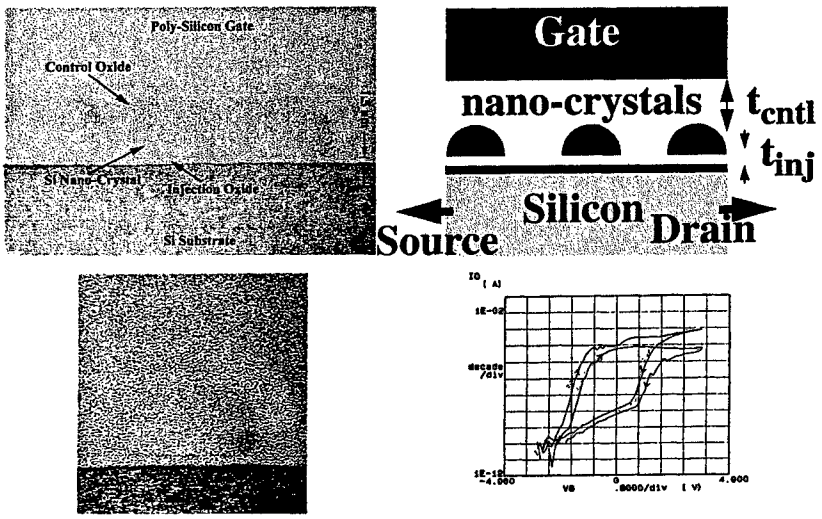


Fig. 1: A cross-section of nano-crystal memory. Three nanocrystals shaped as hemi-spherical bubbles, separated from each other are shown together with the control gate and control and injection SiO_2. A more detailed view of one of the single-crystal quantum-dot is shown on the bottom together with the drain current - gate voltage hysterisis loop.

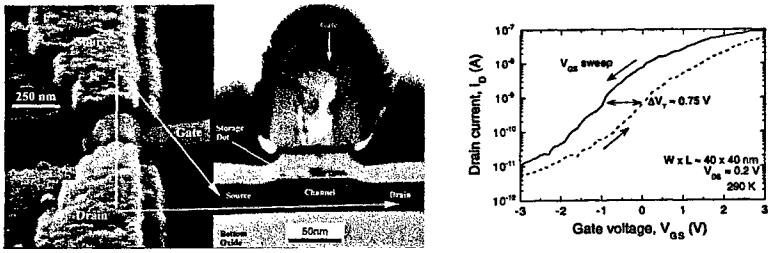


Fig. 2: A cross-section of quantum-dot memory. The storage dot is spaced apart from the control gate by a control oxide that is thick enough to make tunneling transmission negligible for typical bias voltages and is separated from the channel by the tunneling oxide that permits transmission.

Table 1 summarizes a number of characteristics for the poly-silicon/control oxide/sili-

TABLE 1. Spherical charge in SiO_2 gate stack with a 7 nm gate control oxide.

Diameter (nm)	C_Σ *(aF)*	E_c *(eV)*	C_{cntl} *(aF)*	E_0 *(eV)*	*Single electron* V_T *shift (V)*
30	6.68	0.011	5.27	~0.003	0.03
20	4.45	0.018	2.57	0.007	0.062
10	2.23	0.036	0.71	0.03	0.225
5	1.11	0.072	0.19	0.104	0.84
3	0.68	0.118	0.069	0.29	2.31
2	0.45	0.178	0.031	0.65	>5
1	0.22	0.364	0.008	2.6	>10

con island/injection oxide/silicon gate stack. This is an approximate calculation meant to point out the main characteristics of the system. The capacitance is the self-capacitance of the silicon dot used in the calculation of the charging energy. These vary linearly (for capacitance) and inverse linearly (for energy) with dimension. The quantization effect of confinement varies as the inverse square of the dimension. At dimensions below 10 nm, the capacitance is small enough that it requires energy of the order of room temperature thermal energy to place an electron on the silicon island. As the dimension decreases further, the eigen-energy of the confined states allowed become larger than the single electron electrostatic charging energy. When a single electron is stored on the island, it causes the channel threshold voltage to shift by a magnitude that is inversely controlled by the capacitance C_{cntl}. The shift should not exceed the operating voltages of the structure. Thus, dimensions of between 10 nm and 3 nm are usable and provide a substantial and observable effect. Yano et al. [4] and Nakazato et al. [5] describe other very interesting examples of the use of this large influence in a small dimension.

II. SMALL DIMENSION EFFECTS

Single Electron Effects:

Neugebauer and Web[6] recognized nearly four decades ago that, when a capacitance is reduced, the electrostatic energy required to charge the capacitance ($e^2/2C$) can be made to be of the order of magnitude of thermal voltage at dimensions in the 10 nm range which result in a capacitance in the aF (10^{-18} F) range. This implies that discrete single electron transmission or storage events can be observed, and unless the electrostatic energy is available to the electron from the power supply, the transition is prohibited. This is known as Coulomb blockade. Fulton and Dolan[7], in 1987, demonstrated the first single electron transistor, and in recent times, there has been tremendous interest in understanding of this

mesoscopic system [8]. Here, we will summarize some the necessary conditions for observation of the single-electron events [9] in order to connect them to the properties of the small silicon memories. For the single electron events to be clearly observable, a number of requirements must be met. The state that the electron occupies on the particle is confined, and for the event to be observable, the change in system energy upon transmission of an electron, is larger than thermal energy. The uncertainty principle tells us that the width of the eigen-state is $\Delta E \approx h/2\pi\tau$, where $\tau = 1/\Gamma$ is the lifetime (related inversely with the tunneling rate). The change in system energy ($\Delta U = QV = e\,I\,R_T$, where Q is the charge, V is the voltage, I is the current ($e\Gamma$), and R_T is the tunnel resistance), upon transition of an electron, is $\Delta U = e^2\ \Gamma R_T$. The energy width of the eigenstate is, therefore $\Delta E = h/2\pi\,\Gamma = h/2\pi\ \Delta U/(e^2 R_T)$. A clear observation of Coulomb blockade requires $\Delta U >> \Delta E$ which is the condition

$$R_T \gg \frac{(h/2\pi)^2}{e^2} = 4.1k\Omega$$

Note that this resistance is different from that of quantum resistance, usually alluded to in superconducting tunneling of Cooper pairs, of $R_q = h/4e^2$, which has the magnitude of 6.4 kΩ. So, the first condition is that the resistance of the barrier be larger than 4.1 kΩ. The second condition is that the energy $(e^2/2C)$ be larger than kT. The overriding time-constant for the transmission of this electron is an RC time constant, which is greater than 100 fs. This time constant dominates since it is larger than the time constant from uncertainty principle, i.e. of the certainty of observation, of $h/(e^2/2C)$, which is of the order of 10 fs, as well as of the transmission of a wave packet through the barrier, of $h/2\pi\ d(ln(T(E))/dE$ at $E=E_f$, which is very small. This large time constant also implies that a small current flows (1 electron/100 fs is ~ 1.6 μA; in experiments typically a nA) during the electron transmission. Coupling the effect of stored electrons to field-effect of a transistor allows a larger current because carriers are more mobile in the barrier-free channel.

Now, let us consider a small particle which has these requisite properties. Fig. 3 shows the transfer process of electron onto an island with a large density of states, such as a metal. For the moment, we assume that there is no spurious charge (electrically neutral; no trapped electron at interfaces or in the bulk) and hence electric field terminations occur only between the island and the electrodes, when a power supply is connected at the electrodes. Because only discrete tunneling events are allowed for the flow of charge and hence the change in electrochemical potential, the electrochemical potential of the particle - a nano-crystal - follows the inequality $\mu_{nxtl} \le e^2/(2C_\Sigma)$, where C_Σ is the total capacitance

between the particle and its surroundings. This is equivalent to having polarization charge,

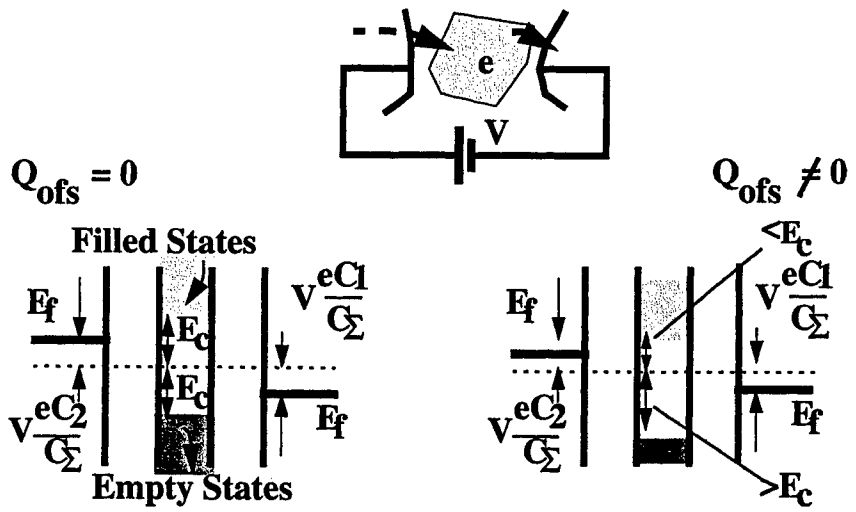


Fig. 3: Schematic of the transfer process of an electron upon application of a bias voltage V between two electrodes that the particle is confined in between. Both diagrams show Coulomb blockade condition, one in the absence of offset charge and another in the presence of offset charge. The capacitances of the two junctions are identified by the subscript 1 and 2.

or an offset charge Q_{ofs}, of

$$Q_{ofs} \approx C_\Sigma \frac{|\mu_{nxtl}|}{e} \leq \frac{e}{2}$$

Consider first the situation where the offset charge is zero, and C_1 and C_2 are the coupling capacitances. The Coulomb charging energy of E_c is accounted for in the energy diagram by raising the energy of the unoccupied states by E_c. Tunneling to the particle occurs when the energy of states in the lead align with the E_c -shifted unoccupied states of the particle. Tunneling from the occupied states of the particle also occur with a change in energy of E_c; the energy diagram accounts for this by shifting the energy of occupied states by E_c. So, a barrier E_c exists for flow of an electron whether it is on to the particle or off the particle. For the moment we assume that there is no spurious charge (electrically neutral; no trapped charge at interfaces or in the bulk) and hence electric field terminations are only between the island and the electrodes, when a power supply is connected at the elec-

trodes. Under favorable conditions, an electron tunnels from the left onto the particle with the expenditure of energy E_c by the power supply. The number of electrons in the occupied states has now increased by one and the electrochemical potential of the particle (aligned with the first electrode) is higher than the second electrode. Tunneling can now occur off the island to the second electrode because it is energetically favorable, and the system returns back to its initial state. Similar arguments hold when the first tunneling event is from the particle to the second electrode. In this case, the first tunneling event occurs upon alignment of the energies between the particle and the second electrode. This leads to the lowering of the energy of the particle, and now empty states are available for tunneling from the first electrode. In both cases the Coulomb blockade energy is still $e^2/2C_\Sigma$. The presence of offset charge makes the condition of transmission asymmetric, one example of which is shown in Fig. 3.

This offset charge represents the polarization of the particle due to electric fields terminated on the small quantum-dot. The electrochemical potential difference, at zero bias, is equivalent to a polarization charge, or an offset charge Q_{ofs}, of

$$Q_{ofs} \approx C_\Sigma \frac{|\mu_{nxtl}|}{e} \leq \frac{e}{2}$$

This offset may be intentional, such as from an electric field due to a gate nearby whose potential can be varied as in a single electron transistor, or it may be due to unintentional causes, such as an electron trapped on a defect or an interface state in the enclosing matrix of barrier. In the event of transfer of an electron from the reservoir on to the island under application of a bias V and in the presence of a polarization charge Q_{ofs}, the change in energy, for $C_1 >> C_2$, is

$$eV = \frac{(e+Q_{ofs})^2}{2C_2} - \frac{Q_{ofs}^2}{2C_2} = \frac{e}{2C_2}\left(1 + \frac{2Q_{ofs}}{e}\right)$$

i.e., if the offset charge is $-e/2$, conduction is allowed. And, the largest Coulomb blockade occurs for e/2, and is e/C_2. The offset can appear due to polarization induced by a gate. Thus, under gate modulation, it is possible to have a condition where there is no blockade, so the conduction can be modulated from off (blockade) to on condition. In the first single electron transistor work of Fulton and Dolan [7], performed on aluminum junctions, both the existence of this offset charge and the tunability of this conduction was demonstrated. Likharev [10] provides a very complete description of the transport properties of the system. A more complete calculation of these capacitances using a self-consistent solution of the Poisson and the Schrodinger equation in the Hartree approximation and ignoring the exchange and correlation effects, can be performed using techniques such as that described

in [11]. It thus includes the quantization effects. Fig. 4 shows e.g. the conduction band-

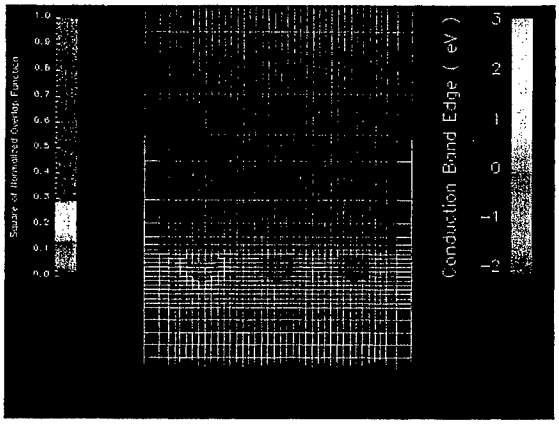


Fig. 4: Normalized overlap function together with conduction band edge for a cross-section through the gate stack of a nano-crystal memory. The magnitudes are intensity modulated.

edge and the envelope function for an example case of the nano-crystal memory containing three nano-crystals. The coupling capacitance to the channel is found to be significantly larger, with additional coupling to the other nano-crystals in the vicinity and, in particular, for the end nano-crystals there is stronger coupling to the source and drain reservoirs. The latter is not surprising; it is one of the major mechanisms for leakage of charge in floating gate memories. While these results are secondarily geometry specific (e.g., box, sphere, and hemisphere shapes) because of the different degree of confinement, the estimates of capacitance described before (self-capacitance) are within 20% of the more sophisticated calculations. The coupling capacitances to the channel and source and drain regions, therefore, have a stronger influence on the characteristics.

Confinement and Random Effects in Semiconductors:

Single charge tunneling, limited by the electrostatic energy argument of above, shows up best in metal systems, where the density of states is enormous and hence confinement does not place severe restrictions on the states occupied by the electron in the island. In practice, we work with semiconductor systems, where the density of states is many orders of magnitude lower. A consequence of this is an additional energy conservation term related to the energy of the confined state occupied by the electron. Hence the arguments of the required bias are modified by the subband energy term. It increases the energy requirement by E_0 for transit of one electron.

Interface states are a major source of the offset charge in these floating-gate structure. If we assume that surface states on the nano-crystals are the largest source of the offset charge, for a cubic quantum-dot, the mean threshold voltage and the standard deviation of

$$\overline{\Delta V_T} = \frac{e}{\varepsilon_{ox}}\left(t_{cntl} + \frac{1}{2}\frac{\varepsilon_{ox}}{\varepsilon_{Si}}t_{dot}\right)\frac{1}{4t_{dot}^2}\bar{v}$$

the threshold-voltage are:

$$\sigma(V_T) = \frac{e}{\varepsilon_{ox}}\left(t_{cntl} + \frac{1}{2}\frac{\varepsilon_{ox}}{\varepsilon_{Si}}t_{dot}\right)\frac{1}{t_{dot}}(6N_{\square T})^{0.5}$$

where $N_{\square T}$ is the interface state density. For oxide/silicon interfaces with thermally grown oxides the interface trap density is typically ~5×10^{10} $cm^{-2}eV^{-1}$ or less. For comparison, the effect of random dopants is given by [12]:

$$\sigma(V_T) = \frac{e}{C_{gate}}\left(\frac{N_A z_d}{3WL}\right)^{0.5}\left(1 - \frac{z_{undop}}{z_d}\right)^{1.5}$$

where z_d is the depletion region of the retrograde implant and z_{undop} is the lightly doped region width. Fig. 5 compares the fluctuation effect due to defects, random dopants and the

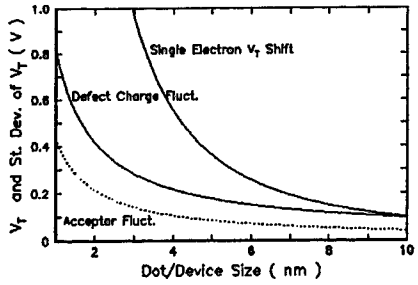


Fig. 5: The threshold voltage and its standard deviation as a function of quantum-dot size for a quantum-dot memory. For comparison the expectation from acceptor fluctuations is also included.

V_T shift to be obtained from a single electron. As dimensions decrease, the magnitude of the variations increases.

Comparison of Magnitudes:

Stray charge has already been seen to have a significant effect on the characteristics. Since the charging energy varies inversely with capacitance the charging energy varies linearly with dimensional variance, i.e.,

$$\frac{\Delta E_c}{E_c} = \frac{\Delta L}{L}$$

Relative dimensional tolerance are similar to the relative voltage tolerances if the effect is an intrinsic part of device operation. Current, ($e\Gamma$), is more severely affected by the dimensions and energy of the confining barrier due to the exponential dependence of quantum tunneling on the barrier height. Subband energies vary as inverse square of the dimensions. Thus the relative variation of the energy dependence is

$$\frac{\Delta E_0}{E_0} = \frac{2\Delta L}{L}$$

a requirement nearly twice as strong as due to the Coulomb effects. This places a stronger constraint on devices structures when dimensions are below ~ 7 nm.

The variance in threshold voltage of bulk MOSFETs increases with decreasing dimensions partly because of the random (Poisson) distribution of dopants and the limited number of dopants used to achieve the threshold voltage. A plausible solution to this is elimination of dopants, such as in double-gate[13] and back-plane structures[14]. In the former, the electrostatics of the structure, through control of silicon channel thickness, allows for a normally off device whose threshold voltage is determined by the material parameters. This threshold voltage can not be made very high. In the latter, a back-gate is used and provides the back-barrier and controls the threshold voltage through an applied potential. In either case, the contribution of channel random doping is eliminated. But now, the variance in threshold voltage is determined by the lateral distribution of the dopants in the shallow contact regions, and can be interpreted as an effective channel length variation across the width of the device. Theoretically, such a variance is in the 1-5 mV range for 25 nm junction spacing, instead of the retrograde channel doping contribution of the order of 20-40 mV. Instead of channel doping, in the back-plane geometry (and with some modifications in the double-gate geometry), the thickness variations of silicon, through the linear electrostatic potential change ($\psi \sim t$ instead of $\psi \sim t^2$ for doped channels), now contributes to threshold voltage variation. Current SOI structures have a thickness variance of ~0.4 nm over 10 μm^2 areas. Assuming that this can be improved to 0.3 nm, a 10 mV threshold voltage variance leads to a limit in usable silicon thickness of > 10 nm. Confinement introduces an inverse square dependence on the subband energy. This is worse than the linear electro-

static potential dependence. Fig. 6 shows the variation of this energy as a function of the

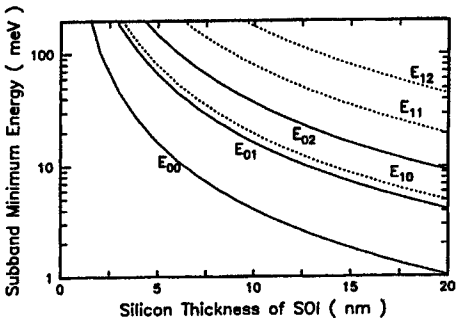


Fig. 6: Subband minimum energy as a function of the silicon thickness of an SOI structure.

thickness of the silicon channel. Below 5 nm in thickness, the subband energies change very rapidly.

Tunneling:

Tunneling in Oxide: At small dimensions, two regions of tunneling are important: oxide tunneling (injection and control oxides) which determines the competing balance between injection and ejection, and between source and drain which determines the smallest limit of the device. Fig. 7 shows a cross-section of thin gate oxide and calculated

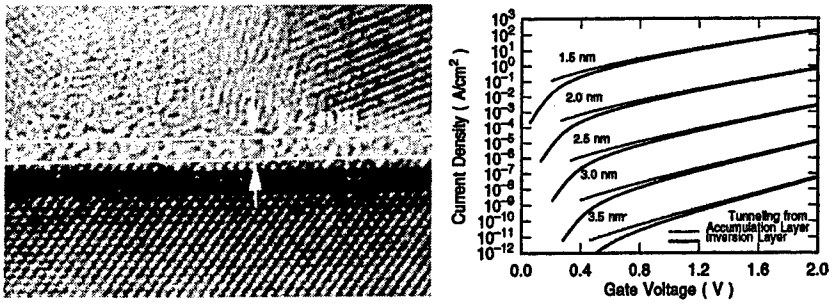


Fig. 7: A cross-section of a thin gate oxide and the calculated gate tunneling current from accumulation regions and inversion region.

tunneling current [15]. As oxide thickness decreases, a large current density can be

obtained through thin barriers. Indeed, a 0.15 nm change in oxide thickness leads to a current density change by a factor of 10. Note that a larger roughness arises from the top poly-silicon gate/SiO_2 interface while the bottom surface is nearly atomically smooth. Random effects should be expected from the random gate control capacitance and dopant activation in this poly-silicon/oxide region.

Tunneling in Silicon: With a bandgap of 1.1 eV and a low transverse effective mass (0.19 m_0, Bohr radius~3-4 nm), tunneling between the source/drain regions and the substrate, and from the source to the drain, becomes significant when the distance scales are ~10 nm. For bulk nMOSFET structures, inter-band tunneling appears when acceptor doping in channel or halo-doped regions approaches $2x10^{19}$ cm^{-3}. This tunneling occurs at the source junction and at the reverse-biased drain-substrate junction, and is a stand-by power constraint similar in nature to that from oxide thickness. In thin silicon structures, inter-band tunneling (conduction to valence band and back) is avoided if the threshold voltage of the device allows $V_D+(V_G-V_T)<E_g/e$, a condition that prevents tunneling at the drain end, and is equivalent to the threshold voltage not exceeding ~0.55 eV for 0.5 V drain bias. This threshold voltage is consistent with requirements of low sub-threshold leakage currents for designs with good sub-threshold swing. So, intra-band tunneling between source and drain through the channel barrier is a fundamental constraint for adequate field-effect operation and needs to be satisfied in the quantum-dot memory. Fig. 8 shows tunneling

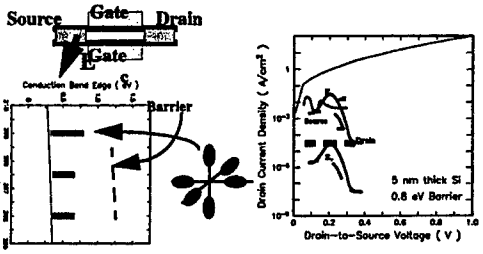


Fig. 8: Model tunneling current calculation between source and drain for a gate bias causing 0.8 eV barrier. Largest tunneling occurs from the low transverse mass valleys.

current between source and drain, for a 5 nm thick sliver of silicon (junctions box doped $5x10^{18}$ cm^{-3} and 10 nm apart) for a quasi-two-dimensional self-consistent Schrodinger-Poisson calculation. The longitudinal masses of the doubly degenerate ellipsoids form the lowest energy ladder with the smaller transverse mass available for tunneling. The 4-fold degenerate in-plane ellipsoids cause tunneling through the longitudinal mass. Tunneling

from the doubly-degenerate states dominates. This tunneling current, between source and drain, establishes a fundamental constraint of 10 nm for channel length, where the field-effect is not subsumed by tunnel effect, and is a practical constraint at which the stand-by current caused by tunneling leads to too high a stand-by power drain during chip operation. Geometries such as the straddle-gate structure can satisfy this constraint while allowing for a small enough quantum-dot.

QUANTUM KINETIC MODELING

Details of the modeling of the charging and discharging process are given elsewhere[16]; here we summarize only the salient steps of this modeling, and then discuss the implications. The Hamiltonian for the coupled system consisting of the channel region (in inversion: two-dimensional electron gas) coupled to the quantum-dot is:

$$H = H_{2deg} + H_{qd} + H_T \qquad or \qquad H = H_0 + H_T$$

$$with \qquad H_0 = H_{2deg} + H_{qd}$$

and

$$H_{2deg} = \sum_n (\varepsilon_n + eV) a_n^\dagger a_n$$

$$H_{qd} = \sum_m \varepsilon_m b_m^\dagger b_m + E_s(v)$$

where $E_s(v)$ is the electrostatic energy and m's and n's identify the quantum-dot and the channel states.

$$H_T = \sum_{n,m} T_{nm} a_n^\dagger b_m + cc$$

The state of the system is $|n_n, n_m\rangle$, where n_n and n_m represent the occupation number in the channel and the quantum-dot. It is useful to write time evolution of the density matrix in the Heisenberg representation:

$$i\frac{h}{2\pi}\frac{\partial}{\partial t}\hat{P}_H(t) = [H, \hat{P}_H(t)]$$

which yields the equation of motion in interaction representation:

$$\frac{\partial}{\partial t}\hat{P}_I(t) = -i\frac{2\pi}{h}[H_T, \hat{P}_I(t_0)] + \left(i\frac{2\pi}{h}\right)^2 \int_{t_0}^{t} [H_T(t), H_T(t'), \hat{P}_I(t')]dt'$$

and which can be formulated as the Rate/Master equation:

$$\frac{\partial}{\partial t}\boldsymbol{P}(t) = \mathbf{W} \bullet \boldsymbol{P}(t)$$

To calculate the time-dependence of the charging and discharging, we first calculate self-consistently for all eigenstates in the channel for a given number of electrons stored in the quantum-dot for all gate voltages, repeat it for the different number of electrons allowed, determine the transition rates, and then determine the time-dependence from the rate equations. Probability of quantum-dot occupation number $\{n_m\}$ is:

$$p(\{n_m\})(t) = \sum_{\{n_n\}} \langle \{n_n\}, \{n_m\} | \hat{P}_I(t) | \{n_n\}, \{n_m\} \rangle$$

and probability of having ν electrons in the quantum-dot $\sum_m n_m = \nu$ with transition

$$p_\nu(t) = \sum_{\{n_m\}} \sum_{\{n_n\}} \langle \{n_n\}, \{n_m\} | \hat{P}_I(t) | \{n_n\}, \{n_m\} \rangle \delta\left(\sum_m n_m, \nu\right)$$

rates determined using the coupling constants and the occupation statistics. The average

$$\bar{\nu} = \langle \nu \rangle = \sum_{\nu=0}^{\nu_0} \nu p_\nu$$

$$\sigma_\nu^2 = \langle \nu^2 \rangle - \langle \nu \rangle^2 = \sum_{\nu=0}^{\nu_0} \nu^2 p_\nu^2 - \left(\sum_{\nu=0}^{\nu_0} \nu p_\nu \right)^2$$

and variance of electrons is:

This now gives us the information from which many of the parameters of interest can be calculated.

Carrier Statistics and Charge Fluctuations:

From the master equation, the stationary solution follows from:

$$\mathbf{W} \bullet \boldsymbol{P}(t) = 0$$

where the transition matrix **W** is of dimensions $\nu_{max} \times \nu_{max}$ where ν_{max} is the number of electrons in the quantum-dot set for computational tractability, and the vector $\boldsymbol{P}(t)$ =

$[p_0(t), p_1(t), p_2(t), \ldots p_{vmax}(t)]$ is the probability of having *0, 1, 2, ...* v_{max} electrons in the quantum-dot.

This now allows determination of the time-dependence. relate to the classical expressions for current, threshold voltage, and also derive the spectrum for single quantum-dot. Fig. 9 shows an evolution of electrons in a dot due to injection from inversion layer under

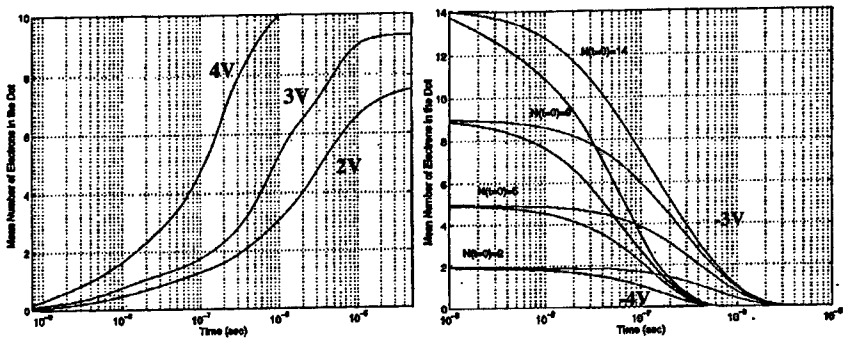


Fig. 9: The evolution of the mean number of electrons in a silicon quantum-dot (10 nm x 10 nm x 6 nm) from an inversion layer due to direct tunneling from an injection oxide of 1.5 nm at three different gate-to-inversion layer potentials. The evolution during ejection is shown on the right.

three different bias conditions. At the 2 V bias condition, it takes nearly 100 ns before the average reaches one electron. The transition rates are too low because of the large oxide barrier height and small overlap. But, it changes rapidly with bias so that less than 10 ns is needed at 4 V bias. The saturation in number of electrons between 100's of ns to 10's of μs for the differing bias voltages represents the effect of reduced dimensions. As the charging process nears flat-band conditions, the injection process begins to slow down for the same reasons that slow the process at low bias voltages. Now consider the same structure during erasure (Fig. 9) when a negative potential is applied at the gate to eject the electrons into the substrate. A number of starting electrons are considered for two differing voltages. The behavior does not have the detailed features of the injection process; the injection process reveals more of the details of the states being tunneled into. The time-constants of ejection are however quite similar to that of injection. At 2 V, not shown, the process has very appreciably slowed down. The lifetime in the dot has become very large.

Fig. 10 shows mean and variance in the number of electrons for a calculation in which

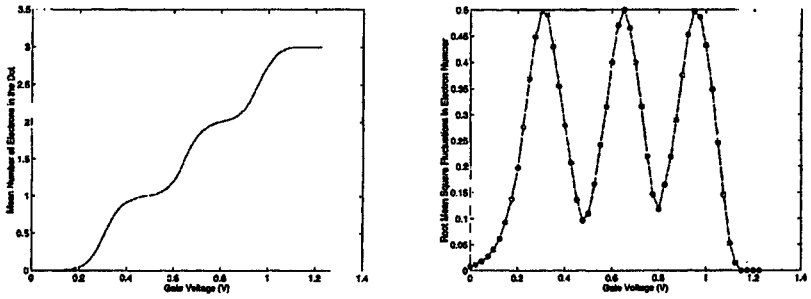


Fig. 10 The mean and variance as a function of gate voltage for occupation in the quantum-dot for a model example of quantum box coupled to the channel and controlled by the gate.

a maximum of 3 electrons is allowed. The variance is 1/2 at gate voltages where the mean number of electrons is integer+1. The actual number of electrons in the quantum dot can take only integer values. A mean number of integer+1/2 implies that the actual number of electrons is fluctuating rapidly between integer and integer+1. The fluctuations in current, etc. follow from these calculations by coupling to the classical transport equations of the field-effect.

III. PERCOLATION EFFECTS

The nano-crystal memory operates by screening of the channel from the gate by stored electrons in the nano-crystal. The nano-crystals have a disordered distribution on the oxide surface. The occupation of the nano-crystals by electrons is modeled to the first order by the rate equation derived before. When only a fraction of the nano-crystals are occupied, and this is a function of applied bias and time, transport takes place underneath through the unscreened areas. This is similar to the classic problem of bond percolation. The conductance of this area, e.g. measured at low drain-to-source voltages, should show percolative behavior with a criticality that is dependent on time and voltage. We model this system approximately by assuming a square lattice whose conductance we calculate between the edges. The occupation is determined using the rates, and for this calculation we do not consider any two-dimensional effects along the channel.

Fig. 11 shows the application of the rates of charging to a square lattice of the quantum-dots as a snapshot in time for a voltage of 2.0 V between the gate and the channel. The occupation of an electron in a quantum-dot is represented by a filled dot. Its presence

depletes the channel area underneath of electrons. A turn-off of the device requires blockage of the resistive conduction path between source and drain. In Fig. 11, this occurs

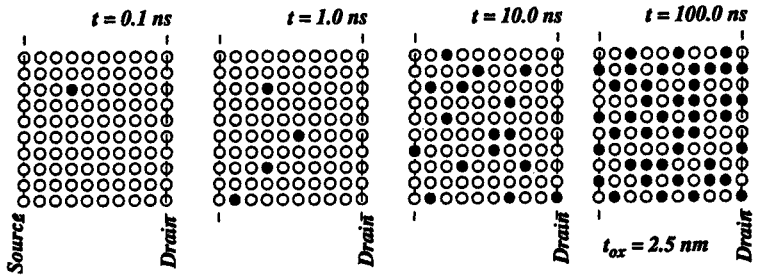


Fig. 11: Charging of a square lattice array of nano-crystals for tunneling injection oxide thickness of 2.5 nm and a gate bias voltage of 2.0 V as a function of time.

between 10 ns and 100 ns. Fig. 12 shows the dependence of conductance on time and voltage with the other as parameter.

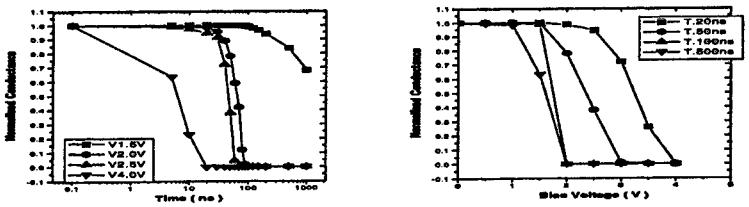


Fig. 12: Normalized conductance as a function of time (a) and bias voltage (b) for the square lattice of the previous example.

Percolation is clearly observable in these simulations, and a minimum necessary nano-crystal density and voltage and time is needed for reproducible operation. Note, however, that not all nano-crystals have to be filled with electrons for conduction to be shut off. Thus, time scales smaller than those required to fill all nano-crystals are sufficient and probabilities significantly smaller than unity still allow operation.

IV. CAN WE AVOID USE OF COLLECTIVE PHENOMENA?

Digital microelectronics optimizes device and interconnection technology with the circuit design to obtain the necessary functions at the characteristics desired (usually a combination of several attributes: speed, power dissipation, voltages of operation, density,

reliability, noise immunity, cost, etc.). It requires a judicious blend, one of whose important component has been the reduction of dimensions. Smaller dimensions lead to faster devices, lesser area, and lower power - all desirable properties. High yields can be maintained only by improvements in technology and use of device designs that minimize variations arising from technology. CMOS, with the use of a rail-to-rail circuits, restores levels and is less sensitive to variations so long as devices maintain reasonable active power gain. The use of collective phenomena has been implicit in this progress because the number of electrons used has always been large enough. It reduces the variances arising from random effects and usually also takes care of variations arising from systematic effects (dimensions, resistances, etc.) arising from the practice of technology. Reduction of dimensions, while reducing the power (usually), also increases the variance due to random effects[1] that appear in statistical fluctuations in voltages (threshold, threshold shifts, etc.) and in currents (magnitude, time and phase). So, implicit in this is a worsening of the noise-margin for operation of devices, in logic and in memory, and minimum voltages that can be tolerated and that can compensate for voltage noise margins. For a CMOS inverter gate driving another inverter gate, the number of electrons that are transferred during a low loaded switching event is shown in Fig. 13 together with energy dissipation during switching. This figure assumes (among many other assumptions) a changing of voltage levels to

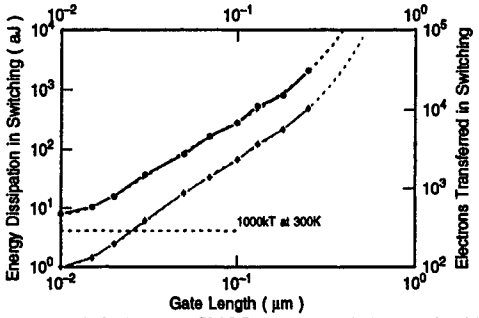


Fig. 13: Number of electrons switched when a CMOS inverters switches another identical CMOS inverter together with the energy dissipated in the process.

accommodate the power dissipation constraints. Nearly 100 electrons still flow through during the switching and their number can be made larger by scaling the width of the device. Deviations in threshold-voltages changes the amount of drive available approximately linearly with an average transconductance as the multiplication factor. A large consequence of any changes in drive current is a proportional change in switching times

1.For a sample N, with Poisson distribution, approximatable by a normal distribution, the standard deviation is $N^{1/2}$.

and hence problems in timing and clocking. For logic, therefore, the consequence of scaling size is serious; however, device design (through width) and circuit design (through careful timing analysis and design) can compensate and allow a functioning design.

For memories, the issues are more difficult. Static RAMs are flip-flops made using CMOS gates. The previous comments apply to it; SRAMs also use lower voltages and are much more sensitive to variances in threshold voltages due to the need to minimize imbalances in the flip-flop. Dynamic memories use a large number of electrons on the capacitors (~40 fC of charge, equivalent to ~250,000 electrons). Fitting such a large number of electrons, as dimensions are scaled, is an increasingly difficult task because we are demanding that the capacitance not be scaled. An increase in the third dimension is needed and higher and higher aspect ratios are more and more difficult to achieve. An equally big problem is that of retention time. Transistors are designed to have fA of off-state current so that the electrons do not leak easily and refresh cycles are slow. However, changes in threshold voltages change the off-state leakage current exponentially for barrier-modulated transport as is the case for electron diffusion. So, the leakage current changes by approximately a factor of 10 for every ~60 mV change in V_T. This is very difficult to design around through a worst case design. Quantum-dot memories and the nano-crystal memories attempt to work around these issues by using the oxide barrier for storage of charge and using a gain cell (conversion of the change in electrostatic potential into the current carried by the device) and do it with low power by reducing the number of electrons needed to obtain the memory effect. Two problems arise: one is the need to work with low voltages and the second is the need to work with the smaller numbers and their consequent Poisson variance problem.

First consider the issue of voltages. Smaller size increases the eigenenergies and the electrostatic charging energy as seen in Table 1. The voltages needed for the charging are increased by the lever effect ($\sim t_{cntl}/t_{inj}$) approximately a factor of 3 to 5. To work with voltages of ~ 3 V, the charging energies should not exceed ~0.6 to 1 eV. To compensate for random variations, in a quantum-dot memory one needs to work with ~5 electrons. So, this implies a size in between 10 nm and 3 nm. These dimensions still maintain a charging energy larger than thermal voltages. For nano-crystal memories, the large number of quantum-dots help in minimizing the variance. A similar size range in dot size is still necessary. Fig. 14 shows the power-speed trade-off that comes with the use of a single electron within the size constraints described. Using larger number of electrons scales it higher. However, it is still significantly smaller than that for alternative semiconductor memory structures. It is therefore quite likely that, if we are willing to trade speed for lower power, we will be

able to work with smaller number of electrons and still achieve the control on electrical variations desired for microelectronics.

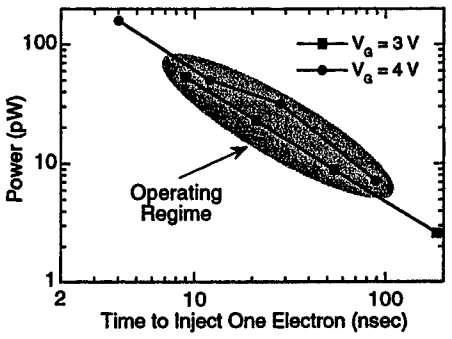


Fig. 14: Power-speed trade-off for single electron operation in quantum-dot memory.

V. CONCLUSIONS

As field-effect devices reach their operational - fundamental and practical - limits, and assimilate semi-classical and quantum-mechanical effects in their operation, increased sensitivity in static and dynamic operational fluctuations are inevitable. Thickness and length control of barriers and channels are clearly a very essential requirement and they have an increasing variation due to quantum effects. And, since tunneling currents vary exponentially, the consequences of leakage can also be quite significant. Small silicon memories, such as the nano-crystal and quantum-dot, combine the field-effect with the discreteness that comes from use of small dimensions. For control of electrical variations, they have to solve similar issues as CMOS, and so long as dimensions, interface states, etc., can be controlled, and a few electrons are used, they can be practical and useful.

ACKNOWLEDGEMENTS

The work summarized in this paper has evolved over a number of years with contributions from many people, and discussions with many have helped clarify ideas. In particular, I express my gratitude to Kevin Chan. Support of IBM and of DARPA through grant N66001-7-1-8908 is also gratefully acknowledged.

REFERENCES

[1] S. Tiwari, F. Rana, K. Chan, H. Hanafi, W. Chan, and D. Buchanan, Tech. Dig. of IEDM, 521, 1995

[2] J. J. Welser, S. Tiwari, S. Rishton, K. Y. Lee, and Y. Lee, IEEE Electron Device Letters, 278, 1997

[3] S. Guo, E. Leobandung, and S. Chou, Science, vol. 175, 649, 1997

[4] K. Yano, T. Ishii, T. Hashimoto, T. Kobayashi, F. Murai, and K. Seki, Tech. Dig. of IEDM, 541, 1993

[5] K. Nakazato, R. J. Blaikie, and H. Ahmed, J. Appl. Phys., vol. 75, 5123, 1994

[6] C. A. Neugebauer and M. B. Webb, J. Appl. Phys., vol. 33, 74, 1962

[7] T. A. Fulton and G. J. Dolan, Phys. Rev. Lett., vol. 59, 109, 1987

[8] H. Grabert and M. H. Devoret, *Single Charge Tunneling*, Plenum Press 1992

[9] M. H. Devoret, in *Single Charge Tunneling* (Ed. H. Grabert and M. H. Devoret) Plenum Press 1, 1992

[10] K. K. Likharev, Phys. Rev. B, vol. 165, 821, 1968

[11] A. Kumar, S. E. Laux, and F. Stern, . Phys. Rev. B, 1990, vol. 42 5166

[12] D. Burnett and S. W. Sun, Proc. SPIE, vol. 2636, 83, 1995

[13] D. J. Frank, S. E. Laux, and M. V. Fischetti, Tech. Dig. IEDM, 553, 1992

[14] I. C. Yang, C. Vieri, A. Chandrakasan, and D. A. Antoniadis, Tech. Dig. IEDM, 877 1995

[15] F. Rana, S. Tiwari, and D. A. Buchanan Appl. Phys. Lett., vol. 69, 1104, 1996

[16] F. Rana, S. Tiwari, and J. J. Welser, Superlattices and Microstructures, Vol. 23, 757, 1998

ELECTRON WAVEGUIDE PUMPED QUANTUM WIRE FAR IR LASER

Erik Forsberg*, Jan-Olof J. Wesström, Lars Thylén
The Laboratory of Photonics and Microwave Engineering, Department of Electronics, Royal Institute of Technology (KTH) Stockholm, Sweden

Thomas Palm
Ericsson Components AB Stockholm, Sweden

ABSTRACT

A novel concept for carrier injection in low-dimensional semiconductor lasers using ballistic electron waveguides is proposed. The concept is studied for a quantum wire far IR laser. Computer simulations on the carrier injection and calculations of threshold current densities and modulation bandwidths are presented

I. INTRODUCTION

Low-dimensional semiconductor lasers, e.g. quantum wires and dots promise significant improvement of characteristics such as threshold current, spectral properties and modulation bandwidths [1]. However, early experiments failed to deliver what was promised and poor luminescence was shown. These results were soon explained as an intrinsic effect of low-dimensional devices, a combination of inefficient energy relaxation due to lack of phonons and orthogonality of carrier quantum states. This was dubbed 'the phonon bottleneck' [2], [3], [4]. Also, the maximum modulation bandwidth is expected to be limited by slow carrier capture. [5], [6], [7]. While this is true for interband lasers the 'phonon bottleneck' can actually be beneficial for intraband lasers.

Since it turned out to be hard to observe the 'phonon bottleneck' experimen-

*email: erikf@ele.kth.se

tally [8], this prompted a long (and still ongoing) discussion about the existence of the 'phonon bottleneck' and what processes limits its effects (multiphonon processes [10], Auger-like mechanisms [11], defect-state related relaxation [12]).

This has led us to study alternative ways of injecting carriers into the active region. In this paper we propose carrier injection using ballistic electron waveguides. Using this approach the carriers are injected selectively into to the upper lasing level using 'wavefunction engineering'. This way the 'phonon bottleneck' problem is completely circumvented, *albeit* at the expense of a more complex manufacturing technology.

We begin by introducing the concept of carrier injection using ballistic electron waveguides and use computer simulations to calculate the excitation efficiency. Based on those calculations the threshold current and small-signal frequency response are calculated using rate equations.

II. CARRIER INJECTION

A. Principle

The most obvious idea as how to avoid time-consuming relaxation processes before the carriers end up in the desired excited state, is direct injection to that specific state. In a low-dimensional semiconductor laser this can be achieved by injecting the electrons ballistically using electron waveguides. In Fig. 1 this type of injection into a quantum wire (labeled central waveguide in the following) is shown schematically.

Electrons from the source are injected through the source waveguide into the central waveguide, which is the active region. The source and central waveguides are connected by two paths. We can tune the phase difference, $\Delta\phi = ak_f - bk'_f$, between these two paths, by adjusting the path lengths a and b (indicated in Fig. 1) and the Fermi vector. This way we can, for electrons having a longitudinal wave vector within a certain range, achieve a predominant injection into a higher transverse subband in the central waveguide and thus create a population inversion. After an optical transition in the central waveguide the electrons empty to the drain through the drain waveguide.

Explaining the concept in more detail we turn to Fig. 2 which shows an energy diagram of the structure from Fig. 1. The source and drain waveguides have only one bound transverse mode whereas the central waveguide has two. As can be seen, the energy levels are aligned in such a way that the energy of the higher of the two bound modes in the central waveguide equals that of the single mode in the source waveguide, whereas the energy of the lower mode equals that of the drain waveguide. The bias across the device is $V = (\mu_1 - \mu_2)/(-e)$. Electrons from the source waveguide populate the central waveguide modes up to μ_1, and

electrons from the drain will populate the mode(s) in the central waveguide up to μ_2. Electrons that populate the upper mode of the central waveguide will contribute to the photon emission as indicated. As will be shown later, it is essential for laser operation that electrons populate the second bound transverse mode in the central waveguide with high probability over a ideally rather broad range of longitudinal electron wave vector. It is also important that the electrons in the lower mode of the central waveguide empty into the drain waveguide with as low reflection as possible.

We define the transmission probabilities as follows: $T_{ij,mn}$ is the probability of transmission from mode m in lead i to mode n in lead j. If we denote the source waveguide lead 1, the central waveguide lead 2 and the drain waveguide lead 3, the ideal transmission coefficients would be

$$\begin{array}{llll} T_{11,11}=0 & T_{21,21}=1 & T_{23,21}=0 & T_{32,11}=1 \\ T_{12,11}=0 & T_{21,11}=0 & T_{23,11}=1 & T_{32,12}=0 \\ T_{12,12}=1 & & & T_{33,11}=0 \end{array}$$

Note that using this terminology, $T_{11,11}$ and $T_{33,11}$ represent reflections. Although all of these are important for the operation of the laser, the transmission coefficients that are crucial are those between the source and central waveguides.

B. Simulations

In order to test the feasibility of the idea of creating a population inversion as proposed in the previous section, computer simulations were made. First the potential in a heterostructurally defined waveguide structure was calculated using a Thomas-Fermi approximation. Then the time-dependent Schrödinger equation was solved for an electron wave packet inbound from the source waveguide using the BPM-method [13]. Fig. 4 shows snapshots from such a simulation. Examining Fig. 4 we clearly see that the second bound mode of the central waveguide is excited.

From these transport simulations we can calculate the transmission coefficients. Fig. 5 shows the transmission coefficients $T_{11,11}$, $T_{12,11}$ and $T_{12,12}$ for the simulated structure. As can be seen the upper level is populated with a high probability within a certain range of the longitudinal wave vector of the inbound electron wave, which is what is required. There seems to be much room for further optimizations of the structure.

III. THRESHOLD CURRENT

We envision two possibilities of using the proposed structure as an active element in a resonant optical cavity, thereby creating a laser. Either in a VCSEL

(Vertical Cavity Surface Emitting Laser) type structure as in Fig. 3 (a) or in an in-plane type laser structure as in 3 (b). In this section we calculate the threshold current for both cases.

A. Absorption cross section

To calculate the threshold current we begin by calculating the absorption cross section σ [14],

$$\sigma = \frac{W\hbar\omega}{0.5E_{opt}^2/Z} \tag{1}$$

E_{opt} is the optical field and ω the optical angular frequency. $Z = (nc\epsilon_0)^{-1}$ is the wave impedance with n, c and ϵ_0 being the refractive index, the speed of light and the permittivity of vacuum respectively. The transition rate W, is given by Fermi's Golden Rule

$$W = \frac{2\pi \mid H_{21} \mid^2}{\hbar^2}\frac{}{\Delta\nu}, \tag{2}$$

where $\Delta\nu$ is the transition linewidth and

$$H_{21} = \langle \Psi_u \mid H'(\vec{r}) \mid \Psi_l \rangle. \tag{3}$$

The interaction Hamiltonian $H'(\vec{r})$ is defined as

$$H'(\vec{r}) = \frac{e}{m}A(\vec{r})\vec{\eta}\cdot\vec{p} = \frac{e}{m}A_0 e^{-\vec{\kappa}\cdot\vec{r}}\vec{\eta}\cdot\vec{p}, \tag{4}$$

where $\vec{p}$ is the momentum operator, $\vec{\eta} = \alpha_x\cdot\hat{x} + \alpha_z\cdot\hat{z}$ is the polarization vector, and $A(\vec{r})$ the vector potential. We set the wavefunctions to be

$$\Psi_u = u_c(\vec{r})\zeta_u(\vec{r}) \tag{5}$$

$$\Psi_l = u_c(\vec{r})\zeta_l(\vec{r}), \tag{6}$$

where $u_c(\vec{r})$ are the Bloch-function and $\zeta_{u,l}$ the envelope-functions. If we assume an infinite hardwall potential we can write the envelope functions as

$$\zeta_u(\vec{r}) = \sqrt{\frac{4}{L_xL_yL_z}}\cos(\frac{\pi z}{L_z})\sin(\frac{2\pi x}{L_x})e^{(\imath k_u y)} \tag{7}$$

$$\zeta_l(\vec{r}) = \sqrt{\frac{4}{L_xL_yL_z}}\cos(\frac{\pi z}{L_z})\cos(\frac{\pi x}{L_x})e^{(\imath k_l y)}. \tag{8}$$

Evaluating (4) using (5)-(8) yields

$$H_{21} = \frac{8i\hbar e A_0 \alpha_x}{3mL_x}\delta_{\vec{k_u},\vec{k_l}} \tag{9}$$

E_{opt} in (1) is related to the vector potential A via $E_{opt} = -i\omega A$. Inserting this together with (2) and (9) we arrive at the following expression for the absorption cross section

$$\sigma = \frac{256\pi\hbar e^2\alpha_x^2}{9c\epsilon_0 n\omega\Delta\nu m^2 L_x^2}. \tag{10}$$

B. Rate equations

We assume the following rate-equations to estimate the threshold current.

$$\frac{\partial n_2}{\partial t} = \frac{\kappa J}{e} - \frac{n_2}{\tau_{21}} - \overline{g}S \tag{11}$$

$$\frac{\partial n_1}{\partial t} = \frac{(1-\kappa)J}{e} + \frac{n_2}{\tau_{21}} + \overline{g}S - \frac{n_1}{\tau_{1out}} \tag{12}$$

$$\frac{\partial S}{\partial t} = \overline{g}S - \frac{S}{\tau_p} + \frac{\beta}{\tau_{sp}}n_2, \tag{13}$$

where n_1 and n_2 are the carrier densities in the two modes of the central waveguide and S is the photon density. τ_{21} and τ_{1out} are the carrier lifetimes of the upper and lower transverse modes respectively. We have accounted for the fact that only a fraction κ of the injected current density J ends up in the upper bound mode, this due to the non-ideal transmission coefficients (Fig. 5). τ_p is the photon lifetime

$$\frac{1}{\tau_p} = \frac{c}{n}[\alpha_i + \frac{1}{L}ln(\frac{1}{\sqrt{R_1R_2}})], \tag{14}$$

where c is the velocity of light, n the group index, α_i the internal loss, L the cavity length and $R_{1,2}$ the mirror reflectivities. The gain is

$$\overline{g} = \frac{c\sigma}{L}(n_2 - n_1), \tag{15}$$

where σ is the absorption cross section.

Steady state, i.e. $\frac{\partial}{\partial t} \rightarrow 0$, yields the following expressions for the carrier densities, using (11) and (12)

$$n_1 = \frac{\tau_{1out}J}{e} \tag{16}$$

$$n_2 = \frac{\tau_{21}\kappa J}{e} - \tau_{21}\overline{g}S. \tag{17}$$

τ_{1out} is essentially determined by the time it takes for the electrons to travel through the central waveguide combined with the transmission probability $T_{23,11}$, which by careful design can be made close to unity. So we can safely assume $\tau_{1out} \ll \tau_{21}$ and can also assume $n_2 \gg n_1$. Above threshold n_2 will be clamped to it's threshold value $n_{2,th}$, which we can estimate using (13)-(15), the assumption above and neglecting the spontaneous emission.

$$n_{2,th} = \frac{L}{c\sigma\tau_p} \tag{18}$$

Inserting this into (11) at threshold ($S = 0$) yields the threshold current density

$$J_{th} = \frac{Le}{\kappa\tau_{21}c\tau_p\sigma} \tag{19}$$

This result emphasizes what was discussed in the previous section, namely that it is vital for the lasers performance that as many as possible of the electrons injected from the source waveguide populates the upper mode in the central waveguide, i.e. we need a sufficiently large κ.

C. A numerical estimate

For a 10 meV (2.4 THz) transition in a 40 nm wide quantum wire we calculate the threshold current densities in the VCSEL and in-plane cases. The transition linewidth is somewhat arbitrary chosen to be $\Delta\nu = 100$ GHz. The relaxation time τ_{21}, has for a V-groove quantum wire been measured to be 200 ps [15], but since we consider etched wires we assume $\tau_{21} = 100$ ps, allowing for faster relaxation through defect states. The material system is GaAs, and we approximate the group index of refraction with the bulk refractive index, which is n=3.62 at the transition wavelength [16]. Further we assume the following parameters.

Parameter	VCSEL	In-Plane
Mirror reflectivity R_1, R_2	99,5%	32%
Internal losses α_i	2000 m^{-1}	500 m^{-1}
Cavity length L	18μm	250 μm
Photon lifetime τ_p, calculated using (14)	5.3 ps	2.2 ps

Setting the polarization vector to be $\vec{\eta} = 1 \cdot \hat{x}$ and using the simulation results to choose $\kappa = 0.7$. With (10) we find $\sigma = 2.8 \cdot 10^{-15}$ m^2. This gives an estimate of the threshold current densities: $J_{th}^{VCSEL} = 0.93$ A/cm^2 and $J_{th}^{In-Plane} = 29$ A/cm^2.

IV. MODULATION BANDWIDTH

We calculate the small signal modulation response $\Delta S(\omega)/\Delta J(\omega)$ for the VCSEL structure. Introduce

$$J = J_{SS} + \Delta J \quad (20)$$
$$n_2 = n_{2,SS} + \Delta n_2 \quad (21)$$
$$n_1 = n_{1,SS} + \Delta n_1 \quad (22)$$
$$S = S_{SS} + \Delta S, \quad (23)$$

where SS denotes steady state. Inserting these into (12)-(13) together with (15) we get (neglecting higher order terms)

$$\frac{\partial \Delta n_2}{\partial t} = \frac{\kappa \Delta J}{e} - \frac{\Delta n_2}{\tau_{21}} - \frac{c\sigma}{L}(n_{2,SS} - n_{1,SS})\Delta S - \frac{c\sigma}{L}(\Delta n_2 - \Delta n_1)S_{SS} \quad (24)$$

$$\frac{\partial \Delta n_1}{\partial t} = \frac{(1-\kappa)\Delta J}{e} + \frac{\Delta n_2}{\tau_{21}} + \frac{c\sigma}{L}(n_{2,SS} - n_{1,SS})\Delta S + \frac{c\sigma}{L}(\Delta n_2 - \Delta n_1)S_{SS} - \frac{\Delta n_1}{\tau_{1out}} \quad (25)$$

$$\frac{\partial \Delta S}{\partial t} = \frac{c\sigma}{L}(n_{2,SS} - n_{1,SS})\Delta S + \frac{c\sigma}{L}(\Delta n_2 - \Delta n_1)S_{SS} - \frac{\Delta S}{\tau_p} + \frac{\beta}{\tau_{21}}\Delta n_2 \quad (26)$$

Making use of the assumption $n_2 \gg n_1$ and assuming harmonic current modulation ($\frac{\partial}{\partial t} \rightarrow j\omega$) we can rewrite (24)-(26) into the following matrix equation

$$\begin{pmatrix} \omega + A & -E & B \\ -A & \omega + F & -B \\ -C & E & \omega - D \end{pmatrix} \begin{pmatrix} \Delta n_2 \\ \Delta n_1 \\ \Delta S \end{pmatrix} = \frac{\Delta J}{e} \begin{pmatrix} \kappa \\ 1-\kappa \\ 0 \end{pmatrix}, \quad (27)$$

where we have defined

$$A = \frac{1}{\tau_{21}} + \frac{c\sigma}{L}S_{SS} \quad (28)$$
$$B = \frac{c\sigma}{L}n_{2,SS} \quad (29)$$
$$C = \frac{c\sigma}{L}S_{SS} + \frac{\beta}{\tau_{sp}} \quad (30)$$
$$D = \frac{c\sigma}{L}n_{2,SS} - \frac{1}{\tau_p} \quad (31)$$
$$E = \frac{c\sigma}{L}S_{SS} \quad (32)$$

$$F = \frac{c\sigma}{L} S_{SS} + \frac{1}{\tau_{1out}}. \quad (33)$$

Since we are operating above threshold $n_{2,SS} = n_{2,th}$ and S_{SS} is, using (11) and (13)

$$S_{SS} = \frac{\tau_p \kappa}{e}(J - J_{th}) + \frac{\beta \tau_p n_{2,th}}{\tau_{sp}} \quad (34)$$

We solve (27) numerically for $\Delta S(\omega)/\Delta J(\omega)$, with $\beta = 0.008$, for varying current densities J. The result is plotted in Fig. 6. As can be seen high modulation bandwidths are in principle achievable. However, one should notice that here we have not taken into account nonlinear gain which will limit the maximum modulation bandwidth [17], thus the modulation bandwidths presented here are somewhat overestimated.

V. CONCLUSIONS

We have presented a new way of injecting carriers into low-dimensional semiconductor laser structures, which circumvents the long-discussed 'phonon bottleneck'. The approach was numerically tested on an intraband quantum wire far IR laser and we found very promising threshold currents and modulation bandwidths. However, we are not limited to just a quantum wire laser, this concept could also be applied to a quantum box type laser.

ACKNOWLEDGMENT

This work was partly supported by the Foundation for Strategic Research and the EU-project Q-SWITCH (Esprit project number 30960). The authors would like to thank Petter Holmström and Ulf Ekenberg at the Royal Institute of Technology and Mats-Erik Pistol at Lund University for helpful discussions.

References

[1] Y. Arakawa, K. Vahala, and A. Yariv, Appl. Phys. Lett. **45**, 950 (1984).

[2] U. Bockelmann and G. Bastard, Phys. Rev. B **42**, 8947 (1990).

[3] H. Bensity, C. M. Sotomayor-Torrès, and C. Weisbuch, Phys. Rev. B **44**, 10645 (1991).

[4] K. Mukai, N. Ohtshuka, H. Shoji, and M. Sugawara, Appl. Phys. Lett. **68**, 3013 (1996).

[5] C. Kan, D. Vassilovski, T. C. Wu, and K. Y. Lau, Appl. Phys. Lett. **61**, 752 (1992).

[6] C. Kan, D. Vassilovski, and K. Y. Lau, Appl. Phys. Lett. **62**, 2307 (1993).

[7] J. Wang, U. A. Griesinger, M. Geiger, D. Ottenwealder, F. Scholz, and H. Schweizer, IEEE Photonics Tech. Lett. **8**, 1585 (1996).

[8] *see for instance* G. Wang, S. Fafard, D. Leonard, J. E. Bowers, J. L. Merz, and P. M. Petroff Appl. Phys. Lett. **64**, 2815 (1992).

[9] T. Inoshita and H. Sakaki, Phys. Rev. B **46** 11, 7260 (1992).

[10] R. Heitz, M. Weit, N. Ledentsov, A. Hoffmann, D. Bimberg, V. M. Ustinov, P. S. Kop'ev, and Zh. I. Alferov, Phys. Rev B **56**, 10435 (1997).

[11] U. Bockelmann and T. Egeler, Phys. Rev. B **46** 15574 (1992).

[12] X.-Q. Li and Y. Arakawa, Phys. Rev. B **56**, 10423 (1997).

[13] T. Palm, J. Appl. Phys. **74**, 3551 (1993).

[14] L. Thylén and T. Palm, IEEE J. Quantum Electron. **30**, 1163 (1994).

[15] M. Grundmann, J. Christen, M. Joschko, O Stier, D. Bimberg and E. Kapon, Semicond. Sci Technol. **9**, 1939 (1994).

[16] E.D. Palik, *ed.* Handbook of Optical Constants in Solids, Academic Press Inc. (1985).

[17] A. Karlsson, R. Schatz, and G. Björk, IEEE Photonic Tech. Lett. **6**, 1312 (1994).

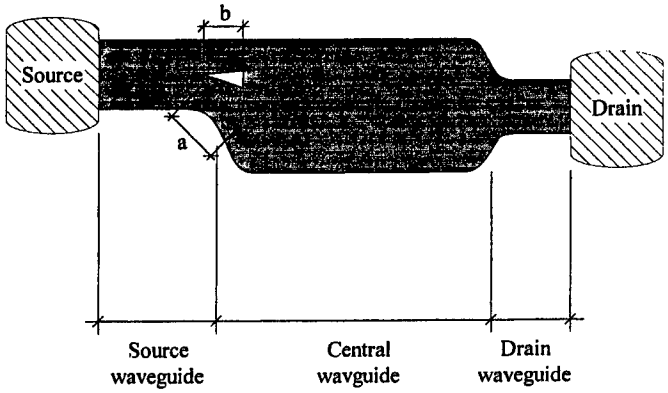


Figure 1: Schematics of the waveguide structure, the gray area is the waveguiding region where the electron transport is ballistic. The central waveguide is the actual quantum wire, or the active region, where the optical transitions take place.

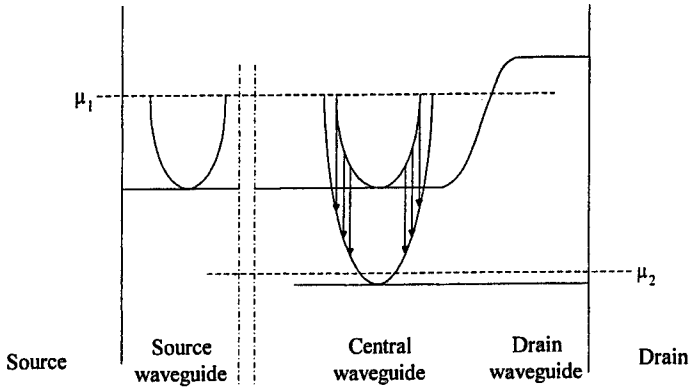


Figure 2: Energy diagram of the waveguide structure. The energy levels seen are the transverse bound modes. The mode spacing is larger in the source and drain waveguides due to smaller widths compared to the central waveguide. The modes of the source and drain waveguides are tuned to match the upper and lower bound modes of the central waveguide respectively.

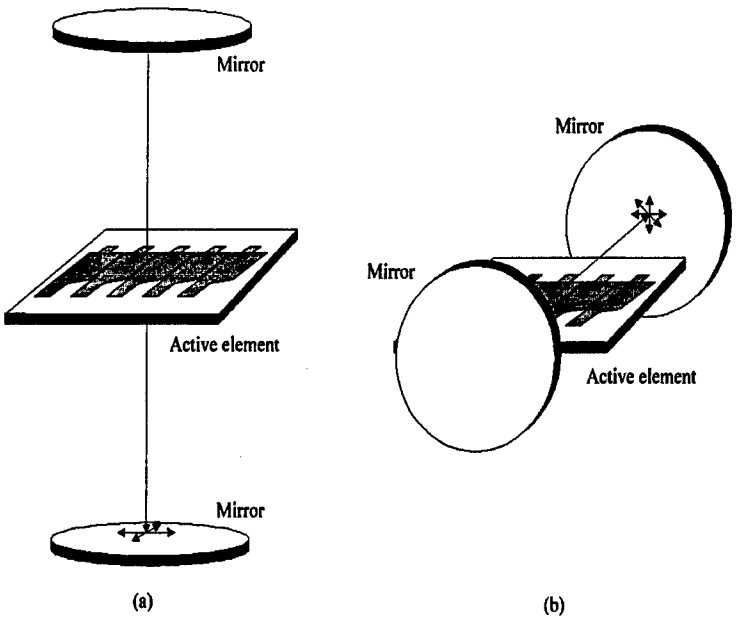


Figure 3: Possible cavity configurations (a) VCSEL-type structure (b) In-plane laser configuration. In the figures the possibility of using multiple quantum wires to enhance the optical output is indicated

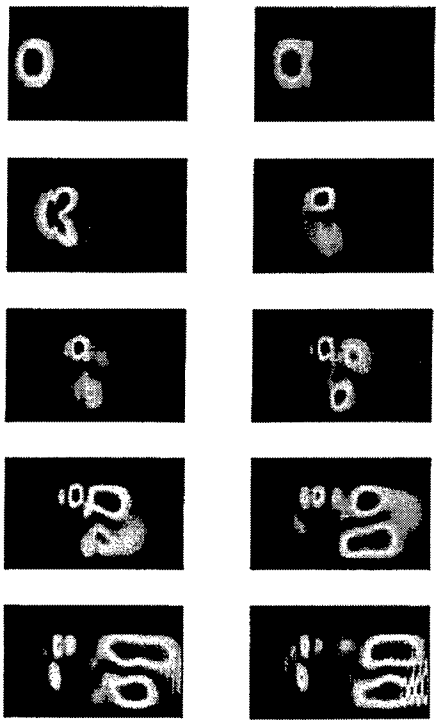


Figure 4: Snapshots from simulation of propagation of an electron wave packet through the source and central waveguides. Time runs from left-right, top-bottom. As can be clearly seen the second transverse mode is excited in the central waveguide. The 'ripple' seen to the right in the last two snapshots are interference effects from numerical reflections (i.e. ghost effects).

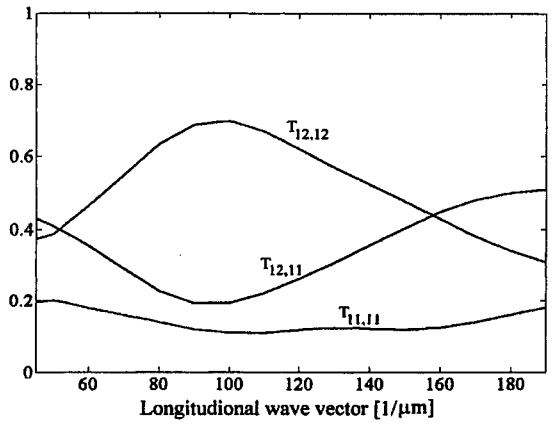


Figure 5: Transmission coefficients $T_{11,11}$, $T_{12,11}$ and $T_{12,12}$ as a function of longitudinal wave vector.

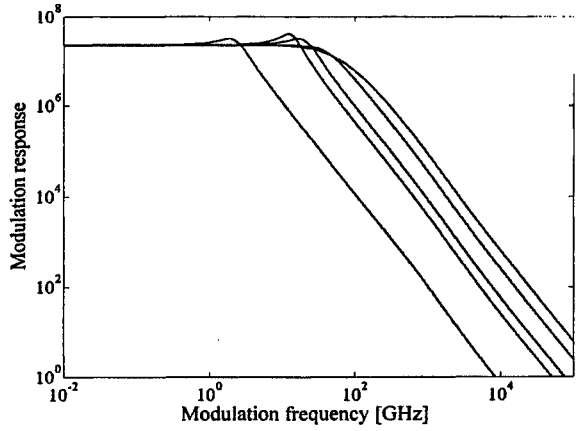


Figure 6: Small signal modulation response for the VCSEL structure for current densities ranging from $1.1 \cdot J_{th}^{VCSEL}$ A/cm^{-2} to $100 \cdot J_{th}^{VCSEL}$ A/cm^{-2}

3D Computer Modeling of Silicon Quantum-Dot Floating Gate Flash Memory Device

A. Thean and J.P. Leburton
Beckman Institute and Coordinated Science Laboratory,
University of Illinois at Urbana-Champaign,
Urbana, IL 61801, USA

ABSTRACT

Simulation of single-electron charging operation of a silicon quantum-dot memory device is performed using self-consistent Schrödinger and Poisson equations. Emphasis is placed on the influence of the poly-wrapped gate on the onset of inversion. We show that the geometry of the control gate causes the inversion to occur on the vertical sides of the channel. The device experiences a strongly nonuniform threshold voltage shift as a function of the number of electrons in the dot to reach about 0.5V when the floating gate quantum-dot is charged from empty to 10 electrons. We analyse the influence of the extent of the control gate overlap on the charging behavior of the device.

INTRODUCTION

Extensive investigations of quantum-dot(QD) physics and technology have been undertaken for years with most of the materials being compound-semiconductors. However, recent advancements in silicon-on-insulator(SOI) fabrication technology have given rise to new silicon quantum-dot devices that could exhibit single-electron charging at room temperature[1],[2]. This has opened new avenues and possiblities for future device integration with existing silicon ultra-large scale integation(ULSI) technology.

In this paper we present a quasi-3D self-consistent Schrödinger-Poisson simulation of a structure similar to the device fabricated by Welser et. al.(Fig. 1). We

studied the charging behavior of the floating gate and the resulting variation of the device threshold voltage. The effects of the poly-wrapped gate geometry are investigated as well.

II. APPROACH

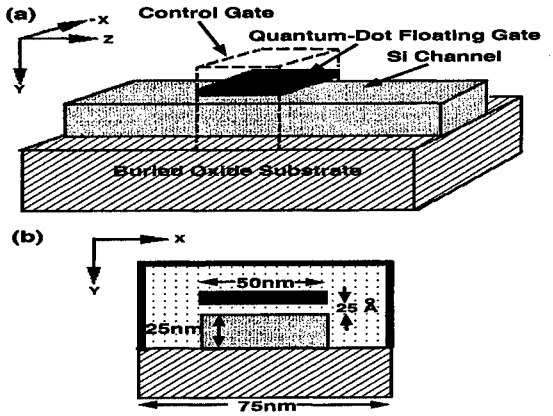


Fig 1 (a) 3D Schematic of Device Structure.(b) X-Y slice of the device, showing the QD floating gate and the channel.

A schematic representation of the simulated device is shown in Fig. 1. The channel is doped at $N_a = 5 \times 10^{18}$ cm^{-3}. The source and drain contacts are kept at zero volts. The control gate overlaps the quantum-dot floating gate and part of the channel. The rest of the channel is assumed to be covered by SiO_2, representing the field oxide or passivation. The electric potential in the device is obtained as a solution of the 3-D nonlinear Poisson equation,

$$\nabla[\epsilon(x,y,z)\nabla\phi(x,y,z)] = -q[p(x,y,z) - n(x,y,z) + N_D^+(x,y,z) - N_A^-(x,y,z)] \quad (1)$$

where, $n(x,y,z)$ and $p(x,y,z)$ are the electrons and holes densities, respectively. The nonuniform doping is described by the ionized donor and acceptor densities, $N_D^+(x,y,z)$, $N_A^-(x,y,z)$. Dielectric permitivity, $\epsilon(x,y,z)$, variation across Si/SiO_2 interface is also taken into account.

Since the floating gate is more than 6 times larger laterally(50nm $\times$ 50nm) than its thickness(8nm), we model only the much stronger confinement in the vertical direction. As such, we solve the 1-D Schrödinger equation adiabatically in

the y-direction. This allows us to study the quantum coupling between the channel and the floating gate easily. The 1-D Schrödinger equation for the electrons at the Si/SiO_2 interface reads,

$$-\frac{\hbar^2}{2}\frac{d}{dy}(\frac{1}{m_l^*(y)}\frac{d}{dy})\psi_{il}(y)+\{-q\phi(y;x,z)+\Delta E_c(y)+\mu_{xc}(n)\}\psi_{il}(y;x,z)=E_{il}(x,z)\psi_{il}(y;x,z) \tag{2}$$

Here $\Delta E_c(y)$ is the material band offsets; $\mu_{xc}(n)$ is the exchange-correlation term and $m_l^*(y)$ are the effective masses of the electron, where l denotes the different effective masses arising from the anisotropy of the Si bandstructure. Exchange and correlation effects to account for electron-electron interaction is treated according to the local density approximation[4],[5],

$$\mu_{xc}(n)=\frac{d[n\epsilon_{xc}(n)]}{dn}. \tag{3}$$

In the QD, we have $p(x,y,z)=0$ and $n(x,y,z)=\sum_i|\psi_{il}|^2$, which requires a self-consistent solution of both the Poisson and Schrödinger equations. The discretized Poisson's equation in finite-difference form is solved by Newton-Raphson technique and the solution process is accelerated with successive over-relaxation. The finite-difference 1-D Schrödinger's equation is solved by direct method using a QR algorithm. A self-consistent loop is employed to iterate between the two equations until convergence is achieved[6]. The averaged electron number, N per quantum dot, which is not necessary an integer number, is computed from the total electron density over the volume element at each grid point in the device,

$$N=\sum n(x,y,z)\Delta x\Delta y\Delta z. \tag{4}$$

This condition which is incorporated in the self-consistent loop, is used to simulate the reading and writing operation of the memory device.

III. RESULTS

Fig. 2 shows a x-y slice of the conduction band profile of the device. The QD floating gate is located between Y = 100Å to 200Å and the channel is located between 200Å and 500Å. The rest of the surrounding regions pertains to silicon dioxide. The variations of the potential in the silicon-dioxide regions around the QD floating gate and the channel are due to the 3-D effects arising from the geometry of the gate structure. Far into the oxide substrate (Y > 1000Å) the potential recovers its linear change showing constant electric field.

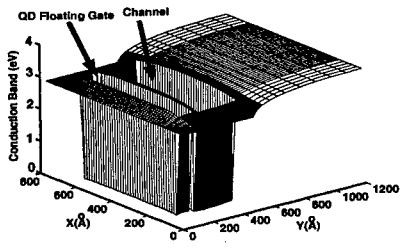


Fig 2 (a) X-Y slice of the conduction band at Z = 1200Å

In Fig. 3 we show the effects of screening of the control gate potential by the QD floating gate electrons on the strong inversion in the channel. The channel electron density is located between 200Å and 500Å. We see that the channel electron density is dramatically reduced right under the quantum-dot.

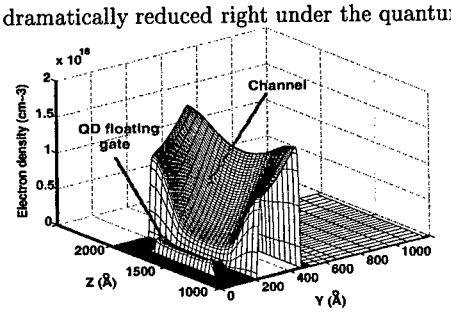


Fig 3. Z-Y slice of electron density in the quantum-dot and the channel

The poly-wrapped gate geometry also causes the initial inversion to occur on the vertical sides of the channel(Fig. 4). This effect is due to the closer proximity of the side gates to the channel as well as, the screening of the top gate by the quantum-dot. This indicates that during device operation, most of the channel is almost empty of electrons, except on the vertical sides. Consequently, the current flow occurs along the vertical sides and could undergo extensive interface roughness scattering.

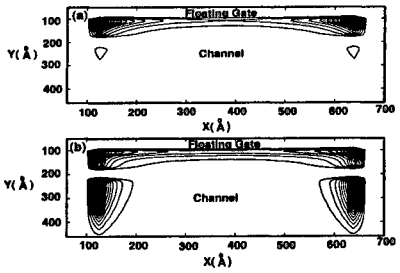


Fig 4.(a) X-Y contour slice of electron density right before inversion. (b) Electron density during inversion. The QD floating gate is located between 100 Å to 200 Å in the Y-direction. The channel is located below Y=200 Å.

Since the control gate only covers a small section of the channel, the rate of increase in channel electrons is initially limited to the region under the QD floating gate As the gate field is increased, the growing fringing fields that extend outside the region under the floating gate start to produce inversion which spread slowly in those regions. In Fig 5(a) and (b) we show the contour lines resulting from the control gate field which extend around the periphery of the dot, reaching the channel, and causing inversion outside the regions underneath the quantum-dot.

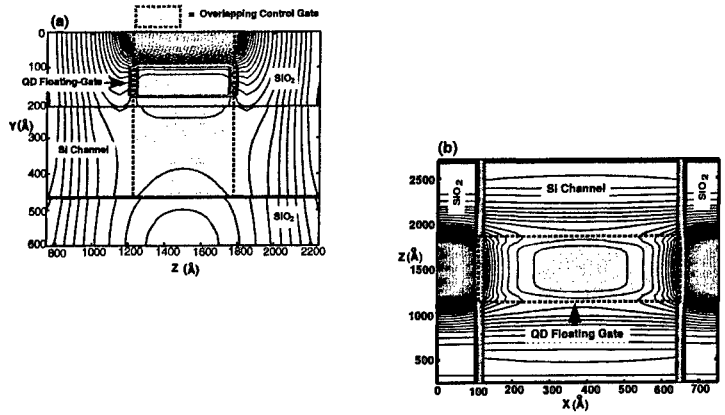


FIG 5.(a) X-Y contour plot of the conduction band potential showing the effects of the control gate fringing fields. (b) X-Z contour plot of the conduction band potential

Fig 6. shows the charging behavior of the channel as the number of electrons in

the QD floating gate is constrained to be integer numbers, which illustrates the read and write operations of the memory device.

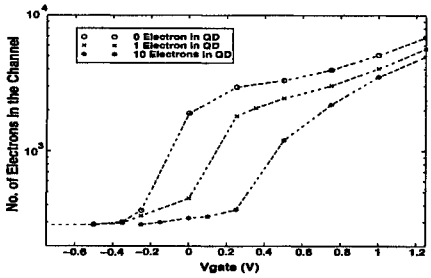


Fig 6. Effects of read/write charging of the quantum-dot floating gate on the number of channel electrons.

The threshold voltage is estimated to be the bias point for which the electron number in the channel, which is proportional to the device conductance, begin its rapid exponential rise. When the quantum-dot is empty, the threshold voltage is about -0.4V. With one electron in the quantum-dot, the threshold voltage shifts to -0.2V. When the number of quantum-dot electrons is increased to ten, the total threshold voltage shift experienced by the device is about 0.5V. This is in qualitative agreement with the behavior of the device demonstrated by Welser et al[1]. The shift in threshold voltage for each additional electron in the quantum-dot is therefore nonuniform. Apparently, the largest shift comes from the transition from an empty dot to the storing of the first electron. This effect is related to the results illustrated in Fig. 2 and is a manifestation of the decrease in the screening effectiveness per electron in the quantum-dot, as the number of stored electrons increases. This also indicates the changing sensitivity of the device channel for single-electron charging of the dot. This reduction in sensitivity of the electron population in the channel is understood as an effect of the 3-D nature of the inversion and the channel screening which have two important contributions: First, as the increase in channel electrons occurs mainly on the vertical wall facing the side gate (Fig.3), the screening from the quantum-dot which is placed on the top of the channel appears to be rather poor. The second contribution stems from the gate fringing field which extent laterally in the z-direction beyond the region under the QD floating gate. This 3-D fringing field effect induces inversion electrons away from the central region which do not experience much screening from the floating gate either.

Finally, we investigate the changes in both the threshold voltage and the charging behavior cause by the gate geometry. This is done by reducing the amount of gate overlap with the channel. In Fig. 7(a), we show the gate covering the

channel and the QD floating gate. In Fig. 7(b), the gate covers only partially the channel. Fig. 7(c) illustrates the case when the gate covers only the QD floating gate but not the channel and in Fig. 7(d) the gate is flat, both the QD floating gate and the channel are completely beneath the gate structure.

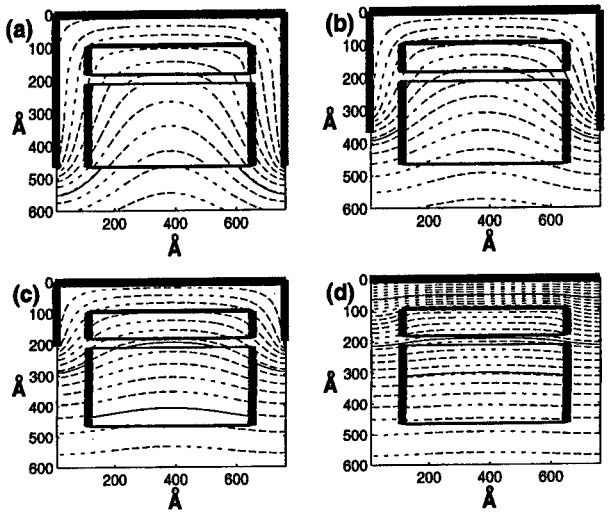


Fig 7. Contour plots of potential profile as the control gate overlap changes. The control gate is shown in bold black lines on top of the structure.

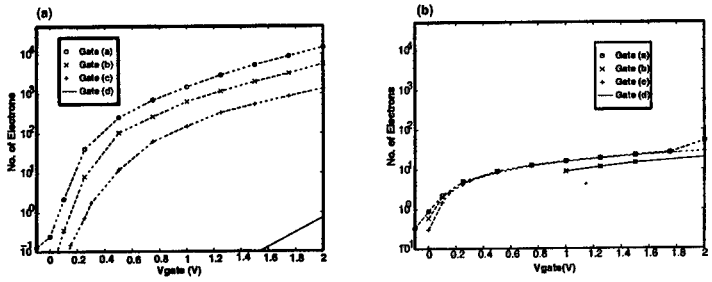


FIG 8.(a) The charging curves for the channel as the control gate structure is varied from gate(a) to gate(d). (b) The corresponding charging curves for the QD floating gate.

In Fig. 8(a), we see that as the gate overlap is decreased from gate (a) to

gate (d), the charging curve of the channel shifts to the right. This means that higher gate biases are required to induce the same amount of channel inversion for a flatter gate. Though the control over the channnel inversion is significant, the control over the QD floating gate charge does not change as much(Fig. 8b). Again, these results illustrates the different ways the electron charge are induced in the floating gate and the channel. Case (d), where the flat gate causes the potential and the charge density in the QD floating gate to be substantially uniform(Fig. 7d), is spectacular, since it corresponds to the largest shift in the charging chracteristic of the channel(Fig. 8a).

IV. CONCLUSIONS

By using a 3-D self-consistent simulation, we have shown the unique behavior of the carrier inversion on the vertical sides of the channel due to the wrap-around geometry of the control gate of a quantum-dot floating gate flash memory. We have also demonstrated that the threshold voltage shift per electron decreases as the number of electrons in the quantum-dot increases. We have shown that substantial shifts in the threshold voltage are experienced by the device when the extent of control gate overlap is changed.

ACKNOWLEDGMENT

This work is supported by the National Science Foundation (ECS-95-09751).

References

[1] J.J. Welser, S. Tiwari, S. Rishton, K.Y. Lee and Y. Lee, "Room temperature operation of a quantum-dot flash memory," *IEEE Electron Device Lett.*, vol. 18, p. 278, 1997.

[2] L.J. Guo, E. Leobandung, and S.Y. Chou, "A room-temperature silicon single-electron metal-oxide-semiconductor memory with nanoscale floating-gate and ultranarraw channel," *Appl. Phys. Lett.*, vol. 70, p. 850, 1997.

[3] A. Nakagima, T. Futatsugi, K. Kosemura, T. Fukano and N. Yokoyama, "Room temperature operation of Si single-electron memory with self-aligned floating dot gate," *Appl. Phys. Lett.*, vol. 70, p. 1742, 1997.

[4] D.Jovanovic and J.P. Leburton,"Self-consistent analysis of single-electron charging effects in quantum-dot nanostructures," Phys Rev B vol. 49, p. 7474, 1994.

[5] R.O. Jones, O. Gunnarsson, "The density functional formalism, its applications and prospects," Rev. of Modern Phys. vol. 61, p. 689, 1989.

[6] V.Y. Thean, S. Nagaraja, and J.P. Leburton, "Three-dimensional self-consistent simulation of interface and dopant disorders in delta-doped grid-gate quantum-dot devices", J. Appl. Phys. vol. 92, p. 1678, 1997.

SIMULATION OF NANOSCALE SILICON CONDUCTION CHANNELS

A. Trellakis and U. Ravaioli
Beckman Institute and Dept. of Electrical Engineering
University of Illinois, Urbana, Illinois 61801

ABSTRACT

Several MOS-type structures are examined for their suitability of implementing quantum wire based conduction channels operating in silicon at room temperature. By solving the self-consistent system of Schrödinger's and Poisson's equation, a setup with a T-shaped gate was identified as the most promising one for both fabrication and operation. For this system, an almost mono-mode room temperature quantum wire can be created, if one uses a highly doped substrate. Furthermore, the barrier height of the the wire confining potential is high enough to contain even hot electrons. However, the same structure implemented with an undoped substrate shows various problems, the most serious ones a very low confining potential and a negative threshold voltage, making the undoped setup quite unsuitable for all practical purposes.

INTRODUCTION

As the dimensions of electronic devices approach nanometer scale, quantum effects are expected to have an ever increasing influence on their electronic properties, until at some point these effects become essential for device operation. While it is possible to conceive completely new devices which are designed to operate solely on the basis of quantum effects, this approach is very costly due to the huge investment in current production technology. Therefore, it would be highly advantageous to develop quantum structures that are in some ways compatible or interfaceable with existing silicon Metal–Oxide–Semiconductor (MOS) technologies, operated at or near room temperature.

Following this line, the authors decided to focus their research on exploring the limits of scalability for MOS devices operated at room temperature. While

great effort has been put into reducing the length of typical conduction channels down to less than 100nm, much less work has been done for shrinking the lateral dimension of the channel, even though the maximum achievable integration density is determined by the product of both dimensions. The goal of this paper is to present self-consistent quantum simulations of quantum wire type conduction channels in order to explore the limits of lateral scalability for MOS devices.

II. PHYSICAL AND COMPUTATIONAL MODEL

The physical model used to achieve a realistic description of electrons in the cross-section of nanoscale conduction channels consists of the coupled system of Schrödinger's and Poisson's equation [1]. Schrödinger's equation in the effective mass approximation is defined as

$$-\frac{\hbar^2}{2}\nabla\cdot\left[\frac{1}{m^*}\nabla\psi_l\right]+\left[V_h-e\phi+V_{\rm xc}(n)\right]\psi_l=E_l\psi_l, \tag{1}$$

where ψ_l denotes the wavefunction belonging to energy level E_l, ϕ the electrostatic potential, V_h the heterojunction step potential, n the quantum electron density, and finally $V_{\rm xc}$ the exchange correlation potential in the local density approximation. e is the unit electric charge and m^* is the tensor describing the effective electron mass.

The electrostatic potential ϕ is determined by a nonlinear Poisson equation

$$\nabla\cdot(\epsilon\nabla\phi)=-e\left[-n+p(\phi)+N_D^+(\phi)-N_A^-(\phi)\right] \tag{2}$$

where ϵ is the dielectric constant, p the hole density, and N_D^+ and N_A^- the ionized donor and acceptor concentrations.

The quantum electron density n occurring in both equations is then obtained from the eigenpairs (E_l,ψ_l) of Schrödinger's equation as

$$n=\sum_l N_l|\psi_l|^2, \tag{3}$$

where

$$N_l=g_V\left(\frac{2m_{\rm w}k_BT}{\pi^2\hbar^2}\right)^{1/2}\mathcal{F}_{-1/2}\left(\frac{E_F-E_l}{k_BT}\right) \tag{4}$$

denotes the occupancy of the eigenstate l, g_V the number of equivalent conduction band valleys, m_w the electron mass along the wire axis, T the Temperature, k_B

Boltzmann's constant, E_F the Fermi level, and $\mathcal{F}_{-1/2}$ the complete Fermi-Dirac integral of order $-1/2$.

In order to obtain an efficient numerical model [2], both Schrödinger's equation as well as Poisson's equation are discretized using a box integration finite difference approach to take material discontinuities into account. Since the quantum wire covers only a small region of the entire simulation domain we employ a non-uniform rectangular mesh condensed around the wire region to minimize computational effort and achieve high accuracy within the region of interest. Furthermore, to avoid the cost of solving Schrödinger's equation in a very large grid we calculate the quantum electron density n only within the region of the actual quantum wire itself, while in the rest of the simulation domain, where the electron density is small, we replace n by its classical value $n_{\text{class}}(\phi)$.

The size of the matrices involved here demands the use of sparse solvers for both equations. The eigenvalue problem for Schrödinger's equation is solved using Chebyshev-Arnoldi iteration [3, 4, 5]. This method allows us to compute only the physically relevant lowest-energy states. The nonlinear Poisson equation is solved by Newton-Raphson iteration with inexact line search. The necessary solution of a sparse linear system at each iteration step is accomplished by a version of the preconditioned conjugate gradient method involving DKR preconditioning [6, 7].

Solving the combined system of the two model equations requires an iterative approach [8, 9]. However, due to the strong nonlinear coupling between both equations underrelaxation yields only slow convergence. Therefore, a predictor-corrector approach for the electron density n is utilized, enabling the outer iteration to converge in less than ten iteration steps [10].

III. RESULTS

For exploring the limits of lateral scalability for MOS devices, the system shown in Fig. 1a should very much define the minimum setup necessary for the creation of an ultra narrow conduction channel in silicon. A 5 nm wide metalized (Al) trench acting as gate is separated from a uniformly p-doped substrate by 2 nm of SiO_2. Under the influence of a positive gate bias a localized inversion forms at the oxide interface under the gate, resulting in a quantum wire type system.

In order to assess the validity of this structure for device operations, the authors did a self-consistent simulation for a highly doped ($N_A = 10^{18}$ cm^{-3}) structure of this type. Both the interface orientation as well as the axis of the channel were assumed to be aligned along a direction of the <100> family, and a typical surface charge density of 4×10^{10} cm^{-2} at the oxide interface was taken into account. The simulation temperature was 300 K.

The result for the lateral cross-section of the conduction band potential in the channel at a gate bias of 1.7 V and an integrated channel charge of $\int n dx = 4.5 \times 10^6$

cm^{-1} is shown by the solid curve in Fig. 2. While postponing a detailed discussion of the simulation results to the next chapter, it is immediately clear that a very narrow (about 20 nm wide) and deep (about 1.1 eV) potential trench is formed, ensuring excellent confinement even for hot electrons.

Unfortunately, manufacturing a 5 nm metal line is quite challenging, even if one allows for future progress in process technology. Therefore it would be highly desirable if one could achieve similar good confinement while relaxing the necessary fabrication tolerances. One attempt in that direction is shown in Fig. 1c. Its main distinction to the system shown in Fig. 1a is that in addition to the 5 nm wide gate the whole surface of the device has been metalized, in effect forming a trench oxide structure comparable to those discussed by Tsukui and Oda [11]. However, a self-consistent simulation of this structure using the same channel fill-in as in the previous case at a gate bias of 1.3 V shows (Fig. 2, long dashed curve), that the depth of the potential trench is with 0.4 eV not sufficient to confine hot electrons, even though the channel width itself has not changed much.

In order to find a solution for this problem, the authors restricted the surface metalization to a 20 nm wide band (Fig. 1b), as compared to the complete metalization used for the previous system. The reasoning behind this structure is that it should be much easier to put a metal line over an oxide trench, if the line is much wider than the trench, thus avoiding the manufacturing difficulties involved with system 1a). At the same time, keeping the total metalization width narrow should prevent the drastic reduction of the confinement potential shown by the fully metalized structure 1c).

Indeed, a self-consistent simulation for this structure shows a lateral confinement potential (Fig. 2, dotted line) that is almost indistinguishable from that of the ideal system 1a). Even if one increases the metalization width to 50 nm, the confinement potential only widens by about 30 nm in its upper flanks (Fig. 2, dashed line), while its depth remains with 1.1 eV unchanged. Thus, of the three structures examined here the T-gate system shown in Fig. 1b appears to be the most promising one for further investigation.

The small dimensions of the T-gate structure allow one to consider in practice only a highly doped or a nearly undoped substrate. While for high dopant concentrations as $N_A = 10^{18}$ cm^{-3} the average distance between dopant atoms (about 10 nm) should be small enough for reliable device operation, for intermediate concentrations as $N_A = 10^{15}$ cm^{-3} this is no longer true, since in this case there would be only a few dopant atoms within the channel, leading to unacceptable statistical fluctuations of device characteristics. Therefore we limit our investigation to T-gate systems with acceptor concentrations of either $N_A = 10^{18}$ cm^{-3} for highly doped devices or $N_A = 10^{10}$ cm^{-3} for nominally undoped ones, where the latter concentration is a typical value for residual impurity concentrations in undoped silicon. As the authors will show, both types of systems are very different in their

physical properties.

This fact becomes immediately obvious if one examines the occupation numbers N_l of the states E_l. As Fig. 3. shows, for a total occupation of $\int n dx$=4.5×10^6 cm^{-1} most energy levels are located above the Fermi level E_F, resulting in an exponential decay of the occupations for increasing l. However, we find that for the same total charge inside of the channel, the number of occupied energy levels is quite different for both systems. While for the highly doped structure only a few states are occupied and 70% of the electrons are concentrated in the ground state (Fig. 3a), there is a dense spectrum of occupied states for the undoped case (Fig. 3b).

The reason for this difference becomes obvious if one examines the cross-sections of the conduction band potential (Fig. 4a) and the quantum electron density n (Fig. 4b) parallel to the Si-SiO_2 interface for the same channel fill-in. We find that for the highly doped structure the conduction band potential forms a very narrow and deep trench, resulting in a very compact and dense quantum wire. The size quantization caused by this tight electron confinement then causes the large separation between energy levels seen in Fig. 3a. On the other hand, for the undoped system electron confinement is much looser, and consequently size quantization is less important here, resulting in the dense quasi-classical energy spectrum seen in Fig. 3b.

The issue of electron confinement is further complicated by the by the emergence of hot electrons. While a potential trench might be nominally deep enough to confine carriers with a kinetic energy of 300 K or 0.025 eV, at high channel currents the electron temperature can be as high as 0.9 eV, necessitating much higher confinement potentials. Examining the barrier height of the potentials shown in Fig. 4a, we find that only highly doped systems with $N_A = 10^{17}$ cm^{-3} or higher can ensure the confinement of hot electrons in the channel, while for lower lower substrate doping the barrier height quickly decreases down to 0.2 eV for the undoped system, making it quite unsuitable to carry any substantial current.

Finally, let us examine the dependence of the integrated charge in the channel $\int n dx$ on the gate bias for different substrate doping. Even though $\int n dx$ is not necessarily proportional to the channel current, its dependence on the bias should be good indicator for the switching behavior of devices using the T-gate structure. Examining Fig. 5 we notice that the threshold voltage seems to decrease with decreasing channel doping. For example, if we define somewhat arbitrarily a total channel charge of 10^6 cm^{-1} as "threshold", we get approximately 1.2 V for the highly doped structure ($N_A = 10^{18}$ cm^{-3}) and -0.1 V for the undoped one.

Further differences between the two cases can be found, if one examines the sub-threshold behavior of the electron density. While the highly doped systems show a consistent decrease in the total charge of at least decade per 0.1 V decrease in gate bias, the corresponding decrease in the undoped system is smaller and

tends to decrease further for negative gate voltages. This behavior of the undoped structure is caused by a considerable number of electrons in the substrate outside of the wire, that persists even at negative gate voltages. As a consequence, it might be quite difficult to switch off the current in the undoped channels even at moderately negative gate voltages.

IV. CONCLUSIONS

We examined several MOS-type structures for their suitability of implementing quantum wire based conduction channels in room temperature silicon, and using self-consistent calculations we identified a structure with a T-shaped gate as the most promising one for both fabrication and operation. Further investigation shows that if one uses a highly doped substrate for this system, an almost mono-mode room temperature quantum wire can be created. Furthermore, the barrier height of the the wire confining potential is with 1.1 eV high enough to contain even hot electrons. The threshold voltage is with about 1.2 V suitable for low-voltage operation, below threshold the total channel charge decreases by one decade per 0.1 V gate bias shift, indicating a benign sub-threshold behavior. Considering these results, the authors believe that this highly doped system is a promising candidate for the implementation of nanoscale conduction channels.

On the other hand, the same structure implemented using an undoped substrate shows various problems, the most important ones a low confining potential of only 0.2 eV and a negative threshold voltage, making this system quite unsuitable for all practical purposes. Despite these problems, structures based on undoped silicon are highly attractive since these systems do not suffer from statistical fluctuations caused by randomly distributed dopant atoms. Therefore the authors are currently trying to improve the undoped structure by adding a highly p-doped ground plane and at the same time reducing the thickness of the top undoped silicon layer down to small values like 50 nm.

The rationale behind this approach would be to limit the number of carriers available outside of the wire region, hopefully improving upon the sub-threshold behavior of the system. At the same time, the wire should be located far enough from the ground plane at the oxide interface to see detrimental influence from impurity scattering. As preliminary results indicate, introducing a ground plane indeed seems to improve both confinement and control significantly, indicating that most of the disadvantages of the original undoped structure could be overcome.

ACKNOWLEDGEMENT

This work was supported by the National Science Foundation grant ECS 95-09751, a Nato Collaborative Grant CRG.950753, and by a graduate fellowship (A.T.) of the CSE program at the University of Illinois.

References

[1] T. Kerkhoven, M.W. Raschke, and U. Ravaioli, Journal of Applied Physics, Vol. 74(2), p. 1199 (1993).

[2] A. Trellakis and U. Ravaioli, "Computational Issues in the Simulation of Semiconductor Quantum Wires", to be published in Computational Methods in Applied Mechanics and Engineering.

[3] G.H. Golub and C.F. Van Loan, *Matrix Computations* (John Hopkins University Press, Baltimore and London, 1996).

[4] A. T. Galick, T. Kerkhoven, and U. Ravaioli, Microwave Theory and Techniques, Vol. 40(4), p. 699 (1992).

[5] Y. Saad, *Numerical methods for large eigenvalue problems* (Manchester University Press, Manchester, 1992).

[6] T. Dupont, R.P. Kendall, and H.H. Rachford, SIAM Journal for Numerical Analysis, Vol. 5(3), p. 559 (1968).

[7] R. Chandra, "Conjugate Gradient Methods for Partial Differential Equations". Ph.D. thesis, Yale University, 1978.

[8] S. E. Laux, p. 270, in *Proceedings of the Fifth International NASECODE Conference*; J. J. H. Miller, Ed. Boole Press, Dublin, Ireland (1987).

[9] T. Kerkhoven, A. T. Galick, U. Ravaioli, J.H. Ahrends, and Y. Saad, Journal of Applied Physics, Vol. 68(7), p. 3461 (1990).

[10] A. Trellakis, A. T. Galick, A. Pacelli, and U. Ravaioli, Journal of Applied Physics, Vol. 81(12), p. 7880 (1997).

[11] T. Tsukui and S. Oda, Jpn. Journal of Applied Physics, Vol. 34(2B), p. 874 (1995).

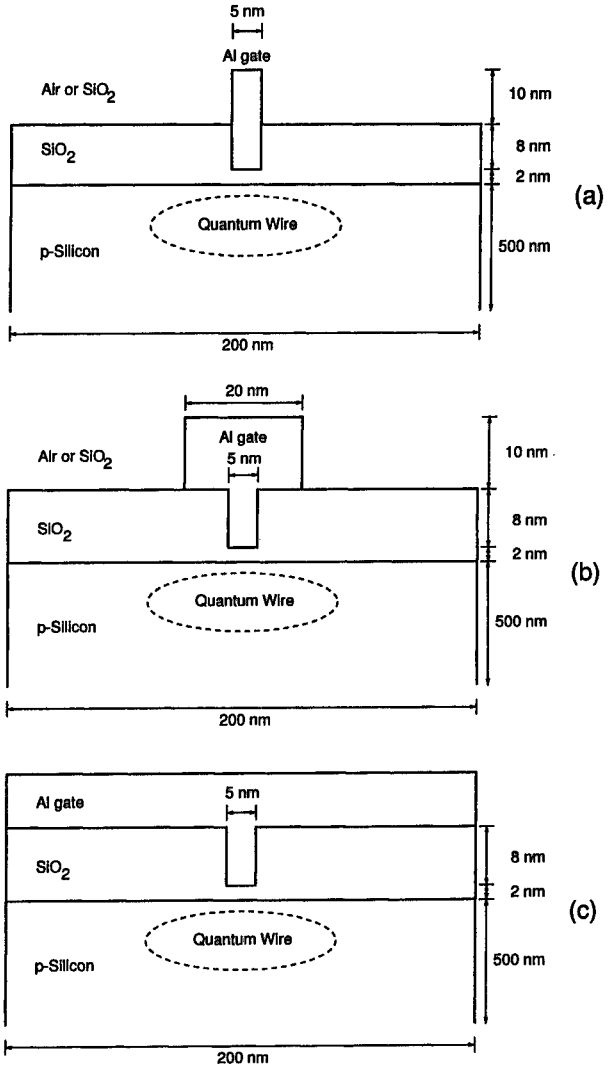


Figure 1: Three Si-SiO_2 based quantum structures. The acceptor concentration in the substrate can vary from nominally undoped ($N_A = 10^{10}$ cm^{-3}) to highly doped ($N_A = 10^{18}$ cm^{-3}) depending on the application.

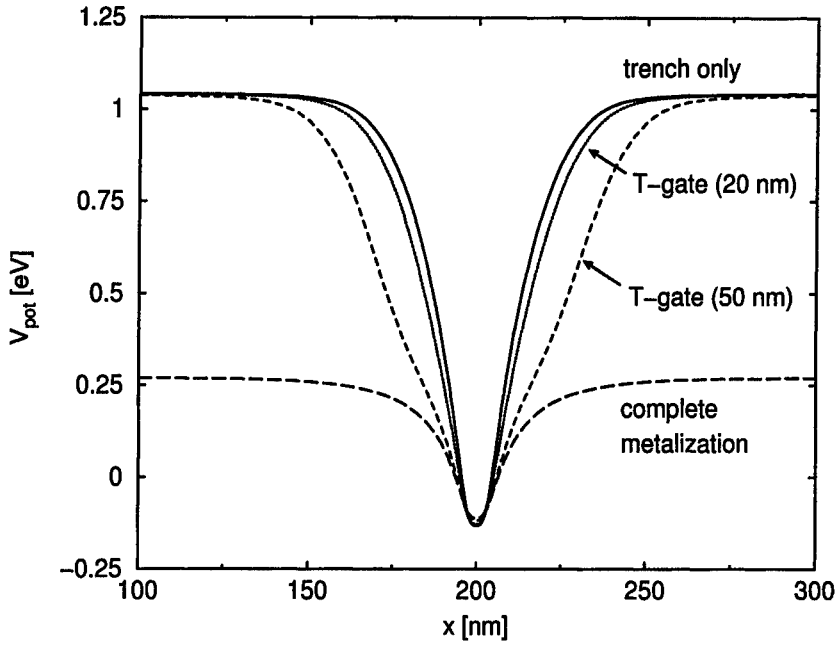


Figure 2: Cross-sections of the conduction band potential V parallel to the Si-SiO_2 interface for three structures shown in Figs. 1a-c. All sections are cut through the maximum of the electron density, and the gate is located at x=200 nm. The total integrated electron density is 4.5×10^6 cm^{-1} in all cases, and the gate biases are 1.7 V, 1.6 V, 1.4 V, and 1.3 V form the inside to the outside.

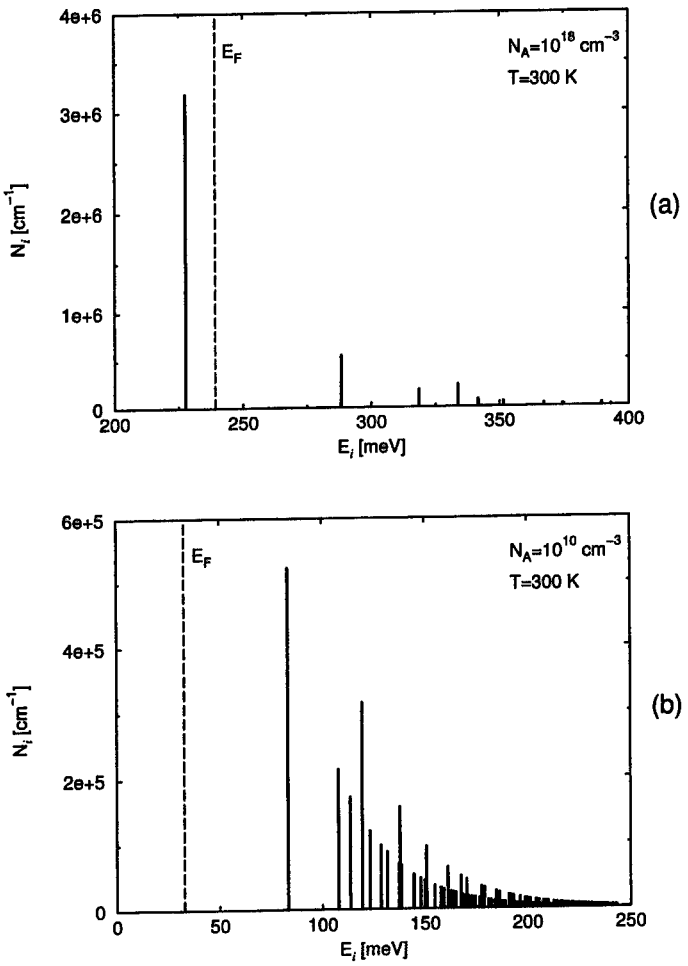


Figure 3: Occupation numbers N_l of states E_l for the T-gate structure shown in Fig. 1b. The Fermi level E_F is indicated by the dashed line and energies are normalized with respect to the bottom of the conduction band potential. The total integrated electron density is 4.5×10^6 cm^{-1} in both cases, and the gate bias is 1.6 V for the highly doped (a) and 0.3 V for the undoped system (b).

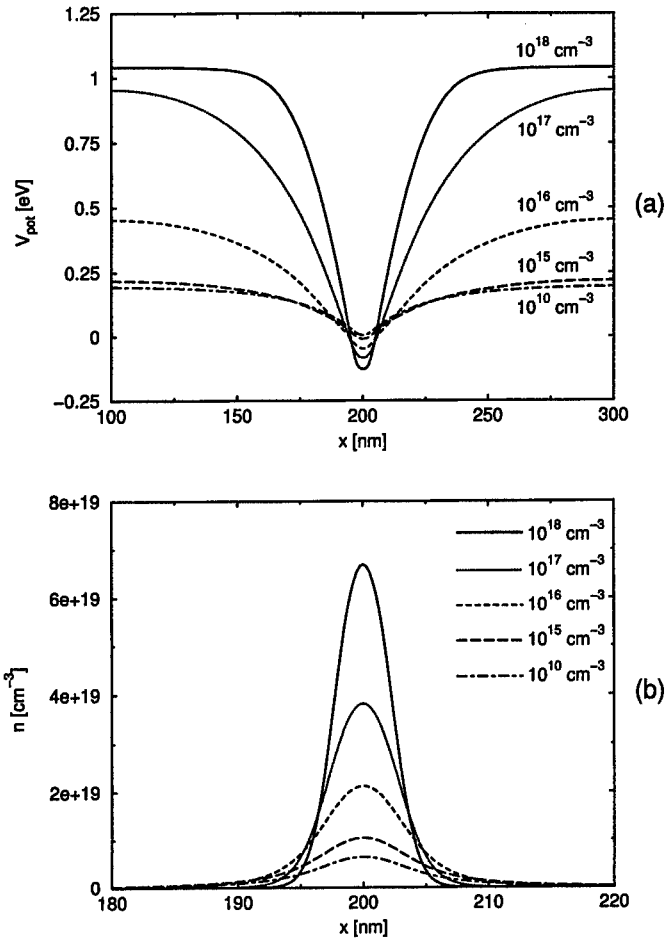


Figure 4: Cross-sections of the conduction band potential V (a) and the quantum electron density n (b) parallel to the Si-SiO_2 interface for the T-gate structure shown in Fig. 1b. All sections are cut through the maximum of the electron density and the distance to the interface is 0.9 nm for the highly doped and 1.6 nm for the undoped case. The gate is located at x=200 nm. The total integrated electron density is 4.5×10^6 cm^{-1} in both cases, and the gate bias is again 1.6 V for the highly doped and 0.3 V for the undoped system.

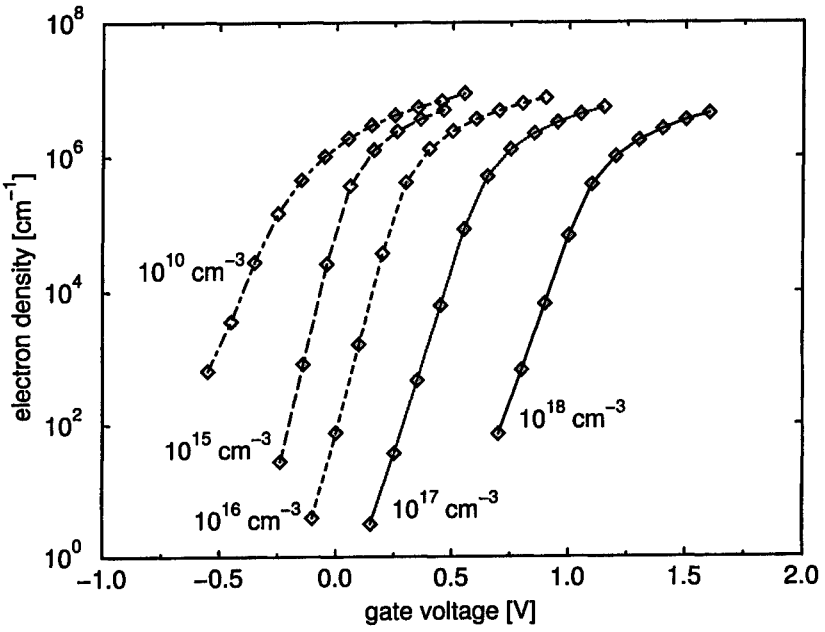


Figure 5: The integrated electron density in the quantum wire of Fig. 1 as function of the gate bias. Gate metal is Al.

MAGNETO-CAPACITANCE OF MULTIPROBE MESOSCOPIC SYSTEMS

Pawel Pomorski
Center for the Physics of Materials and Department of Physics
McGill University, Montreal, PQ, Canada H3A 2T8

ABSTRACT

We analyze the behavior of magnetocapacitance for a multiprobe mesoscopic capacitor. The self-consistent evaluation of the internal potential is found to play a large role in determining quantitative values of the capacitance. For capacitor plates of mesoscopic size, this potential reduces the charge accumulation by a significant factor compared to that obtained with non-interacting models. In general, the broad qualitative behavior of the magnetocapacitance is not substantially altered by the self-consistency, but some new features do appear. A simple but physically motivated model gives an analytical formula which compares well with the numerical data.

INTRODUCTION

For a mesoscopic system the notion of capacitance differs from the familiar classical concept. Classically, capacitance is obtained by solving an electrostatic problem, determining the small bias voltage difference, ΔU, which is needed to transfer a charge ΔQ between two conductors. The electrostatic capacitance is thus $C_e = \Delta Q/\Delta U$, and it is geometrical: C_e only depends on the geometric properties of the two conductors in addition to the dielectric media. On the other hand, in a mesoscopic conductor quantum coherence of the entire system including the leads may be maintained. Furthermore, in a typical mesoscopic system where the density of states is low, the electron screening length may be similar to the size of the conductor. In this case the conductor can no longer be considered to be at an equipotential. In other words, the potential drop ΔU acorss the two conductors of a mesoscopic capacitor may not be the same as the electrochemical potential difference $\Delta\mu$ of the two reservoirs which connect to the capacitor plates[1]. Since experimentally one controls $\Delta\mu$, the experimentally measured capacitance is in

fact an electrochemical one[1], $C = e\Delta Q/\Delta\mu$. For macroscopic metal plates where the screening length is very small, one can prove[1] that for all practical purposes $C_\mu = C_e$. But for mesoscopic plates one may need to consider quantum effects and $C_\mu \neq C_e$. This discussion naturally leads to a dynamic approach to capacitance[2]: the capacitance matrix describes the dynamic charge response when the chemical potential of a reservoir is changed by a small amount $\Delta\mu$. Clearly, the capacitance formulated in this way can be extended to cases where conductors are connected by multiple probes to more than one reservoir.

In this short paper, we describe a self-consistent analysis of electrochemical magneto-capacitance for a mesoscopic system. In particular we consider a multi-probe mesoscopic plate coupled to a nearby metal gate and investigate the behavior of C_μ as a function of the strength of an external uniform magnetic field B. Our numerical results suggest that the specific inclusion of a full self-consistent cycle is not strictly necessary to obtain certain general qualitative properties of magneto-capacitance, such as the symmetry properties under the magnetic field reversal[3]. But it is essential to correctly account for charges induced by the electron-electron interaction and to obtain qualitatively correct pictures. Although the multiprobe capacitor considered here is strictly three-dimensional (3D), we have constructed an effective one-dimensional model which can be solved analytically. The analytical solution gives a clear physical picture of the dependence of capacitance on various densities of states (DOS), as well as very good agreement with our numerical solutions.

In the next two sections of this paper we discuss both the numerical and analytical approaches as well as the results. The final section is reserved for a summary.

II. METHODS

Our theoretical discussion follows the approach of Ref.[1]. To be specific, we consider a general mesoscopic capacitor system which consists of a number of conductors connected by one or more probes to macroscopic reservoirs. In response to a change in the electrochemical potential $\Delta\mu$ in one of the reservoirs from its equilibrium value, there will be a change of the charge density $\Delta\rho$ on the conductors in the system. This $\Delta\rho$ can be thought to consist of two components: the injected and the induced charge densities.

The injected charge comes from the reservoirs due to the variation $\Delta\mu$. Its value can be determined by solving a quantum scattering problem[1]. On the other hand electron-electron interaction establishes an induced charge inside the conductors which act to oppose the external injection. It is this induced charge density which is self-consistently determined by iterating the Poisson equation for the potential distribution $U(\mathbf{r})$ inside the system. The total charge on a conductor is then obtained as $\Delta Q = \int \Delta\rho(\mathbf{r})d\mathbf{r}$, where the integral is restricted to the relevant

conductor volume. Finally the electrochemical capacitance is obtained as $C = e\Delta Q/\Delta\mu$.

The specific system we considered consisted of a square semiconductor plate of size 3300Å×3300Å, connected with up to four reservoirs through quantum wires of width 1650Å(see inset of Fig. 1). The confining potential of the seminconductor plate was taken as zero inside the plate and infinite at boundaries. In the vertical direction the plate was 260Å thick — a reasonable value for electrons confined in heterostructures. Electrons in the plate and the leads move in an applied external uniform magnetic field $\mathbf{B}$, applied in the direction perpendicular to the plate. The second capacitor plate is a metal gate on top of and parallel to the semiconductor plate. The gate has a cross section of 5500Å×5500Å. In the vertical direction the metal gate is much thicker — many times the screening length, so that the interaction is completely screened deep inside the gate along this direction. Between the two plates of the capacitor there is an insulating layer with thickness $d = 360$Å. All space surrounding the plates has a uniform dielectric constant $\epsilon = 13.1$. We self-consistently calculated the magnetocapacitance in two ways, numerical and analytical. In all the following discussions we dropped the minus sign of the electron charge.

To obtain the charge response to a small variation in reservoir electrochemical potentials, the first essential ingredient is to get the local partial densities of states (LPDOS) for the mesoscopic conductor from the scattering problem[1]. We solved it numerically using a finite element method described in Ref.[3,7]. In the gate, the density of states may be set to a high constant value to model metallic behaviour. The injectivity, describing LPDOS for particles arriving from reservoir k, is given by[5, 6] $dn(\mathbf{r},k)/dE = \sum_m |\Psi_m(\mathbf{r})|^2/hv_m$ where the sum is over the scattering state wavefunctions of free electrons at the Fermi energy. Similarly, the emissivity describing the LPDOS for particles which exit the conductor into reservoir k, can also be obtained from the scattering wavefunctions. Our analysis also used another fact that the sum of all injectivities is equal to the sum of all emissivities everywhere. In response to electrochemical variation $d\mu$, the injected charge density is given by

$$d\rho_{inj}(\mathbf{r}) = \sum_i [dn(\mathbf{r},i)/dE]d\mu_i \tag{1}$$

In the Thomas-Fermi approximation the induced charge is[1]

$$d\rho_{ind}(\mathbf{r}) = -\sum_i [dn(\mathbf{r},i)/dE]u_i(r)d\mu_i. \tag{2}$$

where the electrostatic potential drop across the plates is related to the change in reservoir electrochemical potential, through the characteristic function[1] $u_i(r)$ with $edU(r) \approx \sum_i u_i(r)d\mu_i$. Finally we numerically solved the Poisson equation to obtain u_i[4].

The charge accumulation on a single-probe conductor labelled by k in response to a electrochemical potential variation in reservoir l connected to another conductor, gives the electrochemical capacitance[1]

$$C_{kl} = -e^2 \int [u_l(\mathbf{r}) dn(\mathbf{r}, k)/dE] d\mathbf{r} \quad . \tag{3}$$

Our numerical analysis used an approximation that the capacitance is determined primarily by the densities in the plate and the gate. Hence the relatively smaller leads and the distant shielded reservoirs need not be specifically included. The numerical results will be presented below.

As mentioned above, we have also constructed 1D models for the analytical solution of C_{kl}. This approach is reminiscent of basic electrostatics and we now describe how it is carried out. Since there are two parallel conductors (after neglecting the contribution of leads), we could obtain an 1D model by using a constant, average local density of states, and by ignoring edge effects. A priori it is not obvious whether this approach would give correct results, as the densities of states are in fact highly nonuniform for our capacitor. Hence our 1D model requires a numerical comparison with the full 3D results.

As an example of 1D analysis, we consider a two-probe semiconductor plate coupled to the metal gate. The system thus consists of a plate with thickness a, connected by two leads to reservoirs 1 and 2, and a bulk gate at a distance d from the plate. The bulk gate connects to reservoir 3. We need to solve the characteristic potential from the following equation[1]

$$-\nabla^2 u_i(\mathbf{r}) + 4\pi e^2 \left[\sum_{j=1}^{3} \frac{dn(\mathbf{r}, j)}{dE} \right] u_i(\mathbf{r}) = 4\pi e^2 \frac{dn(\mathbf{r}, i)}{dE} \tag{4}$$

where

$\frac{dn(r,1)}{dE} = \frac{dn_1}{dE}$ for $-a < x < 0$ inside plate;

$\frac{dn(r,2)}{dE} = \frac{dn_2}{dE}$ for $-a < x < 0$ inside plate;

$\frac{dn(r,3)}{dE} = \frac{dn_3}{dE}$ for $x > d$ inside gate.

All densities are zero outside above given regions, *i.e.* they vanish outside their respective conductors.

We can solve this equation for u_1 which describes what happens when potential in one of the leads varies. We require that u_1 vanishes deep inside the metal gate (at $x \to \infty$), and is finite in free space far away from the system (at $x \to -\infty$). Hence u_1 must have the form:

$$
\begin{aligned}
u_1(x) &= a_1 & x &< -a \\
u_1(x) &= a_2 e^{-x/\lambda_p} + a_3 e^{x/\lambda_p} + a_4 & -a &< x < 0 \\
u_1(x) &= a_5 x + a_6 & 0 &< x < d \\
u_1(x) &= a_7 e^{-(x-d)/\lambda_g} & x &> d
\end{aligned}
$$

Here we define the screening lengths inside the plate and gate, as:

$$\lambda_p^{-2} = 4\pi e^2 (\tfrac{dn_1}{dE} + \tfrac{dn_2}{dE}),$$

$$\lambda_g^{-2} = 4\pi e^2 \tfrac{dn_3}{dE}.$$

Matching solutions at the region boundaries and making sure the solution inside the plate satisfies Eq. (4), we can find the unknown coefficients. Once these are known, we can thus obtain the charge accumulated on the plate and the gate. In particular, we obtain the charge accumulated on the gate in response to electrochemical potential variation in reservoir 1. Hence from Eq. (3), we have

$$C_{31} = -\frac{A}{4\pi} \frac{\frac{dn_1}{dE}}{\frac{dn_1}{dE} + \frac{dn_2}{dE}} \frac{1}{\frac{2\lambda_p}{1-e^{-2a/\lambda_p}} + \lambda_g - \lambda_p + d} \quad . \tag{5}$$

Next we consider the limit where the plate is made very thin while the integrated density of states is kept constant. In this case the screening length is much larger than the thickness of the plate, $\lambda_p >> a$. On the other hand, the screening length will be much smaller than the separation between the two conductors, $\lambda_p << d$. For a metallic gate, the screening length is also very small: $\lambda_g << d$. In this limit Eq. (5) reduces to

$$C_{31} = -\frac{A}{4\pi} \frac{\frac{dn_1}{dE}}{\frac{dn_1}{dE} + \frac{dn_2}{dE}} \frac{1}{\frac{\lambda_p^2}{a} + d} = -\frac{A}{4\pi} \frac{\frac{d\sigma_1}{dE}}{\frac{d\sigma_1}{dE} + \frac{d\sigma_2}{dE}} \frac{1}{\lambda_{1+2} + d} \quad . \tag{6}$$

where we have defined surface densities of states

$$\frac{d\sigma_{1,2}}{dE} = \frac{dn_{1,2}}{dE} a$$

and characteristic length

$$\lambda_{1+2}^{-1} = 4\pi e^2 (\frac{d\sigma_1}{dE} + \frac{d\sigma_2}{dE}) \quad .$$

The analytical formulas will be compared with our full 3D numerical results (see below).

The above analysis can be easily extended to situations where the semiconductor plate has more than two probes. It is straightforward to verify that the necessary change to the above formula is to use $\lambda_p^{-1} = 4\pi e^2 \sum_j \frac{d\sigma_j}{dE}$ where the sum is over all the reservoirs attached to the semiconductor plate. In the final expression thus obtained, the difference to the above three probe formula (two at the semiconductor plate and one at the gate) is that the sum of densities of states in the denominator of the prefactor (see Eq. (6)) is now over densities from all probes present, and the same holds for the characteristic length due to total density of states.

III. RESULTS AND DISCUSSION

Our self-consistent numerical solution gives results qualitatively similar but quantatively different from the nonself-consistent analysis of Ref.3. The solutions are highly dependent on the magnetic field strength. At higher values of B, Aharonov-Bohm type oscillations are observed[3]. The wavefunctions yielded the necessary local densities of states: our numerical results showed that they are highly nonuniform in space due to interference effects.

First, we present results of the case when the semiconductor plate has four probes. The result of capacitance matrix C_{g1} describing gate response to potential variation in one of the plate's reservoirs are shown in Fig.1. The result obtained by full numerical solution (solid line) is compared with that from equation (6) for the 1D model (dashed line). The 1D line was obtained by using the numerically calculated LPDOS after spatial average. Qualitatively the two results agree very well. Quantitatively, the numerical solution is expected to be consistently larger than the 1D model since 1D model does not include edge effects. Fig. 1 shows this behavior. In addition the inhomogenous densities in the numerical solution will also give larger capacitance over the case where the local densities of states are uniform. When densities are inhomogeneous, screening in the plate is expected to be less efficient so that response in the gate is greater. This nonuniformity is particularly noticable at values of field where there is a resonance. Hence at peaks (see Fig. 1) there is a larger discrepancy between the two lines. This last effect becomes less pronounced as the number of probes is reduced. We conclude that the analytical 1D model actually gives excellent qualitative and reasonable quantitative agreement with the full numerical solution. Therefore the computationally costly step of solving the 3D Poisson equation can be avoided for the cases studied here.

On the other hand, we can demonstrate that the full self-consistency is *quantitatively* important by comparing results to those obtained without self-consistency. A simplest model without full self-consistency uses what is in effect a classical image charge where it is assumed that the charge inside the semiconductor plate is only the injected charge and all the screening takes place in the metal gate:

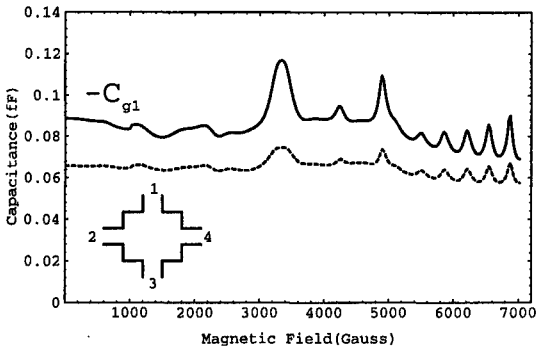


Figure 1: Capacitative gate response to injection from one of the probes by the self-consistent methods: from the numerical solution (solid line) and from analytical 1D model (dashed line)

the gate charge thus being equal in magnitude and opposite in sign to the charge accumulated on the plate. The gate response according to this image model is plotted in Fig.2. One can see that even though there is a qualitative agreement with the self-consistent results of Fig.1, quantitatively the image charge model is off by an order of magnitude. This is because induction does in fact take place in the plate for the mesoscopic system considered here, thus reducing the total gate induced charge. One can also observe that the fully self-consistent response tends to significantly diminish the relative size of resonance features in the capacitance response.

In the highly symmetric four probe plate configuration studied so far, the capacitance matrix element is symmetric under B-field reversal. Furthermore, due to symmetry, the results are the same for all the probes: $C_{g1} = C_{g2} = C_{g3} = C_{g4}$. We also observe that the capacitance is relatively constant as the magnetic field is varied. This is because the symmetry here ensures that resonances in the densities of states for all the probes will occur at the same values of the magnetic field. As shown by Eq. (6), this makes the factor of the ratio of injected to total density of states to be constant for all values of the magnetic field. For a perfectly symmetric conductor, this constant is just the reciprocal of the number of its probes.

The capacitance was also calculated for a three probe plate (see inset of Fig. 3). The capacitance matrix elements for each plate probe obtained using the analytical formula are shown in Figs.3, 4 and 5. The results here are very different from the four probe case. With three probes the structure has significantly less symmetry, so that the densities of states associated with each probe are different

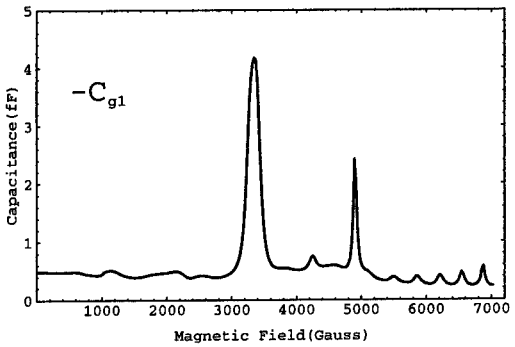


Figure 2: Capacitative gate response to injection from one of the probes in a four probe plate obtained from the classical image charge model. This is to be compared to Fig. 1

and have different magnetic field dependence. This means that C_{g1}, C_{g2} and C_{g3} are in general different. In the three probe structure considered here, the magnetic field reversal properties are $C_{g1}(B) = C_{g3}(-B)$ and $C_{g2}(B) = C_{g2}(-B)$.

For 3-probe plate it may now happen that at some value of the field the injectivity from the probe at which the electrochemical potential is being varied is much less than the emissivity for some other probe. This means that inside the plate the total density of states available for screening is much larger leading to a much more efficient screening at the plate and thus a correspondingly diminished response in the metal gate. The analytical formula dicussed in the last section gives us a quantitative understanding of this effect. The part of the analytical formula Eq. (6) which changes from probe to probe is the factor of the ratio of densities of states. From the analytical expression in Eq. (6),

$$\frac{\frac{dn_{1,2,3}}{dE}}{\frac{dn_1}{dE} + \frac{dn_2}{dE} + \frac{dn_3}{dE}} \tag{7}$$

is different for each probe and it changes as the magnetic field is varied. This is very different from the four probe plate configuration where the high probe symmetry plays an important role.

This factor can become very small if one of the densities in the denominator (see Eq.7) is much larger than the density in the numerator. This is exactly the situation which produces a valley in the capacitance curves of Fig. 3, 4 and 5. At higher B fields, the AB oscillation in capacitance can now take a new form as compared to that reported before[3]. For the three-probe plate system, the AB oscillation may manifest itself as a series of evenly spaced peaks (Fig. 4) as

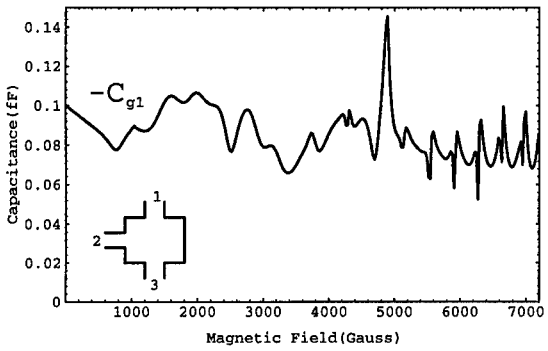


Figure 3: Capacitative gate response to injection from plate probe 1 for a 3-probe plate, obtained from the 1D analytic model

observed before[3] for a two-probe system, or a series of evenly spaced valleys (Fig. 5), or as a more complicated structure due to competition of various densities of states (Fig. 3).

IV.CONCLUSION

We have applied a self-consistent formalism to calculate electrochemical capacitance in multiprobe mesoscopic capacitors. Using a 3D self-consistent numerical solution of the Poisson equation and the quantum scattering problem, we investigated the behavior of magneto-capacitance as the external magnetic field is varied. Our numerical results have shown that self-consistency is essential to obtain quantitatively correct capacitance values, although the more general magnetic field symmetry properties are not affected by the self-consistency. For the cases studied here, the self-consistency reduced the total charge by about a factor of ten as compared to that without self-consistency. The numerical results can be understood using a very simple 1D analytical model, where we use the constant average density of states to make analytical predictions. The analytical formula suggests that the ratio of partial density of states to the total density of states plays the important role in determining the magneto-capacitance behavior. The analytical model is shown to compare very well with the full numerical solution, thus it is useful for predictions of multiprobe mesoscopic capacitors.

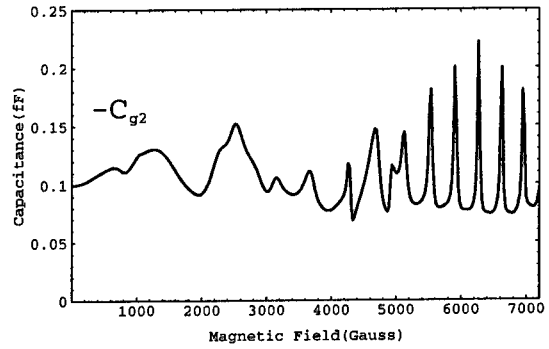


Figure 4: Capacitative gate response to injection from plate probe 2 for a 3-probe plate, obtained from the 1D analytic model

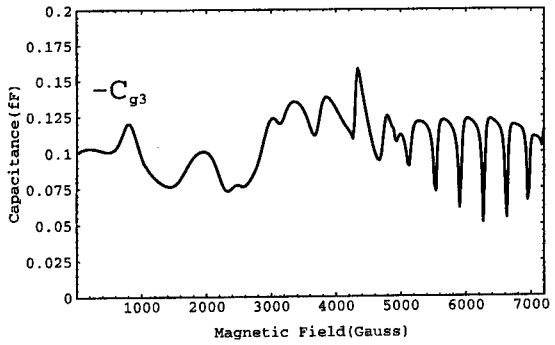


Figure 5: Capacitative gate response to injection from plate probe 2 for a 3-probe plate, obtained from the 1D analytic model

ACKNOWLEDGMENT

I thank the collaboration with Prof. Hong Guo throughout this project, and gratefully acknowledge useful correspondences with Profs. R. Harris and Jian Wang. I am grateful to the financial support provided by NSERC of Canada and FCAR of Québec.

References

[1] M. Büttiker, H. Thomas and A. Prêtre, Phys. Lett. A **100**, 364 (1993); M. Büttiker, J. Phys: Condens. Matter **5**, 9361 (1993).

[2] T. Christen and M. Büttiker, Phys. Rev. Lett. **77**, 143 (1996).

[3] H. Wei, N. Zhu, J. Wang and H. Guo, Phys. Rev. B 56, 9657 (1997).

[4] Pawel Pomorski,Hong Guo, R. Harris, and Jian Wang, Phys. Rev. B 58, 15393 (1998).

[5] M. Büttiker and T. Christen, in *Quantum Transport in Semiconductor Submicron Structures*, ed. B. Kramer (Kluwer Academic Publishers, Dordrecht, 1996).

[6] V. Gasparian, T. Christen, and M. Büttiker, Phys. Rev. A. **54**, 4022 (1996).

[7] Yongjiang Wang, Jian Wang, and Hong Guo, Phys. Rev. B. **49**, 1928 (1994).

Adaptive Control of Single-Electron Circuit Signatures for Computation

R.W. Rendell
Electronics Science & Technology
Naval Research Laboratory
Washington, DC 20375

ABSTRACT

An approach to computation with single-electron circuits is discussed in which information encoded in sensitive circuit signatures is adaptively tuned by adjusting circuit variables to achieve a computationally useful goal. Examples are presented based on numerical simulation of model circuits in which the adapted signatures are (1) conductance spectra of asymmetric coupled quantum dots and (2) the bistable control phase diagram of driven quantum dots.

INTRODUCTION

Physical limitations on the scaling of conventional digital electronics [1] has led to recent studies in search of new scalable nanoelectronics technologies. These have included proposals to utilize single-electron devices controlled by Coulomb blockade, such as quantum dots and tunnel junctions, as building blocks in locally-connected circuits to perform computational or other useful tasks [2-6]. These include logic circuits [2], neural circuits [3], polarization arrays [4], phase-locked arrays [5], and digital circuits [6]. Computational tasks are accomplished in these designs by using applied biases and the mutual electron interactions to control electron transport. Successful operation requires that computational functions be performed with sufficient precision in spite of circuit nonuniformities and undesired interactions from the circuit environment. This results in stringent requirements on design and fabrication because of the sensitivity of single-electron circuits to circuit variables. Circuit architectures and methods of computation, which can mitigate these concerns, are of central interest. An attractive approach to these problems is the use of adaptation and learning both to attain the goal of a computation and enforce immunity to errors caused by material, fabrication, and physical processes [7]. Recently, investigators in the fields of quantum chemistry and classical chaos, which also require control of sensitive systems in

imprecise environments, have successfully implemented adaptive feedback control to tune these systems to desired configurations [8]. Single-electron computational circuits are another class of sensitive systems that should be considered as candidates for use of adaptive feedback control.

In this work, we consider an approach to nanoelectronic computation in which information encoded in a *single-electron circuit signature* is tuned by adjusting experimental variables using an externally applied adaptive algorithm to achieve a computationally useful goal. A circuit signature is any single-electron circuit response that is sensitive to the configuration of circuit variables and is sufficiently flexible to allow useful adaptation toward a computational goal. Examples of circuit signatures include the conductance spectrum for circuits composed of coupled quantum dots, as shown in Figs. 1 or 2, and the phase stability diagram for phase-locked quantum dots, as shown in Fig. 3. These examples will be discussed in more detail below. Such signatures are repeatable for given values of the circuit parameters and applied biases but are extremely sensitive and respond rapidly to changes in these experimental variables. This is precisely the situation in which feedback control is advantageous. The sensitivity of the signatures to external perturbations suggests that adaptive feedback control can be used to quickly tune the signature to a desired pattern that represents the solution to a computation or could be utilized as part of a computational goal. This approach to computation is expected to share the robustness to errors which is generally typical of adaptive processes. The feasibility of this proposal is supported by recent reports [9] that Marcus et al have experimentally demonstrated the damping of conductance fluctuations in quantum dots using feedback control of applied voltages.

In the following, we will study the response of single-electron circuit signatures to feedback control using numerical simulations of model circuits. In section II, we discuss the requirements of single-electron circuits to usefully take advantage of feedback control and the approach used to utilize circuit signatures for achieving computational goals. Section III presents numerical simulations of adaptive control of different choices of circuit signatures for achieving computationally useful goals. Section IV summarizes the results.

II. APPROACH

Achieving non-trivial computation requires that the circuit signature for a quantum dot circuit be sufficiently complex in order to encode large numbers of bits and thereby allow non-trivial computation; i.e. contain sufficient numbers of degrees of freedom to adaptively tune. A sufficient condition for achieving this is to use circuits with *asymmetric* coupled quantum dots. An example is shown in Fig.1(a) which shows a double-dot system with dots of different sizes. This circuit has both a top gate and a back gate. A circuit of this type was built by Blick et al [10] with dots defined by split gates in an $Al_xGa_{1-x}As$-GaAs heterostructure. Two quantum dots of different sizes, and thus different capacitance, were produced by applying appropriate voltages to the split

gates. The conductance of the double-dot system as a function of the top gate voltage is observed to have a complex but repeatable characteristic, similar to that shown in Fig. 1(b). For identically sized dots, the conductance spectrum is symmetric and periodic, whereas an asymmetry in dot sizes produces a complex spectrum, almost random in appearance, due to the mismatch in charging energies of the two dots. This effect is known as the *stochastic Coulomb blockade* [11]. The complexity of the spectrum in such asymmetric circuits means that designs utilizing only a few dots can in principle produce very complex patterns that can be useful toward a computational goal.

The conductance spectrum is extremely sensitive to the size and shape of the dots as well as other experimental parameters such as the applied voltages. In this double-dot circuit, the *conductance versus top gate voltage spectrum* can be considered as a *signature* of the circuit with a complex but unique pattern that characterizes the circuit for particular values of the circuit parameters, source-drain voltage, and back gate voltage. The measured conductance signature was observed to change dramatically as the value of the back gate voltage was changed; see Fig. 1 in Ref. [10]. It is clear from this that if the back gate voltage were changed systematically by means of an externally applied adaptive algorithm, the shape of the signature could be manipulated and controlled to approximate a desired pattern. In general, several adaptive variables could be used to obtain more flexibility in the tuning of the signature. For instance, in addition to the back gate voltage, the relative sizes of the dots could also be changed by means of split gate voltages. There are numerous ways in which this procedure could be used to achieve a computationally useful goal. An illustrative example is shown in Fig. 1(b) in which we consider tuning the conductance signature to conform to training inputs (shown by the black dots) in order to perform classifier training. The tuning can be carried out by applying an adaptive algorithm to find a near minimum of a cost function, such as $Cost = \sum (G - G_{TRAIN,I})^2$,where $G_{TRAIN,I}$ are the training input values. Adaptive algorithms are available which can efficiently find very good, though not necessarily optimum, solutions. The training of circuits for data interpolation, pattern recognition and pattern classification have been successful computational tasks for neural networks and these can be performed by single-electron circuit signatures as well. There are numerous other candidates for both single-electron circuit signatures and methods of implementing computational goals by adaptive tuning. In the following section, two examples based on numerical simulation of model circuit responses to adaptive tuning will be briefly discussed in order to indicate the range of possibilities in this area.

III. RESULTS

In these examples, calculations were carried out using the orthodox Coulomb blockade model [2] to describe the electron transport. Currents were calculated numerically using a Monte Carlo procedure [12]. The nominal values of parameters were $R_J = 10^2$ kΩ, $C_J = 10$ aF, $C_G = 5$ aF, $V_{SD} = 5$ mV, and T = 10 K. The generalized downhill simplex algorithm [13] was used to perform the adaptive tuning of circuit

variables and search for a near optimum solution of minimizing a cost function within a specified error resolution. The simplex algorithm does not require computing derivatives of the cost function and efficiently finds a solution by sweeping over the landscape of the cost function for the adaptive variables. In each case, a cost function is chosen which will implement a computation or result in a circuit which has a computational use.

Figure 2 shows an example of generating Boolean strings by adaptive tuning of a single-electron circuit. The single-electron circuit is composed of two asymmetric quantum dots with two current channels, I_1 and I_2. A tunnel junction couples the two dots so that electrons can move between the two channels. This coupling, along with the asymmetry of the dots, allows the conductance spectra of these channels to be quite complex in shape. The normalized conductance spectrum of channel *1* versus the top gate voltage is used as the circuit signature. To keep the peak structure well defined, conductance peaks are grouped within a resolution ΔV_{GT}, which has the effect of coarse-graining the spectra. To generate the strings, each conductance peak P_i is assigned a digit $S_i = 0$ or 1 by the rule that $S_i = 1$ if $P_i > 0.5$ and $S_i = 0$ if $P_i \leq 0.5$. The adaptive variables used for tuning were the back gate voltage and the relative dot sizes. Applying the adaptive algorithm, it is found that the circuit can readily generate an arbitrary training input binary string by adaptively tuning these adaptive variables as shown in Fig. 2(b). The ability of the circuit to generate the proper string without error is enhanced by the fact that many different conductance spectra can generate the same string. String generation is also robust to random modifications of the circuit. For example, it was found that random offset charge added to each of the dots does not deteriorate the ability of the circuit to find adaptive solutions. This suggests that the approach would be viable for real nonideal circuits. The generated strings corresponded to current channel *1*, but note that there is also a string corresponding to current channel *2*. These strings are interacting due to the coupling between the dots. With additional circuitry, it is possible to actually combine strings and carry out logical functionality by adaptively tuning the circuit.

Figure 3 shows an example of adaptively generating a phase diagram for control of driven single-electron circuits. These are bistable phase-locked single-electron tunneling circuits composed of capacitively coupled quantum dots. They are driven by a common ac pump voltage at frequency $2\omega_{SE}$ and an input ac voltage V_{IN} at frequency ω_{SE}. These circuits were proposed by Kiehl and Oshima [5] as a basis for computational circuitry in which information is stored in the phase state of single-electron tunneling oscillations. They showed that a dc voltage ramped on at time t_{CLOCK} results in bistable steady-state junction voltages that oscillate in one of two modes : mode *1* or mode *2*. The mode is determined by the two phases : the input voltage phase ϕ_{IN} and the dc clock phase $\phi_{CLOCK} = \omega_{SE}\, t_{CLOCK}$. These generate a bistability phase diagram of the type shown in Fig. 3(b) that determines how these circuits are controlled during a computation. The regions occupied by modes *1* and *2* in the phase diagram are sensitive to the values of the circuit parameters and can exhibit a great range of area and shape. Thus the bistability control phase diagram for the phase-locked circuits is another candidate for a sensitive circuit signature which is amenable

to being tuned by adaptive feedback control. An example is shown in Fig. 3(b) in which a training input bistability diagram was used to tune the circuit to a specified pattern : mode *2* within the white square and mode *1* outside the white square. The dot size was adjusted as the adaptive variable and the circuit was tuned to this training input. The adaptive solution correctly generated mode *2* within the white square, although small errors were generally observed in which small regions of mode *2* leak out into mode *1*. The crosshatched areas in Fig. 3(b) show a typical example of these errors. These errors can be reduced by using additional adaptive variables and by increasing the error resolution of the simplex algorithm. Equally good solutions were found with circuits containing additional random offset charge, again demonstrating the robustness of adaptive control methods.

IV. CONCLUSIONS

Adaptive methods are attractive for single-electron computational circuits because of the difficulty of ensuring the stringent specifications of fabrication and materials required for reliable operation of single-electron designs. Uncontrollable modifications of the circuit operation due to random background charge, nonuniformities in circuit parameter values, and error sources such as thermal and cotunneling processes can all deteriorate the operation of single-electron circuits. Adaptive tuning may be able to compensate for these to some extent by finding a circuit configuration that optimizes circuit operation in the presence of these uncontrollable processes. The extent to which this is possible can only be learned by studying the response of individual circuit designs and methods of implementing computation both experimentally and in simulation. One could consider attempting to optimize the performance of existing single-electron circuits, such as SET's, using adaptive methods. However, in this work we have focused on adaptively tuning sensitive and flexible *circuit signatures* to take full advantage of adaptive methods. These can encode a large amount of information using circuits consisting of only a few dots and tunnel junctions and present large numbers of degrees of freedom for adaptive tuning. The simulation examples presented, which tuned conductance spectra and bistability phase diagrams, showed robust ability to obtain good solutions. The adaptive tuning studied here was externally applied and this would need to be implemented by external circuitry in an actual experiment. The recent experimental achievement [9] of feedback control of conductance fluctuations gives confidence in the feasibility of this proposal. However, it would be desirable to go beyond this and find methods for implementing adaptive control locally and autonomously as part of the same circuitry.

ACKNOWLEDGEMENT

The author thanks M.G. Ancona for useful discussions.

References

[1] *National Technology Roadmap for Semiconductors,* Semiconductor Industry Association, San Jose, CA (1994).

[2] D.V. Averin and K.K. Likharev, in *Single Charge Tunneling,* Edited by H. Grabert and M.H. Deverot (Plenum Press, New York, 1992), Chap. 9; A.N. Korotkov, R.H. Chen and K.K. Likharev, J. Appl. Phys. **78**, 2520 (1995).

[3] M.J. Goosens, C.J.M. Verhoeven and A.H.M. van Roermund, *Proceedings of the Fifth International Conference on Microelectronics for Neural Networks and Fuzzy Systems* (IEEE Computer Society Press, Los Alamitos, CA, 1996), p. 125; M, Kirihara and K. Taniguchi, Jpn. J. Appl. Phys. **36**, 4172 (1997).

[4] C.S. Lent, P.D. Tougaw, W. Porod, and G.H. Bernstein, Nanotechnology **4**, 49 (1993); S. Bandyopadhyay, B. Das and A.E. Miller, Nanotechnology **5**, 113 (1994).

[5] R.A. Kiehl and T. Oshima, Appl. Phys. Lett. **67**, 2494 (1995); T. Oshima and R.A. Kiehl, J. Appl. Phys. **80**, 912 (1996).

[6] K. Nakazato and J. White, IEDM Tech. Digest, **487** (1992); M.G. Ancona and R.W. Rendell, J. Appl. Phys. **77**, 393 (1995); M.G. Ancona, J. Appl. Phys. **79**, 526 (1996).

[7] R.W. Rendell and M.G. Ancona, Superlatt. Microstr. **20**, 479 (1996).

[8] W.S. Warren, H. Rabitz and M. Dahleh, Science **259**, 1581 (1993); L.M. Pecora and T.L. Carrol, Phys. Rev. Lett. **64**, 821 (1990).

[9] R.F. Service, Science **279**, 1848 (1998).

[10] R.H. Blick, R.J. Haug, J. Weis, D. Pfannkuche, K.v. Klitzing, and K. Eberl, Phys. Rev. **B53**, 7899 (1996).

[11] I. M. Ruzin, V. Chandrasekhar, E.I. Levin, and L.I. Glazman, Phys. Rev. **B45**, 13469 (1991) ; K. Kemerink and L.W. Molenkamp, Appl. Phys. Lett. **65**, 1012 (1994).

[12] K.P. Hirvi, M.A. Paalanen and J.P. Pekola, J. Appl. Phys. **80**, 256 (1996).

[13] J.A. Nelder and R. Mead, Comput. J. **7**, 308 (1965).

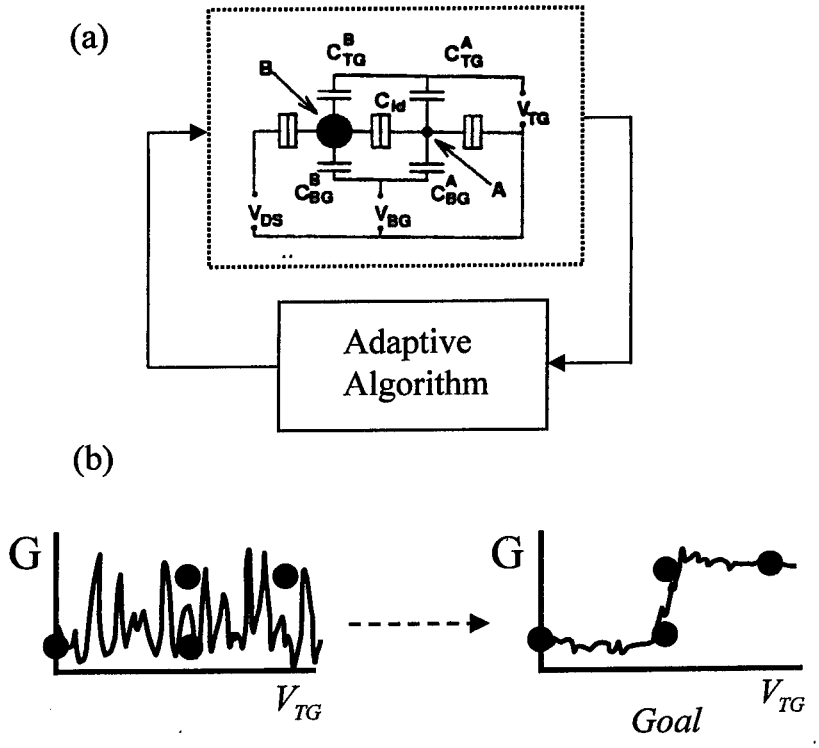


Figure 1 : (a) Circuit composed of two coupled asymmetric quantum dots (after Ref. 10). (b) Schematic illustration of tuning a circuit signature by adaptive feedback. In this example, the circuit signature is the conductance spectrum for the top gate voltage and an externally applied adaptive algorithm tunes the conductance spectrum to conform to training inputs (solid dots), i.e. classifier training, by adaptively adjusting circuit variables such as the back gate voltage and the relative dot size.

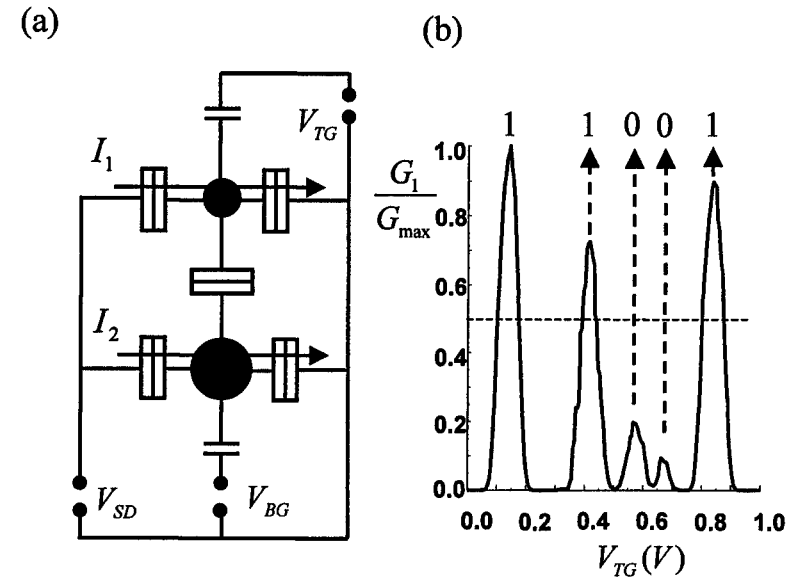


Figure 2 : (a) Circuit composed of two asymmetric quantum dots with two coupled current channels. (b) Adaptive solution for the normalized conductance of channel #1 corresponding to a training input binary string.

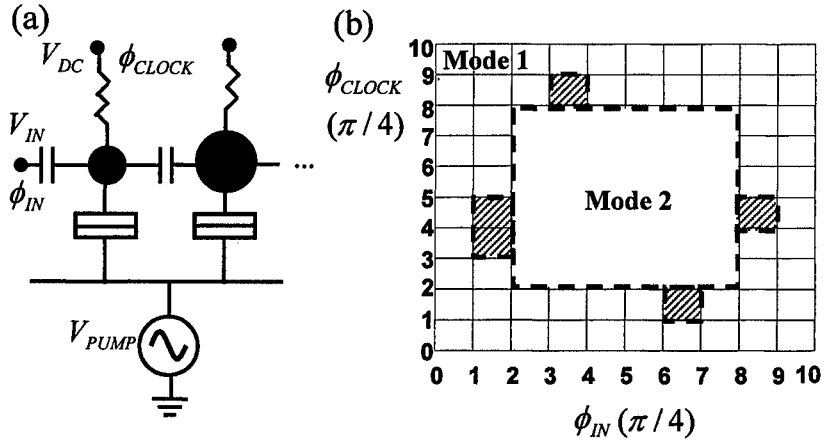


Figure 3 : (a) Bistable phase-locked single-electron circuit. (b) Adaptive solution for the bistability phase diagram corresponding to a training input phase diagram.

FAULT RATES IN NANOCHIPS

S. Spagocci, T. Fountain
University College London
Gower Street, London WC1E 6BT, England

ABSTRACT

In this paper we address the problem of estimating nanochip error rates, taking intrinsic error rates and fault-tolerant techniques into account. In particular we first describe cascaded triple modular redundancy (CTMR), an iterated version of triple modular redundancy that we believe might greatly improve the potentialities of the latter, while retaining its advantages. In particular CTMR is expected to be particularly suitable for online implementation. We then analyze intrinsic error rates for logic gates based on single electron devices and quantum cellular automata, respectively. Intrinsic error rates in such devices clearly show the necessity of fault-tolerant techniques. We then show that, through application of CTMR, chips containing ~ 10^{11} such devices can be made perfectly reliable, at least as far as intrinsic runtime errors are concerned, with a level of redundancy of ~ 100 at worst. This, however, requires carefully tuning the devices' operating conditions and design solutions.

INTRODUCTION

The proposed introduction of nanometer-scale components should make it possible to conceive chips containing up to 10^{12} logic gates. This would be particularly interesting for the implementation of parallel systems on a single chip. For such an assembly to work, the introduction of fault-tolerant techniques seems inevitable. The huge number of devices makes the chip unreliable, even if the devices are highly reliable in themselves.

We believe that triple modular redundancy (TMR) [1] is a fast and easily implemented fault tolerant technique. In TMR, the place of each device is taken by a block of three identical devices and majority voting is performed among them. When TMR is not enough, we propose the use of cascaded triple modular redundancy (CTMR). In this approach, the devices are first clustered and TMR is applied to the clusters. The voting circuits are then suitably clustered and TMR is applied again. The process is iterated for a number of steps.

We first considered single-electron devices, of which the electron pump [2] is a prototype. The electron pump is an array of metallic islands, separated by nanometer-scale junctions, through which an electron is made to tunnel sequentially. Logic gates based on the electron pump have been proposed [3]. At high frequencies, the main error source arises from pumping the electron too fast, so that the desired tunneling process is missed [4-6]. We predict complete reliability for a system with 10^{11} effective devices at GHz frequency and room temperature, with 4 TMR levels.

We also considered quantum cellular automata [7]. A QCA cell is a square array of 4 quantum dots, occupied by two electrons. The cell has two stable states, which are taken

to mean 0 and 1. Due to electrostatic repulsion, each cell interacts with its neighbors. QCA logic gates based on this principle have been proposed [8]. The main error source arises from thermal excitation [9], which may create a kink in a row of previously aligned cells, thus giving a wrong answer. We predict complete reliability for a system with 10^{11} effective devices at GHz frequency and liquid nitrogen temperature, with 3 TMR levels.

2 CASCADED TRIPLE MODULAR REDUNDANCY

Since cascaded triple modular redundancy is an iterated version of the well known technique of triple modular redundancy [1], the latter will be briefly described here. In TMR the place of each potentially faulty unit is taken by a block of three identical units, and majority voting is performed among them. This works well provided one is dealing with binary units, under the assumption that a fault can only flip the unit's answer and the voting circuitry is perfectly reliable. If the working circuitry is not perfectly reliable, the formalism has to be suitably modified.

A TMR unit fails when either two or three units out of three fail. The probability of such an event to occur, $P_{f/tmr}$, can be calculated by a binomial distribution, as follows:

$$P_{f/tmr} = (P_f)^3 + 3 \cdot (P_f)^2 \cdot (1 - P_f) \qquad (1)$$

Eq. (1) takes an even simpler form if one considers the limiting case in which the intrinsic probability for an element to fail is small. As we see in the following sections, this will be the case in our work. By taking a first-order Taylor expansion of Eq. (1), one obtains:

$$P_{f/tmr} = 3 \cdot (P_f)^2 \qquad (2)$$

For the general case of an imperfect voting circuitry, with failing probability P_v, we have to consider that the TMR unit gives a wrong answer if either majority voting would give a wrong answer and the voting circuit works, or majority voting would give a right answer and the voting circuitry fails. If, furthermore, we consider a cluster of N_g gates, Eq. (2) generalises to:

$$P_{f/tmr} = 3 \cdot (N_g \cdot P_f)^2 + P_v \qquad (3)$$

We are now ready to discuss cascaded triple modular redundancy in detail. According to CTMR, the potentially faulty units are first clustered in a suitable way, and triple modular redundancy is applied to the clusters. The voting circuits are then suitably clustered, as well, and triple modular redundancy is applied to each cluster. The process is iterated for a number of steps, as in Fig. (1). The intrinsic reliability of both the functional units and the voting circuitry impose a bound on cluster size and the number of cascaded levels.

Let us consider a chip containing clusters of N_g identical logic gates. The gates have a faulting probability $P_{f;g}$. The voting circuits have a faulting probability $P_{f;v}$. Both probabilities are assumed to be small. We deal with two possible regimes. In the first regime, the voting circuitry can be considered as perfectly reliable in comparison to the TMR units. In the second regime, the TMR units can be considered as perfectly reliable in comparison to the voting circuits. The two regimes will be referred to as the perfect voting circuitry (PVC) regime and the imperfect voting circuitry (IVC) regime.

In the PVC regime, the voting circuitry is supposed to be much more reliable than the clusters. We then require that, in Eq. (3):

$$3 \cdot (N_g \cdot P_{f;g})^2 \geq 10 \cdot P_{f;v} \tag{4}$$

By iterated use of Eq. (3), taking Eq. (4) into account, it is possible to calculate the failing probability of a cluster at the i^{th} CTMR stage, $P_{f/tmr;c}(i)$, and its minimum size, $N_{min}(i)$, under the hypothesis that $P_v = P_{f;g}$.

In particular, one obtains:

$$P_{f/tmr;c}(i) = 10^i \cdot P_{f;g} \tag{5}$$

and:

$$N_{\min}(i) = \sqrt{\frac{10^{2-i}}{3 \cdot P_{f;g}}} \tag{6}$$

The chip's failing probability after i CTMR stages, $P_{f/tmr}(i)$, can be written as:

$$P_{f/tmr}(i) = \frac{N_g}{\prod_{s=1}^{i} N_{\min}(s)} \cdot P_{f/tmr;c}(i) \tag{7}$$

where the product in Eq. (7) can be calculated by making use of decimal logarithms:

$$\prod_{s=1}^{i} N_{\min}(s) = 10^{\frac{i \cdot (3-i)}{4}} \cdot (3 \cdot P_{f;g})^{-\frac{i}{2}} \tag{8}$$

We can then give a final expression for the failing probability of a chip with i CTMR stages.

In particular, we have:

$$P_{f/tmr}(i) = 10^{\frac{i\cdot(1+1)}{4}} \cdot (3 \cdot P_{f;g})^{\frac{i}{2}} \cdot (N_g \cdot P_{f;g}) \qquad (9)$$

Differentiation of Eq. (9) with respect to i shows that $P_{f/tmr}(i)$ is monotonically decreasing with i. It is therefore advisable to have as many CTMR levels as possible. The very nature of the iteration process, however, prevents it from going on forever. In fact, the maximum number of stages is defined by the condition:

$$\frac{N_g}{\prod_{s=1}^{i} N_{\min}(s)} = 1 \qquad (10)$$

Equivalently, the maximum number of stages is given by i_{max}, where i_{max} is the integer part of the number i satisfying Eq. (10) in conjunction with Eq. (8). If a number i_{max} of stages is not enough, it is further possible to apply TMR to the whole chip, by using micron-scale voting circuitry.

The chip's failing probability, then, becomes:

$$P_{f/tmr}(i) = 3 \cdot \{10^{\frac{i\cdot(1+1)}{4}} \cdot (3 \cdot P_{f;g})^{\frac{i}{2}} \cdot (N_g \cdot P_{f;g})\}^2 \qquad (11)$$

where $i = i_{max}$.

In the IVC regime, the clusters are supposed to be much more reliable than the voting circuitry. We will see that, by following a suitable clustering scheme, it is possible to bring the whole chip to have the same faulting probability as that of an individual gate. In order to implement this regime, we require that in Eq. (3):

$$3 \cdot (N_g \cdot P_{f;g})^2 \le \frac{1}{10} \cdot P_{f;v} \qquad (12)$$

It follows than that the clusters must have a maximum size, at any stage and under the hypothesis that $P_{f;g} = P_v$, given by the following expression:

$$N_{\max} = \sqrt{\frac{1}{30 \cdot P_{f;g}}} \qquad (13)$$

We can now calculate the faulting probability of a cluster after i CTMR stages.

In particular, we obtain:

$$P_{f/tmr}(i) = \frac{N_g}{(N_{\max})^i} \cdot P_{f;g} \tag{14}$$

By differentiating Eq. (14), used in conjunction with Eq. (13), with respect to i, $P_{f/tmr}(i)$ is seen to be monotonically decreasing with i. One therefore needs as many CTMR stages as possible. The iteration process, of course, cannot go on indefinitely. The maximum number of stages is defined by the condition:

$$\frac{N_g}{(N_{\max})^i} = 1 \tag{15}$$

which translates into:

$$i_{\max} = [-2 \cdot \frac{Log(N_g)}{Log(30 \cdot P_{f;g})}] + 1 \tag{16}$$

where [.] is the integer part function.

We then obtain a surprising simple expression for the chip's overall failing probability:

$$P_{f/tmr} = P_{f;g} \tag{17}$$

If needed, it is then possible to apply TMR to the chip's output, using a voting circuitry much more reliable than the chip's gates (micron-scale technology, in practice). The system's failing probability then becomes:

$$P_{f/tmr} = 3 \cdot (P_{f;g})^2 \tag{18}$$

The previously derived formulae refer to an idealised clustering scheme. Real-world design solutions, presumably, can only approximate such a scheme.

3 ERROR RATES IN SEDs

The first class of devices we considered was single-electron devices (SEDs), of which the electron pump [2] is a prototype. The electron pump is an array of metallic islands, separated by nanometer-scale junctions, through which an electron is made to tunnel sequentially. A single-electron switch [3], based on the electron pump principle, is shown in Fig. (2). When the control island is free, the input electron is made to turn left. When it is

occupied by an electron, repulsion makes the previous path energetically unfavorable. The input electron, then, turns right.

The single electron switch is the building block of a family of logic gates [3], which we show in Figs. (3) and (4). We first describe the error sources affecting electron pumps, since fault rates for electron pumps have been investigated both theoretically [4,10] and experimentally [5,6,11]. The results are then extended to the previously mentioned SED-based logic gates.

There are three kinds of fault sources affecting an electron pump [4]: frequency, thermal and cotunnelling errors. In frequency errors, the electron is pumped too fast as compared to the half life for the tunnelling process, so that the desired tunnelling process is missed. In thermal errors, the electron goes the wrong way, acquiring the necessary energy through thermal exchange with the environment. In cotunnelling errors, the electron goes the wrong way by simultaneously tunnelling through all its junctions.

Experimentally, the main fault source for electron pumps at the micron scale, operated at more than ~ 1 MHz, is frequency errors [5,6,11]. The corresponding error rate per clock cycle, $P_{f;g}$, is shown to have the form [4]:

$$P_{f;g} = \exp\left(-\frac{\alpha}{R \cdot C \cdot f}\right) \tag{19}$$

with:

$$\alpha = \frac{n-1}{8 \cdot n^2} \tag{20}$$

where R and C are the tunnelling junction's resistance and capacitance, respectively, f is the clock frequency and n is the number of junctions in the pump. Eq. (19) simply represents the probability that the electron has not tunnelled through the junction after the pulsing cycle is completed. If the tunnelling process is missed, the electron goes back through the pump by cotunnelling, in a small time-scale as compared to the clocking time [4].

At frequencies below ~ 1 MHz the error rate approaches an asymptotic value [5,6,11], as shown in Fig. (5). The most likely candidate is photon-assisted cotunnelling [5,6,10,11]. The electron tunnels the wrong way, by absorbing energy from the environmental noise. The most likely noise candidate seems to be charge traps on the device substrate, which slowly relax with time [5]. A fault rate per cycle of ~ 10^{-8} was observed for a 7-junction electron pump operating at 35 mK, with micron-scale islands [6,11]. A fault rate per cycle of ~ 10^{-6} was instead observed for a 5-junction electron pump, under similar conditions [5].

Errors in electron pumps are controlled by suitable adimensional parameters. For frequency and cotunnelling errors the parameter is [4]:

$$R \cdot C \cdot f \tag{21}$$

which is essentially the ratio between the pumping time and the time-scale for the tunnelling process. For thermal errors the relevant parameter is [4]:

$$\frac{e^2}{C \cdot k \cdot T} \tag{22}$$

Eq. (22) essentially represents the ratio between the energy jump due to a tunnelling event and the thermal energy at the operating temperature.

The experimental or calculated data on failure rates we are aware of refer to micron-scale devices. We need them at the nanometer regime. We then introduce a parameter λ, the ratio between the target length scale and the length scale of available results.

As shown in Ref. [12], the effective junction capacitance can be calculated as:

$$C = C_j + C_i \tag{23}$$

where C_j is the junction capacitance and C_i is the island's capacitance to earth. The junction capacitance can be approximated by a parallel-plate capacitor of area A, separated by a gap d [13]. Since the tunnelling junction is already at the nanometer level, we do not need to vary the width d. The effective area A, instead, scales as λ^2. Then:

$$C_j \propto \lambda^2 \tag{24}$$

The island capacity to earth can be calculated by approximating it to a bidimensional metallic sheet [12]. So:

$$C_i \propto \lambda \tag{25}$$

Provided λ is much smaller than one ($\lambda \sim 10^{-3}$ in our case), the stray capacitance C_i will dominate in Eq. (23). The total capacitance, then, has the same scaling law as the stray capacitance, as given by Eq. (25).

Experimentally, C ~ 0.1 fF at the micron scale [5,6]. Consequently, we predict C ~ 0.1 aF at the nanometer scale. Incidentally, it has to be seen whether an electron pump dominated by its stray capacitance would still work.

An expression for the tunneling junction resistance is given in Ref. [14]. Using such an expression, it is possible to show that the effect of the scaling on R can be compensated by shortening the tunnelling barrier by δd, where $\delta d \sim 0.1$ nm. Experimentally, $R \sim 0.1$ MΩ for a micron scale pump [5,6]. Therefore, we assume a similar value for the nanometer scale.

Since the junction resistance R can be kept constant by displacing the tunnel junction, we only have to worry about the products C·f and C·T as long as scaling is concerned. The experimental data for fault rates in micron-scale electron pumps were obtained for a clock frequency of ~ 1 MHz and an operating temperature of ~ 0.3 K. We now need to scale such data to nanometer-scale pumps with a clock frequency of ~ 1 GHz and an operating temperature of ~ 300 K (room temperature). Our change of conditions can be described by the transformations $f \rightarrow 10^3 \cdot f$ and $T \rightarrow 10^3 \cdot T$. On the other hand, since we are passing from the micron to the nanometer scale, $\lambda \rightarrow 10^{-3} \cdot \lambda$. The products C·f and C·T are then kept constant and, according to Eqs. (21), (22) and (25), even the error rates and their relative importance.

To our knowledge, no quantitative treatment on error rates in SED-based logic gates has been proposed. Such gates are affected by two different kinds of errors: switching errors and pump errors. The electron, in fact, can be switched the wrong way, or it can travel back through one of the electron pumps composing the gates. In general, we can imagine two distinct regimes, in which either error dominates. Pumping errors can be made smaller by adding a suitable number of junctions to the input and output lines. However, switching errors fix an upper limit for device dimensions, since above a certain size they dominate over pumping errors, making any improvement in pumping accuracy pointless.

We considered an array of ~ 10^{11} SDE-based electron gates [3]. Simulation results on error rates in single electron switches are described in Ref. [15]. Error probabilities of ~ 10^{-8} and ~ 10^{-4} are reported for right and left switching, respectively. The overall switching error probability is therefore of ~ 10^{-4}. Such an error rate would imply a lifetime of ~ 10^{-2} sec, with 9+1 CTMR levels, which is clearly unacceptable. Therefore, the electron gates have to be redesigned, so as to reduce switching errors to an acceptable level. By adding a suitable number of junctions to the input and output lines, respectively, it is then possible to reduce pumping errors. In the following we assume that the gates have been suitably redesigned. We have preliminary indications that such a redesign process is possible. However, our design solution has to be further checked.

We can now give predictions on the lifetimes and redundancies of SED-based chips. For an array of ~ 10^{11} effective gates working at ~ 1 GHz, a design based on the 7-junction electron pump ($P_{f;g} \approx 10^{-8}$) implies a lifetime of ~ 1 month, with 4+1 CTMR levels. With a design based on the 9-junction electron pump ($P_{f;g} \approx 10^{-10}$, as extrapolated from the error rates of the 5 and 7-junction electron pumps, by using the cotunneling expression of Ref. [4]), this result can be greatly improved. An "infinite" lifetime is predicted, with 3+1 CTMR levels. The corresponding redundancy level is 81.

The linear dimensions of a SED-based chip with ~ 10^{11} effective gates (but ~ 10^{13} total gates) and 3+1 CTMR stages are estimated to be ~ 1 cm. From this point of view, the proposed solution seems to be realistic. However, power dissipation would pose serious difficulties. Powering the devices with nanometer-wide buses feeding rows, in fact, would imply a power dissipation of ~ 100 MW, which is a physically absurd result. On the other hand, widening the buses so as to bring power dissipation at the level of ~ 1 W would imply a chip having one side ~ 10 km long, which is again absurd. A power dissipation of ~ 1 W could be obtained by feeding each gate independently or, equivalently, by making pump islands stick out of a metallic base the size of the chip, which would carry the power. The proposed powering solution would be hardly feasible with the multiphase pulsing scheme proposed in Ref. [4]. Presumably, a single-phase design like that of Ref. [16] should be considered.

4 ERROR RATES IN QCAs

We also considered quantum cellular automata (QCAs) [7]. A QCA cell is a square array of four quantum dots, occupied by two electrons. The cell has two stable states, corresponding to electrons sitting at the ends of each diagonal. Each cell is influenced by its neighbors through electrostatic repulsion. A family of QCA logic gates based on this principle has been proposed [8]. We show them in Figs. (6) and (7).

The main error source in QCA-based devices arises from thermal excitation [9], which may create kinks in a row of previously aligned cells, thus giving a wrong output. See Fig. (8) for the one-kink case. To our knowledge, no detailed account of QCA fault rates has been given. We assume that such error rates can be estimated from thermodynamic considerations, following the qualitative remarks of Ref. [9].

The applicability of thermodynamic considerations is not a priori guaranteed, since the device might not have enough time to explore higher excited states during its clock cycle. However we think that, at least in one of the possible operating regimes for QCAs, the use of thermodynamic arguments can be justified. In the so-called adiabatic switching regime [9], in fact, the clocking time t_c is chosen to be much longer than the time corresponding to the energy splitting between the ground state and the first excited state of a QCA unit (a gate or a wire). If the first excited state has an energy splitting of ΔE with respect to the ground state, the previously mentioned condition translates into [17]:

$$t_c >> \frac{\hbar}{\Delta E} \tag{26}$$

Condition (26) is verified even for the higher rank states, since their energy splitting is $\Delta E' > \Delta E$. The unit is then prevented from getting stuck on a metastable excited state [17]. We think that such a condition also gives the unit time to explore higher rank states through thermal excitation, therefore validating the use of thermodynamic arguments.

We obtained an order-of magnitude estimation for fault rates in a QCA unit by considering the case of a QCA wire. This approach has been invoked for approximated considerations on QCA fault rates [9]. By applying Boltzmann's statistics, the transition probability to the n^{th} excited state of an assembly of N QCA cells is calculated to be:

$$P_{f;g} = g_n \cdot \frac{\exp\left(-\frac{\Delta E_n}{k \cdot T}\right)}{\sum_n \exp\left(-\frac{\Delta E_n}{k \cdot T}\right)} \tag{27}$$

In Eq. (27), g_n is the degeneracy of the n^{th} excited level. In the case of a QCA wire, g_n is the number of ways in which n kinks can be chosen from N-1 positions:

$$g_n = \binom{N-1}{n} \tag{28}$$

while ΔE_n is the splitting of the n^{th} excited level with respect to the ground state. In the case of an infinite wire, ΔE_n is given by the expression [9]:

$$\Delta E_n = n \cdot \Delta E \tag{29}$$

where ΔE is the splitting between the first excited level and the ground state. Eqs. (27) and (29) show that the probabilities of thermal excitation of rank higher than one are exponentially dumped. On the other hand, Eq. (29) is approximately valid even for a finite wire [9]. Therefore, in a first approximation, we can assume that errors arise from the thermal excitation of one kink. Eq. (27), then, takes the form:

$$P_{f;g} = N \cdot \exp\left(-\frac{\Delta E}{k \cdot T}\right) \tag{30}$$

where we have put N-1 ≈ N and approximated the partition function to 1.

Again, we introduce a parameter λ, the ratio between the target length scale and the length scale of available results and we assume the following Coulomb-like scaling law for ΔE:

$$\Delta E \propto \varepsilon^{-1} \cdot \lambda^{-1} \tag{31}$$

where ε is the relative dielectric constant of the device's substrate ($\varepsilon \approx 10$ [7]).

The energy splitting ΔE has been calculated to be ≈ 0.8 meV for an infinite QCA wire with dot centers within a cell spaced by ~ 30 nm [18]. For cells spaced by ~ 1 nm, our change of scale can be expressed by the transformations $\lambda \rightarrow 3 \cdot 10^{-2} \cdot \lambda$, $\varepsilon \rightarrow 10^{-1} \cdot \varepsilon$. The scaling law

for ε derives from the fact that, at the nanometer (i.e. molecular) scale, $\varepsilon \approx 1$, since screening effects are no more present [9]. We estimate that $\Delta E \approx 0.2$ eV for nanometer-level QCA cells.

We can now predict lifetimes and redundancies of QCA-based chips. For a QCA-based gate working at a nanometer scale, room temperature, an error rate of ~ 10^{-4} is predicted. For an array of ~ 10^{11} effective gates, this implies a lifetime of ~ 10^{-2} sec at ~ 1 GHz, with 9+1 CTMR levels. This is clearly unacceptable. However, by operating at liquid Nitrogen temperature (77 K), a gate error rate of ~ 10^{-19} and an "infinite" lifetime might be expected, with 2+1 CTMR levels. The corresponding redundancy level would be 27. However these figures might be subject to revision, due to the doubts concerning the application of thermodynamic considerations to QCA fault rate estimations.

We estimate the linear dimensions of a QCA-based chip with ~ 10^{11} effective gates (but ~ 10^{12} total gates) and 3+1 CTMR stages to be ~ 1 cm. The proposed solution would then seem realistic. The problem of power dissipation in QCA-based chips has not yet been addressed.

5 CONCLUSIONS

CTMR, of course, is not the only possible approach to fault tolerance in nanochips. In particular, the following approaches [11] seem to be feasible:

- n-modular redundancy (plain or cascaded) in space
- n-modular redundancy (plain or cascaded) in time
- duplication (or n-fold replication) with error recovery
- error correcting codes

Apart from error correcting codes, all such ideas can be analyzed by following the same line of thought as TMR. Error correcting codes have still to be considered, though, and the preliminary results on the previously mentioned approaches have to be further checked. Reconfiguration, by its very nature, is unsuitable for taking care of the intrinsic faults of the nanodevices we considered, which are of a transient nature, though it may well be effective in dealing with manufacturing errors.

The intrinsic error rates we analyzed are of a transient nature. Impurities and dislocations, however, could cause permanents faults, which have not yet been considered in our device analysis. The fact that the typical dimensions of the devices we considered are ~ 10 nm, so that their area is ~ 10^4 times smaller than present-day devices suggests that single crystal errors will have more significant effects than in microcircuitry. On the other hand, the high level of redundancy required by the transient gate fault rates might provide protection against permanent faults, as well.

ACNOWLEDGEMENT

This paper and associated research were funded as part of the DARPA ULTRA program. Grant number N00014-96-1-0850. Principal investigator: T J Fountain.

REFERENCES

[1] H. Schepers, Terminology and Paradigms for Fault Tolerance, in: J. Vytopil, Ed., Formal Techniques in Real-Time and Fault-Tolerant Systems, pp. 3-31, Kluwer Academic Publishers, Boston, MA (1993).
[2] H. Pothier, P. Lafarge, C. Urbina, D. Esteve and M.H. Devoret, Europhys. Lett., **17**, 249 (1992).
[3] M.G. Ancona, J. Appl. Phys., **79**, 526 (1996).
[4] H.D. Jensen and J.M. Martinis, Phys. Rev. B, **46**, 13407 (1992).
[5] J.M. Martinis, M. Nahum and H.D. Jensen, Phys. Rev. Lett., **72**, 904 (1994).
[6] M.W. Keller, J.M. Martinis, N.M. Zimmermann and A.H. Steinbach, Appl. Phys. Lett., **69**, 1804 (1996).
[7] C.S. Lent, P.D. Tougaw, W. Porod and G.H. Bernstein, Nanotechnology, **4**, 49 (1993).
[8] P.D. Tougaw and C.S. Lent, J. Appl. Phys., **75**, 1818 (1994).
[9] C.S. Lent, P.D. Tougaw and W. Porod, in PhysComp '94: Proceedings of the Workshop on Physics and Computing, IEEE Computer Society Press, Los Alamitos, CA (1994).
[10] J.M. Martinis and M. Nahum, Phys. Rev. B, **48**, 18316 (1993).
[11] M.W. Keller, J.M. Martinis and R.L. Kautz, Phys. Rev. Lett., **80**, 4530 (1998).
[12] H.D. Jensen and J.M. Martinis, Physica B, **194-196**, 1255 (1994).
[13] L.J. Geerligs. V.F. Anderegg, C.A. van der Jeugd, J. Romijn and J.E. Mooij, Europhys. Lett, **10**, 79 (1989).
[14] M.I. Lutwyche and Y. Wada, J. Appl. Phys., **75**, 3654 (1994).
[15] M.G. Ancona, submitted to the 3rd International Workshop on Quantum Functional Devices, NIST, Gaithersburg MD (1997).
[16] M.G. Ancona, J. Appl. Phys., **81**, 3311 (1997).
[17] C.S. Lent and P.D. Tougaw, Proc. IEEE, **85**, 541 (1997).
[18] C.S. Lent and P.D.. Tougaw, J. Appl. Phys., **74**, 6227 (1993).

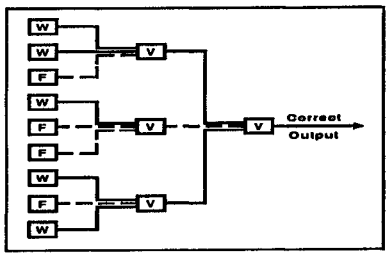


Fig. 1 A 3-stage CTMR unit In the 1st stage there are 9 copies of a device. In the 2nd stage majority voting is performed among triplets of devices of the 1st stage. In the 3rd stage majority voting is performed among the 3 voting units of the 2nd stage. W = working device, F = failing device, V = voting circuit. Wrong outputs are marked with a dashed line.

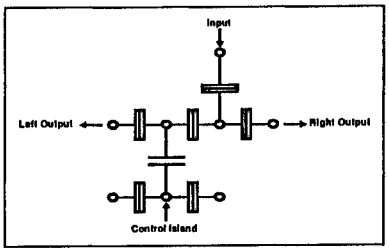


Fig. 2 A single electron switch The input electron is made to sequentially tunnel through the junctions joining the metallic islands. When the control island is free, the input electron turns left. When the control island is occupied by an electron, the input electron turns right. Metallic islands are marked as circles, tunnel junctions as rectangles.

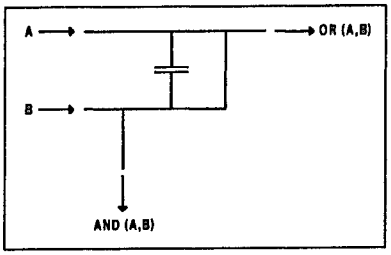


Fig. 3 An AND/OR gate, based on single-electron switching Any electron appearing at input A is driven to the OR (A,B) output. Any electron appearing at input B is either switched to the AND (A,B) output or to the OR (A,B) output, depending on the presence or absence of the electron coming from input A. Driving happens through the principle of electron pumps. Electron pumps in the circuit are represented as solid lines.

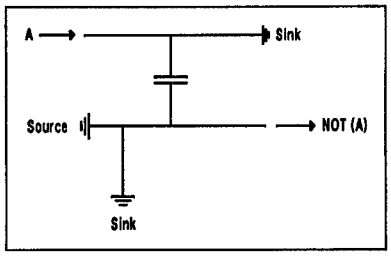


Fig. 4 A NOT gate, based on single electron switching Any electron appearing at input A is driven to a sink. One electron per clock cycle is taken from a source and either switched to a sink or to the NOT (A) output, depending on the presence or absence of the electron coming from input A. Electrons are driven through the principle of electron pumps, which we schematise as solid lines.

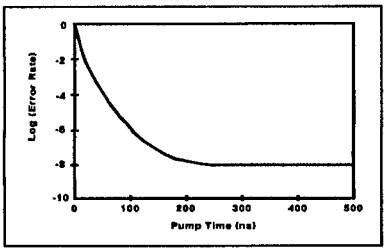


Fig. 5 Error rate vs. pump time for a micron-scale 7-junction electron pump, operating at 35 mK At high frequencies, the error rate is exponentially dependent on pump time. At low frequencies, the error rate approaches an asymptotic value of ~ 10^{-8}.

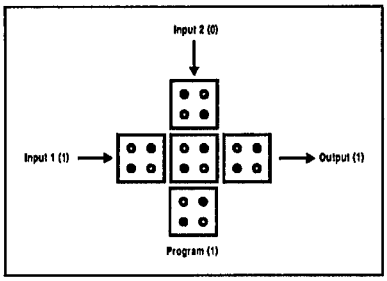


Fig. 6 A programmable AND/OR gate, based on QCAs The central cells performs majority voting among the two input cells and the control cell. Therefore, if the control cell is set to 0 the device works as an AND gate, if 1 as an OR gate. In the example shown the control cell is set to 1, so that we have an OR gate.

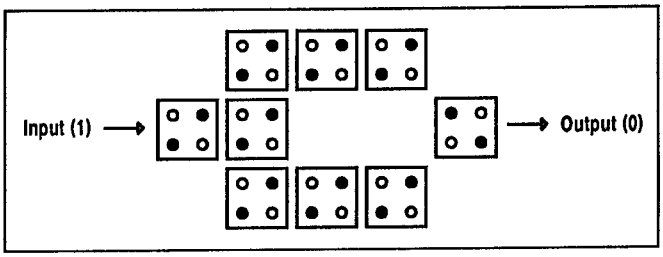


Fig. 7 A NOT gate, based on QCAs The input line extends one cell beyond the beginning of the two circuit branches. The input signal is propagated unaltered through the branches, due to electrostatic repulsion. The two branches, then, converge onto the output line. In this case there is diagonal alignment, so that electrostatic repulsion causes the input signal to be inverted.

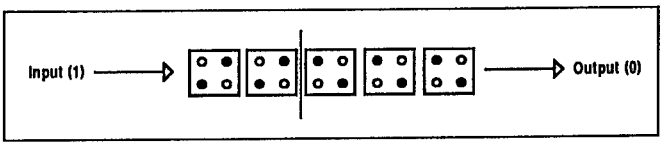


Fig. 8 A kink in a QCA wire Due to thermal fluctuations, the device has absorbed a quantity of energy enough to create a kink in it. The input, which would normally be propagated unaltered through the wire, is then flipped. The wire, then, acts as an inverter and an error arises.

INFLUENCE OF THE SPIN-ORBIT SPLIT-OFF BAND ON THE TUNNELING PROPERTIES OF HOLES ACROSS $InAlAs/InGaAs$ AND $InP/InGaAs$ INTERFACES

S. Ekbote, M. Cahay, and K. Roenker
Department of Electrical Engineering
University of Cincinnati, Cincinnati, Ohio 45221

ABSTRACT

We study the influence of the spin-orbit split-off band on the tunneling of holes across potential steps starting with the 6X6 Luttinger-Kohn Hamiltonian. The latter is diagonalized into 3X3 blocks (upper and lower Hamiltonians) using a unitary transformation. We consider potential steps due to $InP/In_{0.53}Ga_{0.47}As$ and $In_{0.52}Al_{0.48}As/In_{0.53}Ga_{0.47}As$ interfaces which are two of the most widely used materials for Heterojunction Bipolar Transistor technology. The important difference between the two interfaces comes from the difference between the valence band discontinuities and the difference in the spin-orbit split-off energies on both sides of the interfaces. While computing the transmission coefficients of holes incident from either side of the potential step, we show that the influence of the spin-orbit split-off band is quite drastic by comparing the results with those obtained with the 4X4 Luttinger-Kohn Hamiltonian. The implications of the results on the emitter efficiency of Pnp Heterojunction Bipolar Transistors are briefly discussed.

INTRODUCTION

The development of Pnp InP based Heterojunction Bipolar Transistors (HBTs) has received increased interest only over the last few years [1]. There have been only a few reports of Pnp HBTs while high performance Npn transistors have been widely reported [2, 3]. Stanchina et al. have obtained a current gain of 25, an f_T of 10 GHz and an f_{max} of 27 GHz at a collector current density of $7X10^3$ A/cm^2 for an initial, conservatively designed, single heterojunction InAlAs/InGaAs Pnp

transistor [4]. In view of their potential for a wide variety of applications, there is a need to develop accurate models of the device physics of Pnp HBTs. While the importance of electron tunneling through the emitter-base spike of Npn HBTs has been investigated by several groups [5, 6, 7, 8], the importance of hole tunneling across the emitter-base junction of abrupt Pnp HBTs has not been addressed so far. This paper deals with the coherent transport of holes across typical abrupt heterointerfaces ($In_P/In_{0.53}Ga_{0.47}As$ and $In_{0.52}Al_{0.48}As/In_{0.53}Ga_{0.47}As$) used as emitter-base junction in HBT technology. We study both the importance of the anisotropy of the dispersion relation of holes and the effects of band mixing on the tunneling of holes across the emitter-base junction.

A preliminary account of the scattering-matrix approach used here has been published recently [9, 10]. We start with the 6X6 Luttinger-Kohn Hamiltonian which is first reduced to two 3X3 Hamiltonians (referred as upper and lower Hamiltonians in the literature) through a unitary transformation. Because of the Kramers degeneracy is lifted for holes tunneling through a potential step, their tunneling coefficients are expected to be different when calculated with the upper and lower Hamiltonians. This is illustrated in this paper where we also compare the tunneling coefficients of holes incident from either sides of the potential steps.

II. APPROACH

Following Chao and Chuang [11], we start with the Luttinger-Kohn Hamiltonian describing the top of the valence band while including the effects of the spin-orbit split-off band

$$H = -\begin{bmatrix} P+Q & -S & R & 0 & -\frac{1}{\sqrt{2}}S & \sqrt{2}R \\ -S^\dagger & P-Q & 0 & R & -\sqrt{2}Q & \sqrt{\frac{3}{2}}S \\ R^\dagger & 0 & P-Q & S & \sqrt{\frac{3}{2}}S^\dagger & \sqrt{2}Q \\ 0 & R^\dagger & S^\dagger & P+Q & -\sqrt{2}R^\dagger & -\frac{1}{\sqrt{2}}S^\dagger \\ -\frac{1}{\sqrt{2}}S^\dagger & -\sqrt{2}Q & \sqrt{\frac{3}{2}}S & -\sqrt{2}R & P+\Delta & 0 \\ \sqrt{2}R^\dagger & \sqrt{\frac{3}{2}}S^\dagger & \sqrt{2}Q & -\frac{1}{\sqrt{2}}S & 0 & P+\Delta \end{bmatrix} \begin{matrix} |\frac{3}{2},\frac{3}{2}\rangle \\ |\frac{3}{2},\frac{1}{2}\rangle \\ |\frac{3}{2},-\frac{1}{2}\rangle \\ |\frac{3}{2},-\frac{3}{2}\rangle \\ |\frac{1}{2},\frac{1}{2}\rangle \\ |\frac{1}{2},-\frac{1}{2}\rangle \end{matrix} \quad (1)$$

where

$$P = \Gamma_1(k_x^2 + k_y^2 + k_z^2) \quad (2)$$

$$Q = \Gamma_2(k_x^2 + k_y^2 - 2k_z^2) \quad (3)$$

$$R = -\sqrt{3}\tilde{\Gamma}(k_x - ik_y)^2 + \sqrt{3}\left[\frac{\Gamma_3 - \Gamma_2}{2}\right](k_x + ik_y)^2 \quad (4)$$

and

$$S = 2\sqrt{3}\Gamma_3(k_x - ik_y)k_z \tag{5}$$

where the wavevector $\vec{k}$ is interpreted as a differential operator $-i\vec{\Delta}$. In Eq.(1), Δ is the spin-orbit split-off energy. In Eq.(1), the following equations were used: $\Gamma_1 = \frac{\hbar^2\gamma_1}{2m}$, $\Gamma_2 = \frac{\hbar^2\gamma_2}{2m}$, $\Gamma_3 = \frac{\hbar^2\gamma_3}{2m}$, and $\tilde{\Gamma} = (\Gamma_2 + \Gamma_3)/2$, where the γ_i are the Luttinger parameters.

The Hamiltonian in Eq.(1) is a 6X6 matrix in the basis composed of the $(|\frac{3}{2}, \frac{3}{2}))$ heavy-hole, the $(|\frac{3}{2}, \frac{1}{2}))$ light-hole, and the $(|\frac{1}{2}, \frac{1}{2}))$ split-off Bloch wave functions at the center of the Brillouin zone. In the axial approximation, the matrix element R is approximated by

$$R = -\sqrt{3}\tilde{\Gamma}{k_\rho}^2 exp(-2i\phi) \tag{6}$$

where ${k_\rho}^2 = {k_x}^2 + {k_y}^2$. In that case, the Hamiltonian (1) can be block-diagonalized using a similarity transformation as described in [11]. In the new basis set [11], the transformed Hamiltonian can then be written as

$$H = \begin{bmatrix} H_{3X3} & 0 \\ 0 & {H^\dagger}_{3X3} \end{bmatrix} \tag{7}$$

where ${H^\dagger}_{3X3}$ is the Hermitian conjugate of H_{3X3}. The explicit form of the Hamiltonian H_{3X3} is given by

$$H_{3X3} = \begin{bmatrix} P+Q & -R_\rho - iS_\rho & -\sqrt{2}R_\rho + \frac{i}{\sqrt{2}}S_\rho \\ -R_\rho + iS_\rho & P-Q & \sqrt{2}Q + i\sqrt{3/2}S_\rho \\ -\sqrt{2}R_\rho - \frac{i}{\sqrt{2}}S_\rho & \sqrt{2}Q - i\sqrt{3/2}S_\rho & P+\Delta \end{bmatrix} \tag{8}$$

where

$$R_\rho = -\sqrt{3}\tilde{\Gamma}{k_\rho}^2, \tag{9}$$

and

$$S_\rho = 2\sqrt{3}\Gamma_3 k_\rho k_z \tag{10}$$

Starting with the upper or lower Hamiltonian, the eigenenergies and corresponding envelope functions of the valence subbands can then be obtained by solving the effective-mass equation

$$\Sigma_j[H_{ij} + V_h(z)\delta_{ij}]F_j(\vec{k_\rho}, \vec{r}) = E(k_\rho)F_i(\vec{k_\rho}, \vec{r}) \tag{11}$$

where (i,j) = (1,2,3) and $V_h(z)$ is the valence band potential energy profile. In the axial approximation, the envelope function components F_j can be approximated as follows

$$F_j(\vec{k_\rho}, \vec{r}) = F_j(\vec{k_\rho}, z)e^{i\vec{k_\rho}\cdot\vec{\rho}} \tag{12}$$

where z is the direction of growth of the heterostructure. In Eq.(10), $\vec{k_\rho} = k_x\vec{x} + k_y\vec{y}$ and $\vec{\rho} = x\vec{x} + y\vec{y}$.

For a fixed energy E and in-plane wavevector $\vec{k_\rho}$, Eq.(9) will have three complex wave vector solutions k_z and associated wave vectors $\vec{F}(k_{\vec{\rho}}, z)$. We seek solutions of Eq.(9) of the form

$$\vec{F}(k_{\vec{\rho}}, z) = \vec{F}_{\vec{k}} e^{ik_z z} \tag{13}$$

Substituting Eq.(11) into Eq.(9), we find that the eigenvectors $\vec{F}_{\vec{k}}$ must satisfy the following eigenvalue problem

$$H_{3X3}\vec{F}_{\vec{k}} = E\vec{F}_{\vec{k}} \tag{14}$$

where each matrix element in the Hamiltonian H_{3X3} can be written as a second order polynomial in k_z

$$H_{3X3} = H^{(2)}{k_z}^2 + H^{(1)}(k_\rho)k_z + H^{(0)}(k_\rho) \tag{15}$$

where the $H^{(n)}$ are 3X3 matrices whose elements are polynomial at most quadratic in (k_x, k_y, k_z). The explicit forms of the matrices $H^{(2)}, H^{(1)}$ and $H^{(0)}$ are given in appendix A.

To solve the eigenvalue problem associated to the Hamiltonian (13), we first transform it into a standard eigenvalue problem for k_z [12, 13]. The energy dispersion relations for holes in the heavy-,light-, and SO-band can then be obtained by solving the following eigenvalue problem

$$\begin{bmatrix} 0 & 1 \\ -(H^{(2)})^{-1}(H^0(k_\rho) - E) & (H^{(2)})^{-1}H^{(1)}(k_\rho) \end{bmatrix} \begin{bmatrix} \mathbf{C_k} \\ k_z\mathbf{C_k} \end{bmatrix} = k_z \begin{bmatrix} \mathbf{C_k} \\ k_z\mathbf{C_k} \end{bmatrix} \tag{16}$$

This last equation has 6 eigenvalues and 6 corresponding eigenvectors. Three solutions correspond to solutions propagating from left to right. The other three solutions for k_z are just the negative of the first three solutions and correspond to hole propagation from right to left.

Next, we consider tunneling of a heavy-hole between two contacts sandwiching an arbitrary heterostructure. The wavefunction for a heavy-hole incident from the left can be written as

$$\psi_{HH}(r) = \begin{bmatrix} F_{1H} \\ F_{2H} \\ F_{3H} \end{bmatrix} e^{i(\vec{k_\rho}\cdot\vec{\rho} + k_z^{(h)}z)} \tag{17}$$

and the reflected wave can be written as

$$\psi_{refl}(\vec{r}) = \Gamma_{HH} \begin{bmatrix} F_{1H}^- \\ F_{2H}^- \\ F_{3H}^- \end{bmatrix} e^{i(\vec{k_\rho}\cdot\vec{\rho} - k_z^{(h)}z)} + \Gamma_{LH} \begin{bmatrix} F_{1L}^- \\ F_{2L}^- \\ F_{3L}^- \end{bmatrix} e^{i(\vec{k_\rho}\cdot\vec{\rho} - k_z^{(l)}z)} + \Gamma_{SO} \begin{bmatrix} F_{1SO}^- \\ F_{2SO}^- \\ F_{3SO}^- \end{bmatrix} e^{i(\vec{k_\rho}\cdot\vec{\rho} - k_z^{(so)}z)} \tag{18}$$

where $(\Gamma_{HH}, \Gamma_{LH}, \Gamma_{SO})$ are the reflection amplitudes for the incident heavy-hole to be reflected in the heavy-, light-, and SO-band, respectively. The (${F_{1i}}^-, {F_{2i}}^-, {F_{3i}}^-$) with (i = HH,LH,SO) are the components of the wave vector solutions of Eq.(14) for holes propagating from right to left.

In the transmitted region in which the potential energy profile can be different from the left contact, the transmitted wave function can be written as

$$\psi_{trans}(\vec{r}) = \tau_{HH} \begin{bmatrix} {F_{1H}}^t \\ {F_{2H}}^t \\ {F_{3H}}^t \end{bmatrix} e^{i(\vec{k_\rho}\cdot\vec{\rho}+k_z^{(h)}z)} + \tau_{LH} \begin{bmatrix} {F_{1L}}^t \\ {F_{2L}}^t \\ {F_{3L}}^t \end{bmatrix} e^{i(\vec{k_\rho}\cdot\vec{\rho}+k_z^{(l)}z)} + \tau_{SO} \begin{bmatrix} {F_{1SO}}^t \\ {F_{2SO}}^t \\ {F_{3SO}}^t \end{bmatrix} e^{i(\vec{k_\rho}\cdot\vec{\rho}+k_z^{(so)}z)} \tag{19}$$

where the subscript t is a reminder that the quantities must be evaluated in the transmitted region. In Eq.(17), τ_{HH}, τ_{LH},and τ_{SO} are the transmission coefficients from the heavy-hole into the heavy-,light-, and SO-band in the transmitted region, respectively.

An arbitrary valence band energy profile can always be approximated as a series of small steps in which the valence band edge is assumed to be a constant. At the interface between any two steps, the envelope function components (F_1, F_2, F_3) must be chosen such that

$$\begin{bmatrix} F_1(z) \\ F_2(z) \\ F_3(z) \end{bmatrix} \tag{20}$$

and

$$\frac{1}{\hbar} \begin{bmatrix} 2(\gamma_1 - 2\gamma_2)k_z & -2i\sqrt{3}\gamma_3 k_\rho & i\sqrt{6}\gamma_3 k_\rho \\ 2i\sqrt{3}\gamma_3 k_\rho & 2(\gamma_1 + 2\gamma_2)k_z & -4\sqrt{2}\gamma_2 k_z + 3i\sqrt{2}\gamma_3 k_\rho \\ -i\sqrt{6}\gamma_3 k_\rho & -4\sqrt{2}\gamma_2 k_z - 3i\sqrt{2}\gamma_3 k_\rho & 2\gamma_1 k_z \end{bmatrix} \tag{21}$$

are continuous. In Eq.(19), $k_z = -i\frac{d}{dz}$ and k_ρ is the magnitude of the in-plane wave vector. The conditions (20) and (21) are required for the wave function and the current density to be continuous across the interface [14].

In order to calculate the transmission and reflection coefficients of holes incident from the left contact, the probability current density must be calculated along the growth direction for the incident, reflected, and transmitted waves. The transmission coefficients for a heavy-hole incident from the left are then calculated as follows

$$T_{HH} = \frac{|\tau_{HH}|^2 j_{z,H}^{trans}}{j_{z,H}^{inc}},\ T_{LH} = \frac{|\tau_{LH}|^2 j_{z,L}^{trans}}{j_{z,H}^{inc}},\ T_{SOH} = \frac{|\tau_{SOH}|^2 j_{z,SO}^{trans}}{j_{z,H}^{inc}}, \tag{22}$$

and the reflection coefficients are

$$R_{HH} = -\frac{|\Gamma_{HH}|^2 j_{-z,H}^{inc}}{j_{z,H}^{inc}},\ R_{LH} = -\frac{|\Gamma_{LH}|^2 j_{-z,L}^{inc}}{j_{z,H}^{inc}}.\ R_{SOH} = -\frac{|\Gamma_{SOH}|^2 j_{-z,SO}^{inc}}{j_{z,H}^{inc}}. \tag{23}$$

In Eqns.(20-21), the labels *inc* and *trans* mean that the probability current density must be evaluated in the incident and transmitted regions, respectively. Furthermore, the relationship $j_{-z,\alpha} = -j_{z,\alpha}$ holds between the probability current densities corresponding to left ($j_{-z,\alpha}$) and right ($j_{z,\alpha}$) propagating states ($\alpha = H, L$, or SO). Current conservation further requires that $T_{HH} + T_{LH} + T_{SOH} + R_{HH} + R_{LH} + R_{SOH} = 1$, which is helpful to check the accuracy of the numerical simulations. The tunneling problem described above can then be easily repeated for holes incident from the left contact in the light- or SO-band.

III. RESULTS

We apply the formalism described above to the problem of hole tunneling across a potential step. We only report the results for the transmission coefficients of holes incident from either side of the potential step. We compare the results obtained with the upper and lower Hamiltonians and show the importance of including the effects of the Spin-Orbit Split-Off band by also calculating the transmission coefficients starting with the 4X4 Luttinger-Kohn Hamiltonian. The simple potential steps analyzed here roughly approximates the valence band across the emitter-base junction of a Pnp Heterojunction Bipolar Transistor (HBT) under high enough forward bias [9].

We consider two potential steps corresponding to the two lattice-matched interfaces $In_{0.52}Al_{0.48}As/In_{0.53}Ga_{0.47}As$ and $InP/In_{0.53}Ga_{0.47}As$, which are two of the most widely used structures for HBT technology. For these materials, the values of the Luttinger-Kohn parameters and split-off energy were obtained by linear interpolation from the parameters for the binaries [10, 15, 16].

An important difference exists between the two heterojunctions as shown in Fig.1. For the $In_{0.52}Al_{0.48}As/In_{0.53}Ga_{0.47}As$ system, the valence band discontinuity is smaller than the spin-orbit split-off energy in the $In_{0.53}Ga_{0.47}As$ region. Holes incident from the left (emitter) need a kinetic energy around 70 meV before being able to reach the threshold energy for free propagation in the SO-band in the $In_{0.53}Ga_{0.47}As$ region (base). On the other hand, tunneling through the $InP/In_{0.53}Ga_{0.47}As$ will be very sensitive to presence of the SO-band because the spin-orbit split-off energy in the transmitted region ($In_{0.53}Ga_{0.47}As$) is smaller than the valence band discontinuity ($\Delta E_v = 386$ meV). Furthermore, the spin-orbit split-off energy in the left region (InP) is quite small (100 meV) and the dispersion relation for heavy- and light-holes in this region will be strongly affected by the SO-band even for holes with low incident kinetic energy.

In order to understand the various features appearing in the plots of the transmission coefficients of holes discussed below, we first look at the energy dispersion of holes in one of the three regions considered in Fig. 1. As an example, we consider the $In_{1-x}Ga_xAs$ region latticed-matched to InP. In this case, the Gallium

mole fraction x is equal 0.468. We plot in Fig.2 the real ($Realk_z$) and imaginary (Imk_z) parts of the heavy, light, and SO-bands as a function of the incident energy for a given magnitude of the transverse wavevector ($k_0 = 4X10^{-2}\ \pi/a$, where a = 5.83 $\AA$ the lattice constant of InP). For comparison, we also show the real and imaginary parts of the hole bands obtained while neglecting the SO-band. The latter curves were calculated starting with the 4X4 Luttinger-Kohn Hamiltonian [17]. In the axial approximation, this 4X4 Hamiltonian can also be block-diagonalized in two 2X2 Hamiltonians (upper and lower Hamiltonians). In this case, the upper Hamiltonian is formed of the four upper left matrix elements in the Hamiltonian (8).

In Fig.2, the zero of energy is the top of the valence band. The critical energies $(E_h^-, E_h^+, E_1, E_{SO})$ are the values at which there is a sudden break in the energy dependence of the real and imaginary parts of the heavy-,light-,and SO-hole wave vectors. More precisely, E_h^- is the lowest positive energy at which $k_z{}^{(h)}$ is purely real; E_h^+ is the lowest positive energy at which $Imk_z{}^{(l)}$ is equal to zero, E_1 is the energy above which $k_z{}^{(l)}$ is purely real, and E_{SO} is the energy above which $k_z{}^{(so)}$ is purely real. Analytical expressions for (E_h^-, E_h^+, E_1) were derived in [17] when the SO-band is neglected.

The following features are readily seen in Fig. 2: when $\vec{k_\rho}$ is non-zero, the heavy-hole dispersion relation is basically unchanged with the inclusion of the SO-band but the light-hole dispersion relation is strongly affected. Figure 2 shows that the energy threshold for purely propagating states for light holes occurs at a lower energy compared to the case when the SO-band is neglected. A similar feature has been reported by Chao and Chuang in their study of SO-interaction of the valence-band structure of strained semiconductor quantum wells [11]. The change in the energy threshold for propagating light-holes will affect not only the reflection coefficient for light-hole but also the energy dependence of the amount of heavy to light-hole conversion compared to the results with the 4X4 Hamiltonian, as will be shown below. Furthermore, since the matrix elements (1,3) and (2,3) in Hamiltonian (8) are non-zero when $\vec{k_\rho}$ is non-zero, we expect some conversion from heavy- (and light)-band to SO-band past the energy threshold for free propagating states in the SO-band. This will be illustrated in the numerical examples below.

The energies $(E_h^-, E_h^+, E_1, E_{SO})$ are function of the magnitude of the transverse wavevector $\vec{k_\rho}$. These variations with k_ρ were determined numerically and are plotted in Fig.3 for the case of a $In_{0.52}Al_{0.48}As$ region (the trends are the same for the other two materials). In this Figure, we also compare the k_ρ-dependence of (E_h^-, E_h^+, E_1) with the analytical results obtained while neglecting the effects of the SO-band [17].

Since the potential steps in Fig. 1 lack inversion symmetry, the transmission coefficients will be different when calculated with the upper or lower Hamiltonians. This will be illustrated in the numerical examples below. Hereafter, we calculate

the transmission coefficients of heavy-holes incident on the potential steps shown in Fig. 1 from either direction.

Case 1: The $InP/In_{0.53}Ga_{0.47}As$ interface

Left to Right Propagation: Figure 4 shows the transmission coefficients (T_{HH}, T_{LH}) for heavy holes as a function of energy for holes incident from left to right on the structure shown on the left in Fig. 1. In all simulations, the zero of energy is the bottom of the valence band in the InGaAs region, energy is measured positively going into the valence band, and the transverse wavevector k_ρ is set equal to 0.04 ($2\pi/a$) (where a is 5.83 Å, the lattice constant of InP). The lines labeled (3X3) and (2X2) are the results obtained with the 3X3 and 2X2 upper Hamiltonians, respectively. The (2X2) results correspond to the case where the effects of the Spin-Orbit Split-Off band are neglected.

Figure 5 shows the results obtained with the upper and lower (3X3) Hamiltonians are quite different over the full range of incident energy investigated here. The large difference between the results with the upper and lower Hamiltonians are due to the lack of inversion of symmetry of the potential steps in Fig. 1 lifting the Kramers degeneracy of the hole bulk states [17].

In Figures 4 and 5, there are cusps in the transmission coefficient T_{HH} appearing at incident energy equal to the threshold energies for free propagation in the SO-bands on either side of the interface. This is best illustrated by plotting the real part of the longitudinal component of the hole wavevectors on either side of the heterointerface as a function of the hole incident energy. These results are plotted in Fig. 6. In Figures 4 and 5, T_{SOH} is non-zero past the energy threshold E_{SO} in the $InGaAs$ region (around 500 meV according to Fig. 6). However, T_{SOH} goes back down close to zero above 535 meV because there is a finite probability to be reflected in the SO-band in the InP region beyond that energy. Indeed, Figure 6 shows that the SO-band is opened in the InP region for incident energy above 535 meV.

Figures 7 and 8 are plots similar to Figures 4 and 5 for a light-hole incident from the InP region. Figure 7 shows that the probability of light- to heavy-hole conversion (T_{HL}) is much smaller than the probability of heavy- to light-hole conversion (T_{LH}) shown in Fig. 4. This can be understood using a simple estimate based on the well-known result for electron tunneling through a potential step [18]

$$T_{ji} = \frac{2k_j^{\mathbf{trans}}/k_i^{\mathbf{inc}}}{[k_j^{\mathbf{trans}}/k_i^{\mathbf{inc}} + 1]^2} \tag{24}$$

where ji = HL or LH for an incident light-hole or heavy-hole, respectively. Referring to Fig. 6, the ratio of the z-component of the wave vectors is closer to unity past $E_1(InGaAs)$ when ji = LH which explains why T_{LH} is larger than T_{HL}.

Similar arguments explain why the probability of heavy- to SO-band (T_{SOH})

or light- to SO-band (T_{SOL}) transition in Figures (4,5) and (7,8) are fairly small. Figure 6 shows that the real part of the hole wavevector in the InGaAs SO-band is indeed much smaller that the real parts of the the heavy- and light-hole longitudinal wavevector components in the InP region past the energy E_{SO} in the InGaAs region.

Right to Left Propagation: Figure 9 is a plot of the transmission coefficients of heavy holes incident from the right. The results are shown for the upper Hamiltonian only. Once again, there is a large difference between the results calculated with the upper (2X2) and (3X3) Hamiltonians. T_{HH} rises sharply past the threshold energy $E_h^-(InP)$ for free propagation in the heavy-hole band in the InP region. Kinks in T_{HH} appear at the energy thresholds for free propagation in the light-hole band in the InP region and in the SO-bands on either sides of the interface. The conversion probabilities T_{LH} and T_{SOH} are quite small as a result of the large difference in the longitudinal components on either sides of the potential step (See Fig. 6).

The transmission coefficient T_{LH} is identically zero below $E_1(InP)$, the threshold energy for free propagation in the light-hole band in the InP region. This is different from the results in Fig. 4 where T_{LH} was found to be non-zero for incident energy above $E_h^-(InP)$. This results from the fact that, for holes incident from the left, the threshold energy for free propagation in the ligh-hole band in the InGaAs region is below $E_h^-(InP)$ for the transverse wavevector considered here (k_ρ = 0.04 $(2\pi/a)$, where a is 5.83 $\AA$, the lattice constant of InP). Therefore, there is a finite probably for heavy to light hole conversion for heavy-holes tunneling from the left as soon as free propagation for heavy-holes is allowed in the InP region. Since the threshold energy for free propagation in the light-hole band is quite large ($E_1(InP)$, the probability for heavy- to light-hole conversion for heavy-holes incident from the left contact is accordingly smaller than its value for heavy-holes incident from the InP region. Similarly, the probability T_{SOH} is also smaller for holes incident from the right contact.

Figure 10 is a plot of the transmission coefficients for light-holes incident from the left. The results are shown for the upper (2X2) and (3X3) Hamiltonians only. In addition to the large difference between the results obtained with the (2X2) and (3X3) Hamiltonians, the following features are noticeable: (1) the probability for light- to heavy-hole conversion reaches a maximum of 0.3 in the energy range [$E_h^-(InP)$ - $E_1(InP)$] where only heavy-holes can propagate freely in the InP region; (2) as soon as free propagation is allowed in the light-hole band in InP, T_{HL} suddenly decreases and, simultaneously, T_{LL} rises sharply; (3) another drop in T_{HL} appears past $E_{SO}(InGaAs)$ when free propagation in the SO-band is possible in the InGaAs region. Simultaneously, T_{LL} decreases because there is a finite probability for light-holes to be reflected in the SO-band. Past this threshold, there is a very small probability for light to SO-band transition while crossing the interface. The

strong coupling between the SO- and light-hole bands leads to an increase of T_{LL} past $E_{SO}(InP)$.

Case 2: The $In_{0.52}Al_{0.48}As/In_{0.53}Ga_{0.47}As$ interface

To stress the importance of the Spin-Orbit Split-Off band, we again plot the results obtained with the 2X2 and 3X3 Hamiltonians hereafter. The general trends observed in the transmission coefficients of heavy- and light-holes incident from either side are fairly similar to those observed for the InP/InGaAs interface. Hereafter, we only focuss on the major differences between the two potential steps due to the difference in the valence band edge discontinuity and the position of the minima of the SO-bands as illustrated in Fig. 1. Figures 11 and 12 compare the tunneling coefficients of heavy-holes incident from either side and Figures 13 and 14 show similar results for incident light-holes.

Left to right propagation: Comparing Figures 4 and 11, we see that the transmission coefficients for heavy-holes propagating from left to right across the $In_{0.52}Al_{0.48}As/In_{0.53}Ga_{0.47}As$ interface have features similar to the case of the $InP/In_{0.53}Ga_{0.47}As$ interface. However, there are noticeable differences. For the $In_{0.52}Al_{0.48}As/In_{0.53}Ga_{0.47}As$ interface, (1) T_{HH} is larger past the energy threshold (E_h^- (InAlAs)). This is due to the smaller valence band discontinuity at the InAlAs/InGaAs interface compared to the InP/InGaAs case and the closer match between the longitudinal components of the heavy-hole wavevectors on both sides of the interface for the $InAlAs/InGaAs$ case; (2) there is a smaller drop in T_{HH} past the energy threshold for free propagation in the InGaAs SO-band. This is due to the fact that T_{HH} is already close to unity upon approaching the energy threshold E_{SO} (InGaAs) for free propagation in the InGaAs region. This is confirmed by the plot of T_{SOH} showing a very small probability for heavy- to SO-band conversion; (3) the kink in T_{HH} past the threshold energy for free propagation in the $InAlAs$ SO-band is not seen in Fig.11 because the threshold energy E_{SO} (InAlAs) is above 700 meV for the value of the transverse wavevector considered here.

Comparing Figures 7 and 13, we see that the T_{LL}, T_{HL}, and T_{SOL} coefficients behave qualitatively the same in both structures. T_{SOL} is much larger past the energy threshold $E_{SO}(InGaAs)$ for the InP/InGaAs structure. There is another kink in T_{LL} past the energy threshold $E_{SO}(InAlAs)$ occuring outside the energy range plotted in Fig. 14.

Right to left propagation: for holes propagating from right to left, the trends in Figures 12 and 14 are similar to those observed in Figures 9 and 10 for the InP/InGaAs interface. The following differences are pointed out: (1) the small drop in T_{HH} occuring at an energy above $E_{SO}(InGaAs)$ is due to the finite probability However, the probability of reflection R_{SOH} is small because of the large mismatch between the longitudinal component of the holes in the heavy- and SO-

bands; (2) As shown in Fig. 14, the drop in T_{LL} also occurs at $E_{SO}(InGaAs)$ when the light-hole is allowed to be reflected in the SO-band. However, the drop in T_{LL} is sharper than the drop in T_{HH} past this threshold because of the stronger coupling between the light- and SO-bands and the closer match between the longitudinal components of the light- and SO-hole wavevectors.

IV. CONCLUSIONS

We have used the 6X6 Luttinger-Kohn Hamiltonian to study the effects of the Spin-Orbit Split-Off band on the transmission coefficients of holes through the potential steps $InP/In_{0.53}Ga_{0.47}As$ and $In_{0.52}Al_{0.48}As/In_{0.53}Ga_{0.47}As$ which are two of the most widely used material systems to form abrupt emitter-base junctions in HBT technology. The tunneling coefficients of heavy and light holes were calculated using the upper and lower Hamiltonians obtained through a unitary transform of the 6X6 Luttinger-Kohn Hamiltonian.

Our results indicate that the Spin-Orbit Split-Off band has a profound influence on the tunneling coefficients of both heavy and light holes and also on the amount of heavy-to-light (or the reverse) conversion for holes tunneling across the potential steps. Therefore, the hole conversion process must be appropriately taken into account when calculating the emitter injection efficiency of the emitter-base junction of Pnp HBTs. Simply modeling the tunneling current of holes across the emitter-base junction using the well-known expression [5] for electrons while using an average effective mass (density of states effective mass) for holes may lead to substantial error in the tunneling current density and its dependence on the emitter-base bias. This, in turn, would affect the ideality factor of the emitter current.

Furthermore, if holes end up in the SO-band in the base, the corresponding scattering rates for holes in the SO-band must be included in a Monte-Carlo description of carriers across the base for an accurate determination of the average base transit time. Indeed, it is well-known for Npn HBTs that a small amount of scattering can greatly affect the average base transit time of electrons [19]. It is anticipated that the same must be true for holes crossing the base of Pnp HBTs. These issues will be addressed in a forthcoming publication.

ACKNOWLEDGEMENT

This work is supported by the National Science Foundation (ECS-9525942). We also acknowledge the Ohio-Cray supercomputing center for the use of their facilities.

References

[1] M. E. Kim, B. Bayraktaroglu, and A. Gupta, Chapter 5, in *HEMTs and HBTs: Device, Fabrication, and Circuits*; F. Ali and A. Gupta, Eds. Artech House, Boston (1991).

[2] J. F. Jensen, W. E. Stanchina, R. A. Metzger, D. B. Rensch, R. F. Lohr, R. W. Quen, M. W. Pierce, Y. K. Allen, and P. F. Lou, IEEE Journal of Solid State Circuits, Vol. 26, p. 415 (1991).

[3] W. L. Chen, J. P. Sun, G. I. Haddad, M. E. Sherwin, G. O. Munns, J. R. East, and R. K. Mains, Appl. Phys. Letters, Vol. 61, p.189 (1992).

[4] W. E. Stanchina, R. A. Metzger, D. B. Rensch, L. M. Burns, J. F. Jensen, R. H. Walden, L. E. Larson, and P. T. Greiling, GOMAC-91 Digest (1991).

[5] R. J. Ferro, R. G. Wilson, J. F. Jensen, D. B. Rensch, W. E. Stanchina, R. A. Metzger, M. W. Pierce, T. V. Kargodorian and Y. K. Allen, Solid State Electronics, Vol.34(12), p. 1319 (1991).

[6] A. Das and M.S. Lundstrom, Journal of Applied Physics, Vol.66(5), p.2168 (1989).

[7] T. Kumar, M. Cahay, S. Shi, K. Roenker, and W. E. Stanchina, Journal of Applied Physics, Vol. 77(11), p. 5786 (1995).

[8] T. Kumar, M. Cahay, S. Shi, and K. Roenker, Journal of Applied Physics, Vol. 78(11), p. 6814 (1995).

[9] T. Kumar, M. Cahay, and K. Roenker, "Hole Tunneling Through the Emitter-base Junction of Heterojunction Bipolar Transistors" Physical Review B, Vol.56(8), p.4836 (1997).

[10] S. Ekbote, M. Cahay and K. Roenker, "Influence of the Spin-Orbit Split-Off Band on the Tunneling of Holes Through Heterostructures ", submitted to Phys. Rev. B, October 1997.

[11] C.Y. Chao and S.L. Chuang. Phys. Rev. B, vol.43(9), p.7027 (1991).

[12] J. H. Wilkinson, *The Algebraic Eigenvalue Problem* (Oxford University Press, Oxford, 1965), pp. 633 and 634

[13] Y. C. Chang and J. N. Schulman, Phys. Rev. B, Vol. 25, p. 3975 (1982)

[14] S. L. Chuang, Phys. Rev. B, Vol.43(12), p.9649 (1991).

[15] For the $InP/In_{0.53}Ga_{0.47}As$ interface, we use 1.344 eV and 0.324 + 0.7x + 0.4 x^2 for the energy gap of InP and $In_{1-x}Ga_xAs$, respectively. For the conduction- and valence-band offsets, we follow [16] and use $\Delta E_c = 0.36\ \Delta E_g$ and $\Delta E_v = 0.64\ \Delta E_g$.

[16] C. D. Lee and S. R. Forrest, Appl. Phys. Lett., Vol. 57, p. 469 (1990).

[17] S. L. Chuang, Phys. Rev. B., vol.40(15), p.10379 (1989).

[18] S. Datta, "Quantum Phenomena", Modular Series, Volume 8, p.19 (1989).

[19] P. Dodd and M. S. Lundstrom, Appl. Phys. Letters, Vol. 61, p.465 (1992).

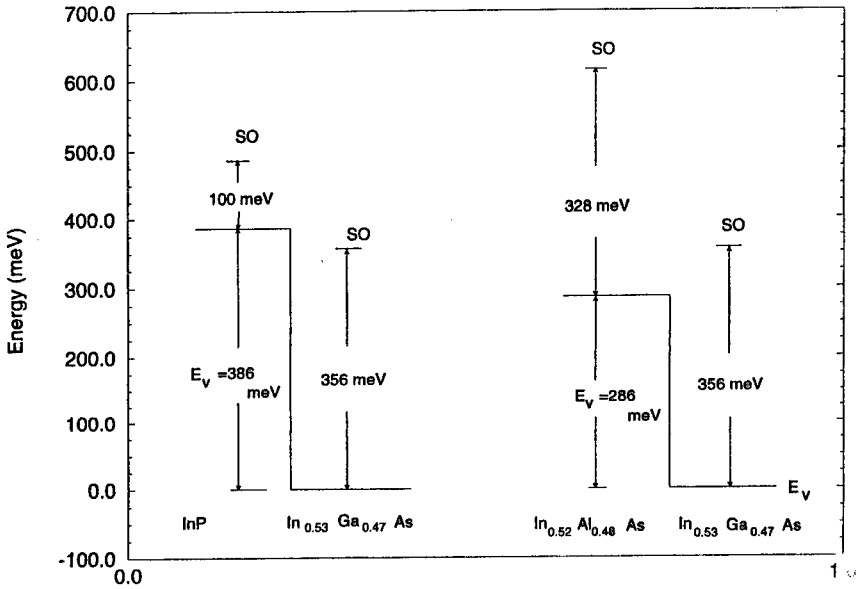


Figure 1: Illustration of the valence band discontinuity across the $In_{0.52}Al_{0.48}As$ $/In_{0.53}Ga_{0.47}As$ and $InP/In_{0.53}Ga_{0.47}As$ interfaces. Energies are measured positively going into the valence band. The horizontal lines labeled "SO" are the locations of the spin-orbit split-off energy band minimum on both sides of the structure. The energy threshold E_{SO} for free propagation in the SO-band coincides with the "SO" level for $k_\rho = 0$, but shifts upward in energy with the magnitude of the transverse wave vector increases as shown in Fig. 3.

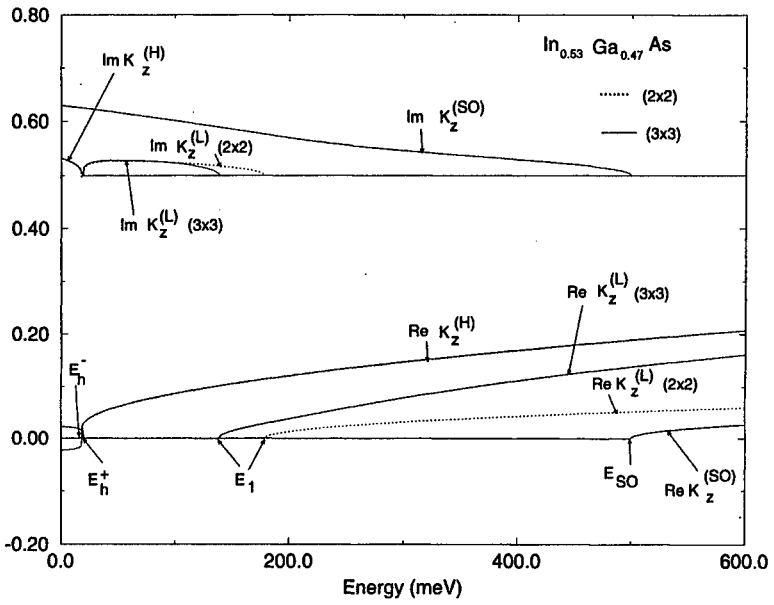


Figure 2: Real and Imaginary parts of the hole wave vectors solutions of the eigenvalue problem in Eq.(16) for a bulk $In_{0.53}Ga_{0.47}As$ region as a function of energy for a value of $k_\rho = 0.04\ (2\pi/a)$ (a is 5.83 $\AA$, the lattice constant of InP). The zero of energy is the top of the valence band. The real and imaginary parts are expressed in units of $2\pi/a$. For clarity, the imaginary parts have been shifted vertically by an amount equal to 0.5 $(2\pi/a)$. Also shown are the results obtained while neglecting the effects of spin-orbit coupling [9, 17] (curves labeled with 2X2 symbol). The energies (E_h^-, E_h^+, E_1, E_{SO}) defined in the text are also shown.

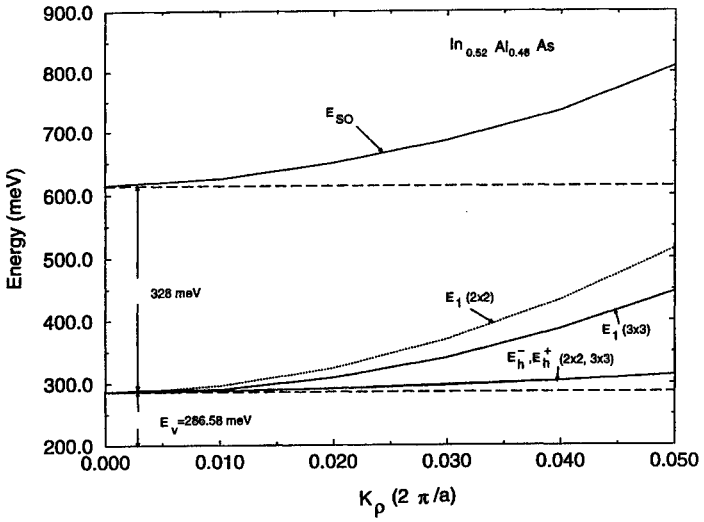


Figure 3: k_ρ dependence of the energies $(E_h^-, E_h^+, E_1, E_{SO})$ defined in the text in $In_{0.52}Al_{0.48}As$. The results obtained with the (2X2) and (3X3) Hamiltonians are shown. E_{SO} is only defined for the (3X3) Hamiltonian.

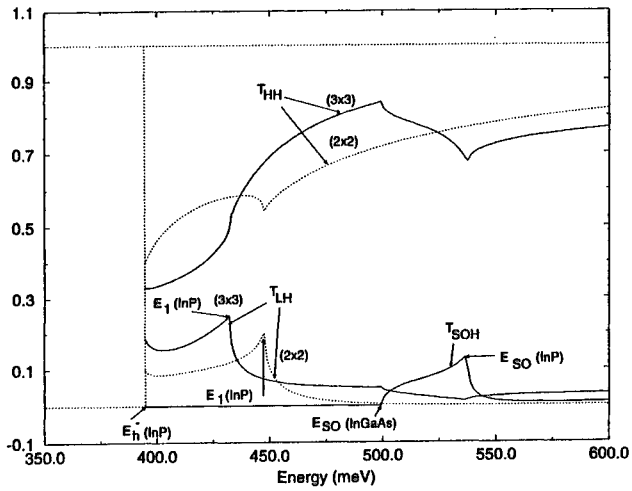


Figure 4: Transmission coefficients of a heavy-hole incident from the left side of the $InP/In_{0.53}Ga_{0.47}As$ potential step shown in Fig. 1. The results are shown for the upper 2X2 and 3X3 Hamiltonians. The zero of energy is the bottom of the $In_{0.53}Ga_{0.47}As$ region in Fig. 1. The in-plane wave vector is set equal to $k_\rho = 0.04$ $(2\pi/a)$ (where a is 5.83 $\AA$, the lattice constant of InP).

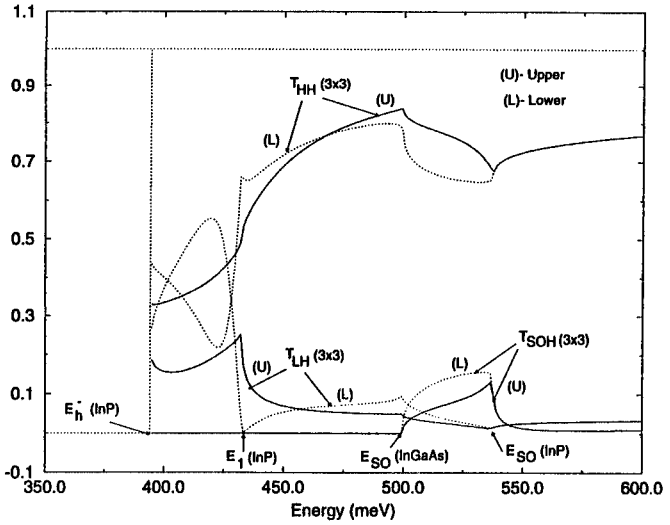


Figure 5: Comparison of the results obtained with the upper and lower Hamiltonians for the transmission coefficients of a heavy-hole incident from the left on the $InP/In_{0.53}Ga_{0.47}As$ interface shown in Fig. 1. The in-plane wave vector is set equal to $k_\rho = 0.04\ (2\pi/a)$ (where a is 5.83 $\AA$, the lattice constant of InP).

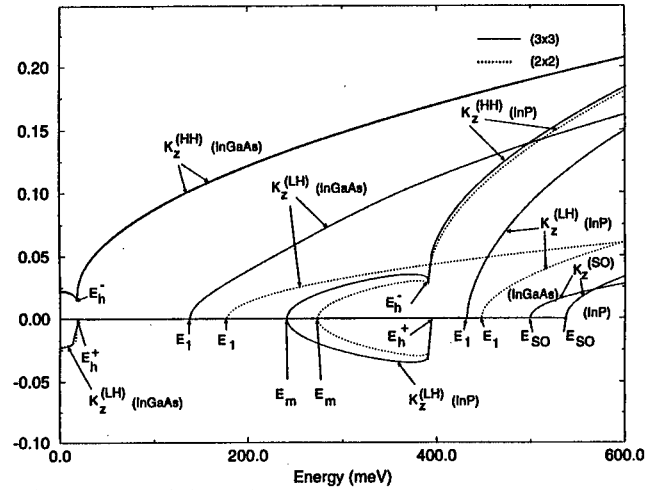


Figure 6: Comparison of the real parts of the longitudinal components of the hole wavevectors obtained from Eq.(16) for the InP and $In_{0.53}Ga_{0.47}As$ regions. The results for the InP region are shifted upward in energy by an amount equal to the band discontinuity at the heterointerface (See Fig. 1).

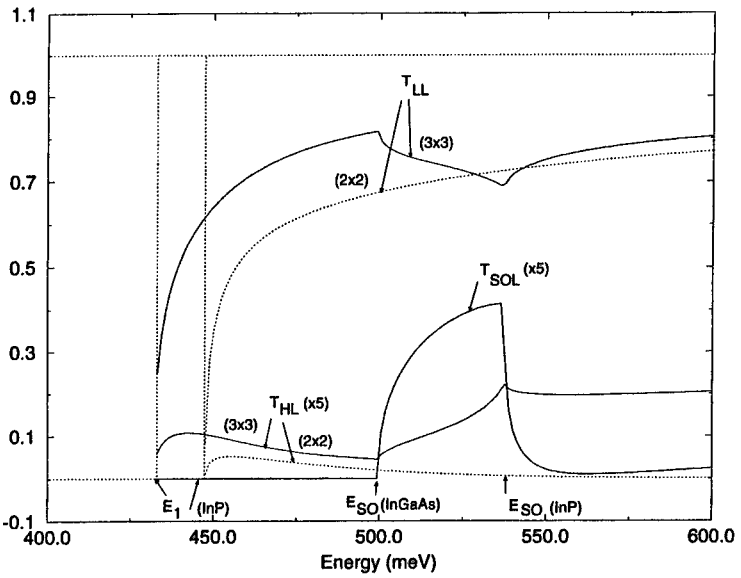


Figure 7: Same as Fig.4 for a light-hole incident from the left on the $InP/In_{0.53}Ga_{0.47}As$ potential step shown in Fig. 1. The in-plane wave vector is set equal to $k_\rho = 0.04$ $(2\pi/a)$ (where a is 5.83 $\AA$, the lattice constant of InP).

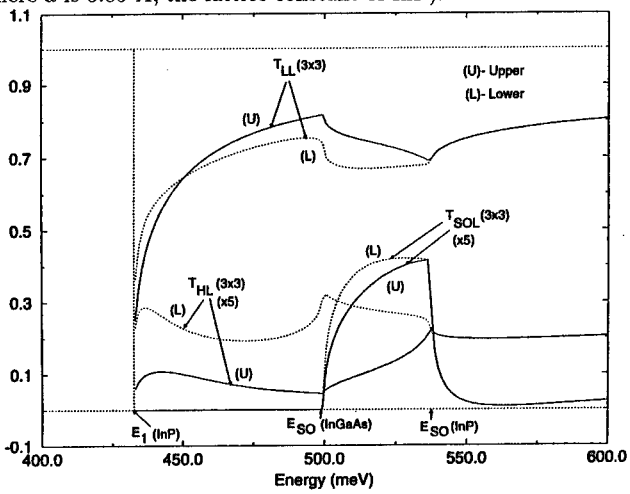


Figure 8: Same as Fig.5 for a light-hole incident from the left on the $InP/In_{0.53}Ga_{0.47}As$ potential step shown in Fig. 1. The in-plane wave vector is set equal to $k_\rho = 0.04$ $(2\pi/a)$ (where a is 5.83 $\AA$, the lattice constant of InP).

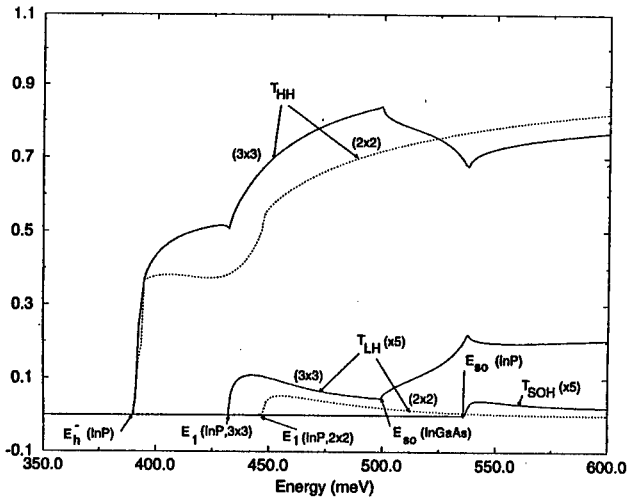


Figure 9: Same as Fig.4 for a heavy-hole incident from the right on the $InP/In_{0.53}Ga_{0.47}As$ potential step.

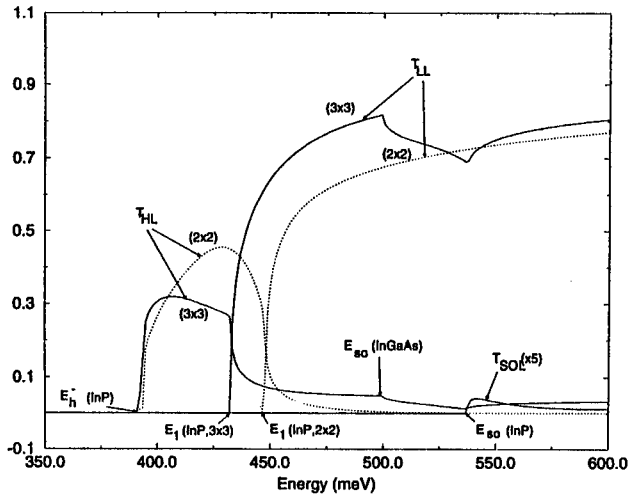


Figure 10 : Same as Fig.7 for a light-hole incident from the right on the $InP/In_{0.53}Ga_{0.47}As$ potential step.

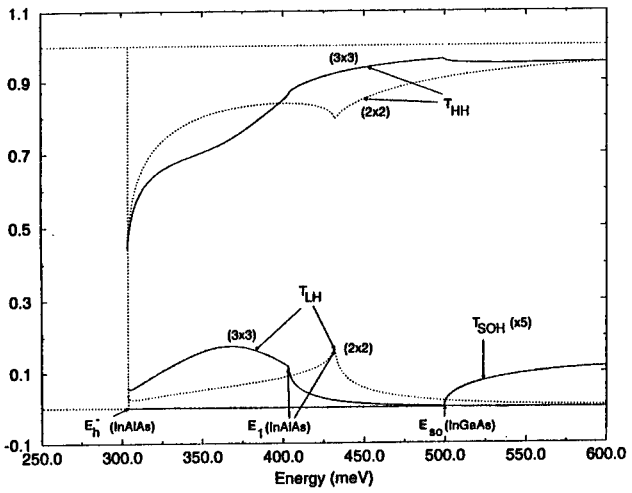


Figure 11: Same as Fig.4 for a heavy-hole incident from the left on the $In_{0.52}Al_{0.48}As/In_{0.53}Ga_{0.47}As$ potential step shown in Fig. 1.

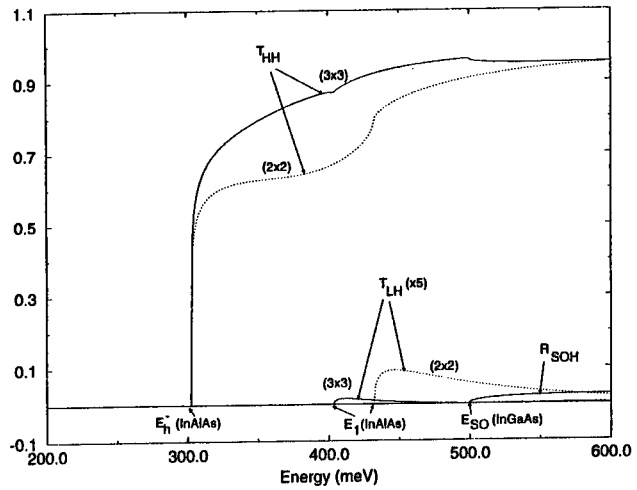


Figure 12: Same as Fig.11 for a heavy-hole incident from the right on the $In_{0.52}Al_{0.48}As/In_{0.53}Ga_{0.47}As$ interface. Also shown is the reflection coefficient R_{SOH}.

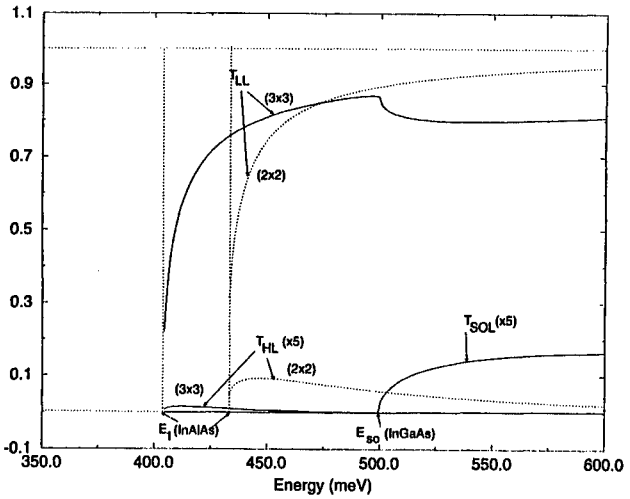


Figure 13: Same as Fig.7 for a light-hole incident from the left on the $In_{0.52}Al_{0.48}As/In_{0.53}Ga_{0.47}As$ potential step.

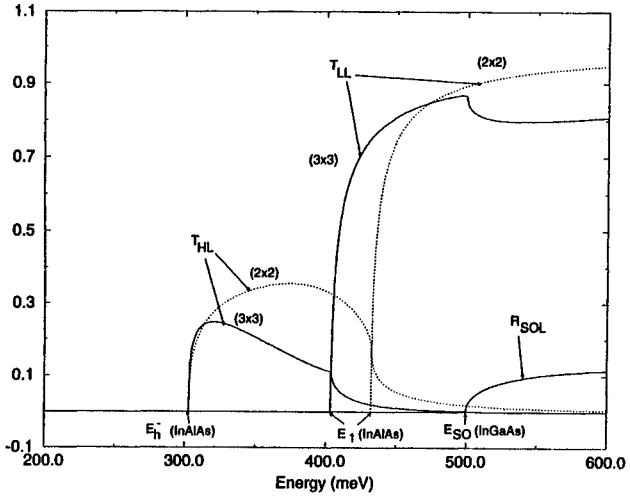


Figure 14: Same as Fig.13 for a light-hole incident from the right on the $In_{0.52}Al_{0.48}As/In_{0.53}Ga_{0.47}As$ potential step. Also shown is the reflection coefficient R_{SOL}.

Johnson Noise in Quantum Wires: Temperature Dependence and the Effect of High Electric Fields

A. Svizhenko and S. Bandyopadhyay
Department of Electrical Engineering
University of Nebraska
Lincoln, Nebraska 68588

M. A. Stroscio
US Army Research Office
P. O. Box 12211
Research Triangle Park, North Carolina 27709

Abstract

We have studied electron velocity fluctuations and Johnson noise in a free-standing GaAs quantum wire at different lattice temperatures and for different driving electric fields using a Monte Carlo approach. The noise spectral density and the carrier diffusivity were found to decrease with increasing temperature and increasing electric field strengths. The latter effects is due to the fact that a high field tends to induce streaming and promotes oscillations in the velocity autocorrelation function. An external magnetic field, applied transverse to the wire's axis, suppresses noise and diffusivity at low temperatures, but increases then at high temperatures.

1 Introduction

There is significant current interest in the application of quasi one-dimensional semiconductor structures for high-speed and low noise electronic devices such as quantum-wire field-effect-transistors (QWFET). Such devices are expected to exhibit high transconductance and unity-gain-frequency as a result of the enhancement of carrier mobility [1]. In this paper, we have investigated the noise characteristics of a quantum wire structure since noise is also an important device parameter.

Johnson noise in a solid is caused by fluctuations in the velocity of current carriers (electrons or holes) interacting with scatterers. We have found these fluctuations from a Monte Carlo simulation of carrier transport under a driving electric field. Additionally, we have investigated the effect of an external magnetic field on velocity fluctuations and how it affects noise characteristics.

This paper is organized as follows. In the next section, we briefly describe our theoretical approach and the Monte Carlo simulator. This is followed by results and discussion. The last section details our conclusions.

2 Theory

We will calculate the velocity autocorrelation function and noise spectral density in a free-standing GaAs quantum wire of rectangular cross-section. An electric field is applied along the length of the wire to induce carrier transport and an external magnetic field is applied in a transverse direction parallel to the thickness as shown in the inset of Fig. 1.

We first solve the Schrödinger equation in the quantum wire (with only the transverse magnetic field present) to obtain the wave functions and the energy dispersion relations of the confined hybrid magnetoelectric states of electrons [3]. These wave functions and the dispersion relations are used to calculate the matrix elements and density of final states for scattering. All scattering rates are evaluated from Fermi's Golden Rule and used in a Monte Carlo simulator to obtain the velocity autocorrelation function in the presence of a driving electric field.

The Monte Carlo simulator is a modified code for quantum wires. The basic algorithm is described in refs. [4, 5, 7, 6] and it was modified to account for the presence of a magnetic field which necessitates searching for the right phonon (with the right energy and wavevector) to mediate a scattering process. We collect velocity statistics after steady state is achieved by using a uniform sampling in time.

The velocity autocorrelation function is calculated as

$$C(T) = < \delta v(t) \delta v(t+T) > , \tag{1}$$

where $\delta v = v(t) - v_d$ (where $v(t)$ is the instantaneous carrier velocity at an instant of time t and v_d is the steady state (ensemble average) drift velocity). The noise spectral

density is obtained by evaluating the Fourier transform of the autocorrelation function:

$$S(f) = 4\int_0^\infty dT e^{-2\pi fT} C(T) \,, \tag{2}$$

and it is related to the dc component of the diffusivity $D(0)$ by the Wiener-Khintchine theorem

$$S(f) = \frac{4D(0)}{1 + (2\pi f \tau_m)^2} \tag{3}$$

where τ_m is the ensemble-average momentum relaxation time. A corollary of the above theorem is that the dc component of the diffusivity is related to the dc component of the noise spectral density as $D(0) = S(0)/4$.

3 Results and Discussion

We consider a GaAs quantum wire of width 300 Å and thickness 40 Å. The Monte Carlo simulation was carried out with an ensemble of 1000 particles at lattice temperatures of 30 K and 77 K and magnetic flux densities of 0 and 10 tesla. The number of particles is more than sufficient to make the quantities in Equations (1)-(3) independent of the ensemble size. The simulations were carried out at different electric field strengths.

In Figs. 1 and 2, we show the temporal decay of the velocity autocorrelation function for two different temperatures of 30 K and 77 K. The driving electric field is 200 V/cm. The upper panel shows the results in the absence of any magnetic field and the lower panel shows the results in the presence of a transverse magnetic flux density of 10 tesla.

Looking at Fig. 1, we find oscillations in the autocorrelation function. These oscillations are a well-known signature of streaming and arise when polar optical phonon scattering is the dominant energy relaxation mechanism. The autocorrelation function oscillates because an electron will be rapidly accelerated to the polar optical phonon emission threshold by the electric field, emit and fall to the bottom of the subband, repeating this process again and again. This oscillation in k-space (or energy space) leads to permanent oscillations in the velocity and mean energy *if* the entire ensemble is more or less in phase. When polar optical phonon scattering is overwhelmingly dominant, the ensemble remains in phase for a long time and the oscillations show up in the velocity autocorrelation function. This is characteristic of "streaming" transport and has been examined in ref. [8, 9, 6].

It is obvious that the phase of the oscillation will be randomized if there is significant acoustic phonon scattering since that will randomly kick electrons out of phase with the rest of the ensemble. At a low driving electric field of 20 V/cm, acoustic phonon scattering usually dominates transport. Hence, the oscillations are ordinarily suppressed. But at intermediate electric field strengths of around 200 V/cm, polar optical phonon scattering is overwhelmingly dominant over acoustic phonon scattering and hence the electron

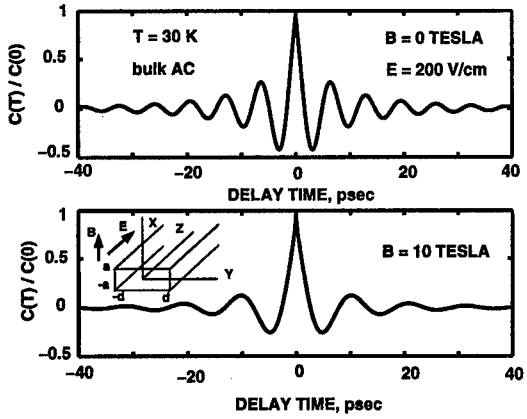


Figure 1: Temporal evolution of the velocity autocorrelation function at a magnetic flux density of 0 tesla (upper panel) and 10 tesla (lower panel). The driving electric field is 200 V/cm and the lattice (as well as the electron) temperature is 30 K. A bulk acoustic phonon model has been assumed. The inset shows the geometry of the quantum wire and the orientations of the electric and magnetic fields.

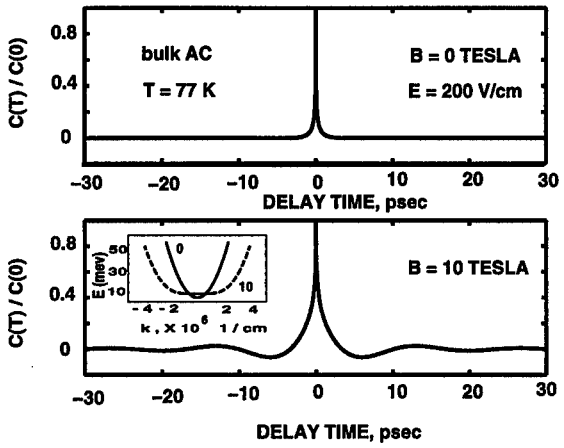


Figure 2: Temporal evolution of the velocity autocorrelation function at a magnetic flux density of 0 tesla (upper panel) and 10 tesla (lower panel). The driving electric field is 200 V/cm and the lattice (as well as the electron) temperature is 77 K. A bulk acoustic phonon model has been assumed.

ensemble stream in phase. A magnetic field increases the period of the oscillation. The oscillation period t_p is given by [4]

$$t_p = \frac{\hbar \Delta k}{eE} + \tau_{op} \ , \tag{4}$$

where e is the electronic charge, E is the driving electric field, τ_{op} is the mean time that elapses after an electron crosses the polar optical phonon emission threshold and before it emits, and Δk is the change in the electron's wavevector (caused by the accelarating field E) during the free flight between two successive polar optical phonon scattering events.

A magnetic field has two effects (which show up prominently in Figs. 1 and 2): (i) it reduces the decay rate of the velocity autocorrelation function, and (ii) it increases the period of the oscillations. The first effect has an obvious source. Since a magnetic field suppresses backscattering [2], the momentum relaxation rate is reduced and this reduces the decay rate of the autocorrelation function. The second effect is somewhat more subtle and is discussed below.

In a magnetic field, the momentum p of an electron transforms according to $\vec{p}' = \vec{p} + e\vec{A}$ where $\vec{A}$ is the magnetic vector potential. As a result, the electron trajectories are elongated in k-space. Another way of viewing this is to look at the electron dispersion relations with and without a magnetic field as shown in the inset of Fig. 2. Obviously, in a magnetic field, an electron's wavevector will have to increase more to gain the same amount of energy as in the absence of a magnetic field. Since Δk is larger in a magnetic field, the oscillation period increases (see Equation (4)).

We can check the validity of our picture with a simple comparison. If we assume that an elecron scatters soon after it reaches the threshold for polar optical phonon emission and that such a scattering drops the electron down to near the bottom of the conduction band, then we can show that

$$t_p = \frac{\tau_{op}}{2} + \sqrt{\left(\frac{\tau_{op}}{2}\right)^2 + \frac{\sqrt{2m^*\hbar\omega_0}(\sqrt{2m^*\hbar\omega_0} + eE\tau_{op})}{e^2E^2}} \ , \tag{5}$$

in the absence of any magnetic field.

For $E = 200$ V/cm, the above equation yields a value of $t_p = 8$ ps ($\tau_{op} \approx 0$). The observed period in Fig. 1 ($B = 0$ tesla) is about 7 ps which is close enough to the estimated value to confirm that this simple picture originally presented in ref. [4, 8, 9, 6] is quite reasonable.

In Fig. 2, we find that there are no oscillations in the absence of any magnetic field at 77 K. This is because acoustic phonon scatterings are much more frequent at 77 K than at 30 K and they randomize the phase of the oscillations rapidly. As a result, no oscillation is visible. One might think that polar optical phonon scattering will also be more frequent at the higher temperature and this should counter the effect of increased acoustic phonon scattering. In reality, only polar optical phonon *emission* matters and emission

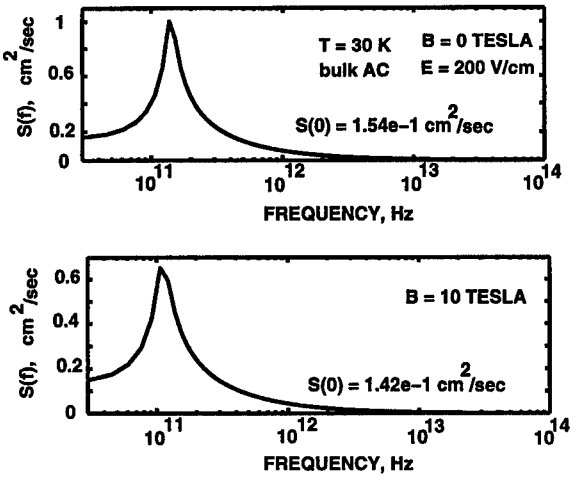


Figure 3: The spectral density of Johnson (or Nyquist) noise at a magnetic flux density of 0 tesla (upper panel) and 10 tesla (lower panel). The driving electric field is 20 V/cm and the lattice (as well as the electron) temperature is 30 K. A bulk acoustic phonon model has been assumed.

is dominated by spontaneous processes rather than stimulated processes. At 77 K, the ratio of the rates of the two processes is approximately $(1/\tau_{spontaneous})/(1/\tau_{stimulated}) = exp[(\hbar\omega_0)/(kT)] - 1 = 215$ (ω_0 is the polar optical phonon frequency in GaAs). Thus, the spontaneous processes are most frequent and since they are relatively independent of temperature, the net emission rate does not increase significantly at 77 K.

A magnetic field brings out the oscillations since it suppresses acoustic phonon scattering (more specifically backscattering) [2] and increases polar optical phonon scattering. This is what we see in the lower panel of Fig. 2. Additonally, the magnetic field also reduces the deacy rate of the autocorrelation function since it increases the momentum relaxation time by suppressing backscattering [2].

In Figs. 3 and 4, we plot the Johnson noise spectral densities which are the Fourier transforms of the velocity autocorrelation functions. At a temperature of 30 K (Fig. 3), the noise is definitely "colored" and has a well-resolved peak at millimeter wave frequency which arises from the streaming oscillations in the velocity autocorrelation function. A magnetic field red-shifts the peak (see the lower panel of Fig. 3) because it increases the period of the oscillation by elongating the electron's trajectory in k-space.

At 77 K (Fig. 4), we get the conventional "white" noise up to millimeter wave frequency. A magnetic field makes the noise colored and introduces a peak at millimeter wave frequency by promoting streaming oscillation.

We point out that the correlation functions do not decay exponentially with time

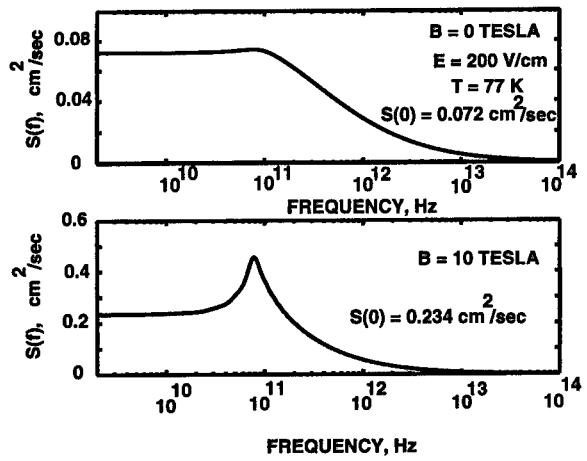


Figure 4: The spectral density of Johnson (or Nyquist) noise at a magnetic flux density of 0 tesla (upper panel) and 10 tesla (lower panel). The driving electric field is 20 V/cm and the lattice (as well as the electron) temperature is 77 K. A bulk acoustic phonon model has been assumed.

since the scattering processes are not Markovian, and consequently the lineshapes of the noise spectral density peaks are not Lorentzian.

In Fig. 5 and 6, we show the dc component of diffusion coefficient $D(0)$ as a function of driving electric field at two different magnetic field strengths and at two different temperatures. At a temperature of 30 K (Fig. 5), the magnetic field decreases the diffusivity at low electric field strengths. Note that diffusivity is given by

$$D(0) = S(0)/4 = \int_0^\infty dTC(T) \; . \tag{6}$$

Hence it is the *area* under the autocorrelation function.

A magnetic field decreases the decay rate of the autocorrelation function thus increasing the area under the autocorrelation curve. On the other hand, at low electric electric field strengths, a magnetic field brings out oscillations in the autocorrelation function by promoting carrier streaming. This tends to reduce the area under the autocorrelation curve since the function oscillates between positive and negative values. At low electric fields and at low temperature, the second effect is more important and hence the diffusivity is reduced by a magnetic field. At higher temperatures, the first effect is always more important and hence the diffusivity increases.

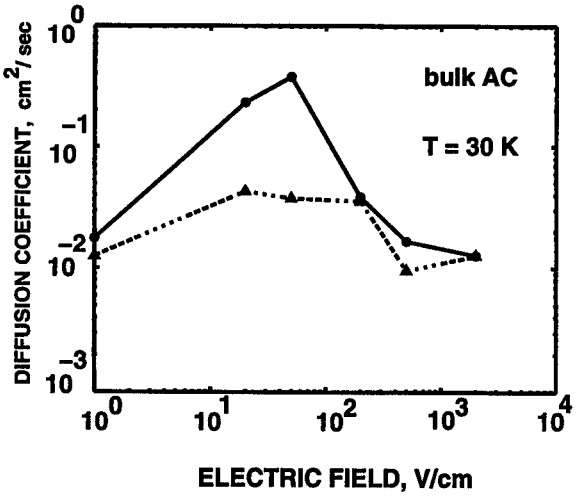


Figure 5: The diffusivity versus electric field at a magnetic flux density of 0 tesla (solid line) and 10 tesla (broken line). The lattice temperature is 30 K. A bulk acoustic phonon model has been assumed.

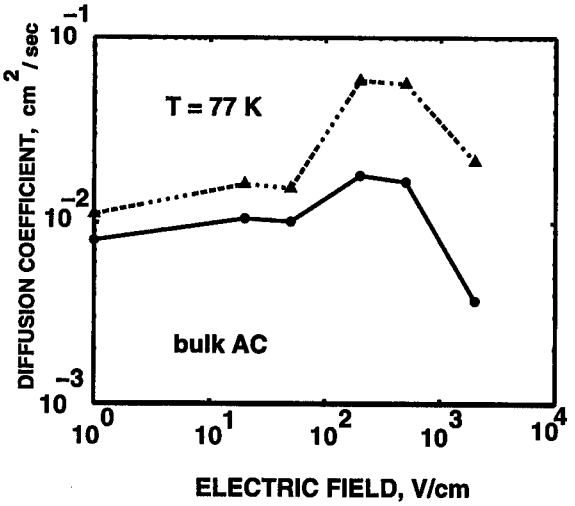


Figure 6: The diffusivity versus electric field at a magnetic flux density of 0 tesla (solid line) and 10 tesla (broken line). The lattice temperature is 77 K. A bulk acoustic phonon model has been assumed.

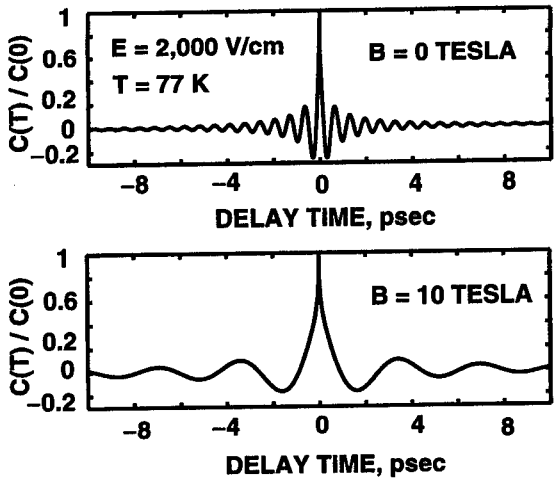


Figure 7: Temporal evolution of the velocity autocorrelation function at a magnetic flux density of 0 tesla (upper panel) and 10 tesla (lower panel). The driving electric field is 2000 V/cm and the lattice (as well as the electron) temperature is 77 K. A bulk acoustic phonon model has been assumed.

3.1 Temperature dependence of diffusivity

It is interesting to see that in the absence of a magnetic field, the diffusion coefficient is larger at 30 K than at 77 K. The diffusion coefficient should increase with increasing electron temperature and mobility even though the exact Einstein relation may not hold (in fact, the Einstein relation does not hold in our case). Obviously, the reduction in the carrier mobility from 30 K to 77 K more than offsets the increase of the electron temperature (electron and lattice temperatures are the same at these low electric fields) to make the diffusivity at 30 K higher than that at 77 K.

3.2 Effect of high electric field

In Figs. 7 and 8, we show the velocity autocorrelation function and the noise spectral densities at a high electric field of 2000 V/cm. The lattice temperature is 77 K.

Note that there are very distinct oscillations in the autocorrelation function and corresponding well-resolved peaks in the noise spectral densities. The oscillations are pronounced because it is easier to stream at higher electric fields. A condition for effective streaming can be expressed as

$$t_p < \tau_{acoustic} \tag{7}$$

where t_p is the oscillation period given in Equation (4) and $\tau_{acoustic}$ is the mean time between two successive acoustic phonon interactions which dephase the streaming oscillations. Since t_p scales inversely with the electric field (assuming $\tau_{op} << t_p$), the

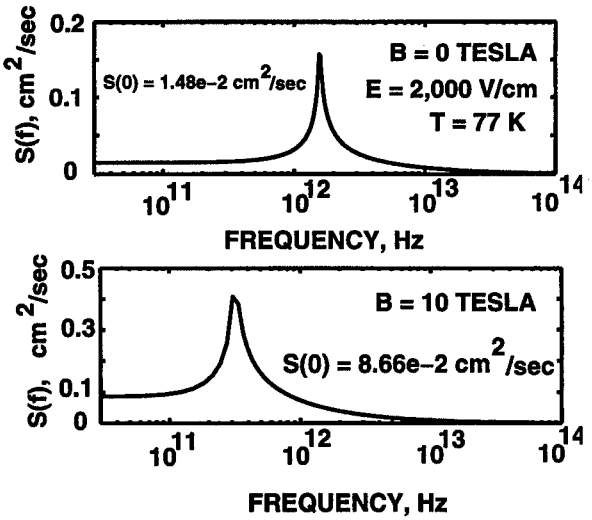


Figure 8: The spectral density of Johnson (or Nyquist) noise at a magnetic flux density of 0 tesla (upper panel) and 10 tesla (lower panel). The driving electric field is 2000 V/cm and the lattice (as well as the electron) temperature is 77 K. A bulk acoustic phonon model has been assumed.

inequality of Equation (7) is much easier to satisfy at higher electric fields. This is the reason that oscillations become very pronounced at high electric fields. By the same token, the area under the autocorrelation curve decreases significantly at high electric fields because the oscillations make the autocorrelation function alternate between positive and negative values. The decay rate of the autocorrelation curve also increases since the momentum relaxation time is reduced. All of this combine to cause the sharp fall in the dc component of diffusivity at high electric fields as seen in Fig. 6.

Finally, one other feature that deserves a discussion is the strong influence of the magnetic field on the period of the oscillation when the driving electric field is high. Note that in Fig. 1 (E = 200 V/cm), the magnetic field increases the period by only $\sim$ 50%, whereas in Fig. 7 (E = 2000 V/cm), the period increases by about 400 %. This difference is a multi-subband effect. In a high electric field, several subbands are occupied in the absence of a magnetic field. Consequently, the value of Δk associated with a polar optical phonon emission can be quite small since the emission may be taking place from a higher to a lower subband. In other words, the polar optical phonon emission is often an inter-subband process which does not involve a significant momentum transfer. Hence the period of the oscillation (see Equation 4) is small. However, when a magnetic field is applied, the subband energy spacing increases. As a result, polar optical phonon emission tends to be more of an intra-subband process. Consequently, the associated Δk is much larger. This accounts for the large increase in the period (caused by the

magnetic field) when the driving electric field is high. By the same token, the magnetic field induced red shift of the noise spectral density peak is much more significant at high driving electric field strengths.

4 Conclusions

In this paper, we have showed the effects of lattice temperature and electric/magnetic fields on Johnson noise. These effects reveal interesting features of carrier transport in quasi one-dimensional systems and may ultimately find use in creative "noise engineering".

References

[1] H. Sakaki, *Jpn. J. Appl. Phys.*, **19**, L735 (1980).

[2] N. Telang and S. Bandyopadhyay, *Appl. Phys. Lett.*, **62**, 3161 (1993).

[3] S. Chaudhuri and S. Bandyopadhyay, *J. Appl. Phys.*, **71** 3027 (1992).

[4] S. Briggs and J. P. Leburton, *Phys. Rev. B*, **38**, 8163 (1988).

[5] D. Jovanovic and J. P. Leburton, in *Monte Carlo Device Simulation: Full Band and Beyond*, ed. K. Hess (Kluwer Academic, Boston,1991), pp.191-218.

[6] R. Mickevicius, V. V. Mitin, U. K. Harithsa, D. Jovanovic and J. P. Leburton, *J. Appl. Phys.*, **75**, 973 (1994).

[7] N. Telang and S. Bandyopadhyay, *Phys. Rev. B*, **51**, 9728 (1995).

[8] D. Jovanovich and J. P. Leburton, *Superlat. Microstruct.*, **11**, 141 (1992).

[9] V. Mitin and C. M. VanVliet, *Phys. Rev. B*, **41**, 5332 (1990).

[10] N. Telang and S. Bandyopadhyay, *Phys. Rev. B*, **48**, 18002 (1993).

[11] SeGi Yu, K. W. Kim, M. A. Stroscio, G. J. Iafrate and A. Ballato, *Phys. Rev. B*, **50**, 1733 (1994).

VISIBLE LIGHT EMITTING DEVICE WITH SCHOTTKY CONTACT ON ULTRA-THIN AMORPHOUS SILICON LAYER CONTAINING SILICON NANOCRYSTALS

S. Fujita and N. Sugiyama
Toshiba Corporation, Research and Development Center,
Advanced Research Laboratory
1, Komukai Toshiba-cho, Saiwai-ku, Kawasaki 210-8582, Japan

ABSTRACT

We have fabricated light emitting diodes (LEDs) with Schottky contacts on a single ultra-thin amorphous silicon (Si) layer containing Si nanocrystals formed by simple techniques as used for standard Si devices. Orange or red electroluminescence (EL) from these LEDs could be seen with the naked eye at room temperature when a reverse bias voltage was applied. The operation voltage is reduced to 3.5-5 V, which is low enough to be applied by a standard Si transistor. The origin of luminescence is also discussed.

INTRODUCTION

It has been expected that high-efficiency light emitting diodes (LEDs) using silicon (Si) - related materials can be realized for monolithic optoelectronic integrated circuits (ICs). Of the Si-related materials investigated, porous Si (PS) has been studied most actively. The quantum efficiency and stability of LEDs based on PS have gradually been improved [1]. Recently, Si-based nanostructures such as Si-based quantum wells and Si nanocrystals (Si-NC) have also been studied for their light-emitting characteristics. These Si nanostructures can be formed using methods which better match standard silicon technology as compared with PS, since electrochemical processes are not needed. Based on previous theoretical studies, the optical band gap is increased [2] and the probability of radiative recombination for excitons is enhanced with a decrease in the feature size of nanostructures owing to the quantum confinement effect [3,4]. The quantum size effect has been experimentally demonstrated for an amorphous Si(a-Si)/SiO_2 superlattice even at room temperature [5]. Visible photoluminescence (PL) with high efficiency has been reported with Si-NCs formed by various methods [6-10]. The reported photon energy of the PL peak spectra is 1.5 to 1.9 eV (red) for most Si-NCs.

The number of the reports on electroluminescence (EL) from the Si-based nanostructures [11-13] is very small as compared with those on PL. This is principally because carrier injection induced electrically is more difficult than that induced optically in the case of Si-based materials. In the investigations reported, visible EL was obtained from Si-NCs in an SiO_2 matrix formed by chemical vapor deposition (CVD) [11] or by Si^+-implantation into SiO_2 [12], and from a multi-quantum-well (MQW) composed of 40 couples of crystallized a-Si/silicon-nitride (SiN_x)

formed by plasma-enhanced CVD and laser annealing [13]. The EL in some of these cases was strong enough to be seen with the naked eye. These results indicate that Si-based nanostructures show promise in realizing LEDs based on Si-related materials. However, the operating voltage is still rather high (10~25 V or more) for the devices to be driven by standard Si-ICs. This is because the Si-NCs in these cases are sandwiched between multiple insulating layers or embedded in thick insulating layers, through which the carriers must pass by direct tunneling. In this study, we fabricated simple LEDs with Schottky contacts on a "single" ultra-thin a-Si layer containing Si-NCs and without the insulating layers. Visible orange and red EL was observed from this LED with a relatively low operating voltage.

EXPERIMENTS

The ultra-thin a-Si layers containing Si-NCs were formed as follows. The *p*-type Si wafer had a diameter of 150 mm and low resistivity (0.01 Ωcm). The surface was etched by HF solutions before the deposition of a-Si. A molecular beam of Si, formed by resolving disilane using a graphite cracking heater [14], was deposited and a-Si 3 nm or 18 nm thick was formed on the Si substrate at room temperature. The Si substrate was heated at 700, 800, and 850°C for 1 minute in purified nitrogen or oxygen gas in order to convert a-Si partially to nanocrystals. It took about 3 minutes to increase the temperature from room temperature to the heating temperature. After heating, the samples were cooled passively in purified nitrogen. During the heating in oxygen, an oxide thinner than 1 nm may be formed simultaneously [15]. PL measurements for these samples were performed using an Ar^+ laser (488 nm) at room temperature. The structure of these samples was observed using a high-resolution transmission electron microscope (HR-TEM). Metal contacts composed of titanium and gold (Ti/Au) were formed by electron beam (EB) evaporation on the back of the substrate. Ti/Au contacts 100 x 100 μm^2 in area were formed on the surface of the Si-NCs by the lift-off process. Device isolation was not employed. Figure 1 shows a cross-sectional scheme of the resulting device. For reference, *p*-type Si substrates were also annealed in oxygen gas and the devices with Schottky contacts were fabricated on them. The current-voltage (I-V) characteristics were measured at room temperature. EL was measured at room temperature using a monochromator and a photomultiplier.

RESULTS

At room temperature, the PL signals with a peak photon energy of about 1.9 eV and weak intensity were obtained from the a-Si layers 3 nm thick heated at 700°C in both nitrogen and oxygen. From those heated at 800°C in nitrogen, the PL signals with a peak photon energy of about 1.7 eV and very weak intensity were obtained. On the other hand, there were no detectable PL signals from the other specimens. These results are summarized in Table 2.

Figure 2 shows a cross-sectional HR-TEM lattice image of an a-Si layer 3 nm thick heated

at 700°C in oxygen. Tiny Si-nanocrystal islands of almost hemispherical shape, 2-3 nm wide and about 1 nm high, which were not seen in the case of a non-annealed sample, are seen in the a-Si layer. The presence of stacking faults between the islands and the substrate indicates that these islands are formed after the deposition of the a-Si layer and that there is an interfacial layer. The thickness of the surface oxide is thought to be comparable to that of the native oxide. In the case of heating in nitrogen, similar tiny islands of almost the same size were formed. A previous report indicated that 2-3 nm rectangular nanocrystals were formed inhomogeniously in the [111] direction by a similar method and that strong blue PL was observed[16]. The structures converted from a-Si layers heated under several conditions are summarized in Table 1. In the case of a-Si 3 nm thick heated at 800°C in nitrogen, the nanocrystal islands were 3 nm wide and 1.5 nm high. In the case of a-Si 3 nm heated at 850°C in nitrogen, most of the a-Si was converted to polycrystalline silicon. In the case of a-Si 3 nm thick heated at 800 and 850°C in oxygen, most of the a-Si was converted to silicon oxide. It has been found that the size of the nanocrystal islands formed from a-Si 3 nm thick was larger than that formed from a-Si 18 nm thick under the same heating conditions. This is probably because crystallization is suppressed owing to surface stress in the a-Si layer in the case of ultra-thin a-Si.

The I-V characteristics of the devices fabricated using these samples show rectifying behavior. Figure 3 shows typical I-V characteristics measured for the devices fabricated using samples heated at 700 and 800°C in nitrogen. The I-V characteristics approach those of ohmic contacts as the heating temperature is increased. On the other hand, in the case of heating in oxygen, the I-V characteristics approach those of MIS diodes as the heating temperature is increased.

Visible EL emission was observed from some of these Si-NC devices. Orange EL emission was obtained from the devices fabricated using samples heated at 700°C in nitrogen or oxygen, and the emission was clearly seen with the naked eye at room temperature when a reverse bias voltage was applied. In the case of the devices fabricated using samples heated in oxygen, the critical reverse current (I_{cr}) for the observation of light emission with the naked eye was 30-40 mA, where the applied voltage was 4.0-4.5 V. These I-V characteristics were stable and changed little after repeated observation of the EL. The I_{cr} of the devices fabricated using samples heated for 1 minute in nitrogen was about 60mA, where the applied voltage was about 5 V. The external quantum efficiency for these devices was $1x10^{-3}$-$1x10^{-2}$ %. The reverse current increased and EL intensity decreased every time the I-V characteristics were measured. This is because the surface oxidation due to heating in oxygen is effective in stabilizing the operation of the EL device. Red EL emission was obtained at 3.5-4.0 V from the devices fabricated using samples heated at 800°C in nitrogen. However, no visible EL was observed from the devices fabricated using samples heated at 800 or 850°C in oxygen, where a-Si was almost completely converted to oxide. In addition, visible EL emission was not obtained from the devices fabricated using samples without heating or those heated at 850°C in nitrogen, where most of the a-Si was converted to polycrystalline Si. The results for EL emission from the devices fabricated using a-Si heated under several conditions are summarized in Table 2. The results in Table 2 indicate that the visible EL is related to the existence of Si-NCs less than 3 nm in lateral diameter formed in the a-Si layer.

Figure 4 shows typical EL spectra for devices fabricated using samples heated at 700 and 800°C in nitrogen. The spectra were measured at room temperature when the reverse current was 60 mA. The EL spectra for devices fabricated using samples heated at 700°C in oxygen were similar to the spectrum for 700°C heating. In Fig. 4, two peaks are visible in the spectrum for 700°C heating. In this spectrum, the peak wavelength, equivalent photon energy and full-width at half-maximum (FWHM) are 650 nm, 1.9 eV and 110 nm for the major peak, and 570 nm, 2.2 eV and 30 nm for the minor peak, respectively. The peak wavelength and FWHM of the main peak are close to those obtained from an MQW of crystallized a-Si/a-SiN_x [13]. In the spectrum for 800°C annealing, there is a single peak with a peak wavelength of 720 nm, an equivalent photon energy of 1.7 eV and an FWHM of 50 nm. If quantum confinement of carriers in Si-NCs is responsible for the EL emission, it can be thought that this peak shift by increasing the size of Si-NCs is due to the quantum size effect.

ORIGIN OF LUMINESCENCE

It should be noted that the spectra shown in Fig. 4 are quite different from the spectrum produced by a reverse-biased p-n junction of silicon, where the spectrum spans the entire visible range and the emitted light is white [17]. Furthermore, since the a-Si where hydrogen is effused by annealing can not exhibit detectable PL at room temperature owing to the defect states for a non-radiative recombination process [18], the EL is not thought to be emitted from the a-Si layer. This is also confirmed by the result that no EL was emitted from the devices fabricated on an a-Si layer 18nm thick annealed in oxygen or nitrogen, where larger crystals were easily formed in a-Si compared with a-Si layer 3nm thick. This result also indicates that the origin of EL is neither defects at the a-Si surface or interface nor those related to SiO_x [19], in which the defect states are not dependent on the thickness of the a-Si. Thus, the results summarized in Table 2 can not be explained by the existence of emission centers in a-Si or at the interface of a-Si/Si-NC or SiO_x/a-Si. Although the origin of EL is still unclear at this stage, the authors speculate on the origin as follows. This light emission is related to the formation of Si-NCs in an ultra-thin a-Si layer, considering the fact that luminescence was obtained only when Si-NCs with a lateral size less than 2 nm and height less than 1.5 nm were present. The luminescence may be due to some confinement effect, considering the fact that no luminescence was emitted from a-Si layers 18nm thick annealed in oxygen or nitrogen, where crystals larger than 5nm were easily formed. The red shift of the luminescence peak wavelength with increasing Si-NC size also suggests the quantum confinement effect in Si-NCs. Although there is not enough evidence to show the confinement effect in Si-NCs at present, it is likely that the luminescence is emitted from Si-NCs.

Figure 5(a) shows the schematic band diagram of this structure expected by the authors. The very thin surface oxide (or native oxide) and interfacial layer may act as a barrier to electrons and holes. It has been reported that the band gap of ultra-thin a-Si is 1.6-1.7 eV, and this may be substantially increased as compared with bulk a-Si because of the confinement effect [5]. However, the efficiency of radiative recombination in a-Si is very low [18]. The

electrons may be confined in the Si-NC/a-Si or *p*-type-Si/Si-NC interface region when a reverse voltage is applied, as shown in Fig. 5(b). Some of the electrons may be trapped at the interface states between a-Si and Si-NC since a-Si contains high-density trap sites [18]. Although the holes, which pass through the surface oxide by tunneling, cannot be confined in NCs, they can be trapped at the interface states between a-Si and Si-NC. It is likely that the recombination of "confined" electrons and "trapped" holes is responsible for the luminescence, since the recombination of "trapped" electrons and "trapped" holes may be non-radiative [18]. The reason for the weak intensity of PL is thought to be that the density of NC is low and the carrier confinement is not strong when no bias voltage is applied. However, further study is needed for the confirmation of this model.

REASON FOR THE OBSERVATION OF EL AT LOW VOLTAGE

The fact that EL was emitted only under reverse bias is unique as compared with those on PS or Si-NCs. The authors think that EL is obtained when the electrons and holes are produced in *p*-type Si, a-Si or Si-NC by impact ionization (i.e. avalanche breakdown occurs) [20] when a large reverse bias voltage is applied, and the electrons are transferred into NC-Si, where they contribute to EL, as shown in Fig. 5(b). Holes are also injected from the metal contact through the surface SiO_x layer into a-Si or Si-NCs. Since avalanche breakdown occurs easily in our devices because of the thin a-Si thickness and high acceptor concentration in the *p*-type substrate, the operation voltage for visible EL can be reduced to 3.5-5 V, which is so low that these diodes can be driven by a standard Si bipolar transistor. The external quantum efficiency of EL will be improved by increasing the density of NCs and strengthening the carrier confinement. Thus, the LED that the authors have demonstrated is a promising device for realizing a monolithic optoelectronic ICs.

It should be noted that strong EL can be obtained from just a single ultra-thin layer. The volume of the light-emitting layer for our devices is 30 to 500 times smaller than that of EL cells of Si-based nanostructures in which a bright EL is visible to the eye [12-13]. This result suggests that the LED based on the Si/SiO_2 (or SiN_x)-MQW with an even smaller number of Si well-layers can exhibit EL strong enough to be seen with the naked eye, although, in general, it is thought that a large number of well-layers is needed.

SUMMARY

The authors have fabricated LEDs with Schottky contacts on an single ultra-thin a-Si layer including Si-NCs formed by a simple method. These LEDs exhibit orange or red EL that can be seen with the naked eye at room temperature. The authors inferred that the origin of EL is related to the quantum confinement effect of the Si-NCs embedded in a-Si. The turn-on voltage for light emission was 3.5-5 V, which is low enough to be applied by a standard Si device. These results suggest that the LEDs based on the Si/SiO_2 (or SiN_x)-MQW even with a small number of

Si well-layers can exhibit strong EL.

ACKNOWLEDGMENTS

The authors would like to express their gratitude to Dr. T. Sakai of the Advanced Semiconductor Laboratories and S. Hosoi of the Microelectronics Center of Toshiba Corporation for their valuable suggestions and technical support in device fabrication. They would also like to thank Dr. A. Toriumi, M. Ishikawa, and Dr. A. Kurobe of the Research and Development Center of Toshiba Corporation for their helpful discussion. The first author would like to express gratitude to Dr. L. Sedarcreek for helpful advice.

References

[1] P.M. Fauchet, J. Lumines. **70**, 294(1996).
[2] J.P. Proot, C. Delerue, and G. Allan, Appl. Phys. Lett. **61**, 1948 (1992).
[3] T. Takagawara and K. Takeda, Phys. Rev. B, **46**, 15578 (1992).
[4] J.B. Khurgin, E.W. Forsythe, G.S. Tompa, and B.A. Khan, Appl. Phys. Lett. **69**, 1241 (1996).
[5] Z.H. Lu, D.J. Lookwood and J.-M. Baribeau, Nature **378** (1995) 258.
[6] H. Takagi, H. Ogawa, Y. Yamazaki, A. Ishizaki, and T. Nakagiri, Appl. Phys. Lett. **56**, 2379 (1990).
[7] Y. Kanemitsu, T. Ogawa, K. Shiraishi, and K. Takeda, Phys. Rev. B, **48**,4883 (1993).
[8] S. Schupper, S.L. Friedman, M.A. Marcus, D.L. Adler, Y.-H. Xie, F.M. Ross, T.D. Harris, W.L. Brown, Y,J, Chabal, L.E. Brus, and P.H. Citrin, Phys. Rev. Lett. **72**, 2648 (1994).
[9] T. S-. Iwayama, S. Nakao, K. Saitoh, Appl. Phys. Lett. **65**, 1814 (1994).
[10] X. Zhao, O. Schoenfeld, J. Kusano, Y. Aoyagi, and T. Sugano, Jpn. J. Appl. Phys. 2, **33**, 649 (1994). J. Appl. Phys. 2, **33**, 899 (1994).
[11] G.S. Tompa, D.C.Morton, F.T. Monmouth, B.S. Sywe, Y. Lu, E.W. Forsythe, J.A. Ott, D. Smith, J.B. Khurgin, B.A. Khan, N.A.Phlips, Mater. Res. Soc. Symp. Proc. **358** 701(1995).
[12] L.-S.Liao X.-M.Bao, N.-S. Li, X.-Q.Zheng, and N.-B Min, Solid State Commun.97,1039(1996). 409(1994).
[13] K. Chen, M. Wang, W. Shi, L. Jiang, W. Li, J. Xu, and X. Huang, J. Non-Cryst. Solids, **198**, 833 (1996).
[14] N. Sugiyama, J. Crystal Growth, **172** 376(1997).
[15] The thickness of oxide formed on a crystalline Si substrate for one and three minutes of heating was about 0.5 and 0.7 nm, respectively.
[16] O. Schoenfeld, X. Zhao, J. Christen, T. Hempel, S. Nomura, and Y. Aoyagi, Solid State Electron. 40, 605 (1996).

[17] J. Bude, N. Sano, and A. Yoshii, Phys. Rev. B **45**, 5848(1992).
[18] *The Physics and Applications of Amorphous Semiconductors*, edited by A. Madan and M. Shaw (San Diego, 1988) p. 106.
[19] L. N. Skuja, A. R. Silin, and A.G. Boganov, J. Non-cryst. Solids **63**, 431(1984).
[20] The reverse I-V characteristics does not exhibit "sharp" break down, which is typical avalanche breakdown characteristics, since the major part of reverse current pass through the a-Si area where NC does not exit and a-Si (without hydrogen) contain high density defects for electron hopping.

Atmosphere	Temperature (°C)	Thickness of a-Si (nm)
N_2	700	3
N_2	800	3
N_2	850	3
O_2	700	3
O_2	800	3
O_2	850	3
N_2	700	18
N_2	800	18
O_2	700	18
O_2	800	18

Table 1 : Annealing conditions and initial thickness of a-Si layer

Atmosphere	Temperature (°C)	PL /peak wavelength (nm)	EL /peak wavelength (nm)
N_2	700	△ / 650	○ / 650
N_2	800	▲ / ~720	○ / 720
N_2	850	-	-
O_2	700	△ / 650	○ / 650
O_2	800	-	-
O_2	850	-	-

Table 2 : Correlation between luminescence and annealing conditions for formation of Si-NCs using a-Si layer 3nm thick . (Intensity : ○: strong, △: weak, ▲: very weak) Note that no luminescence was observed from those using a-Si layer 18 nm.

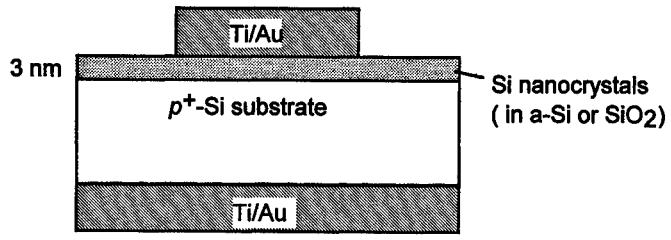


Figure 1 : Cross-sectional scheme of the device.

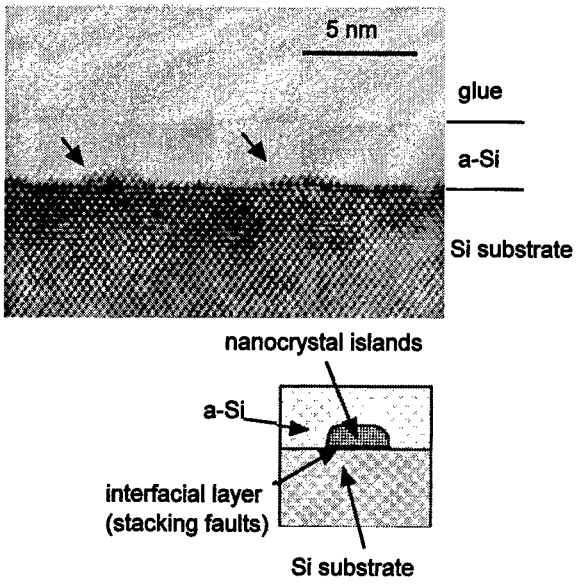


Figure 2 : Cross sectional high resolution TEM lattice image of the a-Si layers heated for one minute in oxygen.

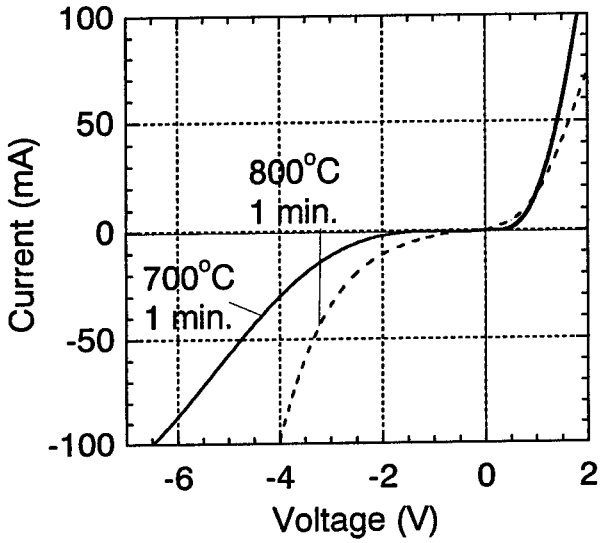


Figure 3 : Typical I-V characteristics for the device fabricated using samples heated at 700 and 800°C in nitrogen.

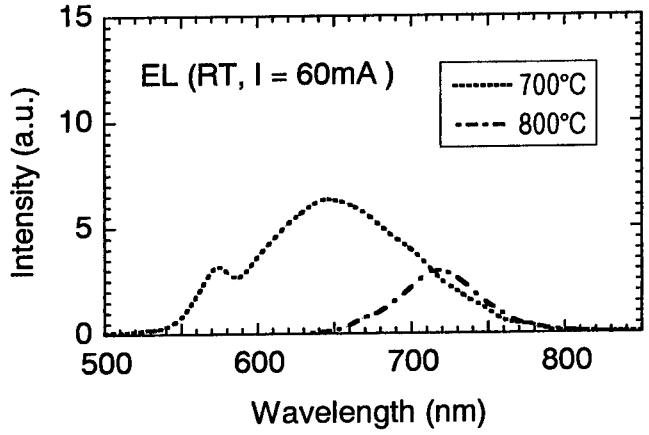


Figure 4 : Typical EL spectra for devices fabricated using samples heated at 700 and 800°C in nitrogen.

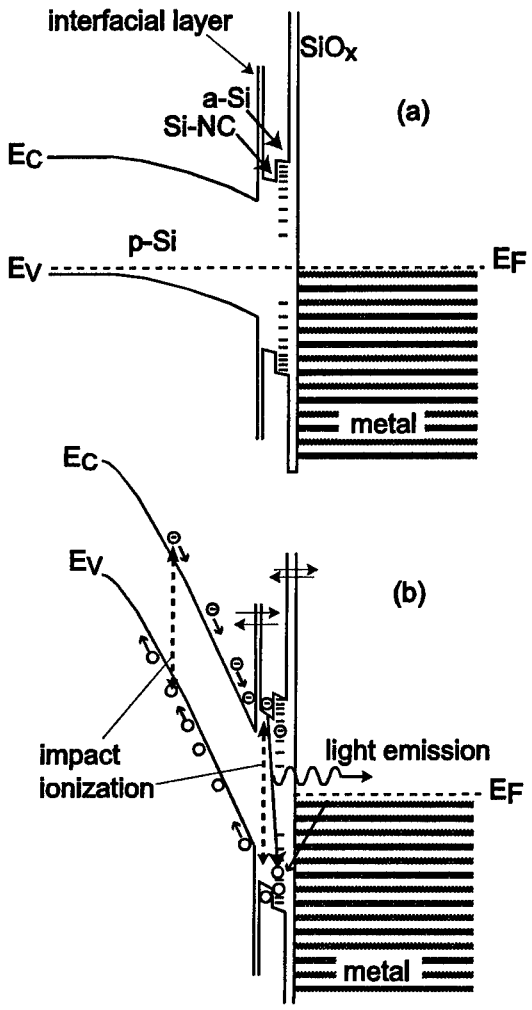


Fig.5 Schematic band diagram of device structure under no bias voltage (a), and under reverse bias voltage(b)

QUANTUM TRANSPORT THROUGH AN ATOMIC CLUSTER

Jeremy Taylor[1], Hong Guo[1] and Jian Wang[2]
1. Centre for the Physics of Materials, Department of Physics
McGill University, Montreal, CANADA H3A 2T8
2. Department of Physics
The University of Hong Kong, Hong Kong, China

ABSTRACT

A quantitative prediction of quantum transport properties of atomic scale devices requires detailed knowledge of the microscopic degrees of freedom. To this end, we have developed an *ab initio* method for calculating transport properties of atomic scale devices. Our method combines quantum molecular dynamics, evaluation of the single electron scattering potential within density functional theory, and finally the solution of the three-dimensional quantum scattering problem. In this work we investigate the effects of ionic thermal fluctuations on the transport properties of an atomic scale junction consisting of an Al_{13} cluster coupled to metallic leads. For ionic temperatures of $150K$ and $450K$, the conductance of the atomic junction fluctuates around $3 \times G_o$, where $G_o = 2e^2/h$, with a fluctuation amplitude less than G_o. On the other hand, the electro-chemical capacitance is found to fluctuate between two values due to the position of the Fermi energy.

INTRODUCTION

In a ballistic nanoscale constriction, conductance is quantized in units of $G_o = 2e^2/h$, representing the conductance of a single spin-degenerate transport channel. Recent experiments have shown that the conductance in a single-atom constriction is approximately e^2/h times the valence of the atom [1]. *Ab initio* calculations of

transport in Si atomic chains predict quantized conductance and the development of a conductance gap as the length increases [2]. It was also predicted that, in a single Si atom tunnel junction, resonant transmission occurs at the energy levels of the isolated atom [3]. In addition, for atomic wires made of Carbon atoms, conductance oscillates as the number of atoms changes from odd to even and vice-versa [4]. These investigations demonstrate that transport in atomic scale nano-systems is strongly coupled to microscopic degrees of freedom.

The relevant energy scale in these atomic systems is of the order of atomic energy level spacing. This spacing is of the order $\Delta E \sim 1eV \gg k_B T$, so that conductance quantization is not smeared out by electronic fluctuations resulting from a finite temperature. Many experiments have confirmed this fact [5]. On the other hand, the energy levels of an atomic junction depend sensitively on its atomic structure. At room temperature, the atoms of an atomic device fluctuate about their equilibrium position causing rearrangements of the energy levels. Hence it is interesting to ask how these thermal fluctuations affect transport properties on average, and further on the time domain. Ref. 6 is the first to address this question from an atomic point of view, by investigating the Kubo conductivity in a Na cluster. For a Na atomic junction, an interesting discovery was that the Kubo conductivity has large fluctuations [6] as a function of time in the range of picoseconds. These fluctuations were certainly a reflection of the thermal fluctuation of the Na atoms at a finite temperature.

Since transport in a coherent conductor is intrinsically a quantum scattering problem, and since experimentally it is the conductance (as opposed to conductivity) which is measured, it is desirable to solve the quantum scattering problem for atomic junctions to directly obtain conductance in the theoretical framework of Landauer and Büttiker [7, 8]. In this work we report our investigations in this direction, and focus on thermal effects on transport in atomic junctions. In particular, we focus on an atomic junction formed by an Al_{13} cluster which couples to the outside world through two high density metallic leads. In this work the leads are modeled by the jellium model.

Our numerical calculations are from first principles. Our method combines quantum molecular dynamics, evaluation of single electron scattering potential within the density functional theory, and finally a direct solution of the scattering problem using a transfer matrix. For temperatures at $150K$ and $450K$, the conductance of the atomic junction fluctuates around $3 \times G_o$ with a fluctuation amplitude less than G_o. On the other hand the electro-chemical capacitance is found to fluctuate between two values due to the position of the Fermi energy. In the following sections we first discuss the computational method, followed by our

results for the Al_{13} cluster.

II. Computational Method

To make the discussion clearer, it is appropriate to state what we mean by an atomic device. In this work an atomic device consists of an atomic cluster with atomic positions at $\{\vec{R}_I\}$, coupled to outside world through metallic leads. The leads extend far away from the cluster and connect to electron reservoirs with chemical potential μ_L. In the Landauer-Büttiker theoretical framework [7, 8], we can relate the electronic transport properties to the scattering matrix for a single electron interacting with an effective potential V_{eff} which describes the device. The effective potential includes the relevant microscopic degrees of freedom: the nature of the leads, the atomic positions, the electron-electron interactions, the ion-electron interactions, the boundary conditions, and the external bias voltages. We give a brief description of how we describe these degrees of freedom.

A. Leads

In our theoretical analysis, the leads play the role of connecting the device with the outside world and guide the incoming and outgoing waves to and from the device. The electronic structure of the leads must be solved together with the device. We may consider two models for the leads, *atomic leads* and *jellium leads*. An atomic lead consists of a unit cell repeated in the lead direction. The band structure of the lead can be non-trivial. For example, Si atomic chains develop a band gap as the length of the chain increases [2]. The eigenfunctions of atomic leads are Bloch states $\{\psi^E_{\vec{k}_z}\}$. The scattering problem involves the propagation of an incoming Bloch wave through the atomic lead, scattering by the lead-device junction, traversing and scattering through the atomic section, and again scattering by the other lead-device junctions, and finally transmitting through or reflecting back. While atomic leads can be employed, the calculation tends to be more complicated.

A simpler model for the leads is the jellium model which is used in this work. For a transport problem, jellium leads reasonably mimic the high density electrodes [4]. A jellium lead consists of a rectangular block of uniform positive compensating background screened by the valence electron density. The compensating density is chosen so that the electron density of the lead is the same as the electron density of the bulk substance being studied. The eigenfunctions of the leads are plane waves in the lead direction (the z-direction) multiplied by transverse eigenfunctions. The dispersion relation in the z-direction is trivial: $E_{\vec{k}_z,n} = \frac{\vec{k}_z^2}{2} + \epsilon_n$

where n indexes the transverse subband. For an electron of energy E inside the incoming lead, we only need consider subbands $\epsilon_n < E$ because higher subbands cannot propagate. We emphasize that while the positive charges in a jellium lead are spread uniformly throughout the lead volume, the electrons of the lead must be included into our density functional analysis which produces the effective scattering potential.

B. Atomic Positions

Transport properties of atomic devices can depend sensitively on atomic structures. Thus we must obtain the structure before calculating the scattering matrix. Furthermore, in this paper we will be interested in the effects of thermal fluctuations of the atomic positions. In general, obtaining the equilibrium structure is a time-consuming process. To speed this up, we decided to minimize a non-self consistent density functional (the Harris functional) $E[\rho_0(\vec{r}); \{\vec{R}_I\}]$ to determine the equilibrium structure. This is done using a localized basis set and an isolated neutral-atom reference density $\rho_0(\vec{r})$ [11]. With the atomic forces calculated this way, the dynamics of the atomic motion is governed by the usual Langevin equation with the proper temperature dependent noise term. This first principles quantum molecular dynamics (QMD) method is computationally faster than the QMD based on self-consistent density functional theory, but it is slower than empirical tight-binding methods. The procedure is similar to tight-binding methods in that the Hamiltonian and overlap matrices are sparse and well-suited to $O(N)$ electronic structure approaches. Using this QMD, the instantaneous atomic positions, $\{\vec{R}_I(t)\}$, are obtained as a function of time t for the Al_{13} cluster at $150K$ and $450K$.

C. Electronic Degrees of Freedom

The electronic degrees of freedom consist of the electron-electron interaction, ion-electron interaction and boundary conditions. A scattering state is extended, connecting the two macroscopic leads. The scattering states interact weakly with the electrons in the device so that we can separate the two and describe the interaction in terms of the effective potential mentioned before.

We further separate the electrons in the device into valence electrons and core electrons. The core electrons are included in a pseudopotential that describes the ion-electron interaction. For this work, we use a local pseudopotential [12]. Standard non-local norm-conserving pseudopotentials can also be applied [13] but the scattering problem becomes very difficult in the presence of a non-local potential.

The electron-electron interactions are described within the LDA of density functional theory. Here we note that the standard Hartree mean-field expression for the electrostatic energy,

$$V_H = \int d\vec{r}' \frac{\rho(\vec{r}')}{|\vec{r} - \vec{r}'|},$$

represents a choice of "free" boundary conditions or boundaries at infinity. The presence of boundaries at a finite distance introduces a surface term which is proportional to the surface charge density. We can separate the surface charges from the device charges so that it is appropriate to describe the interaction between the device electrons and the surface electrons using a classical electrostatic potential. Equivalently, we can solve the Poisson equation with appropriate boundary conditions to describe the effect of surface charges. In our work, the large three-dimensional (3D) Poisson equation is solved using a multigrid boundary value solver.

Once the boundary conditions are chosen, we solve the Kohn-Sham equations self-consistently. The self-consistent solution includes the response of the device to all orders in the external bias voltage so that we can probe the non-linear transport characteristics of the device. In the low-bias regime, the lead and the device are at equilibrium and there is no surface charge so we can solve the problem in the zero bias limit. The results presented in this work are calculated in this limit.

The effective potential that describes the device is just the Kohn-Sham effective potential

$$V_{\text{eff}} = \frac{\delta E[\rho(\vec{r}); \{\vec{R}_I\}]}{\delta \rho(\vec{r}')}.$$

We note that the density of the scattering state is not included in the effective potential and so the scattering states are naturally self-interaction free. As discussed above, it is important to include the charge densities of the leads into the calculation of V_{eff}.

III. Scattering Calculation

The Landauer-Büttiker formalism relates the conductance and other transport properties to the scattering matrix $S(E)$ [7, 8]. To obtain the scattering matrix for our system, we write the scattered state $\tilde{\Psi}_n^L$:

$$\tilde{\Psi}_i^L = \begin{cases} \Psi_i^L = \psi_i^L + \sum_j r_{ij}\psi_j^R & z < 0 \\ \Psi_i^D & 0 \le z < \ell \\ \Psi_i^R = \sum_j t_{ij}\psi_j^L & z \ge \ell \end{cases}$$

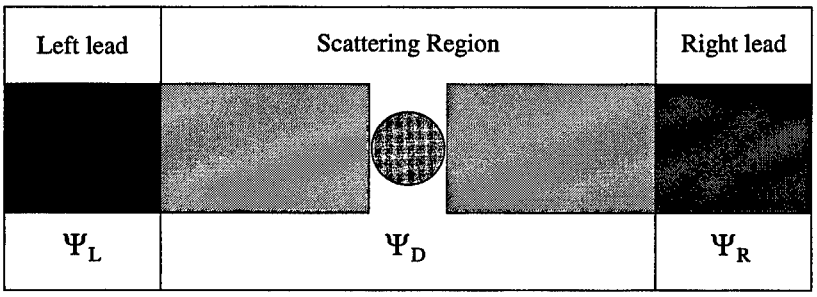


Figure 1: Schematic representation of scattering calculation. Electrons in the left lead will be partially reflected and transmitted because they are scattered off the device. The inner scattering region is described by the self-consistent effective potential. Part of the leads must be included in the self-consistent calculation to properly couple the lead and the device.

where $\{\psi^{L/R}\}$ are the left/right moving states of the leads. For jellium leads, $\{\psi^{L/R}\}$ consist of transverse eigenfunctions multiplied by left/right plane waves. For atomic leads, $\{\psi^{L/R}\}$ are Bloch states.

The transfer matrix method enables us to solve for the transmission and reflection coefficients $\{r_{ij}, t_{ij}\}$. Essentially, we divide the device into slices along the z-direction and expand the wavefunctions Ψ_i^D on each slice. We impose continuity at each slice. This allows us to relate the wavefunction at $z = 0$ and $z = d$. Matching boundary conditions allows us to solve for the unknown coefficients. We then use this to construct the scattering matrix and evaluate quantities such as conductance and capacitance [7, 8, 9].

IV. Results and Discussion

There are two possible sources of fluctuations in our system: *electronic fluctuations* and *ionic fluctuations*. In atomic scale systems, the energy level spacing is of the order of $\Delta E \sim 1eV$ so the electronic excitations are gapped. The thermal energy scale at room temperature is much smaller than ΔE, thus the electronic fluctuations are unimportant to conductance. It is also possible to consider the effect of electronic excitations by considering a free-energy density functional [14]. This would yield a new thermally averaged effective potential $V_{\text{eff}}(T)$. The electronic excitations will still be gapped, thus they will not change the transport

properties in any substantial way. On the other hand, the ionic fluctuations are inherently soft modes which will be populated at any temperature. Given that the transport properties are strongly coupled to atomic structure, it is interesting to ask whether ionic fluctuations affect the transport properties.

Using our QMD, we simulated a fluctuating Al_{13} cluster. After each 5 QMD time steps of $3fs$, we calculated an effective potential V_{eff} which we use to evaluate the conductance and the capacitance at that time. We repeated the procedure for two temperatures of $150K$ and $450K$. The conductance and capacitance are plotted as a function of time in Figure 2.

Conductance is plotted as a function of time in **A**. Note that the value for both temperatures is always approximately $G(t) \approx 3G_o$. At the higher temperature $T = 450K$, $G(t)$ shows larger fluctuations than that at $150K$, but the quantization $G = 3G_o$ is not destroyed by fluctuations at either temperature. Since G is determined by the atomic junction (essentially the most narrow part), this indicates that the number of propagating modes inside the atomic junction region is not affected by the atomic position fluctuation. In addition, the amplitude of the fluctuations is not large, in the range of $0.5G_o$. This is quite different from that of the Na atomic junctions [6] where larger fluctuations in the Kubo conductivity have been obtained. This difference reflects, perhaps, the non-universal nature of the fluctuation for different atomic junctions. It is also possible that the Na junction [6] studied before had a very narrow part which fluctuates much more to alter the propagation subbands, leading to a larger fluctuation in conductivity.

Using the scattering approach we also computed the electro-chemical capacitance [9] C of the Al_{13} atomic junction. $C(t)$ does not stay constant but seems to jump between $0.01aF$ and $0.03aF$. These jumps coincide with the variations in the Fermi energy of the system. C is plotted in **B** (for $150K$) and **C** (for $450K$). The data is qualitatively the same. An explanation of this behavior may be offered as the following. The electro-chemical capacitance of the system measures the non-equilibrium charge distribution accumulated near the two lead-device interfaces as discussed in Ref. 10. Such an accumulation is proportional to the local density of states below the Fermi level. When the Fermi level varies due to the atomic position fluctuation, the local density of states changes leading to the variation of the non-equilibrium charge. Hence C changes its value as well. Although a quantized capacitance is not predicted in this system, it appears that the capacitance happens to jump between $0.01aF$ and $0.03aF$ for this range of temperatures. This is illustrated in Figure 3. For both temperatures, $C \approx 0.01aF$ for Fermi energies below a cutoff energy $E_c \approx -0.087Ry$, and $C \approx 0.03aF$ for Fermi energies above this cutoff energy. It is interesting to note that, in other systems, such jumps

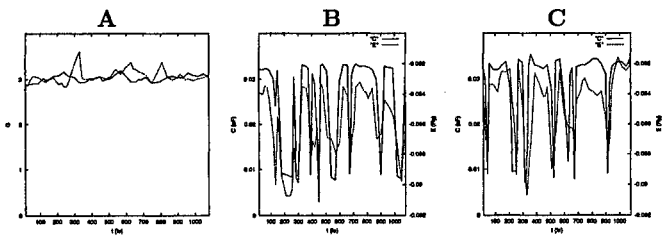


Figure 2: **A.** DC conductance G (in units of G_o) plotted as a function of time. The fluctuations at $150K$ (solid line) are slightly smaller than those at $450K$ (dashed line) but the conductance quantization is not destroyed in either case. **B.** Capacitance C and Fermi energy E plotted as a function of time for $T = 150K$. **C.** Capacitance C and Fermi energy E plotted as a function of time for $T = 450K$. Note that the jumps in capacitance follow the jumps in the Fermi energy.

between two level states are thought to lead to random telegraph noise.

VI. Summary

In summary, the powerful tool described in this paper is suitable to calculate transport properties of atomic scale devices when electron-electron interactions can be accounted for in the density functional formalism. In this work, we have investigated the importance of ionic fluctuations in an Al_{13} cluster. Our results show that thermal fluctuations of the ions do not destroy conductance quantization at least for the atomic device studied here, although the conductance does fluctuate in a sub-picosecond range. The amplitude of the conductance fluctuation is smaller than that found for a Na junction, reflecting the non-universal nature of these temporal fluctuations. The electro-chemical capacitance is found to be affected by ionic fluctuations due to related fluctuations in the Fermi energy. For this atomic junction it is interesting that the capacitance jumps between two levels for the two temperatures studied. Finally we note that investigations of transport phenomena at the atomic scale are still in the early stages. The ability to make quantitative measurements and theoretical predictions at this scale offers exciting opportunities in fundamental nano-science and technology.

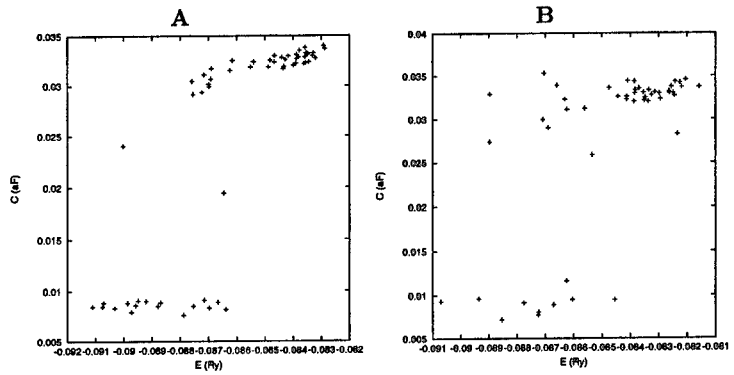


Figure 3: **A.** Capacitance C plotted as a function of Fermi energy E for $T = 150K$. **B.** C plotted as a function of Fermi energy E for $T = 450K$. Note that for E less than a cutoff $E_c \sim -0.087Ry$, $C \sim 0.01aF$ and $C \sim 0.03aF$ for $E > E_c$.

ACKNOWLEDGMENTS

We thank useful discussions at early stages of this work with Dr. C.C. Wan of the University of Toronto; Qingrong Zheng of the University of Hong Kong; Dr. J-L. Mozos of the Helsinki University of Technology, Finland; and Gianni Taraschi of MIT. We gratefully acknowledge financial support by NSERC of Canada and FCAR of Québec.

References

[1] E. Scheer, N. Agraït, J. C. Cuevas, A. L. Yeyati, B. Ludoph, A. Martín-Rodero, G. R. Bolliner, J. M. van Ruitenbeek and C. Urbina, Nature, Vol. 294, p. 154 (1998).

[2] J.-L. Mozos, C. C. Wan, G. Taraschi, J. Wang, and H. Guo, Phys. Rev. B, Vol. 56, p. 4351 (1997).

[3] J.-L. Mozos, C. C. Wan, G. Taraschi, J. Wang, and H. Guo, J. Phys. C, Vol. 10, 2663, (1998).

[4] N. D. Lang and Ph. Avouris, Phys. Rev. Lett., Vol. 81, 3515 (1998).

[5] J. I. Pascual *et. al.*, Science, Vol. 267, 1793 (1995).

[6] R. N. Barnett and U. Landman, Nature, Vol. 387, 788 (1997).

[7] R. Landauer, IBM J. Res. Develop., Vol. 1, 233 (1957).

[8] M. Büttiker, IBM J. Res. Develop., Vol. 32, 317 (1988).

[9] M. Büttiker, J. Phys. C., Vol. 5, 9361 (1993).

[10] T. Christen and M. Büttiker, Phys. Rev. Lett., Vol. 77, 143 (1996).

[11] O. F. Sankey and D. J. Niklewski, Phys. Rev. B, Vol. 40, p. 3979 (1989).

[12] L. Goodwin, R. J. Needs, and V. Heine, J. Phys. C., Vol. 2, 351 (1990).

[13] G. B. Bachelet, D. R. Hamman, and M. Schlüter, Phys. Rev. B, Vol. 26, p. 4199 (1982).

[14] R. G. Parr and W. Yang, *Density Functional Theory of Atoms and Molecules*, Oxford University Press, New York (1989).

NONLINEAR RESONANT TUNNELLING THROUGH DOUBLY DEGENERATE LOCAL STATE IN THE PRESENCE OF STRONG ELECTRON-PHONON INTERACTION

V.N. Ermakov

Bogolyubov Institute for Theoretical Physics
Kiev 252143, Ukraine

ABSTRACT

In an approach of low transparency of the barrier the tunneling of electrons through doubly degenerate local state has been considered with an account of Coulomb and electron-phonon interactions. It is shown that in the case of weak electron-phonon and strong electron-electron interactions the dependence of tunneling current on applied voltage has a steplike character at low temperature. For small applied bias there is a threshold value in the current-voltage characteristic. In the region of large applied bias, the bistable state of the tunneling current is possible. For both of the strong electron-phonon and weak electron-electron interactions, the tunneling current threshold can be bistable.

INTRODUCTION

Resonant electron tunneling through a local state is very sensitive to its position in the barrier similarly to the case of quantum wells [1-3]. This circumstance can be used for effective control of the tunneling process [4]. For example, it is possible to change potential field in the well by accumulation of electric charge in it under the tunneling. Manyparticle effects can be important in this case. However, this process assumes the existence of many electronic states which is not valid in the case of a local state. Nevertheless, as it has been shown in Ref.[5] the manyparticle effects are already essential even in the case of doubly degenerate resonant level of the quantum well. For this reason the manyparticle effects can exist in for the resonant tunneling through degenerated local state. However, the strong electron-phonon interaction is possible in the local state [6] which can essentially change the process of tunneling.

In the present paper, we consider this problem for the case of double degenerated electronic state when the accumulation up to four electrons in the local state is possible. Taking into account the interaction between electrons and electron-phonon interaction one can derive a number of properties characteristic of nonlinear tunneling, including the appearance of steplike current-voltage curves and the bistability of threshold tunneling, among others. The detailed consideration is restricted to one-dimensional case of resonant tunneling. Study of fluctuations in these systems shows that they can be practically suppressed [7]. The later is typical for double level systems.

II. HAMILTONIAN OF THE SYSTEM

We consider a model of tunneling with a double-degenerate local state in the barrier. The energy profile of this structure is shown in Fig.1. Electrons are supposed to interact via Coulomb interaction and with phonons in the local state. The Hamiltonian describing the electrons in this system can be written as follows

$$H = H_o + H_W + H_T. \tag{1}$$

The first term of this Hamiltonian

$$H_o = \sum_{k\sigma} \varepsilon_L(k) a^+_{k\sigma} a_{k\sigma} + \sum_{p\sigma} \varepsilon_R(p) a^+_{p\sigma} a_{p\sigma} \tag{2}$$

describes electrons in the left electrode (emitter) and in the right electrode (collector) (regions 1 and 3 in Fig.1.). Here $a^+_{k\sigma}(a_{k\sigma})$ and $a^+_{p\sigma}(a_{p\sigma})$ are the creation (annihilation) operators, respectively; $\varepsilon_L(k) = \varepsilon_L + \hbar^2 k^2/2m_L$ is the energy of electrons in the emitter, $\hbar k$ and m_L are their quasimomentum and effective mass, respectively, σ is the electron spin. In the collector (with an external potential V applied across the barrier), $\varepsilon_R(k) = \hbar^2 k^2/2m_R + \varepsilon_R - V$, where m_L is the effective mass.

In Eq.(1) the Hamiltonian H_W describes electrons and their interactions in a local state (region 2 in Fig.1). We consider the case when the local state is doubly degenerate. Then H_W can be written as follows

$$H_W = \sum_{\alpha} E_o a^+_\alpha a_\alpha + \sum_i \hbar\omega_i b^+_i b_i$$

$$+ \sum_{\alpha i} \phi_{\alpha i} a^+_\alpha a_\alpha (b_i + b^+_i) + \frac{1}{2} \sum_{\alpha_1 \neq \alpha_2} V_{\alpha_1\alpha_2} a^+_{\alpha_1} a^+_{\alpha_2} a_{\alpha_2} a_{\alpha_1}. \tag{3}$$

Here $a^+_\alpha(a_\alpha)$ are the creation (annihilation) operators for electrons in the local state. $\alpha = (l, \sigma)$, σ is a spin number, l is the quantum state number, which takes values 1 or 2. The energy of the local state taking into account the applied bias is written as follows $\bar{E}_o = \varepsilon_o - \gamma V$, where ε_o is the energy of the local state and γ is the

coefficient, $\gamma = a_L/a$, $a = (a_L + a_R)$. a_L and a_R are distances of local state from left and right borders of the barrier, respectively. V_{α_1,α_2} is a matrix element describing electron interaction in the local state. For simplicity, we approximate it by the positive constant $V_{\alpha_1,\alpha_2} = U_c$, corresponding to repulsion. $b_i^+(b_i)$ are the creation (annihilation) operators for phonons of the i-th mode ($\hbar\omega_i$ is their energy). $\phi_{i\alpha}$ is the matrix element of the electron-phonon interection for local states. The Hamiltonian H_T in Eq.(1) describes the tunneling transition of electrons through the barrier and has the conventional form [8]:

$$H_T = \sum_{k\alpha} T_{k\alpha} a_{k\sigma}^+ a_\alpha + \sum_{\alpha p} T_{p\alpha} a_{p\sigma}^+ a_\alpha + \sum_{kp} T_{kp} a_k^+ a_p + c.c., \tag{4}$$

where $T_{k\alpha}$ and $T_{p\alpha}$ are matrix elements of tunneling transition to the local states from the left and right electrode, respectively. T_{kp} is the matrix element for direct tunneling transition from the emitter to the collector. In the general case, the matrix elements depend on the applied bias.

III. DENSITY OF STATES

Before considering the density of states it is convenient to transform the Hamiltonian H_W using the unitary transformation

$$S = \exp\left\{-\sum_{i\alpha} \frac{\phi_{\alpha i}^*}{\hbar\omega_i} a_\alpha^+ a_\alpha (b_i - b_i^+)\right\}. \tag{5}$$

Thus H_W get the form

$$\tilde{H}_W = \sum_\alpha E_o a_\alpha^+ a_\alpha + \sum_i \hbar\omega_i b_i^+ b_i + \frac{1}{2} \sum_{\alpha_1 \neq \alpha_2} U a_{\alpha_1}^+ a_{\alpha_2}^+ a_{\alpha_2} a_{\alpha_1}. \tag{6}$$

Where

$$U = U_c - \sum_i \frac{|\phi_i|^2}{\hbar\omega_i},$$

and

$$E_0 = \varepsilon_0 - \gamma V - \sum_i \frac{|\phi_i|^2}{\hbar\omega_i}$$

For the Hamiltonian H_T we obtain respectively

$$\tilde{H}_T = \sum_{k\alpha} T_{k\alpha} S_b a_{k\sigma}^+ a_\alpha + \sum_{\alpha p} T_{p\alpha} S_b a_{p\sigma}^+ a_\alpha + \sum_{k,p} T_{kp} a_k^+ a_p + c.c., \tag{7}$$

where S_b is determined below

$$S_b = \exp\left\{-\sum_i \frac{\phi_{\alpha i}^*}{\hbar\omega_i}(b_i - b_i^+)\right\}.$$

Next we confine our consideration to the case of electron tunneling without radiation and absorption of phonons. After averaging Hamiltonians (6) and (7) over phonon states we get

(8)

$$H_t = \sum_{k\alpha} \tilde{T}_{k\alpha} a^+_{k\sigma} a_\alpha + \sum_{\alpha p} \tilde{T}_{p\alpha} a^+_{p\sigma} a_\alpha + \sum_{kp} T_{kp} a^+_k a_p + c.c., \tag{9}$$

where $\tilde{T}_{p\alpha}$ is

$$\tilde{T}_{p\alpha} = T_{p\alpha} \exp\left\{ -\sum_i \left| \frac{\phi_{\alpha i}}{\hbar\omega_i} \right|^2 \left(n_i + \frac{1}{2} \right) \right\}. \tag{10}$$

$$n_i = \left\{ \exp\left(\frac{\hbar\omega_i}{k_B T} \right) - 1 \right\}^{-1} \tag{11}$$

The density of states $\rho(E)$ of local levels can be determined with the help of Fourier transform of the retarded Green's function $G(\alpha, \alpha, E)$

$$\rho(E) = -\frac{1}{\pi} \sum_\alpha \mathrm{Im} G(\alpha, \alpha, E), \tag{12}$$

where

$$G(\alpha, \alpha, t) = -i\theta(t) \langle [a^+_\alpha(t), a_\alpha(0)]_+ \rangle \tag{13}$$

and $\theta(t)$ is a unit Heaviside function.

Using the Hamiltonian H_W, the Green's function can be calculated explicitly. For example, for the state α one obtain

$$G(\alpha, \alpha, E) = \frac{1}{(E' - E_o)} \left\{ 1 + \sum_{m=1}^{3} \sum_{\substack{\alpha_1, \ldots \alpha_m \neq \alpha \\ \alpha_1 \neq \alpha_2 \neq \ldots \alpha_m}} \prod_{m_1=1}^{m} n_{\alpha_{m_1}} \frac{U}{E' - E_o - m_1 U} \right\}, \tag{14}$$

with $E' = E + i\eta$ at $\eta \to +0$. Here $n_\alpha = \langle a^+_\alpha a_\alpha \rangle$ are average values of the occupation numbers of the α-th state. The Green's function has poles at $E_m = E_o + mU$, where $m = 0, 1, 2, 3$. So, the electon-phonon interaction as well as the electron-electron interaction lead to a splitting of the local degenerated states. New states are separated by the value U. However in this case U may also take negative values. With the help of Eq.(7), the density of states ρ for the local states in the barrier can be calculated. These states depend on the occupation numbers of states n_α which are functions of the applied voltage. This is the reason behind the nonlinearity of the tunneling current.

IV. OCCUPATION NUMBERS

When the constant external voltage is applied to the system, a nonequilibrium steady-state distribution of electrons sets in. It is assumed that the electron distribution functions in the electrodes are at equilibrium because of their large spatial extent, but their chemical potentials do change. The latter are connected through the relation $\mu_L - \mu_R = V$ (where μ_L and μ_R are the chemical potentials of the emitter and the collector, respectively). The electron distribution function $g(E)$ in the local state is essentially nonequilibrium. It can be determined from the condition of equality of the tunneling current through the emitter and the collector [8,9]

$$g(E) = \frac{1}{\Gamma(E)}[\Gamma_L(E)f_L(E) + \Gamma_R(E)f_R(E)], \tag{15}$$

where

$$\Gamma(E) = \Gamma_L(E) + \Gamma_R(E),$$

$$\Gamma_L(E) = \sum_k |T_{k\alpha}|^2 \delta[E - \varepsilon_L(k)], \tag{16}$$

$$\Gamma_R(E) = \sum_p |T_{p\alpha}|^2 \delta[E - \varepsilon_R(p)].$$

$f_L(E)$ and $f_R(E)$ are electron distribution functions in the emitter and the collector, respectively. The occupancy of local states in the barrier can be determined with the help of the expression [10]:

$$n_\alpha = -\frac{1}{\pi}\int dE g(E)\mathrm{Im}G(\alpha, \alpha, E). \tag{17}$$

As it follows from (7), the expression for n_α does not depend on the index α. Therefore, mean values of occupation numbers are also independent of the number of the quantum state, and we can assume that $n_\alpha = n$. Thus, we finally obtain

$$n = F(n) \tag{18}$$

where

$$F(n) = \sum_{m=0}^{3} C_3^m g_m (1-n)^{3-m} n^m, \quad C_3^m = \frac{3!}{m!(3-m)!}.$$

The functions $g_m = g(E_m)$ determine the occupancy of new states. Thus, Eq.(18) is a cubic equation for the occupation numbers n. In the general case, this equation can have three solutions in the interval $0 \leq n \leq 1$. According to Eq.(11), for $g_m = g$ we get $n = g$. The equation admits three solutions when $g_0 = g_1 = 0$, i.e. if two states are vacant. These solutions have the form:

$$n_1 = 0,$$

$$n_{2,3} = -\frac{3}{2}\frac{g_2}{g_3 - 3g_2} \pm \sqrt{\frac{9g_2^2 + 4(g_3 - 3g_2)}{4(g_3 - 3g_2)^2}}. \tag{19}$$

According to the condition $0 < n < 1$, expression (19) leads to

$$0 < \frac{3g_2}{3g_2 - g_3} < 2,$$

$$9g_2^2 - 4(3g_2 - g_3) > 0. \tag{20}$$

These inequalities (15) are compatible when

$$g_2 \geq \frac{2}{3}(1 + \sqrt{1 - g_3}), \quad g_3 > 3/4. \tag{21}$$

Thus, Eq.(18) has three solutions when the values of g_1 and g_3 are close to unity. The two solutions n_1 and n_3 are stable, while the third one n_2 is unstable. The stable states correspond to the cases when the local state does not contain electrons or contains four electrons occupying two upper levels. The latter is possible since the system is essentially out of equilibrium.

Matrix elements for tunneling in the one dimentional case are given in the Appendix by Eqs.(A1),(A2). The functions $\Gamma_L(E)$ and $\Gamma_R(E)$ can be approximated by the value

$$\Gamma_{L,R} = \alpha_{L,R}\sqrt{E - \varepsilon_{L,R}(0)}. \tag{22}$$

Here α_L and α_R are the proportionality factors for the emitter and the collector, respectively.

$$\alpha_L = \frac{m_L V_L^2 B(0, a_L; E)}{4\pi m E_s \sqrt{V_0 - \varepsilon_0}(V_0 - \varepsilon_L)},$$

$$\alpha_R = \frac{m_R V_R^2 B(a_L, a; E)}{4\pi m E_s \sqrt{V_0 - \varepsilon_0}(V_L - \varepsilon_R)},$$

and

$$E_s = \frac{\hbar^2}{2\,m\,a^2}$$

Substituting (22) into (15) and taking into account that

$$f_{L,R} = \left\{\exp\left(\frac{E - \mu_{L,R}}{k_B T}\right) + 1\right\}^{-1}, \tag{23}$$

where k_B is Boltzman constant and T is temperature, we obtain the expression for the electron distribution function g_m. For more detailed investigation of the properties of Eq. (18) we will consider same particular cases.

a. The case of $U > 0$.
A plot of the dependence of the occupancy n on the applied voltage obtained by solving Eq.(18), at low temperatures ($k_BT/\epsilon = 0.01$ and 0.05) and pameters $m_L/m_R = 1$, $\gamma = 0,5$, $\varepsilon_o/\epsilon = 1.6$, $U/\epsilon = 0.2$, is represented in Fig.2. Here ϵ is a normalizing constant having the order of magnitude μ. It follows that with the applied voltage increases, the occupancy of the local state increasing step-wize due to consecutive occupation of split states. Above the critical value V_2, the occupation drops abruply to zero due to the departure of the local states from resonance. If the voltage is lowered below V_2, a jump in the occupation number is observed at a lower value of voltage V_1. Thus, the voltage range from V_1 to V_2 contains a bistability region, which is connected with the removal of electrons from the lower levels and with their attachment to the upper split states.

b. The case of $U < 0$.
In this case the dependence of the occupancy n on the applied voltage is more complicated. This dependence is shown in Fig.3 at $U = -0.2$ and the same values of parameters as in Fig.2. It follows that, with the applied voltage increasing, the occupancy of the local state abruply jumps to one above the critical value V_2. If the voltage is lowered below V_2, the occupation drops aleruptly to zero at a lower value of voltage V_1. Thus, there is a voltage range from V_1 to V_2 that contains a bistable region. The voltage interval $(V_2 - V_1)$ decreases with an increase in temperature. Such character of bistability is a consequence of the negative value U.

V. TUNNELING CURRENT

In the case of a constant applied voltage the tunneling current through the double-barrier structure can be calculated in various ways (see, for example, Refs.[9,11]). The following simple expression was obtained for this quantity:

$$J_{cd} = \frac{e}{\hbar}\int dE \frac{\Gamma_L(E)\Gamma_R(E)}{\Gamma(E)}[f_L(E) - f_R(E)]\rho(E)$$
$$+ \frac{e}{\hbar}\int dE P(E)[f_L(E) - f_R(E)], \qquad (24)$$

where e is the electron charge. The second term in Eq.(24) is caused by the direct tunneling of electrons from emiter to collector. The transparency coefficient $P(E)$ is defined as follows

$$P(E) = \sum_{k,p} |T_{kp}|^2 \delta[E - \varepsilon_L(k)]\delta[E - \varepsilon_R(p)]$$

Where T_{kp} is given by Eq.(A3) in the Appendix. For a low barrier transparency, $\Gamma \ll U$, the density of states ρ can be calculated using formulas (12) and (14), which

give

$$\rho(E) = \sum_{m=0}^{3} C_3^m (1-n)^{3-m} n^m \delta(E - E_m). \tag{25}$$

Then, Eq.(24) becames

$$J_{cd} = \frac{e}{\hbar} \sum_{m=0}^{3} \frac{\Gamma_R(E_m)\Gamma_L(E_m)}{\Gamma(E_m)} \{f_L(E_m) - f_R(E_m)\} (1-n)^{3-m} n^m C_3^m$$

$$+ \frac{e}{\hbar} \int dE P(E)[f_L(E) - f_R(E)] \tag{26}$$

The results of numerical calculations of $J_{cd}(V)$ for the same parameters as those used for constructing the curves in Fig.2 and Fig.3 for different values of temperature are illustrated in Fig.4 and Fig.5. A bistability of tunneling current is due to the filling of electrons in the upper energy levels of splitting state. The toothed form of the current in Fig.5 is due to the process of the departure of local states from resonance.

VI. CONCLUSION

Thus, the electron-electron and electron-phonon interactions in the local degenerate state result in the conductance oscillations of the tunneling system. The later is connected with the splitting of electron states by the Coulomb or electron-phonon interactions. The value of splitting defines a period of the conductance oscillations. The steplike form of the current-voltage curve and its threshold character have some analogy with an effect of single-electron tunneling [5] in the case $U > 0$. The bistability takes place in the interval of negative differential conductance. The sign of U determines the chape of the current-voltage characteristics. In the case of a strong electron-phonon interaction ($U < 0$), the steplike character of the current-voltage curve takes place in the interval of negative differential conductance. The bistability takes place in the interval of positive differential conductance. An important feature of the present model is its stability with respect to the fluctuations. A simple consideration of the fluctuations of the occupation numbers of the local states results in

$$\langle \delta n^2 \rangle = \langle (\hat{n} - n)^2 \rangle = n(1-n). \tag{27}$$

In the region of bistability, n takes values in the vicinity of unity or zero. At these values $\sqrt{\langle \delta n^2 \rangle} \ll n$. However, in the region of the current steps the fluctuations are comparable with the charge value. This conclusion is confirmed by experiment [10]. With increasing of temperature the steps quickly smooth out, due to the smoothing of the Fermi distribution functions. The region of their existance is limited by temperature $kT \ll U$. The temperature dependence of bistability is due to the change in functions g_m. They are not so sensitive to temperature. The bistability dissapears, when $\max g(E) \leq 3/4$, and this can be achieved at sufficiently large temperatures comparable to μ. In the range of these temperatures one can neglect the

spin dependence and the situation becomes similar to the one considered in Ref.[2]. In the case $U < 0$, increasing the temperature leads to suppression of the bistability.

Appendix

When a constant voltage is applied to the system, the wave function of an electron in the barrier can be fond in WKB approximation

$$\psi_k(x) = \frac{1}{\sqrt{L}} B(0, x; \varepsilon_L(k))$$

$$\psi_p(x) = \frac{1}{\sqrt{R}} B(x, a; \varepsilon_R(p))$$

$$\psi_\alpha(x) = \frac{1}{\sqrt{r}} \begin{cases} B(x, a_L; \varepsilon_\alpha), & \text{if } x < a_L \\ B(a_L, x; \varepsilon_\alpha), & \text{if } x > a_L \end{cases}$$

Where

$$B(x_1, x_2; E) = \exp\left\{ - \int_{x_1}^{x_2} \frac{dx}{\hbar} \sqrt{2m(V(x) - E)} \right\}$$

L and R are the collector and emitter regions, respectively; r is the radius of the local state. It is supposed that $r \ll a_L, a_R$. Under the condition that $E = \varepsilon_L(k) = \varepsilon_R(p) = \varepsilon_\alpha$ is the energy of the tunneling electron, matrix elements $T_{\alpha,k}$, $T_{\alpha,p}$, $T_{k,p}$ are

$$T_{k\alpha} = \int_0^{a_L} \psi_k^*(x)\, V(x)\, \psi_\alpha(x)\, dx = \bar{V}_L\, B(0, a_L; E)\, \frac{a_L}{\sqrt{a_r L}} \qquad (A1)$$

$$T_{p\alpha} = \int_{a_L}^{a} \psi_p^*(x)\, V(x)\, \psi_\alpha(x)\, dx = \bar{V}_R\, B(a_L, a; E)\, \frac{a_R}{\sqrt{a_r L}} \qquad (A2)$$

$$T_{kp} = \int_0^{a} \psi_k^*(x)\, V(x)\, \psi_p(x)\, dx = \bar{V}\, B(0, a; E)\, \frac{a}{\sqrt{R\, L}} \qquad (A3)$$

Where $\bar{V}_L, \bar{V}_R, \bar{V}$ are the average value of $V(x)$

$$\bar{V} = \frac{1}{a} \int_0^a V(x)\, dx,$$

$$\bar{V}_L = \frac{1}{a_L} \int_0^{a_L} V(x)\, dx,$$

$$\bar{V}_R = \frac{1}{a_R}\int_{a_L}^{a} V(x)\,dx$$

When $V(x)$ is a linear function of x and the applied voltage V

$$V(x) = V_0 - V\frac{x}{a_R + a_L}$$

$B(x_1, x_2; E)$ can be written in the form

$$B(x_1, x_2; E) = \begin{cases} \exp\{Z(x_1) - Z(x_2)\}, & \text{if } x_2 < x_0 \\ \exp\{Z(x_1)\}, & \text{if } x_2 > x_0 \end{cases}$$

where

$$x_0 = \frac{x_2 - x_1}{V}\left\{V(x_1) + \frac{x_1 V}{x_2 - x_1} - E\right\}$$

$$Z(x) = -\frac{2(x_0 - x)^{\frac{3}{2}}}{3}\sqrt{\frac{2Vm}{\hbar(x_2 - x_1)}}$$

References

1. B. Ricco and M.Ya. Azbel, Phys. Rev. B 29 (1984) 1970.
2. A.S. Davydov and V.N. Ermakov, Physica D 28 (1987) 168.
3. A.S. Davydov and V.N. Ermakov, in: Molecular electronics and molecular electronic devices, Vol. 2, ed. K.Sienicki (CRC Press, Boca Raton, 1993).
4. M.A. Reed, I.W. Lee, R.K. Albert and Wetsel. J. Mater. Res., 1, (1986), 337.
5. V.N. Ermakov, E.A. Ponezha J. Phys.: Condens.Matter 10 (1998) 2993
6. Walter A.Harrison, Solid State Theory, Mc. Graw-Hill Book Company, New York, 1970.
7. J.H. Davis, P. Hydgaard, S. Hershfield, and J.W. Wilkins, Phys. Rev. B 46 (1992) 9620.
8. E. Runge, H. Ehrenreich, Phys. Rev. B 45 (1992) 9145.
9. L.Y. Chen, C.S. Ting, Phys. Rev. B 43 (1991) 2097.
10. A.S. Davydov, Quantum mechanics, (Pergamon Press, 1968).
11. D.V. Averin, A.N. Korotkov, and K.K. Likharev, Phys. Rev. B 44 (1991) 6199.

12. Bo Su, V.J. Goldman, and J.E. Cunningham, Phys. Rev. B 46 (1992) 7644.

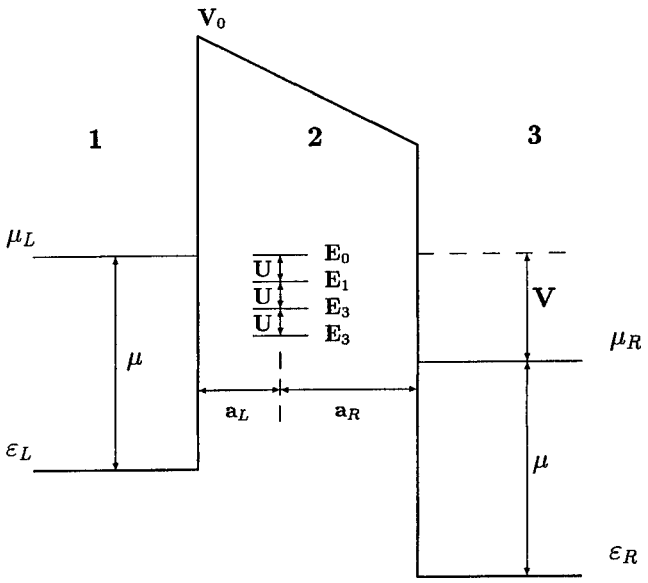


Figure 1: Energy profile under applied voltage V of a barrier structure with localized energy levels.

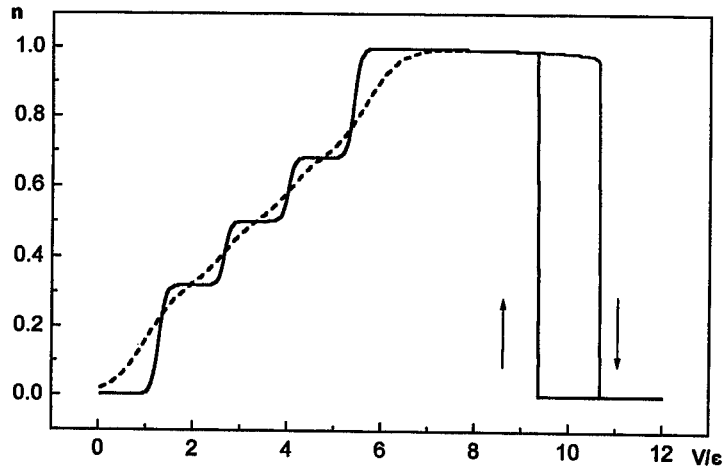


Figure 2: Dependence of the population density n of the local state on applied voltage V for $U/\epsilon = 0.2$. Solid line is for $k_BT = 0.01$; dashed line is for $k_BT = 0.05$.

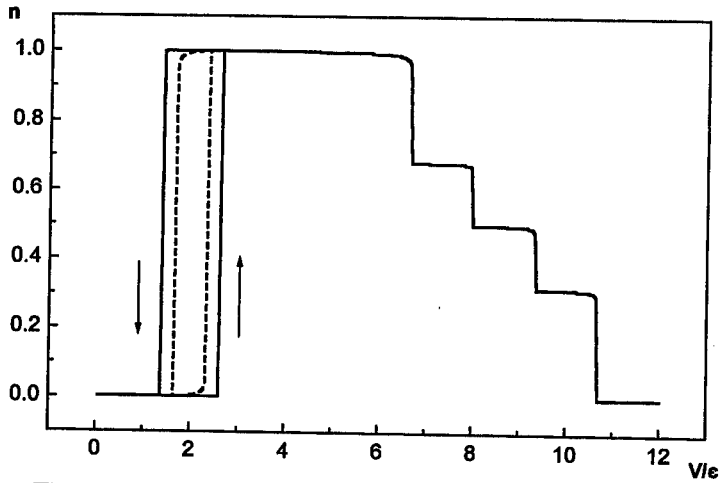


Figure3: Dependence of the population density n of the local state on applied voltage V for $U/\epsilon = -0.2$. Solid line is for $k_BT = 0.01$; dashed line is for $k_BT = 0.05$.

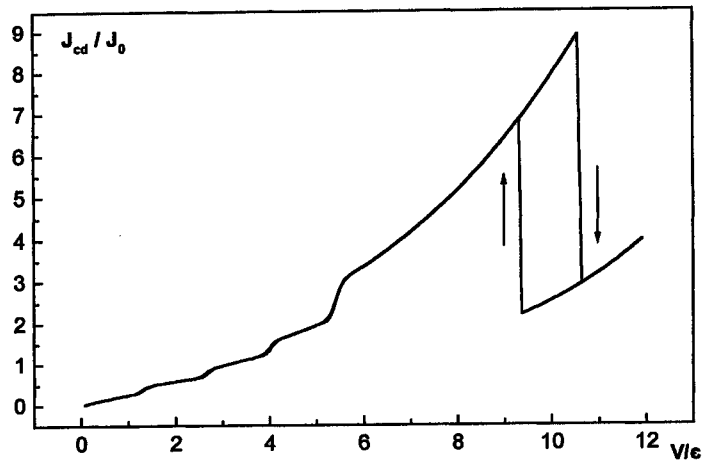


Figure4: Dependence of the tunneling current J_{cd}/ J_0, where $J_0 = e\mu\ 10^{-4} / h$, on the applied voltage V for $U/\epsilon = 0.2$.

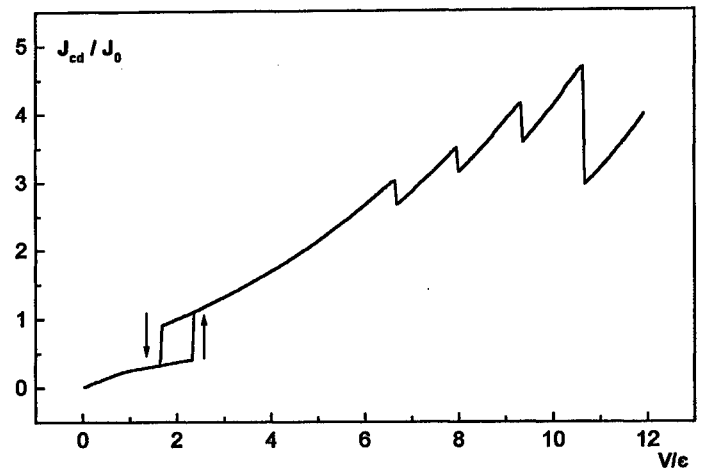


Figure 5: Dependence of the tunneling current J_{cd}/ J_0, where $J_0 = e\mu\ 10^{-4} / h$, on the applied voltage V for $U/\epsilon = - 0.2$.

The domains of current in the resonant tunneling diodes

M. N. Feiginov and V. A. Volkov
Institute of Radioengineering and Electronics of
Russian Academy of Sciences
11 Mokhovaya St., Moscow, 103907, Russia
E-mail: misha@mail.cplire.ru

Abstract

The resonant tunneling is accompanied by the accumulation of the 2D electrons in the well between the barriers of the double-barrier heterostructures. It leads to the I-V curve of Z-type in the high-quality structures. We have shown that it also leads to the instability of the 2D plasmons in the quantum well. The build up of the instability can give rise to the lateral static domains in the tunnel current, that in its turn results in the kinks in the region of the central arm of Z of the I-V curve.

1 Introduction

The double-barrier heterostructures (DBHS) has the I-V curves of N-type [1]. Approximately 10 years ago it has been predicted that the accumulation of the 2D electrons in the quantum well (QW) of the DBHS is to result in the transformation of the I-V curve of N-type to that of Z-type [2] - [6]. If one uses the ordinary experimental technique (say, the load line is close the vertical one), it is seen as hysteresis or bistability in the I-V curve. A new experimental technique has been proposed recently, where a negative load resistance is realized [7]. The technique allows one to measure the I-V curves of Z-type. An additional peak in the region of the central arm of Z was observed with the help of the technique [8]. The interpretation of the experimental results [7], [8] depends on the solution of the stability problem of the homogeneous (along the QW) distribution of the currents and charges in the DBHS with respect to the inhomogeneous perturbation in the Z-type region of the I-V curve. The first part of the paper is devoted to the solu-

tion of the problem. The problem is formulated in the terms of the 2D plasmons – low-frequency charge oscillations in the QW. From our point of view, the language is the most adequate to the problem at hand.

The second part of the paper is devoted to the the static nonlinear nonhomogeneous distribution of the tunnel current and charge density in the QW. It should be noted here, that the similar problem has been considered in [9]. The results depend in a complicated way on the parameters of the system. Unfortunately, the situation considered in [9] (very thin barriers and the external circuit being neglected) is not applicable to the experiments [7] and [8].

In the paper the properties of the 2D plasmons (screened by the high conducting emitter and collector) in the QW of DBHS are considered. The problem of the linear stability of the plasmons is solved. It is shown that the static nonlinear domain-like solutions for the tunnel current and charge in the QW are possible and it is demonstrated how they affect the I-V curve.

2 Basic equations.

We consider the DBHS in the sequential tunneling model [10]. The set of equations describing the time and spatial (x, y) distribution of the currents and potentials in the QW consists of the material equation (1), continuity equation (2), the equation (3) that follows from the Poisson equation in the local capacitance approximation, the equations for the emitter-well (J_{ew}) (4) and well-collector (J_{wc}) (5) tunnel currents, respectively:

$$\frac{\partial \mathbf{J}}{\partial t} + \nu \mathbf{J} = \frac{\sigma \nu}{e} \nabla E_{fw}, \tag{1}$$

$$-e\frac{\partial}{\partial t} N_{2D} + \nabla \mathbf{J} = J_{ew} - J_{wc}, \tag{2}$$

$$V - V_0 = \frac{e^2}{C} N_{2D} - (E^0_{fe} - E^0_{fc}) \frac{d}{L+d}, \tag{3}$$

$$J_{ew} = -\left[E_{fe} - E_{fw} - (E_{fe} - U_w)\,\theta(U_w - E_{fe})\right] \rho_{2D} \frac{e}{\tau_e} \tilde{\theta}(V), \tag{4}$$

$$J_{wc} = -N_{2D} \frac{e}{\tau_c}, \tag{5}$$

see the notations in Fig. 1. $\mathbf{J}(x,y)$ is the density of the 2D current in the QW; $V = U_w - U_e$. For simplicity we supposed that the bottom of the 2D subband in the QW is higher than the Fermi energy in the emitter, when the energy shift due to the external bias (V_{ext}) is equal to zero, $V = V_0$ in the case. ρ_{2D} is the 2D density

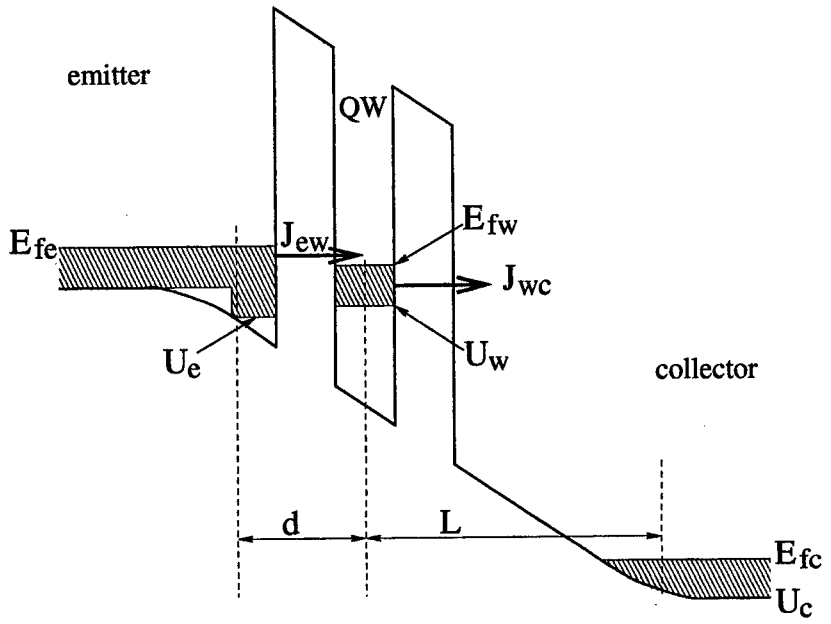


Figure 1: The energy diagram of the DBHS in the regime of the resonant tunneling.

of states in the QW, $N_{2D} = [E_{fw} - U_w]\rho_{2D}$ is the local 2D concentration of the electrons in the QW, τ_e and τ_c are the life times of electrons in the QW due to the tunneling to the emitter and collector, respectively. $C = \epsilon(L+d)/4\pi Ld$, $\nu = 1/\tau$ is the reciprocal momentum relaxation time in the QW, $\sigma = N_{2D}e^2/m^*\nu$ is the static 2D conductance of the QW. The form-factor $\tilde{\theta}(V)$ describes the broadening of the resonant levels. If the broadening is neglected, $\tilde{\theta}(V) = \theta(V)$, where $\theta(V)$ is the step function. One gets the known Z-type I-V curve from the set of Eqs. (1-5) if all the variables are supposed to be static and homogeneous (we use the superscript "0" for the solution).

3 Inhomogeneous linear solution.

Linearizing the Eqs. (1-5) in the vicinity of the homogeneous static solution, one gets [11] the set of equations describing the screened 2D plasmon in the QW. The dispersion Eq. of the 2D plasmons is:

$$(\omega + i\nu)(\omega + i\nu_T) = \frac{\sigma^0 \nu}{C}\left(1 + \frac{C}{e^2\rho_{2D}}\right) q^2, \tag{6}$$

$$\nu_T = \frac{1}{\tau_c} + \frac{\tilde{\theta}(V^0)}{\tau_e} + \frac{e^2\rho_{2D}}{C}\left[\frac{\tilde{\theta}(V^0)}{\tau_e} - \frac{[E_{fe} - U_e - V^0]}{1 + \tilde{\theta}(V^0)\tau_c/\tau_e}\frac{\tilde{\theta}'(V^0)}{\tau_e}\right], \tag{7}$$

here q is the 2D wavevector of the plasmons. The plasmons are unstable in time when $Im(\omega) > 0$. The analysis of the Eqs. (6) and (7) (see [11]) shows that the 2D plasmons are always unstable in the central arm of Z of the I-V curve if $q < q_0$ (when $-\nu < \nu_T < 0$ and the width, W, of DBHS is sufficiently large: $W > \pi/q_0$) and when q is arbitrary (if $-\nu_T > \nu$), see Fig.2; here

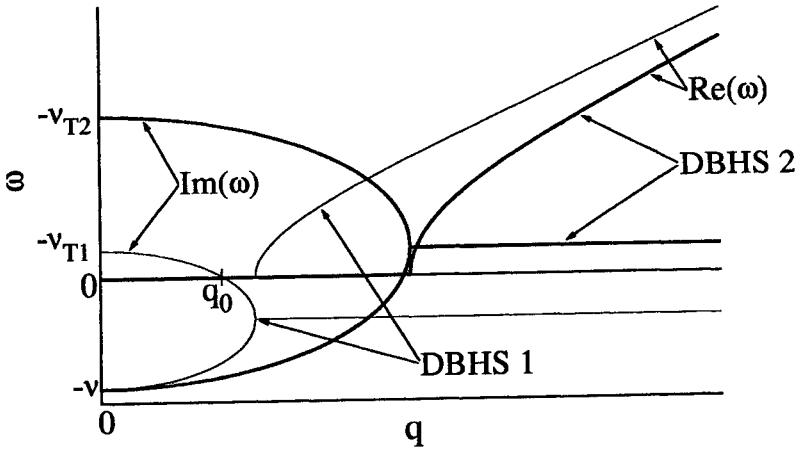


Figure 2: The complex frequency of the 2D screened plasmons as a function of the wave-vector q in the plane of the QW. The plasmons are unstable if $Im(\omega) > 0$. In the DBHS 1 $-\nu < \nu_T < 0$ and the 2D plasmons with $q < q_0$ are unstable only; in the DBHS 2 $-\nu_T > \nu$ and the plasmons with arbitrary q are unstable.

$$q_0 = \sqrt{-\frac{\nu_T C}{\sigma^0}\left(1 + \frac{C}{e^2\rho_{2D}}\right)^{-1}}. \tag{8}$$

The instability does not depend on the external circuit. For the parameters of DBHS taken from Refs. [7], [8] the length $\pi/q_0 \approx 150\ \mu m$.

4 Inhomogeneous nonlinear solution.

If $-\nu < \nu_T < 0$ the 2D plasmons build up without oscillations in time in the central arm of Z of the I-V curve. The increase in amplitude should be stopped by the nonlinear effects. The nonlinear static solutions follow from the set of Eqs. (1-5). They describe the domain-like distribution of the tunnel current and the 2D charge in the QW. For the illustration of the phenomenon we present here the calculation result of the inhomogeneous tunnel current distribution (see Fig.3) and the I-V curve (see Fig.4). The parameters of the DBHS where taken from the papers [7], [8]. Due to the appearance of the domain structure in the tunnel current, the kinks appear in the central arm of Z of the I-V curve (see Fig. 4) that qualitatively corresponds to the experimentally observed [8] features of the I-V curve of Z-type.

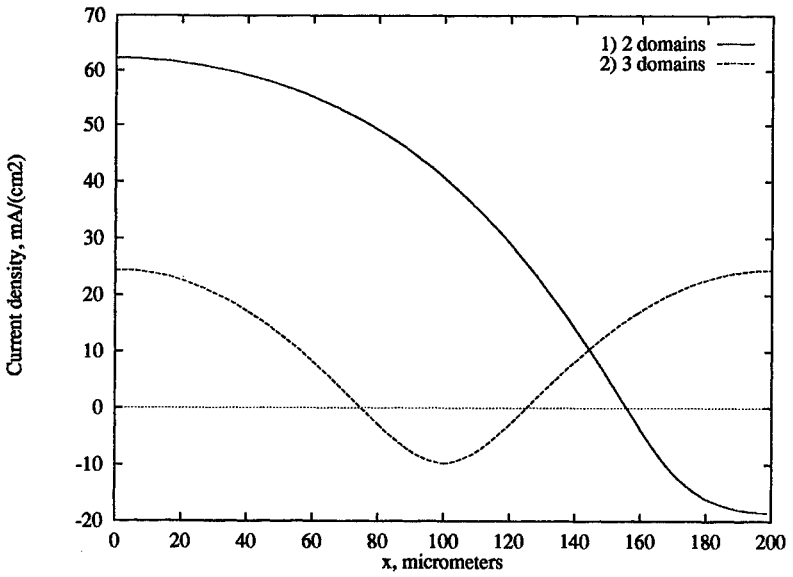


Figure 3: The deviation of the tunnel current from the homogeneous solution in the case of 2 domains (1) and 3 domains (2).

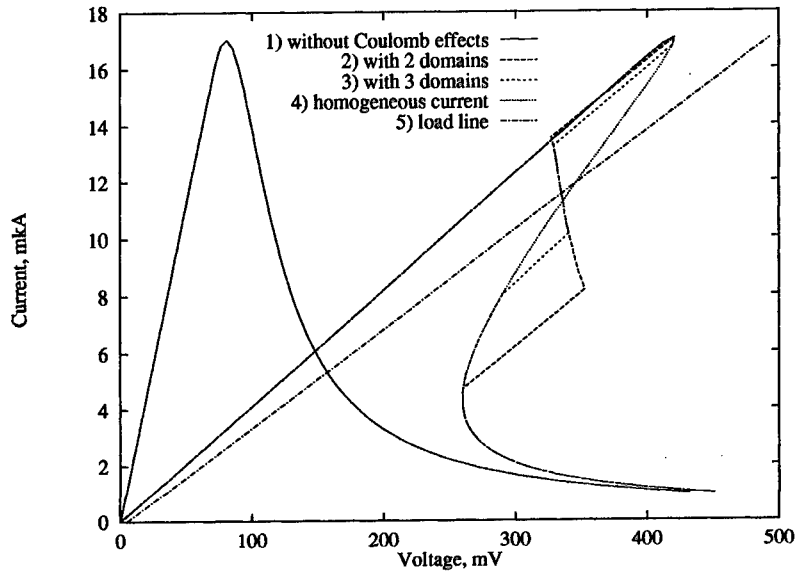


Figure 4: The I-V curves of the DBHS.

5 Conclusions.

We have shown that in the high quality DBHS with the I-V curve of Z-type, the 2D screened plasmons are unstable in the central arm of the Z in the following cases: 1) in the structures of any width (W) if $\nu_T < -\nu$; 2) in sufficiently wide structures ($W > \pi/q_0$) if $-\nu < \nu_T < 0$. The instability does not depend on the external circuit and the load resistance may be positive as well as negative. The build up of the instability can give rise to the static domains in the tunnel current, that in its turn results in the kinks in the Z-region of the I-V curve. The result is in a qualitative agreement with the experiment [8].

Acknowledgements

The work is partially supported by RFBR (96-02-18811), INTAS-RFBR (95-0849) and CRDF (RC1-220).

References

[1] H. Mizuta and T. Tanoue, "The physics and applications of resonant tunneling diodes". Cambridge University Press, 1995.

[2] F. W. Sheard and G. A. Toombs, Appl. Phys. Lett. **52**, 1228 (1988).

[3] V. J. Goldman, D. C. Tsui, and J. E. Cunningham, Phys. Rev. Lett. **58**, 1256 (1987).

[4] A. Zaslavsky, V. J. Goldman, D. C. Tsui, and J. E. Cunningham, Appl. Phys. Lett. **53**, 1408 (1988).

[5] R. K. Mains, J. P. Sun and G. I. Haddad, Appl. Phys. Lett. **55**, 371 (1988).

[6] H. L. Berkowitz and R. A. Lux, J. Vac. Sci. Technol., **B5**, 967 (1987).

[7] A. D. Martin *et al*, *Appl. Phys. Lett.* **64**, 1248 (1994).

[8] C. Zhang *et al*, *Phys. Rev. Lett.* **72**, 3397 (1994).

[9] B. A. Glavin, V. A. Kochelap and V. V. Mitin, Phys. Rev. B **56**, 13346 (1997).

[10] S. Luryi, Appl. Phys. Lett. **47**, 490 (1985).

[11] M. N. Feiginov and V. A. Volkov, *JETP Lett.* **68** (8), 633 (1998).

RADIOACTIVITY - INDUCED DEGRADATION OF Si PIN PHOTODETECTORS

Emmanuel A. Anagnostakis
The Laboratory of Physics , Hellenic Army Academy .
72 Cyprus Str. , GR 112 57 Athens , Greece .
Electronic Mail Address : emmanagn@otenet.gr

ABSTRACT

A study is undertaken concerning the performance degradation of Si PIN infrared photodetectors induced by α - particle bombardment . The performance degradation is traced against the experimental dependence of detection photocurrent upon incident infrared photonic flux with the α - particle cumulative exposure dose as a parameter . Furthermore , an experimental investigation is performed regarding the incident illumination wavelength selectivity in the photoconductive response of Si PIN photodiodes . The processing of the experimental results traces the differing detection yield for typical visible and infrared wavelength illumination , on the basis of the photocurrent versus photonic flux optoelectronic characteristics .

I. INTRODUCTION

The obvious technological importance of optoelectronic semiconductor photodetectors has been paid attention to by several researchers , as in [1 - 6] , examining in particular elemental and composite homostructures and heterostructures [7 - 12] .

Si PIN photodiodes , combining ease of fabrication with variety and effectiveness of application , belong to the extremely interesting of such microelectronic devices , as exemplified by their integration in fiber optic waveguide communication systems .

Unfavourable performance degradation is , on the other hand , known to result from exposure of semiconductor photodetectors to a particle irradiation environment , as is the obviously interesting case of optoelectronic devices carried by Space vehicles [4 - 6] . And yet , appropriate assessment of these functional consequences may allow for an alternative way of radioactivity sensing and counting in ecological and nuclear research .

The non-ionising energy loss of the incoming bombardment particle has been monitored for GaAs and Si structures as leading to displacement damage [13] .

Such lattice disruptions are believed to invoke deep level defect states modifying the electrical properties of the device active material and even onsetting relaxation - like and semi - insulating behaviour [14] .

In the present Paper , recent results are outlined concerning the performance degradation of Si PIN infrared photodetectors induced by α-particle bombardment. Furthermore , the present work addresses a frequently encountered yet not thoroughly resolved aspect of Si PIN photodiode optoelectronic performance : The detection yield underlying their photoconductive response to regulated incident photonic beams parametrised by the corpuscular photonic flux and illumination wavelength entailed .

II. EXPERIMENT

The experimental configuration comprises the infrared LASER beam emitter unit , an optical fiber waveguide , and the Si PIN photodetector part : Double heterojunction AlGaAs infrared LASER diodes emitting in the 0.78 μm band are launched into the front end of a 1 m long , 3 mm in diametre , single mode , Eska high performance plastic optical fiber connected at its rear end to commercially conventional , narrow receiving angle , linear response , fast switching time , Si PIN photodiodes exhibiting peak responsivity for incoming wavelengths between 0.75 and 1.00 μm .

Each double heterostructure AlGaAs infrared LASER diode is controlled through a special , high fidelity , current source sustaining up to 54 mA of injection current . The optical power at the output port of the Eska fiber waveguide is exactly measured at each LASER diode injection current level utilised by a Melles Griot , 4 digit , universal optical power metre bearing a 10 mm aperture Si detector head . These optical power P measurements along with the illuminated Si PIN photodiode area A lead to the respective energetic intensity $\Theta = P/A$ (μW/cm2) values , which - through the straightforward relation $\Theta = h\,(c/\lambda)\,\Phi$ - furnish the photonic flux Φ (photons / (cm2 s)) data , as witnessed by the Si PIN photodetectors , for the successive LASER diode injection current levels employed .

The optoelectronic response of the Si photodiodes , sensing the incident infrared beam, is - on the other hand - monitored at each experimental step in terms of the photocurrent I flowing through the detector . For the series of optoelectronic experiments reported here , performed at room temperature , the order of magnitude of the infrared photonic flux Φ impinging upon the tested Si PIN photodetectors ranges from 10E15 to 10E16 photons/(cm2 s) , whereas the resulting detection

photocurrent I permeating the Si photodiodes varies from , around , 2 to 70 μA .

For each Si PIN infrared photodetector studied , the optoelectronic response I-Φ curve is experimentally traced both prior to and after exposure to some decided cumulative radioactive α - particle dose Δ (α - particles/cm2) materialising through the bombarding of the photodetector at a constant α - particle flux (α - particles/(cm2 s)) for a predetermined time interval .

The radioactive α - particle source utilised for the experiments described here is of 241Am nuclide with a 2.87 mm face diametre and a mean emitted α - particle energy value of approximately 5 MeV . Care is taken that the 241Am source is properly situated in almost direct contact to each exposed Si PIN photodiode for the time period desired . The exact cumulative α - particle dose to which the photodetector has been , thus , exposed is evaluated by consideration of this time interval along with the accurate α - particle flux at the site of the exposed photodiode , measured by a Leybold Heraeus Geiger - Muller counter .

As for the Si PIN photodiode optoelectronic response to typical visible illumination , the same experimental configuration is utilised but with GaAsP LEDs producing a photonic beam with nominal wavelength of 650 nm as the light emitters . The visible photonic flux Φ impinging upon the tested photodiodes evolves from 0.72 x 10E15 to 1.72 x 10E15 photons / (cm2 s) , whilst the resulting detection photocurrent I increases from 2.7 to 8.2 μA . Each GaAsP LED employed is controlled through a current source allowing for injection currents up to 200 μA .

III. DETECTION YIELD

The exact definition of detection yield Y employed in this study refers to the number of photogenerated charge carriers per incident illumination photon and may be expressed as the ratio of the time rate of creation of flowing photocarriers (1/e)I (with e being the elementary electron charge and I the detection photocurrent responding to the illumination beam impinging upon the studied photodiode) over the time rate of incidence of illumination photons AΦ (with A being the exposed photodiode surface area and Φ the illuminating beam photonic flux (photons / (cm2 s))) :

$$Y = (1/e)\, I / (A\Phi) \; . \qquad (1)$$

On the other hand , the number (1/e)I of charge carriers photogenerated per unit time is given by that part of the number AΦ of illumination photons striking the exposed device per unit time which having escaped reflection at the illuminated surface (by a probability of (1-R) , R being the reflectivity of the exposed surface semiconductor at the specific illumination wavelength) inhabit mainly [15] the

photodiode depletion zone (by a cumulative occupation probability of [1 - exp(-αW)] - with α being the depletion zone material absorption coefficient for the specific illumination wavelength and W the depletion zone width valid for the value of reverse bias applied to the tested photodiode- , deriving as the difference between probability of photonic entrance into and probability of photonic exit from the depletion zone extension - under the assumption of shallow depletion region , materialising for the technologically conventional PIN photodiodes) and , furthermore , succeed (by a quantum efficiency of F corresponding to the specific illumination wavelength) in being absorbed within the depletion zone , ultimately energetically liberating initially bound (in the semiconductor valence band or at impurity or lattice defect trap levels) charge carriers :

$$(1/e)I = F [1 - \exp(-\alpha W)] (1-R) A\Phi \ . \qquad (2)$$

It is , then , obvious that the Si PIN photodiode detection yield Y , as defined by (1) , is expressible , by virtue of (2) , as

$$Y = F [1 - \exp(-\alpha W)] (1-R) \ , \qquad (3)$$

which describes the detection yield dependence upon chosen illumination wavelength λ (through the λ - related quantities F , α , and R) and applied reverse bias V (through the photodiode depletion region width W) .

The experimentally measured , now , conductivity current through the illuminated reverse biased photodiodes comprises the optoelectronic response photocurrent I and the dark saturation - recombination current (saturation of the dark reverse current having been reached at the sufficiently high reverse bias of 9 V applied) , both flowing in the reverse sense with respect to a forward biased diode dark conduction situation .

As , then , is well known [16 - 18] , the dark saturation - recombination current is at a given absolute photodiode ambient temperature determined by the dark depletion zone built - in voltage value and for the typical growth parameters of technologically conventional Si PIN photodiodes is always of the order of some tens or , at most , hundreds of a nA . Indeed , in the series of the experiments reported here the maximum value of dark saturation - recombination current for the 6 commercially typical photodetectors studied does not exceed 300 nA , which compared to the corresponding total conductivity current values (equal to several units or tens of a μA) under any illuminating photonic flux level utilised may be approximately ignored , thus rendering the directly measured overall conductivity current adequately approaching the net detection photocurrent I .

In Fig. 1 , plotted for a representative couple of GaAsP visible LED and commercially conventional encapsulated Si PIN photodiode , the photodetector optoelectronic response experimental characteristic of detection photocurrent I versus incident visible photonic flux Φ is shown : The visible photonic flux Φ impinging upon the tested photodiodes evolves from 0.72 x 10E15 to 1.72 x 10E15 photons / (cm2 s) , whilst the resulting detection photocurrent I increases from 2.7 to 8.2 μA .

Similarly , the photoconductive I-Φ characteristic of the previous representative Si PIN photodiode illuminated by means of one of the double heterojunction AlGaAs infrared LASER diodes is presented in Fig. 2 : Here , the incident infrared photonic flux Φ ranges from 1.25 x 10E15 to 8.75 x 10E15 photons / (cm2 s) , whereas the optoelectronic response photocurrent I varies from , around , 10 to about 70 μA .

A first processing of the experimental I-Φ characteristics of the tested Si PIN photodiodes furnishes the absolute values (in photogenerated flowing charge carriers per incident visible or infrared illumination photon) of the device detection yield Y , which in accordance with its notion and definition (1) may be obtained through the photodetector optoelectronic response curve slope ($\Delta I / \Delta \Phi$) as

$$Y = [1 / (eA)] (\Delta I / \Delta \Phi) , \qquad (4)$$

the slope ($\Delta I / \Delta \Phi$) having been calculated by a least squares fitting to the I-Φ characteristic .

Thus , given that the photodetector optoelectronic characteristic slope ($\Delta I / \Delta \Phi$) is computed against Fig. 1 and 2 to be equal to 5.5 μA / [10E15 photons / (cm2 s)] and 8.0 μA / [10E15 photons / (cm2 s)] for , respectively , visible and infrared illumination of the studied Si PIN photodiodes , the detection yield Y absolute value of 14 photogenerated flowing charge carriers per incident visible photon and 21 photogenerated flowing charge carriers per incident infrared photon is attained .

A second , straightforward , processing of the experiment leads to the determination of relative detection yield (Y / Y*) for comparing the photodiode photoconductive responsivity Y valid under visible at λ = 650 nm illumination to its optoelectronic gain Y* exhibited for infrared at λ = 780 nm illumination (taken as a reference) : (Y / Y*) = 2 / 3 .

Obviously , in this manner , a realistic calibration - in terms of (Y / Y*) versus λ - of any specific kind of Si PIN photodiode is achievable , against a prechosen reference (for instance , once more , its detection yield Y* under ifrared at λ = 780 nm illumination) for a technologically applicable spectrum of distinct illumination wavelengths λ .

Such a calibration plot might , then , serve - among other - the purpose of incident illumination wavelength recognition via , initially , experimental tracing of the calibrated Si PIN photodiode I-Φ characteristic and , consecutively , determination of its relative detection yield (Y / Y*) , with Y being the absolute value of the detection yield corresponding to the illumination wavelength λ under recognition .

IV. RADIOACTIVITY - INDUCED DEGRADATION

Detailed investigations during the experiments have reproducibly yielded an α - particle cumulative dose threshold of , around , 4.2 x 10E9 α - particles/cm2 for the 241Am , 5 MeV , α - particle beam used , necessary to be surpassed for clearly measurable radioactivity - induced performance degradation effects in the conventional encapsulated Si PIN photodetectors studied . This is to be compared to relevant findings referring to traceable particle irradiation - produced operation modifications in GaAs/AlGaAs quantum well infrared photodetectors [19] .

A systematic experimental correlation between magnitude of radioactivity - induced performance degradation and α - particle cumulative dose entailed for the exposed conventional encapsulated Si PIN infrared photodetectors being currently conducted , first evidence of the fundamental features of the radioactivity effect upon the Si photodiode optoelectronic functionality is here recorded :

As shown in Fig. 3 , plotted for a representative couple of double heterojunction AlGaAs infrared at nominally 0.78 μm LASER diode and commercially conventional encapsulated Si PIN infrared photodetector , the photodetector optoelectronic response I - Φ experimental curve exhibits the following major features of alteration after the photodiode exposure to a cumulative α - particle dose Δ of 3.9 x 10E10 α - particles/cm2 , well above the aforementioned threshold :

1. Overall attenuation of the detection photocurrent I for each photonic flux Φ impinging upon the photodetector illuminated area by a factor ranging , approximately, from 2 (for high photonic flux values) to 9 (for low photonic flux values) . The relative magnitude (4.5 - 5 : 1) of the detection photocurrent I after - exposure attenuation factors for low and high Φ values appears uniform for the specific different α - particle cumulative exposure dose Δ levels already employed , though -expectedly- their absolute values are connected with the respective radioactivity total dose level for each experimentally traced I - Φ curve .
2. Splitting of the single pre-exposure optoelectronic response linearity into two distinct consecutive after - exposure linearity regimes of different slope , stemming away from a clearly defined kink observed at an incoming photonic flux level of about 5 x 10E15 photons/(cm2 s) - in the middle of the employed photonic flux range . It is noteworthy that the high photonic flux after - exposure linearity regime extends with a slope essentially equal to the one marking the single pre-exposure I - Φ linearity , for any α - particle cumulative exposure dose Δ surpassing the relevant threshold and utilised in the experiments to - date .
3. Optoelectronic response stability , as manifested by the inverse of the relaxation time preceding the fully reliable reading of the successive detection photocurrent I values , degraded by almost a factor of 2 .

The above prime characteristics of the after - exposure optoelectronic performance of the tested Si PIN infrared photodetectors appear understandably consistent with the adequately established observation of other researchers that particle bombardment - invoked lattice displacement damage results in degradation of carrier mobility and lifetime , causing a decrease in optoelectronic device dark current and responsivity [20 , 21] .

V. CONCLUSIONS

In conclusion , first evidence of the character of α - particle bombardment - induced optoelectronic performance degradation of commercially conventional encapsulated Si PIN infrared photodetectors is obtained , conducive to reliable predictions for the devices functioning either in a Space application environment or as intended radioactivity sensors and counters .

Furthermore , the present work reports recent experimental studies of the detection yield of Si PIN photodiodes illuminated by typical visible and infrared wavelength photonic beams , on the basis of detection photocurrent I dependence upon evolving incident photonic flux Φ . The absolute value (in photogenerated flowing charge carriers per incident visible or infrared illumination photon) of the device detection yield Y is extracted , as well as the photodiode relative detection yield (Y / Y^*) for an illumination wavelength λ of interest with respect to its optoelectronic response to an established reference wavelength λ^* .

ACKNOWLEDGEMENT

The author is grateful to the Hellenic Army General D. Bakas for his , as Commandant's of the Hellenic Army Academy , inspiring strategic charisma and exceptional academic mentality , having produced a fruitful programmatic and functional upgrading of The Laboratory of Physics , advantageous for scheduling and fulfilling novel , Defence - oriented , optoelectronic experiments , partially conducted within the framework of collaboration between The Laboratory of Physics at the Hellenic Army Academy and **HO** , the Hellenic Centre for the Study of Optoelectronics . (**HO**'s Electronic Page visited at the WWW Site : http://users.otenet.gr/~emmanagn)

REFERENCES

[1] E. A. Anagnostakis , Appl. Phys. A **54** , 68 (1992) .
[2] E. A. Anagnostakis , Phys. Rev. B **46** , 7593 (1992) .
[3] E. A. Anagnostakis and D. E. Theodorou , J. Appl. Phys. **73** , 4550 (1993) .
[4] D. T. Wilhelm , R. K. Purvis , A. Singh , D. Z. Richardson , R. A. Jr. Hahn , J. R. Duffey , W. T. Roberts , and J. A. Ruffner , Proc. SPIE **2217** , 307 (1994) .
[5] D. V. Lang and L. C. Kimmerling , Inst. Phys. Conf. Ser. **23** , p 581 (1975) .
[6] D. Pons and J. C. Bourgoin , J. Phys. C : Solid State Phys. **18** , 3839 (1985) .
[7] D. C. Herbert , Semicond. Sci. Technol. **8** , 1993 (1993) .
[8] D. C. Herbert , Compel **11** , 413 (1992) .
[9] R. Van Overstraeten and H. De Man , Solid State Electron. **13** , 583 (1970) .
[10] P. H. Wilson , M. Lamm , H. C. Liu , Jianmeng Li , M. Buchanan , Z. R. Wasilewski , J. G. Simmons , and W. J. Schaff , Semicond. Sci. Technol. **8** , 2010 , (1993) .
[11] E. Rosencher , B. Vinter , and B. F. Levine (Editors) , *Intersubband Transitions in Quantum Wells* (Plenum , New York , 1992) .
[12] B. F. Levine , A. Zussman , S. D. Gunapala , M. T. Asom , J. M. Kuo , and W. S. Hobson , J. Appl. Phys. **72** , 4429 (1992) .
[13] G. P. Summers , E. A. Burke , P. Shapiro , S. R. Messenger , and R. J. Walters , IEEE Trans. Nucl. Sci. **40** , 1373 (1993) .
[14] M. McPherson , B. K. Jones , and T. Sloan , Semicond. Sci. Technol. **12** , 1187 (1997) .
[15] D. Wood, *Optoelectronic Semiconductor Devices* (Prentice Hall International Ltd. , London , 1994) , Chap. 6 .
[16] S. M. Sze , *Physics of Semiconductor Devices* (Wiley - Interscience Ltd. , New York , 1969) , Chap. 3 .
[17] E. A. Anagnostakis , Phys. Stat. Sol. A **127** , 153 (1991) .
[18] E. A. Anagnostakis , Phys. Stat. Sol. B **172** , K61 (1992) .
[19] L. Li , H. C. Liu , P. H. Wilson , M. Buchanan , and S. M. Khanna , Semicond. Sci. Technol. **12** , 947 (1997) .
[20] H. Gamlouch , M. Aubin , C. Carlone , and S. M. Khanna , J. Appl. Phys. **74** , 4357 (1993) .
[21] A. Jorio , M. Parenteau , M. Aubin , C. Carlone , S. M. Khanna , and J. W. Jr. Gerdes , IEEE Trans. Nucl. Sci. **41** , 1937 (1994) .

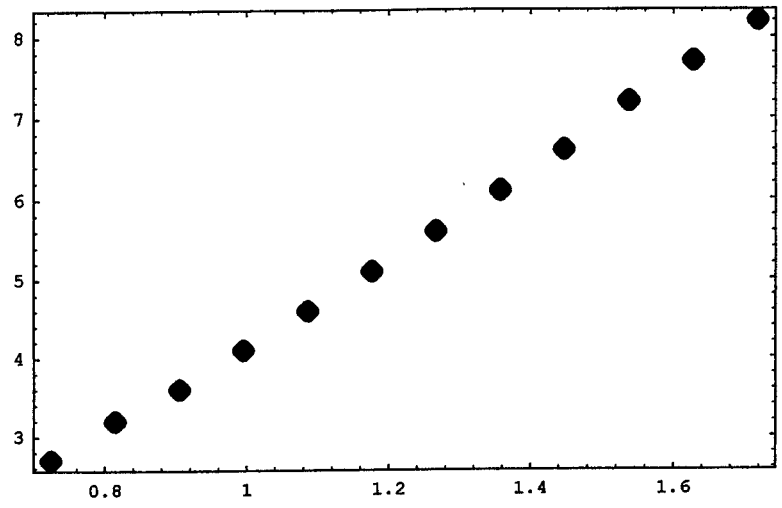


Fig.1 : Experimental characteristic of detection photocurrent I (μA) versus incident visible at λ = 650 nm photonic flux Φ (x 10E15 photons/(cm2 s)) for a representative commercially conventional encapsulated Si PIN photdiode .

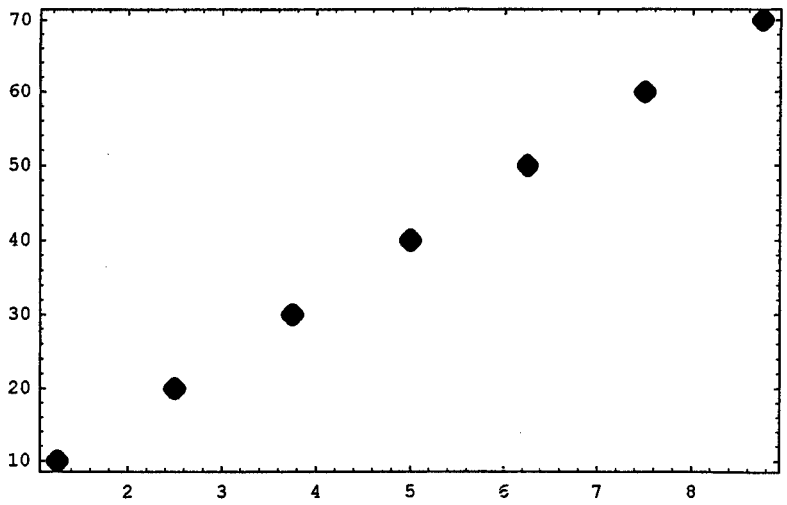


Fig.2 : Experimental characteristic of detection photocurrent I (μA) versus infrared at λ = 780 nm photonic flux Φ (x 10E15 photons/(cm2 s)) for the representative typical Si PIN photodiode .

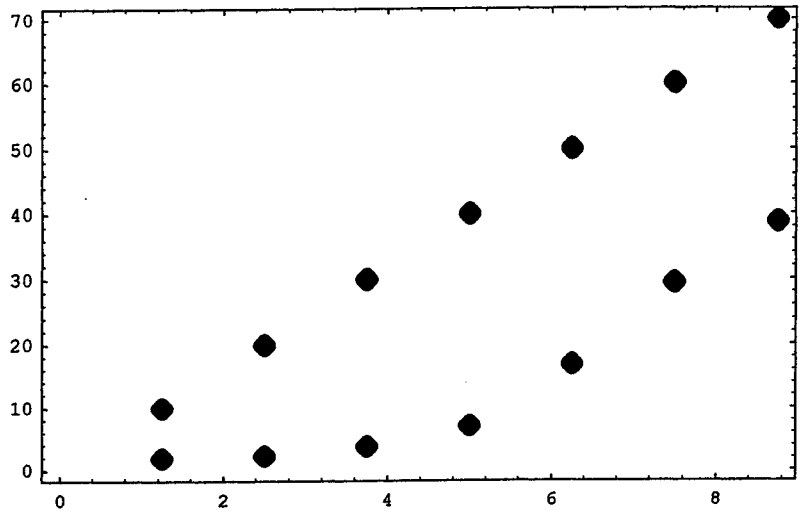


Fig.3 : Si PIN infrared photodetector optoelectronic response I - Φ representative experimental curves (I in μA , Φ in x10E15 photons/(cm2 s)) prior to (upper dots) and after (lower dots) the photodiode exposure to a cumulative α-particle dose of 3.9 x 10E10 α-particles / cm2 , well above the pertinent threshold .

AUTHOR INDEX

Akikusa, J., 410
Alferov, Zh.I., 320
Anagnostakis, E.A., 670
Andreev,A.D., 312
Aoki, M., 464
Averboukh, B., 118
Avrutin, E.A., 320
Aymerich, X., 27
Balandin, A., 371
Bandyopadhyay,S., 371, 618
Baribeau, J.M., 76
Bawendi, M.G., 280
Ben-Chorin, M., 118
Bhattacharyya, D., 320
Bimberg, D., 320
Black, C.T., 507
Bläsing, J., 94
Botti, S., 17
Boucaud, P., 357
Braginsky, L., 489
Broido, D., 227
Bryce, A.C., 320
Cahay, M.M., 597
Canham, L.T., 163
Chandrasekharan, N., 454
Chen, Y., 61
Cheong, H.D., 227
Coffer, J.L., 61
Datsiev, R.M., 312
Dennis, W.M., 430
Dneprovskii, V., 241
Dzyubenko, A.B., 227
Efros, Al.L., 177
Ekbote, S., 597
Empedocles, S.A., 280
Erickson, L.E., 141
Ermakov, V.N., 650
Fafard, S., 348
Fauchet, P.M., 76,94
Feiginov, M.N., 663
Feng, Y., 270
Feng, S.L., 318
Feofilov, S.P., 430
Fountain, T., 582
Forsberg, E., 529
Fujishima, A., 402
Fujita, S., 629
Garcia, J., 213
Garriga, M., 27
Gerard, J.-M., 357
Glotin, F., 357
Glozman, A., 381
Gorer, S., 454
Gould, C., 270
Gray, J.M., 320
Grom, G.F., 76
Guo, H., 640
Haginoya, C., 335
Hamilton, B., 163
Hashimoto, K., 402
Hawrylak, P., 270
Heckler, H., 118, 128
Heintichsdorff, F., 320
Henderson, D.O., 106,439
Herold, G.S., 227
Hirschman, K.D., 94
Hodes, G., 454
Ishibashi, M., 335
Ishii, K., 49
Ivanov, S.V., 312
Iyoda, T., 402
Jacobs, J., 163
Jiang, D.S., 318
Jiang, L., 402
Jin, F., 297
Kahn, S.U.M., 410
Kenyon, A.J., 17
Khurgin, J.B., 297
Kikuchi, R., 475
Kim, Y., 402
Kioseoglou, G., 227
Kitazawa, K., 402

Kiyama, K., 151
Koch, F., 118, 128
Koike, K., 335
Kouklin, N., 371
Kovalev, D., 118, 128
Kumar, A., 507
Kunze, U., 213
Labbe, H.J., 76
Leburton, J.P., 542
Ledentsov, N.N., 320
Lemaitre, A., 357
Leon, R., 286
Li, J., 402
Lifshitz, E., 381
Lockwood, D.J., 76, 141
Maeda, T., 49
Malone, K., 439
Marsh, J.H., 320
Martin, F., 27
Martinez, X., 27
Masuda-Jindo, K., 464,475
Masumoto, Y., 241
McCaffrey, J.P., 76
McCombe, B.D., 227
Medeiros-Ribeiro, G., 213
Meijerink, A., 392
Meldrum, A., 106
Meltzer, R.S., 430
Menon, L., 371
Menon, M., 464
Meulenkamp, E.A., 392
Mills, G., 439
Morris, D., 286,348
Mu, R., 106,439
Mulyarov, E., 241
Neuhauser, R., 280
Nickel, H.A., 227
Okumura, T., 151
Onishchenko, A.I., 320
O'Reilly, E.P., 320
Ortega, J.M., 357
Palm, T., 529
Perret, N., 286
Petroff, P.M., 213
Petrou, A., 227
Pinizzotto, R.F., 61
Pitt, C.W., 17
Polisski, G., 128
Pomorski, P., 563
Poteanu, H-.E., 381
Prazeres, R., 357
Rana, F., 507
Ravaioli, U., 551
Rendell, R.W., 574
Roenker, K.P., 597
Rosen, M., 177
Sachradja, A.S., 270
Sakata, I., 49
Sato, H., 40
Sauvage, S., 357
Schmidt, K.H., 213
Schmuki, P., 141
Seisyan, R.P., 312
Shibata, K., 40
Shimizu, K., 280
Shimura, M., 151
Shklover, V., 489
Sivachenko, A.Yu., 227
Spagocci, S., 582
Sproule, G.I., 76
St John, J.V., 61
Stroscio, M. A., 618
Subbaswamy, K.R., 464
Sugimura, A., 40
Sugiyama, N., 629
Sun, B.Q., 318
Suzuki, E., 49
Svizhenko, A, 618
Takagahara, T., 192
Taylor, J., 640
Teehan, D., 163
Tereshin, S., 371

Thean, A., 542
Thierry-Mieg, V., 357
Thylen, L., 529
Tikodeev, S., 241
Tissue, B.M., 430
Tiwari, S., 507
Trellakis, A., 551
Trwoga, P.F., 17
Tsu, R., 3
Tsybeskov, L., 76,94
Ueda, A., 106,439
Umezu, I., 40
Ustinov, V.M., 320
Van Dijken, A., 392
Vanmaekelberg, D., 392
Varfolomeev, A., 371
Veit, P., 94
Vizoso, J., 27
Volkov, V.A., 663
Wang, J., 640
Wang, Z.M., 318
Wasilewski, Z., 270
Wessler, J.J, 507
Wesström, J.-O.J., 529
White, C.W., 106
Wu, M.H., 106,439
Yamada, Y., 40
Yamaguchi, S., 40
Yamanaka, M., 49
Yang, H.-S., 430
Yeo, T., 227
Yoshida, T., 40
Zacharias, M., 94
Zaitsev, S.V., 320
Zaretsky, D., 371
Zawadzki, P., 270
Zheng, H. Z., 318
Zhu, H., 318
Zhukov, E., 241
Zinov'ev, N. N., 128
Zuhr, A., 106
Zunger, A., 259

SUBJECT INDEX

Al_{13} cluster, 640
alcoholic OH groups, 151
α-particle bombardement, 670
amorphous Silicon, 76,629
anodic alumina, 335
anodic oxydation, 151
atomic cluster, 640
atomic force microscopy, 402
Au nanocrsytals, 439
Auger processes, 348
Auger recombination, 318
Auger scattering, 286
bistability, 371,663
capacitance spectroscopy, 213
C_{60} single crystals, 402
carrier capture, 286
carrier recombination, 286
carrier relaxation, 286
$CdSe$ nanocrystals, 454
$CdSe$ quantum dots, 280,312
chemical vapor deposition, 49
colloidal suspension, 392
colloidal synthesis, 280
control gate, 542
control phase diagram, 574
Coulomb blockade, 259
Coulomb energy, 259,270
Coulomb interaction, 241
$CuCl$ nanocrystals, 192
Curie temperature, 297
density functional theory, 640
dielectric matrix, 241
electro-chemical capacitance, 640
electroluminescence, 629
electron charging effect, 49
electron-electron interaction, 650
electron-hole pairs, 118,213
electron-phonon interaction, 650
electron waveguide, 529
epitaxial Si/O superlattice, 3
Erbium-doped Si nanocrystals, 61
exchange energy, 259,270
exciton, 241
exciton band excitation, 402
exciton binding energy, 312
exciton confinement, 128
exciton dephasing, 192
excitonic optical nonlinearity, 192
excitonic spectrum, 259
Far IR laser, 529
fault rate, 582
fault tolerance, 582
ferro-magnetic properties, 297
ferro-electric properties, 297
few electron lateral dots, 270
floating gate flash memory, 542
focused ion beam, 141
free-carrier absorption, 17
furnace annealing, 94
Green function, 11
growth rate, 28
high resolution electron
microscopy, 61
hole burning, 118
hole spin, 177
Huang-Rhys Theory, 192
$InAs/GaAs$ self-assembled
quantum dots, 357
InAs nanocrystals, 177
InAs-quantum dots, 213, 318
incubation time, 27
interdiffusion, 287
interface disorder, 475
interface light absorption, 489
intermixing, 287
intraband absorption, 357
intradot relaxation time, 357
Johnson noise, 618
laser pyrolysis, 17
lateral static domains, 663
light emitting diode, 629
light-emitting Si, 61

Luttinger-Kohn Hamiltonian, 597
magneto-capacitance, 563
magneto-exciton, 227
magneto-exciton Hamiltonian, 227
magnetospectroscopy, 128
mesoscopic capacitor, 563
misfit dislocation, 475
mode grouping, 320
modulation bandwidth, 529
MOS structure, 551
Mott-Schottky plot, 410
mulitphonon processes, 286
multiphonon scattering, 348
nanochip, 582
nanocrystal, 28,177
nanocrystalline ZnO particles, 392
nanocrystalline Si, 94
nanocrystalline Si/SiO_2 SLs, 3
nanocrystallites, 40
nanoparticle thin films, 163
nanostructures, 28,489
n-Fe_2O_3 thin film electrodes, 410
nonlinear absorption, 241
nonlinear resonant tunneling, 650
nonradiative Auger process, 118
optically detected resonance spectroscopy, 227
percolation clusters, 163
phonon bottleneck, 529
photocarrier lifetime, 17
photocurrent, 213,410,670
photocurrent spectroscopy, 213
photoelectrochemical response, 454
photo-induced nanopatterns, 402
photoluminescence, 40,106,392
photoluminescence spectroscopy, 213
photon echo method, 192
photoreduction, 439
Pidgeon and Brown model, 177
Poisson equation, 542,551
polysterene sphere, 335
polywrapped gate, 542
pore formation potential, 141
porous silicon, 128,141,151,163
porous Vycor Glass, 439
potential step, 597
pulsed laser ablation, 40
pulsed laser irradiation, 439
quantum cellular automata, 582
quantum confinement, 8
quantum dot, 28,177,192,348,371,454
quantum dot laser, 320
quantum molecular dynamics, 640
quantum wire, 241,529,551,618
radioactivity-induced degradation, 670
ramp-up furnace annealing, 76
rapid thermal annealing, 94
rapid thermal oxidation, 49
rare earth ions, 61
reactive ion etching, 335
recombination, 40
red photoluminescence, 151
relaxation oscillations, 320
relaxation time, 348
resonant tunneling diode, 663
RTCVD, 27
Schottky barrier breakdown, 141
Schroedinger equation, 357,542,551
self-assembled quantum dots, 213,259,287,348,371
self-assembly, 335
self-organization, 76
semiconductor-atomic-superlattice, 4
semiconductor cluster, 464,475
Si dot, 28
Si light emitter, 3
Si nanoclusters,
Si nanocrystals, 49,61,106,118,629
Si nonapowder, 17
Si PIN photodetectors, 670
Si quantum-dot, 542
single-electron charging, 542

single electron device, 582
single electron circuits, 574
Si/SiO_2 superlattices, 3,94
spin-orbit split-off band, 597
spray-pyrolytic method, 410
Stark effect, 280
Stark spectroscopy, 280
Stern-Volmer relation, 151
strained quantum dot, 297
surface reconstruction, 402
TEM imaging, 454
thermal annealing, 286
thermal budget, 28
thermal crystallization, 94
threshold current density, 320,529
threshold voltage shift, 542
time resolved photoluminescence, 287,348
triple modular redundancy, 582
T-shaped gate, 551
ultrathin gate oxide, 49
water-splitting reaction, 410
$Y_2O_3 : Eu^{3+}$ nanocrystals, 430
Zeeman splitting, 128